Controlled Self-Assembly of Cage-like Structures and their Applications in Fullerene Chemistry

Thesis for receiving the degree of “Doctor rerum naturalium” in chemistry

TU Dortmund

Fakultät für Chemie und Chemische Biologie

technische universität dortmund

Bin Chen

from Jiangsu, China

May, 2019

Seek the truth from facts.

Principal advisor:	Prof. Dr. Guido Clever
Secondary surveyor:	JProf. Dr. Sebastian Henke
Filed on:	May 29th, 2019

Eidesstattliche Versicherung (Affidavit)

Name, Vorname
(Surname, first name)

Matrikel-Nr.
(Enrolment number)

Belehrung:
Wer vorsätzlich gegen eine die Täuschung über Prü- fungsleistungen betreffende Reg(Surname, first name)(Enrolment number)elung einer Hochschul-prüfungsordnung verstößt, handelt ordnungswidrig. Die Ordnungswidrigkeit kann mit einer Geldbuße von bis zu 50.000,00 € geahndet werden. Zuständige Verwaltungs- behörde für die Verfolgung und Ahndung von Ordnungs- widrigkeiten ist der Kanzler/die Kanzlerin der Techni- schen Universität Dortmund. Im Falle eines mehrfachen oder sonstigen schwerwiegenden Täuschungsversu- ches kann der Prüfling zudem exmatrikuliert werden, § 63 Abs. 5 Hochschulgesetz NRW.
Die Abgabe einer falschen Versicherung an Eides statt ist strafbar.
Wer vorsätzlich eine falsche Versicherung an Eides statt abgibt, kann mit einer Freiheitsstrafe bis zu drei Jahren oder mit Geldstrafe bestraft werden, § 156 StGB. Die fahrlässige Abgabe einer falschen Versicherung an Eides statt kann mit einer Freiheitsstrafe bis zu einem Jahr oder Geldstrafe bestraft werden, § 161 StGB.
Die oben stehende Belehrung habe ich zur Kenntnis genommen:

Official notification:
Any person who intentionally breaches any regulation of university examination regulations relating to deception in examination performance is acting improperly. This offence can be punished with a fine of up to EUR 50,000.00. The competent administrative authority for the pursuit and prosecution of offences of this type is the chancellor of the TU Dortmund University. In the case of multiple or other serious attempts at deception, the candidate can also be unenrolled, Section 63, paragraph 5 of the Universities Act of North Rhine-Westphalia.

The submission of a false affidavit is punishable.
Any person who intentionally submits a false affidavit can be punished with a prison sentence of up to three years or a fine, Section 156 of the Criminal Code. The negligent submission of a false affidavit can be punished with a prison sentence of up to one year or a fine, Section 161 of the Criminal Code.

I have taken note of the above official notification.

Ort, Datum
(Place, date)

Unterschrift
(Signature)

Titel der Dissertation:
(Title of the thesis):

Ich versichere hiermit an Eides statt, dass ich die vorliegende Dissertation mit dem Titel selbstständig und ohne unzulässige fremde Hilfe angefertigt habe. Ich habe keine anderen als die angegebenen Quellen und Hilfsmittel benutzt sowie wörtliche und sinngemäße Zitate kenntlich gemacht.
Die Arbeit hat in gegenwärtiger oder in einer anderen Fassung weder der TU Dortmund noch einer anderen Hochschule im Zusammenhang mit einer staatlichen oder akademischen Prüfung vorgelegen.

I hereby swear that I have completed the present dissertation independently and without inadmissible external support. I have not used any sources or tools other than those indicated and have identified literal and analogous quotations.
The thesis in its current version or another version has not been presented to the TU Dortmund University or another university in connection with a state or academic examination.*

*Please be aware that solely the German version of the affidavit ("Eidesstattliche Versicherung") for the PhD thesis is the official and legally binding version.

Ort, Datum
(Place, date)

Unterschrift
(Signature)

Abstract

The coordination-driven self-assembly of discrete nanostructures has resulted in numerous amazing architectures such as molecular rings, cages and capsules over the last few decades. On the basis of rational design, the combination of banana-shaped bis-monodentate ligands and the square-planar coordination geometry of metal ions (e.g. Pd^{II}) has proven to be a reliable strategy for the self-assembly of discrete structures. Moreover, hosts assembled from extended aromatic panels and metal ions can encapsulate a variety of neutral guest molecules, including fullerenes and their derivatives. Work with these compounds, known as electroactive materials, is currently limited due to tedious and expensive methodologies for their purification.

This thesis entitled "Controlled Self-Assembly of Cage-like Structures and their Applications in Fullerene Chemistry" focuses on the donor-site-controlled self-assembly of supramolecules as well as their distinct fullerene binding abilities. In Chapter 3, Pd^{II}-mediated assemblies ranging from monomeric cage $[Pd_2L_4]^{4+}$ to bowl-like structure $[Pd_2L_3(MeCN)_2]^{4+}$ and ring $[Pd_2L_2(MeCN)_4]^{4+}$, are described to be realized by means of steric effects of terminal coordination groups, i.e. pyridine, quinoline and acridine. The employment of a precisely designed backbone, which shows shape complementarity for the convex surface of fullerenes, endows these assembled nanostructures with binding abilities towards fullerenes (C_{60} and C_{70}). The in-depth studies deduced from crystal structures of these supramolecular assemblies, reveal different binding behaviors owing to their structural flexibility. Afterwards, applications of the assembled cage and bowl in fullerene chemistry are introduced in Chapter 4. Cage $[Pd_2\mathbf{L^1}_4]^{4+}$, able to selectively bind C_{60} from fullerene soot, allows solubilization of fullerenes in acetonitrile, acetone, nitromethane and DMF, and develops into a recyclable system of C_{60} purification controlled by solvent effects. The novel bowl structure is not only found to serve as a supramolecular protecting group, which allows selective mono-functionalization of its guest, but is also capable of being connected by a second ligand to hierarchically assemble into a molecular capsule which can accommodate two fullerene molecules within its inner cavity. In addition, self-assembly of heteroleptic cages with advanced complexity and functionalities has gained increasing attention in recent years. Another non-traditional nitrogen donor, namely naphthyridine, was shown to manifest a dislocated arrangement in the Pd^{II} coordination sphere owing to the repulsive effect between adjacent electron-pairs. A synergy between quinoline donors and naphthyridine donors as well as template effect of guests was further exploited to generate heteroleptic cages. At last, a newly designed fullerene-based ligand $\mathbf{L^6}$ can assemble with Pd^{II} into a coordination cage bearing four fullerene molecules in the periphery, whose diameter is about 3 nm.

In summary, this thesis showcases the donor-site engineering in Pd^{II}-mediated coordination complexes, yielding distinctive supramolecular architectures, including the molecular cage, bowl, ring and capsule. These assemblies have practical application in fullerene chemistry, involving selective binding, purification and derivatization. The exploration of promising fullerene receptors contributes to addressing urgent problems in fullerene chemistry. All compounds have been fully characterized by multiple analytic techniques, such as NMR spectroscopy, mass spectrometry and single crystal X-ray structural analysis.

Zusammenfassung

Die koordinationsgesteuerte Selbstassemblierung diskreter Nanostrukturen führte in den letzten Jahrzehnten zu zahlreichen Architekturen wie molekularen Ringen, Käfigen oder Kapseln. Basierend auf rationalem Design zeigte sich die Kombination von bananenförmigen doppelt-einzähnigen Liganden und der quadratisch-planaren Koordinationsgeometrie von Metallionen (z.B. Pd^{II}) als verlässliche Strategie für die Selbstassemblierung diskreter Strukturen. Außerdem können Wirtsverbindungen, die aus ausgedehnten aromatischen Flächen und Metallionen zusammengesetzt sind, eine Vielzahl neutraler Gastmoleküle aufnehmen, darunter Fullerene und deren Derivate. Die Anwendung dieser Verbindungen, als elektroaktive Materialien bekannt, ist zurzeit noch aufgrund der mühsamen und teuren Aufreinigungsmethoden eingeschränkt.

Diese Arbeit mit dem Titel „Kontrollierte Selbstassemblierung von käfigartigen Strukturen und deren Anwendungen in der Fullerenchemie" setzt den Schwerpunkt auf Donorregion-kontrollierte Selbstassemblierung von Supramolekülen sowie auf deren Fähigkeit, Fullerene zu binden. In Kapitel 3 werden Pd^{II}-vermittelte Strukturen, anfangend bei Käfigen $[Pd_2L_4]^{4+}$ über schalenähnliche Gebilde $[Pd_2L_3(MeCN)_2]^{4+}$ bis zu Ringen $[Pd_2L_2(MeCN)_4]^{4+}$, beschrieben, die durch sterische Effekte der terminalen koordinierenden Gruppe, z.B. Pyridin, Chinolin und Acridin, erhalten werden. Die Verwendung eines präzise designten Rückgrats, das eine komplementäre Oberflächenwölbung zu Fullerenen aufzeigt, verleiht diesen Nanostrukturen die Fähigkeit zur Bindung von Fullerenen (C_{60} und C_{70}). Tiefgehende Untersuchungen, abgeleitet von Kristallstrukturen dieser supramolekularen Gebilde zeigen verschiedene Bindungseigenschaften aufgrund ihrer strukturellen Flexibilität. Anschließend werden in Kapitel 4 Anwendungen der assemblierten Käfige und Schalen in der Fullerenchemie vorgestellt. Der Käfig $[Pd_2\mathbf{L^1}_4]^{4+}$, der selektiv C_{60} aus einer Fullerenrohmischung binden kann, macht es möglich, Fullerene in Acetonitril, Aceton, Nitromethan und DMF zu lösen und erlaubt ein recycelbares System zur Aufreinigung von C_{60}, kontrolliert durch Lösungsmitteleffekte. Die neuartige Schalenstruktur stellt nicht nur eine supramolekulare Schutzgruppe dar, die eine selektive Monofunktionalisierung gebundener Gäste erlaubt, sondern sie kann auch über einen zweiten Liganden in einer hierarchischen Anordnung zu einer molekularen Kapsel verbunden werden, die zwei Fullerenmoleküle in ihrer inneren Kavität aufnehmen kann. Des Weiteren hat die Selbstassemblierung heteroleptischer Käfige mit fortschreitender Komplexität und Funktionalität in den letzten Jahren gesteigerte Aufmerksamkeit erlangt. Es wurde gezeigt, dass Naphthyridin, ein anderer unüblicher Stickstoffdonor, eine verdrehte Anordnung in der Pd^{II} Koordinationsumgebung aufweist, die mit abstoßenden Effekten zwischen benachbarten Elektronenpaaren zu begründen ist. Das Zusammenwirken zwischen Chinolin- und Naphthyridindonoren sowie der Templateffekt von Gästen wurde ausgenutzt, um heteroleptische Käfige zu bilden. Zum Schluss konnte sich ein neu designter Ligand $\mathbf{L^6}$ mit Pd^{II} zu einem Koordinationskäfig zusammenschließen, der vier Fullerenmoleküle in der Peripherie trägt und einen Durchmesser von circa 3 nm aufweist.

Zusammenfassend demonstriert diese Arbeit die Manipulation der Donorregion von Pd^{II}-vermittelten Koordinationskomplexen, die zu supramolekularen Architekturen wie molekularen Käfigen, Schalen, Ringen und Kapseln führt. Diese Assemblierungen finden praktische Anwendung in der Fullerenchemie, darunter selektive Bindung, Aufreinigung und Derivatisierung. Die Untersuchung vielversprechender Fullerenrezeptoren trägt dazu bei, die drängenden Probleme in der Fullerenchemie anzugehen. Alle Verbindungen wurden vollständig durch analytische Methoden wie NMR-Spektroskopie, Massenspektrometrie und Röntgenkristallstrukturanalyse charakterisiert.

List of Publications and Conference Contributions

Publications

1. "Pd(II) coordination sphere engineering: pyridine cages, quinoline bowls and heteroleptic pills binding one or two fullerenes"

B. Chen, J. J. Holstein, S. Horiuchi, W. G. Hiller, G. H. Clever, *J. Am. Chem. Soc.* **2019,** *141,* 8907.

2. "Dinuclear ruthenium complex based on a π-extended bridging ligand with redox-active tetrathiafulvalene and 1,10-phenanthroline units"

B. Chen, Z. P. Lv, C. Hua, C. F. Leong, F. Tuna, D. M. D'Alessandro, D. Collison, J. L. Zuo, *Inorg. Chem.* **2016,** *55,* 4606.

3. "Crystal structures, gas adsorption, and electrochemical properties of electroactive coordination polymers based on the tetrathiafulvalene-tetrabenzoate ligand"

B. Chen, Z. P. Lv, C. F. Leong, Y. Zhao, D. M. D'Alessandro, J. L. Zuo, *Cryst. Growth Des.* **2015,** *15,* 1861.

4. "Charge-transfer supra-amphiphiles built by water-soluble tetrathiafulvalenes and viologen-containing amphiphiles: supramolecular nanoassemblies with modifiable dimensions"

Z. P. Lv, B. Chen, H. Y. Wang, Y. Wu, J. L. Zuo, *Small* **2015,** *11,* 3597.

5. "Four coordination clusters using fluorenyl and carbazyl phosphonates as ligands"

Y. S. Ma, W. S. Cai, B. Chen, J. Y. Chang, X. Y. Tang, R. X. Yuan, *CrystEngComm* **2013,** *15,* 7615.

Manuscripts in preparation

6. "Steric ligand tuning yields cage-, bowl- and ring-shaped metallosupramolecules with differential fullerene affinities"

B. Chen, S. Horiuchi, J. J. Holstein, J. P. Dürholtand, K. Stracke, R. Schmid, G. H. Clever.

7. "Synergetic interactions of electronic complementarity donors in self-assembly of heteroleptic cages"

B. Chen, J. J. Holstein, A. Platzek, L. Schneider, G. H. Clever.

Conference contributions

1. Poster, The 14th International Symposium on Macrocyclic and Supramolecular Chemistry (ISMSC), **2019**, Lecce, Italy (IUPAC Poster Prize)

2. Poster, The 4th Erlangen Symposium on Synthetic Carbon Allotropes, **2017**, Erlangen, Germany

3. Poster, The 12th International Symposium on Macrocyclic and Supramolecular Chemistry (ISMSC), **2017**, Cambridge, UK

Acknowledgements

First of all, I want to thank my supervisor Prof. Dr. Guido Clever for giving me the opportunity to conduct my PhD study in his lab, equipped with a lot of advanced instruments. I sincerely appreciate all his contributions of time, ideas and guidance in my research projects during the last three and a half years. I am very grateful for all his understanding and endless support, especially during my tough times. He is the most easy-going and creative professor I have met so far. I am also thankful to JProf. Dr. Sebastian Henke for being part of the examination committee.

I would like to thank China Scholarship Council as well as European Research Council for financial support, allowing me to have this opportunity to study in Germany.

Special thanks goes to Dr. Julian Holstein for his guidance in the X-ray structure determination, and Dr. Shinnosuke Horiuchi for his help in the publication of crystal data. I would like to thank Prof. Dr. Wolf Hiller and André Platzek for their support in NMR measurement, Laura Schneider, Christiane Heitbrink and Dr. David Engelhard for measuring ESI mass spectra. I would like to thank Dr. Mark Johnstone, Dr. Thorben Schulte and Marcel Krick for helping me solve software problems. Meanwhile, I would like to thank our cooperation partners Prof. Dr. Rochus Schmid and Prof. Dr. Max von Delius as well as the related students for their contributions in terms of theoretical calculation and the supply of a fullerene compound.

I would like to thank all current and former members of the Clever-lab for creating such an enjoyable working atmosphere and organizing social activities with a lot of fun. I really enjoyed the last three years with these friendly and helpful colleagues. Special thanks goes to Dr. Gabriele Trötscher-Kaus, Birgit Thormann and Kristian Surich for all their help over the last three years. Huge thanks to Dr. Subhadeep Saha, Dr. Jacopo Tessarolo, Dr. Susanne Löffler, Dr. Sudhakar Ganta, Irene Regeni, Lukas Stratmann, André Platzek for the proof reading of this thesis. In addition, I would like to thank Dr. Susanne Löffler, Dr. Rongmei Zhu, Kristina Ebbert, Dr. Sonja Pullen, Irene Regeni for sharing the girls' office with me for three years and Dr. Sudhakar Ganta for sharing a desk with me in the last several months. Likewise, thanks to Dr. Witold Bloch, Dr. Mark Johnstone, Dr. Rongmei Zhu, Kristina Ebbert, Dr. Shinnosuk Horiuchi, Dr. Hironobu Tahara, Dr. Jacopo Tessarolo, Dr. Kai Wu for creating a positive working atmosphere and valuable discussions in the "Foreigner Lab".

I really appreciate all the timely help and continuous encouragement from Dr. Soham Mandal and Dr. Thorben Schulte when I was in the most difficult situation.

Last but not least, I am grateful to my parents for their understanding and support, which allows me to pursue my dream in this far-away country. Special thanks to my wife Yun for endless love and encouragement during this long period.

Table of Contents

1 Introduction

1.1 Design of fullerene receptors

1.1.1 The relevance of fullerene separation

Since the first discovery of buckyball C_{60} by Kroto *et al.* in 1985,[1] fullerene and its derivatives have gained considerable attention during the last three decades.[2] In 1996, the Nobel Prize in Chemistry was awarded to Robert F. Curl, Sir Harold W. Kroto and Richard E. Smalley for their discovery of fullerenes.[3-5] Fullerenes are one of the most stable allotropes of carbon. They are soluble in organic solvents, unlike diamond and graphite. This property of fullerene facilitates the chemical modification of this kind of carbon material via solution-phase processing, thus yielding more functional and sophisticated fullerene derivatives.

The intensive study on fullerene chemistry started from the year of 1990, when Krätschmer and Huffman firstly realized the preparation of fullerenes in the multigram scale,[6] which allowed scientists to access raw materials to do further research and process. This vital finding was also recognized by Robert F. Curl, stating: ''this work took it from mass spectrometers to the laboratory''. This method produces fullerene-containing soot via arc-discharge between high-purity graphite rods in a helium atmosphere, which is still the main production method for fullerenes up to now. Apart from this approach, there are two other reliable methods to yield fullerenes in industry: hydrocarbon combustion in deficiency of oxygen[7] and condensation of polycyclic aromatic hydrocarbons.[8-9]

Until now, fullerene soot produced by arc-discharge or laser-vaporization is still the main source of fullerenes, and the commercially available fullerene soot generally includes C_{60} and C_{70} as the major components as well as few amounts of higher-order fullerenes (C_n, $n > 70$) and fullerene oxides. Preliminary separation of fullerenes from the carbon soot can be accomplished via multiple extraction and concentration steps. However, the extraction of target fullerenes from solid-state carbon soot by using chloroform or toluene is quite slow due to the poor solubility of fullerenes, whereas the use of dichlorobenzene or CS_2 as solvents can speed up this process but need to be removed in an energy-consuming process under high vacuum.[10] Nowadays, the advanced purification of fullerene compounds predominantly relies on chromatographic techniques, promoted by the development of diverse stationary phases and eluents, but still complicated by some problems, such as huge consumption of solvents and irreversible absorption.[11-12] In order to enhance the purity of separated fullerene compounds, these methods can be employed in combination with recrystallization, if necessary. Additionally, controlled sublimation under vacuum can afford purer fullerenes, although often accompanied by partial decomposition and the occurrence of side reactions with impurities at high temperature. In a nutshell, purification of fullerenes remains a time- and energy-consuming process.

Owing to their curved π-conjugated surfaces, fullerenes are considered as very promising electroactive materials. They possess cage-like geometries, which allows them to entrap metal atoms/molecules inside the cavity (endohedral fullerenes) or attach additional atoms/groups at the outer surface (exohedral fullerenes). The tunability of inherent electronic and geometric features makes fullerenes and their derivatives attractive candidates as functional molecular materials, widely applied in molecular electronics,[13] liquid crystalline materials,[14] photovoltaic devices,[15-19] medical therapy[20-23] and so on.

Application of these fullerene-based functional materials for practical use, however, is limited by the high price of fullerene compounds, owing to the tedious purification of fullerenes from carbon soot. This pressing problem has attracted attention of the community of chemists and efforts are being made to develop artificial fullerene receptors, capable of selectively binding fullerenes and their derivatives.

1.1.2 Design principles of fullerene receptors

From the design perspective, artificial fullerene receptors are generally required to exhibit complementarity towards target fullerenes in terms of electronic nature and spatial geometry for the purpose of accessing greater binding affinities and selectivities towards fullerenes. In the regard of electronic complementarity, extended π-conjugated systems, particularly those moieties that behave as electron donors in the excited state, are extensively utilized as backbones in the majority of reported fullerene receptors, thus facilitating the interaction between these hosts and fullerenes that generally act as electron acceptor moieties. Moreover, fullerenes with well-defined geometries and volumes, e.g. spherical C_{60} with a van-der-Waals volume of 547 $Å^3$ and ellipsoidal C_{70} with a van-der-Waals volume of 646 $Å^3$,[24] tend to be entrapped in those receptors with suitable shape and size on the basis of their structural complementarity. Relatively strong binding can be provided by the concave-convex π-π interaction between hosts and fullerenes.[25] Among known fullerene receptors, metallo-porphyrins are one of the most used backbones, thanks to the favorable electronic interaction between porphyrin and fullerene (Figure 1.1).[26-27] Cyclotriveratrylene (CTV)[28-29] features a bowl-shaped geometry which complements to the shape of fullerenes, whereas corannulenes[30-33] and extended tetrathiafulvalenes (TTF)[34-35] with curved π-conjugated surfaces, to a certain extent, both exhibit concave-convex π-π interaction upon binding fullerenes. Apart from these above-mentioned basic principles, the flexibility of supramolecular hosts can also be fine-tuned to achieve selectivity in some cases.[36] Besides, solvent effects, like the hydrophobic effect, sometimes play an important role in the binding process.[37]

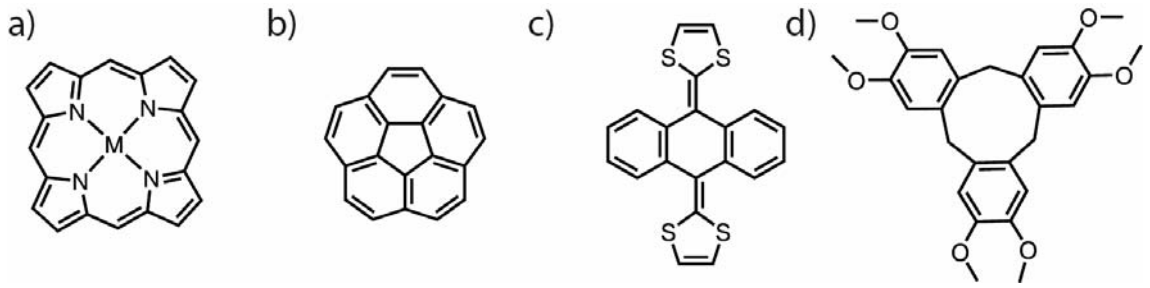

Figure 1.1 Popular backbones used in artificial fullerene receptors: (a) Metallo-porphyrin; (b) corannulene; (c) π-extended tetrathiafulvalene; (d) cyclotriveratrylene.

1.2 Discrete coordination-driven fullerene receptors

A number of fullerene receptors have been reported in the last two decades and can be divided into three categories: (a) fully covalent receptors, for example, conjugated aromatic belts;[38] (b) receptors that are constructed by weak non-covalent interactions, e.g. hydrogen bonding;[39-40] (c) receptors that are assembled from organic ligands and metal ions via coordination bonding.[41] Herein, coordination-driven fullerene receptors will be mainly discussed considering their comparative advantages over the other receptors due to the following reasons. Firstly, intricate synthetic procedures are not required to synthesize them, unlike fully covalent receptors, which implies greater possibilities of the large-scale preparation. Secondly, coordination bonding is relatively stronger than labile hydrogen bonding, thus constructing more stable systems for further investigation and application. Thirdly, the shape and size of cavities within coordination-driven assemblies can be precisely tuned based on tailor-made ligands and metal ions. In contrast to infinitely extended metal-organic frameworks that are able to bind fullerenes,[42-44] discrete coordination cages as fullerene receptors can be more readily tuned via chemical manipulation in the solution phase, thus achieving the desired properties. Accordingly, discrete coordination-driven fullerene receptors have become more attractive and will be presented in detail in the following sections.

1.2.1 Binding capacity

Binding capacity is one of the crucial properties for fullerene binders and its definition is the maximum binding number of fullerenes within each host. Despite that chemists have been aiming to prepare supramolecular hosts capable of accommodating multiple fullerenes in proximity to study peculiar electronic properties of fullerene aggregates,[45-46] this kind of host materials has so far rarely reported. This section will showcase some characteristic metal-organic cages with single-fullerene binding ability as well as other fullerene receptors with higher capacities.

1.2.1.1 Single fullerene binding

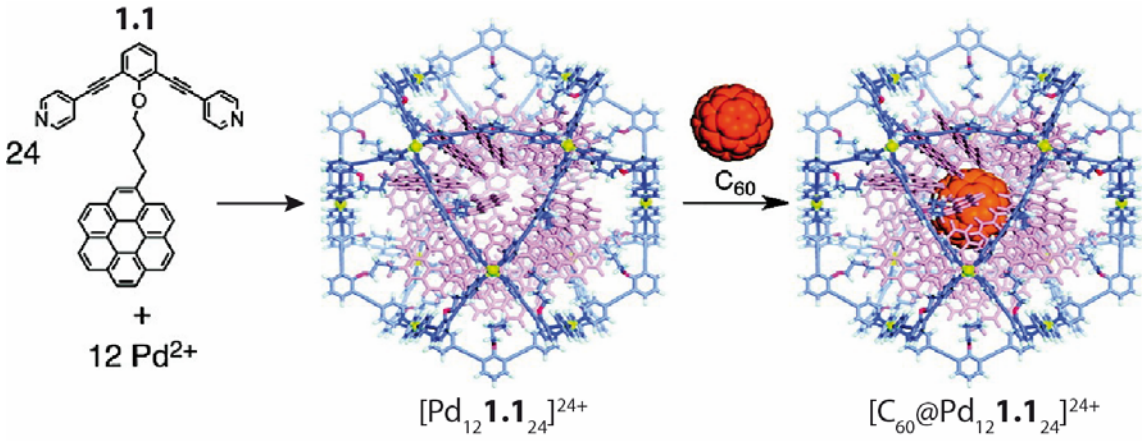

Figure 1.2 Self-assembly of cage $[Pd_{12}\mathbf{1.1}_{24}]^{24+}$ based on Pd^{II} cations and ligands **1.1** bearing the coronene moiety, after being treated with excess C_{60} to partially convert into the host-guest complex $[C_{60}@Pd_{12}\mathbf{1.1}_{24}]^{24+}$ (40%). Reprinted with permission from reference.[47] Copyright © (2010) American Chemistry Society.

In view of the endohedral functionalization of self-assembled $[Pd_{12}L_{24}]^{24+}$ spheres,[48] Fujita and co-workers employed a bis-monodentate ligand **1.1** bearing a pendant coronene moiety to assemble with square-planar Pd^{II} cations into a 4.6 nm-sized cage $[Pd_{12}\mathbf{1.1}_{24}]^{24+}$, containing 24 coronene molecules within its cavity (Figure 1.2).[47] These aromatic coronene molecules, flexibly linked to the ligand backbones, are enriched in the confined cavity, hence facilitating the binding of one C_{60} inside.

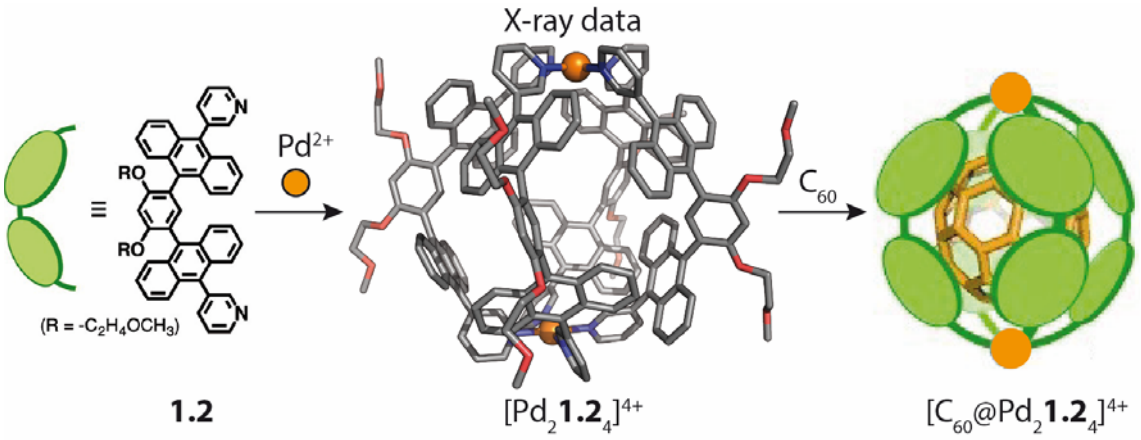

Figure 1.3 Self-assembly of spherical cage $[Pd_2\mathbf{1.2}_4]^{4+}$ based on Pd^{II} cations and bis-monodentate ligands **1.2** containing two anthracene moieties. The cage $[Pd_2\mathbf{1.2}_4]^{4+}$ can bind one C_{60} within its cavity to form host-guest complex $[C_{60}@Pd_2\mathbf{1.2}_4]^{4+}$ quantitatively. Adapted with permission from reference.[49] Copyright © (2011) American Chemistry Society.

In 2011, Yoshizawa and co-workers utilized aromatic anthracene molecules as components of the backbone and synthesized the spherical cage $[Pd_2\mathbf{1.2}_4]^{4+}$ consisting of Pd^{II} cations and the rigid banana-shaped ligand **1.2** (Figure 1.3).[49] The resulting cavity is basically segregated from the surroundings owing to the large dimension of eight anthracene units on the edges, producing a microenvironment for planar molecules and spherical fullerenes. Fullerene binding experiments suggested the cage $[Pd_2\mathbf{1.2}_4]^{4+}$ could only accommodate one C_{60} inside, and it even shows size exclusion towards C_{70}. Quantitative inclusion of C_{60} was confirmed by heating the acetonitrile solution of cage $[Pd_2\mathbf{1.2}_4]^{4+}$ in the presence of C_{60} powder.

Subcomponent self-assembly is an effective way to achieve sophisticated supramolecular architectures through the one-pot assembly of multiple building blocks, which allows for the guest inclusion/liberation in a dynamic equilibrium.[50-52] On the basis of this approach, Nitschke's group reported a series of self-assembled cubic and tetrahedral cages, capable of binding fullerenes within their cavities, as a consequence of the implementation of π-conjugated systems on panels or edges to enhance the host-guest interaction. In 2011, the same group published the assembly of Ni-centered tetrakis(4-aminophenyl)porphyrin and 2-formylpyridine with $Fe(OTf)_2$ into cubic cage $[Fe_8\mathbf{1.3}_6]^{16+}$ with a void space of 1340 $Å^3$ (Figure 1.4).[53] This cubic cavity wrapped by six electron-donating Ni-porphyrin panels shows the ability to accommodate three densely stacked coronene molecules. Moreover, subsequent fullerene-binding investigations suggest that the binding affinity of this cubic cage for C_{70} is significantly greater than that for C_{60} due to the larger surface area of the former which can interact with the internal surface of the host. Driven by the curiosity about whether this giant cage could encapsulate higher fullerenes (C_n, $n > 70$), the binding study of cage $[Fe_8\mathbf{1.3}_6]^{16+}$ with a 9-fold amount (by weight based on cage) of commercial fullerene soot was carried out and

monitored by ESI mass spectrometry. The mass spectrum of the reaction product shows the peaks belonging to a series of host-guest complexes, including $[C_{70}@Fe_8\mathbf{1.3}_6]^{16+}$, $[C_{76}@Fe_8\mathbf{1.3}_6]^{16+}$, $[C_{78}@Fe_8\mathbf{1.3}_6]^{16+}$, $[C_{82}@Fe_8\mathbf{1.3}_6]^{16+}$, $[C_{84}@Fe_8\mathbf{1.3}_6]^{16+}$. However, the absence of free cage $[Fe_8\mathbf{1.3}_6]^{16+}$ and C_{60}-occupied cage $[C_{60}@Fe_8\mathbf{1.3}_6]^{16+}$ in the mixture confirms that the large cavity shows a greater binding affinity for higher fullerenes. In 2017, Lützen's group used alternatively imidazolylimines instead of pyridylimines to construct a cubic cage showing a spin-crossover phenomenon and comprising eight Fe^{2+} vertices.[54] Intriguingly, the binding of C_{70} within the cage's cavity stabilizes the high-spin state with the corresponding spin-transition temperature reduced by 20 K relative to the empty cage.

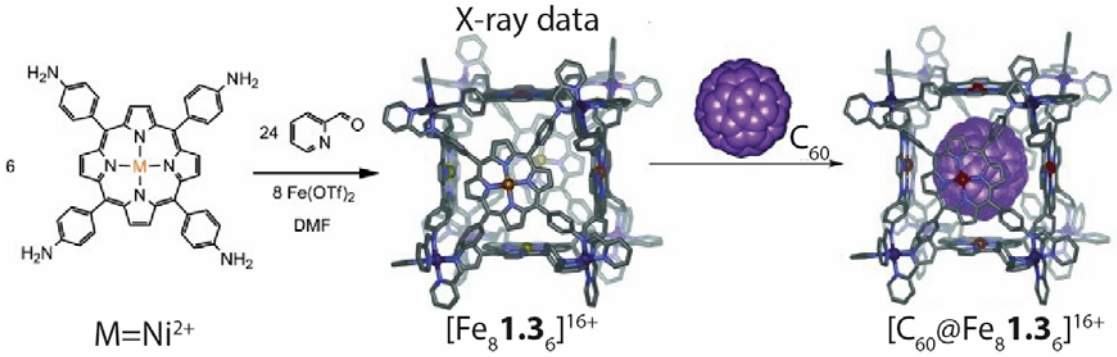

Figure 1.4 Subcomponent self-assembly of cubic cage $[Fe_8\mathbf{1.3}_6]^{16+}$ based on Fe^{2+} cations and tetrakis-bidentate ligands **1.3** containing metal-porphyrin units. The cage $[Fe_8\mathbf{1.3}_6]^{16+}$ after being treated with 5 eq. amounts of C_{60} converted into C_{60}-containing cage $[C_{60}@Fe_8\mathbf{1.3}_6]^{16+}$ (35%). Adapted with permission from reference.[53] Copyright © (2011) Wiley-VCH Verlag GmbH & Co. KGaA, Weinheim.

The classic subcomponent self-assembly of tetrahedral cages $[Fe_4L_6]^{8+}$ was also studied in depth, and is accessed via the direct combination of Fe^{2+}, 2-formylpyridine and C_2-symmetric aromatic diamines (Figure 1.5). In 2014, two isomeric cages based on differently substituted pyrene edges were prepared, wherein the cage $[Fe_4\mathbf{1.4a}_6]^{8+}$ based on the 1,6-pyrene scaffold, was able to host one C_{60}/C_{70} inside to form a 1:1 host-guest complex.[55] Moreover, fullerene binding can induce a geometrical conversion from three diastereomers of free cage $[Fe_4\mathbf{1.4a}_6]^{8+}$ into two favorable geometries of fullerene-containing tetrahedral cages with *T*-symmetry and C_3-symmetry, accompanied by the disappearance of the previous S_4-symmetric diastereomer, consistent with the results of DFT calculations. In contrast, cage $[Fe_4\mathbf{1.4b}_6]^{8+}$ based on the 2,7-pyrene scaffold possesses a more open cavity without sufficient surface enclosure, thus losing the ability to capture C_{60} or C_{70} inside.

Later, the same group utilized an 1,5-anthracene scaffold to substitute the previous pyrene scaffold, giving rise to tetrahedral cage $[Fe_4\mathbf{1.4c}_6]^{8+}$ with reactive anthracene moieties on six edges.[56] Upon addition of C_{60}, three adjacent anthracene-based edges covalently bound to the internal C_{60} guest via Diels-Alder cycloaddition, notably distinct from the non-covalent interaction between C_{60} and other fullerene receptors. By treating the reactive cage $[Fe_4\mathbf{1.4c}_6]^{8+}$ with excess electron-deficient tetracyanoethylene molecules prior to guest inclusion, this post-assembly modified cage without reactivity can still bind C_{60} owing to their shape and size complementarities.

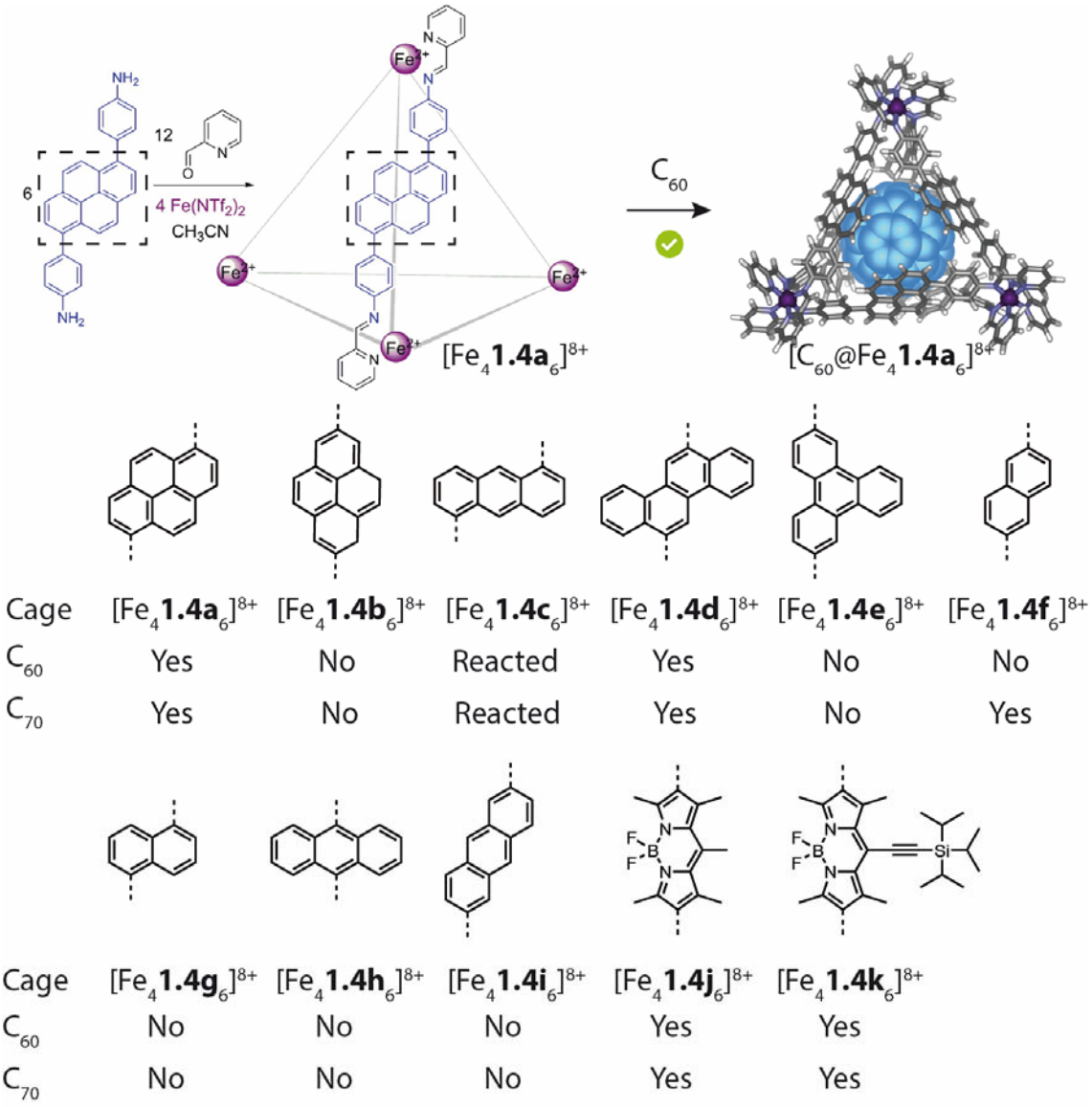

Figure 1.5 Subcomponent self-assembly of tetrahedral cages $[Fe_4L_6]^{8+}$ based on different aromatic edges, which show distinct binding abilities towards C_{60} and C_{70}. Adapted from reference.[55]

Using this modular self-assembly concept based on dynamic-covalent and coordination bonding, additional six different aromatic edges in the comparison with the above-mentioned pyrene and anthracene edges were introduced to construct corresponding tetrahedral cages (cage $[Fe_4\mathbf{1.4d}_6]^{8+}$ — cage $[Fe_4\mathbf{1.4i}_6]^{8+}$) and their respective guest-binding abilities were investigated to elucidate the structure-property relationship.[57] The comprehensive study of this series of cages as well as their binding performances on fullerenes, aromatic hydrocarbons as well as cholesterol, suggests that larger and more offset backbones can provide a more enclosed cavity to maximally constrain the guest molecules inside, thus achieving a stronger binding.

In 2017, two BODIPY moieties were also used as edges to form two homoleptic cages $[Fe_4\mathbf{1.4j}_6]^{8+}$ and $[Fe_4\mathbf{1.4k}_6]^{8+}$, respectively, and an equal mixture of these two distinct bis(aminophenyl)-BODIPY units assembled with 2-formylpyridine and $Fe(OTf_2)_2$ into the heteroleptic cage system $[Fe_4\mathbf{1.4j}_n\mathbf{1.4k}_{(6-n)}]^{8+}$ as a statistical mixture.[58] Both

homoleptic and heteroleptic cages are capable of hosting a C_{60}/C_{70} within the cavity and corresponding fullerene-containing complexes exhibit ultrafast host-guest electron transfer.

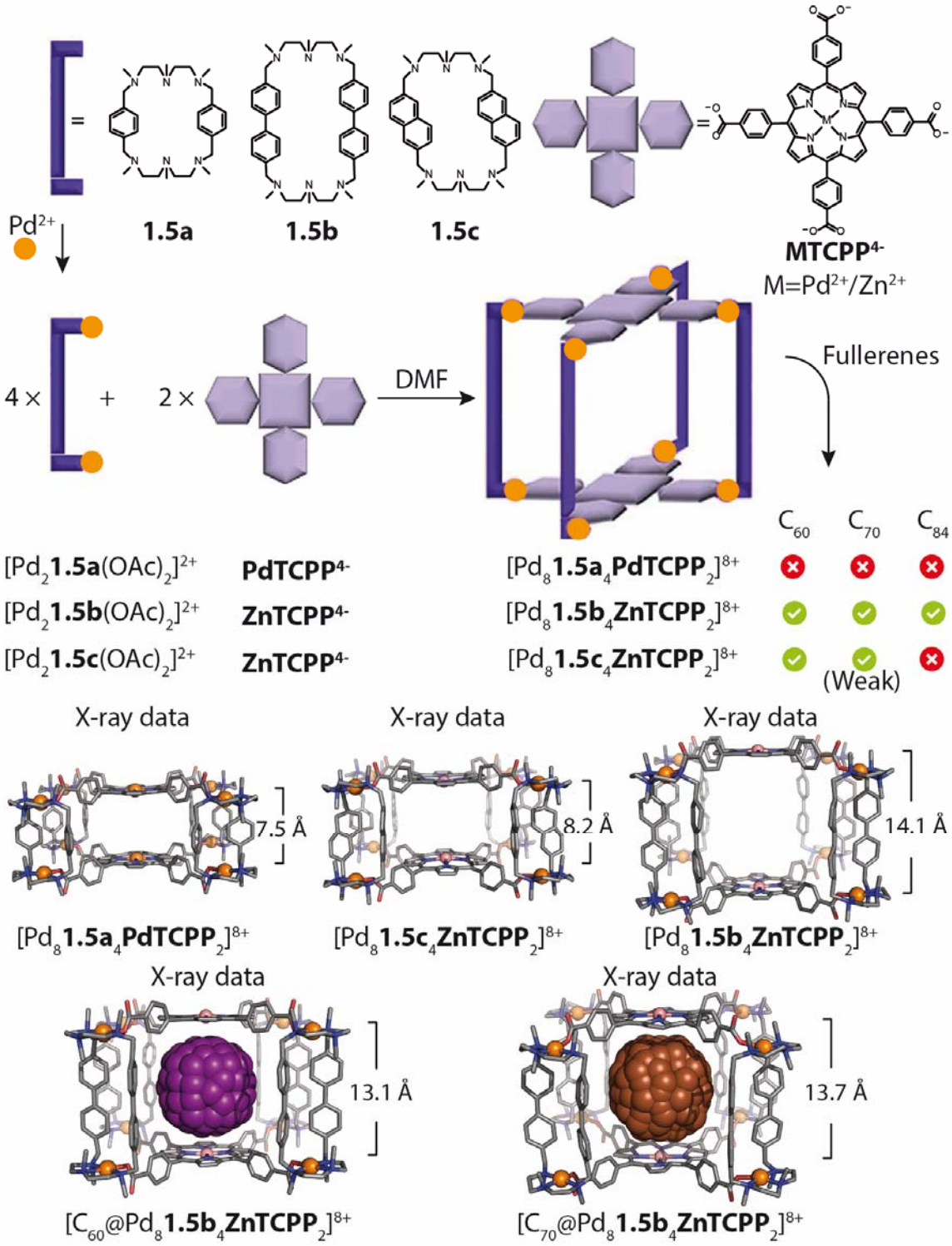

Figure 1.6 Self-assembly of tetragonal prismatic cages based on different Pd-precursors and tetracarboxylated metal-porphyrin, and X-ray structures of these free cages as well as fullerene-filled cages. Adapted with permission from reference.[59] Copyright © (2014) Springer Nature.

Ribas and co-workers took advantage of the strategy of the hierarchical assembly to achieve tetragonal prismatic cages through the combination of pre-synthesized molecular clips ($[Pd_2$**1.5a**$(OAc)_2]^{2+}$ — $[Pd_2$**1.5c**$(OAc)_2]^{2+}$) and metal-porphyrin tetracarboxylate (**PdTCPP**$^{4-}$/**ZnTCPP**$^{4-}$) (Figure 1.6). In 2013, the cage $[Pd_8$**1.5a**$_4$**PdTCPP**$_2]^{8+}$ was first reported by them with a Pd–Pd distance of 7.5 Å between opposite Pd-porphyrin-based panels.[60] This vertical distance is much smaller than the van der Waals diameter of C_{60} (10.1 Å), which hinders the inclusion of C_{60} or higher fullerenes within the cavity of cage $[Pd_8$**1.5a**$_4$**PdTCPP**$_2]^{8+}$.

One year later, the biphenyl moiety was utilized to substitute the previous single phenyl moiety, affording the longer molecular clip $[Pd_2$**1.5b**$(OAc)_2]^{2+}$, which assembled with **ZnTCPP**$^{4-}$ into the larger cage $[Pd_8$**1.5b**$_4$**ZnTCPP**$_2]^{8+}$.[59] X-ray analysis shows that the distance between parallel porphyrin panels is up to 14.1 Å in the free cage, whereas the distances in fullerene-filled cages $[C_{60}@Pd_8$**1.5b**$_4$**ZnTCPP**$_2]^{8+}$ and $[C_{70}@Pd_8$**1.5b**$_4$**ZnTCPP**$_2]^{8+}$ shrink to 13.1 and 13.7 Å, respectively, for the sake of maximizing the porphyrin-fullerene interaction. The large cavity of cage $[Pd_8$**1.5b**$_4$**ZnTCPP**$_2]^{8+}$ allows for the encapsulation of higher fullerenes, such as C_{76}, C_{78} and C_{84}. It is worth noting that this cage exhibits a 'breathing' behavior during the fullerene-binding process as shown in crystal structures, which relies on the flexibility of molecular clips holding the integral structure.

Most recently, they prepared an intermediate-sized cage through the employment of the 2,6-naphthalene-based molecular clip $[Pd_2$**1.5c**$(OAc)_2]^{2+}$, whose length was between single phenyl to biphenyl clips.[61] A crystal structure of the free cage $[Pd_8$**1.5c**$_4$**ZnTCPP**$_2]^{8+}$ shows the relative distance between two porphyrin panels to be 8.2 Å, less than the diameter of C_{60} (10.1 Å). Since cage $[Pd_8$**1.5c**$_4$**ZnTCPP**$_2]^{8+}$ possesses a similar breathing ability, it is still capable of binding C_{60} under structural adjustment. For the larger-sized C_{70}, this cage shows a significantly lower binding affinity relative to that for C_{60}, presumably due to the more unfavorable distortion of the host during the C_{70}-binding process. In addition, fullerene binding studies suggests that this cage exhibits a remarkable selectivity towards C_{60} compared to N-methylpyrrolidine-C_{60}, which allows the cage to selectively bind C_{60} from the mixture of both, being potentially useful for fullerene purification in the near future.

1.2.1.2 Double fullerene binding

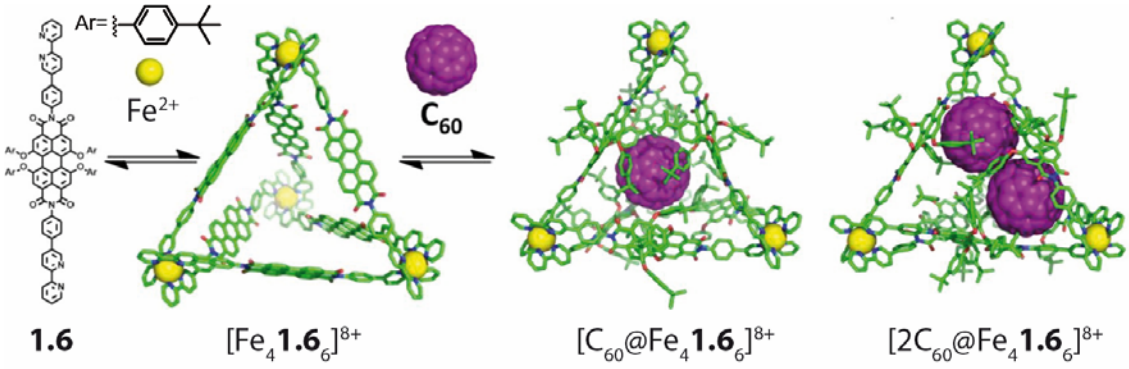

Figure 1.7 Self-assembly of the tetrahedral cage $[Fe_4$**1.6**$_6]^{8+}$ based on perylene bisimide-paneled ligands **1.6** and Fe^{2+} vertices (*p*-tert-butylphenyl chains are omitted in the cage $[Fe_4$**1.6**$_6]^{8+}$ for clarity). This giant cage can bind two C_{60} maximally, confirmed by mass spectrometry. Adapted with permission from reference.[62] Copyright © (2013) American Chemistry Society.

Close inspection of so far reported fullerene receptors points out that a majority of them can merely host one fullerene within their cavities. For those fullerene binders capable of accommodating more than one fullerene molecules, on the one hand, they entail larger cavities with enough space and suited shape for more fullerenes. On the other hand, the binding sites of hosts ought to have strong interactions towards target fullerenes and the cavity should be relatively enclosed to avoid the escape of central fullerenes.

In 2013, Würthner's group published a giant tetrahedral cage $[Fe_4\mathbf{1.6}_6]^{8+}$ assembled by PBI-based bis-bidentate ligands **1.6** and Fe^{2+} cations quantitatively (Figure 1.7), and the electroactive nature of PBI backbones was retained in the resulting coordination cage, presenting a series of reversible redox potentials.[62] This fairly long edge makes its assembled cage one of the largest tetrahedral cages with an estimated void space over 950 Å^3. Besides, the side chain *p*-tert-butylphenyl connected to PBI backbones encircles the whole tetrahedra, conducive to the binding of guests inside the cavity to a certain extent. Afterwards, the encapsulation of C_{60} by cage $[Fe_4\mathbf{1.6}_6]^{8+}$ was demonstrated by UV-Vis spectroscopy, ^{13}C NMR spectra as well as ESI mass spectra, which clearly suggested the existence of $(C_{60})_2$-binding species. Molecular force field analysis shows two encapsulated C_{60} tend to locate close to two corners of this tetrahedral cage.

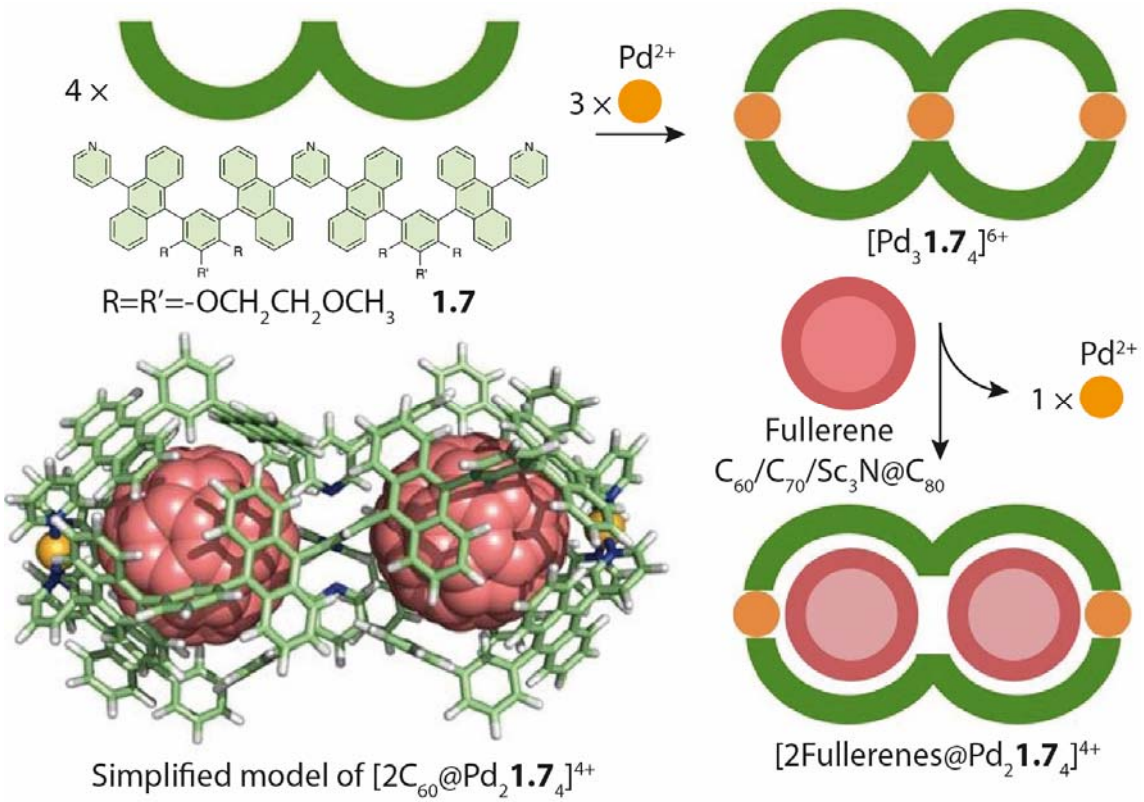

Figure 1.8 Self-assembly of a peanut-like cage $[Pd_3\mathbf{1.7}_4]^{6+}$ based on Pd^{II} cations and polyaromatic ligands **1.7**, followed by adding fullerenes (C_{60}/C_{70}/$Sc_3N@C_{80}$) to form fullerenes-filled cages. The optimized structure of the simplified cage $[2C_{60}@Pd_2\mathbf{1.7}_4]^{4+}$ shows that internal C_{60}s are wrapped by external anthracene moieties. Adapted from reference.[63]

On the basis of their previous work, Yoshizawa *et al.* designed and prepared a novel W-shaped polyaromatic ligand **1.7** comprising four anthracene moieties, and the decoration of six methoxyethoxy groups contributes to enhancing its solubility in organic solvents (Figure 1.8).[63] The self-assembly of the tris-monodentate ligand **1.7** with square-planar Pd^{II}

cations quantitatively yields the peanut-like cage $[Pd_3\mathbf{1.7}_4]^{6+}$ with two inner pockets. Subsequent addition of C_{60} into the cage solution can expel the central Pd^{II} node, thus giving the C_{60}-filled cage $[2C_{60}@Pd_2\mathbf{1.7}_4]^{4+}$, which is also observed in the binding process of two higher fullerenes, such as C_{70} and endohedral fullerene $Sc_3N@C_{80}$. Noteworthy, this peanut-like cage $[Pd_3\mathbf{1.7}_4]^{6+}$ is able to host two different guests in an allosteric binding mode.

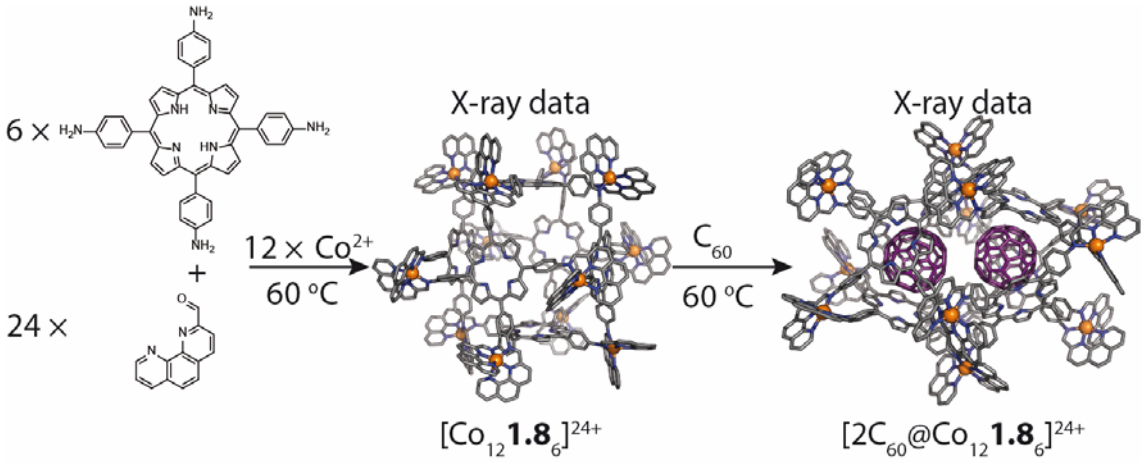

Figure 1.9 Subcomponent self-assembly of the *O*-symmetric cage $[Co_{12}\mathbf{1.8}_6]^{24+}$ based on Co^{2+}, 2-formyl-phenanthroline and porphyrin panels. The cage reorganizes to S_6-symmetric cage $[2C_{60}@Co_{12}\mathbf{1.8}_6]^{24+}$ upon binding two C_{60}.

In light of the reliable subcomponent self-assembly, Nitschke and co-workers successfully employed 2-formyl-phenanthroline instead of the often used 2-formyl-pyridine in the self-assembly with tetrakis(4-aminophenyl) porphyrin and octahedral Co^{2+} cations, thus achieving the D_4-symmetric cage $[Co_{12}\mathbf{1.8}_6]^{24+}$ at room temperature (Figure 1.9).[64] Upon heating, the cage geometry changes into the *O*-symmetric cage $[Co_{12}\mathbf{1.8}_6]^{24+}$ as the thermodynamic stable species, manifesting the evident plasticity of this cage system. Fullerene-binding studies on the cage $[Co_{12}\mathbf{1.8}_6]^{24+}$ suggests it undergoes geometric conversion into S_6-symmetric cage upon binding of two fullerenes (C_{60}/C_{70}/C_{60}PCBM) inside the reconfigured cavity, in the interest of maximizing the host-fullerene interaction. More interestingly, the $(C_{60})_2$-filled cage $[2C_{60}@Co_{12}\mathbf{1.8}_6]^{24+}$ can continually bind two large-sized anions ($CB_{11}H_{12}^-$/$B_{12}F_{12}^{2-}$/BPh_4^-) inside the remaining cavities. Compared to the original anion-binding performance of the free cage, the $(C_{60})_2$-filled cage exhibits different cooperativities in the binding process of two anions.

1.2.1.3 Multiple fullerene binding

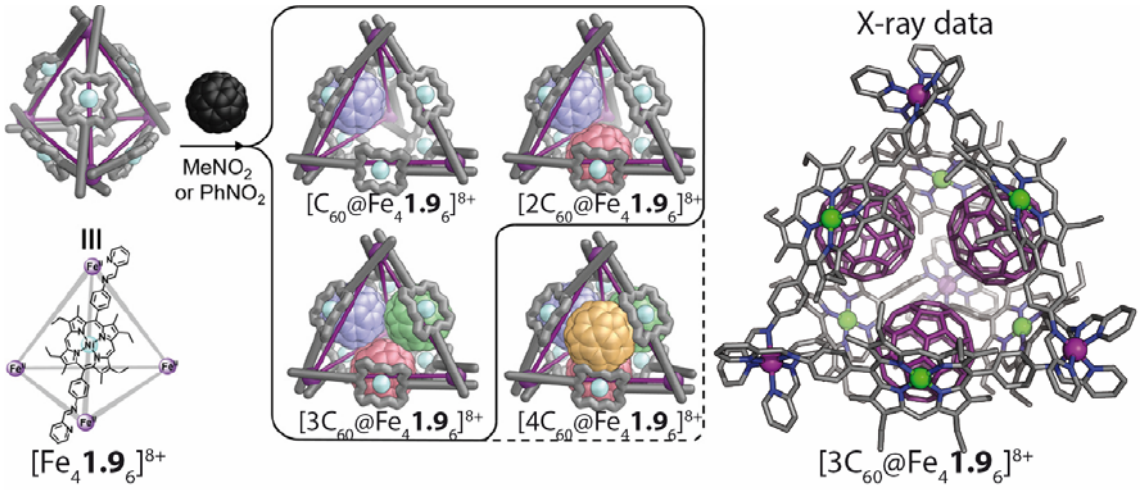

Figure 1.10 Tetrahedral cage $[Fe_4\mathbf{1.9}_6]^{8+}$ that can encapsulate one to three C_{60} in $MeNO_2$. This cage can even accommodate up to four C_{60} within the cavity in $PhNO_2$ to yield the fully filled complex $[4C_{60}@Fe_4\mathbf{1.9}_6]^{8+}$. Adapted with permission from reference.[65] Copyright © (2017) American Chemistry Society.

In 2015, a Ni-porphyrin-edged tetrahedral cage $[Fe_4\mathbf{1.9}_6]^{8+}$ was reported by the group of Nitschke based on the well-established subcomponent self-assembly.[66] Induced by the addition of C_{60} or C_{70} in acetonitrile, this tetrahedron is confirmed to reorganize into a cone-like fullerene-containing complex $[fullerene@Fe_3\mathbf{1.9}_4]^{6+}$, consisting of four bis-bidentate ligands and two coordinatively saturated Fe^{2+} centers as well as one unsaturated Fe^{2+} center. This abnormal transformation from the saturated coordination complex to the unsaturated coordination complex is driven by the strong host-guest interaction between multiple Ni-porphyrin moieties and the fullerene guest in the favorable geometry of $[fullerene@Fe_3\mathbf{1.9}_4]^{6+}$. Moreover, further addition of Cu^+ can completely replace the unsaturated Fe^{2+} and form the heterometallic cage $[fullerene@CuFe_2\mathbf{1.9}_4]^{5+}$. After two years, another work associated with this tetrahedral cage $[Fe_4\mathbf{1.9}_6]^{8+}$ was reported and indicated that the guest-induced transformation of cage $[Fe_4\mathbf{1.9}_6]^{8+}$ only occurred in acetonitrile, which could act as ligand to stabilize the unsaturated coordination metal center.[65] The binding number of C_{60} inside the cavity remarkably relates with the solvent used (Figure 1.10): in $MeNO_2$, the mixture of the cage $[Fe_4\mathbf{1.9}_6]^{8+}$ and 10 eq. amount of C_{60} at room temperature gives a mixture of host-guest complexes $[nC_{60}@Fe_4\mathbf{1.9}_6]^{8+}$ (n = 1 – 3), supported by mass spectrometry; under the same condition, the cage can even bind up to four C_{60} within the cavity in $PhNO_2$ and ESI mass spectrum showed triple-C_{60}-filled and quadruple-C_{60}-filled cages arises as major species in the mixture of $[nC_{60}@Fe_4\mathbf{1.9}_6]^{8+}$ (n = 1 – 4) unlike the situation in $MeNO_2$. This solvent-driven discrepancy in inclusion of fullerenes can be attributed to that the greater solubility of C_{60} in $PhNO_2$ relative to $MeNO_2$ promotes more C_{60} present in solution, thus facilitating the binding of more C_{60}s inside the cavity. The crystal structure of $[3C_{60}@Fe_3\mathbf{1.9}_4]^{6+}$ further confirms this existence of multiple-fullerenes-filled cage species in solid state and cyclic voltammograms studies of these assemblies elucidate that the close arrangement of multiple fullerenes in a confined environment can alter the electron affinity of fullerenes through the non-covalent interaction.

1.2.2 Binding selectivity

Another crucial property of fullerene receptors is the binding selectivity towards different fullerenes and their derivatives, a prerequisite for effective separation of the particular fullerene compound from the fullerene mixture. The acquirement of fullerene receptors with higher selectivity is still a challenging task until now, which is limited by similar physicochemical properties of fullerene compounds. This section will discuss the selective binding of C_{60} and C_{70}, two of the most abundant fullerenes, as well as other uncommon fullerene compounds, such as C_{60} bisadducts, $Sc_3N@C_{80}$, $U_2@I_h\text{-}C_{80}$, $Sc_2CU@I_h\text{-}C_{80}$.

1.2.2.1 Selective binding of C_{60}

C_{60}, the most common fullerene compound, has been investigated as guests in most of the potential fullerene binders owing to its high-symmetric spherical geometry and facile availability. Among these known fullerene receptors, self-assembled coordination cages capable of selectively binding of C_{60} over C_{70} have been seldomly reported.[49, 61] This kind of cages to a large extent relies on the precisely designed host and its cavity, which possesses the ability to distinguish the tiny size difference between C_{60} and C_{70}.

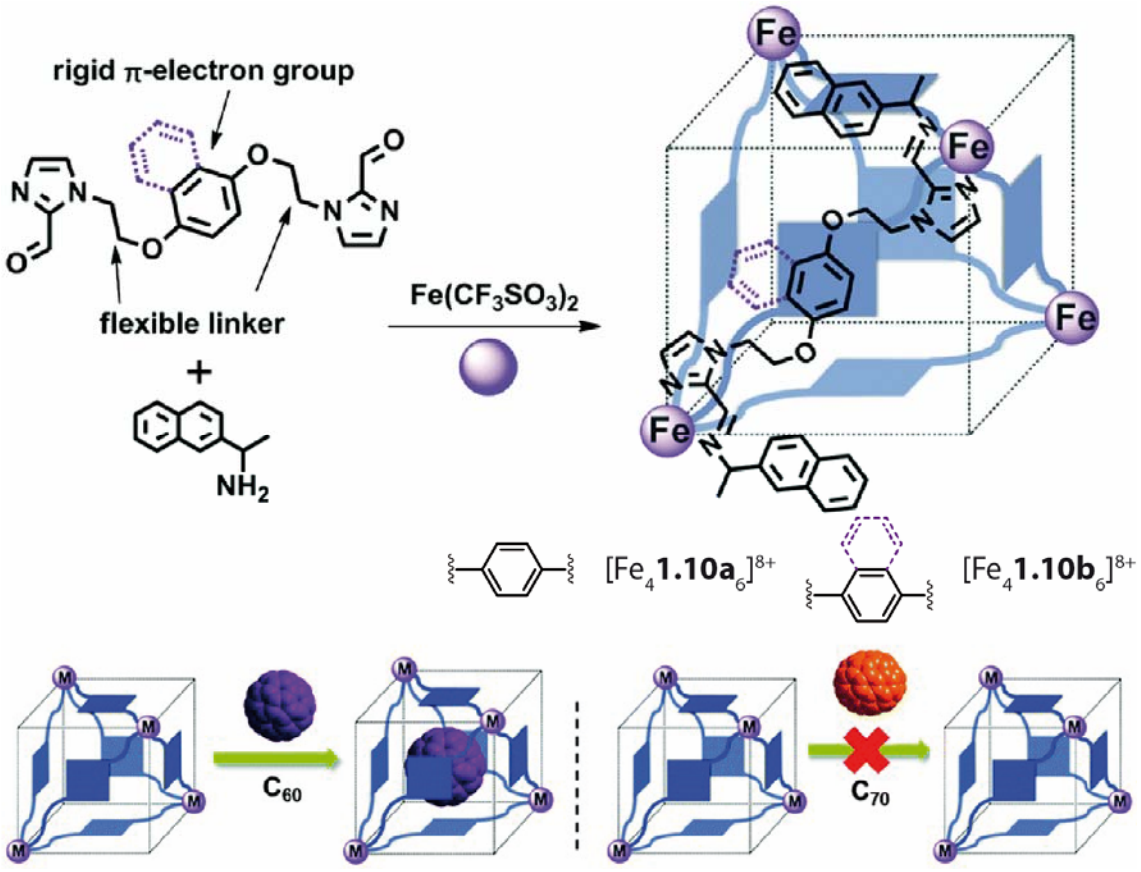

Figure 1.11 Subcomponent self-assemblies of tetrahedral cages $[Fe_4\mathbf{1.10a}_6]^{8+}$ and $[Fe_4\mathbf{1.10b}_6]^{8+}$ based on Fe^{2+}, (R)-1-(naphthalen-2-yl)ethanamine and corresponding aldehydes. Both of these two cages selectively bind C_{60} instead of C_{70}. Reproduced from reference[67] with permission from the Royal Society of Chemistry.

In 2018, Gu and co-workers synthesized two tetrahedral cages with a cubic cavity, wherein the employed panels to interact with target fullerenes are benzene and naphthalene moieties in cage $[Fe_4\mathbf{1.10a}_6]^{8+}$ and $[Fe_4\mathbf{1.10b}_6]^{8+}$, respectively (Figure 1.11).[67] Unlike other known fullerene binders, a flexible linker was utilized here to endow the overall flexibility of cage, which allows for the free guest entering and exiting from the cavity. Experimental results suggested merely C_{60} rather than C_{70} could be captured by these two cages, which was inferred to the higher shape and size complementarity between C_{60} and these two hosts. Furthermore, the encapsulation of C_{60} within these spin-crossover cages stabilizes the high-spin state of Fe^{2+}, confirmed by the lower spin transition temperature ($T_{1/2}$) for host-guest complexes compared to that for free cages.

1.2.2.2 Selective binding of C_{70}

Coordination cages that can bind the large-sized C_{70} are prone to possess the ability to host the small-sized C_{60}, likewise. In this case, in order to selectively capture C_{70} from the mixture of C_{60} and C_{70}, fullerene receptors are required to exhibit significant binding preference towards C_{70} over C_{60}. This difference on binding affinities can be somewhat provided by the larger surface area of C_{70}, benefiting from the increased host-guest interaction.

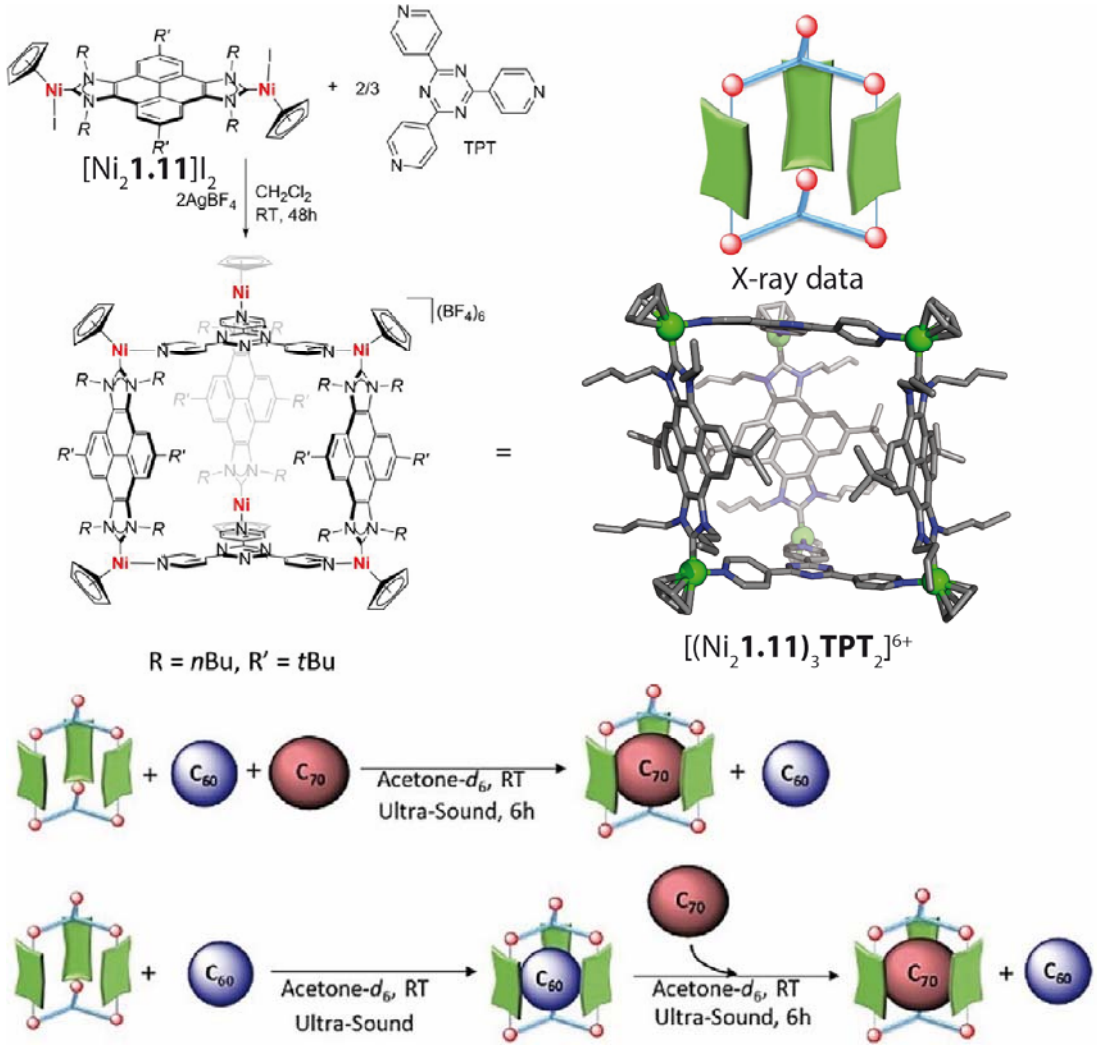

Figure 1.12 Synthesis of the trigonal prismatic metallorganic cage $[(Ni_2\mathbf{1.11})_3\mathbf{TPT}_2]^{6+}$. This cage shows higher binding affinity towards C_{70} over C_{60}. Adapted with permission from reference.[68] Copyright © (2018) Wiley-VCH Verlag GmbH & Co. KGaA, Weinheim.

In 2018, Peris and co-workers reported an organometallic supramolecular cage $[(Ni_2\mathbf{1.11})_3\mathbf{TPT}_2]^{6+}$ assembled by the Ni-based organometallic prism and 1,3,5-tripyridyl-triazine, giving rise to a large cavity (Figure 1.12).[68] This D_{3h}-symmetric trigonal prism was confirmed by X-ray analysis, suggesting the cavity covered by multiple aromatic panels, and the peripheral butyl chains contributed to the enclosure of the inner cavity. The guest inclusion of this molecular cage was studied with fullerenes (C_{60}/C_{70}), indicating that the cage shows binding abilities towards both. Introduction of a mixed solvent (acetone/dichlorobenzene 1:4) facilitates the calculation of binding constants for the encapsulation of C_{60} and C_{70} within the cavity: 4.7×10^3 and 3.5×10^4 M^{-1}, respectively. Considering this discrepancy, the addition of the 1:1 mixture of C_{60} and C_{70} into the acetone solution of the cage $[(Ni_2\mathbf{1.11})_3\mathbf{TPT}_2]^{6+}$ exclusively yielded the C_{70}-filled cage, identified by the ^{13}C NMR spectrum and ESI spectrum. Furthermore, another competitive experiment showed the subsequent addition of C_{70} can completely replace the initially trapped C_{60} in the host-guest complex $[C_{60}@(Ni_2\mathbf{1.11})_3\mathbf{TPT}_2]^{6+}$. Accordingly, both of these two experiments indicated the preferred binding of this cage toward C_{70}, which could be applied in the practical fullerene separation.

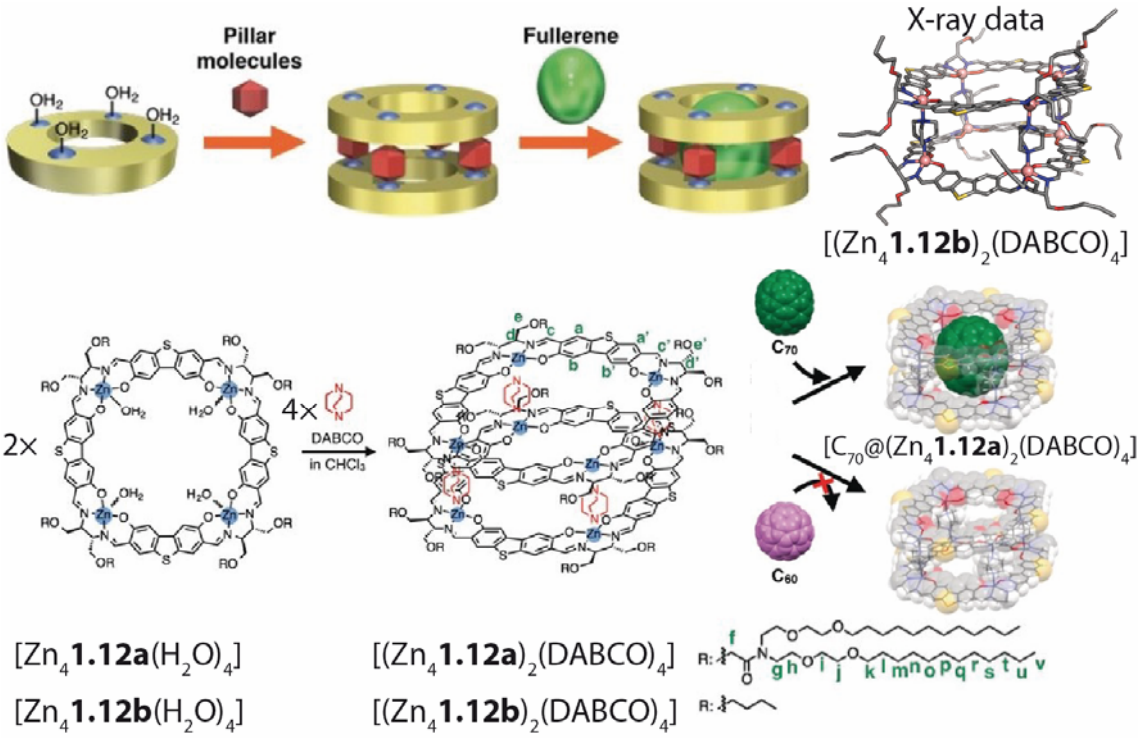

Figure 1.13 Assemblies of cylindrical cages $[(Zn_4\mathbf{1.12a})_2(DABCO)_4]$ and $[(Zn_4\mathbf{1.12b})_2(DABCO)_4]$ based on two macrocycles and four DABCO molecules as connecting pillars. X-ray structure of the cage $[(Zn_4\mathbf{1.12b})_2(DABCO)_4]$ confirms the cylindrical geometry. And the cage $[(Zn_4\mathbf{1.12a})_2(DABCO)_4]$ can selectively bind C_{70} instead of C_{60}. Adapted with permission from reference.[69] Copyright © (2018) Wiley-VCH Verlag GmbH & Co. KGaA, Weinheim.

Different from the fullerene binders that can encapsulate both C_{60} and C_{70} but with the significant binding preference for C_{70}, another rare example among selective receptors, was the neutral cage $[(Zn_4\mathbf{1.12a})_2(DABCO)_4]$, which merely binds C_{70} within its special cavity (Figure 1.13). This cylindrical cage was constructed by shape-persistent Zn-salen-based macrocycles and the linear bridging ligand DABCO as pillars, confirmed by the crystal structure of the simplified cage $[(Zn_4\mathbf{1.12b})_2(DABCO)_4]$. It is worth noting that binding is mainly provided by the CH–π interaction between inward-

pointing protons of the host and the π surface of the entrapped fullerene, in contrast to the common face-to-face aromatic interaction observed in the majority of fullerene receptors. The theoretical calculation showed the shorter distance between inner protons and the surface of the larger-sized C_{70} compared to C_{60}, thus stabilizing the C_{70}-binding within this rigid cavity.

1.2.2.3 Selective binding of other fullerene derivatives

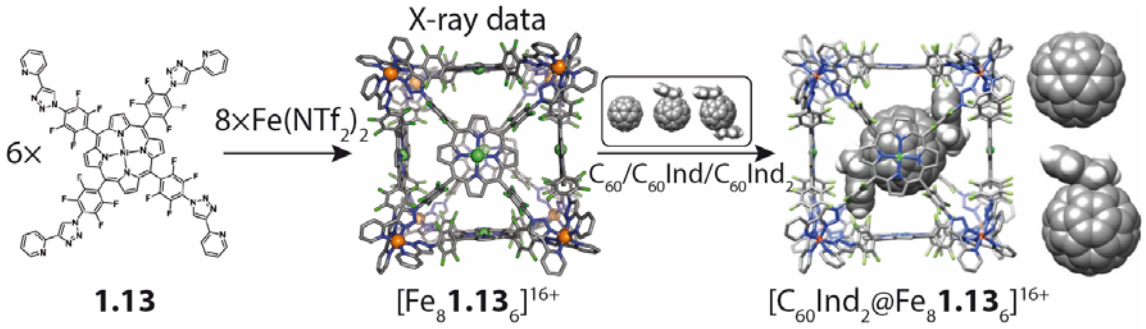

Figure 1.14 Self-assembly of the cubic cage $[Fe_8\mathbf{1.13}_6]^{8+}$ based on tetrakis-bidentate ligands **1.13** and Fe^{2+} cations. The cage can selectively bind the C_{60}-indene bisadduct from the reaction mixture including the unmodified C_{60} and C_{60}-indene monoadduct. Adapted from reference.[70]

Based on the previous works, Nitschke and co-workers synthesized a cubic cage $[Fe_8\mathbf{1.13}_6]^{8+}$ comprising six Ni-porphyrin-based ligands **1.13** and eight octahedral Fe^{2+} cations (Figure 1.14).[70] The X-ray structural analysis of this assembled cage confirms the pseudo-*O*-symmetric cage with a large cavity of 3183 Å^3. The perfluorophenylene linkers with the electron-withdrawing nature are introduced here to construct this electron-deficient coordination cage, potentially used for the binding of those more electron-deficient guests to enhance the binding affinity and selectivity, inspired by the insight from the Fujita's work.[71] On account of the large inner cavity and deviation from the Rebek's 55% rule (the optimum volume ratio of host and guest),[72] unmodified fullerenes, as well as some large anions, are not suitable to be encapsulated inside, reflected by the experimental results. The binding of fullerene Diels-Alder-functionalized adducts with larger volumes was tested in the acetonitrile solution of cage $[Fe_8\mathbf{1.13}_6]^{8+}$ with the solid sample of pure fullerene adducts, indicating that only C_{60}-indene bisadduct ($C_{60}Ind_2$) and C_{60}-anthracene bisadduct ($C_{60}Ac_2$) could be encapsulated within this cubic cage. More intriguingly, this cage can selectively bind $C_{60}Ind_2$ from the reaction mixture containing C_{60} and C_{60}Ind. In a similar manner, the mixture of C_{60} and anthracene in the presence of cage $[Fe_8\mathbf{1.13}_6]^{8+}$ exclusively formed the bisadduct $C_{60}Ac_2$ within the cage cavity, contrary to that no adduct forms in the absence of cage under the same condition. In other words, the introduction of this supramolecular cage into the chemical manipulation of fullerenes is conducive to enhance the chemical reactivity and selectivity of Diels-Alder adduct reaction on C_{60}, thus giving the specific bisadduct, which is applied in organic photovoltaics.[18]

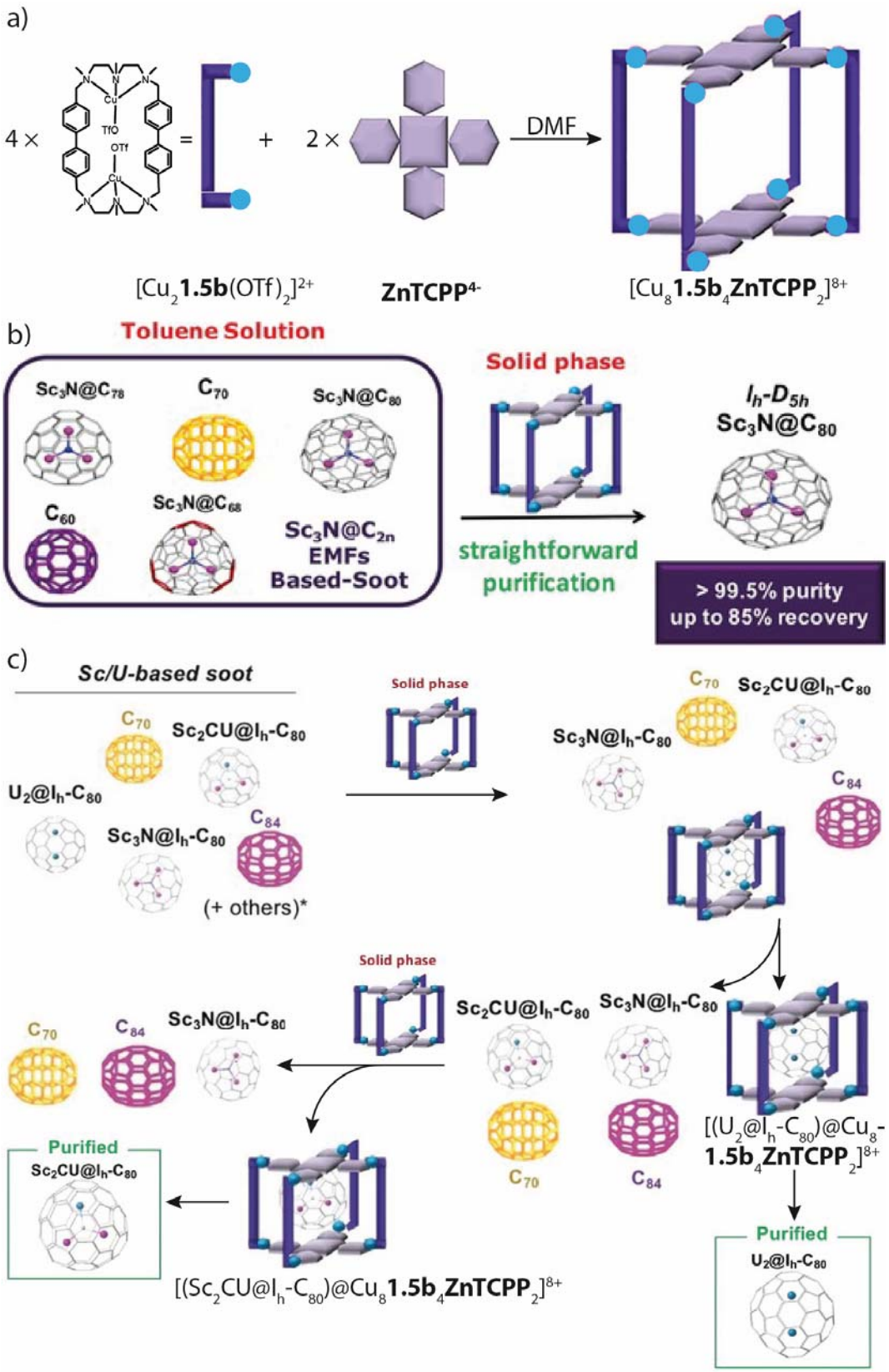

Figure 1.15 Self-assembly of the tetragonal prismatic cage $[Cu_8$**1.5b**$_4$**ZnTCPP**$_2]^{8+}$ and its application in fullerene separation. (a) The cage was assembled by Cu-precursors and tetracarboxylated Zn-porphyrin panels. (b) This cage can separate the $Sc_3N@C_{80}$ from the Sc_3N-based fullerene soot. Reproduced with permission from reference.[73] Copyright © (2017) Wiley-VCH Verlag GmbH & Co. KGaA, Weinheim. (c) Sequential purification of $U_2@C_{80}$ and $Sc_2CU@C_{80}$ from Sc/U-based soot is realized by using this cage. Adapted with permission from reference.[74] Copyright © (2018) Wiley-VCH Verlag GmbH & Co. KGaA, Weinheim.

Based on the above-mentioned cage $[Pd_8\mathbf{1.5b}_4\mathbf{ZnTCPP}_2]^{8+}$ that can bind fullerenes, ranging from C_{60} to C_{84}, Ribas *et al* replaced the Pd-based molecular clip by a novel Cu-based molecular clip, which was more labile in the coordination center, facilitating the guest uptake/release in the assembled cage $[Cu_8\mathbf{1.5b}_4\mathbf{ZnTCPP}_2]^{8+}$ compared to the analogous Pd-mediated cage.[73] The solid sample of cage $[Cu_8\mathbf{1.5b}_4\mathbf{ZnTCPP}_2](OTf)_8$ was treated with a toluene solution of Sc_3N-based fullerene mixture, comprising C_{60}, C_{70}, $Sc_3N@C_{68}$, $Sc_3N@C_{78}$, $Sc_3N@C_{80}$. This experiment reflects that the relatively small fullerene derivatives tend to be captured by the cage in the solid phase, thus remaining the single species, namely $Sc_3N@C_{80}$, in toluene solution (Figure 1.15b). HPLC monitoring of this isolated supernatant shows the purity of $Sc_3N@C_{80}$ is up to 99.5 % after merely one simple separation, and the separated $Sc_3N@C_{80}$ consists of two isomers, i.e. $Sc_3N@I_h\text{-}C_{80}$ and $Sc_3N@D_{5h}\text{-}C_{80}$. More intriguingly, the fullerene-filled cages in the solid phase can release the entrapped fullerenes, thus being reusable by means of their solvent-washing approach, which will be explained in the following section.

One year later, the same first author published another related work, involving the anion-exchanged counterpart, namely cage $[Cu_8\mathbf{1.5b}_4\mathbf{ZnTCPP}_2](BArF)_8$.[74] They utilized this cage to realize the purification of particular fullerene derivatives from the Sc/U-based soot, consisting of C_{70}, C_{84}, $Sc_3N@I_h\text{-}C_{80}$, $Sc_2CU@I_h\text{-}C_{80}$, $U_2@I_h\text{-}C_{80}$ as well as other minor species (Figure 1.15c). Soaking the solid of cage $[Cu_8\mathbf{1.5b}_4\mathbf{ZnTCPP}_2](BArF)_8$ in the toluene solution of the Sc/U-based fullerene mixture promotes the cage to bind all the $U_2@I_h\text{-}C_{80}$ from the solution phase after 6 h, monitored by LDI-TOF mass spectra of the supernatant solution during this process. On the virtue of the classic solvent-washing approach, the entrapped $U_2@I_h\text{-}C_{80}$ can be readily isolated, thus regenerating the empty hosts. Subsequent addition of this host into the toluene solution of the remaining fullerene mixture suggests that the cage is able to selectively encapsulate $Sc_2CU@I_h\text{-}C_{80}$ in a similar manner to $U_2@I_h\text{-}C_{80}$. Accordingly, this cage system can purify two different metallofullerenes sequentially in this fairly simple and fast way. It is noteworthy that these two isolated metallofullerenes ($U_2@I_h\text{-}C_{80}$ and $Sc_2CU@I_h\text{-}C_{80}$) as well as another co-existed metallofullerene ($Sc_3N@I_h\text{-}C_{80}$), cannot be separated from each other using HPLC techniques. The different binding abilities of this cage towards these three metallofullerenes is presumably caused by their distinct electron density distribution, originating from their inner metal clusters. All in all, the recyclable nature and efficient separation shows the promising prospect of this coordination cage in fullerene purification, particularly for endohedral metallofullerenes.

1.2.3 Controllable release of the entrapped fullerene

Another crucial property for fullerene receptors is the controllable release of the entrapped fullerenes from the inner cavities under different stimuli, which facilitates reusing the host material and collecting the isolated fullerene derivatives. Due to the initial design of fullerene receptors for the enhanced binding affinity, a majority of them are unable to liberate guests once bound, which precludes their practical application in fullerene purification. In recent years, chemists have been devoting themselves to developing supramolecular host materials with controllable guest absorption/release.[75] Some harsh conditions, such as high temperature and acidic/basic treatment, have been employed in the supramolecular fullerene receptors to achieve this aim. Temperature, as a common stimulus, can adjust the binding affinity of hosts for fullerenes, thus releasing guests at the particular temperature.[76-77] This method,

generally entailing the regulation of reaction temperature in a broad range, however, is often criticized for the consumption of large amounts of energy in its industrialization process. Another frequently-used protocol is utilizing acid to alter the charge properties of hosts or destroy the linking hydrogen/coordination bonds of frameworks, hence liberating the encapsulated fullerenes.[29, 78] The subsequent addition of a base contributes to the recovery of hosts' fullerene-binding abilities. This strategy requires the continuous addition of acid/base to realize multiple cycles of fullerene separation and is disturbed by the gradually increasing concentration of salt. Herein, we will present other proven approaches to control the fullerene binding/liberation from the following three aspects: adjustment on the coordination environment of backbones or metal nodes as well as solvent effects.

1.2.3.1 Adjustment of the coordination environment of backbones

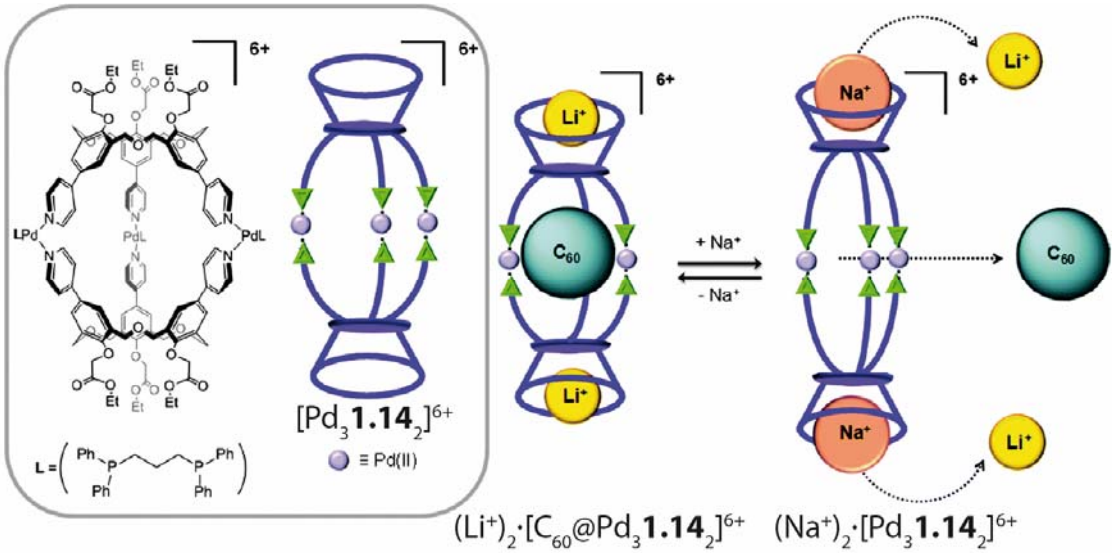

Figure 1.16 Self-assembly of the cage $[Pd_3\mathbf{1.14}_2]^{6+}$. Binding of cations in the external ester pocket triggers to the alteration of the binding affinities towards C_{60} in the central pocket. Reproduced from reference[41] with permission from the Royal Society of Chemistry.

In 1999, Shinkai and co-workers reported the first coordination-driven cage $[Pd_3\mathbf{1.14}_2]^{6+}$ that can act as a fullerene binder.[79] The ligand **1.14** is based on oxacalix[3]arene with ester chains and coordinates to the cis-protected Pd-precursors to yield the cage with a large inner cavity (Figure 1.16). The binding constant for the formation of the 1:1 host-guest complex $[C_{60}@Pd_3\mathbf{1.14}_2]^{6+}$ is 54 M^{-1} in 1,2-dichloroethane at 298 K. Besides the binding abilities of the central cavity, the peripheral ester chains in proximity allow for the complexation of small cations, for example, Li^+ and Na^+. Combination of Li^+ cations induces the adjacent phenyl groups becoming more flattened, thus altering the shape and size of the center cavity.[80] The resulting cavity of $(Li^+)_2[Pd_3\mathbf{1.14}_2]^{6+}$ is more suitable for the rigid, spherical C_{60}, resulting in the enhanced binding constant, up to 2100 M^{-1}. On the contrary, when the larger-sized Na^+ cations are bound to the ester pockets, the shrinkage of the inner cavity in the cage $(Na^+)_2[Pd_3\mathbf{1.14}_2]^{6+}$ is observed, accompanied by the significant decrease of binding constant for the C_{60}-binding (smaller than 5 M^{-1}). Accordingly, the cation-triggered adjustment on binding affinities of this host is employed to realize the guest uptake/release in a reversible manner.

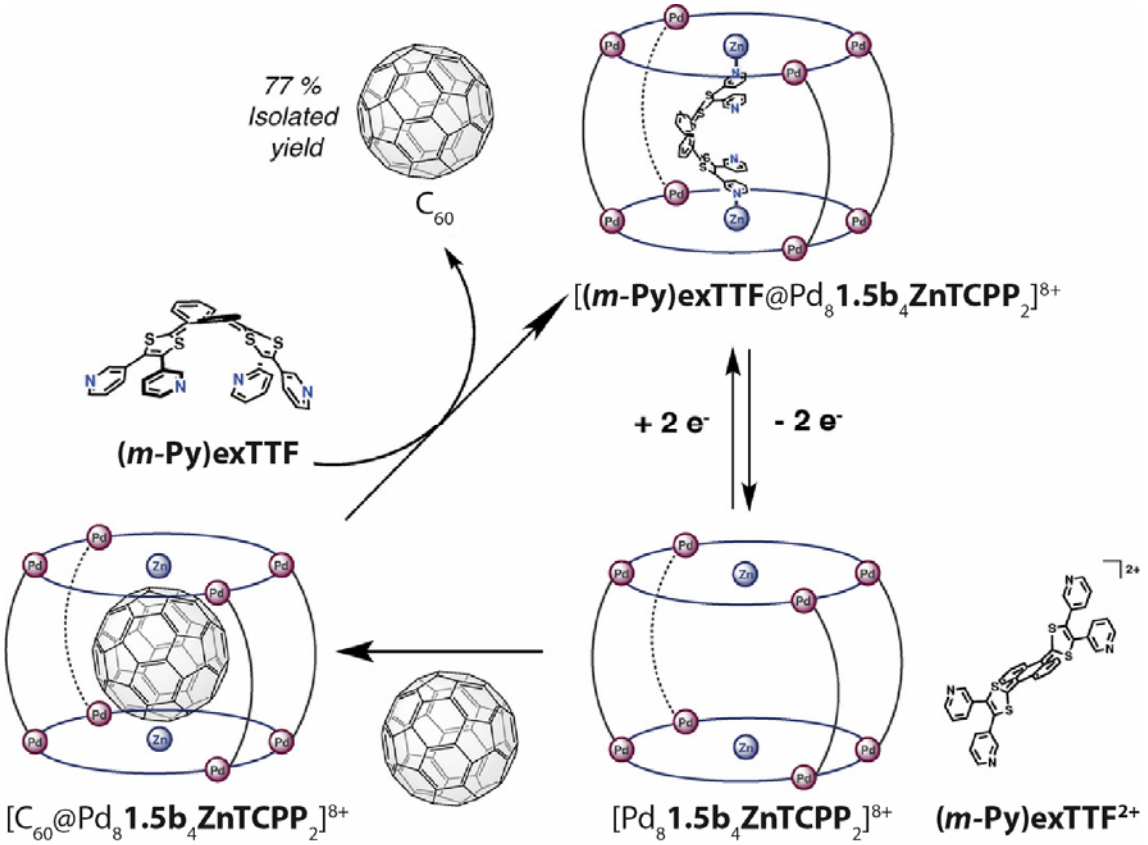

Figure 1.17 Schematic representation of C_{60} uptake/release from the cage $[Pd_8$**1.5b**$_4$**PdTCPP**$_2]^{8+}$ controlled by competitive guest **(*m*-Py)exTTF**. Reproduced with permission from reference.[81] Copyright © (2017) Wiley-VCH Verlag GmbH & Co. KGaA, Weinheim.

For the above described tetragonal prismatic cage $[Pd_8$**1.5b**$_4$**PdTCPP**$_2]^{8+}$ that can host C_{60} within its cavity, Ribas and Sallé *et al* employed another stronger competitive guest **(m-Py)exTTF** to replace the initially entrapped C_{60} owing to the former's coordination preference to the Zn nodes on the porphyrin panels (Figure 1.17).[81] Moreover, the bent geometry of the neutral **(m-Py)exTTF** can change into the planar geometry of the dicationic **(m-Py)exTTF^{2+}** through chemical oxidation, and vice versa. By taking advantage of this reversible redox property, the release/uptake of this competitive guest in the cage cavity can be triggered by chemical oxidation/reduction. Indeed, the oxidation of the host-guest complex $[$**(m-Py)exTTF**$@Pd_8$**1.5b**$_4$**PdTCPP**$_2]^{8+}$ induces the ejection of the **(m-Py)exTTF^{2+}** owing to the evident alteration in its length and charge nature, which is unsuitable to be encapsulated inside the cage. Once the competitive TTF-based guest is oxidized, the cage with the re-obtained empty cavity is capable of binding C_{60}, thus realizing the fullerene binding/release in a controlled manner. The combination of chemical stimulus and redox stimulus in this system provides the new idea to fulfill a recyclable fullerene purification system.

1.2.3.2 Adjustment of the coordination environment of metal nodes

Apart from altering the coordination environment of backbones, the more straightforward method is the direct adjustment of the metal nodes, thus disassembling/reassembling the fullerene receptors. This approach is generally controlled by chemical stimuli, and here we showcase three unique systems to accomplish the efficient release of the sequestered fullerenes.

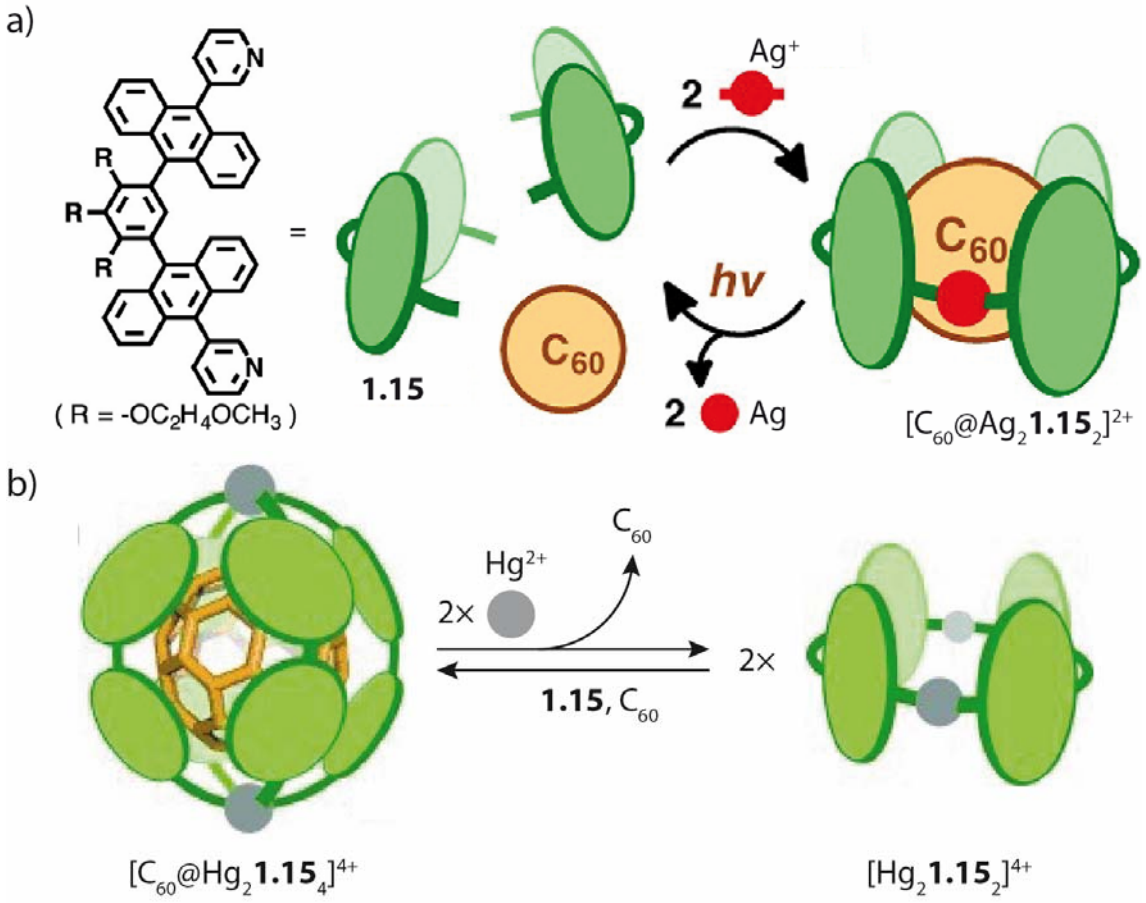

Figure 1.18 (a) Self-assembly of the C_{60}-filled ring $[C_{60}@Ag_2\mathbf{1.15}_2]^{2+}$ and its disassembly triggered by photoirradiation. Adapted with permission from reference.[82] Copyright © (2013) American Chemistry Society. (b) The metal-ligand stoichiometry-induced conversion between cage $[Hg_2\mathbf{1.15}_4]^{4+}$ and ring $[Hg_2\mathbf{1.15}_2]^{4+}$ as well as their distinct C_{60}-binding abilities. Adapted with permission from reference.[83] Copyright © (2014) Wiley-VCH Verlag GmbH & Co. KGaA, Weinheim.

With the participation of C_{60}, the anthracene-paneled ligands **1.15** assemble with Ag^+ cations into the molecular ring $[C_{60}@Ag_2\mathbf{1.15}_2]^{2+}$, a novel open structure compared to the enclosed Pd-mediated cage $[Pd_2\mathbf{1.2}_4]^{4+}$ (Figure 1.18a).[82] This molecular ring can not only selectively encapsulate C_{60} from a fullerene mixture like the spherical cage $[Pd_2\mathbf{1.2}_4]^{4+}$, but also accommodate a series of fullerene derivatives bearing large substituents due to its open geometry. Remarkably, upon photoirradiation to reduce the Ag^+ nodes, the C_{60}-filled ring $[C_{60}@Ag_2\mathbf{1.15}_2]^{2+}$ decomposes and liberates the central C_{60} simultaneously. Furthermore, the supplementary addition of Ag^+ into the decomposed solution can regenerate the host-guest complex $[C_{60}@Ag_2\mathbf{1.15}_2]^{2+}$. This strategy adopts the readily tunable light as a stimulus to release fullerenes, motivating supramolecular chemists to develop more photoswitchable fullerene receptors.

One year later, the same first author reported the molecular cage $[Hg_2\mathbf{1.15}_4]^{4+}$ and the molecular ring $[Hg_2\mathbf{1.15}_2]^{4+}$, quantitatively prepared in the corresponding metal-ligand stoichiometry at room temperature (Figure 1.18b).[83] The different enclosure degree of the cage and ring leads to their distinct fullerene-binding abilities: the cage $[Hg_2\mathbf{1.15}_4]^{4+}$ is able to host C_{60} and C_{70}, whereas the ring $[Hg_2\mathbf{1.15}_2]^{4+}$ loses binding abilities towards both. On the basis of this experimental phenomenon, the modulation of metal-ligand stoichiometry can effectively realize the structural conversion between cage and ring, thus binding or releasing fullerenes.

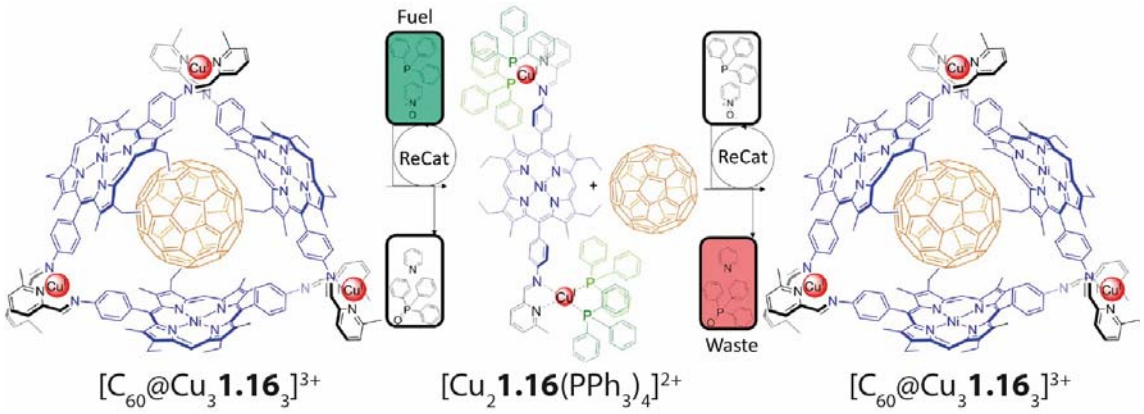

Figure 1.19 The disassembly/reassembly of the C_{60}-occupied triangle $[C_{60}@Cu_3\mathbf{1.16}_3]^{3+}$ triggered by the addition of triphenylphosphine, pyridine N-oxides as well as the oxo-transfer catalyst (ReCat). Reproduced from reference.[84]

In 2015, Nitschke and co-workers built molecular triangle $[Cu_3\mathbf{1.16}_3]^{3+}$ based on Ni-porphyrin-paneled ligands **1.16** and tetrahedral Cu^+ cations.[84] This molecular triangle can encapsulate C_{60} on account of the face-to-face aromatic interaction between fullerene and porphyrin (Figure 1.19). Inspired by the preferred formation of the heteroleptic complex $[CuN_2P_2]^+$ in the presence of both nitrogen and phosphine ligands,[85] the addition of another competitive ligand PPh_3 can alter the coordination mode of Cu^+ nodes, forming $[Cu_2\mathbf{1.16}(PPh_3)_4]^{2+}$ and liberating the inner C_{60}. In addition, the transfer of oxygen from pyridine *N*-oxides to PPh_3 can be rapidly realized with the help of a rhenium-based oxo-transfer catalyst (ReCat).[86] Indeed, application of this method helps reassemble the molecular triangle from the fragment $[Cu_2\mathbf{1.16}(PPh_3)_4]^{2+}$ through the addition of pyridine *N*-oxides and ReCat to react with PPh_3, generating the non-coordinating $OPPh_3$. This combined usage of PPh_3 and pyridine *N*-oxides determines the uptake and release of C_{60} within the molecular triangle, and the reaction rate can be even controlled by the amount of used PPh_3 and the concentration/choice of the oxo-transfer catalyst.

1.2.3.3 Solvent-induced release

Most of the aforementioned approaches to collect the entrapped fullerenes rely on chemical stimuli, but the continuous introduction of chemical stimuli certainly hinders reusing the host material in multiple cycles. In the meantime, it will engender some practical problems, particularly in terms of separation cost, time- and energy-consumption. In 2014, Ribas *et al* presented a fast and efficient protocol, i.e. solvent washing, to release the encapsulated fullerene from the tetragonal prismatic cage $[Pd_8\mathbf{1.5b}_4\mathbf{ZnTCPP}_2]^{8+}$.[59] The separation process could be divided into the following steps (Figure 1.20): firstly, the solid sample of $[Pd_8\mathbf{1.5b}_4\mathbf{ZnTCPP}_2](BArF)_8$ suspended in ethyl ether is filled up in a celite column; secondly, the toluene solution of C_{60} is used as the eluent to pass through the column, enabling the cage to absorb the C_{60} from the solution phase until reaching the saturated state, monitored by mass spectrometry; thirdly, the mixed solvent (1,2-dichlorobenzene/carbon disulfide 1/1, v/v), which has the high solubility for C_{60} and the low solubility for the cage species, facilitates the effective extraction of all the sequestered C_{60} from the cage cavity through washing the stationary phase of column after 5 runs; afterwards, the solid of the cage recovers its empty cavity and can re-bind C_{60} from the toluene solution in multiple cycles, supported by mass spectrometry monitoring; at last, the treatment of the solid phase with pure acetonitrile allows to re-obtain 91.4% of

host material after five times binding-release processes. This solvent-washing strategy is based on distinct solubility of fullerenes and cage, and does not entail other chemical inputs and specific instruments to fulfill the fullerene separation, which has practical applications in fullerene purification.

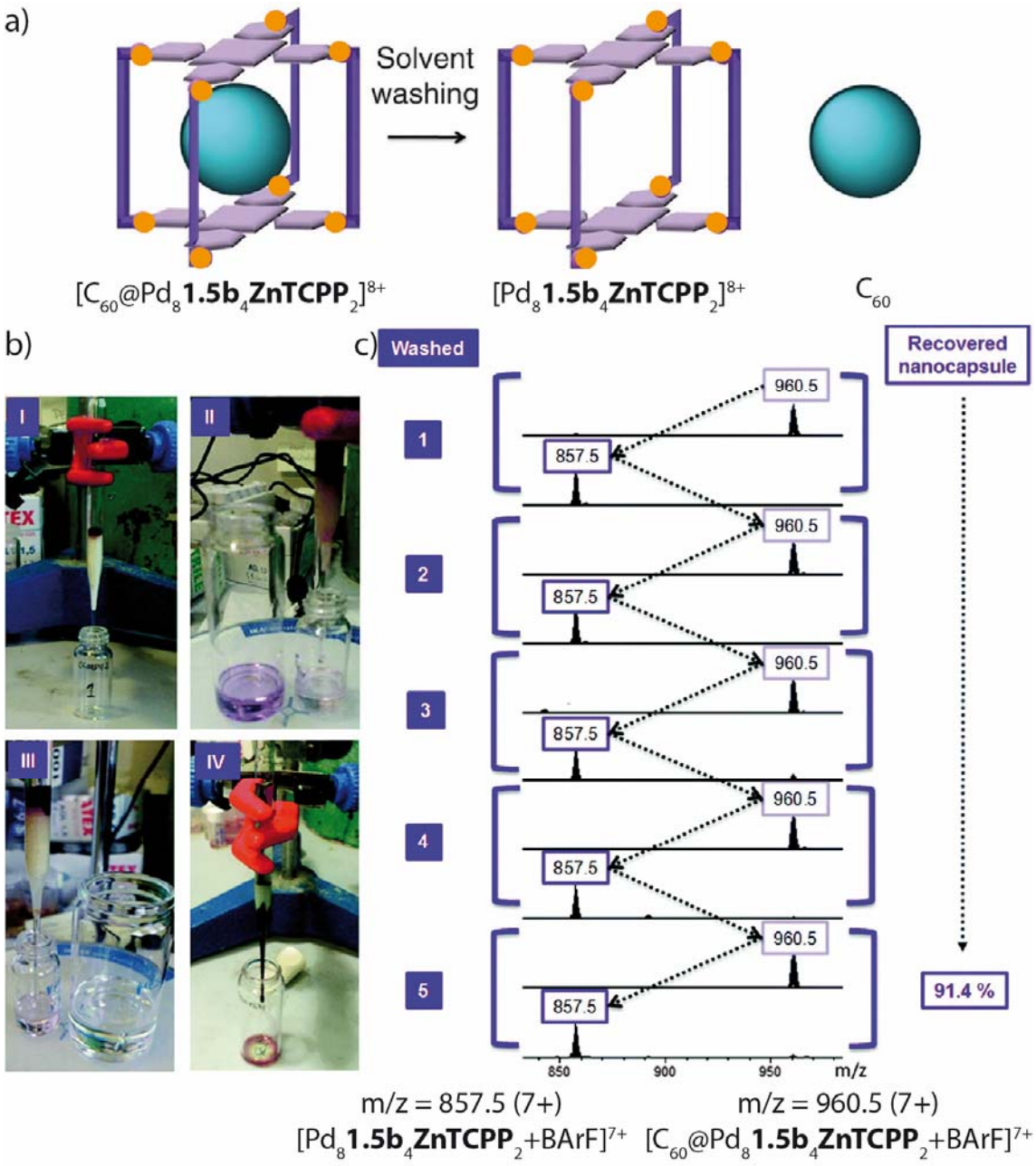

Figure 1.20 (a) The ejection of C_{60} from the tetragonal prismatic cage $[Pd_8\mathbf{1.5b_4ZnTCPP_2}]^{8+}$ accomplished by the solvent washing approach. (b) and (c) images and mass spectrometry monitoring of these related solvent-extraction processes. Adapted with permission from reference.[59] Copyright © (2014) Springer Nature.

1.3 Strategies for achieving Pd-mediated heteroleptic cages

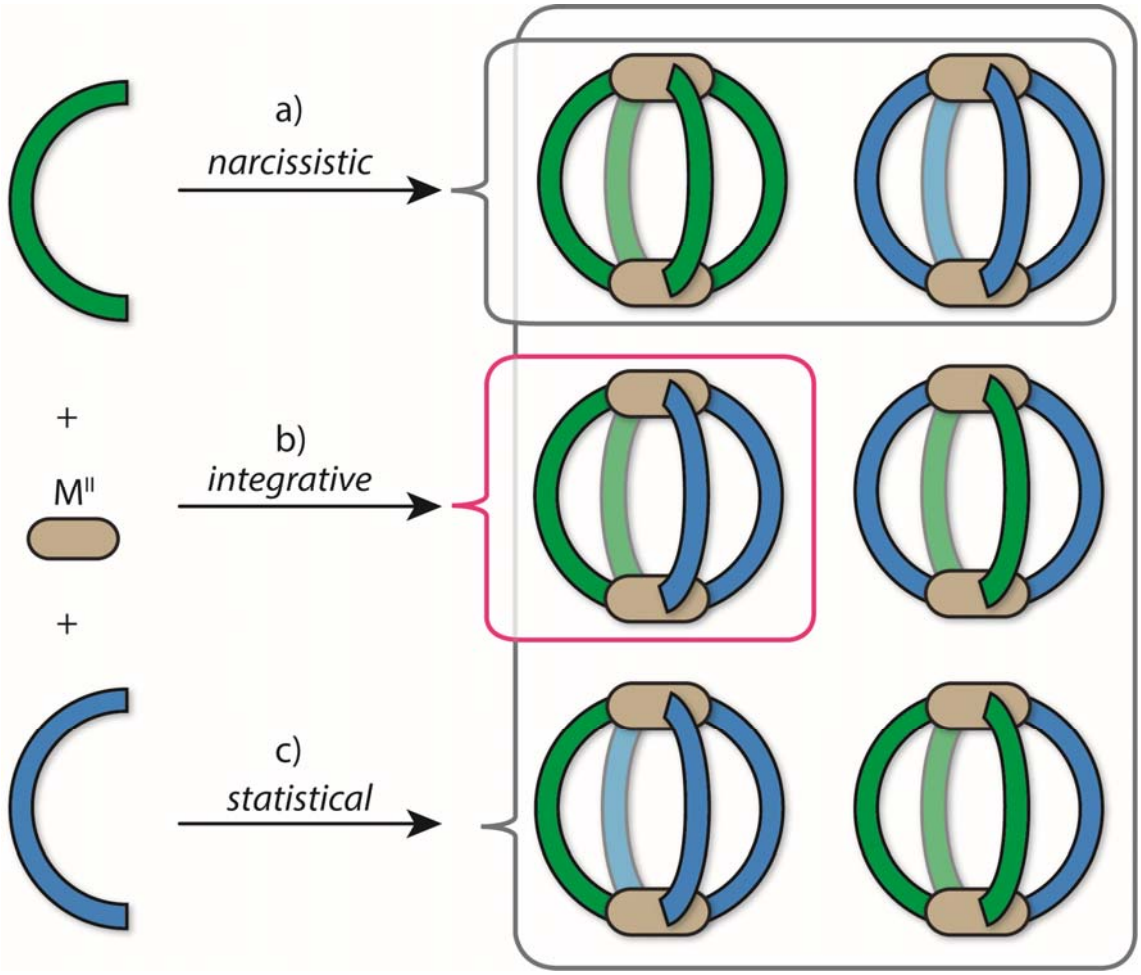

Figure 1.21 Coordination-driven self-assemblies based on square-planar M^{II} and two different ligands: (a) Narcissistic self-sorting that gives the mixture of two homoleptic cages; (b) integrative self-sorting that generates a single heteroleptic cage (here *cis*-$[Pd_2L_2L'_2]^{4+}$ as an example); (c) statistical mixture based on these two ligands. Reproduced from reference[87] published by The Royal Society of Chemistry.

Among the plethora of reported coordination cages, Pd-mediated coordination cages based on nitrogen donor ligands have gained a lot of attention due to these following features: stable square-planar coordination geometry of Pd^{II} cations conducive for molecular design; diamagnetic property that allows the facile characterization by NMR spectroscopy; dynamically reversible Pd–N bonds that facilitate the cage formation under equilibrium conditions.[88] The design and preparation of homoleptic cages $[Pd_nL_{2n}]^{2n+}$ comprising the square-planar Pd^{II} nodes and bis-monodentate ligands L, has been intensively discussed according to different factors, in particular, ligands' shape, size, bending angle and flexibility.[89-90] For the sake of introducing more functionalities, construction of heteroleptic cages affords the possibility to install two different ligands within a single cage framework. With regard to the self-assembly of two banana-shaped ligands with a square-planar metal ion, such as Pd^{II}/Pt^{II}, the outcome generally could be three scenarios (Figure 1.21): (a) narcissistic self-sorting forms the mixture of two homoleptic cages due to the huge differences between two used ligands in terms of shape and size, which hampers the formation of heteroleptic cages; (b)

integrative self-sorting generates only one heteroleptic cage species on the basis of particular interactions; (c) statistical mixture consists of a collection of cages with different ligand ratios, i.e. $[Pd_2L_nL'_{4-n}]^{4+}$ (n = 0 – 4). Of great interest is the self-assembly of heteroleptic cages in a controllable manner by virtue of precise design, a challenging task limited by the entropic propensity during the assembly process. Several known strategies to access Pd-mediated heteroleptic cages have been established, roughly divided into three categories (Figure 1.22): assembly-dependent approaches, coordination-dependent approaches as well as hierarchical assembly.[87, 91] Herein, we mainly discussed heteroleptic cages constructed by unprotected Pd^{II} cations that can link four ligands, instead of the *cis*-protected Pd/Pt precursors with the remaining two coordination sites, such as $[Pd(en)]^{2+}$, $[Pt(PEt_3)_2]^{2+}$, which have been studied in depth by Stang, Fujita, and Mukherjee *et al*.[92-94]

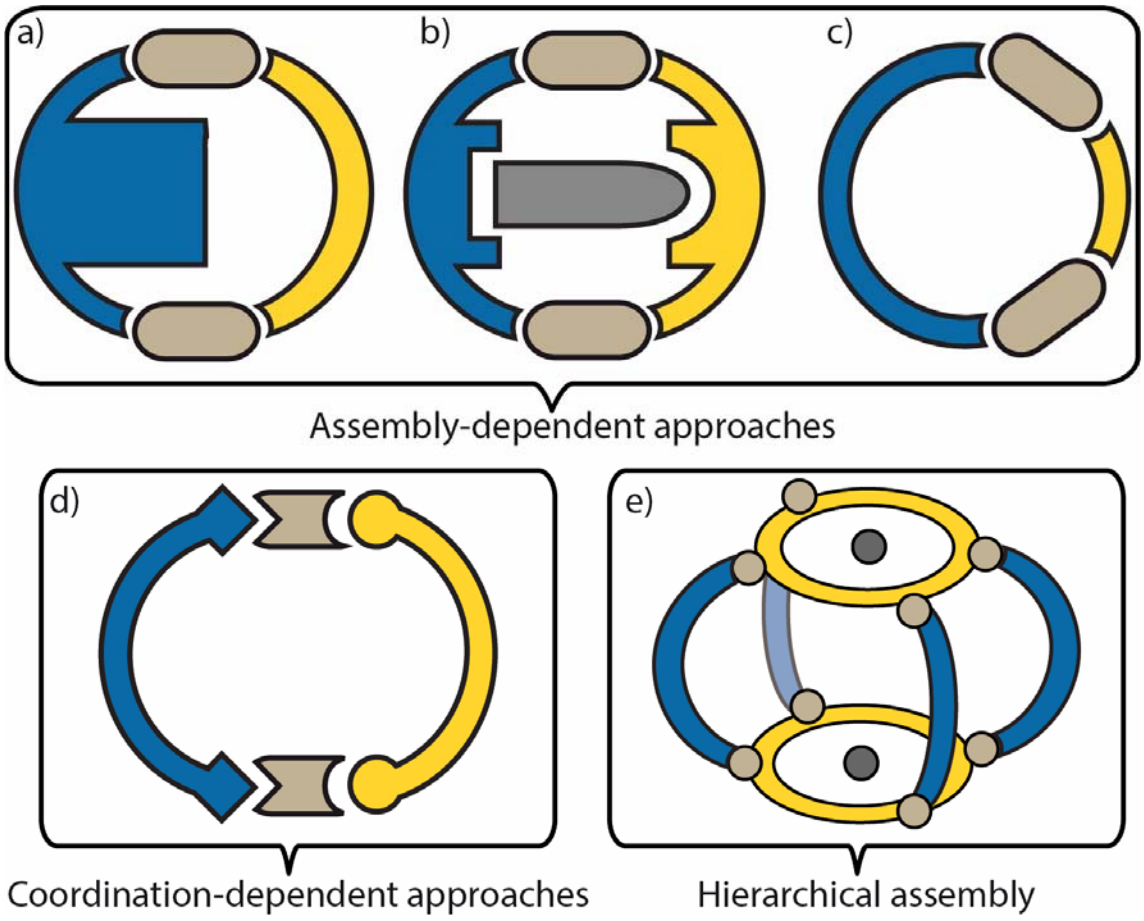

Figure 1.22 Different strategies to achieve heteroleptic coordination cages: (a) Endohedral modification of the bulky group to induce the formation of the heteroleptic cage; (b) the introduction of template molecules to stabilize the host-guest complex; (c) the employment of two shape-complementary ligands in cage formation; (d) coordination-dependent approaches, involving steric constraint and hydrogen bonding; (e) the hierarchical assembly of pre-organized molecular units and bridging ligands. Adapted from reference.[91]

1.3.1 Assembly-dependent approaches

1.3.1.1 Endohedral functionalization

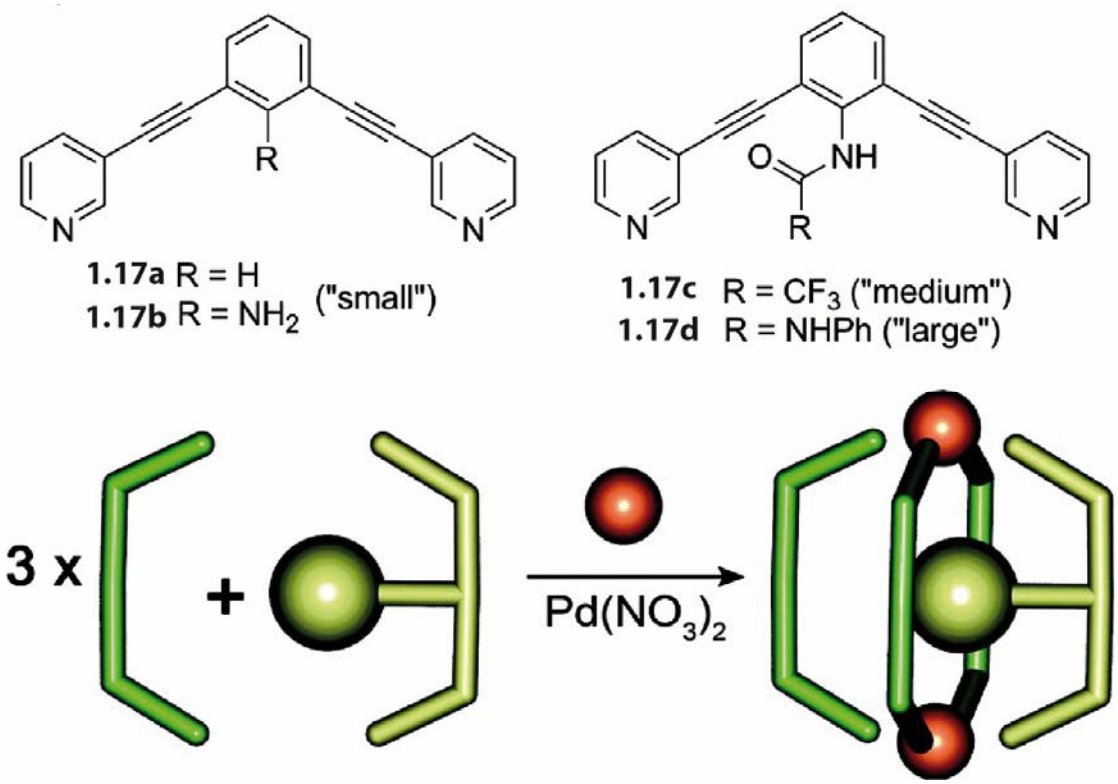

Figure 1.23 Ligands used in the study of the steric effect between internally bulky substituents in the cage formation. The combination of ligands with small and large-sized substituents induces the formation of $[Pd_2L_3L']^{4+}$. Adapted with permission from reference.[95] Copyright © (2011) American Chemistry Society.

In 2011, Hooley *et al* systemically studied the steric constraints within the prototypical $[Pd_2L_4]^{4+}$ cage, originating from internal substituents (Figure 1.23). For the banana-shaped ligands (**1.17a** and **1.17b**) bearing small inward-pointing groups, they can form respective homoleptic cages smoothly.[95-96] The weakly nucleophilic amine group of ligand **1.17b** allows for the further modification by reacting with trifluoroacetic anhydride or phenylisocyanate to yield the medium-sized ligand **1.17c** or large-sized ligand **1.17d**, respectively. Experimentally, ligand **1.17c** with the medium-sized trifluoroacetate group cannot give identifiable NMR signals after treating with $Pd(NO_3)_2$ in deuterated DMSO, consistent with the unfavorable result of molecular simulation. Thereafter, the examination of heteroleptic cage formation was performed between ligands **1.17a** and **1.17b** with Pd^{II} cations which gave a statistical mixture, identified by NMR spectra and ESI mass spectra. In contrast, the 3:1 mixture of ligand **1.17a** and **1.17c** reacts with Pd^{II} cations under similar condition, exclusively generating the mixture of $[Pd_2\mathbf{1.17a}_4]^{4+}$ and $[Pd_2\mathbf{1.17a}_3\mathbf{1.17c}]^{4+}$ with the ratio of about 3:1. That points out that the introduction of internally bulky substituents triggers the selective formation of heteroleptic cages, affected by the steric constraint within the cage cavity. By using a similar strategy, Fujita's group reported the sole formation of heteroleptic cage $[Pd_{12}L_{23}L']^{24+}$, which accommodates a protein fragment within a giant cavity.[97]

1.3.1.2 Templating effects

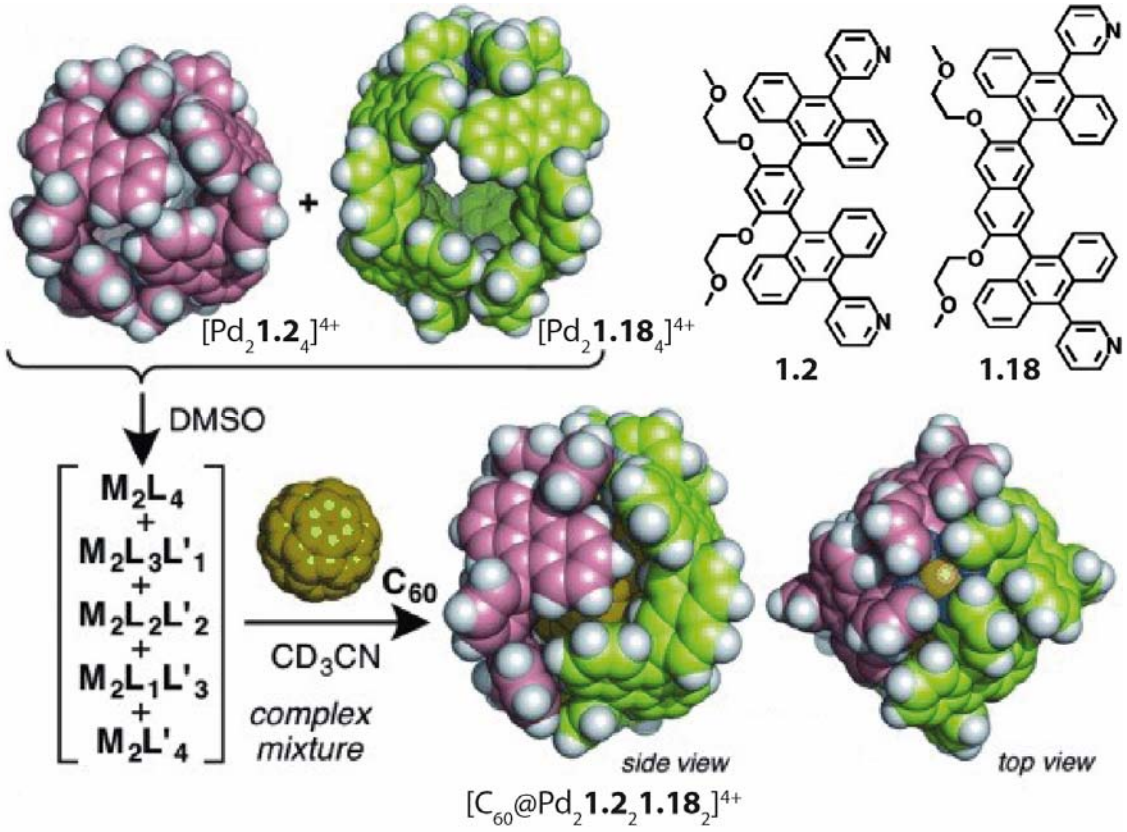

Figure 1.24 C_{60}-induced self-assembly of the heteroleptic cage *cis*-$[C_{60}@Pd_2\mathbf{1.2}_2\mathbf{1.18}_2]^{4+}$. The 1:1 mixture of two homoleptic cages based on the short ligand **1.2** and the long ligand **1.18** gives the statistical mixture with the formula $[Pd_2L_nL'_{4-n}]^{4+}$ (n = 0 – 4), followed by adding C_{60} to form *cis*-$[C_{60}@Pd_2\mathbf{1.2}_2\mathbf{1.18}_2]^{4+}$ exclusively. Adapted with permission from reference.[98] Copyright © (2015) Wiley-VCH Verlag GmbH & Co. KGaA, Weinheim.

The above-mentioned anthracene-functionalized ligand **1.2** can assemble with Pd^{II} into the homoleptic cage $[Pd_2\mathbf{1.2}_4]^{4+}$, which shows the selective binding behavior towards C_{60} over C_{70} owing to the limited cage cavity.[49] Yoshizawa and co-workers synthesized another longer ligand **1.18** to expand the inner pocket in the resulting cage $[Pd_2\mathbf{1.18}_4]^{4+}$, which allows it to accommodate larger guests, such as C_{70} and a mono-functionalized fullerene derivative (Figure 1.24).[98] The initial mixture of the equimolar amount of two homoleptic cages in DMSO indicates the formation of a statistical mixture, but subsequent addition of C_{60} into the acetonitrile solution of the complex mixture drives the dynamic equilibrium towards a single product, identified as $[C_{60}@Pd_2\mathbf{1.2}_2\mathbf{1.18}_2]^{4+}$ by ESI mass spectrum. The determination of *cis*-configuration for $[C_{60}@Pd_2\mathbf{1.2}_2\mathbf{1.18}_2]^{4+}$ is supported by force-field calculation, wherein the *cis*-isomer is 22.2 kcal/mol lower than its *trans*-isomer. In combination with other template effects,[66, 99-100] the guest acts as template molecules to form heteroleptic cages or specific geometries, which seems to be an effective protocol to achieve energetically favorable structures.

1.3.1.3 Shape-complementarity

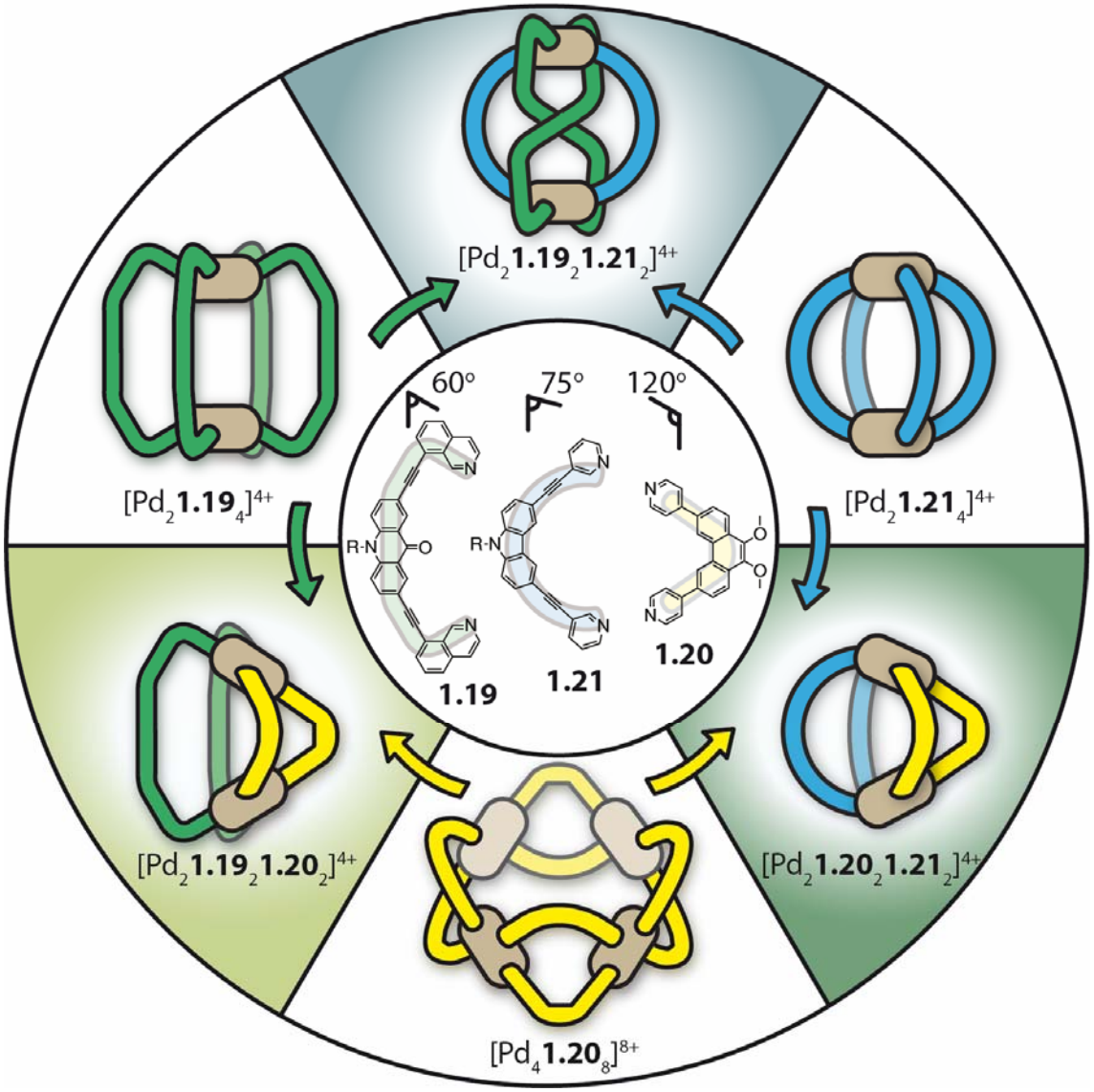

Figure 1.25 Heteroleptic and homoleptic cages based on three shape-complementary ligands as well as their interconversions. Adapted from reference.[101]

In 2016, Clever and co-workers reported a pair of precisely designed ligands **1.19** and **1.20** exhibiting shape complementarity, wherein the native donor angles of inward-pointing isoquinoline donors and outward-pointing pyridine donors are 60° and 120°, respectively (Figure 1.25).[102] For the Pd-mediated assemblies of homoleptic cages, ligands **1.19** and **1.20** give the cages $[Pd_2\mathbf{1.19}_4]^{4+}$ and $[Pd_4\mathbf{1.20}_8]^{4+}$ by heating with $[Pd(CH_3CN)_4](BF_4)_2$ in DMSO, respectively, owing to different bending angles between these two ligands. Based on the geometrical complementarity of ligands, the 1:1:1 mixture of ligand **1.19**, ligand **1.20** and Pd^{II} salt generates a single product upon heating, which is confirmed by ESI mass spectrum with the signals assigned to the cage species $[Pd_2\mathbf{1.19}_2\mathbf{1.20}_2]^{4+}$. The definition of $[Pd_2\mathbf{1.19}_2\mathbf{1.20}_2]^{4+}$ as *cis*-arrangement is strongly favored by theoretical calculation, and also exactly matches the coordination mode of square-planar Pd^{II} cations. Afterwards, the carbazole-based ligand **1.21** with the bite angle of 75° was also examined in the formation of heteroleptic cages. The homoleptic cage $[Pd_2\mathbf{1.21}_4]^{4+}$ was confirmed to

reorganize to the interpenetrated double cage [3Cl@Pd_4**1.21**$_8$]$^{5+}$ in the presence of 1.5 eq. amount of chloride anions (based on the molar amount of cage [Pd_2**1.21**$_4$]$^{4+}$).[103] Heating the mixture of ligands **1.20**, **1.21** and Pd^{II} cations in a 1:1:1 ratio in CD_3CN quantitatively form the heteroleptic cage *cis*-[Pd_2**1.20**$_2$**1.21**$_2$]$^{4+}$, unambiguously characterized by NMR, MS and X-ray analysis, indicating that the shape-complementary principle is still applicable in these two ligands.[101] Surprisingly, ligands **1.19** and **1.21** with relatively close bite angles can assemble with Pd^{II} into an unprecedented architecture *trans*-[Pd_2**1.19**$_2$**1.21**$_2$]$^{4+}$, whose crystal structure shows severely distorted ligands **1.19** bridging opposite Pd atoms like a ''figure eight''. Additionally, it is worth noting that all these three heteroleptic cages can be achieved through cage-to-cage transformation from corresponding homoleptic cages in an appropriate stoichiometry. Also, the ligand displacement occurs upon addition of the third ligand in the solution of heteroleptic cage *cis*-[Pd_2**1.20**$_2$**1.21**$_2$]$^{4+}$ or *trans*-[Pd_2**1.19**$_2$**1.21**$_2$]$^{4+}$, both forming the optimally geometry-matched cage *cis*-[Pd_2**1.19**$_2$**1.20**$_2$]$^{4+}$ due to the efficient design. This shape-complementary principle creates more possibilities to position two different functional backbones in a confined structure.

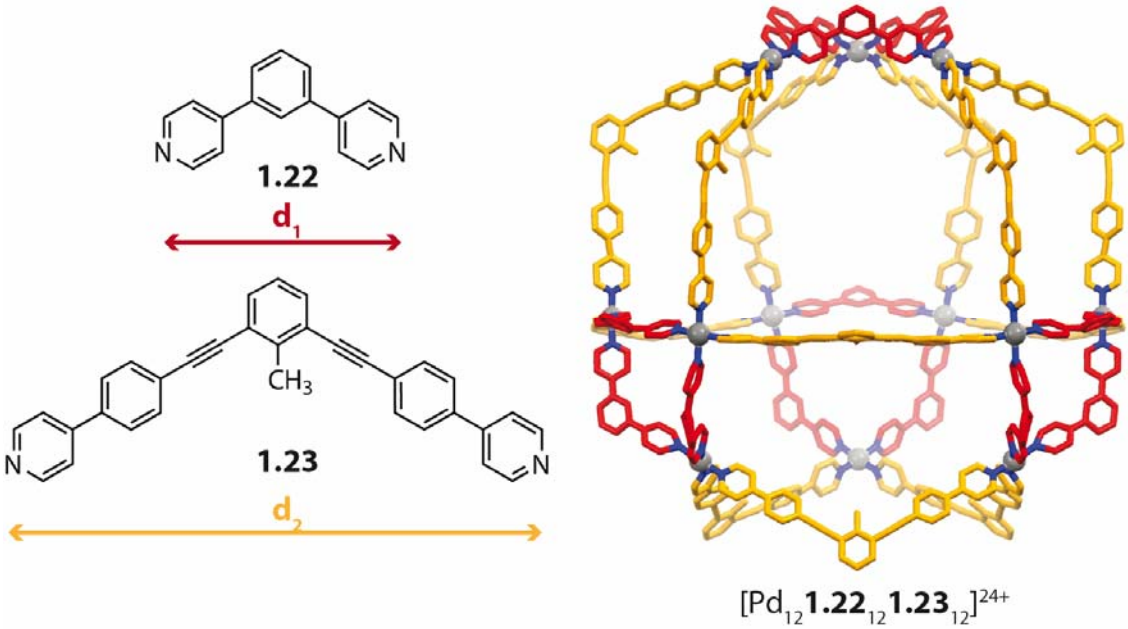

Figure 1.26 Self-assembly of the heteroleptic cage [Pd_{12}**1.22**$_{12}$**1.23**$_{12}$]$^{24+}$ based on two shape-similar ligands with different length. Adapted from reference.[87]

In 2014, another case of heteroleptic cages reported by Fujita and co-workers utilized the same-shaped ligands bearing a bend angle of 120^o but with different lengths between donor sites (Figure 1.26).[104] With regard to the formation of homoleptic cages based on these two ligands, previous works revealed the Pd-mediated self-assemblies of giant architectures [Pd_{12}**1.22**$_{24}$]$^{24+}$ and [Pd_{12}**1.23**$_{24}$]$^{24+}$.[105-106] The equimolar mixture of ligands **1.22**, **1.23,** as well as Pd^{II} cations, exclusively produces a single product, identified as [Pd_{12}**1.22**$_{12}$**1.23**$_{12}$]$^{24+}$ by CSI-TOF mass spectrum. Molecular modeling shows that the most favorable isomer of [Pd_{12}**1.22**$_{12}$**1.23**$_{12}$]$^{24+}$ ought to be the cantellated tetrahedral geometry with the T_d-symmetry, but the synchrotron analysis of crystals indicates its isomer with C_{3v}-symmetry. Moreover, screening of several bis-monodentate pyridine ligands reveals that the ratio of ligand lengths (r = d_2/d_1) greater than 2 contributes to form the defined heteroleptic cage, like the herein case (r ≈ 2.2), whereas the r value

ranging from 1.1 to 1.6 induces the formation of random mixtures assembled by two different ligands. This length-ratio-induced self-assembly of heteroleptic cages further enriches the assembly-dependent strategies.

1.3.2 Coordination-dependent approaches

Coordination-dependent approaches mainly rely on the employment of finely-designed donors to trigger the formation of heteroleptic cages, which can be more exactly described as donor-site engineering. Three pronounced advantages compared to assembly-dependent approaches: (a) the cage cavity of heteroleptic cages can be retained in the largest degree, not entailing the introduction of internally bulky substituents and template molecules; (b) there is no specific requests on geometries of backbones, which allows for the facile installation of more functional backbones into cage-like structures; (c) the chemical modification of donor groups is more straightforward to control the coordination modes of metal nodes, conducive for the more rational molecular design.

1.3.2.1 Steric constraints between donor-sites

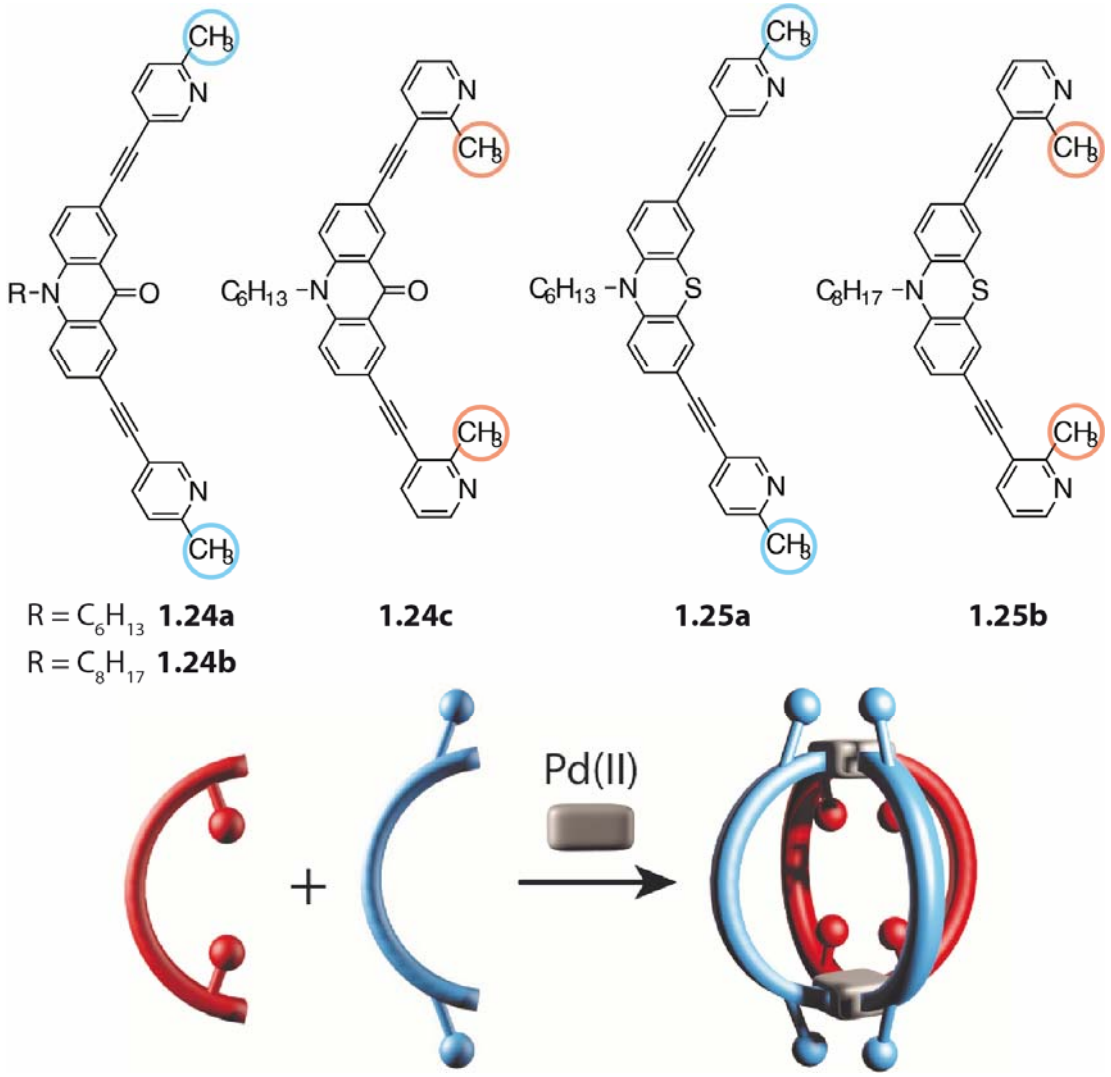

Figure 1.27 The acridone and phenothiazine picolyl ligands as well as their self-assembly of the heteroleptic cage $[Pd_2L_2L'_2]^{4+}$ induced by steric hindrance. Adapted from reference.[107]

Inspired by Fujita's and Schmittel's works introducing bulky-substituted donor ligands to construct mixed-ligand structures successfully,[108-109] Clever and co-workers prepared several ligands based on acridone or phenothiazine backbones with picolyl groups (Figure 1.27).[107] The over-congested coordination environment in the expected cage $[Pd_2L_4]^{4+}$ originated from methyl groups in proximity, and was meant to hinder the formation of homoleptic cages based on these ligands. Therefore, attempted assemblies of Pd-mediated homoleptic cages reveal that ligands **1.24c** and **1.25b** bearing inward-pointing methyl groups both generate the novel bowl species with the formula of $[Pd_2L_3(CD_3CN)_2]^{4+}$, whereas ligands **1.24b** and **1.25a** bearing outward-pointing methyl groups even yield the mixture of molecular bowl $[Pd_2L_3(CD_3CN)_2]^{4+}$ and ring $[Pd_2L_2(CD_3CN)_4]^{4+}$. In light of the severe steric restrictions caused by adjacent methyl groups on the same side, the combination of ligands **1.24b** and **1.24c** was considered to form a heteroleptic cage. Indeed, heating the mixture of ligands **1.24b**, **1.24c** and Pd^{II} cations in the 1:1:1 ratio for 8 h exclusively affords the heteroleptic cage *cis*-$[Pd_2$**1.24b**$_2$**1.24c**$_2]^{4+}$, a more favorable isomer relative to its *trans*-isomer supported by DFT calculation. The crystal structure of the prototypical Pd complex $[Pd(2\text{-picoline})_4]^{2+}$ also displays the *cis*-configured geometry. Afterwards, the construction of the heteroleptic cage incorporating two distinct backbones is also successfully realized between the acridone-based ligand **1.24b** and phenothiazine-based ligand **1.25b**, demonstrating the efficient acquirement of heteroleptic cages driven by designed donor sites.

1.3.2.2 Hydrogen-bonding between donor-sites

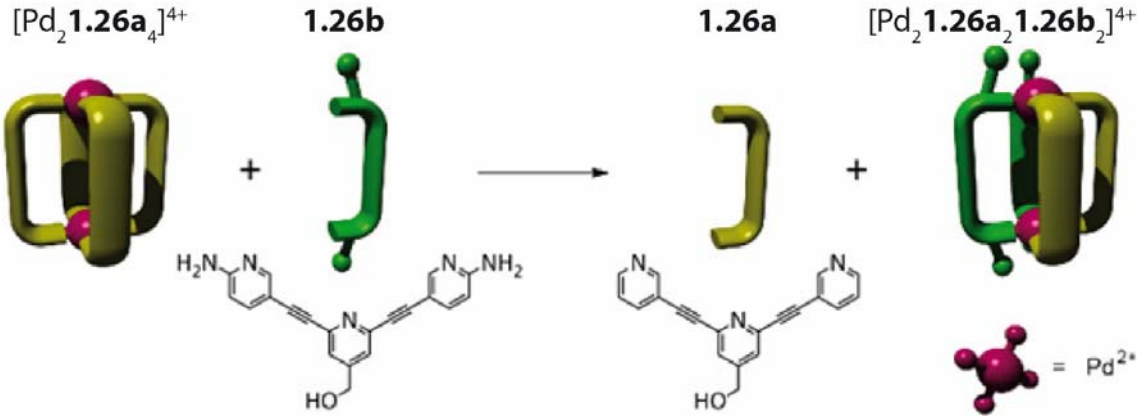

Figure 1.28 The conversion from the homoleptic cage $[Pd_2$**1.26a**$_4]^{4+}$ to the heteroleptic cage $[Pd_2$**1.26a**$_2$**1.26b**$_2]^{4+}$ by ligand displacement. Reprinted with permission from reference.[110] Copyright © (2016) American Chemistry Society.

In 2016, Crowley and co-workers used an *o*-amino-substituted pyridine ligand **1.26b** to partially replace the pristine ligand **1.26a** from the homoleptic cages $[Pd_2$**1.26a**$_4]^{4+}$, leading to the reassembly into a heteroleptic cage $[Pd_2$**1.26a**$_2$**1.26b**$_2]^{4+}$ (Figure 1.28).[110] The 2D NMR spectra and high-resolution ESI mass spectrum both support the existence of this heteroleptic cage species, whilst the *cis*-configuration is indicated by theoretical calculation. Relative to the archetypical ligand **1.26a**, the adjacent amino group with the electron-donating nature can enhance the donor strength of the coordination site as well as the steric hindrance in the surrounding of the coordination center. For the cage *cis*-$[Pd_2$**1.26a**$_2$**1.26b**$_2]^{4+}$, complementary hydrogen-bonding is deemed to form between amino groups of ligand **1.26b** and adjacent hydrogen atoms of ligand **1.26a** around the coordination center. This supplementary hydrogen-bonding interaction, as well as the steric clash between amino groups themselves, determine the exclusive formation of

cis-[Pd_2**1.26a**$_2$**1.26b**$_2$]$^{4+}$ instead of a complete displacement, albeit in the presence of excess ligand **1.26b**. This method provides a new idea to access heteroleptic cages, stabilized by hydrogen-bonding interactions from a particular pair of donor-sites.

1.3.3 Hierarchical assembly

A majority of the aforementioned strategies can realize a one-pot synthesis of heteroleptic cages through the straightforward reaction between multiple components in the correct stoichiometry, based on the precise design of supramolecular architectures. In contrast, for the sake of accessing more sophisticated structures, the hierarchical assembly has gained increasing attention in recent years.[91] The assembly of tetragonal prismatic cages reported by Ribas *et al* as mentioned above, is a classic case based on this approach in two steps (Figure 1.6). At first, each hexa-aza macrocyclic ligand (**1.5a** – **1.5c**) can bind two square-planar Pd^{II} cations, in which one of coordination positions of the Pd atoms is occupied by weakly ligated solvent molecules or anions. These two weakly coordinated ligands in the pre-organized molecular clip are oriented to the same side, ascertained by the crystal structure of [Pd_2**1.5a**$(OAc)_2$]$(OAc)_2$, which allows bridging ligands to link multiple molecular clips into 2D or 3D supramolecular architectures.[60, 111-112] Indeed, the treatment of these molecular clips with porphyrin-based tetracarboxylate affords tetragonal prismatic cages by ligand substitution. On the virtue of porphyrin-based panels, the 3D heteroleptic cages can selectively bind anionic π-conjugated guests, fullerenes as well as the Rh-based catalyst according to the length of the employed molecular clips.[59, 61, 113] These examples highlight the importance of the hierarchical assembly approach, thus accessing more complex and functional coordination cages through tailor-made ligands.

1.4 Aims and objectives

1.4.1 Aims

Considering the tedious purification of fullerenes and their derivatives to date, burgeoning coordination-driven fullerene receptors have been investigated with regards to binding capacity, guest selectivity as well as the controlled release with the expectation to address related problems. In addition, a plethora of conjugated macrocycles is employed as binding sites in most of the known fullerene binders, which requires synthetically demanding procedures and hinders the large-scale preparation. For the further simplification of host materials and the enhanced atomic economy, we turned our attention to develop a low-molecular-weight backbone capable of interacting with fullerenes, and this kind of backbone has been scarcely reported so far.[114] By means of well-studied self-assemblies of Pd-mediated coordination cages,[89, 115] the spherical cavity of the typical [Pd_2L_4]$^{4+}$ cage is envisioned to be constructed and show the high shape-complementarity towards fullerene guests. In this thesis, donor-sites engineering will be studied in depth to yield various Pd-mediated assemblies with distinct fullerene-binding abilities. Taking advantage of these resulting particular cavities, the purification, separation, and derivatization of fullerenes will be explored within these supramolecular assemblies.

1.4.2 Objectives

This thesis will introduce coordination-driven supramolecular assemblies of a variety of nitrogen donor ligands with square-planar Pd^{II} cations and discuss the structure-property relationship between these assemblies. All the related compounds are fully characterized by comprehensive techniques, such as NMR spectroscopy, mass spectrometry as well as X-ray crystallography. The objectives achieved are listed as below: (a) development of a novel low-molecular-weight motif to interact with fullerenes based on the curved dibenzo-2.2.2-bicyclo-octane backbone with a pre-designed shape complementarity for fullerenes, inspired by the shape of triptycene; (b) compared to the traditional nitrogen donor (pyridine), the implementation of non-traditional nitrogen donors (quinoline and acridine) leads to the switch of controlled self-assemblies from molecular cage $[Pd_2L_4]^{4+}$ to molecular bowl $[Pd_2L_3(MeCN)_2]^{4+}$ and ring $[Pd_2L_2(MeCN)_4]^{4+}$ owing to steric effects originating from hydrogen atoms placed near the donor nitrogen atoms; (c) the selective binding of C_{60} by cage $[Pd_2\mathbf{L^1}_4]^{4+}$ allows for the purification of C_{60} from fullerene soot in a recycling manner controlled by solvent changes; (d) the bowl-shaped assembly $[Pd_2\mathbf{L^2}_3(MeCN)_2]^{4+}$ is capable of protecting the encapsulated C_{60}, hence controlling the stoichiometry of the Diels-Alder reaction between C_{60} and anthracene; (e) the hierarchical assembly of ''unsaturated'' metallosupramolecular bowl $[Pd_2\mathbf{L^2}_3(MeCN)_2]^{4+}$ with terephthalate bridges generates a heteroleptic pill $[Pd_4\mathbf{L^2}_6(BDC)_2]^{4+}$, capable of accommodating two fullerene molecules within its inner cavity; (f) the introduction of electronic-complementary donor, i.e. naphthyridine, helping to construct heteroleptic cages by means of the combination of steric effects, synergetic effects of donor-sites as well as template effects of guests; (g) the fullerene-based banana-shaped ligand $\mathbf{L^6}$ assembles with Pd^{II} to afford a giant cage $[Pd_2\mathbf{L^6}_4]^{4+}$ bearing four fullerene spheres in the periphery, which is expected to construct more complex structures via the non-covalent host-guest interaction.

2 Materials and methods

2.1 Materials

All chemicals were obtained from commercial sources and used without further purification. Fullerenes C_{60} and C_{70} were purchased from ABCR with a purity of 99.95% and Sigma-Aldrich with a purity of 98%, respectively; the commercially available fullerene soot was composed of 78.3% C_{60}, 19.0% C_{70}, 1.6% of higher-order fullerenes and 1.1% of fullerene oxides as mentioned in the analysis report, obtained from Alfa Aesar.

2.2 Purification techniques

Gel permeation chromatography (GPC) purification of ligands was performed on a JASCO LC-9210 II NEXT running with $CHCl_3$ (HPLC grade) containing 0.5% (v/v) triethylamine. Flash chromatography was performed on a Biotage Isolera One fraction collector with Biotage SNAP Ultra columns.

2.3 Analytical techniques

NMR measurements were all conducted at 298 K on Avance-500 and Avance-600 instruments from Bruker and an INOVA 500 MHz machine from Varian. Chemical shifts for ^{1}H and ^{13}C are reported in ppm on the δ scale; ^{1}H and ^{13}C signals were referenced to the residual solvent peak: acetonitrile (1.94 ppm, 1.32 ppm); chloroform (7.26 ppm, 77.16 ppm); dimethyl sulfoxide (2.50 ppm, 39.52 ppm); o-dichlorobenzene (6.93 ppm, 132.390 ppm); nitromethane (4.33 ppm, 62.80 ppm); methanol (4.78 ppm, 49.15 ppm); methylene chloride (5.32 ppm, 54.00 ppm); acetone (2.05 ppm, 206.68 ppm); dimethylformamide (8.03 ppm, 163.15 ppm); tetrahydrofuran (3.58 ppm, 67.57 ppm); benzene (7.16 ppm, 128.39 ppm). The following abbreviations are used to describe signal multiplicity for ^{1}H NMR spectra: s: singlet, d: doublet, t: triplet, dd: doublet of doublets; dt: doublet of triplets; m: multiplet, br: broad. All proton signals of supramolecular compounds were assigned with the aid of 2D NMR spectra. The ^{1}H DOSY NMR spectra were recorded with a dstebpgp3s pulse sequence with diffusion delays D20 of 0.09 – 0.12 s and gradient powers P30 of 1200 – 1700 µs. High resolution electrospray ionization mass spectrometry (ESI HRMS) was performed on Bruker Apex IV ESI-FTICR, Bruker compact and Bruker ESI timsTOF mass spectrometers. The samples were diluted with spectrum-grade CH_3CN (1:10) prior to the measurement. UV-Vis spectra were recorded on an Agilent DAD HP-8453 UV-Vis spectrophotometer using quartz cuvettes with an optical path length of 1 mm. The photos of crystals were taken by using Leica DM2500LED polarization microscope equipped with a camera.

2.4 X-ray crystallography

2.4.1 General procedures for small molecules

Crystal data were collected using a Bruker D8 VENTURE diffractometer equipped with an Incoatec microfocus source (Iμs 2.0) using Mokα radiation (λ = 0.71073 Å) or Cukα radiation (λ = 1.54178 Å) on a four axis κ-goniometer, employing an Oxford Cryostream 800 and a Photon 100 detector. A single crystal in mother liquor was mounted onto a nylon loop using NVH oil. Data integration was done with SAINT. Data scaling and absorption correction were performed with SADABS. The space group was determined using XPREP.[116] The structure was solved by intrinsic phasing/direct methods using SHELXT[117] and refined with SHELXL[118] for full-matrix least-squares routines on F^2 and ShelXle[119] as a graphical user interface.

2.4.2 General procedures for supramolecules

Crystals of supramolecular assemblies were extremely sensitive to loss of organic solvent. Due to very thin (5 – 20 γm) plate-like crystals, the analysis was further hampered by the limited scattering power of the samples, not allowing to reach the desired (sub-)atomic resolution using our a modern microfocussed X-ray in-house CuK_α source. Gaining detailed structural insight thus required cryogenic crystal handling and highly brilliant synchrotron radiation. To avoid collapse of the crystal lattice, crystals were quickly mounted onto a nylon loop and immediately flash cooled in liquid nitrogen. Crystals were stored at cryogenic temperature in dry shippers, in which they were safely transported to macromolecular beamline P11 at Petra III, DESY, Germany.[120] Single crystal X-ray diffraction data was collected at 80(2) K on a single axis goniometer, equipped with an Oxford Cryostream 800 a Pilatus 6M. Data integration and reduction were undertaken using XDS.[121] The structure was solved by intrinsic phasing/direct methods using SHELXT[117] and refined with SHELXL[118] by full-matrix least-squares routines on F^2 and ShelXle[119] as a graphical user interface and the DSR program plugin was employed for modeling.[122] Modelling of C_{60}/C_{70} disorder as well as counterion and solvent flexibility required carefully adapted macromolecular refinement protocols employing geometrical restraint dictionaries, similarity restraints and restraints for anisotropic displacement parameters (ADPs). Stereochemical restraints were generated by the GRADE program using the GRADE Web Server (http://grade.globalphasing.org) and applied in the refinement. A GRADE dictionary for SHELXL contains target values and standard deviations for 1,2-distances (DFIX) and 1,3-distances (DANG), as well as restraints for planar groups (FLAT). All displacements for non-hydrogen atoms were refined anisotropically. The refinement of ADP's for carbon, nitrogen and oxygen atoms was enabled by a combination of similarity restraints (SIMU) and rigid bond restraints (RIGU).[123] The contribution of the electron density from disordered counterions and solvent molecules, which could not be modeled with discrete atomic positions were handled using the SQUEEZE[124] routine in PLATON.[125] The solvent mask file (.fab) computed by PLATON were included in the SHELXL refinement via the ABIN instruction leaving the measured intensities untouched.

2.4.3 Analysis of the host–guest interaction

At first, the main position of all disordered C_{60} guest (Part 1) was used to create a PDB file for further analysis in the Olex2 program.[126] The 'CENT' and 'MPLN' commands were used to create the centroid of C_{60} and the mean planes of interest situated on the ligands and fullerene surfaces. The corresponding distances in between centroids of the ligands benzene rings, hydrogen atoms, C_{60} centroids and centroids of C_{60} rings were analyzed by using the 'Distances and angles' function.

2.4.4 Calculation of the cavity volumes

In order to calculate the cavity volumes of cage system, crystallographically determined structures of cages were symmetry expanded and BF_4^- counter ions or encapsulated fullerenes within the cavity were removed. Resulting inner cavities were calculated with VOIDOO[127] using a primary grid and plot grid spacing of 0.1 Å and 10 cycles of volume refinement with the size probe radius of 3.2 Å, the minimum radius such that it would not exit the cavity of all the structures.

2.4.5 Molecular visualization

Molecular visualization of all the structures was done using PyMol.[128] Color scheme: H, light grey; B, pink; C, dark grey; N, blue; O, red; F, green; Pd, orange; Cl, yellow; C_{60}/C_{60}Ac, purple; C_{70}, brown.

2.5 Molecular modeling

Related models shown in this thesis were constructed using Wavefunction SPARTAN '14[129] and first optimized on semiempiric PM6 level of theory without constraints. The resulting structures were then further refined by DFT structure optimization (B3LYP/C, H, N, O = 6-31g(d)/Pd LANL2DZ) using GAUSSIAN 09,[130] if not stated otherwise.

3 Controlled self-assembly using steric effect

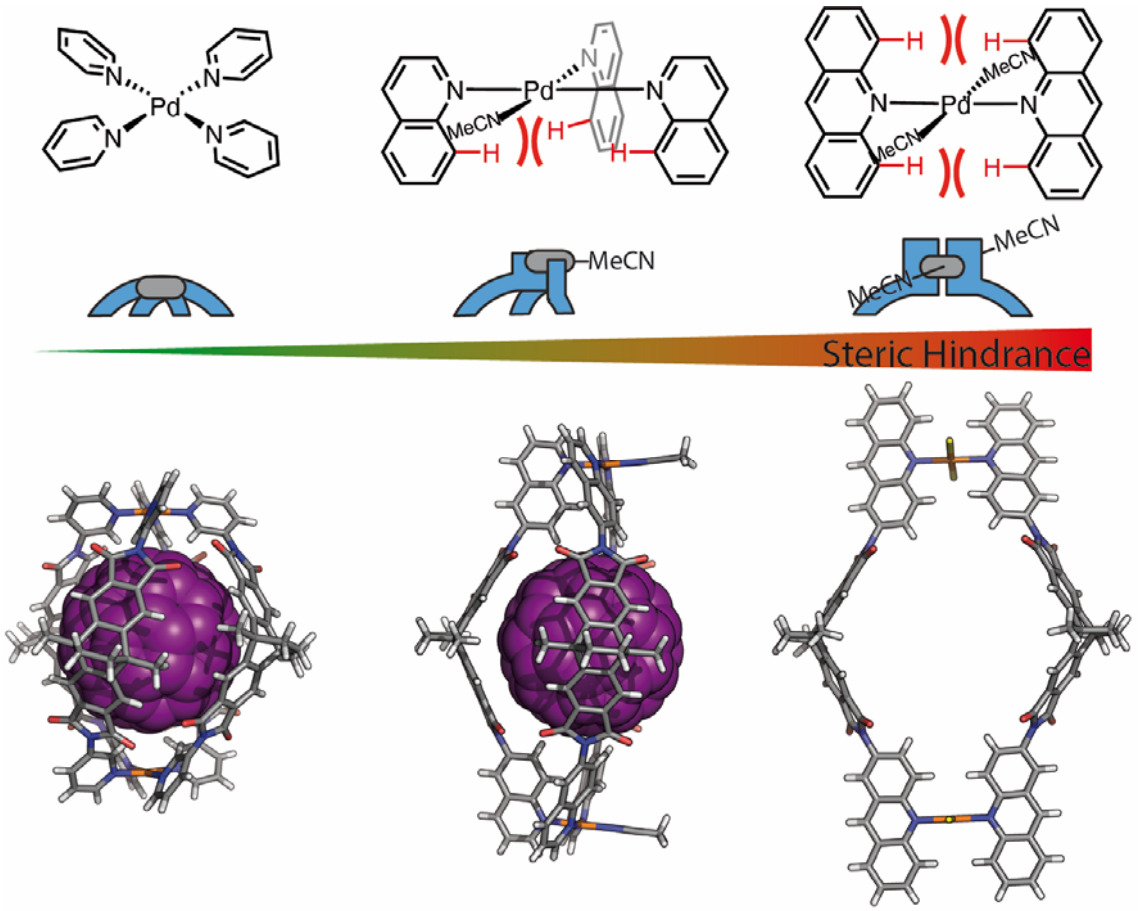

3.1 Introduction

Fullerenes, featuring a unique spherical shape and electronic properties, raised considerable attention in the last two decades, particularly in materials science.[2] The widespread application of fullerene-based materials, however, is still limited by the arduous purification of fullerene compounds from the mixture owing to their similar physicochemical properties, generally accomplished by time- and energy-consuming techniques, such as sublimation, multiple extraction and chromatography.[131]

For the purpose of providing a practical solution for efficient separation and derivatization of fullerenes, a number of precisely designed metallosupramolecules that can act as fullerene receptors, have been constructed by supramolecular chemists.[41, 61, 67, 70] On one hand, coordination-driven assemblies have their inherent advantages, especially in terms of modular assembly and adjustable cavity;[88, 90, 132] On the other hand, close inspection of these so far reported hosts with high affinities towards fullerenes reveals that extended π-conjugated systems, such as

porphyrins, triptycenes and extended tetrathiafulvalenes, are popularly utilized as backbones, thus enhancing the host-guest interaction.[25, 37-38, 133-134]

From the perspective of atomic economy, we then turned out attention to constructing Pd^{II}-mediated metallorganic cages based on a low-molecular-weight moiety with pre-designed shape complementarity towards the convex surface of fullerenes. Taking inspiration from a published X-ray co-crystal structure, we choose the triptycene molecule as a starting building block, since its curved surface structurally matches the spherical shape of C_{60}.[135] By virtue of a computed model, first we simplified the backbone into dibenzo-2.2.2-bicyclo-octane lacking the third benzene ring. Then we introduced phthalimide units as joints to pyridines that coordinate to Pd^{II}, thus assembling into the cage-like structure with an appropriate spherical cavity inside, which showed a geometric match with C_{60} in calculated models (Figure 3.111). To test this hypothesis, herein we synthesized a bis-pyridyl ligand (**L^1**) with the designed backbone, and characterized its self-assembled cage, capable of selectively binding C_{60} instead of C_{70} due to the size exclusion.

Furthermore, employment of sterically demanding donor groups (here termed ''terminal'') has been verified as an effective protocol to achieve heteroleptic assemblies.[91] Fujita and his co-workers reported the side chain-directed self-assembly of heteroleptic prisms by mixing 2,6-dimethyl pyridine donor ligands and pristine pyridine derivatives with *cis*-protected Pd^{II} cations.[92, 136] Similarly, Clever's group recently prepared a heteroleptic cage *cis*-$[Pd_2L_2L'_2]$ on the basis of two pyridine ligands featuring inward-pointing or outward-pointing methyl groups.[107] Additionally, Crowley modified one pyridine donor ligand with an amino group at 2-position, taking advantage of the hydrogen bonding between terminals, to yield a well-defined *cis*-$[Pd_2L_2L'_2]$ cage.[110] Moreover, Schmittel and co-workers utilized more sterically demanding mesityl group to generate heteroleptic rectangles and triangular prisms.[99, 137]

In this chapter, the terminal-induced steric effect in the self-assembly of Pd^{II} coordination cages was systematically studied by the introduction of sterically demanding donor groups, namely quinoline and acridine, surprisingly yielding a molecular bowl and a ring in a controllable manner (Figure 3.1). Moreover, these self-assembled supramolecules based on distinct nitrogen donor ligands, exhibit completely different binding abilities towards C_{60} and C_{70}, which can be explained by means of the comprehensive analysis of all the obtained crystal data, also revealing the breathing behavior of this cage system. All the related metallosupramolecules were analyzed by NMR spectroscopy and mass spectrometry as well as single crystal X-ray structure analyses of most of them.

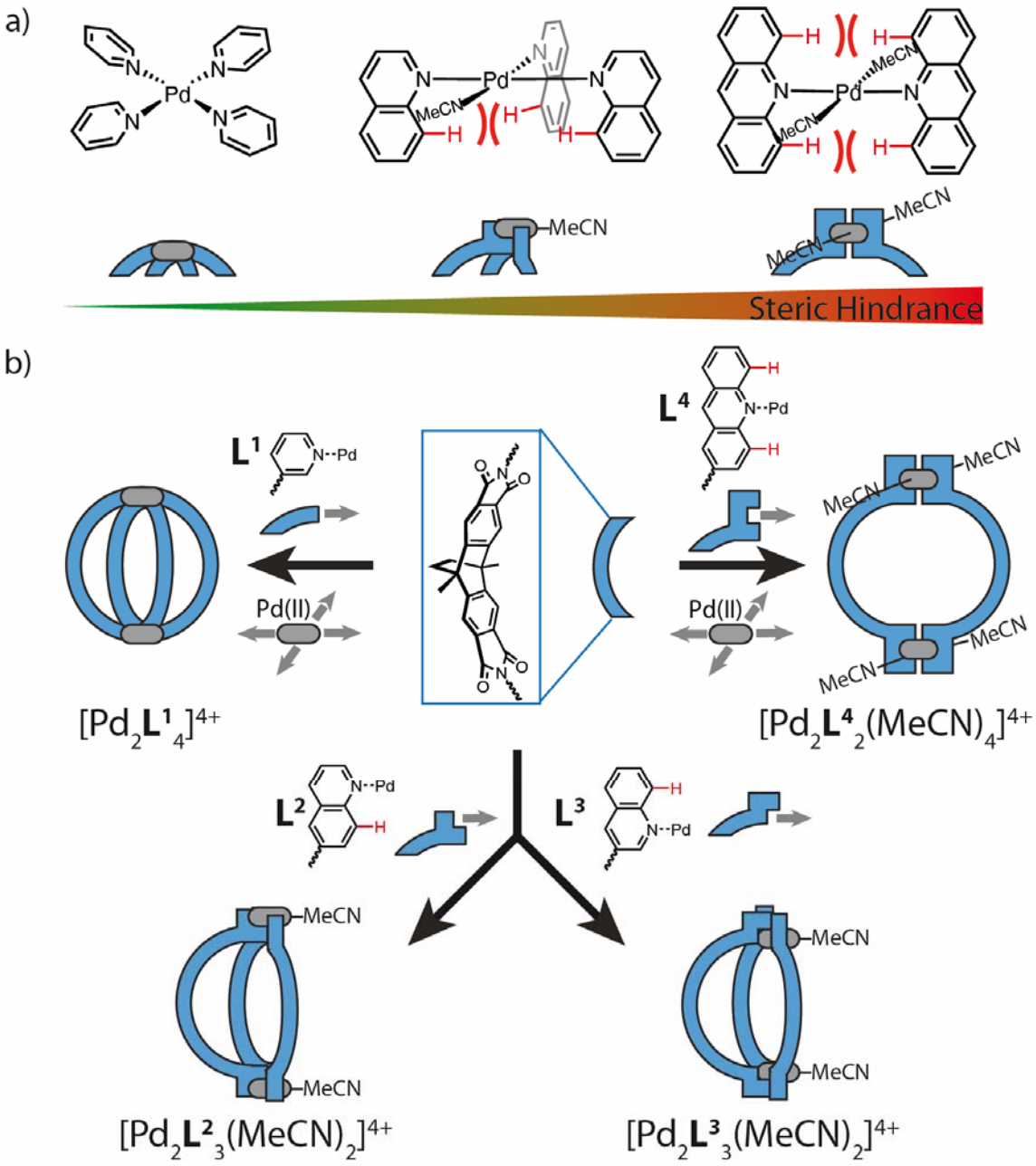

Figure 3.1 Schematic representation of the controlled self-assembly of a family of cage-like structures: (a) The different Pd^{II}-mediated coordination centers induced by sterically demanding nitrogen donors; (b) self-assembly of diverse metallosupramolecules using these designed nitrogen donor ligands with the same curved backbone in acetonitrile.

3.2 Cage assembly based on L^1

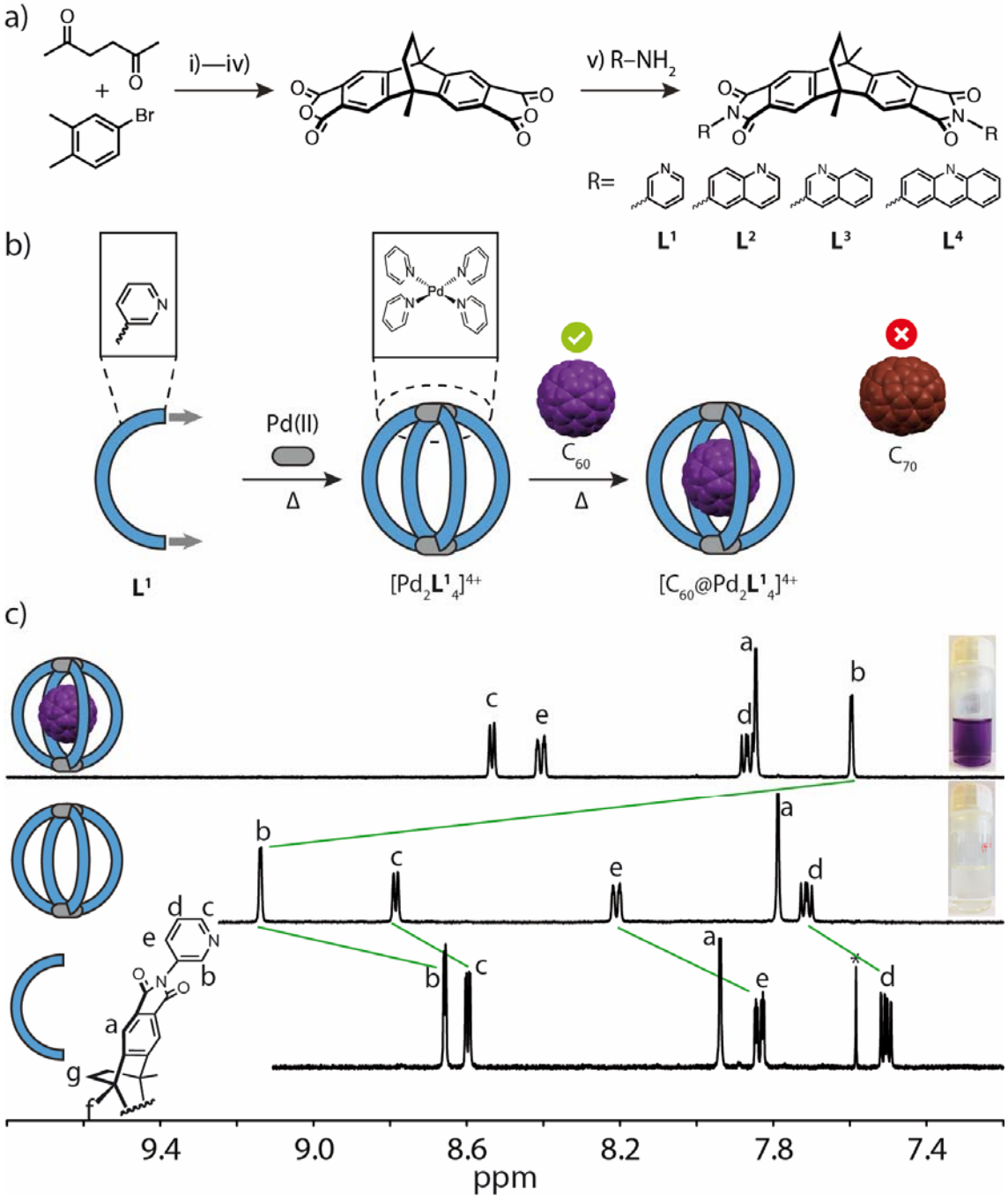

Figure 3.2 Ligand and cage synthesis: (a) Preparation of ligands starting from 4-bromo-1,2-dimethylbenzene and 2,5-hexanedione; (b) the self-assembly of cage $[Pd_2\mathbf{L^1}_4]^{4+}$ based on ligand $\mathbf{L^1}$ and Pd^{II} cations, showing selective binding of C_{60}; (c) ^1H NMR spectra (600 MHz, 298 K, CD_3CN) of Ligand $\mathbf{L^1}$ (2.56 mM), cage $[Pd_2\mathbf{L^1}_4]^{4+}$ (0.64 mM), host-guest complex $[C_{60}@Pd_2\mathbf{L^1}_4]^{4+}$ (0.64 mM) obtained from mixing free cage $[Pd_2\mathbf{L^1}_4]^{4+}$ with pure C_{60} at 70 °C (from bottom to top).

According to a proven synthetic route, the desired curved backbone was synthesized in four steps starting from 4-bromo-1,2-dimethylbenzene and 2,5-hexanedione, as shown in Figure 3.2.[138] This backbone dianhydride allowed for the facile and straightforward introduction of distinct terminals by reacting with the corresponding aromatic amines at

high temperature for few minutes (Figure 3.2a). Like other well-known $[Pd_2L_4]^{4+}$ cages based on banana-shaped ligands,[115] **L¹** reacted with $[Pd(MeCN)_4](BF_4)_2$ in a 2:1 ratio in deuterated acetonitrile at 70 °C to form cage $[Pd_2\mathbf{L^1}_4]^{4+}$ quantitatively, as confirmed by NMR and ESI mass analysis (Figure 3.19). The downfield-shifted signals of pyridine protons were observed in the ^{1}H NMR spectrum of cage $[Pd_2\mathbf{L^1}_4]^{4+}$ due to metal complexation (Figure 3.2c). Afterwards, the binding ability of cage $[Pd_2\mathbf{L^1}_4]^{4+}$ towards fullerene (C_{60} and C_{70}) was investigated by stirring cage solution in the presence of fullerene powder at room temperature or 70 °C (Figure 3.83–Figure 3.86). Interestingly, cage $[Pd_2\mathbf{L^1}_4]^{4+}$ exhibits the effective binding of C_{60} merely as expected, while C_{70} shows no binding at all. This effect is likely due to the shape- and size-difference between C_{60} and C_{70} (spherical C_{60} vs. ellipsoidal C_{70}; 547 Å^3 van-der-Waals volume of C_{60} vs. 646 Å^3 of C_{70}).[24, 54] The process of C_{60} binding could be easily deduced from the color change of the acetonitrile solution, in which fullerene itself is practically insoluble (Figure 3.2c). More convincingly, inward-pointing proton (H_b) upfield-shifted significantly, up to 1.54 ppm, in the ^{1}H NMR spectrum, suggesting the shielding effect of fullerene. More evidences of C_{60} absorption were provided by UV-Vis spectrometry (Figure 3.96) and ESI mass spectrometry (Figure 3.23).

For the structural characterization of supramolecular assemblies, single crystal X-ray diffraction is unambiguously one of the most powerful techniques. In order to obtain crystals with good quality, a lot of anti-solvents were screened and then diffused into the acetonitrile solution of cage species. Diffusion of isopropyl ether into the acetonitrile solution of $[C_{60}@Pd_2\mathbf{L^1}_4](BF_4)_4$ gave red plate crystals (Figure 3.109), identified as the anticipated structure of cage $[C_{60}@Pd_2\mathbf{L^1}_4]^{4+}$ by synchrotron X-ray diffraction analysis (Figure 3.100). Instead, colorless block crystals were obtained from the diffusion of THF into the identical acetonitrile solution of $[C_{60}@Pd_2\mathbf{L^1}_4](BF_4)_4$, surprisingly resulting in the structure of $[Pd_2\mathbf{L^1}_4]^{4+}$ without containing a bound fullerene (Figure 3.99).

In the asymmetric unit of cage $[C_{60}@Pd_2\mathbf{L^1}_4]^{4+}$, there were three crystallographically independent C_{60}-occupied cages with their subtly different Pd–Pd distances (14.66, 14.61 and 14.55 Å, respectively), attributed to the flexible backbone of the ligand. Considering the mean distance of 6.72 Å measured from the centroids of benzene rings on the backbone to the encapsulated C_{60} centroids (Table 3.9), the idea that this cage-fullerene system could show significant π-π interactions owing to the pre-designed concave-convex shape complementarity between them, was further reinforced. Likewise, strong CH-π interactions between pyridine hydrogen atoms and fullerene were indicated by the mean distance of 6.11 Å from pyridine hydrogen H_b to the C_{60} centroid, compared with corresponding distances in other reported fullerene receptors.[139-141] With regard to cage $[Pd_2\mathbf{L^1}_4]^{4+}$, it contained D_{4h}-symmetry in the crystal structure with the opposing Pd–Pd distance of 15.94 Å and two BF_4^- counter anions were found in the cavity (Figure 3.99). By comparison of crystal structures of free and fullerene-occupied cages, a shrinkage of the Pd–Pd distance from 15.94 Å to 14.61 Å was found after hosting fullerene inside the cage, leading to a twisted helical geometry around the entrapped C_{60}, presented by the significant difference of dihedral angles between two pyridine arms of the same ligand (1.0° for $[Pd_2\mathbf{L^1}_4]^{4+}$ vs. 62.3° for $[C_{60}@Pd_2\mathbf{L^1}_4]^{4+}$). This proved that cage $[Pd_2\mathbf{L^1}_4]^{4+}$ underwent a structural rearrangement to accommodate C_{60} inside the cavity, in an induced-fit binding manner.

3.3 Bowl/cage assembly based on L^2

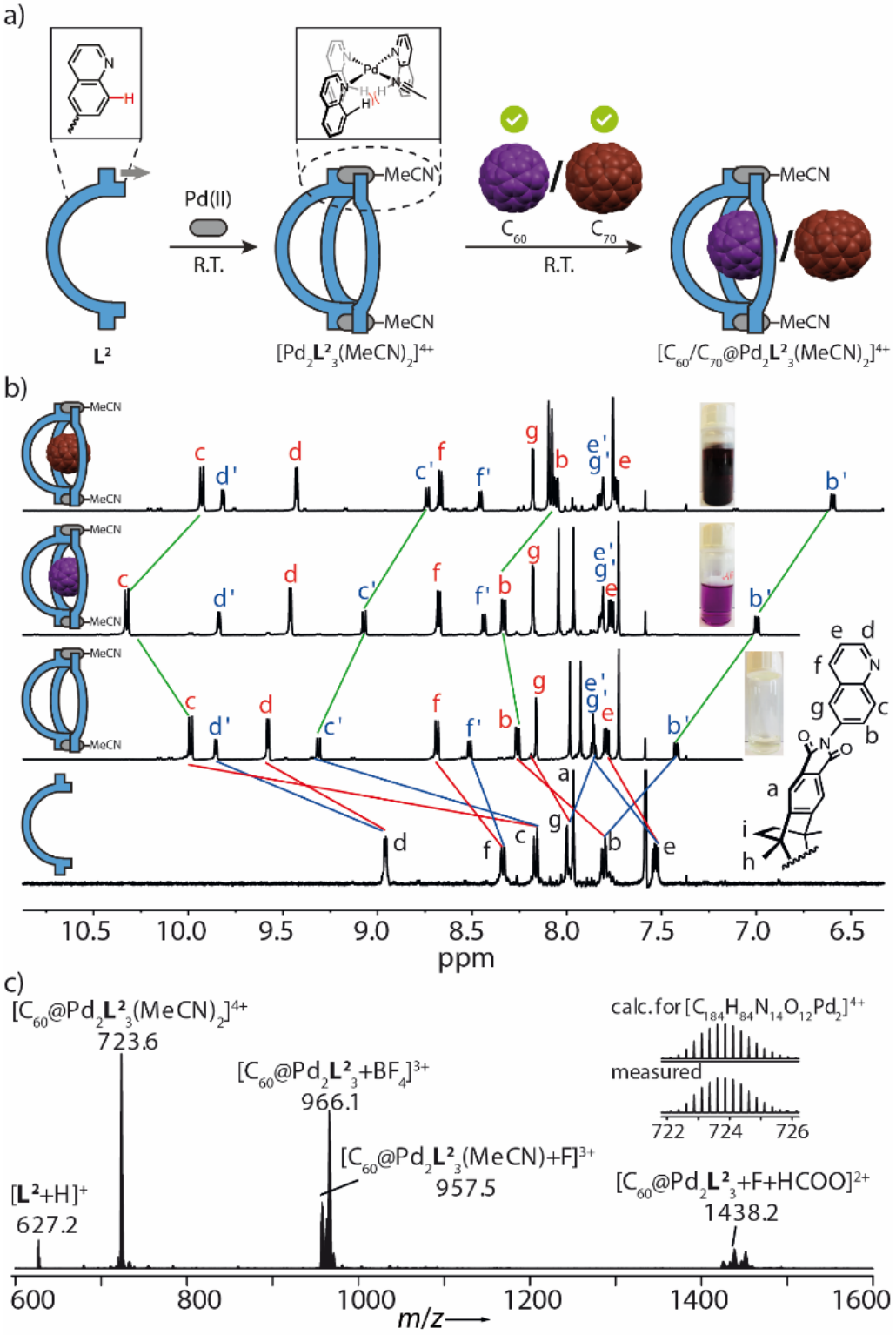

Figure 3.3 Self-assembly and characterization of bowl geometry: (a) The self-assembly of bowl $[Pd_2L^2_3(MeCN)_2]^{4+}$ based on ligand L^2 and Pd^{II} cations, showing C_{60}/C_{70} binding at room temperature; (b) ^1H NMR spectra (600 MHz, 298 K, CD_3CN)of ligand L^2 (saturated), bowl $[Pd_2L^2_3(MeCN)_2]^{4+}$, $[C_{60}@Pd_2L^2_3(MeCN)_2]^{4+}$, $[C_{70}@Pd_2L^2_3(MeCN)_2]^{4+}$ (all 0.64 mM) and photos of solutions. Red and blue marked proton signals are assigned to edge and central ligands, respectively. (c) ESI high resolution mass spectrum of $[C_{60}@Pd_2L^2_3(MeCN)_2]^{4+}$, prepared in pure CH_3CN.

For the initial purpose of improving the cage size for larger guests' binding, a non-traditional nitrogen donor, i.e. 6-amino-quinoline, reacted with the dianhydride backbone to give the ligand **L²** with a longer N–N distance compared with the pyridine-based ligand **L¹**. Unlike other banana-shaped ligands, three sets of proton signals from the ligand were found after the self-assembly of **L²** and $[Pd(MeCN)_4](BF_4)_2$ in a 2:1 ratio in acetonitrile, despite prolonged heating at 70 °C (Figure 3.30). Through the analysis of NMR spectra as well as the clear mass spectrum, the mixture of a new bowl-shaped species $[Pd_2\mathbf{L^2}_3(MeCN)_2]^{4+}$ and the anticipated cage species $[Pd_2\mathbf{L^2}_4]^{4+}$ in the ratio of 4:1 in solution was identified. The bowl formation was presumably attributed to the steric hindrance stemming from adjacent quinolines' hydrogen atoms (H_c) around the coordination centre. To test this hypothesis, the reaction of ligand **L²** with $[Pd(MeCN)_4](BF_4)_2$ in the stoichiometry of 3:2 was performed at room temperature for 2 days to give a single species, identified as the bowl $[Pd_2\mathbf{L^2}_3(MeCN)_2]^{4+}$ by ^1H NMR spectrum (Figure 3.24). Two sets of proton signals of the quinoline moieties with 2:1 integral ratio were observed and ^1H–^1H NOESY NMR spectrum showed the prominent cross peak between the suggested neighbouring protons (H_c and $H_{c'}$) (Figure 3.26). More convincingly, the characteristic peak at m/z 543.6 was in good agreement with the simulated isotopic pattern of the formula $[Pd_2\mathbf{L^2}_3(MeCN)_2]^{4+}$, along with several peaks assigned for bowl species in combination with different anions, i.e. $[Pd_2\mathbf{L^2}_3(MeCN)+X]^{3+}$ (X=F^-, Cl^-, BF_4^-) (Figure 3.28). To our surprise, crystals of cage $[Pd_2\mathbf{L^2}_4]^{4+}$ were obtained from the diffusion of isopropyl ether into the acetonitrile solution of bowl $[Pd_2\mathbf{L^2}_3(MeCN)_2]^{4+}$, suggesting the cage species to be the energetically favourable geometry in the solid state (Figure 3.103).

Considering the open geometry of this molecular bowl, the host-guest behavior of $[Pd_2\mathbf{L^2}_3(MeCN)_2]^{4+}$ towards fullerenes was studied. This assembly was capable of binding both C_{60} and C_{70} at room temperature, thus generating fullerene-occupied $[C_{60}@Pd_2\mathbf{L^2}_3(MeCN)_2]^{4+}$, $[C_{70}@Pd_2\mathbf{L^2}_3(MeCN)_2]^{4+}$, respectively, along with the noticeable color change of the solution upon fullerene binding. NMR analysis revealed a distinct shifts for the inward-pointing protons H_b, $H_{b'}$, H_c and $H_{c'}$, caused by the occupation of the cavity by fullerenes (Figure 3.3 b). In their ESI mass spectra (Figure 3.3c and Figure 3.46), the signals for the bowl species with various trace anions were observed, further indicating the weak bonding of acetonitrile ligands. Hence, the titration of bowl $[Pd_2\mathbf{L^2}_3(MeCN)_2]^{4+}$ with a concentrated acetonitrile solution of tetrabutylammonium chloride was carried out. Addition of two equivalents of chloride anions led to a quantitative conversion into the chloride-coordinated bowl $[Pd_2\mathbf{L^2}_3Cl_2]^{2+}$ (Figure 3.81). The same experiment was likewise applicable in the case of C_{60}-occupied bowl (Figure 3.57). In order to evaluate the thermal stability of these bowl compounds in solution state, the samples were heated at 70 °C for several days. No change was observed in the solution of bowl $[C_{60}@Pd_2\mathbf{L^2}_3(MeCN)_2]^{4+}$ (Figure 3.40), whereas partial conversions of $[Pd_2\mathbf{L^2}_3(MeCN)_2]^{4+}$ and $[C_{70}@Pd_2\mathbf{L^2}_3(MeCN)_2]^{4+}$ to the corresponding cage species $[Pd_2\mathbf{L^2}_4]^{4+}$ and $[C_{70}@Pd_2\mathbf{L^2}_4]^{4+}$ were found (Figure 3.29 and Figure 3.47). These results were consistent with the phenomenon that crystallization of bowl $[Pd_2\mathbf{L^2}_3(MeCN)_2]^{4+}$ or $[C_{70}@Pd_2\mathbf{L^2}_3(MeCN)_2]^{4+}$ both gave the crystals of cage species, as determined by single crystal X-ray analysis.

Single crystal X-ray structures of ligand **L²**, cage $[Pd_2\mathbf{L^2}_4]^{4+}$, cage $[C_{70}@Pd_2\mathbf{L^2}_4]^{4+}$ and bowl $[C_{60}@Pd_2\mathbf{L^2}_3(MeCN)_2]^{4+}$ were obtained, facilitating the comparison of this system's structural features (Figure 3.6). The crystal structures of ligand **L²** and cage $[Pd_2\mathbf{L^2}_4]^{4+}$ show that the dihedral angles between benzene planes of the backbone are 119.8° and 120.2°, respectively, whereas the corresponding angles widened slightly in cases of $[C_{70}@Pd_2\mathbf{L^2}_4]^{4+}$ (124.3°) and $[C_{60}@Pd_2\mathbf{L^2}_3(MeCN)_2]^{4+}$ (123.9°). Correspondingly, the Pd–Pd distance of bowl $[C_{60}@Pd_2\mathbf{L^2}_3(MeCN)_2]^{4+}$ is 20.22 Å, in

contrast to the N–N distance of the ligand (19.11 Å) and Pd–Pd distance of $[Pd_2\mathbf{L^2}_4]^{4+}$ (18.80 Å) and $[C_{70}@Pd_2\mathbf{L^2}_4]^{4+}$ (19.33 Å) (Table 3.1), indicating a slight opening of the cavity in bowl geometry when the fourth ligand is missing. It is worth noting that the hypothesised steric effect originating from the adjacent hydrogen atoms, to a certain degree, reflects on the distances between them which can be measured from the crystal structures. For example, four hydrogen atoms (H_c) were squeezed under the coordination centre in the quinoline-based cage $[Pd_2\mathbf{L^2}_4]^{4+}$, and the resulting average H–H distance of 2.31 Å is less than double the van-der-Waals radius of hydrogen (1.2 Å), indicative of the existence of steric hindrance. In the case of $[C_{60}@Pd_2\mathbf{L^2}_3(MeCN)_2]^{4+}$, H_c hydrogen atoms of opposite quinolines were pushed outward by the hydrogen atom $H_{c'}$ of the central ligand, leading to H–H distances of 2.56, 2.50 and 2.47 Å. For the comparison of host-guest interaction in cage $[C_{60}@Pd_2\mathbf{L^1}_4]^{4+}$ and bowl $[C_{60}@Pd_2\mathbf{L^2}_3(MeCN)_2]^{4+}$, the average distance of 6.79 Å measured from the centroids of benzene rings on the backbone to the encapsulated C_{60} centroids as well as and the average distance of 6.39 Å from quinoline H_b hydrogens to the C_{60} centroid in $[C_{60}@Pd_2\mathbf{L^2}_3(MeCN)_2]^{4+}$ are slightly longer than them observed in $[C_{60}@Pd_2\mathbf{L^1}_4]^{4+}$, but still reveal the relatively strong fullerene-bowl interaction (Table 3.15).

3.4 Bowl/cage assembly based on $\mathbf{L^3}$

In comparison with the pyridine-modified ligand $\mathbf{L^1}$ and quinoline-modified ligand $\mathbf{L^2}$, the new quinoline-modified ligand $\mathbf{L^3}$ bearing a protruding hydrogen atom outside the metal-binding nitrogen atom was initially considered to exhibit a similar behavior with $\mathbf{L^2}$ in the Pd^{II}-mediated self-assembly, thus forming the bowl-shaped structure. Indeed, bowl $[Pd_2\mathbf{L^3}_3(MeCN)_2]^{4+}$ was quantitatively formed by stirring a 3:2 mixture of $\mathbf{L^3}$ and $[Pd(MeCN)_4](BF_4)_2$ in deuterated acetonitrile for 2 hours at room temperature, as verified by NMR spectroscopy (Figure 3.63) and mass spectrometry (Figure 3.67). The ^{1}H NMR spectrum of fresh-prepared bowl $[Pd_2\mathbf{L^3}_3(MeCN)_2]^{4+}$ revealed the quinoline moieties' ^{1}H signals splitting into two sets with 2:1 integral ratio as well as the downfield shifts of most proton signals associated with metal complexation. The bowl-shaped geometry was further supported by the observation of prominent peaks in the ESI mass spectrum, consistent with the formula $[Pd_2\mathbf{L^3}_3(MeCN)_2]^{4+}$ and $[Pd_2\mathbf{L^3}_3+BF_4]^{3+}$, along with three feeble signals for ions of $[Pd_2\mathbf{L^3}_4+nBF_4]^{4-n+}$ (n = 0–2) owing to partially structural reorganization of the unstable bowl species. Unlike the corresponding bowl obtained from $\mathbf{L^2}$, the bowl $[Pd_2\mathbf{L^3}_3(MeCN)_2]^{4+}$ exhibited instability even at room temperature, partially converting to the cage $[Pd_2\mathbf{L^3}_4]^{4+}$ after prolonged standing (Figure 3.68). Afterwards, heating a 2:1 mixture of $\mathbf{L^3}$ and $[Pd(MeCN)_4](BF_4)_2$ at 70 °C for 2 days yielded the more thermodynamic stable cage $[Pd_2\mathbf{L^3}_4]^{4+}$ quantitatively (Figure 3.69). This result was in contrast to the phenomenon observed in the case of $\mathbf{L^2}$, where the expected cage $[Pd_2\mathbf{L^2}_4]^{4+}$ only arose as a minor product under the same heating condition (Figure 3.30). This dissimilarity was likely due to the different energy change during the conversion from bowl to cage, as confirmed for both cases by virtue of DFT calculation (Figure 3.112 and Figure 3.113). Cage $[Pd_2\mathbf{L^3}_4]^{4+}$ assembled and stably existed in solution state as a single species, identified by NMR spectra (Figure 3.63) as well as ESI mass spectrum (Figure 3.69). Suitable crystals for X-ray analysis were obtained from the diffusion of methyl tert-butyl ether into an acetonitrile solution of the intact cage. Intriguingly, the whole cage with C_4-symmetry showcases a severely twisted helical geometry (Figure 3.106), attributed by its self-adjusting of quinoline terminals in a Pd^{II}-coordination center, for the sake of reducing the steric hindrance between squeezed hydrogen atoms. This is structurally confirmed by the average distance of 2.82 Å between adjacent

hydrogen atoms (H_c), slightly longer than double the van-der-Waals radius of hydrogen (1.2 Å). Correspondingly, the Pd–Pd distance elongates to 16.19 Å along with the concomitant decrease of VOIDOO-calculated cavity volume (518 Å^3). Compared with the original pyridine cage $[Pd_2\mathbf{L^1}_4]^{4+}$ (572 Å^3), the smaller cavity of $[Pd_2\mathbf{L^3}_4]^{4+}$ restricts its fullerene-binding ability, which is in agreement with the experimental investigation (Figure 3.93 and Figure 3.94): neither C_{60} nor C_{70} can be encapsulated inside the cage $[Pd_2\mathbf{L^3}_4]^{4+}$ no matter whether they are added initially or after cage formation.

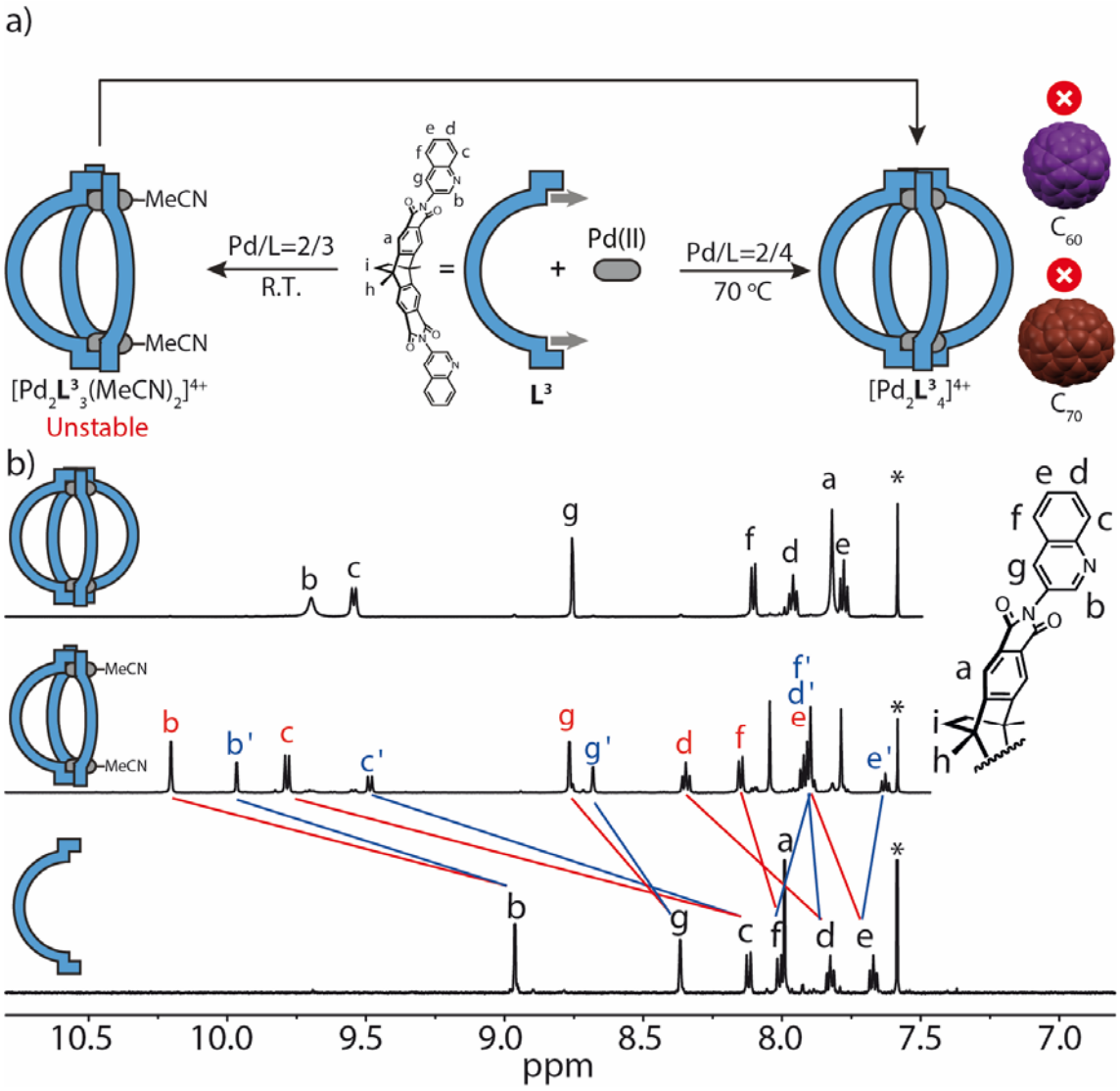

Figure 3.4 Self-assembly and characterization of bowl-shaped $[Pd_2\mathbf{L^3}_3(MeCN)_2]^{4+}$ and cage $[Pd_2\mathbf{L^3}_4]^{4+}$: (a) Self-assembly of bowl $[Pd_2\mathbf{L^3}_3(MeCN)_2]^{4+}$ based on ligand $\mathbf{L^3}$ and Pd^{II} cations in a 3:2 ratio at room temperature, and the self-assembly of cage $[Pd_2\mathbf{L^3}_4]^{4+}$ based on ligand $\mathbf{L^3}$ and Pd^{II} cations in a 4:2 ratio at 70 °C; (b) ^{1}H NMR spectra (600 MHz, 298 K, CD_3CN), of ligand $\mathbf{L^3}$, bowl $[Pd_2\mathbf{L^3}_3(MeCN)_2]^{4+}$(0.64 mM), cage $[Pd_2\mathbf{L^3}_4]^{4+}$(0.64 mM) from bottom to top. Red and blue marked proton signals are assigned to edge and central ligands in the bowl-shaped geometry.

3.5 Ring assembly based on L^4

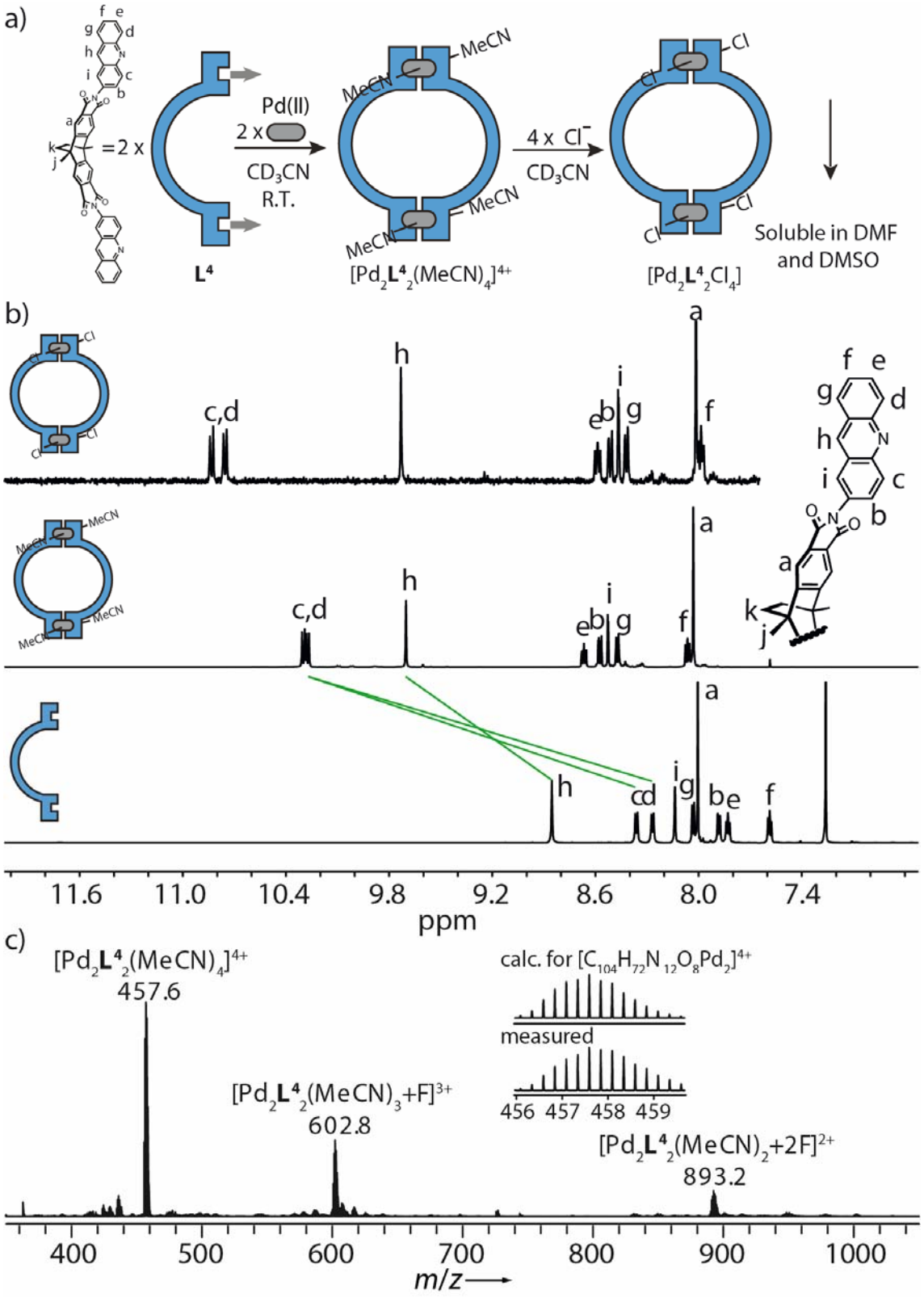

Figure 3.5 Self-assembly and characterization of ring-shaped $[Pd_2\mathbf{L^4}_2(MeCN)_4]^{4+}$ and $[Pd_2\mathbf{L^4}_2Cl_4]$: (a) Self-assembly of ring $[Pd_2\mathbf{L^4}_2(MeCN)_4]^{4+}$ based on ligand $\mathbf{L^4}$ and Pd^{II} cations in a 2:2 ratio at room temperature, followed by the formation of an insoluble neutral ring $[Pd_2\mathbf{L^4}_2Cl_4]$ upon addition of four equivalents of chloride anion; (b) ^1H NMR spectra (600 MHz, 298 K) of ligand $\mathbf{L^4}$ (1.28

mM, $CDCl_3$), ring $[Pd_2\mathbf{L^4}_2(MeCN)_4]^{4+}$ (0.64 mM, CD_3CN), ring $[Pd_2\mathbf{L^4}_2Cl_4]$ (saturated, DMSO-d_6) (from bottom to top); (c) ESI-HRMS of ring $[Pd_2\mathbf{L^4}_2(MeCN)_4]^{4+}$.

For ligand $\mathbf{L^4}$, the acridine terminal was regarded as more sterically demanding group than quinoline-modified ligands ($\mathbf{L^2}$ and $\mathbf{L^3}$) due to the existence of two protruding hydrogen atoms (H_c and H_d) located near the metal-binding site with respect to the ring topology. Stirring a 1:1 mixture of sparingly soluble $\mathbf{L^4}$ and $[Pd(MeCN)_4](BF_4)_2$ in deuterated acetonitrile at room temperature for 1 d gave a clear yellow solution, identified as a single species $[Pd_2\mathbf{L^4}_2(MeCN)_4]^{4+}$ by NMR spectroscopy and mass spectrometry (Figure 3.5). ^{1}H NMR spectrum showed the downfield shifts of three proton signals (H_c, H_d, H_g) mainly caused by metal complexation instead of the possibly minor solvent effect. More convincingly, the pronounced peak at *m/z* 457.6 was fully consistent with the calculated isotopic pattern of formula $[Pd_2\mathbf{L^4}_2(MeCN)_4]^{4+}$. Noteworthy was that this mass spectrum was recorded under a mild ionization temperature through multiple attempts owing to the extremely thermal instability of ring $[Pd_2\mathbf{L^4}_2(MeCN)_4]^{4+}$. In addition, titration of the postulated ring $[Pd_2\mathbf{L^4}_2(MeCN)_4]^{4+}$ with chloride anions in acetonitrile was performed to further confirm this ring geometry, resulting in the precipitate arising in the bottom of NMR tube upon addition of four equivalents of chloride anions (Figure 3.82). The resulting precipitate was washed with chloroform to remove the partially released ligand and then could only be dissolved in DMSO or DMF. ^{1}H NMR analysis in deuterated DMSO allowed to identify the product as the neutral compound $[Pd_2\mathbf{L^4}_2Cl_4]$ even though it was quite thermally unstable (Figure 3.77). Comparison of proton resonances of the assumed ring $[Pd_2\mathbf{L^4}_2Cl_4]$ with the ligand $\mathbf{L^4}$ in DMSO solution revealed the unambiguous Pd^{II}-coordination environment in the ring $[Pd_2\mathbf{L^4}_2Cl_4]$. Crystallization of the pristine ring geometry was challenging, and single crystals were finally obtained from the diffusion of benzene into an acetonitrile solution of $[Pd_2\mathbf{L^4}_2(MeCN)_4]^{4+}$, after addition of five equivalents of tetrabutylammonium periodate as a co-crystallization agent. Synchrotron analysis confirms the *trans*-arranged coordination, wherein two opposing acridine donor ligands coordinate to Pd^{II} (Figure 3.107), in line with DFT energy-minimized model (Figure 3.114). Nevertheless, four coordinated acetonitrile molecules are substituted by chloride anions, which may stem from the decomposition of $CHCl_3$ utilized for GPC purification or impurities of the added tetrabutylammonium periodate used for co-crystallization. The average Pd–Cl bond distance of 2.33 Å observed in the crystal is quite close to the corresponding bond distance of 2.30 Å in the reported complex $Pd(acridine)_2Cl_2$.[142] The average distance between hydrogen atoms (H_c and H_d) of opposing acridine donor ligands is below to 2.29 Å, less than double the van-der-Waals radius of hydrogen (1.2 Å), indicative of the steric hindrance around the coordination centre. Hence, opposite acridine rings cannot locate in the same plane, and adjust themselves to reduce the steric effect as observed in the crystal structure. Fullerene binding studies were also carried out for the ring $[Pd_2\mathbf{L^4}_2(MeCN)_4]^{4+}$ and ^{1}H NMR spectra exhibit broad signals for the inward-pointing protons (H_b and H_c) (Figure 3.95). Combination with the color change after addition of fullerene powder in an acetonitrile solution of the ring (Figure 3.98), suggested the fast exchange between the fullerene guest and the ring with open structure in solution state.

3.6 Comparison of structural details

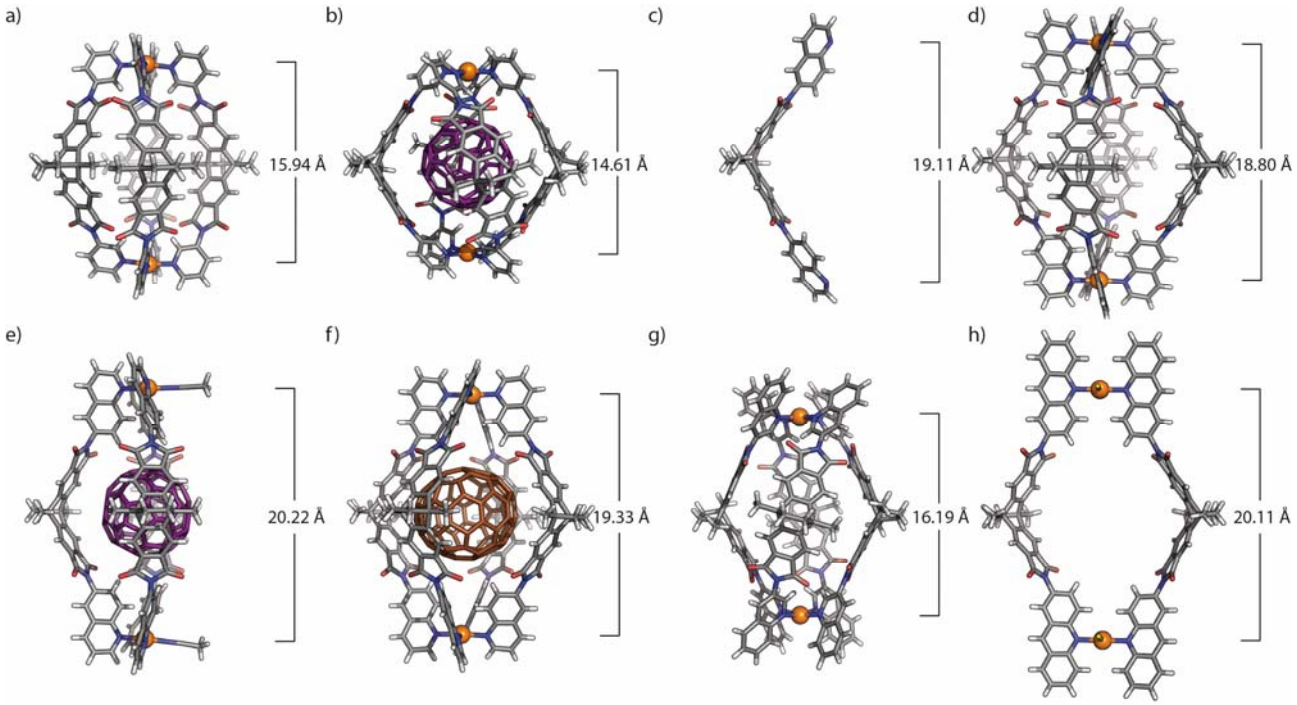

Figure 3.6 X-ray crystal structures: (a) $[Pd_2\mathbf{L^1}_4]^{4+}$, (b) $[C_{60}@Pd_2\mathbf{L^1}_4]^{4+}$, (c) $\mathbf{L^2}$, (d) $[Pd_2\mathbf{L^2}_4]^{4+}$, (e) $[C_{60}@Pd_2\mathbf{L^2}_3(MeCN)_2]^{4+}$, (f) $[C_{70}@Pd_2\mathbf{L^2}_4]^{4+}$, (g) $[Pd_2\mathbf{L^3}_4]^{4+}$ and (h) $[Pd_2\mathbf{L^4}_2Cl_4]$. Solvent molecules, anions and guest disorder are omitted for clarity (Pd^{II}, orange; C, gray; N, blue; O, red; Cl, yellow; H, white; C_{60} and C_{70}, brown).

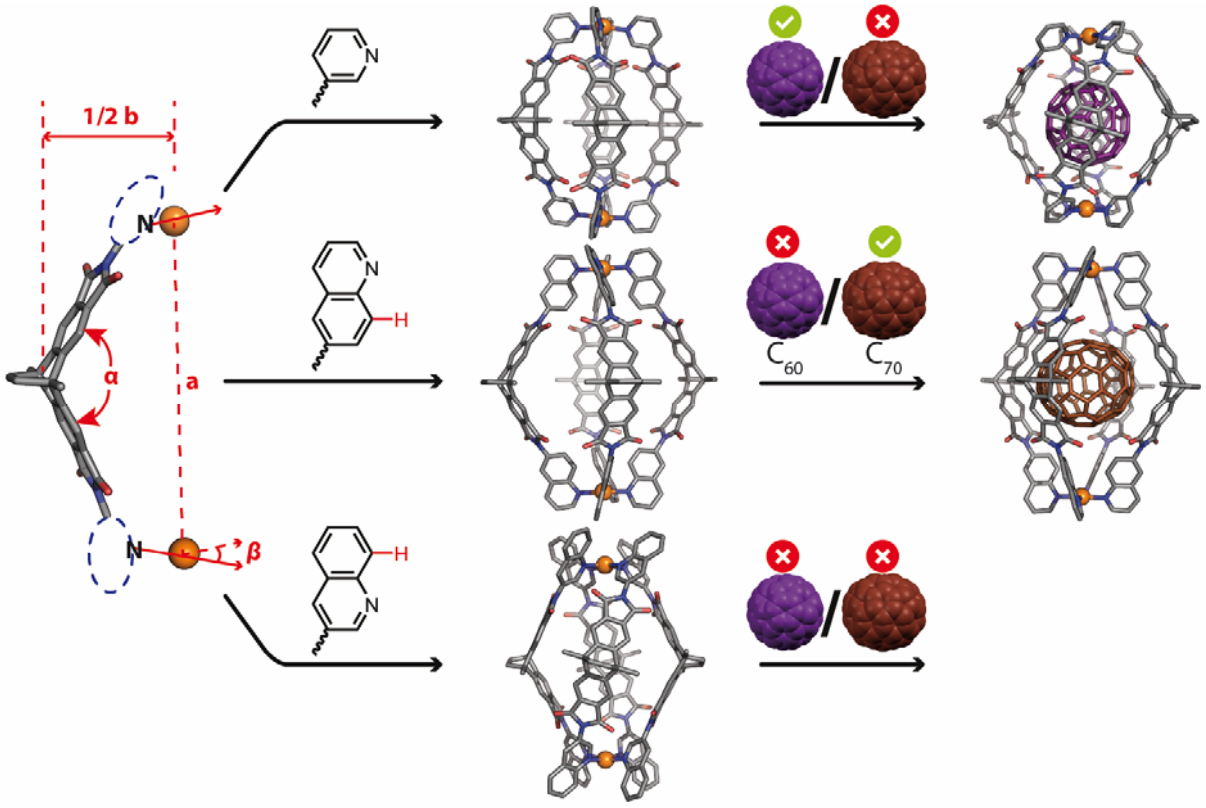

Figure 3.7 Comparison of cage systems with their fullerene-binding abilities.

Table 3.1 Comparison of structural details from X-ray analysis.

	$[C_{60}@Pd_2\mathbf{L^1}_4]^{4+}$	$[Pd_2\mathbf{L^1}_4]^{4+}$	$[Pd_2\mathbf{L^3}_4]^{4+}$	$[Pd_2\mathbf{L^2}_4]^{4+}$	$[C_{70}@Pd_2\mathbf{L^2}_4]^{4+}$	$[C_{60}@Pd_2\mathbf{L^2}_3(MeCN)_2]^{4+}$
Pd-Pd distance a (Å)	14.61[a]	15.94	16.19	18.80	19.33	20.22
Horizontal distance b (Å) [b]	15.12[a]	14.12	13.15	16.90	16.17	15.14
Dihedral angle α (°) [c]	122.1[a]	124.3	126.9	120.2	124.3	123.9
Dihedral angle β (°) [d]	62.8[a]	1.0	76.9	1.2	1.4	0.6
Volume of cavity (Å^3) [e]	780[a]	572	518	1099	995	-

[a] average value of these parameters in three crystallographically independent cages of $[C_{60}@Pd_2\mathbf{L^1}_4]^{4+}$
[b] distance between opposite backbones as defined by the line connecting the midpoint of atom C2 and C5
[c] dihedral angle between the backbone's benzene planes C16_C17_C18_C22_C23_C24 and C7_C8_C9_C13_C14_C15
[d] dihedral angle between planes formed by coordinated N atoms and Pd atoms
[e] VOIDOO-calculated void space with the size probe radius of 3.2 Å

The series of crystal structures (Figure 3.6) allows a systematic elucidation of these terminal-regulated cages as well as their distinct binding abilities towards C_{60} and C_{70}. In this regard, cage $[Pd_2\mathbf{L^1}_4]^{4+}$ exhibits the induced-fit binding of C_{60} within the cavity, whereas cage $[Pd_2\mathbf{L^2}_4]^{4+}$ is capable of accommodating C_{70} inside in contrast to the incapable cage $[Pd_2\mathbf{L^3}_4]^{4+}$ (Figure 3.7). Compared with the referential free cage $[Pd_2\mathbf{L^1}_4]^{4+}$, cage $[Pd_2\mathbf{L^3}_4]^{4+}$ with extra capped benzene rings on both ends, was initially thought to possess the cavity with similar shape and size, thus being able to host C_{60}, however the aforementioned experimental results demonstrated the contrary (Figure 3.93 and Figure 3.94). Given the structural parameters of $[C_{60}@Pd_2\mathbf{L^1}_4]^{4+}$, $[Pd_2\mathbf{L^1}_4]^{4+}$ and $[Pd_2\mathbf{L^3}_4]^{4+}$ (Table 3.1), the elongation of opposing Pd–Pd distance from 14.61 Å to 15.94 Å and even 16.19 Å are found and accompanied with the synchronous decrease of the horizontal distance of cages, since the gradually increased dihedral angle (α) of flexible backbones ranges from 122.1° to 124.3° and 126.9°, respectively. Furthermore, the bonds connecting backbone and coordination groups can freely rotate to reach the energy-optimized positions for the sake of maximizing the host-guest interaction or minimizing steric hindrance around the congested coordination centre, as presented in helical geometries of $[C_{60}@Pd_2\mathbf{L^1}_4]^{4+}$ and $[Pd_2\mathbf{L^3}_4]^{4+}$ with their corresponding dihedral angles (β) of 62.8° and 76.9°. Additionally, more squashed cages on the horizontal direction seems to possess smaller cavities (572 Å^3 for $[Pd_2\mathbf{L^1}_4]^{4+}$, 518 Å^3 for $[Pd_2\mathbf{L^3}_4]^{4+}$) under the overall allosteric effects (Figure 3.108). Analogously, these findings are also applicable in the cage system based on the elongated terminal, i.e. $[Pd_2\mathbf{L^2}_4]^{4+}$ and $[C_{70}@Pd_2\mathbf{L^2}_4]^{4+}$, wherein the squeezed latter shows the longer Pd–Pd distance and shorter horizontal distance as well as a smaller cavity (Table 3.1).

These above-mentioned assumptions and geometrical details deduced from crystal structures, make it possible to explain an unexpected experimental phenomenon: cage $[Pd_2\mathbf{L^2}_4]^{4+}$ can accommodate C_{70} within the cavity, instead of the smaller-sized C_{60}. After inspecting X-ray structures of C_{60}-entrapped cage and bowl, the horizontal distance of 15.12 Å in $[C_{60}@Pd_2\mathbf{L^1}_4]^{4+}$ is astoundingly similar with the corresponding horizontal distance between edge ligands in bowl-shaped $[C_{60}@Pd_2\mathbf{L^2}_3(MeCN)_2]^{4+}$, i.e. 15.14 Å, which can be seen as a structural feature for the C_{60}-binding system. Shorter distances between the surface of C_{60} and interactive sites of the host, namely herein benzene rings of the backbone and inward-pointing hydrogen atoms, offers relatively strong host-guest interaction as well as enough space for encapsulated C_{60}.

For the C_{60}-binding process within cages, the host presumably adapts themselves, thus reaching the suited position with the horizontal distance of around 15.14 Å. Nevertheless, this compression of the cage certainly leads to the increase of its structural tension and more severe steric hindrance around the coordination centre owing to this extra structural requirement. Consequently, the occurrence of fullerene-binding within a cage depends on whether host-guest interaction, namely π–π interaction and CH–π interaction, can overcome the binding-induced energy disadvantage. The non-existent species $[C_{60}@Pd_2\mathbf{L^2}_4]^{4+}$ can be explained by this hypothesis: the favorable host-guest interaction is not strong enough to conquer the unfavourably structural strain, thus yielding the strain-released bowl geometry $[C_{60}@Pd_2\mathbf{L^2}_3(MeCN)_2]^{4+}$. For the C_{70}-binding process, the enhanced host-guest interaction owing to the C_{70}'s larger surface area for the interplay with the host, can cope with the reduced structural tension, as shown in the crystal structure of $[C_{70}@Pd_2\mathbf{L^2}_4]^{4+}$, where the horizontal distance of the cage is merely required to change from 16.90 Å to 16.17 Å instead of more demanding 15.14 Å thanks to the longer axis of C_{70}.

The above-mentioned cage system exhibits a breathing behavior, which stems from flexible dihedral angles of the curved dibenzo-2.2.2-bicyclo-octane and rotatable bonds linking backbone and terminals, manifesting on three specific aspects: (a) three crystallographically independent cages with different Pd–Pd distances are observed in asymmetrical unit for the identical cage of $[C_{60}@Pd_2\mathbf{L^1}_4]^{4+}$ (Figure 3.100); (b) the dihedral angles of the identical backbone measured from this series of cages with distinct terminals, i.e. $[Pd_2\mathbf{L^1}_4]^{4+}$, $[Pd_2\mathbf{L^2}_4]^{4+}$, $[Pd_2\mathbf{L^3}_4]^{4+}$, range from 120.2° to 126.9° along with the decrease of horizontal distances (16.90 Å — 13.15 Å) (Table 3.1); (c) free cages undergo structural adjustment to entrap fullerenes in order to optimize host-guest interactions, presented in solid state of $[C_{60}@Pd_2\mathbf{L^1}_4]^{4+}$ and $[C_{70}@Pd_2\mathbf{L^2}_4]^{4+}$.

3.7 Conclusion

Benefiting from the computation-assisted design, a novel low-weight backbone can be used for the construction of fullerene receptors and the straightforward incorporation of multiple nitrogen donors (pyridine, quinoline and acridine) was used to synthesize a series of new ligands. These nitrogen donor ligands ($\mathbf{L^1}$–$\mathbf{L^4}$) can react with square-planar Pd^{II} cations to yield terminal-induced assemblies with distinct geometries: (a) normally encountered $[Pd_2L_4]^{4+}$ cages are assembled by traditional pyridine donor ligands; (b) sterically demanding quinoline donor ligands are able to form supramolecular $[Pd_2L_3(MeCN)_2]^{4+}$ bowls; (c) the acridine donor ligand, with more severe steric hindrance, is forced to generate a ring geometry. This strategy of controlled self-assembly renders chemists be able to construct anticipated geometries by means of steric effects of donor groups, a novel approach to fine-tune supramolecular structures. Modified terminals have significant effects on the properties of these self-assembled cages, simultaneously exhibiting breathing behaviors. In summary, this modular synthetic approach will certainly contribute to the diversity in supramolecular chemistry in the near future and the practical applications of the herein reported fullerene binders will be presented in next chapters.

3.8 Experimental section

3.8.1 Synthesis of ligands

All the ligands were prepared from reported bis-anhydride (9,10-dimethyl-9,10-dihydro-9,10-ethanoanthracene-2,3,6,7-dianhydride)[138] (**S1**) and the corresponding powdered aromatic amines under nitrogen atmosphere as described below.

3.8.1.1 ligand L^1

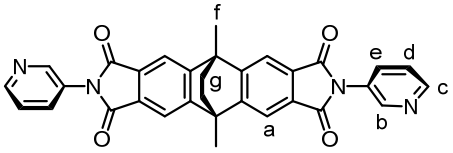

L^1

Under a nitrogen atmosphere, bis-pyridyl ligand **L^1** was prepared from reported bis-anhydride **S1** (149.7 mg, 0.40 mmol, 1 eq.) and powdered 3-aminopyridine (753.0 mg, 8.0 mmol, 20 eq.) by heating the mixture of solids without solvent in a preheated oil bath to 165 °C for 10 min. After the black melt cooled to room temperature, it was taken up into 5 mL chloroform, sonificated and the suspension was immediately subjected to flash column chromatography on silica gel (0–2 % MeOH in $CHCl_3$) to give the crude product. This was further purified via recycling gel permeation chromatography and the solvent was removed under reduced pressure to yield the desired product as a white powder (139.0 mg, 66 %).

^{1}H NMR (500 MHz, 298 K, CD_3CN): δ (ppm) = 8.65 (d, J = 2.4 Hz, 2H), 8.59 (dd, J = 4.8, 1.6 Hz, 2H), 7.91 (s, 4H), 7.83 (ddd, J = 8.2, 2.5, 1.6 Hz, 2H), 7.50 (dd, J = 8.2, 4.8 Hz, 2H), 2.19 (s, 6H), 1.77 (s, 4H).

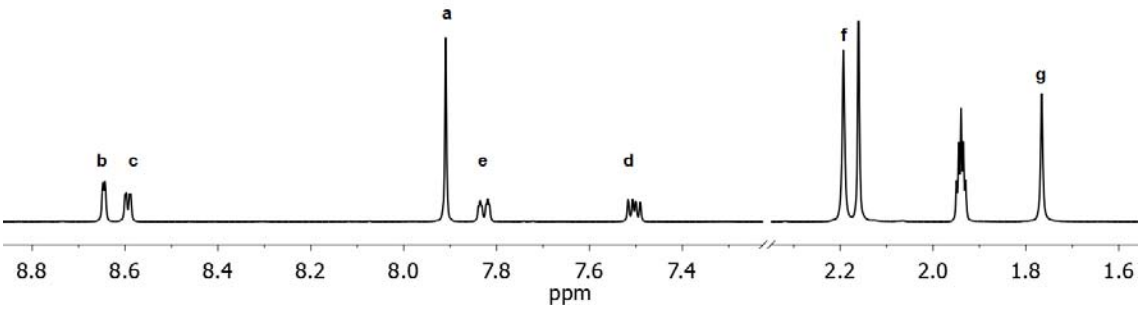

Figure 3.8 ^{1}H NMR spectrum (500 MHz, 298 K, CD_3CN) of **L^1**.

^{13}C NMR (126 MHz, 298 K, CD_3CN): δ (ppm) = 168.02, 153.68, 149.68, 148.57, 135.07, 131.01, 130.03, 124.64, 117.32, 45.09, 35.30, 18.62.

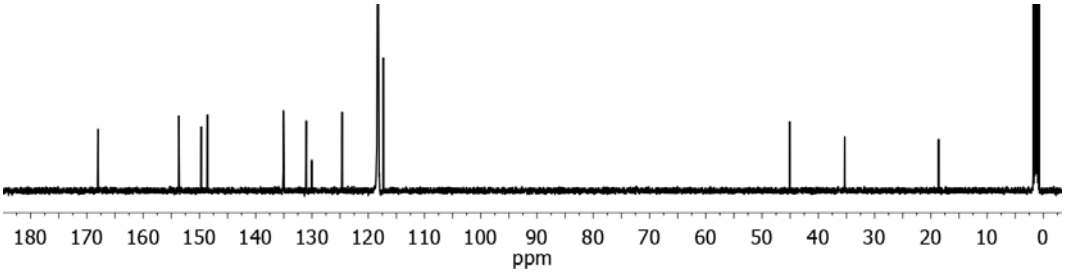

Figure 3.9 ^{13}C NMR spectrum (126 MHz, 298 K, CD_3CN) of **L¹**.

ESI HRMS ($C_{32}H_{22}N_4O_4$): $[M + H]^+$ calcd. for $C_{32}H_{23}N_4O_4$ 527.1710; found 527.1708; $[M + 2H]^{2+}$ calcd. for $C_{32}H_{24}N_4O_4$ 264.0894; found 264.0894.

3.8.1.2 Ligand L²

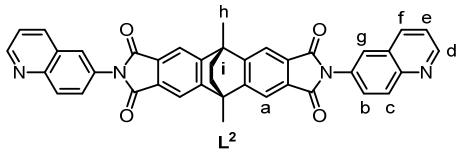

Under a nitrogen atmosphere, ligand **L²** was prepared from reported bis-anhydride **S1** (198.4 mg, 0.53 mmol, 1 eq.) and powdered 6-aminoquinoline (1540.0 mg, 10.7 mmol, 20 eq.) by heating the mixture of solids without solvent in a preheated oil bath to 165 °C for 10 min. After the black melt cooled to room temperature, it was taken up into 20 ml acetonitrile, sonificated and the suspension was filtered to afford a white precipitate. Then it was dissolved in $CHCl_3$ and further purified via recycling gel permeation chromatography and the solvent was removed under reduced pressure to yield the desired product as a white powder (196.2 mg, 59 %).

¹H NMR (500 MHz, 298 K, $CDCl_3$): δ (ppm) = 8.95 (dd, J = 4.4, 1.6 Hz, 2H), 8.21 (m, 4H), 7.95 (s, 4H), 7.92 (d, J = 2.2 Hz, 2H), 7.78 (dd, J = 9.0, 2.3 Hz, 2H), 7.44 (dd, J = 8.4, 4.2 Hz, 2H), 2.19 (s, 6H), 1.78 (s, 4H).

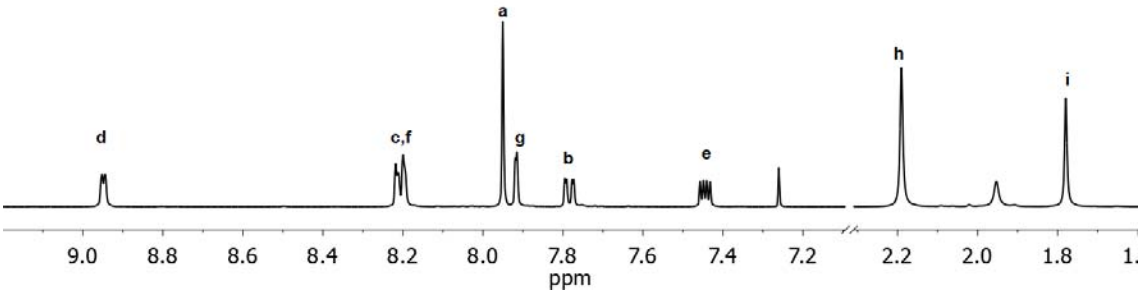

Figure 3.10 ^1H NMR spectrum (500 MHz, 298 K, $CDCl_3$) of **L²**.

^{13}C NMR (126 MHz, 298 K, $CDCl_3$): δ (ppm) = 167.47, 152.67, 151.25, 147.20, 136.40, 130.65, 130.08, 129.86, 128.22, 127.75, 125.07, 121.81, 116.80, 44.29, 34.94, 18.82.

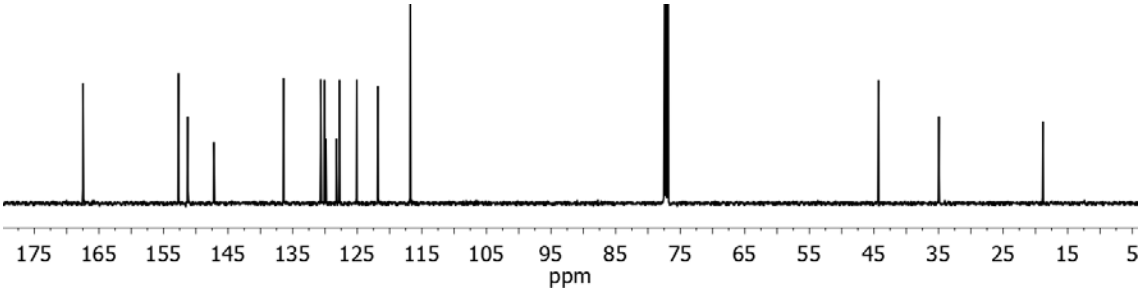

Figure 3.11 ^{13}C NMR spectrum (126 MHz, 298 K, $CDCl_3$) of **L²**.

ESI HRMS ($C_{40}H_{26}N_4O_4$): $[M + H]^+$ calcd. for $C_{40}H_{27}N_4O_4$ 627.2027; found 627.2026; $[M + 2H]^{2+}$ calcd. for $C_{40}H_{28}N_4O_4$ 314.1051; found 314.1051.

3.8.1.3 Ligand L³

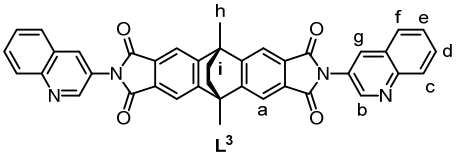

Under a nitrogen atmosphere, ligand **L³** was prepared from reported bis-anhydride **S1** (93.6 mg, 0.25 mmol, 1 eq.) and powdered 3-aminoquinoline (720.7 mg, 5.00 mmol, 20 eq.) by heating the mixture of solids without solvent in a preheated oil bath to 165 °C for 10 min. After the black melt cooled to room temperature, it was taken up into 5 mL chloroform, sonificated and the suspension was immediately subjected to flash column chromatography on silica gel ($CHCl_3$: MeOH = 50 : 1) to give the crude product. This was further purified via recycling gel permeation chromatography and the solvent was removed under reduced pressure to yield the desired product as a white powder (100.10 mg, 64 %).

¹H NMR (600 MHz, 298 K, $CDCl_3$): δ (ppm) = 9.02 (d, J = 2.4 Hz, 2H), 8.28 (d, J = 2.4 Hz, 2H), 8.17 (d, J = 8.4 Hz, 2H), 7.99 (s, 4H), 7.90 (d, J = 8.1 Hz, 2H), 7.78 (ddd, J = 8.3, 6.8, 1.4 Hz, 2H), 7.64 – 7.59 (m, 2H), 2.22 (s, 6H), 1.81 (s, 4H).

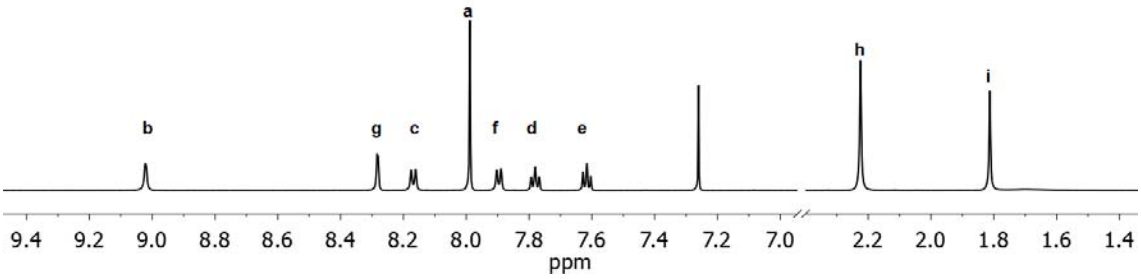

Figure 3.12 ^{1}H NMR spectrum (600 MHz, 298 K, $CDCl_3$) of **L³**.

¹³C NMR (151 MHz, 298 K, $CDCl_3$): δ (ppm) = 167.28, 152.84, 147.99, 147.02, 132.63, 130.31, 130.17, 129.52, 128.20, 127.76, 127.53, 125.74, 116.96, 44.39, 35.00, 18.86.

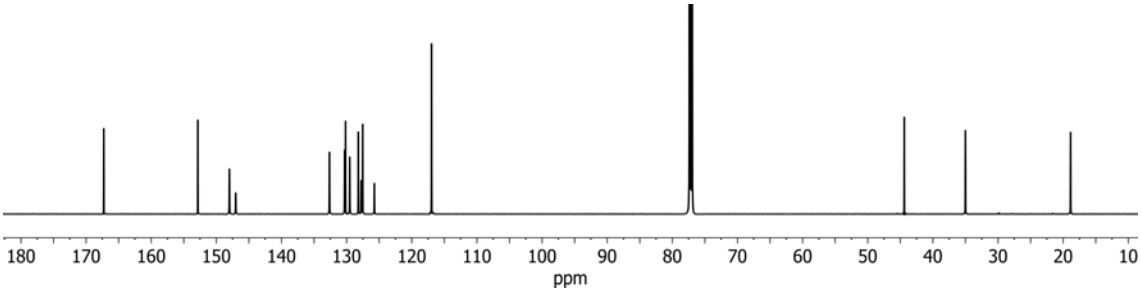

Figure 3.13 ^{13}C NMR spectrum (151 MHz, 298 K, $CDCl_3$) of **L^3**.

ESI HRMS ($C_{40}H_{26}N_4O_4$): $[M + H]^+$ calcd. for $C_{40}H_{27}N_4O_4$ 627.2027; found 627.2015.

3.8.1.4 Ligand L^4

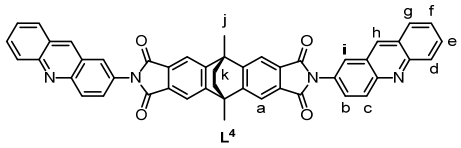

Under a nitrogen atmosphere, ligand **L^4** was prepared from reported bis-anhydride **S1** (37.4 mg, 0.10 mmol, 1 eq.) and powdered 2-aminoacridine (194.2 mg, 1.00 mmol, 10 eq.) by heating the mixture of solids without solvent in a preheated oil bath to 230 °C for 10 min. After the black melt cooled to room temperature, it was taken up into 10 mL chloroform, sonificated and the suspension was immediately subjected to flash column chromatography on silica gel ($CHCl_3$: MeOH = 30 : 1) to give the crude product. This was further purified via recycling gel permeation chromatography and the solvent was removed under reduced pressure to yield the desired product as a pale yellow powder (41.6 mg, 57 %).

^{1}H NMR (700 MHz, 298 K, $CDCl_3$): δ (ppm) = 8.85 (s, 2H), 8.36 (d, J = 9.3 Hz, 2H), 8.27 (d, J = 8.8 Hz, 2H), 8.14 (d, J = 2.3 Hz, 2H), 8.03 (d, J = 8.4 Hz, 2H), 8.00 (s, 4H), 7.88 (dd, J = 9.3, 2.3 Hz, 2H), 7.83 (ddd, J = 8.4, 6.5, 1.3 Hz, 2H), 7.60 – 7.57 (m, 2H), 2.25 (s, 6H), 1.83 (s, 4H).

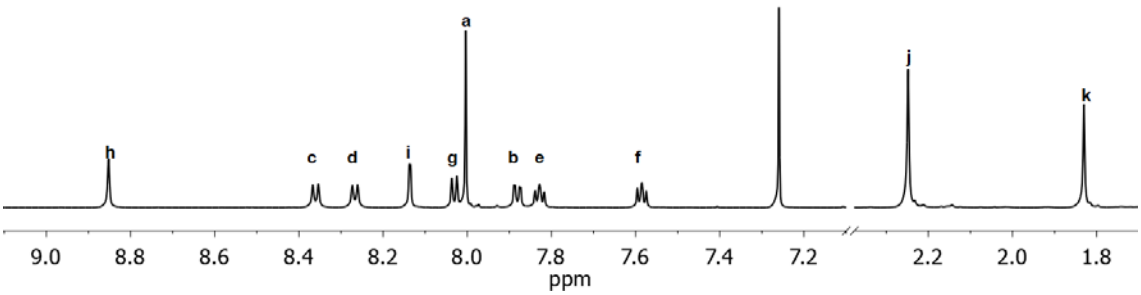

Figure 3.14 ^{1}H NMR spectrum (700 MHz, 298 K, $CDCl_3$) of **L^4**.

^{13}C NMR (151 MHz, 298 K, $CDCl_3$): δ (ppm) = 167.56, 152.80, 149.69, 147.91, 136.69, 130.93, 130.83, 130.25, 129.72, 129.13, 128.69, 128.36, 126.92, 126.40, 126.21, 125.20, 116.90, 44.40, 35.05, 18.94.

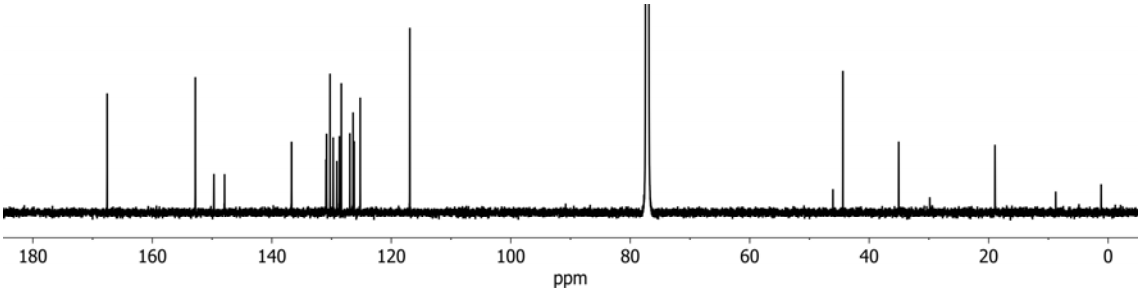

Figure 3.15 ^{13}C NMR spectrum (151 MHz, 298 K, $CDCl_3$) of **L^4**.

ESI HRMS ($C_{48}H_{30}N_4O_4$): $[M + H]^+$ calcd. for $C_{48}H_{31}N_4O_4$ 727.2340; found 727.2445; $[M + 2H]^{2+}$ calcd. for $C_{48}H_{32}N_4O_4$ 364.1206; found 364.1260.

3.8.2 Formation and characterization of metallosupramolecules

3.8.2.1 Cage $[Pd_2L^1_4]^{4+}$

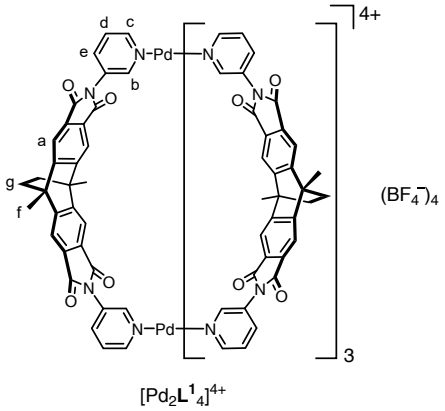

A solution of $[Pd(MeCN)_4](BF_4)_2$ (233.8 µL, 15 mM/CD_3CN, 3.51 µmol, 1 eq.) was combined with ligand **L^1** (3.7 mg, 7.01 µmol, 2 eq.) in CD_3CN (2505 µL) and heated at 70 °C for 1 d to give a 0.64 mM solution of cage $[Pd_2L^1_4]^{4+}$.

^{1}H NMR (600 MHz, 298 K, CD_3CN): δ (ppm) = 9.14 (d, J = 2.2 Hz, 8H), 8.78 (dd, J = 5.8, 1.2 Hz, 8H), 8.21 (dt, J = 8.5, 1.6 Hz, 8H), 7.79 (s, 16H), 7.71 (dd, J = 8.4, 5.7 Hz, 8H), 2.13 (s, mixed with water peak in CD_3CN), 1.79 (s, 16H).

A signal at 2.13 ppm overlapping with the solvent residual peak in the aliphatic region could be assigned via 2D NMR spectroscopy.

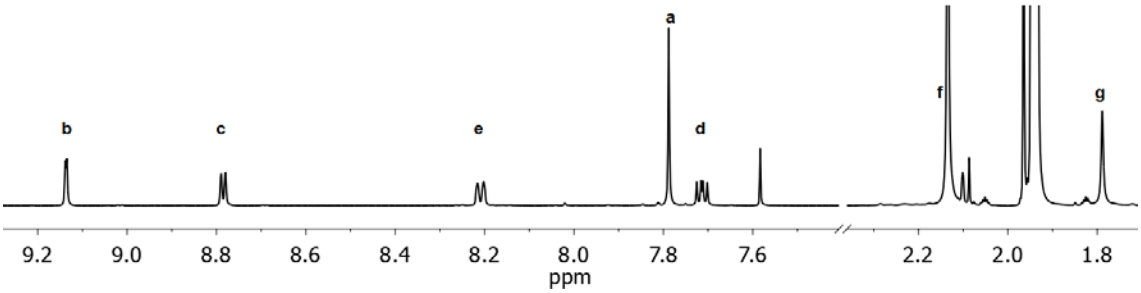

Figure 3.16 ^{1}H NMR spectrum (600 MHz, 298 K, CD_3CN) of $[Pd_2L^1_4]^{4+}$.

^{13}C NMR (151 MHz, 298 K, CD_3CN): δ (ppm) = 166.49, 154.35, 150.36, 149.08, 138.41, 132.74, 130.34, 128.39, 117.71, 45.22, 35.00, 18.61.

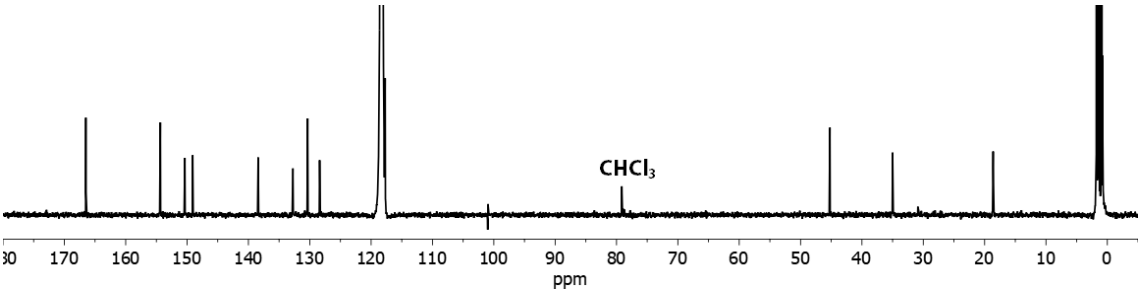

Figure 3.17 ^{13}C NMR spectrum (151 MHz, 298 K, CD_3CN) of $[Pd_2\mathbf{L^1}_4]^{4+}$.

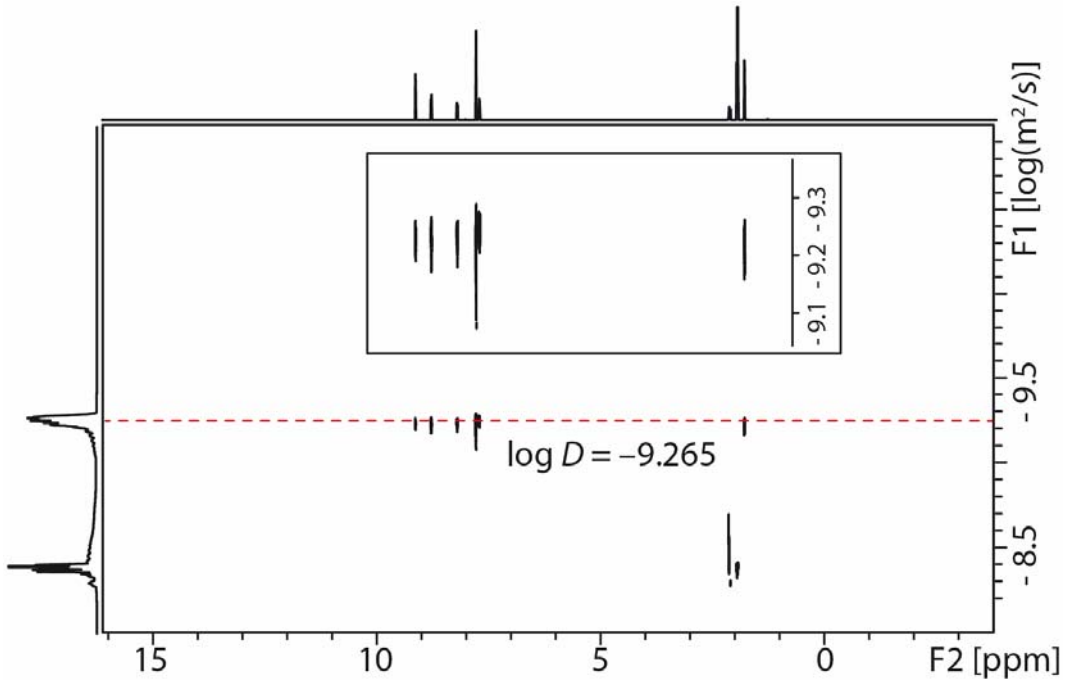

Figure 3.18 DOSY spectrum (500 MHz, 298 K, CD_3CN) of $[Pd_2\mathbf{L^1}_4]^{4+}$: diffusion coefficient = 5.4 x 10^{-10} m^2s^{-1}, log D = –9.26, r = 11.7 Å.

ESI HRMS ($C_{128}H_{88}N_{16}O_{16}Pd_2B_4F_{16}$): $[Pd_2\mathbf{L^1}_4]^{4+}$ calcd. for $C_{128}H_{88}N_{16}O_{16}Pd_2$ 579.6166; found 579.6176; $[Pd_2\mathbf{L^1}_4+BF_4]^{3+}$ calcd. for $C_{128}H_{88}N_{16}O_{16}Pd_2BF_4$ 801.8236; found 801.8256; $[Pd_2\mathbf{L^1}_4+2BF_4]^{2+}$ calcd. for $C_{128}H_{88}N_{16}O_{16}Pd_2B_2F_8$ 1246.2376; found 1246.2416.

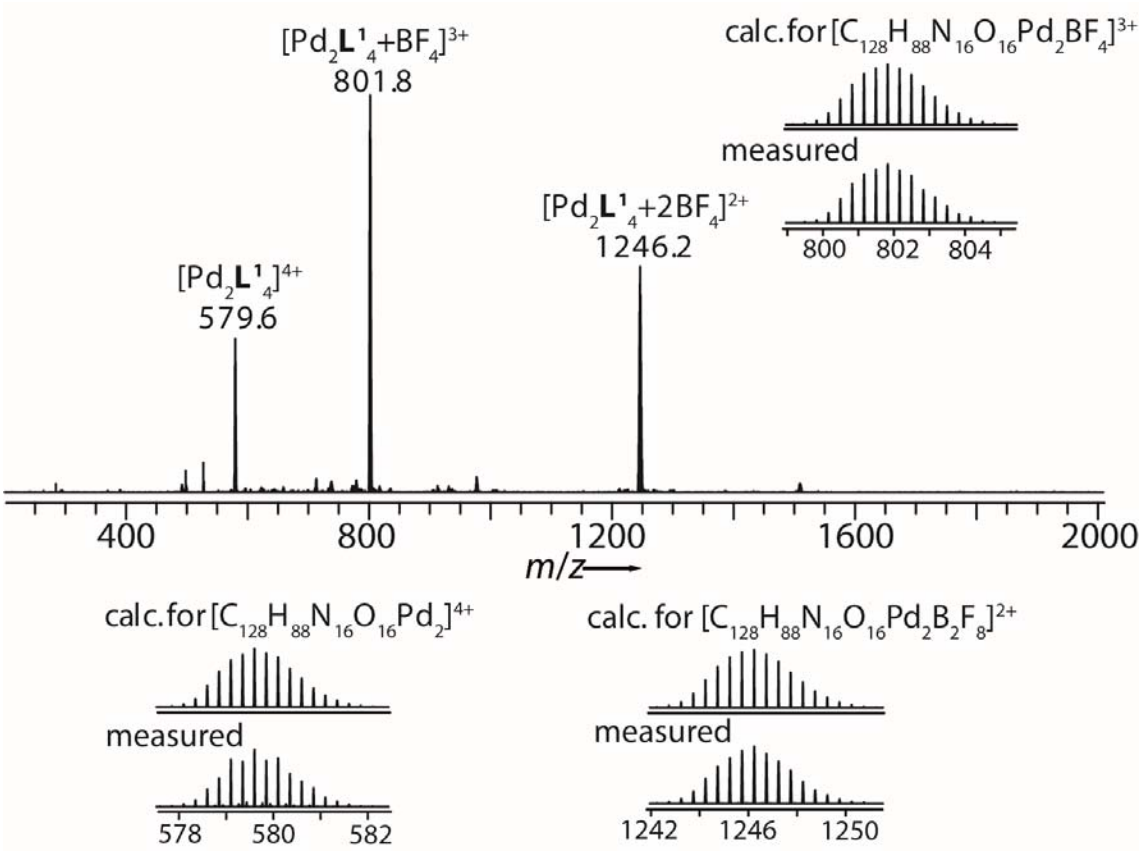

Figure 3.19 ESI mass spectrum of $[Pd_2\mathbf{L^1}_4]^{4+}$.

3.8.2.2 Cage $[C_{60}@Pd_2L^1_4]^{4+}$

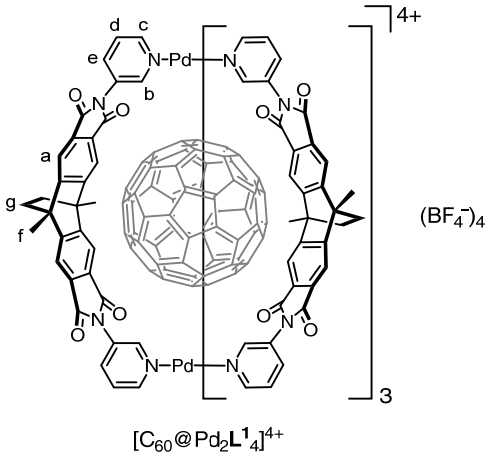

$[C_{60}@Pd_2\mathbf{L^1}_4]^{4+}$

A solution of $[Pd(MeCN)_4](BF_4)_2$ (226.8 µL, 15 mM/CD_3CN, 3.40 µmol, 1 eq.) was combined with ligand $\mathbf{L^1}$ (3.6 mg, 6.80 µmol, 2 eq.) and C_{60} (3.7 mg, 5.11 µmol, 1.5 eq.) in CD_3CN (2505 µL) and heated at 70 °C for 1 d. Excess C_{60} solid was removed by filtration to give a 0.64 mM pale purple solution of host-guest complex $[C_{60}@Pd_2\mathbf{L^1}_4]^{4+}$.

^{1}H NMR (600 MHz, 298 K, CD_3CN): δ (ppm) = 8.54 – 8.52 (m, 8H), 8.41 (ddd, J = 8.4, 2.2, 1.2 Hz, 8H), 7.87 (dd, J = 8.5, 5.8 Hz, 8H), 7.85 (s, 16H), 7.59 (d, J = 2.2 Hz, 8H), 2.22 (s, 24H), 1.82 (s, 16H).

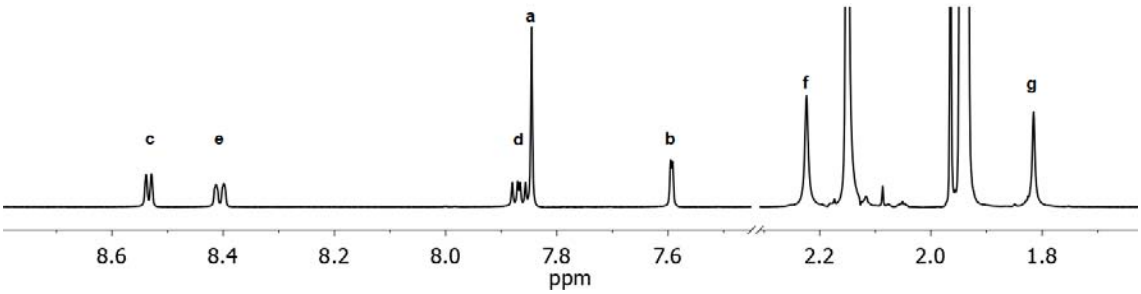

Figure 3.20 ^{1}H NMR spectrum (600 MHz, 298 K, CD_3CN) of $[C_{60}@Pd_2\mathbf{L^1}_4]^{4+}$.

^{13}C NMR (151 MHz, 298 K, CD_3CN): δ (ppm) = 166.14, 154.73, 152.32, 147.64, 141.83 (C_{60}), 140.46, 132.71, 130.80, 129.54, 118.60, 45.44, 34.87, 18.52.

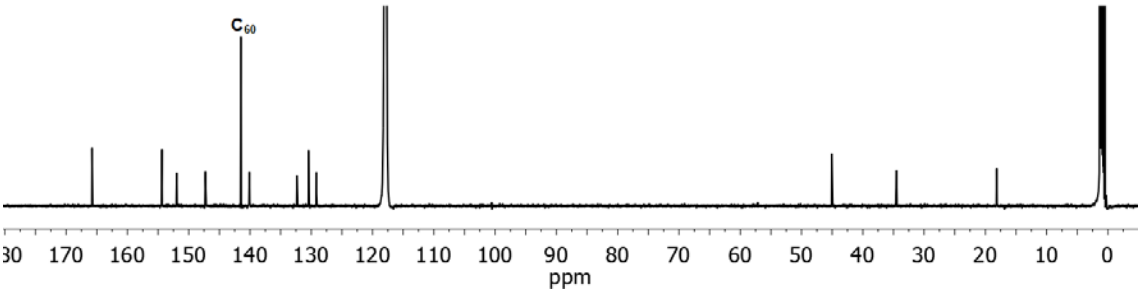

Figure 3.21 ^{13}C NMR spectrum (151 MHz, 298 K, CD_3CN) of $[C_{60}@Pd_2\mathbf{L^1}_4]^{4+}$. A single signal at 141.83 ppm corresponds to the encapsulated C_{60}.

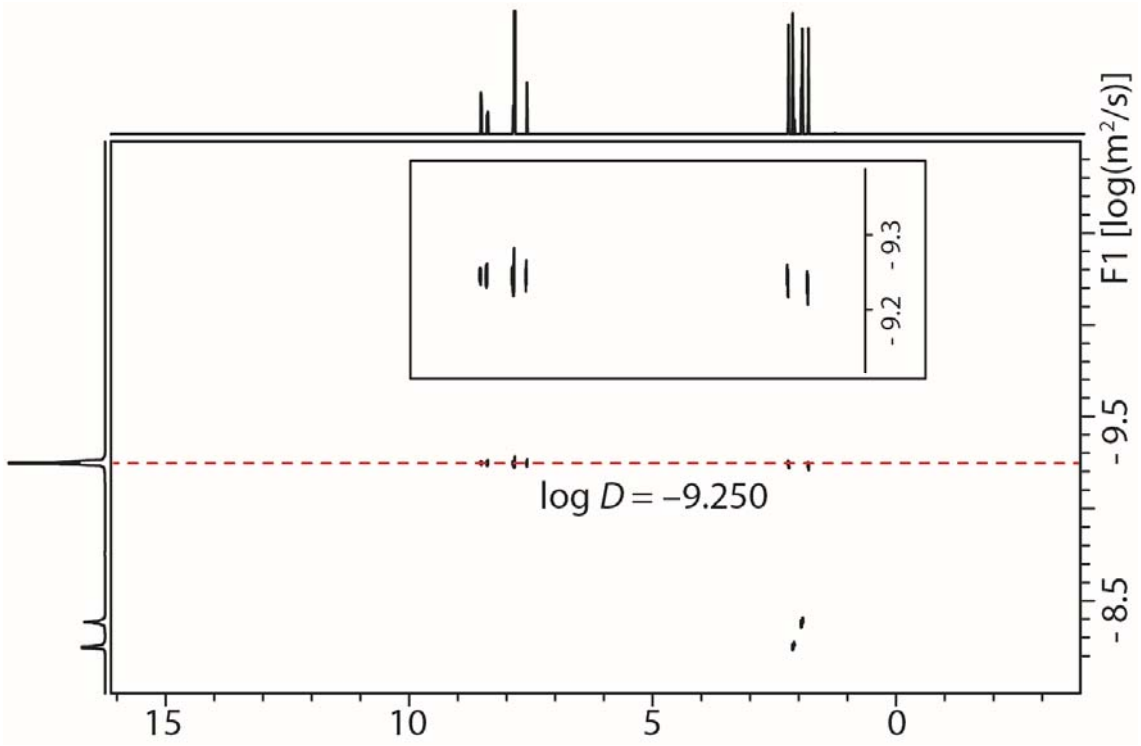

Figure 3.22 DOSY spectrum (500 MHz, 298 K, CD_3CN) of $[C_{60}@Pd_2\mathbf{L^1}_4]^{4+}$: diffusion coefficient = 5.6 x 10^{-10} m^2s^{-1}, log D = –9.25, r = 11.3 Å.

ESI HRMS ($C_{188}H_{88}N_{16}O_{16}Pd_2B_4F_{16}$): $[C_{60}@Pd_2\mathbf{L^1}_4]^{4+}$ calcd. for $C_{188}H_{88}N_{16}O_{16}Pd_2$ 759.8673; found 759.8696; $[C_{60}@Pd_2\mathbf{L^1}_4+BF_4]^{3+}$ calcd. for $C_{188}H_{88}N_{16}O_{16}Pd_2BF_4$ 1042.1578; found 1042.1617; $[C_{60}@Pd_2\mathbf{L^1}_4+2BF_4]^{2+}$ calcd. for $C_{188}H_{88}N_{16}O_{16}Pd_2B_2F_8$ 1606.2385; found 1606.2454.

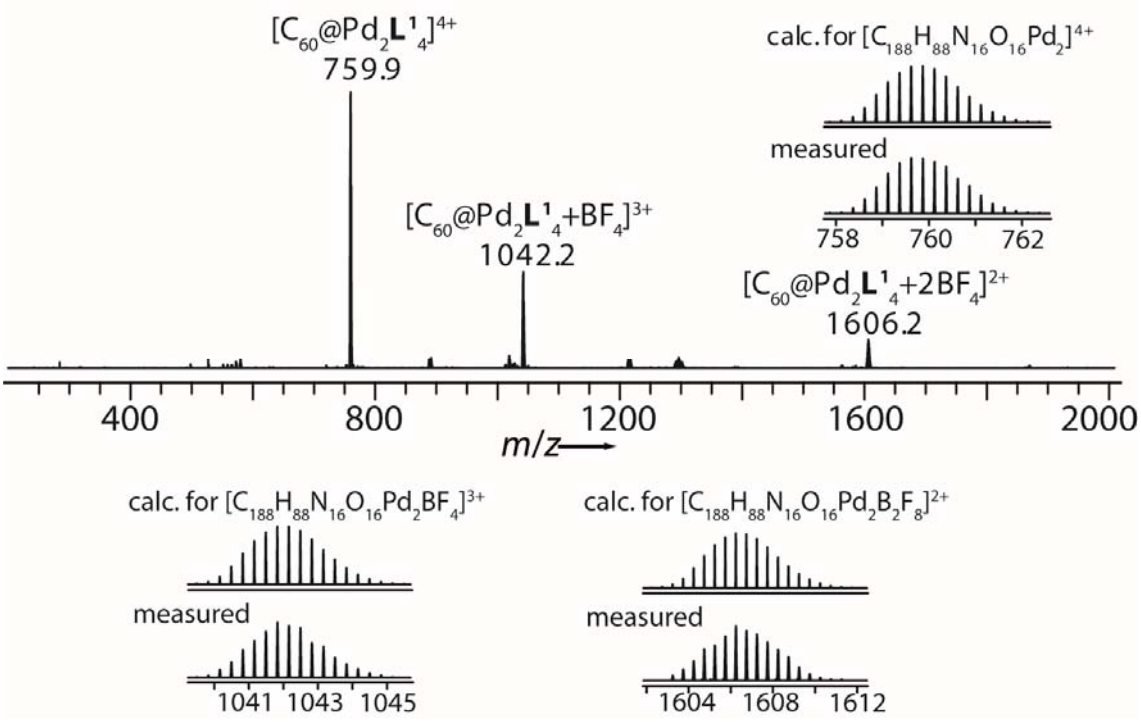

Figure 3.23 ESI mass spectrum of $[C_{60}@Pd_2\mathbf{L^1}_4]^{4+}$.

3.8.2.3 Bowl $[Pd_2\mathbf{L^2}_3(MeCN)_2]^{4+}$

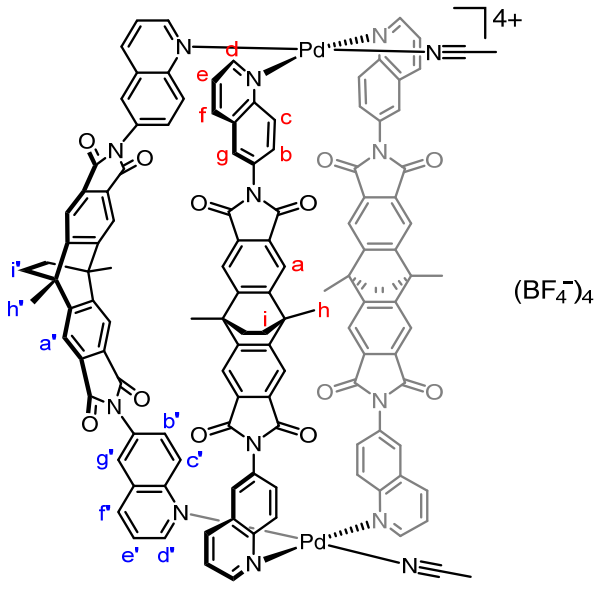

$[Pd_2\mathbf{L^2}_3(MeCN)_2]^{4+}$

A solution of $[Pd(MeCN)_4](BF_4)_2$ (732.4 µL, 15 mM/CD_3CN, 10.99 µmol, 1 eq.) was combined with ligand $\mathbf{L^2}$ (10.3 mg, 16.47 µmol, 1.5 eq.) in CD_3CN (7848 µL) and stirred at room temperature for 2 d to give a 0.64 mM solution of bowl $[Pd_2\mathbf{L^2}_3(MeCN)_2]^{4+}$.

^{1}H NMR (600 MHz, 298 K, CD_3CN): δ (ppm) = 9.99 (d, J = 9.1 Hz, 4H), 9.85 (dd, J = 5.7, 1.3 Hz, 2H), 9.58 (dd, J = 5.5, 1.3 Hz, 4H), 9.31 (d, J = 9.0 Hz, 2H), 8.69 (d, J = 8.3 Hz, 4H), 8.51 (d, J = 8.3 Hz, 2H), 8.26 (dd, J = 9.1, 2.2 Hz, 4H), 8.16 (d, J = 2.2 Hz, 4H), 7.98 (s, 4H), 7.93 (s, 4H), 7.87 – 7.84 (m, 4H), 7.79 (dd, J = 8.3, 5.5 Hz, 4H), 7.73 (s, 4H), 7.42 (dd, J = 9.1, 2.3 Hz, 2H), 2.26 (s, 6H), 2.22 (s, 6H), 2.08 (s, 6H), 1.88 (s, 8H), 1.77 (s, 4H).

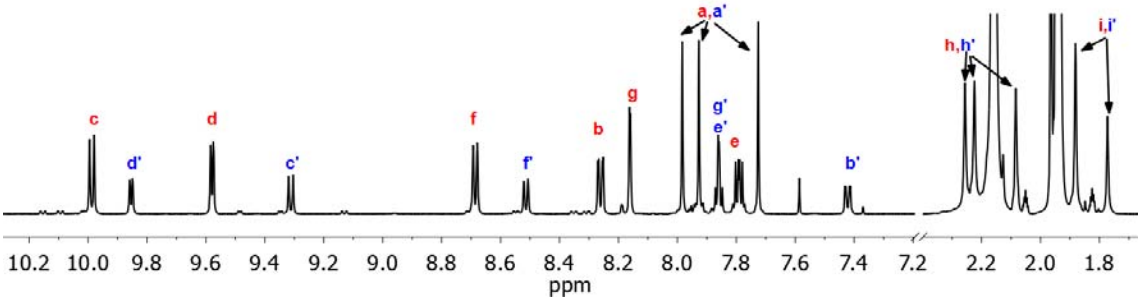

Figure 3.24 ^{1}H NMR spectrum (600 MHz, 298 K, CD_3CN) of $[Pd_2\mathbf{L^2}_3(MeCN)_2]^{4+}$.

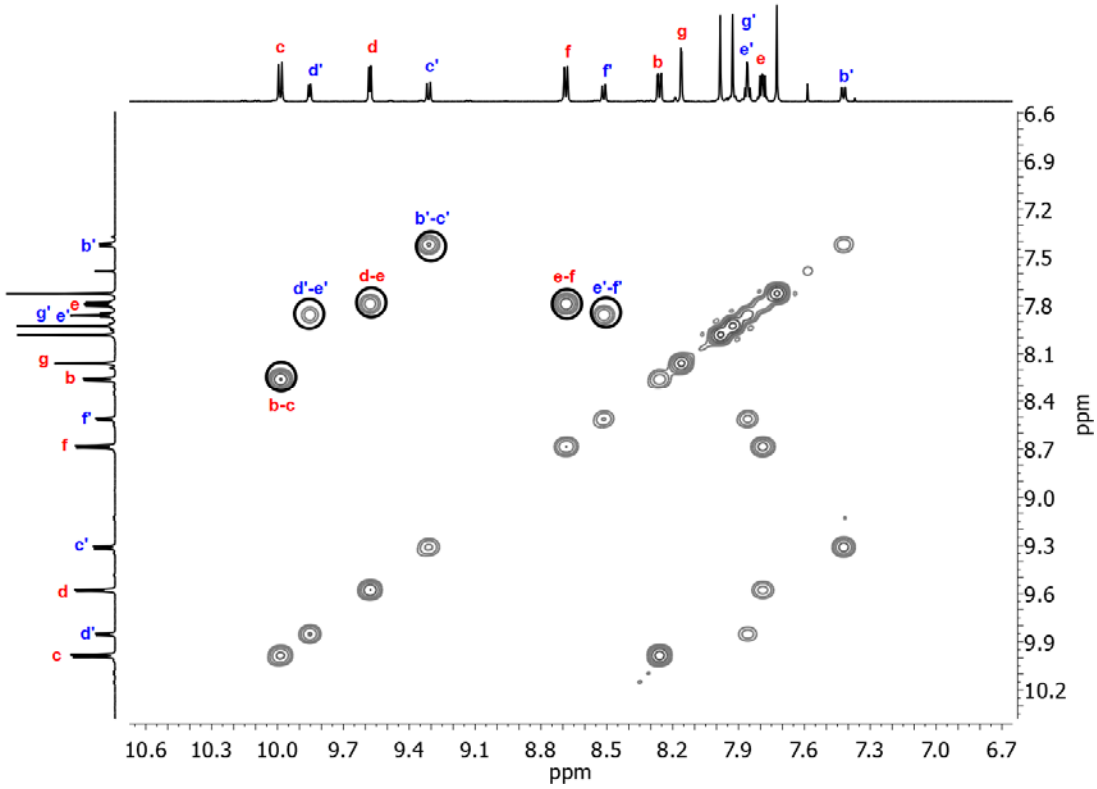

Figure 3.25 Partial ^{1}H – ^{1}H COSY spectrum (600 MHz, 298 K, CD_3CN) of $[Pd_2\mathbf{L^2}_3(MeCN)_2]^{4+}$.

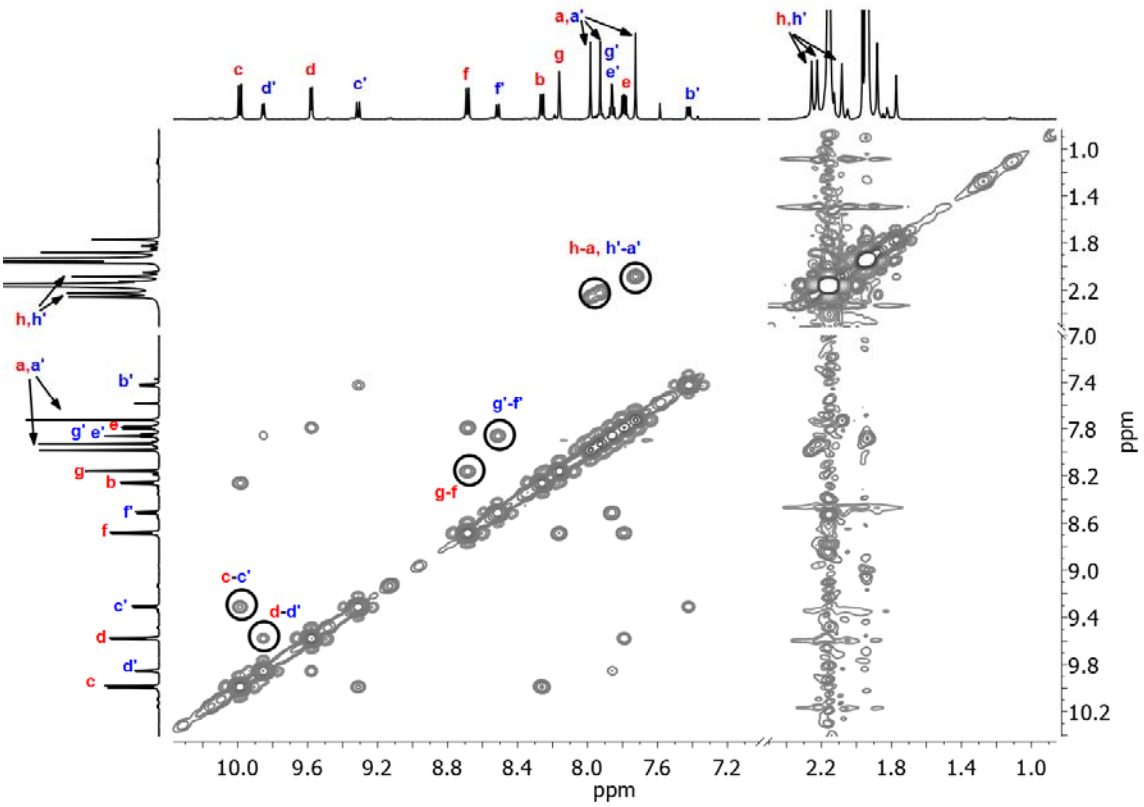

Figure 3.26 Partial $^{1}H - {}^{1}H$ NOESY spectrum (600 MHz, 298 K, CD_3CN) of $[Pd_2\mathbf{L^2}_3(MeCN)_2]^{4+}$.

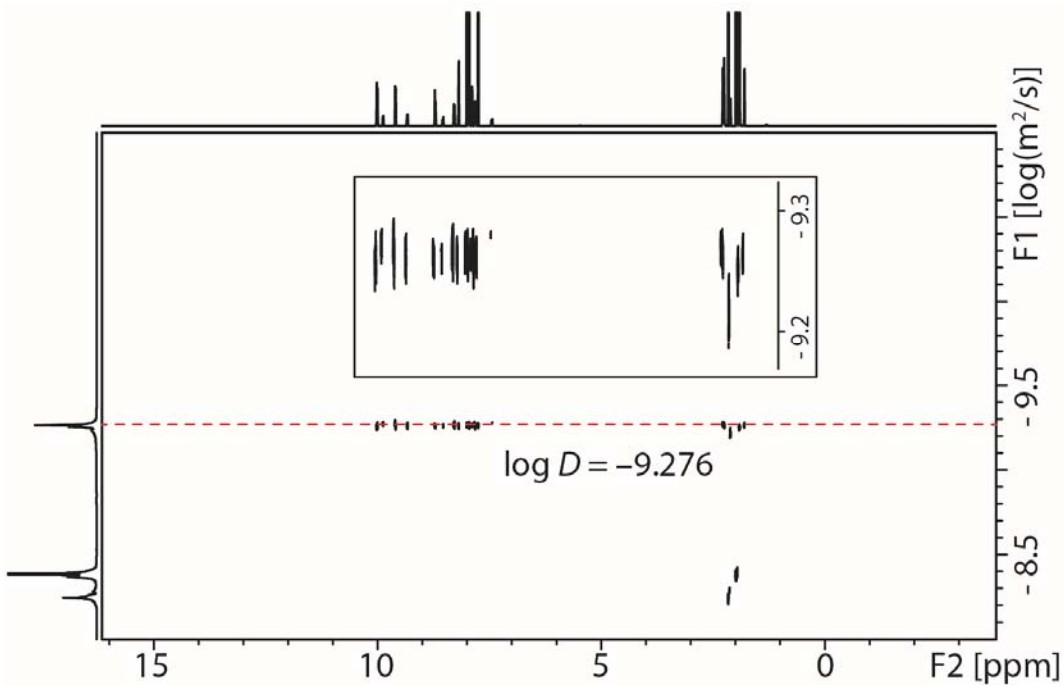

Figure 3.27 DOSY spectrum (500 MHz, 298 K, CD_3CN) of $[Pd_2\mathbf{L^2}_3(MeCN)_2]^{4+}$: diffusion coefficient = 5.3 x 10^{-10} m^2s^{-1}, log *D* = −9.28, r = 12.0 Å.

ESI HRMS ($C_{124}H_{84}N_{14}O_{12}Pd_2B_4F_{16}$): $[Pd_2\mathbf{L^2}_3(MeCN)_2]^{4+}$ calcd. for $C_{124}H_{84}N_{14}O_{12}Pd_2$ 543.6123; found 543.6134; $[Pd_2\mathbf{L^2}_3(MeCN)+F]^{3+}$ calcd. for $C_{122}H_{81}N_{13}O_{12}Pd_2F$ 717.4739; found 717.4762; $[Pd_2\mathbf{L^2}_3(MeCN)+Cl]^{3+}$ calcd. for

$C_{122}H_{81}N_{13}O_{12}Pd_2Cl$ 723.1307; found 723.1325; $[Pd_2\mathbf{L^2}_3+BF_4]^{3+}$ calcd. for $C_{120}H_{78}N_{12}O_{12}Pd_2BF_4$ 726.1335; found 726.1418; $[Pd_2\mathbf{L^2}_3+2F]^{2+}$ calcd. for $C_{120}H_{78}N_{12}O_{12}Pd_2F_2$ 1065.1970; found 1065.2010.

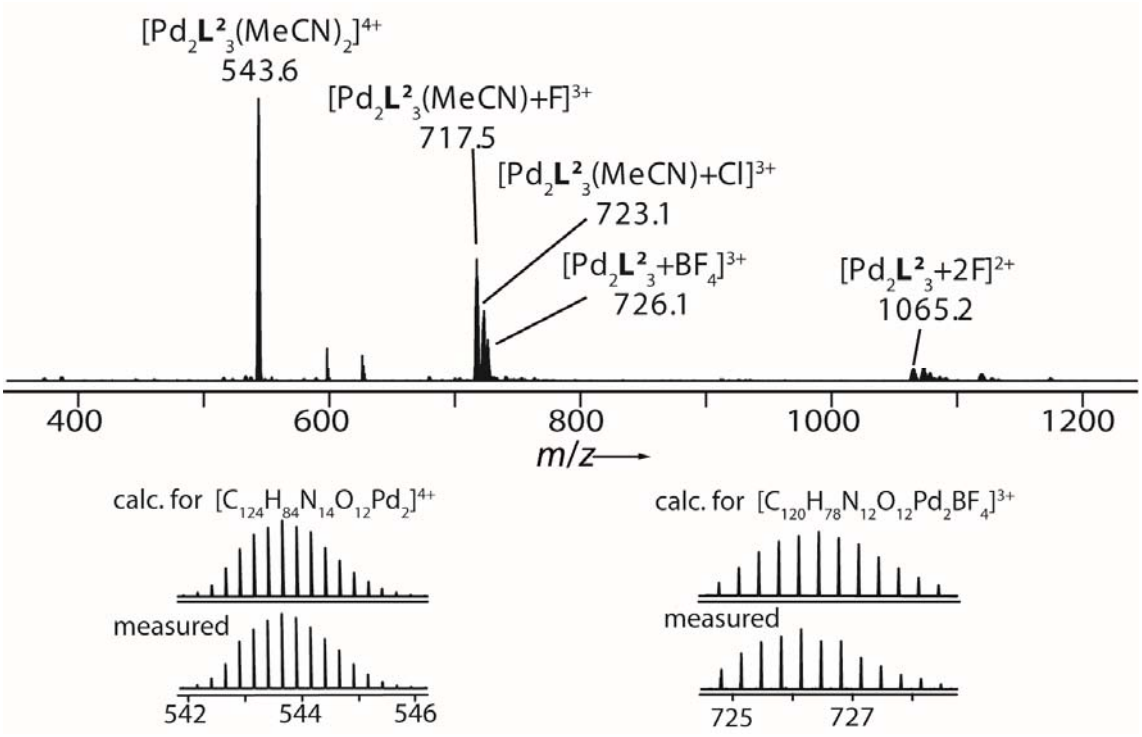

Figure 3.28 ESI mass spectrum of $[Pd_2\mathbf{L^2}_3(MeCN)_2]^{4+}$. The presence of the $[Pd_2\mathbf{L^2}_3(MeCN)+F]^{3+}$, $[Pd_2\mathbf{L^2}_3(MeCN)+Cl]^{3+}$ and $[Pd_2\mathbf{L^2}_3+2F]^{2+}$ species is due to substitution of coordinated CH_3CN by traces of various anions under the measurement conditions.

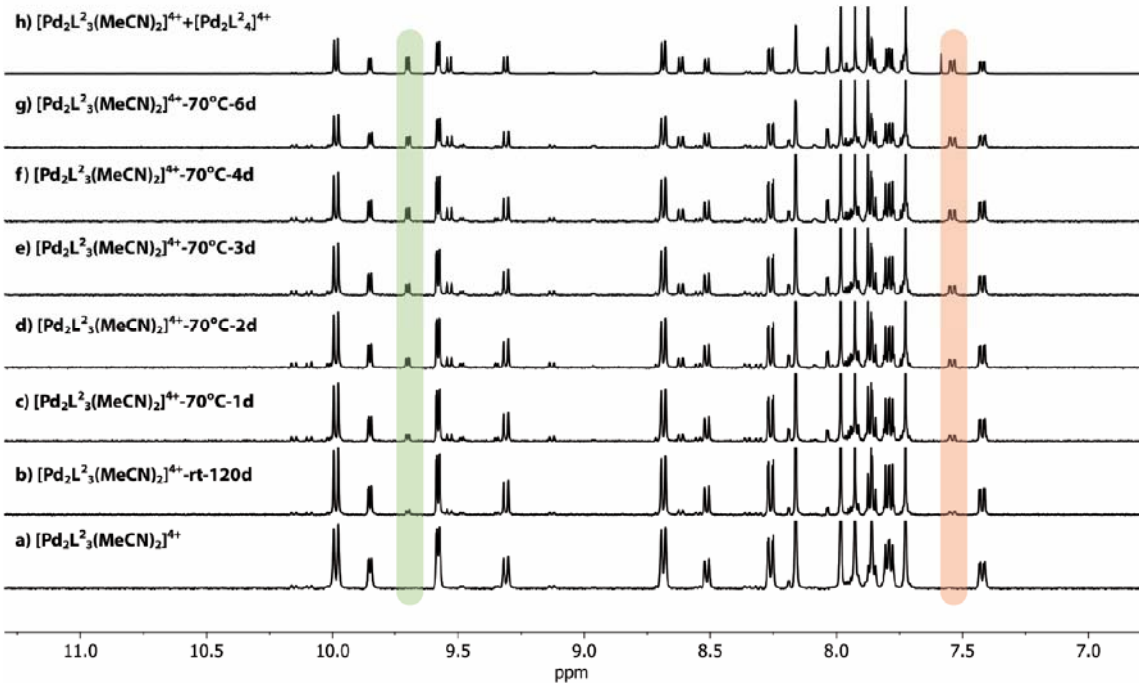

Figure 3.29 ^{1}H NMR spectra (500 MHz, 298 K, CD_3CN) following the integrity of $[Pd_2\mathbf{L^2}_3(MeCN)_2]^{4+}$ at rt or 70 °C, indicating partial conversion into cage $[Pd_2\mathbf{L^2}_4]^{4+}$ after heating for several days. The quinoline proton D and proton B of $[Pd_2\mathbf{L^2}_4]^{4+}$ are highlighted in green and red, respectively.

3.8.2.4 The mixture of bowl $[Pd_2L^2_3(MeCN)_2]^{4+}$ and cage $[Pd_2L^2_4]^{4+}$

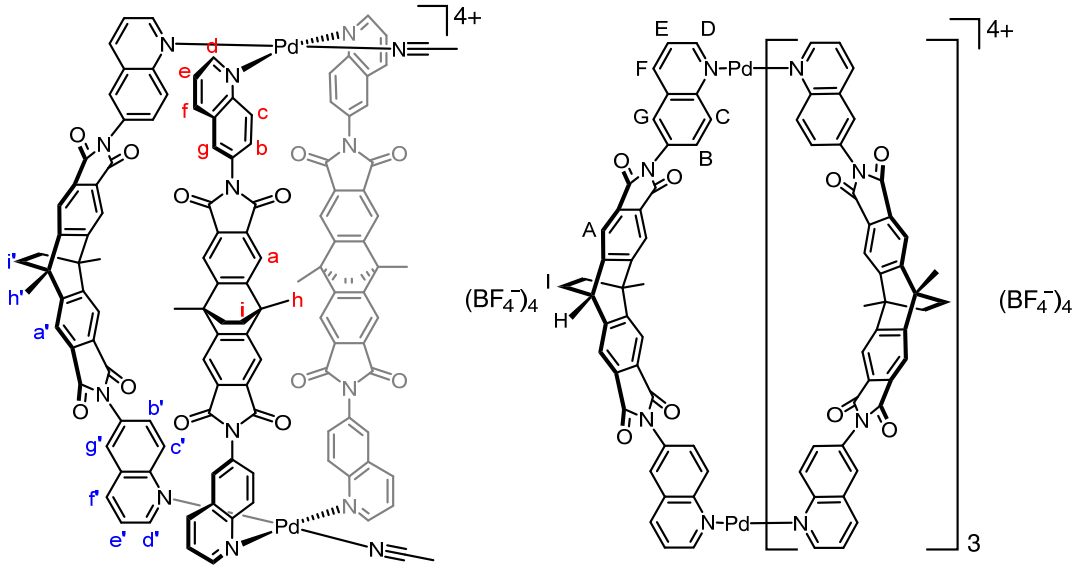

A solution of $[Pd(CH_3CN)_4](BF_4)_2$ (281.9 µL, 15 mM/CD_3CN, 4.23 µmol, 1 eq.) was combined with ligand **L²** (5.3 mg, 8.46 µmol, 2 eq.) in CD_3CN (3020 µL) and heated at 70 °C for 3 d. Remaining ligand was removed by filtration to give a mixture of bowl $[Pd_2L^2_3(MeCN)_2]^{4+}$ and cage $[Pd_2L^2_4]^{4+}$ (ratio: ca. 4:1).

^{1}H NMR (600 MHz, 298 K, CD_3CN): δ (ppm) = δ 9.99 (d, J = 9.1 Hz, 2H), 9.85 (dd, J = 5.7, 1.3 Hz, 1H), 9.70 (dd, J = 5.5, 1.3 Hz, 1H), 9.58 (dd, J = 5.5, 1.3 Hz, 2H), 9.54 (d, J = 9.2 Hz, 1H), 9.31 (d, J = 9.0 Hz, 1H), 8.69 (d, J = 8.3 Hz, 2H), 8.62 (d, J = 8.3 Hz, 1H), 8.51 (d, J = 8.3 Hz, 1H), 8.26 (dd, J = 9.1, 2.3 Hz, 2H), 8.16 (d, J = 2.3 Hz, 2H), 8.03 (d, J = 2.2 Hz, 1H), 7.98 (s, 2H), 7.93 (s, 2H), 7.87 (s, 2H), 7.86 (d, J = 2.4 Hz, 2H), 7.79 (dd, J = 8.2, 5.5 Hz, 2H), 7.75 – 7.72 (m, 3H), 7.54 (dd, J = 9.2, 2.3 Hz, 1H), 7.42 (dd, J = 9.0, 2.3 Hz, 1H), 2.26 (s, 3H), 2.22 (s, 3H), 2.20 (s, 3H), 1.89 (d, J = 5.6 Hz, 6H), 1.77 (s, 2H).

All the signals in the aromatic region could be assigned via 2D NMR spectroscopy.

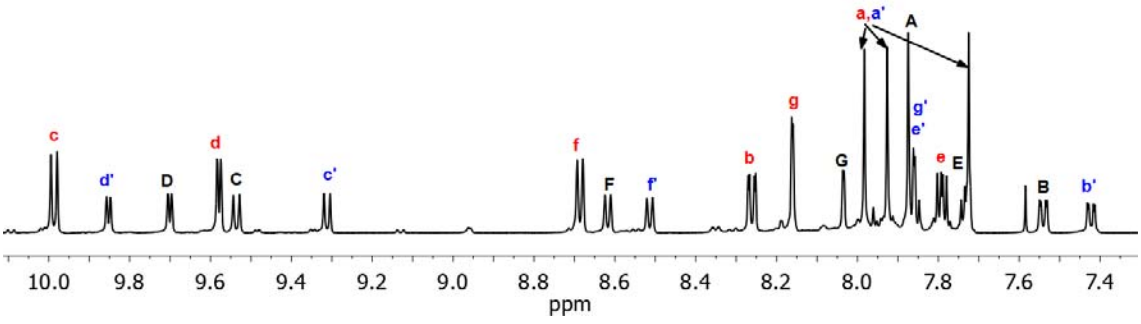

Figure 3.30 ^{1}H NMR spectrum (600 MHz, 298 K, CD_3CN) of the mixture of bowl $[Pd_2L^2_3(MeCN)_2]^{4+}$ and cage $[Pd_2L^2_4]^{4+}$.

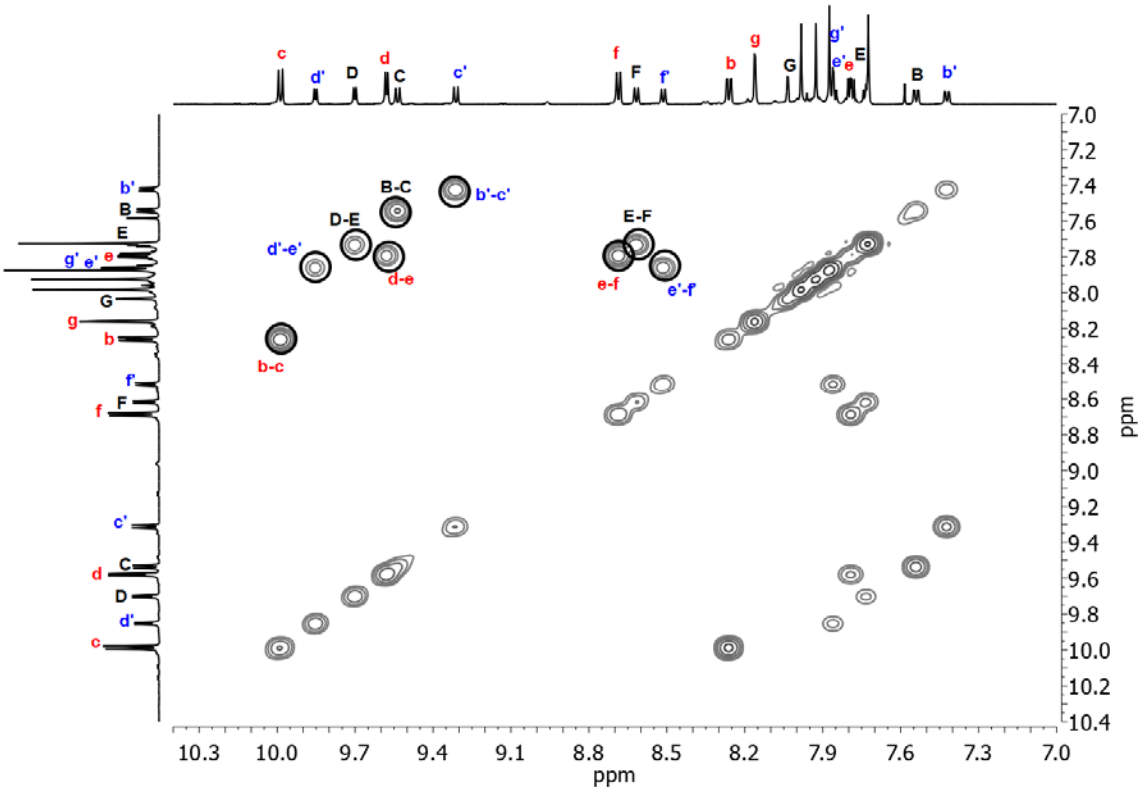

Figure 3.31 Partial ^{1}H – ^{1}H COSY spectrum (600 MHz, 298 K, CD_3CN) of the mixture of bowl $[Pd_2\mathbf{L^2}_3(MeCN)_2]^{4+}$ and cage $[Pd_2\mathbf{L^2}_4]^{4+}$.

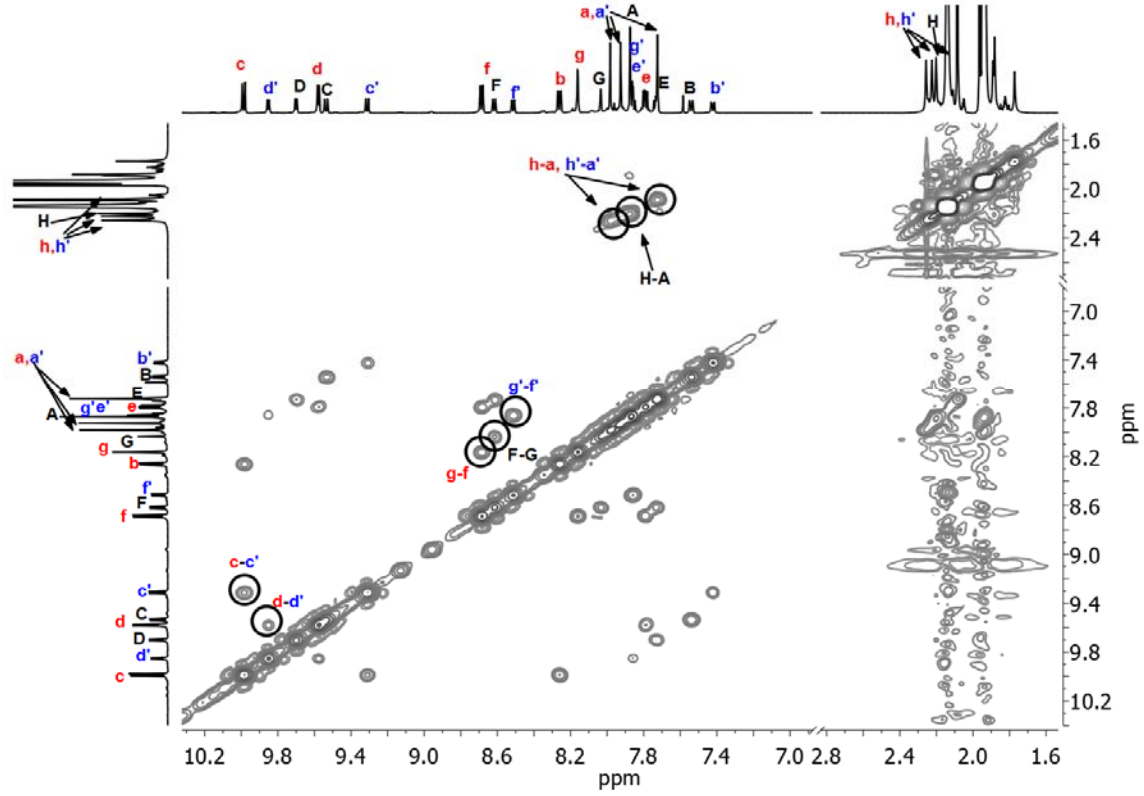

Figure 3.32 Partial ^{1}H – ^{1}H NOESY spectrum (600 MHz, 298 K, CD_3CN) of the mixture of bowl $[Pd_2\mathbf{L^2}_3(MeCN)_2]^{4+}$ and cage $[Pd_2\mathbf{L^2}_4]^{4+}$.

ESI HRMS ($C_{124}H_{84}N_{14}O_{12}Pd_2B_4F_{16}$ and $C_{160}H_{104}N_{16}O_{16}Pd_2B_4F_{16}$): $[Pd_2\mathbf{L^2}_4]^{4+}$ calcd. for $C_{160}H_{104}N_{16}O_{16}Pd_2$ 679.8984; found 679.8983; $[Pd_2\mathbf{L^2}_4+BF_4]^{3+}$ calcd. for $C_{160}H_{104}N_{16}O_{16}Pd_2BF_4$ 935.1988; found 935.2001; $[Pd_2\mathbf{L^2}_4+2BF_4]^{2+}$ calcd. for

$C_{160}H_{104}N_{16}O_{16}Pd_2B_2F_8$ 1446.3000; found 1446.3028. Other peaks come from the bowl $[Pd_2\mathbf{L^2}_3(MeCN)_2]^{4+}$ species as shown before.

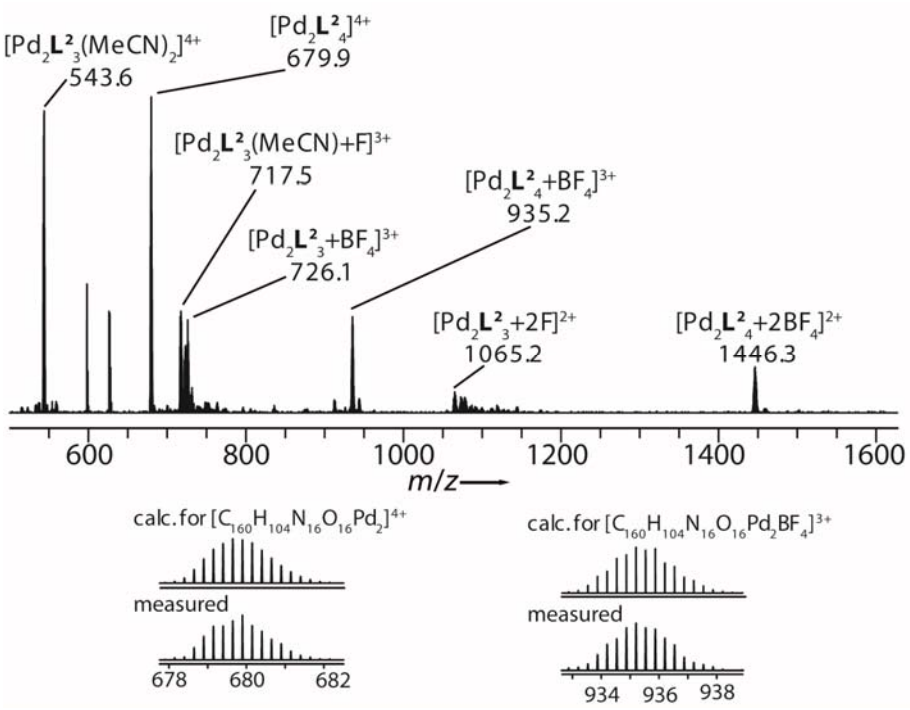

Figure 3.33 ESI mass spectrum of the mixture of bowl $[Pd_2\mathbf{L^2}_3(MeCN)_2]^{4+}$ and cage $[Pd_2\mathbf{L^2}_4]^{4+}$. The presence of the $[Pd_2\mathbf{L^2}_3(MeCN)+F]^{3+}$ and $[Pd_2\mathbf{L^2}_3+2F]^{2+}$ species is due to substitution of coordinated CH_3CN by traces of various anions under the measurement conditions.

3.8.2.5 Bowl $[C_{60}@Pd_2\mathbf{L^2}_3(MeCN)_2]^{4+}$

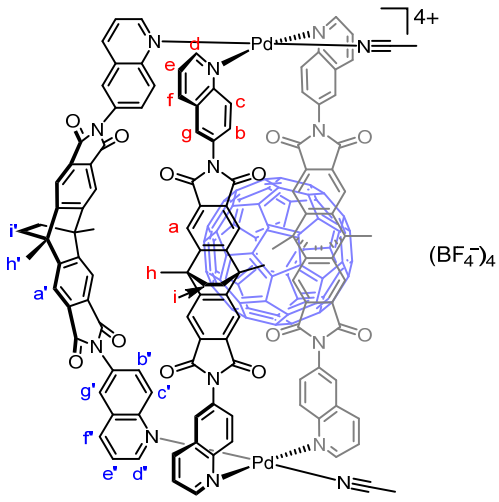

$[C_{60}@Pd_2\mathbf{L^2}_3(MeCN)_2]^{4+}$

A solution of $[Pd(MeCN)_4](BF_4)_2$ (797.0 µL, 15 mM/CD_3CN, 11.96 µmol, 1 eq.) was combined with ligand $\mathbf{L^2}$ (11.2 mg, 17.92 µmol, 1.5 eq.) and C_{60} (5.0 mg, 6.97 µmol, 0.6 eq.) in CD_3CN (8540 µL) and stirred at room temperature for 2 d (or at 70 °C for 1 d). Excess C_{60} solid was removed by filtration to give a 0.64 mM pale purple solution of bowl $[C_{60}@Pd_2\mathbf{L^2}_3(MeCN)_2]^{4+}$.

^{1}H NMR (600 MHz, 298 K, CD_3CN): δ (ppm) = 10.32 (d, J = 9.1 Hz, 4H), 9.84 (dd, J = 5.7, 1.3 Hz, 2H), 9.46 (dd, J = 5.5, 1.3 Hz, 4H), 9.07 (d, J = 9.0 Hz, 2H), 8.68 (d, J = 8.2 Hz, 4H), 8.44 (d, J = 8.2 Hz, 2H), 8.33 (dd, J = 9.1, 2.3 Hz, 4H), 8.18 (d, J = 2.3 Hz, 4H), 8.04 (s, 4H), 7.96 (s, 4H), 7.84 – 7.80 (m, 4H), 7.77 (dd, J = 8.3, 5.5 Hz, 4H), 7.73 (s, 4H), 7.00 (dd, J = 9.1, 2.2 Hz, 2H), 2.26 (s, 6H), 2.24 (s, 6H), 2.09 (s, 6H), 1.79 (s, 8H), 1.67 (s, 4H).

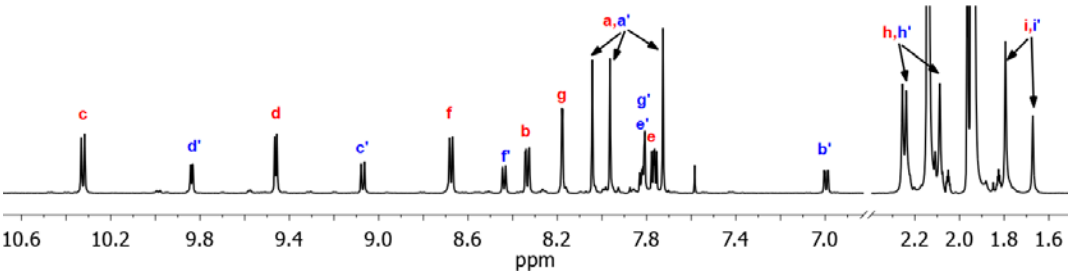

Figure 3.34 ^{1}H NMR spectrum (600 MHz, 298 K, CD_3CN) of $[C_{60}@Pd_2\mathbf{L^2}_3(MeCN)_2]^{4+}$.

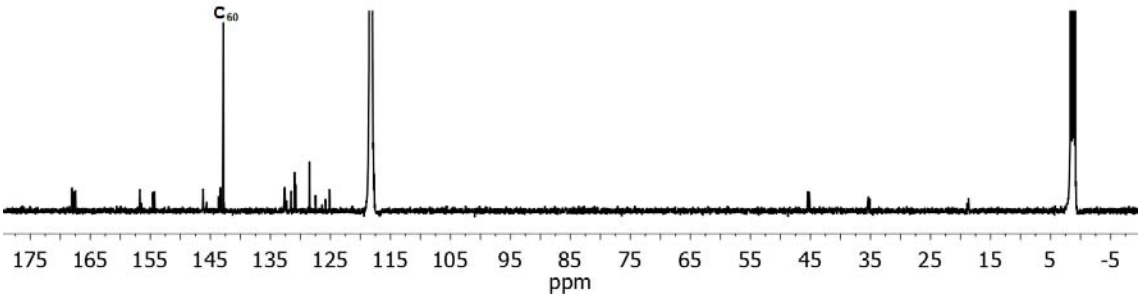

Figure 3.35 ^{13}C NMR spectrum (151 MHz, 298 K, CD_3CN) of $[C_{60}@Pd_2\mathbf{L^2}_3(MeCN)_2]^{4+}$. A single signal at 142.83 ppm corresponds to the encapsulated C_{60}.

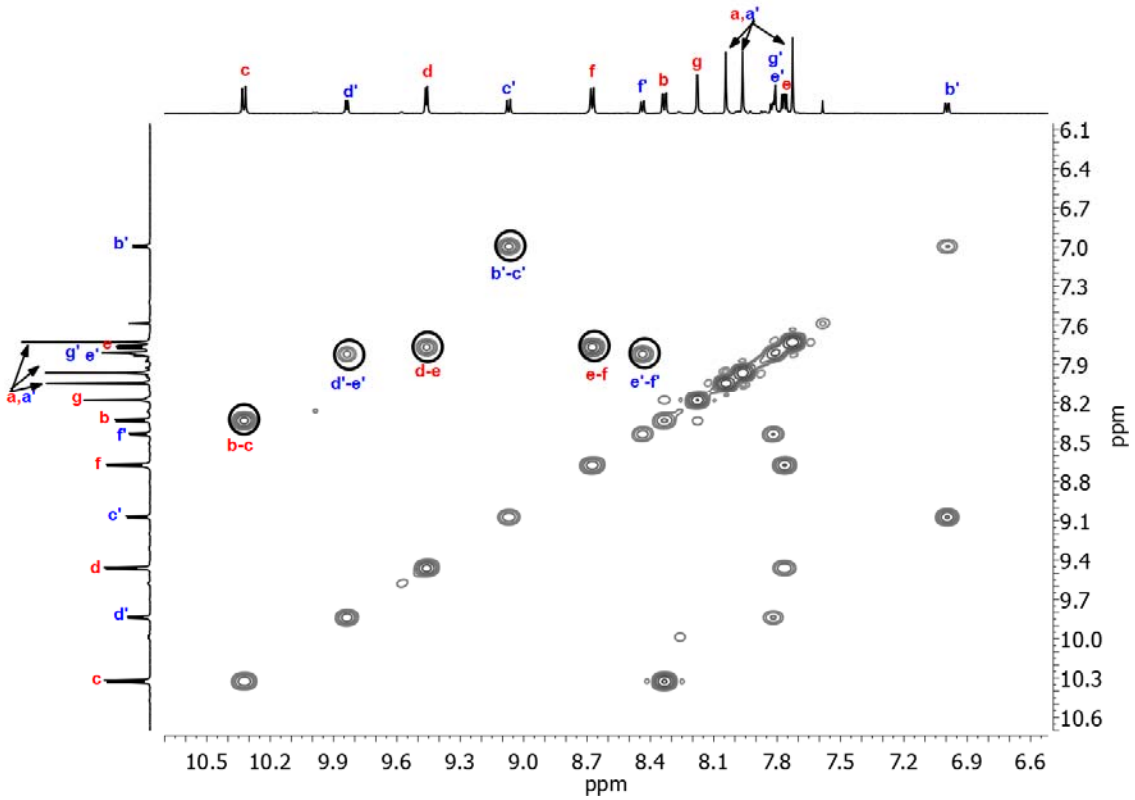

Figure 3.36 Partial ^{1}H – ^{1}H COSY spectrum (600 MHz, 298 K, CD_3CN) of $[C_{60}@Pd_2\mathbf{L^2}_3(MeCN)_2]^{4+}$.

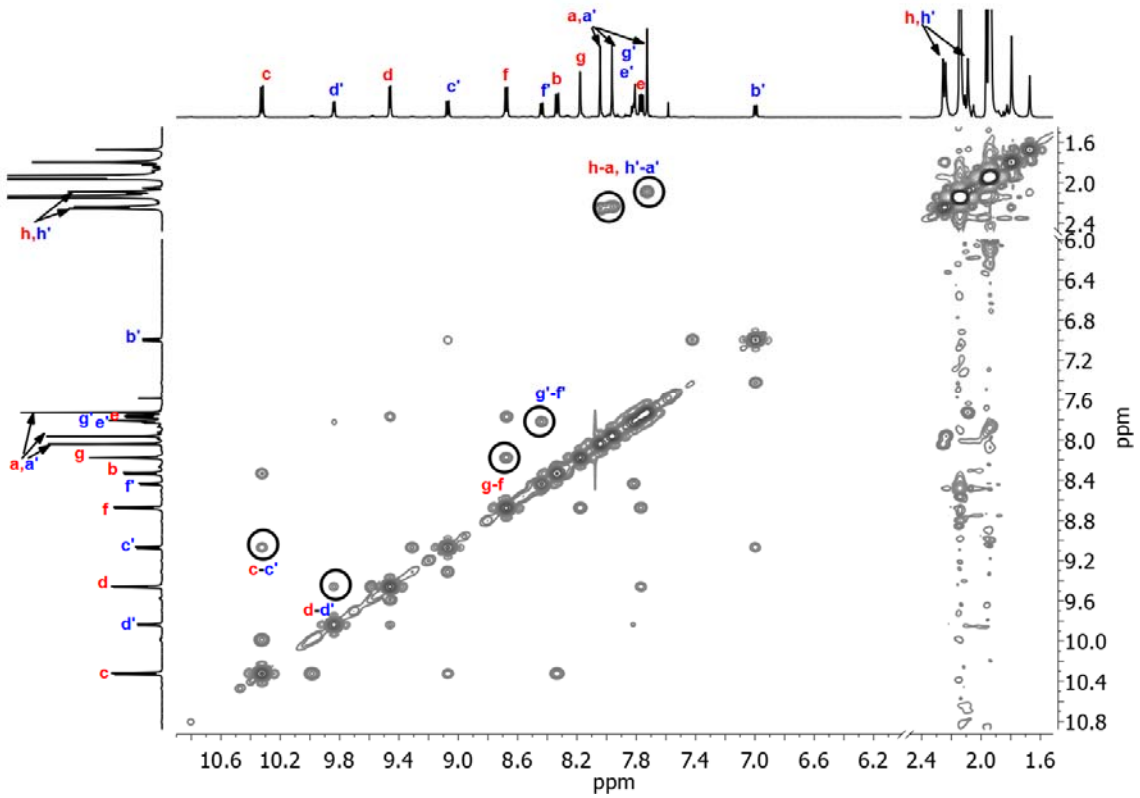

Figure 3.37 Partial $^{1}H - {}^{1}H$ NOESY spectrum (600 MHz, 298 K, CD_3CN) of $[C_{60}@Pd_2\mathbf{L^2}_3(MeCN)_2]^{4+}$.

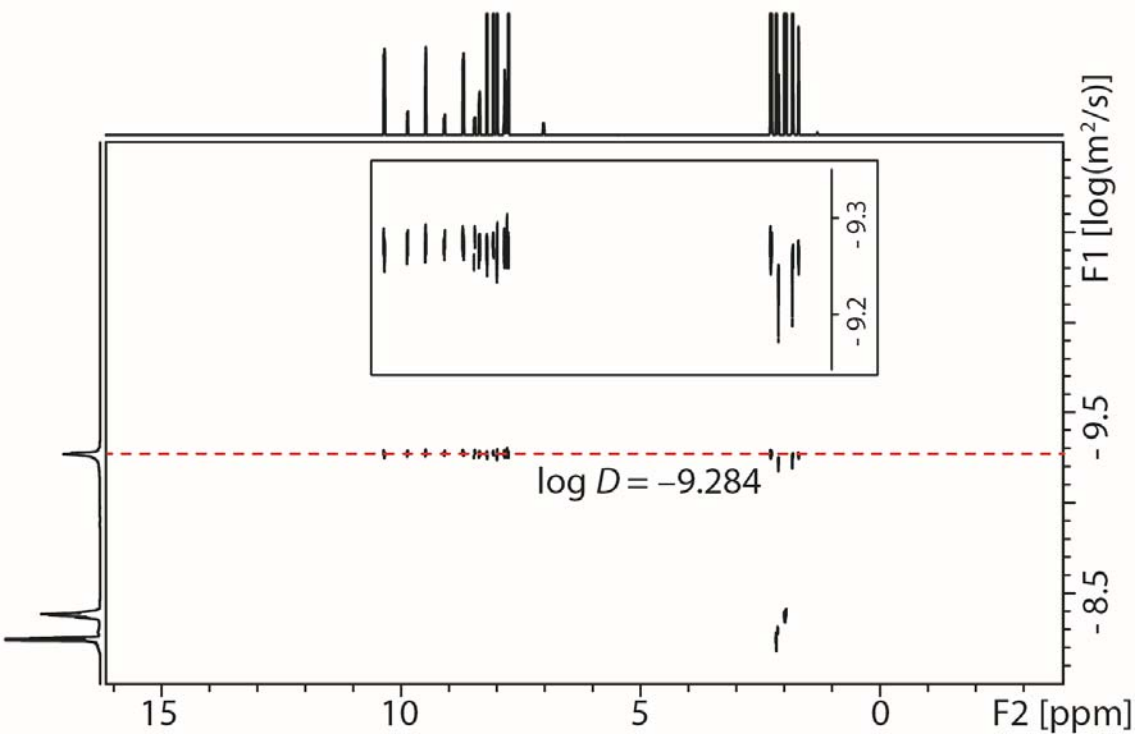

Figure 3.38 DOSY spectrum (500 MHz, 298 K, CD_3CN) of $[C_{60}@Pd_2\mathbf{L^2}_3(MeCN)_2]^{4+}$: diffusion coefficient = 5.2 x 10^{-10} m^2s^{-1}, log *D* = –9.28, r = 12.2 Å.

ESI HRMS ($C_{184}H_{84}N_{14}O_{12}Pd_2B_4F_{16}$): $[C_{60}@Pd_2\mathbf{L^2}_3(MeCN)_2]^{4+}$ calcd. for $C_{184}H_{84}N_{14}O_{12}Pd_2$ 723.6129; found 723.6137; $[C_{60}@Pd_2\mathbf{L^2}_3(MeCN)+F]^{3+}$ calcd. for $C_{182}H_{81}N_{13}O_{12}Pd_2F$ 957.4745; found 957.4773; $[C_{60}@Pd_2\mathbf{L^2}_3+BF_4]^{3+}$ calcd. for $C_{180}H_{78}N_{12}O_{12}Pd_2BF_4$ 966.1340; found 966.1425; $[C_{60}@Pd_2\mathbf{L^2}_3+F+HCOO]^{2+}$ calcd. for $C_{181}H_{79}N_{12}O_{14}Pd_2F$ 1438.1976; found 1438.2014.

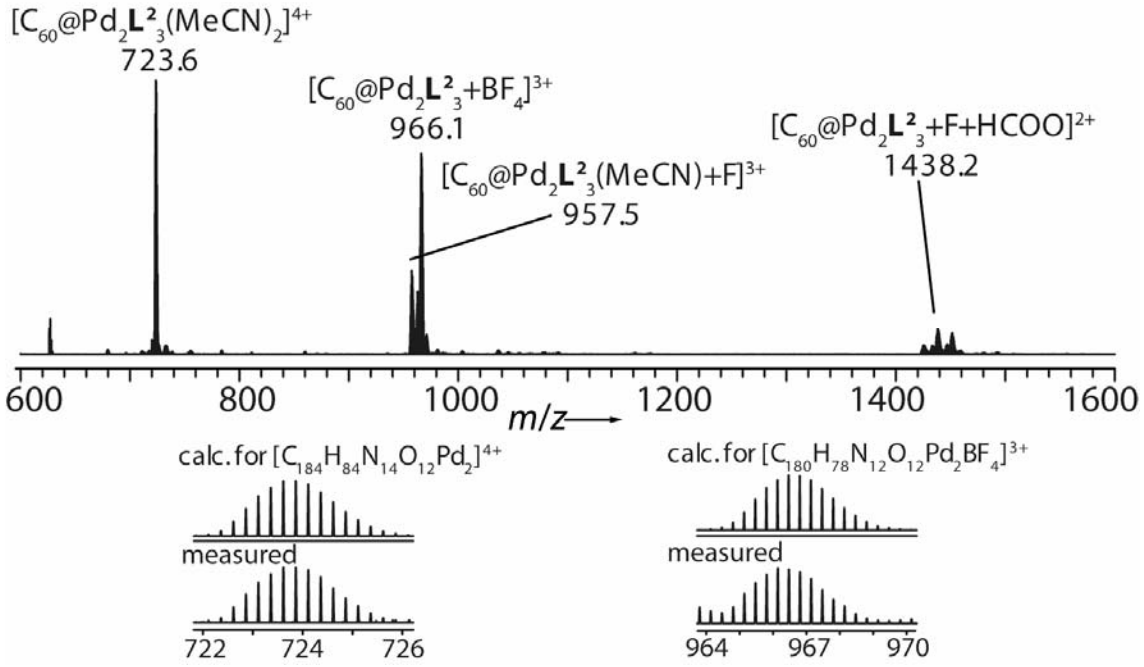

Figure 3.39 ESI mass spectrum of $[C_{60}@Pd_2\mathbf{L^2}_3(MeCN)_2]^{4+}$. The presence of the $[C_{60}@Pd_2\mathbf{L^2}_3(MeCN)+F]^{3+}$, $[C_{60}@Pd_2\mathbf{L^2}_3+F+HCOO]^{3+}$ and species is due to substitution of coordinated CH_3CN by traces of various anions under the measurement conditions.

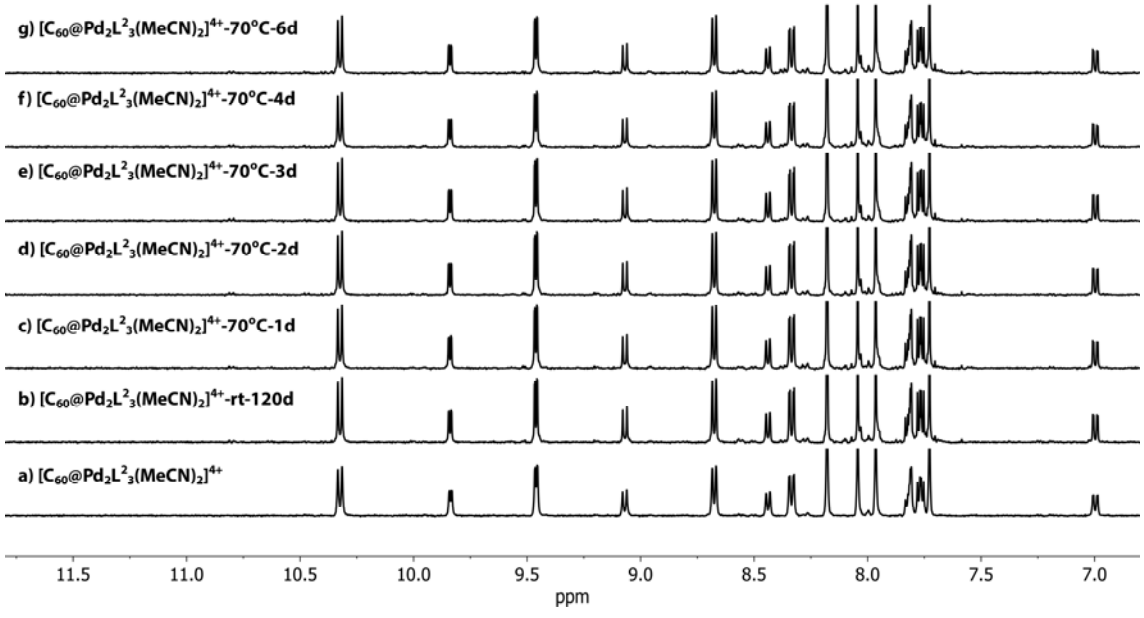

Figure 3.40 ^1H NMR spectra (500 MHz, 298 K, CD_3CN) following the integrity of $[C_{60}@Pd_2\mathbf{L^2}_3(MeCN)_2]^{4+}$ at rt or 70 °C, indicating its high thermal stability at 70 °C.

3.8.2.6 Bowl $[C_{70}@Pd_2L^2_3(MeCN)_2]^{4+}$

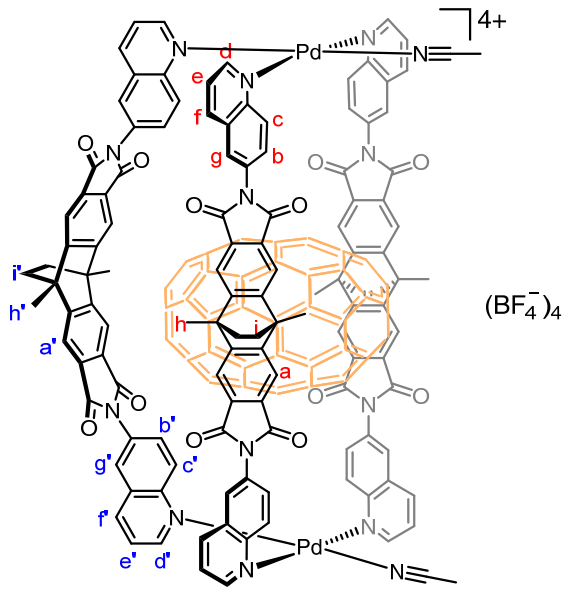

A solution of $[Pd(MeCN)_4](BF_4)_2$ (772.2 µL, 15 mM/CD_3CN, 11.58 µmol, 1 eq.) was combined with ligand **L²** (10.9 mg, 17.36 µmol, 1.5 eq.) and C_{70} (5.6 mg, 6.67 µmol, 0.6 eq.) in CD_3CN (8273 µL) and stirred at room temperature for 2 d. Excess C_{70} solid was removed by filtration to give a 0.64 mM brown solution of the bowl $[C_{70}@Pd_2L^2_3(MeCN)_2]^{4+}$.

^{1}H NMR (600 MHz, 298 K, CD_3CN): δ (ppm) = 9.93 (d, J = 9.1 Hz, 4H), 9.82 (dd, J = 5.7, 1.3 Hz, 2H), 9.43 (dd, J = 5.5, 1.3 Hz, 4H), 8.74 (d, J = 9.1 Hz, 2H), 8.67 (d, J = 8.3 Hz, 4H), 8.46 (d, J = 8.3 Hz, 2H), 8.18 (d, J = 2.3 Hz, 4H), 8.10 (s, 4H), 8.08 (s, 4H), 8.06 (dd, J = 9.1, 2.3 Hz, 4H), 7.84 – 7.80 (m, 4H), 7.76 – 7.73 (m, 8H), 6.59 (dd, J = 9.1, 2.2 Hz, 2H), 2.34 (s, 6H), 2.31 (s, 6H), 2.11 (s, 6H), 1.86 (s, 8H), 1.67 (s, 4H).

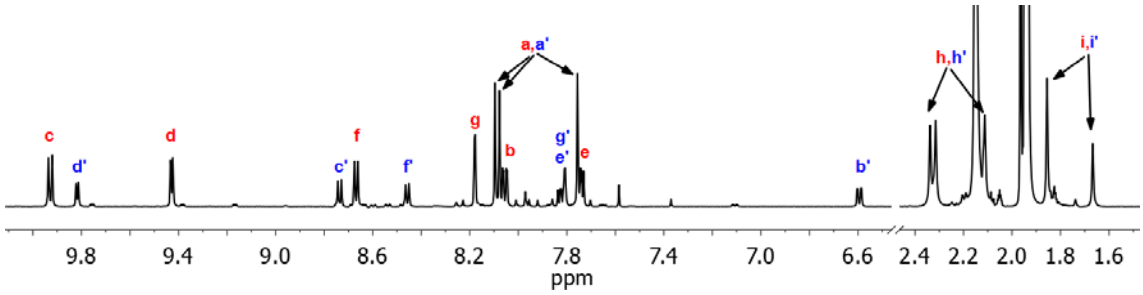

Figure 3.41 ^{1}H NMR spectrum (600 MHz, 298 K, CD_3CN) of $[C_{70}@Pd_2L^2_3(MeCN)_2]^{4+}$.

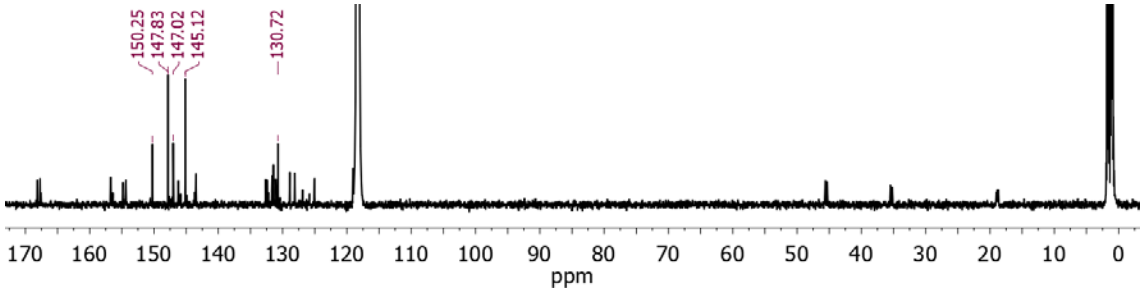

Figure 3.42 ^{13}C NMR spectrum (151 MHz, 298 K, CD_3CN) of $[C_{70}@Pd_2L^2_3(MeCN)_2]^{4+}$. Five single signals at 150.25, 147.83, 147.02, 145.12, 130.72 ppm correspond to the encapsulated C_{70}.

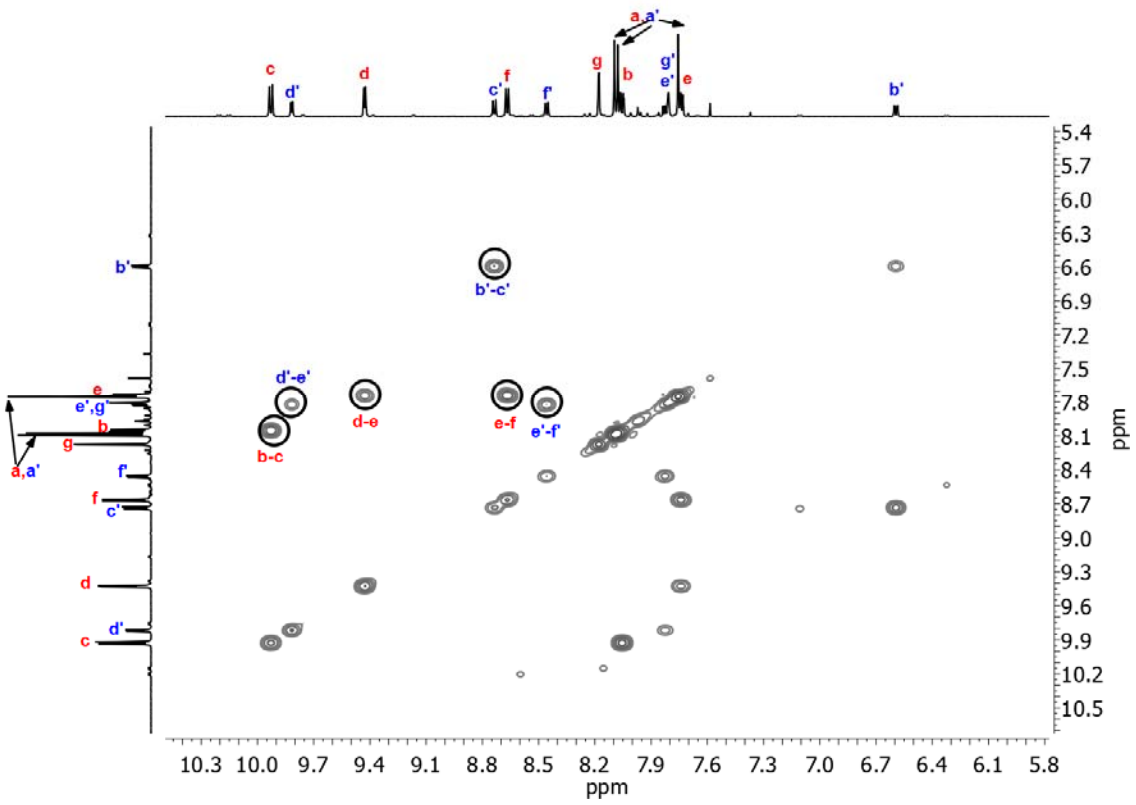

Figure 3.43 Partial $^{1}H - {}^{1}H$ COSY spectrum (600 MHz, 298 K, CD_3CN) of $[C_{70}@Pd_2\mathbf{L^2}_3(MeCN)_2]^{4+}$.

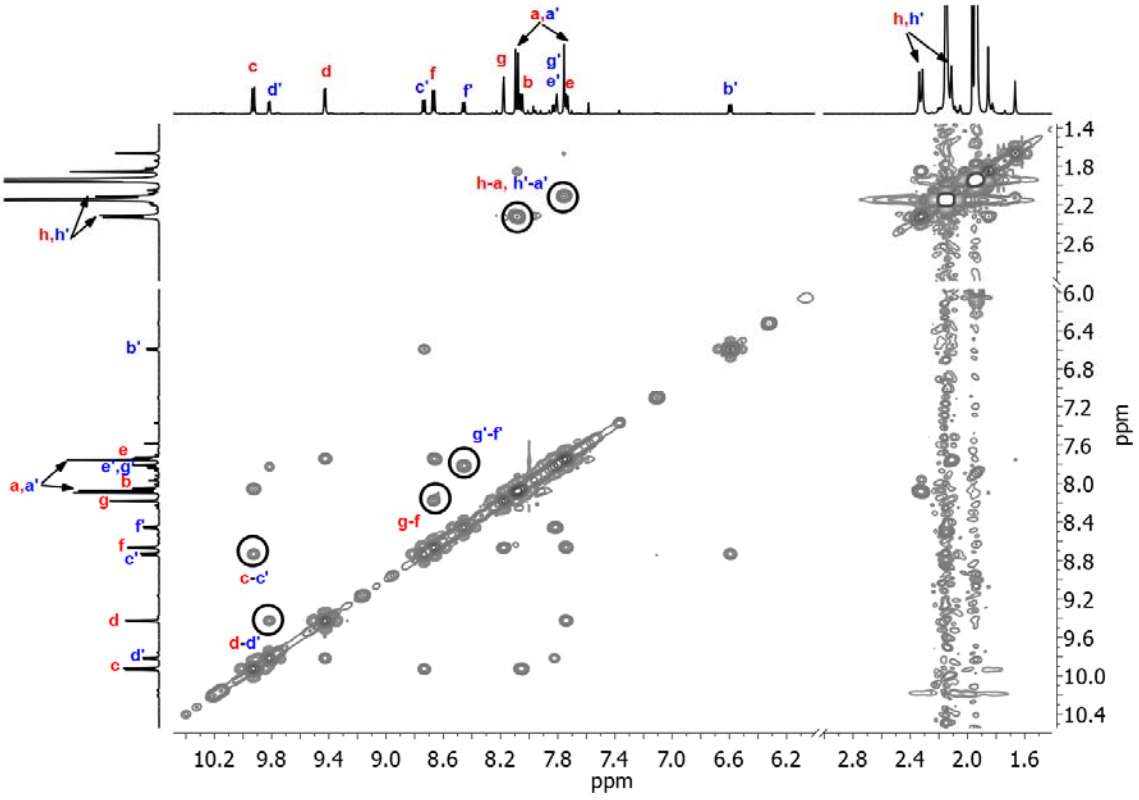

Figure 3.44 Partial $^{1}H - {}^{1}H$ NOESY spectrum (600 MHz, 298 K, CD_3CN) of $[C_{70}@Pd_2\mathbf{L^2}_3(MeCN)_2]^{4+}$.

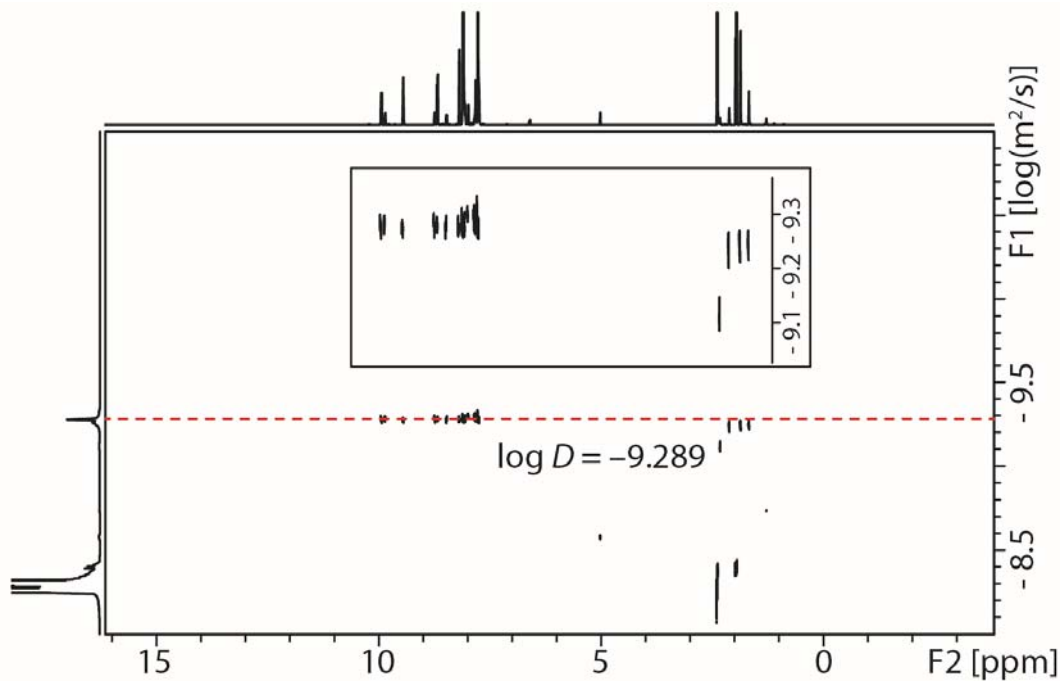

Figure 3.45 DOSY spectrum (500 MHz, 298 K, CD_3CN) of $[C_{70}@Pd_2\mathbf{L^2}_3(MeCN)_2]^{4+}$: diffusion coefficient = 5.1 x 10^{-10} m^2s^{-1}, log *D* = −9.29, r = 12.4 Å.

ESI HRMS ($C_{194}H_{84}N_{14}O_{12}Pd_2B_4F_{16}$): $[C_{70}@Pd_2\mathbf{L^2}_3(MeCN)_2]^{4+}$ calcd. for $C_{194}H_{84}N_{14}O_{12}Pd_2$ 753.6130; found 753.6165; $[C_{70}@Pd_2\mathbf{L^2}_3+BF_4]^{3+}$ calcd. for $C_{190}H_{78}N_{12}O_{12}Pd_2BF_4$ 1006.4675; found 1006.4797; $[C_{70}@Pd_2\mathbf{L^2}_3+2HCOO]^{2+}$ calcd. for $C_{192}H_{80}N_{12}O_{16}Pd_2$ 1511.6978; found 1511.7045.

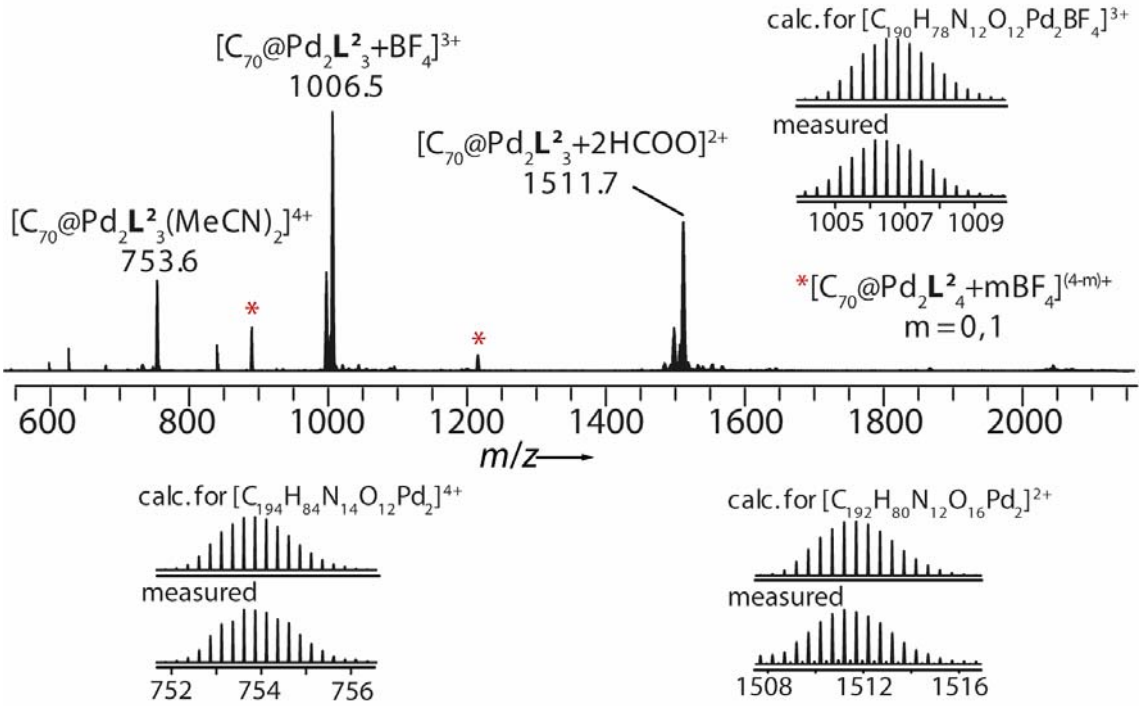

Figure 3.46 ESI mass spectrum of $[C_{70}@Pd_2\mathbf{L^2}_3(MeCN)_2]^{4+}$. The presence of the $[C_{70}@Pd_2\mathbf{L^2}_3+2HCOO]^{2+}$ species is due to substitution of coordinated CH_3CN by traces of formate under the measurement conditions. The $[C_{70}@Pd_2\mathbf{L^2}_4]^{4+}$ species is caused by the partial structural reorganization of the thermodynamic unstable species $[C_{70}@Pd_2\mathbf{L^2}_3(MeCN)_2]^{4+}$.

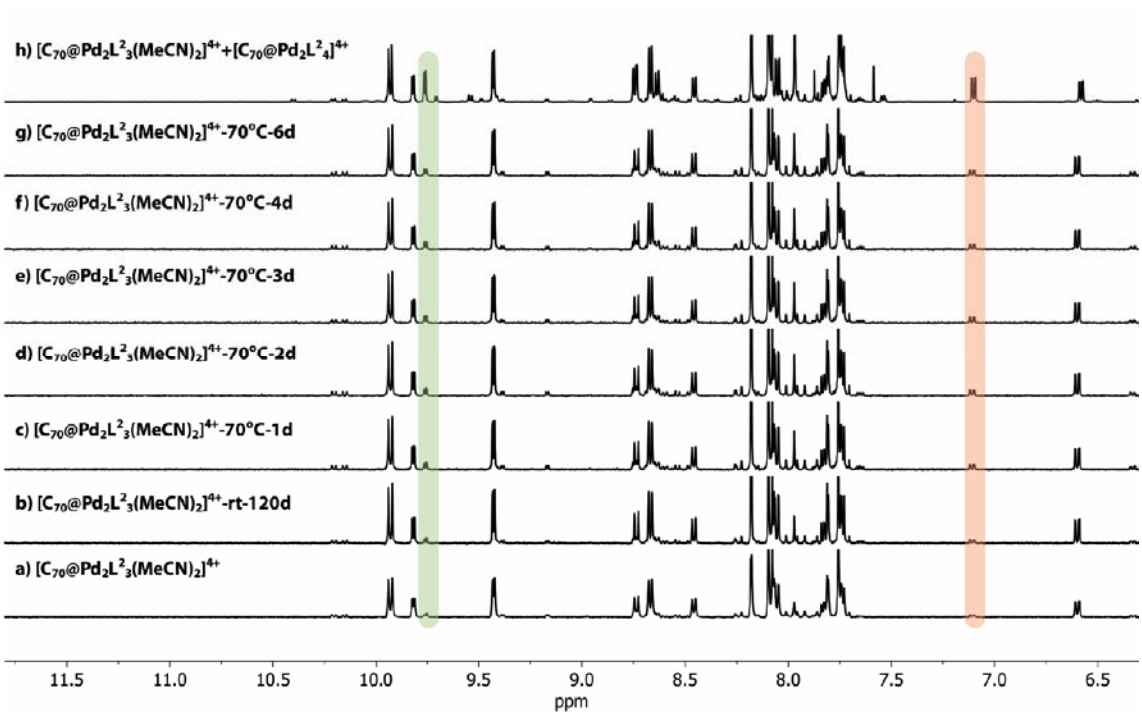

Figure 3.47 ^{1}H NMR spectra (500 MHz, 298 K, CD_3CN) following the integrity of $[C_{70}@Pd_2\mathbf{L^2}_3(MeCN)_2]^{4+}$ at rt or 70 °C, indicating partial conversion into cage $[C_{70}@Pd_2\mathbf{L^2}_4]^{4+}$ after heating for several days. The quinoline proton D and proton B of $[C_{70}@Pd_2\mathbf{L^2}_4]^{4+}$ are highlighted in green and red, respectively.

3.8.2.7 The mixture of bowl $[C_{70}@Pd_2\mathbf{L^2}_3(MeCN)_2]^{4+}$ and cage $[C_{70}@Pd_2\mathbf{L^2}_4]^{4+}$

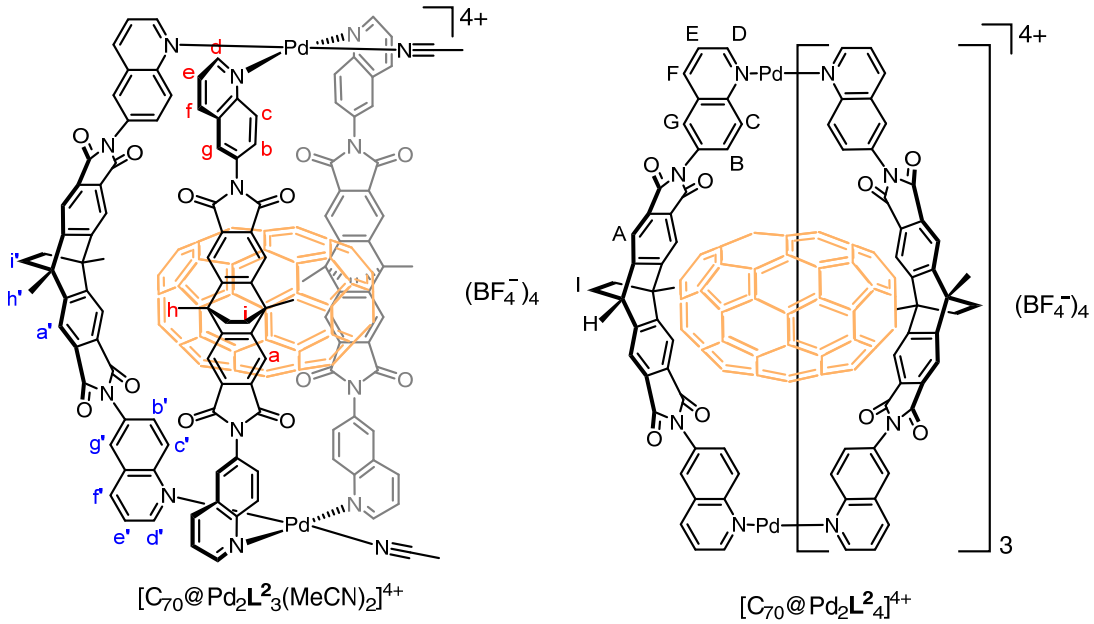

A solution of $[Pd(CH_3CN)_4](BF_4)_2$ (192.0 µL, 15 mM/CD_3CN, 2.88 µmol, 1 eq.) was combined with ligand $\mathbf{L^2}$ (3.6 mg, 5.76 µmol, 2 eq.) and C_{70} (1.3 mg, 1.55 µmol, 0.5 eq.) in CD_3CN (2057 µL) and heated at 70 °C for 3 d. Remaining ligand and C_{70} were removed by filtration to give bowl $[C_{70}@Pd_2\mathbf{L^2}_3(MeCN)_2]^{4+}$ and cage $[C_{70}@Pd_2\mathbf{L^2}_4]^{4+}$ (ratio: ca. 4:1).

^{1}H NMR (600 MHz, 298 K, CD_3CN): δ (ppm) = 9.93 (d, J = 9.2 Hz, 2H), 9.82 (dd, J = 5.6, 1.3 Hz, 1H), 9.76 (dd, J = 5.5, 1.3 Hz, 1H), 9.43 (dd, J = 5.4, 1.3 Hz, 2H), 8.74 (dd, J = 9.2, 2.5 Hz, 2H), 8.67 (d, J = 8.3 Hz, 2H), 8.64 (d, J = 8.4 Hz, 1H), 8.46

(d, J = 8.4 Hz, 1H), 8.18 (d, J = 2.4 Hz, 2H), 8.09 (d, J = 3.0 Hz, 3H), 8.08 (s, 2H), 8.05 (dd, J = 9.1, 2.3 Hz, 2H), 7.97 (s, 2H), 7.84 – 7.80 (m, 2H), 7.77 – 7.72 (m, 5H), 7.10 (dd, J = 9.2, 2.3 Hz, 1H), 6.58 (dd, J = 9.1, 2.2 Hz, 1H), 2.36 – 2.30 (m, 9H), 2.11 (s, 3H), 1.85 (d, J = 9.1 Hz, 6H), 1.66 (s, 2H).

All the signals in the aromatic region could be assigned via 2D NMR spectroscopy.

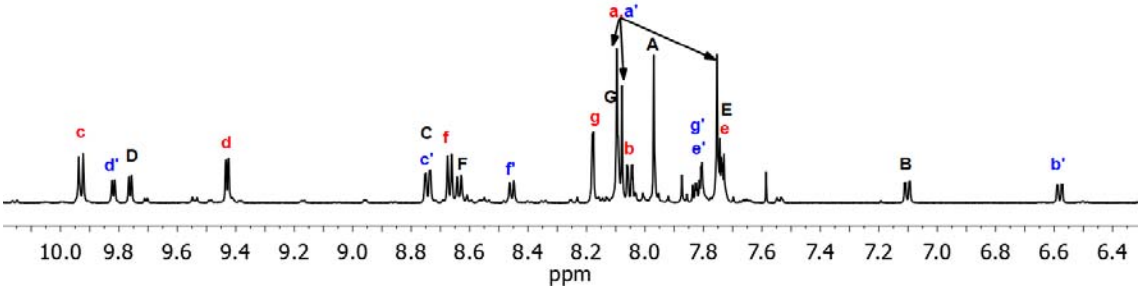

Figure 3.48 ^{1}H NMR spectrum (600 MHz, 298 K, CD_3CN) of the mixture of bowl $[C_{70}@Pd_2\mathbf{L^2}_3(MeCN)_2]^{4+}$ and cage $[C_{70}@Pd_2\mathbf{L^2}_4]^{4+}$.

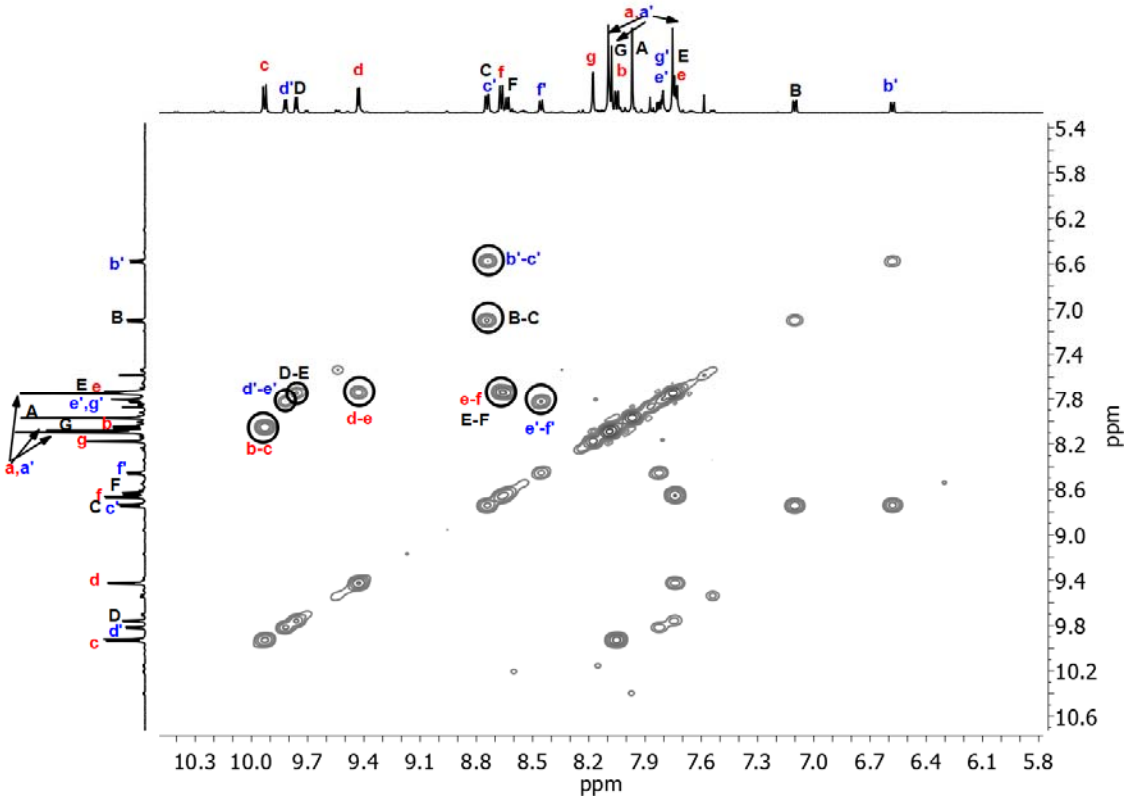

Figure 3.49 Partial ^{1}H – ^{1}H COSY spectrum (600 MHz, 298 K, CD_3CN) of the mixture of bowl $[C_{70}@Pd_2\mathbf{L^2}_3(MeCN)_2]^{4+}$ and cage $[C_{70}@Pd_2\mathbf{L^2}_4]^{4+}$.

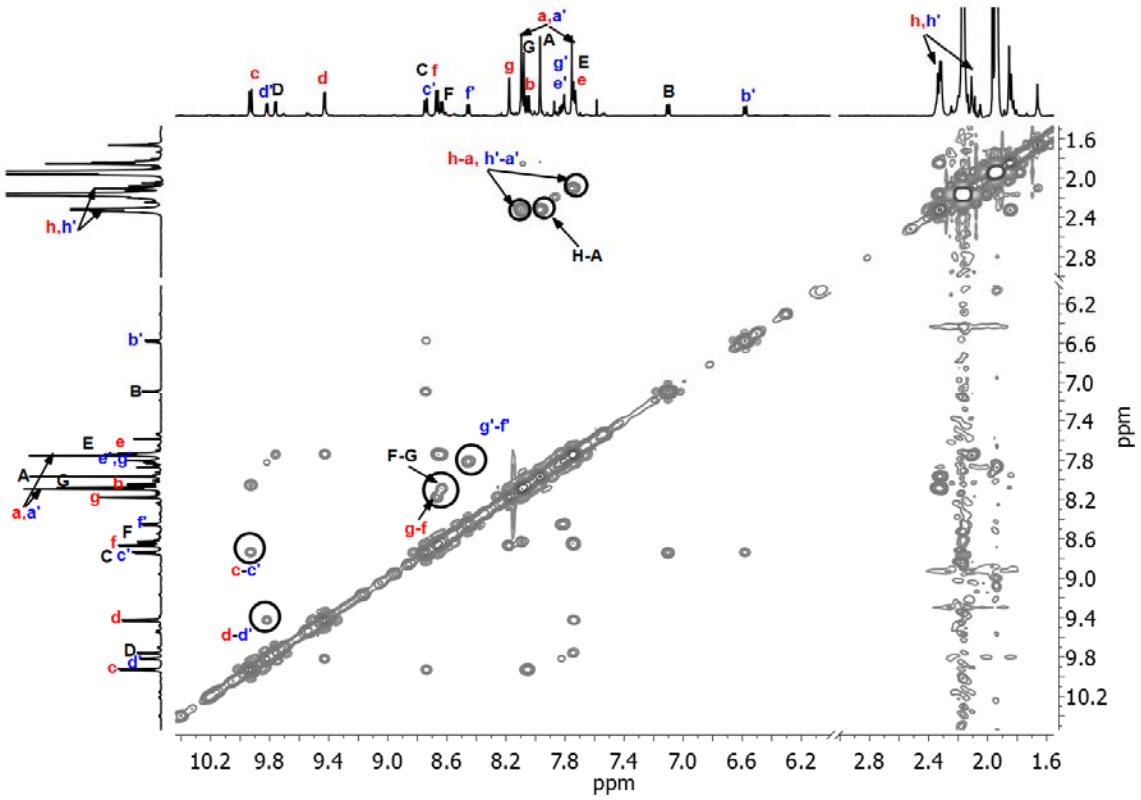

Figure 3.50 Partial ^{1}H – ^{1}H NOESY spectrum (600 MHz, 298 K, CD_3CN) of the mixture of bowl $[C_{70}@Pd_2\mathbf{L^2}_3(MeCN)_2]^{4+}$ and cage $[C_{70}@Pd_2\mathbf{L^2}_4]^{4+}$.

ESI HRMS ($C_{194}H_{84}N_{14}O_{12}Pd_2B_4F_{16}$ and $C_{230}H_{104}N_{16}O_{16}Pd_2B_4F_{16}$): $[C_{70}@Pd_2\mathbf{L^2}_4]^{4+}$ calcd. for $C_{230}H_{104}N_{16}O_{16}Pd_2$ 889.8989; found 889.9022; $[C_{70}@Pd_2\mathbf{L^2}_4+BF_4]^{3+}$ calcd. for $C_{230}H_{104}N_{16}O_{16}Pd_2BF_4$ 1215.5333; found 1215.5389. Other peaks come from the bowl $[C_{70}@Pd_2\mathbf{L^2}_3(MeCN)_2]^{4+}$ species as shown before.

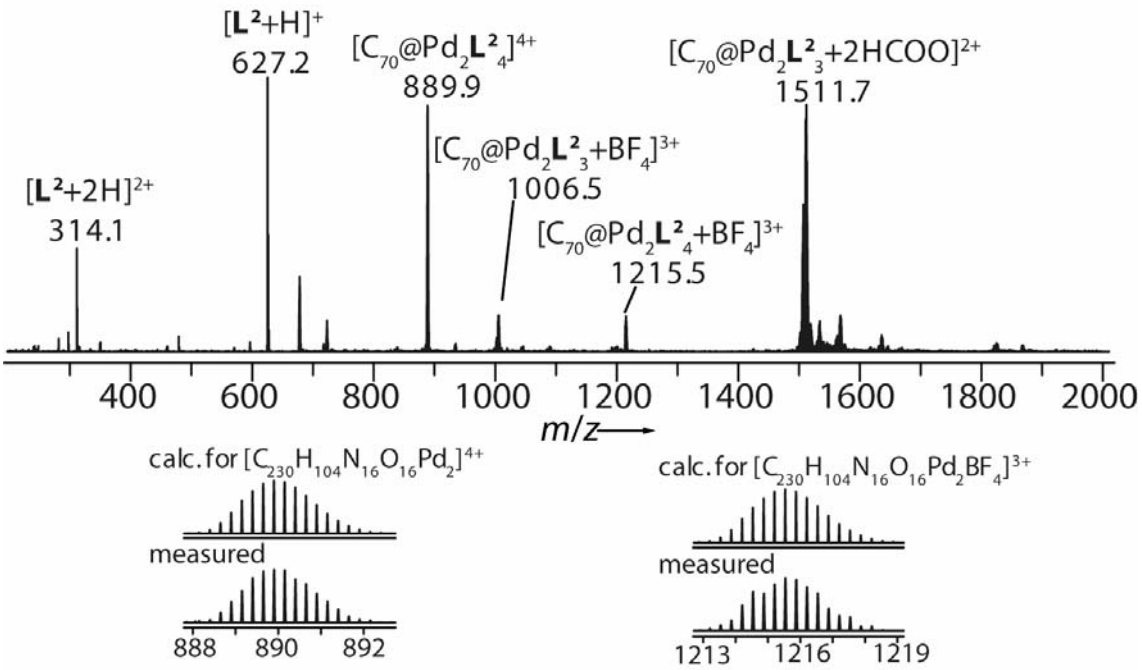

Figure 3.51 ESI mass spectrum of the mixture of bowl $[C_{70}@Pd_2\mathbf{L^2}_3(MeCN)_2]^{4+}$ and cage $[C_{70}@Pd_2\mathbf{L^2}_4]^{4+}$. The presence of the $[C_{70}@Pd_2\mathbf{L^2}_3+2HCOO]^{2+}$ species is due to substitution of coordinated CH_3CN by traces of forma under the measurement conditions.

3.8.2.8 Bowl $[Pd_2L^2{}_3Cl_2]^{2+}$

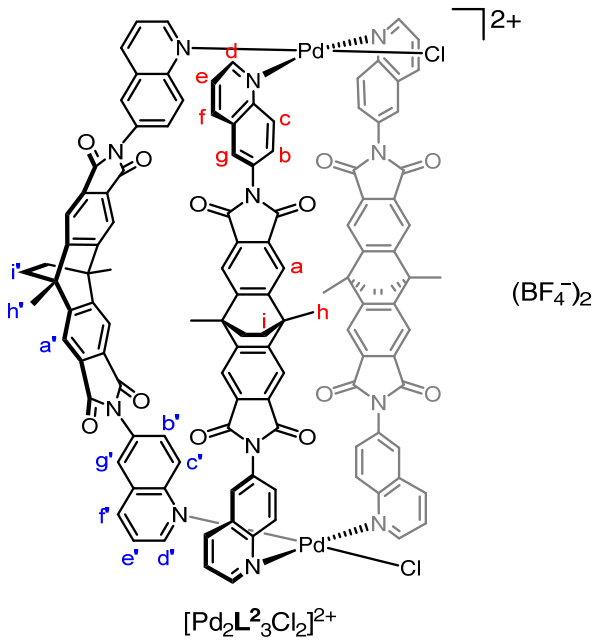

The $[Pd_2\mathbf{L^2}_3Cl_2]^{2+}$ solution (0.56 mM) was formed by stirring a mixture of the CD_3CN solution of $[Pd_2\mathbf{L^2}_3(MeCN)_2]^{4+}$ (4000 µL, 0.64 mM, 2.56 µmol, 1 eq.) and CD_3CN solution of NBu_4Cl (585.4 µL, 8.75 mM, 5.12 µmol, 2 eq.) at room temperature for 2 min.

^{1}H NMR (600 MHz, 298 K, CD_3CN): δ (ppm) = 10.32 (d, J = 9.1 Hz, 4H), 10.00 (dd, J = 5.4, 1.4 Hz, 2H), 9.65 (dd, J = 5.4, 1.3 Hz, 4H), 9.54 (d, J = 9.0 Hz, 2H), 8.58 (d, J = 8.3 Hz, 4H), 8.45 (d, J = 8.3 Hz, 2H), 8.16 (dd, J = 9.1, 2.2 Hz, 4H), 8.08 (d, J = 2.2 Hz, 4H), 7.99 (s, 4H), 7.91 (s, 4H), 7.84 (d, J = 2.2 Hz, 2H), 7.81 (dd, J = 8.4, 5.4 Hz, 2H), 7.74 – 7.70 (m, 8H), 7.40 (dd, J = 9.0, 2.2 Hz, 2H), 2.26 (s, 6H), 2.22 (s, 6H), 2.09 (s, 6H), 1.87 (s, 8H), 1.77 (s, 4H).

All the peaks in aromatic region could be assigned via 2D NMR spectroscopy.

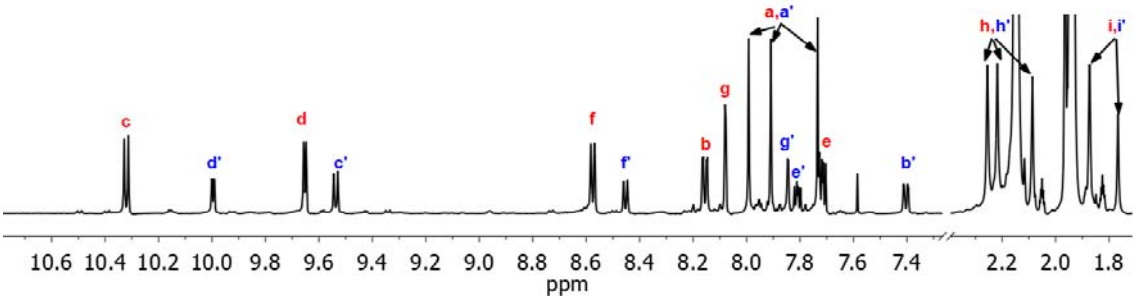

Figure 3.52 ^{1}H NMR spectrum (600 MHz, 298 K, CD_3CN) of $[Pd_2\mathbf{L^2}_3Cl_2]^{2+}$.

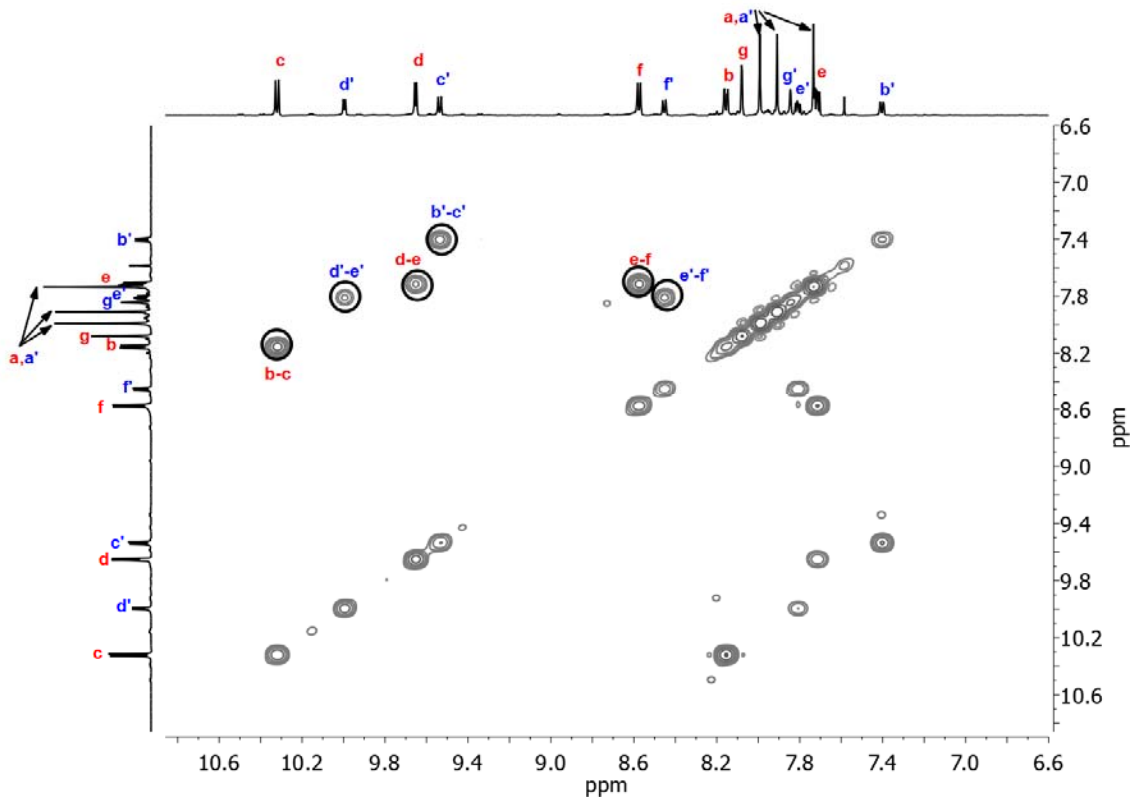

Figure 3.53 Partial $^{1}H - {}^{1}H$ COSY spectrum (600 MHz, 298 K, CD_3CN) of $[Pd_2\mathbf{L}^{2}{}_3Cl_2]^{2+}$.

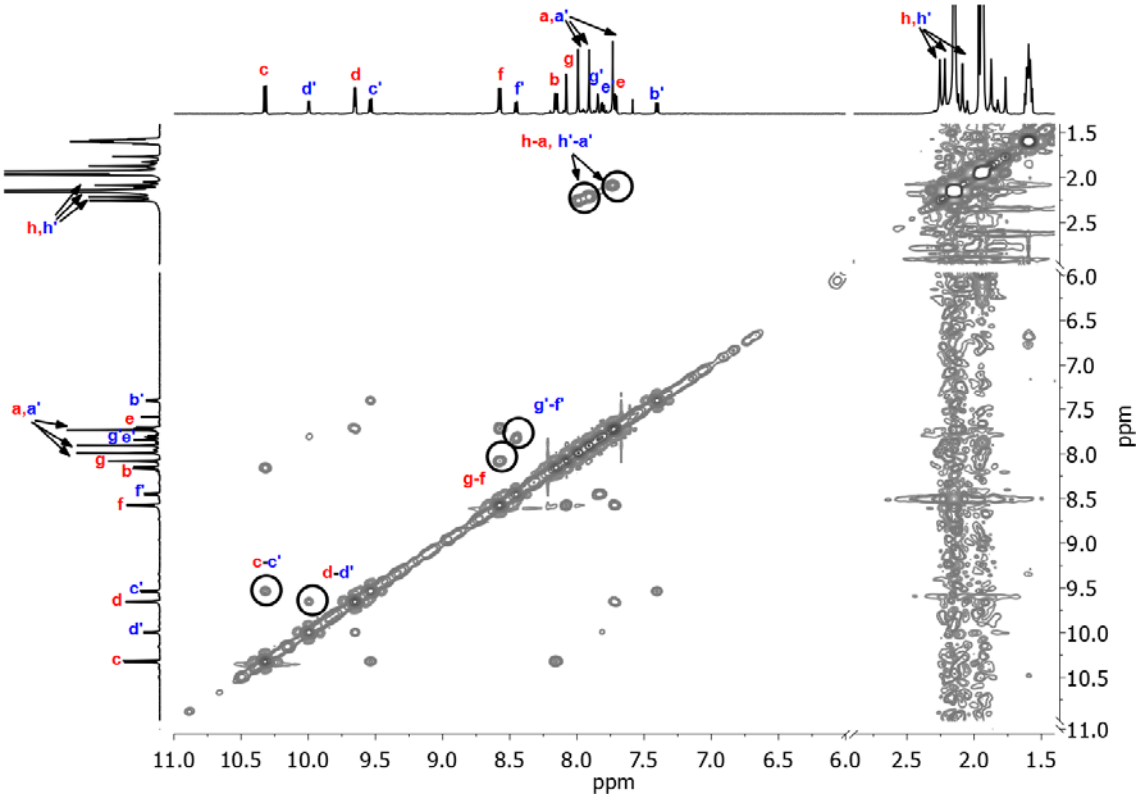

Figure 3.54 Partial $^{1}H - {}^{1}H$ NOESY spectrum (600 MHz, 298 K, CD_3CN) of $[Pd_2\mathbf{L}^{2}{}_3Cl_2]^{2+}$.

ESI HRMS ($C_{120}H_{78}N_{12}O_{12}Pd_2Cl_2B_2F_8$): $[Pd_2\mathbf{L}^{2}{}_3Cl_2]^{2+}$ calcd. for $C_{120}H_{78}N_{12}O_{12}Pd_2Cl_2$ 1081.1668; found 1081.1723.

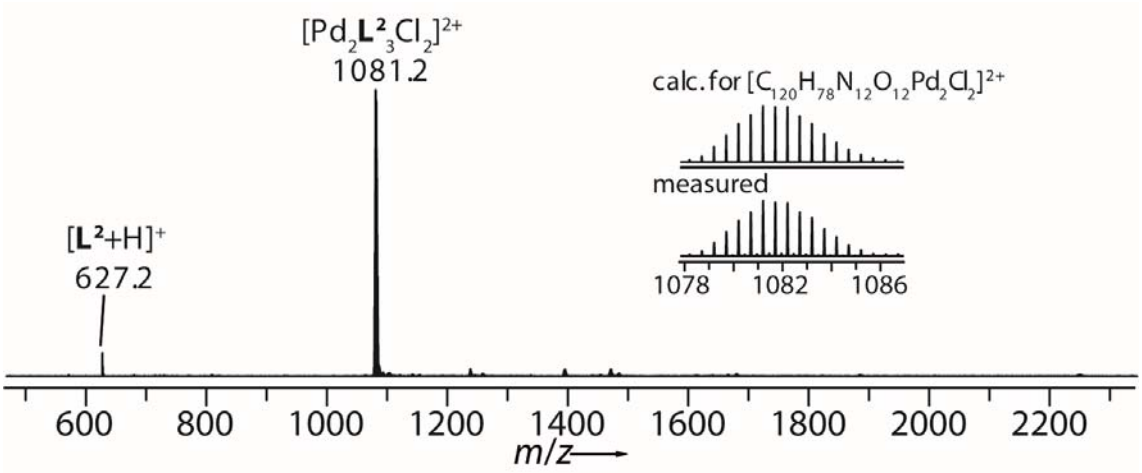

Figure 3.55 ESI mass spectrum of $[Pd_2\mathbf{L^2}_3Cl_2]^{2+}$.

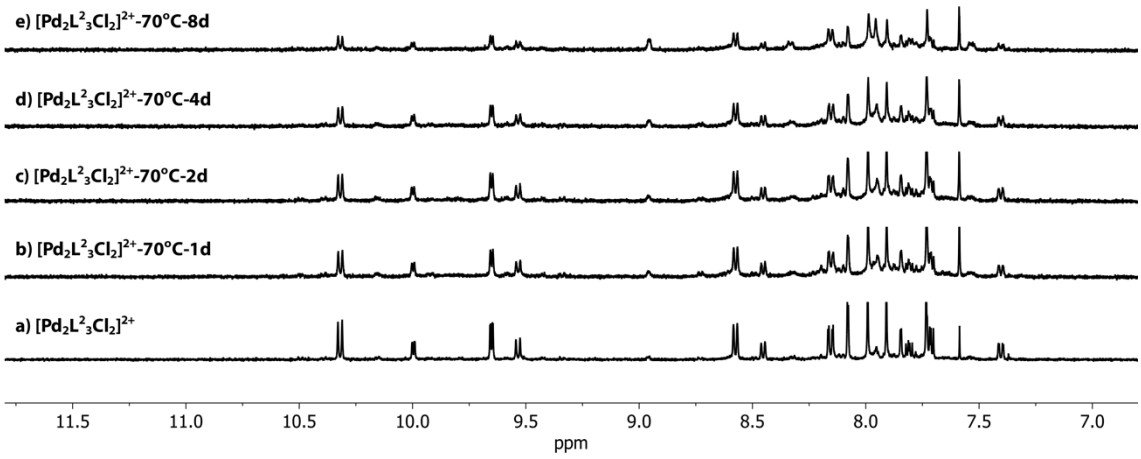

Figure 3.56 ^{1}H NMR spectra (500 MHz, 298 K, CD_3CN) following the integrity of $[Pd_2\mathbf{L^2}_3Cl_2]^{2+}$ at 70 °C, indicating partial decomposition after several days.

3.8.2.9 Bowl $[C_{60}@Pd_2\mathbf{L^2}_3Cl_2]^{2+}$

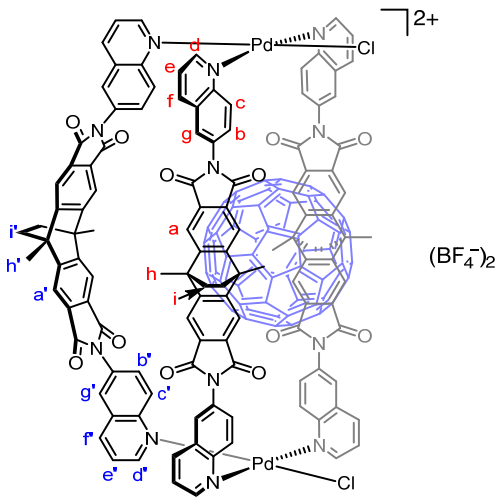

$[C_{60}@Pd_2\mathbf{L^2}_3Cl_2]^{2+}$

The $[C_{60}@Pd_2\mathbf{L^2}_3Cl_2]^{2+}$ solution (0.56 mM) was formed by stirring a mixture of the CD_3CN solution of $[C_{60}@Pd_2\mathbf{L^2}_3(MeCN)_2]^{4+}$ (3000 µL, 0.64 mM, 1.92 µmol, 1 eq.) and the CD_3CN solution of NBu_4Cl (439.0 µL, 8.75 mM, 3.84 µmol, 2 eq.) at room temperature for 2 min.

^{1}H NMR (600 MHz, 298 K, CD_3CN): δ (ppm) = 10.80 (d, J = 9.1 Hz, 4H), 10.01 (d, J = 5.4 Hz, 2H), 9.51 (dd, J = 5.4, 1.3 Hz, 4H), 9.18 (d, J = 9.1 Hz, 2H), 8.56 (d, J = 8.3 Hz, 4H), 8.38 (d, J = 8.3 Hz, 2H), 8.27 (dd, J = 9.1, 2.3 Hz, 4H), 8.09 (d, J = 2.2 Hz, 4H), 8.06 (s, 4H), 7.94 (s, 4H), 7.79 (d, J = 2.2 Hz, 2H), 7.77 (dd, J = 8.3, 5.4 Hz, 2H), 7.73 (s, 4H), 7.68 (dd, J = 8.3, 5.4 Hz, 4H), 7.01 (dd, J = 9.0, 2.2 Hz, 2H), 2.24 (s, 6H), 2.22 (s, 6H), 2.09 (s, 6H), 1.77 (s, 8H), 1.67 (s, 4H).

All the peaks in aromatic region could be assigned via 2D NMR spectroscopy.

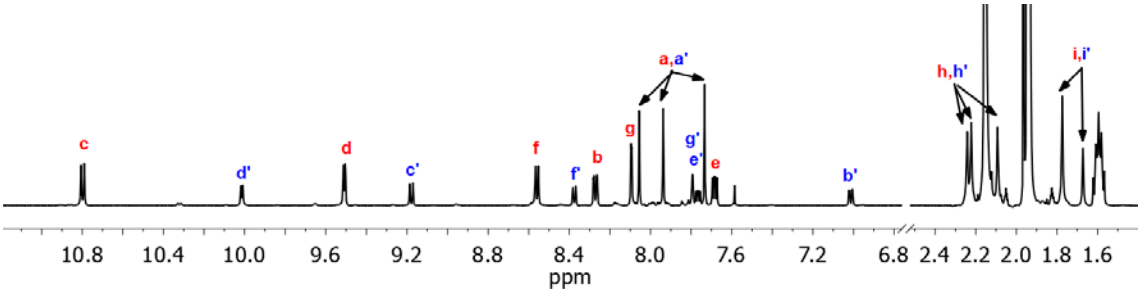

Figure 3.57 ^{1}H NMR spectrum (600 MHz, 298 K, CD_3CN) of $[C_{60}@Pd_2\mathbf{L^2}_3Cl_2]^2$.

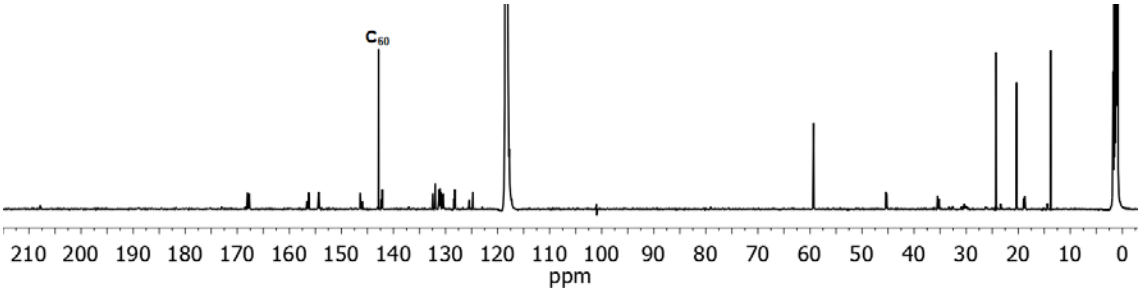

Figure 3.58 ^{13}C NMR spectrum (151 MHz, 298 K, CD_3CN) of $[C_{60}@Pd_2\mathbf{L^2}_3Cl_2]^{2+}$. A single signal at 142.85 ppm corresponds to encapsulated C_{60}.

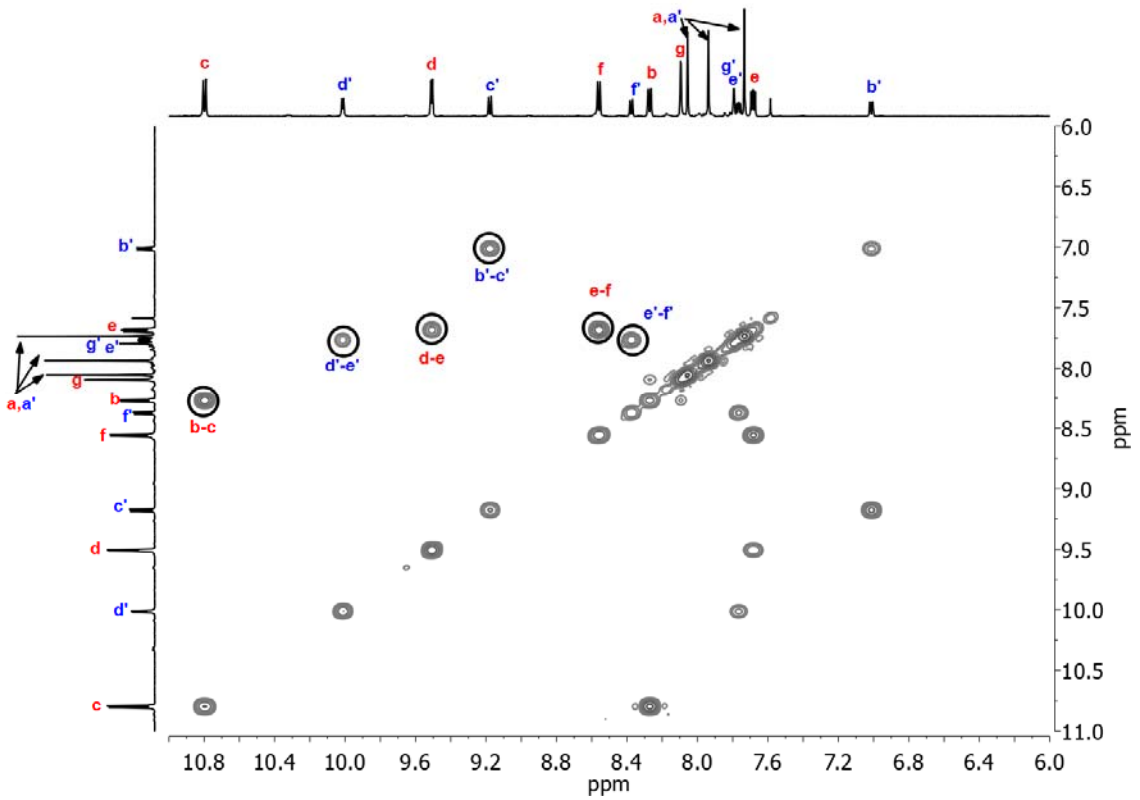

Figure 3.59 Partial $^{1}H - {}^{1}H$ COSY spectrum (600 MHz, 298 K, CD_3CN) of $[C_{60}@Pd_2\mathbf{L^2}_3Cl_2]^{2+}$.

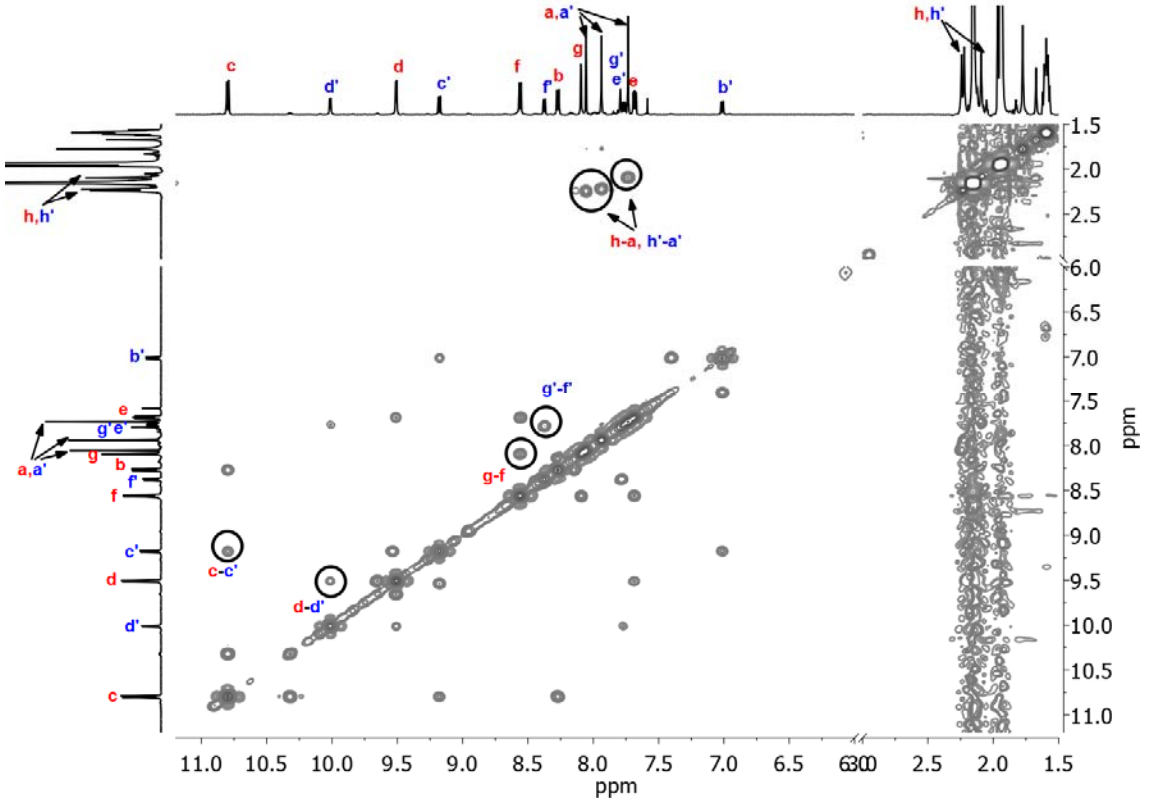

Figure 3.60 Partial $^{1}H - {}^{1}H$ NOESY spectrum (600 MHz, 298 K, CD_3CN) of $[C_{60}@Pd_2\mathbf{L^2}_3Cl_2]^{2+}$.

ESI HRMS ($C_{180}H_{78}Cl_2N_{12}O_{12}Pd_2B_2F_8$): $[C_{60}@Pd_2\mathbf{L^2}_3Cl_2]^{2+}$ calcd. for $C_{180}H_{78}Cl_2N_{12}O_{12}Pd_2$ 1441.6679; found 1441.6661.

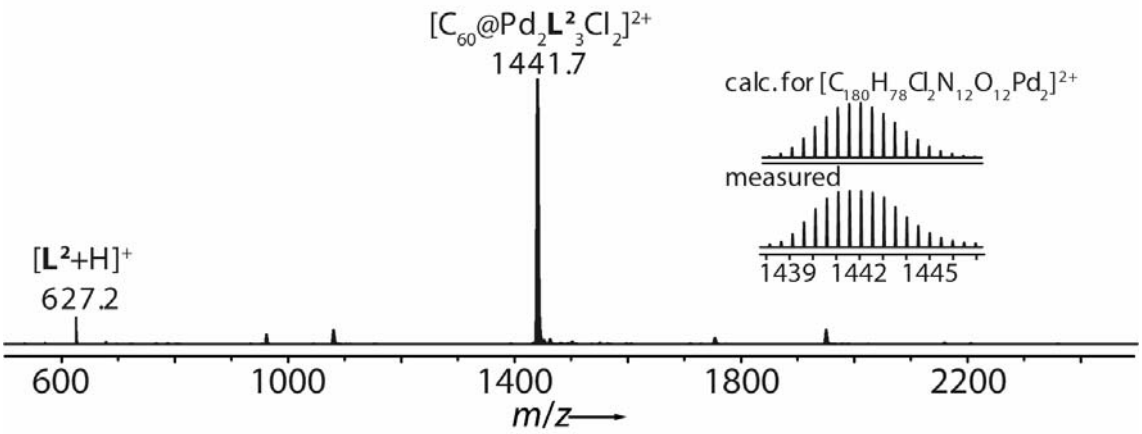

Figure 3.61 ESI mass spectrum of $[C_{60}@Pd_2\mathbf{L^2}_3Cl_2]^{2+}$.

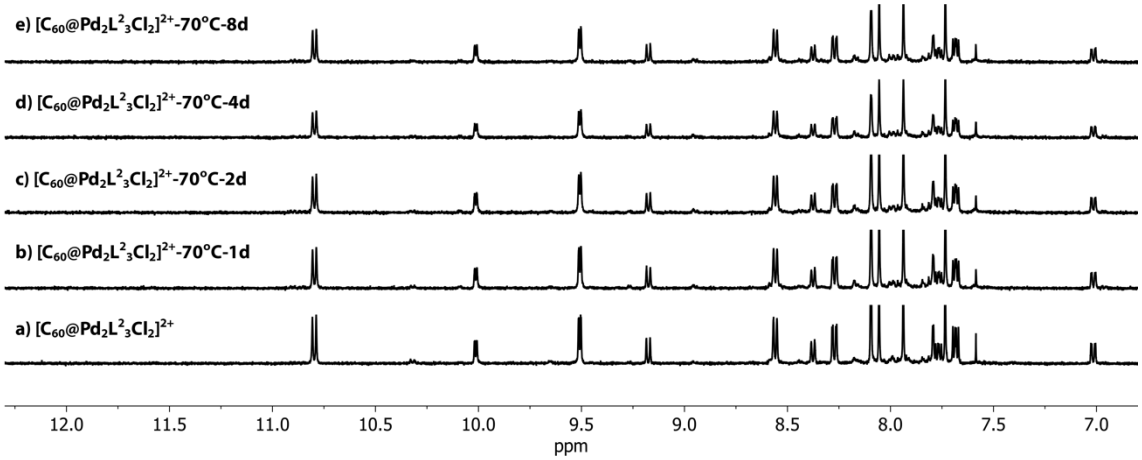

Figure 3.62 ^{1}H NMR spectra (500 MHz, 298 K, CD_3CN) following the integrity of $[C_{60}@Pd_2\mathbf{L^2}_3Cl_2]^{2+}$ at 70 °C, indicating stability for several days.

3.8.2.10 Bowl $[Pd_2\mathbf{L^3}_3(MeCN)_2]^{4+}$

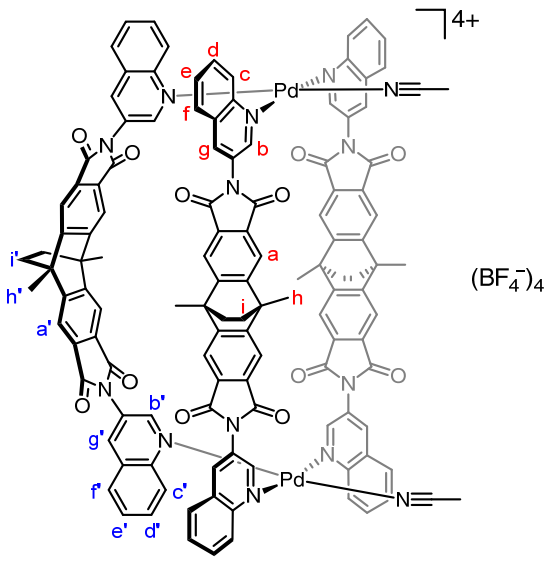

A solution of $[Pd(MeCN)_4](BF_4)_2$ (114.3 µL, 15 mM/CD_3CN, 1.71 µmol, 1 eq.) was combined with ligand **L³** (1.6 mg, 2.57 µmol, 1.5 eq.) in CD_3CN (1224 µL) and stirred at room temperature for 2 h to give a 0.64 mM solution of bowl $[Pd_2\mathbf{L^3}_2(MeCN)_2]^{4+}$. NMR characterization was performed right after preparation of a fresh sample.

^{1}H NMR (600 MHz, 298 K, CD_3CN): δ (ppm) = 10.20 (d, J = 2.1 Hz, 4H), 9.97 (d, J = 2.1 Hz, 2H), 9.78 (d, J = 8.6 Hz, 4H), 9.49 (d, J = 8.8 Hz, 2H), 8.77 (d, J = 2.1 Hz, 4H), 8.68 (d, J = 2.0 Hz, 2H), 8.35 (ddd, J = 8.5, 7.1, 1.4 Hz, 4H), 8.15 (dd, J = 8.3, 1.3 Hz, 4H), 8.04 (s, 4H), 7.92 (dd, J = 14.7, 7.4 Hz, 12H), 7.79 (s, 4H), 7.63 (t, J = 7.7 Hz, 2H), 2.23 (s, 6H), 2.20 (s, 6H), 2.15 (s, mixed with water peak in CD_3CN), 1.87 (s, 4H), 1.76 – 1.72 (m, 4H), 1.71 – 1.67 (m, 4H).

A signal at 2.15 ppm overlapping with the solvent residual peak in the aliphatic region could be assigned via 2D NMR spectroscopy.

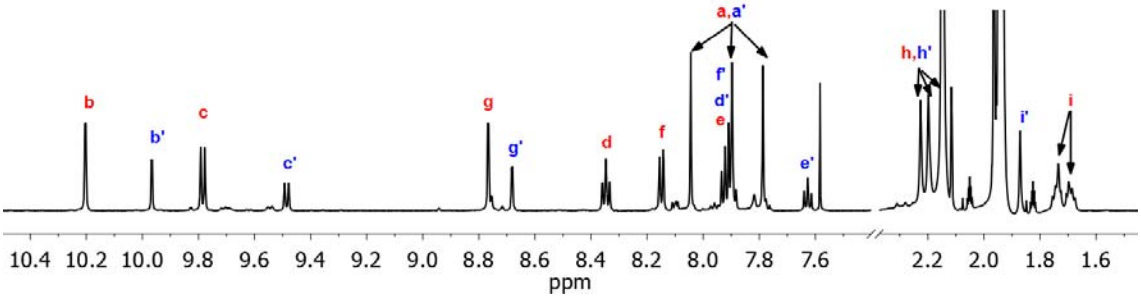

Figure 3.63 ^{1}H NMR spectrum (600 MHz, 298 K, CD_3CN) of $[Pd_2\mathbf{L^3}_3(MeCN)_2]^{4+}$.

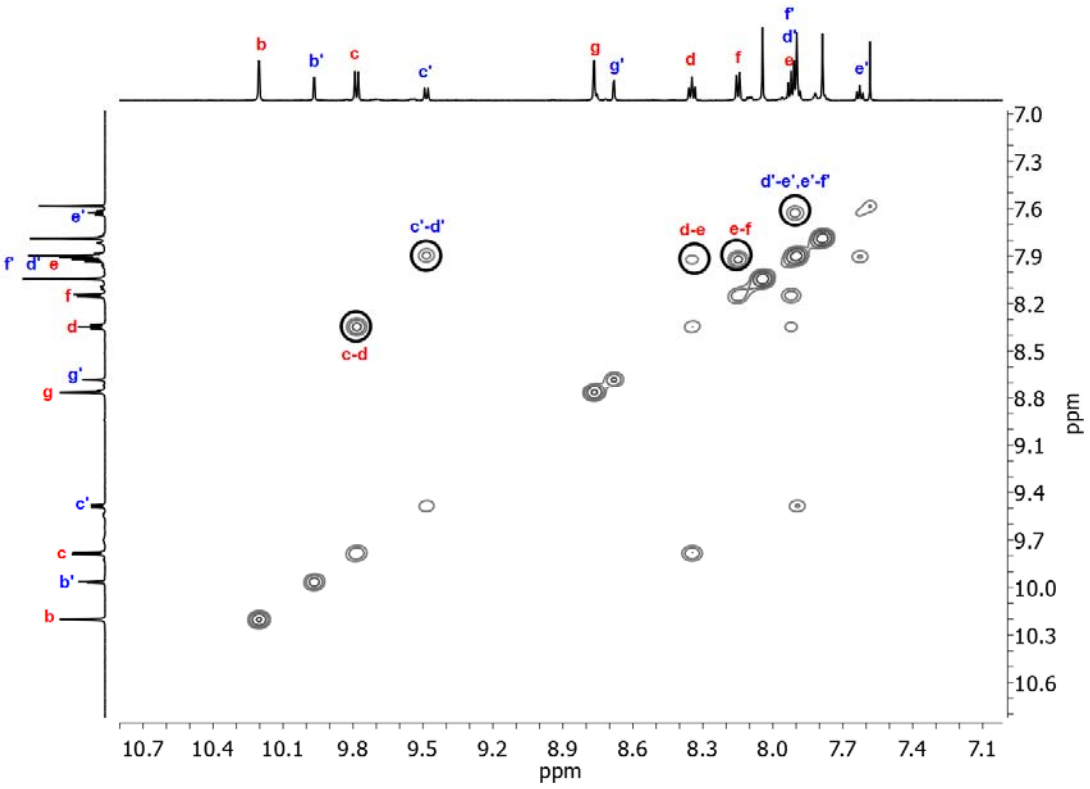

Figure 3.64 Partial ^{1}H – ^{1}H COSY spectrum (600 MHz, 298 K, CD_3CN) of $[Pd_2\mathbf{L^3}_3(MeCN)_2]^{4+}$.

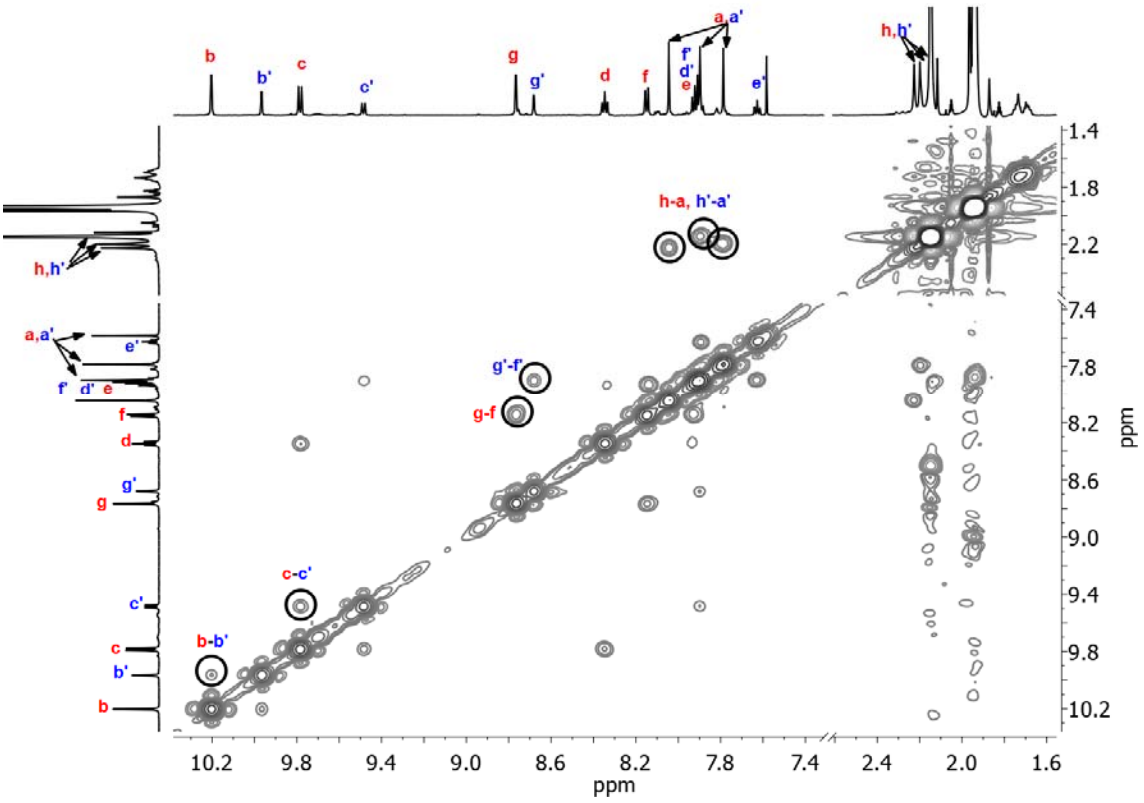

Figure 3.65 Partial ^{1}H – ^{1}H NOESY spectrum (600 MHz, 298 K, CD_3CN) of $[Pd_2\mathbf{L^3}_3(MeCN)_2]^{4+}$.

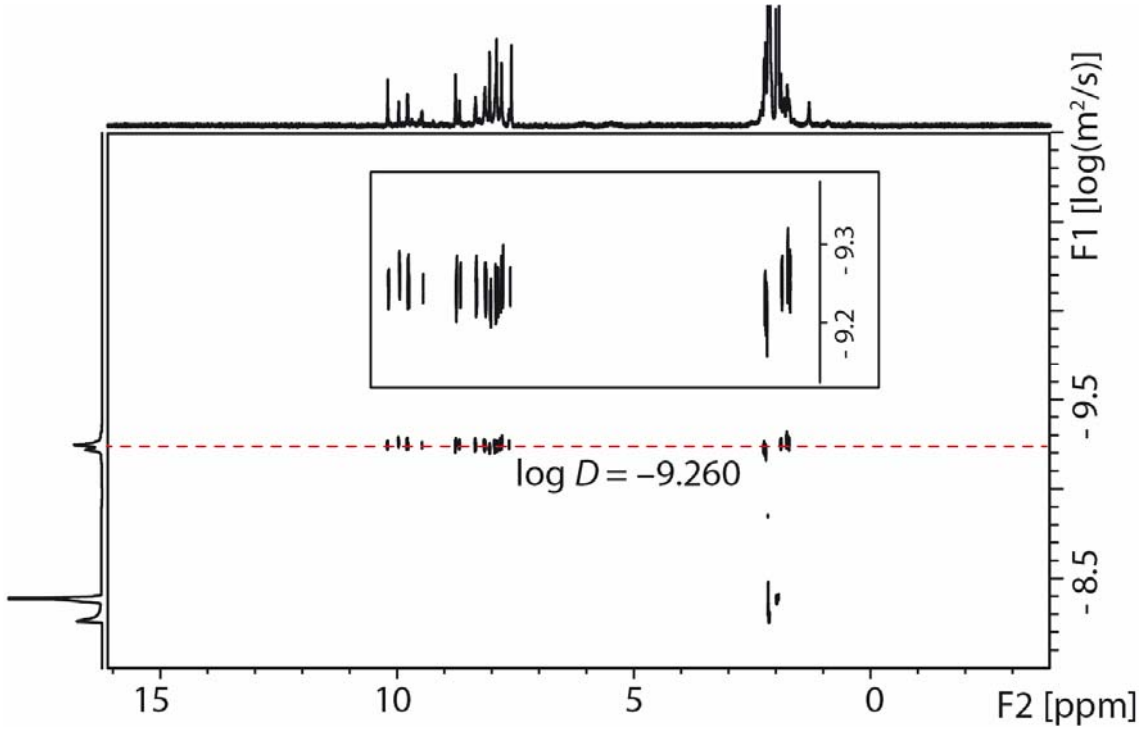

Figure 3.66 DOSY spectrum (500 MHz, 298 K, CD_3CN) of $[Pd_2\mathbf{L^3}_3(MeCN)_2]^{4+}$: diffusion coefficient = 5.5 x 10^{-10} m^2s^{-1}, log D = –9.26, r = 11.5 Å.

ESI HRMS ($C_{124}H_{84}N_{14}O_{12}Pd_2B_4F_{16}$): $[Pd_2\mathbf{L^3}_3(MeCN)_2]^{4+}$ calcd. for $C_{124}H_{84}N_{14}O_{12}Pd_2$ 543.6123; found 543.6161; $[Pd_2\mathbf{L^3}_3+BF_4]^{3+}$ calcd. for $C_{120}H_{78}N_{12}O_{12}Pd_2BF_4$ 726.1335; found 726.1458; $[Pd_2\mathbf{L^3}_3+2BF_4]^{2+}$ calcd. for $C_{120}H_{78}N_{12}O_{12}Pd_2B_2F_8$ 1132.7023; found 1132.7227.

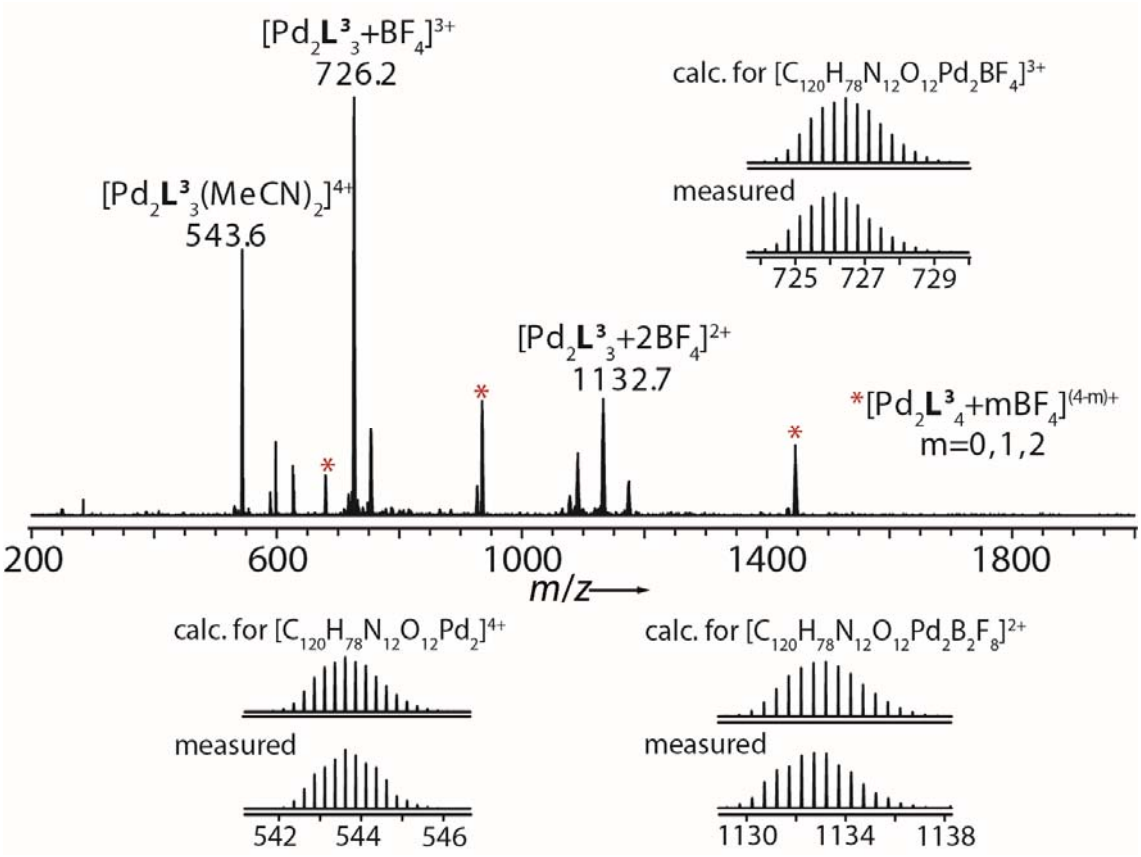

Figure 3.67 ESI mass spectrum of $[Pd_2\mathbf{L^3}_3(MeCN)_2]^{4+}$. Asterisks represent the observed $[Pd_2\mathbf{L^3}_4]^{4+}$ species, caused by partial structural reorganization of the thermodynamically unstable species $[Pd_2\mathbf{L^3}_3(MeCN)_2]^{4+}$.

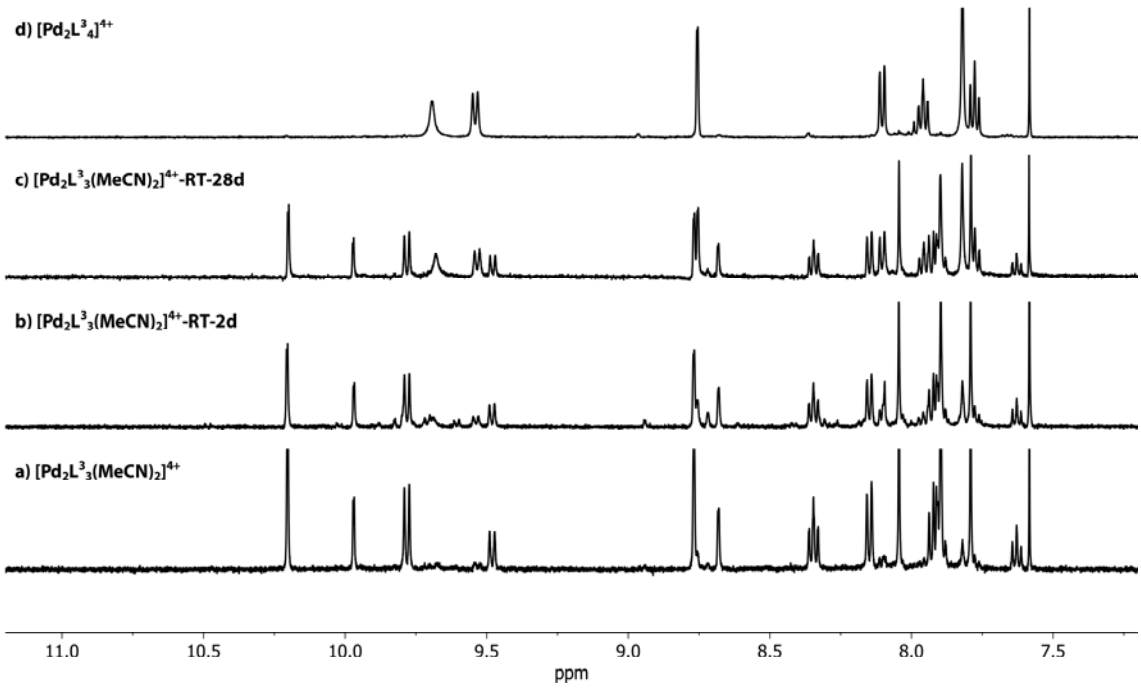

Figure 3.68 ^{1}H NMR spectra (500 MHz, 298 K, CD_3CN) of (a) freshly prepared $[Pd_2\mathbf{L^3}_3(MeCN)_2]^{4+}$ (0.64 mM), (b) and (c) partial conversion of $[Pd_2\mathbf{L^3}_3(MeCN)_2]^{4+}$ to $[Pd_2\mathbf{L^3}_4]^{4+}$ after standing for 2 d or 28 d at room temperature, indicating the instability of bowl $[Pd_2\mathbf{L^3}_3(MeCN)_2]^{4+}$, (d) pure $[Pd_2\mathbf{L^3}_4]^{4+}$ (0.64 mM).

3.8.2.11 Cage $[Pd_2L^3_4]^{4+}$

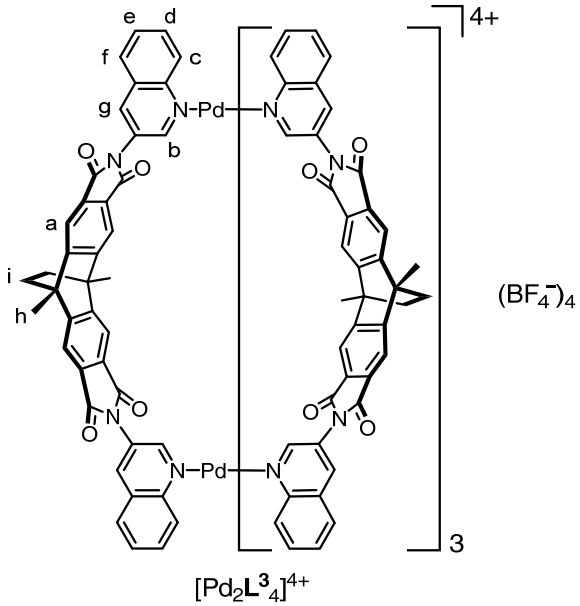

$[Pd_2L^3_4]^{4+}$

A solution of $[Pd(MeCN)_4](BF_4)_2$ (638.8 µL, 15 mM/CD_3CN, 9.58 µmol, 1 eq.) was combined with ligand **L³** (12.0 mg, 19.16 µmol, 2 eq.) in CD_3CN (6844 µL) and heated at 70 °C for 2 d to give a 0.64 mM solution of cage $[Pd_2L^3_4]^{4+}$.

^{1}H NMR (600 MHz, 298 K, CD_3CN): δ (ppm) = 9.70 (s, 8H), 9.54 (d, J = 8.7 Hz, 8H), 8.76 (d, J = 2.0 Hz, 8H), 8.10 (dd, J = 8.3, 1.3 Hz, 8H), 7.96 (ddd, J = 8.6, 7.1, 1.3 Hz, 8H), 7.82 (s, 16H), 7.78 (t, J = 7.6 Hz, 8H), 2.19 (s, 24H), 1.74 (s, 16H).

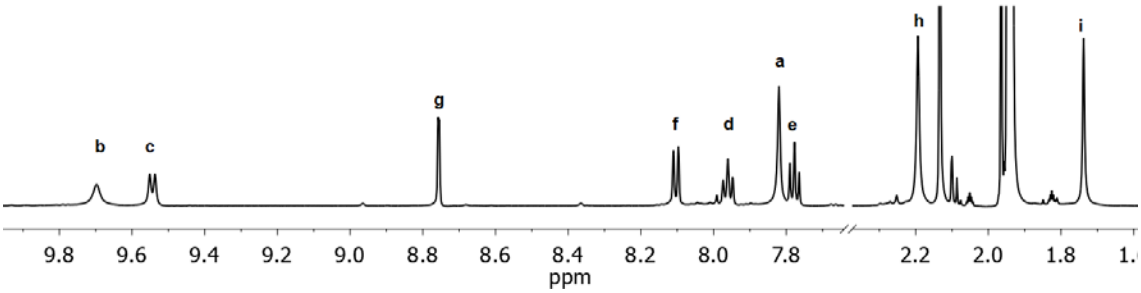

Figure 3.69 ^{1}H NMR spectrum (600 MHz, 298 K, CD_3CN) of $[Pd_2L^3_4]^{4+}$.

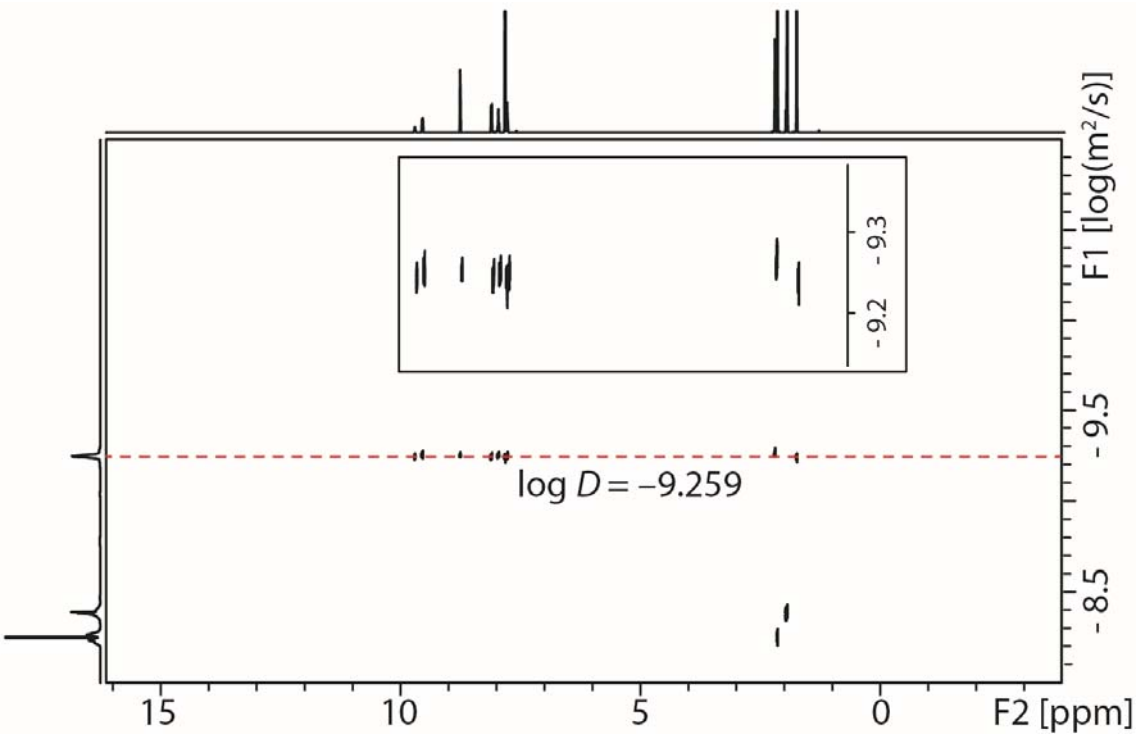

Figure 3.70 DOSY spectrum (500 MHz, 298 K, CD_3CN) of $[Pd_2\mathbf{L^3}_4]^{4+}$: diffusion coefficient = 5.5 x 10^{-10} m^2s^{-1}, log *D* = −9.26, r = 11.5 Å.

ESI HRMS ($C_{160}H_{104}N_{16}O_{16}Pd_2B_4F_{16}$): $[Pd_2\mathbf{L^3}_4]^{4+}$ calcd. for $C_{160}H_{104}N_{16}O_{16}Pd_2$ 679.6482; found 679.6539; $[Pd_2\mathbf{L^3}_4+BF_4]^{3+}$ calcd. for $C_{160}H_{104}N_{16}O_{16}Pd_2BF_4$ 935.1990; found 935.2072; $[Pd_2\mathbf{L^3}_4+2BF_4]^{2+}$ calcd. for $C_{160}H_{104}N_{16}O_{16}B_2F_8$ 1446.3007; found 1446.3137.

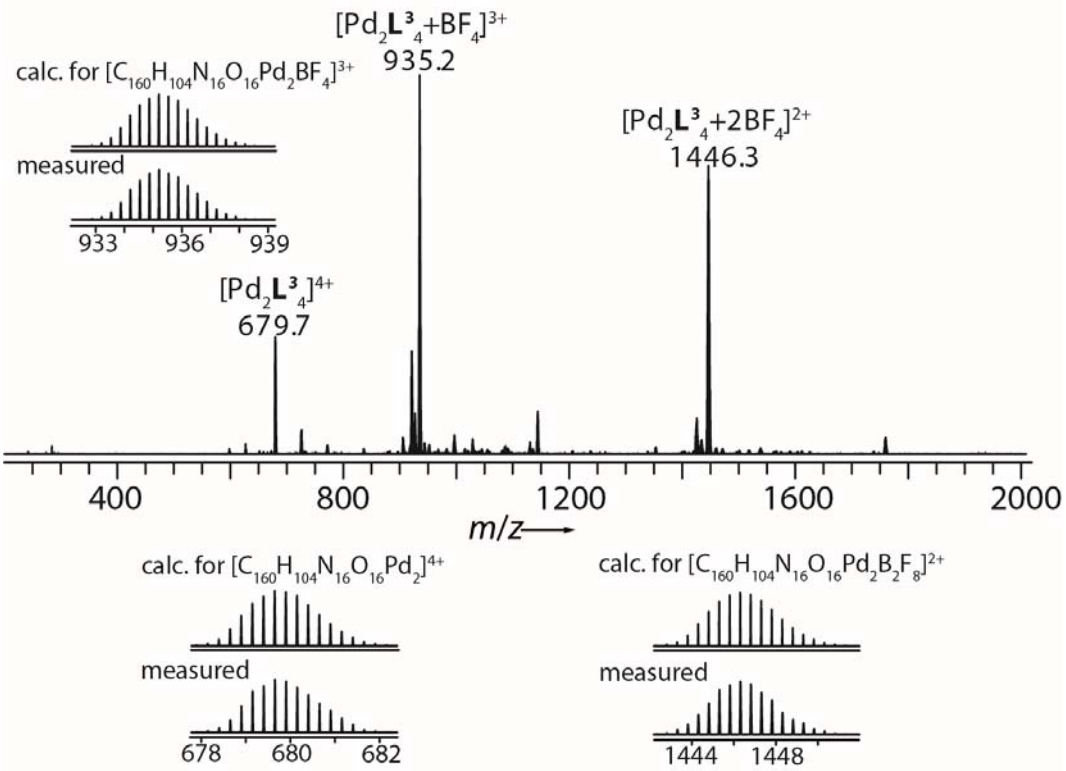

Figure 3.71 ESI mass spectrum of $[Pd_2\mathbf{L^3}_4]^{4+}$.

3.8.2.12 Ring $[Pd_2L^4{}_2(MeCN)_4]^{4+}$

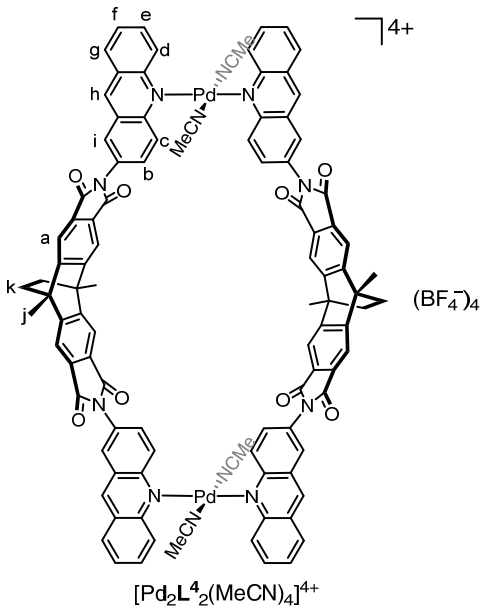

A solution of $[Pd(MeCN)_4](BF_4)_2$ (162.4 µL, 15 mM/CD_3CN, 2.44 µmol, 1 eq.) was combined with ligand **L⁴** (1.8 mg, 2.44 µmol, 1 eq.) in CD_3CN (1740 µL) and stirred at room temperature for 1 d to give a 0.64 mM solution of ring $[Pd_2L^4{}_2(MeCN)_4]^{4+}$.

^{1}H NMR (600 MHz, 298 K, CD_3CN): δ (ppm) = 10.30 (d, J = 9.4 Hz, 4H), 10.27 (d, J = 8.9 Hz, 4H), 9.70 (s, 4H), 8.67 (ddd, J = 8.4, 6.7, 1.4 Hz, 4H), 8.57 (dd, J = 9.3, 2.3 Hz, 4H), 8.52 (d, J = 2.2 Hz, 4H), 8.47 (d, J = 8.3 Hz, 4H), 8.08 – 8.05 (m, 4H), 8.03 (s, 8H), 2.30 (s, 12H), 1.89 (s, 8H).

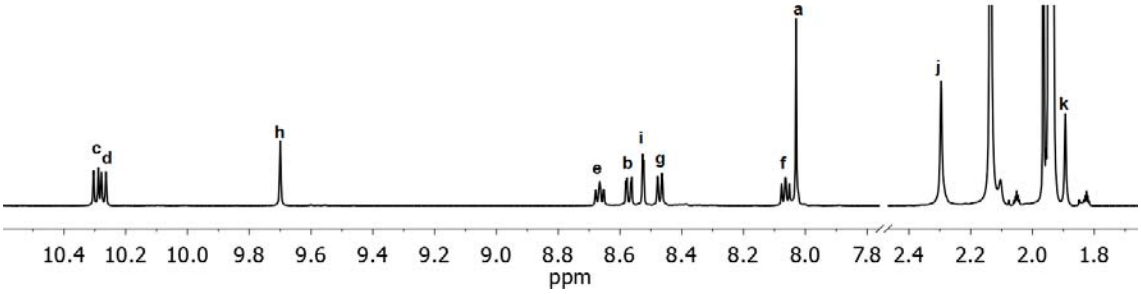

Figure 3.72 ^{1}H NMR spectrum (600 MHz, 298 K, CD_3CN) of $[Pd_2L^4{}_2(MeCN)_4]^{4+}$.

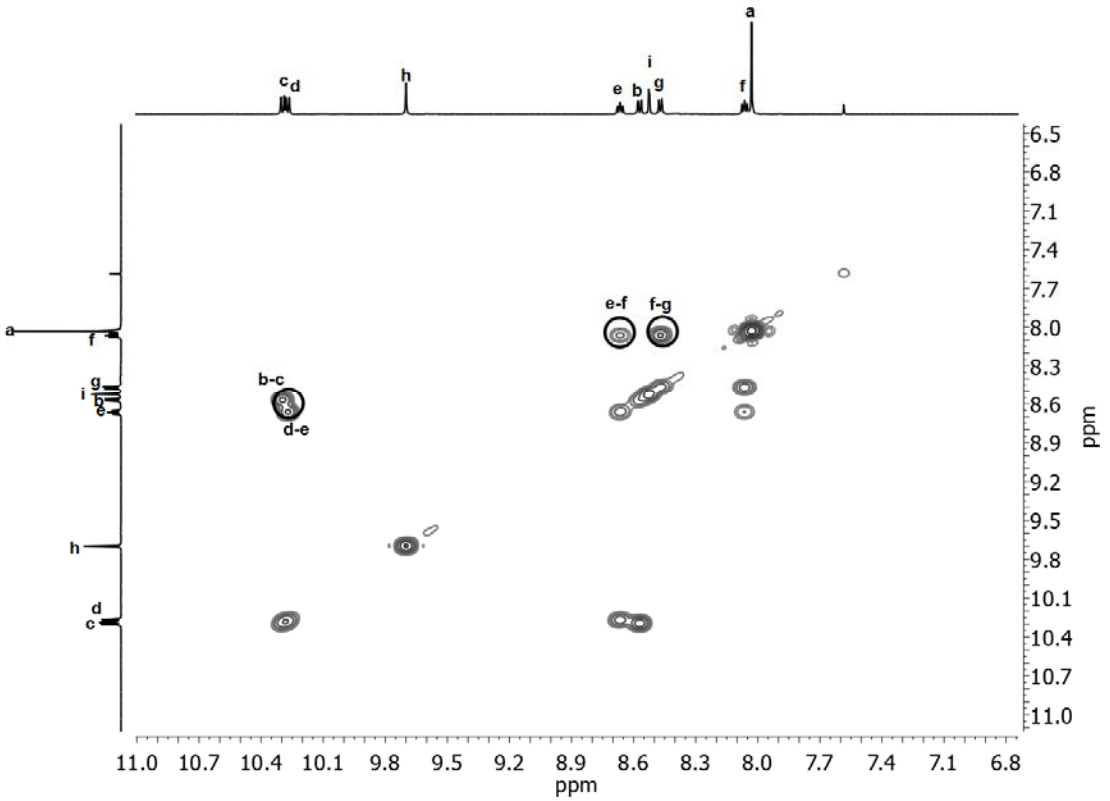

Figure 3.73 Partial $^{1}H - {}^{1}H$ COSY spectrum (600 MHz, 298 K, CD_3CN) of $[Pd_2\mathbf{L^4}_2(MeCN)_4]^{4+}$.

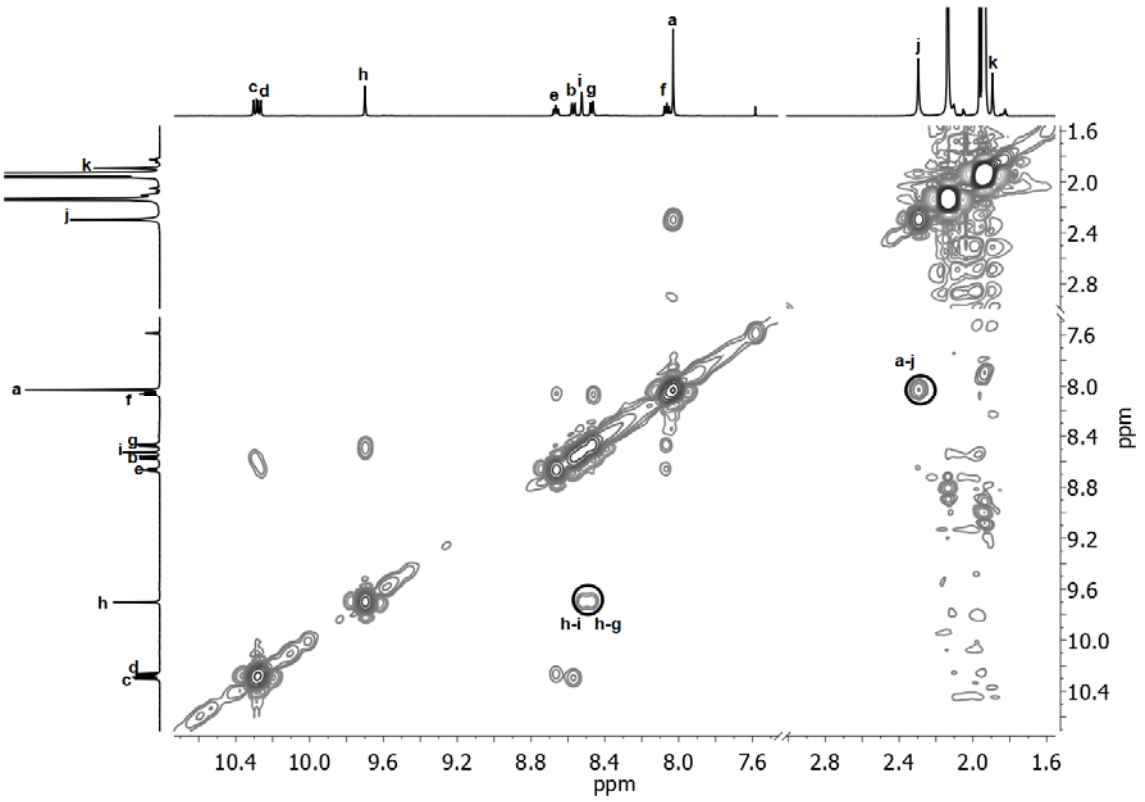

Figure 3.74 Partial $^{1}H - {}^{1}H$ NOESY spectrum (600 MHz, 298 K, CD_3CN) of $[Pd_2\mathbf{L^4}_2(MeCN)_4]^{4+}$.

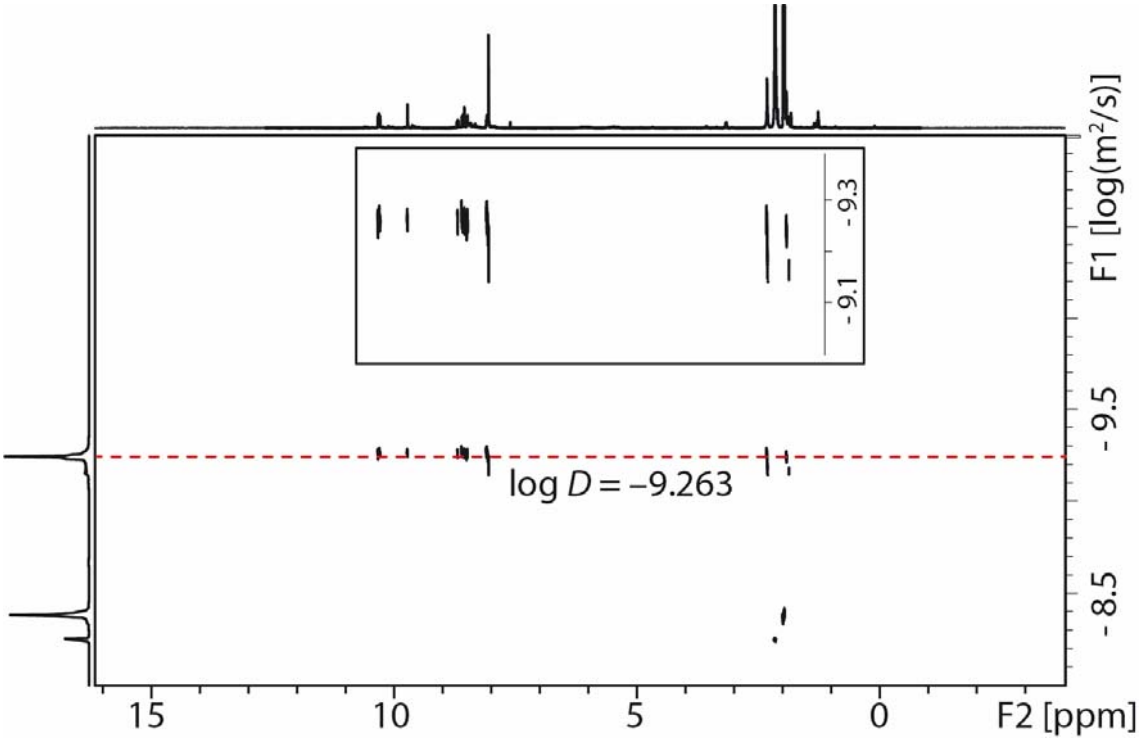

Figure 3.75 DOSY spectrum (500 MHz, 298 K, CD_3CN) of $[Pd_2\mathbf{L^4}_2(MeCN)_4]^{4+}$: diffusion coefficient = 5.5 x 10^{-10} m^2s^{-1}, log *D* = –9.26, r = 11.6 Å.

ESI HRMS ($C_{104}H_{72}N_{12}O_8Pd_2B_4F_{16}$): $[Pd_2\mathbf{L^4}_2(MeCN)_4]^{4+}$ calcd. for $C_{104}H_{72}N_{12}O_8Pd_2$ 457.5922; found 457.5932; $[Pd_2\mathbf{L^4}_2(MeCN)_3+F]^{3+}$ calcd. for $C_{102}H_{69}N_{11}O_8Pd_2F$ 602.7804; found 602.7814; $[Pd_2\mathbf{L^4}_2(MeCN)_2+2F]^{3+}$ calcd. for $C_{100}H_{66}N_{10}O_8Pd_2F_2$ 893.1568; found 893.1576.

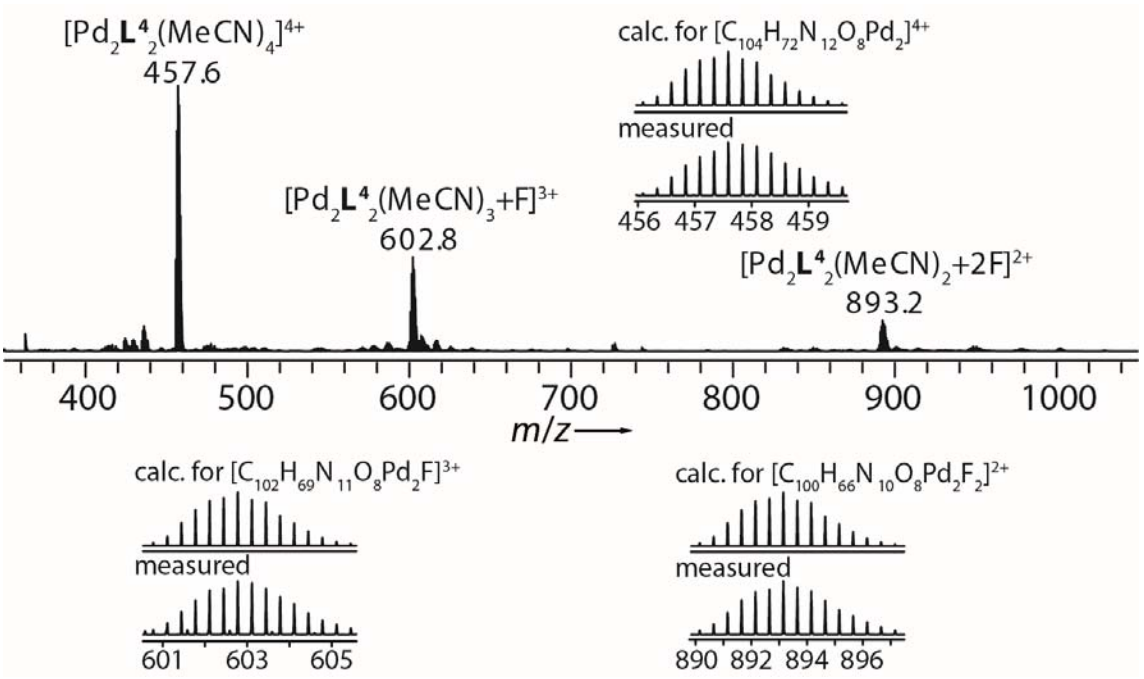

Figure 3.76 ESI mass spectrum of $[Pd_2\mathbf{L^4}_2(MeCN)_4]^{4+}$. The presence of the $[Pd_2\mathbf{L^4}_2(MeCN)_3+F]^{3+}$ and $[Pd_2\mathbf{L^4}_2(MeCN)_2+2F]^{2+}$ species is due to substitution of coordinated CH_3CN by traces of fluoride anions under the measurement conditions.

3.8.2.13 Ring $[Pd_2L^4{}_2Cl_4]$

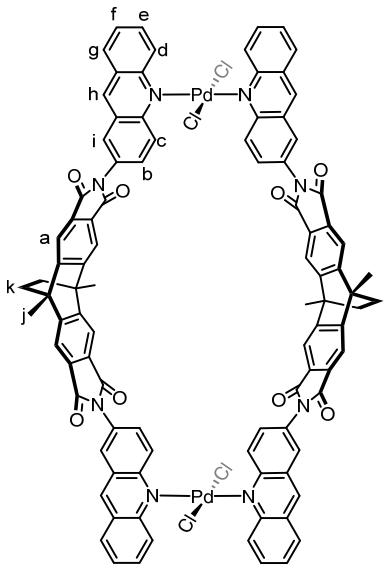

$[Pd_2\mathbf{L^4}{}_2Cl_4]$

A CD_3CN solution of the ring $[Pd_2\mathbf{L^4}{}_2(MeCN)_4]^{4+}$ (5080 µL, 0.64 mM, 3.25 µmol, 1 eq.) was mixed with CD_3CN solution of NBu_4Cl (433 µL, 30 mM, 13.00 µmol, 4 eq.) at room temperature for several minutes to give the neutral compound $[Pd_2\mathbf{L^4}{}_2Cl_4]$ as precipitate. The product was collected via centrifugation, washed with pure chloroform and dried in vacuum to give a yellow solid (4.0 mg, 68%). The solid is soluble in DMSO and DMF, however, proton signals of the free ligand and a second species (presumably mono-coordinated ligand) were found to arise after standing for several hours.

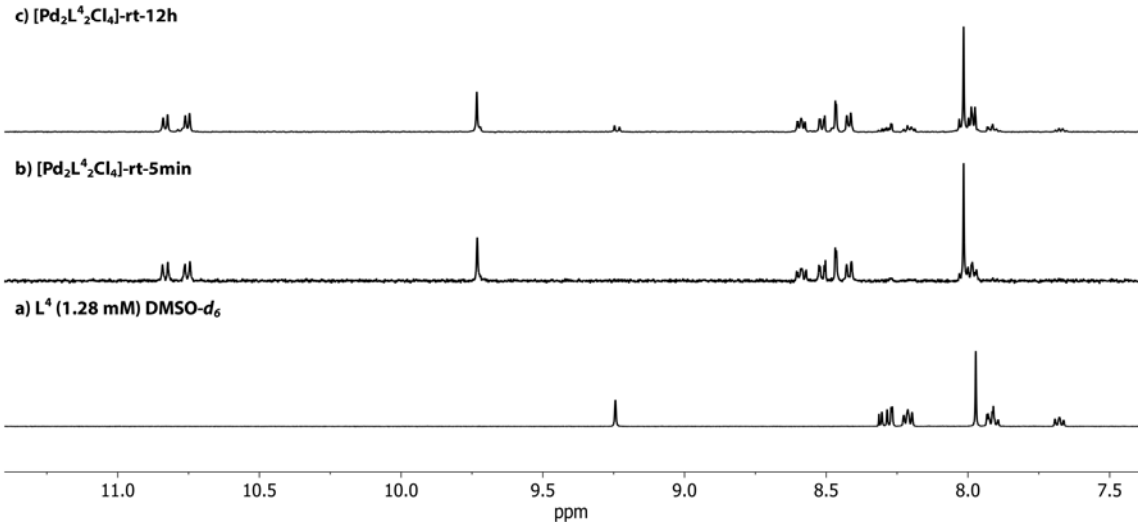

Figure 3.77 ^{1}H NMR spectra (298 K, DMSO-d_6) of (a) $\mathbf{L^4}$ (1.28mM), (b) and (c) re-dissolved $[Pd_2\mathbf{L^4}{}_2Cl_4]$ in DMSO-d_6 for 5 min or 12 h at room temperature, indicating decomposition of $[Pd_2\mathbf{L^4}{}_2Cl_4]$ in DMSO.

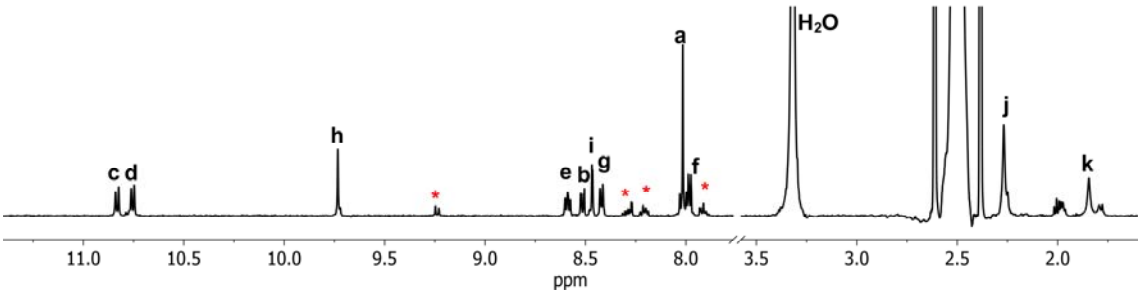

Figure 3.78 ^{1}H NMR spectrum (600 MHz, 298 K, DMSO-d_6) of $[Pd_2\mathbf{L^4}_2Cl_4]$. Asterisks represent proton signals of released ligand after standing for several hours during the 2D NMR experiments.

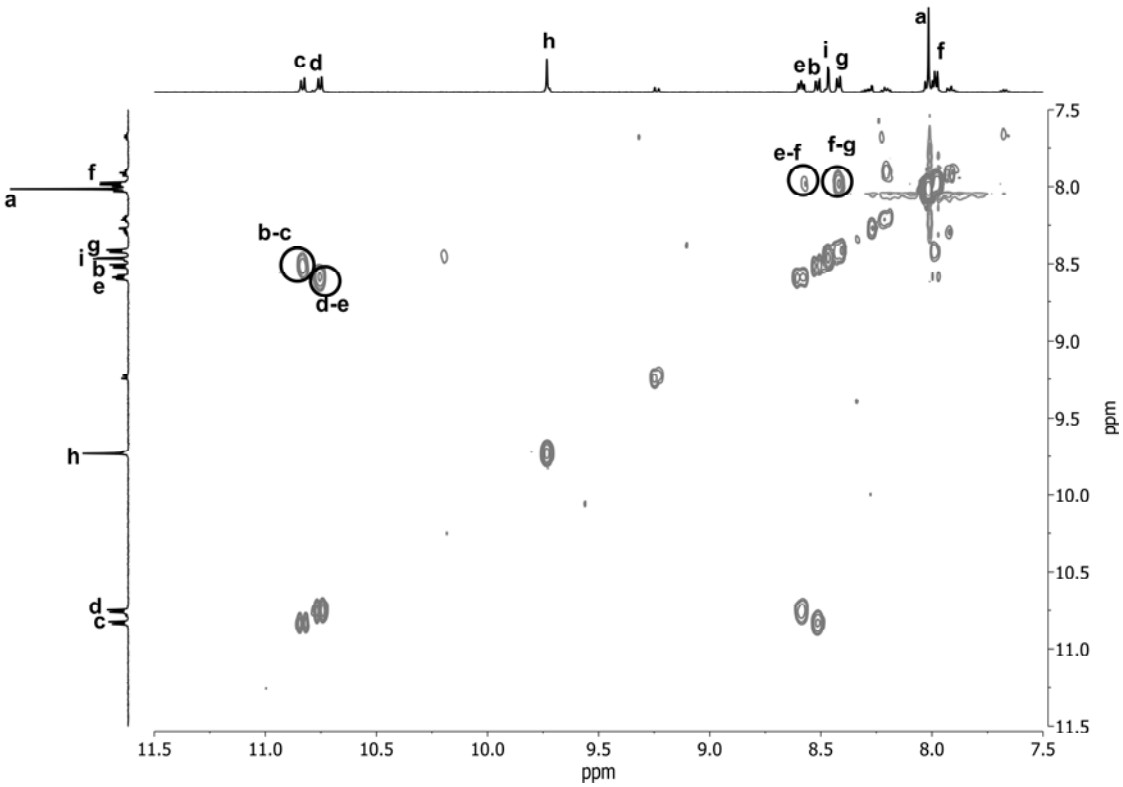

Figure 3.79 Partial ^{1}H – ^{1}H COSY spectrum (600 MHz, 298 K, DMSO-d_6) of $[Pd_2\mathbf{L^4}_2Cl_4]$.

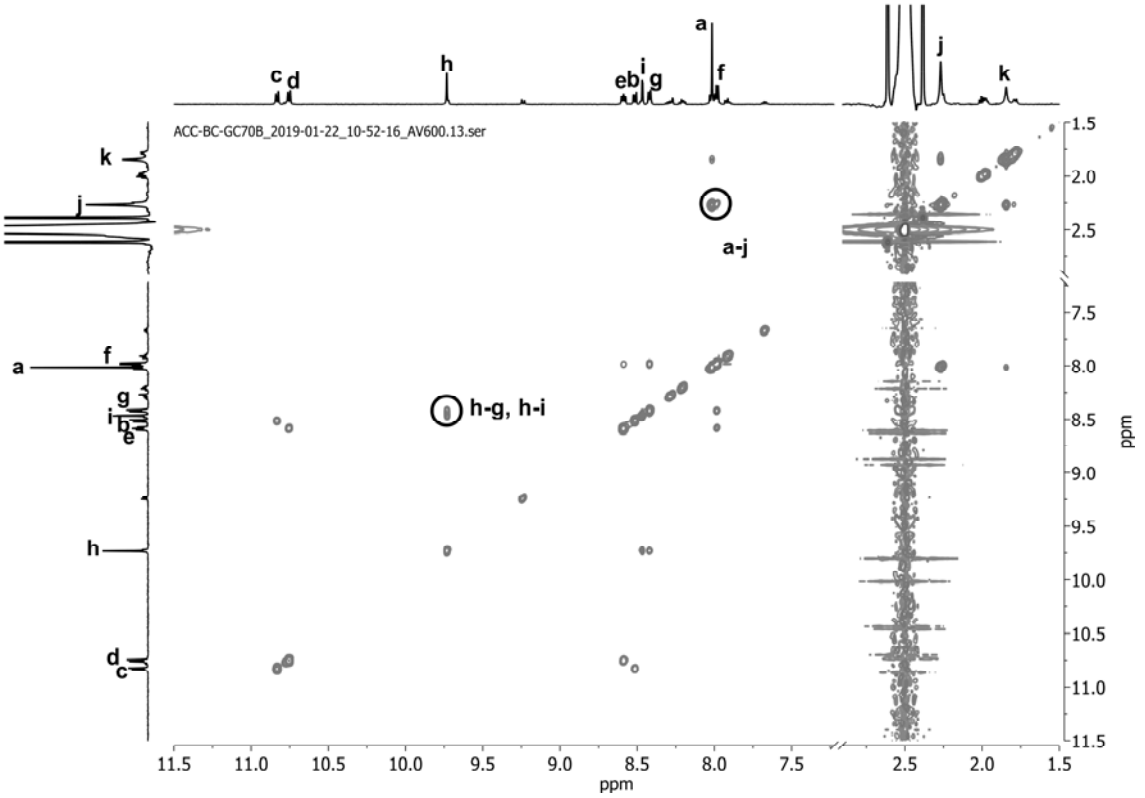

Figure 3.80 Partial $^{1}H - {}^{1}H$ NOESY spectrum (600 MHz, 298 K, DMSO-d_6) of $[Pd_2\mathbf{L^4}_2Cl_4]$.

3.8.3 Titration of bowl/ring with chloride anions

3.8.3.1 Titration of bowl $[Pd_2\mathbf{L^2}_3(MeCN)_2]^{4+}$ with chloride anions

A 500 µL solution of the bowl $[Pd_2\mathbf{L^2}_3(MeCN)_2]^{4+}$ (0.64 mM) in CD_3CN was titrated with a concentrated solution of tetrabutylammonium chloride (NBu_4Cl) (8.75 mM) in CD_3CN. Upon each addition, the solution was shaken before acquiring the spectrum, which allowed equilibrium to be reached.

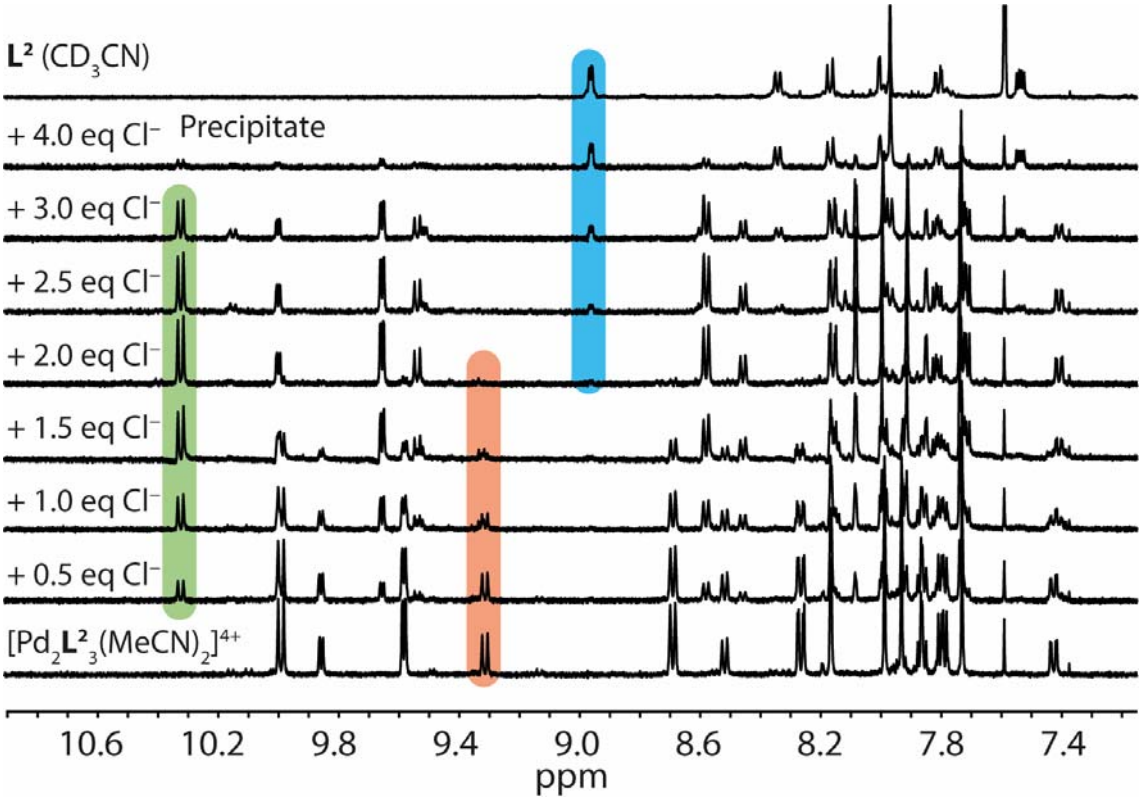

Figure 3.81 ^{1}H NMR titration (500 MHz, 298 K, CD_3CN) of $[Pd_2\mathbf{L^2}_3(MeCN)_2]^{4+}$ with NBu_4Cl. Upon addition of two equivalents of chloride, bowl $[Pd_2\mathbf{L^2}_3(MeCN)_2]^{4+}$ transforms into bowl $[Pd_2\mathbf{L^2}_3Cl_2]^{2+}$. Excess addition of chloride leads to disassembly of the bowl. The quinoline proton c of $[Pd_2\mathbf{L^2}_3Cl_2]^{2+}$, proton c' of $[Pd_2\mathbf{L^2}_3(MeCN)_2]^{4+}$ and proton d of $\mathbf{L^2}$ are highlighted in green, red and blue, respectively.

3.8.3.2 Titration of ring $[Pd_2\mathbf{L^4}_2(MeCN)_4]^{4+}$ with chloride anions

A 600 µL solution of the ring $[Pd_2\mathbf{L^4}_2(MeCN)_4]^{4+}$ (0.64 mM) in CD_3CN was titrated with a concentrated solution of tetrabutylammonium chloride (NBu_4Cl) (30 mM) in CD_3CN. Upon each addition, the solution was shaken before acquiring the spectrum, which allowed equilibrium to be reached.

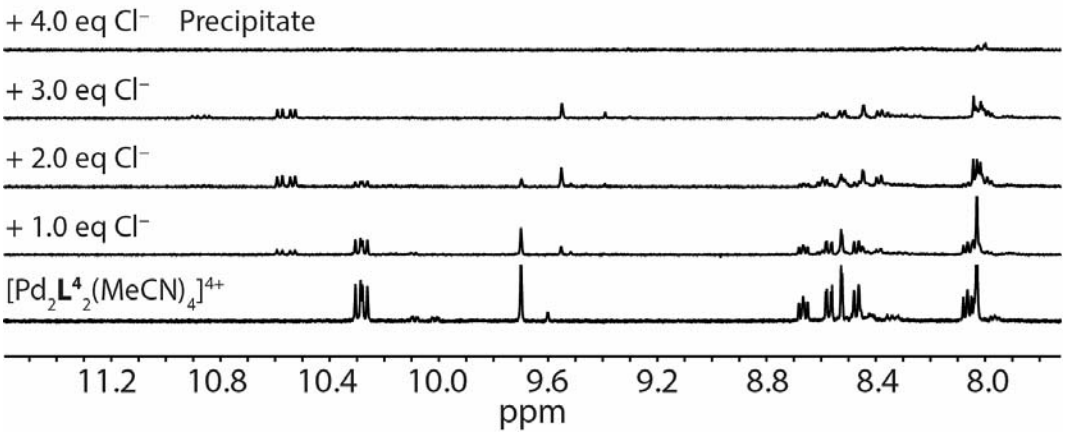

Figure 3.82 ^{1}H NMR titration (500 MHz, 298 K, CD_3CN) of $[Pd_2\mathbf{L^4}_2(MeCN)_4]^{4+}$ with NBu_4Cl. Upon addition of four equivalents of chloride, charged ring $[Pd_2\mathbf{L^4}_2(MeCN)_4]^{4+}$ transforms into neutral ring $[Pd_2\mathbf{L^4}_2Cl_4]$ which was found to precipitate from the polar solvent. The characterization of ring $[Pd_2\mathbf{L^4}_2Cl_4]$ is described above in detail.

3.8.4 Fullerene binding studies

General procedure: To a CD_3CN solution of the host compounds (0.64 mM for $[Pd_2\mathbf{L^1}_4]^{4+}$, $[Pd_2\mathbf{L^2}_3(MeCN)_2]^{4+}$, $[Pd_2\mathbf{L^3}_4]^{4+}$ and $[Pd_2\mathbf{L^4}_2(MeCN)_4]^{4+}$, 0.56 mM for $[Pd_2\mathbf{L^2}_3Cl_2]^{2+}$) in a sealed vessel, excess fullerene (C_{60}, C_{70}) was added as finely grounded powders. The mixtures were sonicated for 3 minutes, then stirred at room temperature or left standing at 70 ^oC for several days. Upon cooling, the supernatant was collected and transferred to NMR tubes.

3.8.4.1 Fullerene binding experiment with cage $[Pd_2L^1_4]^{4+}$

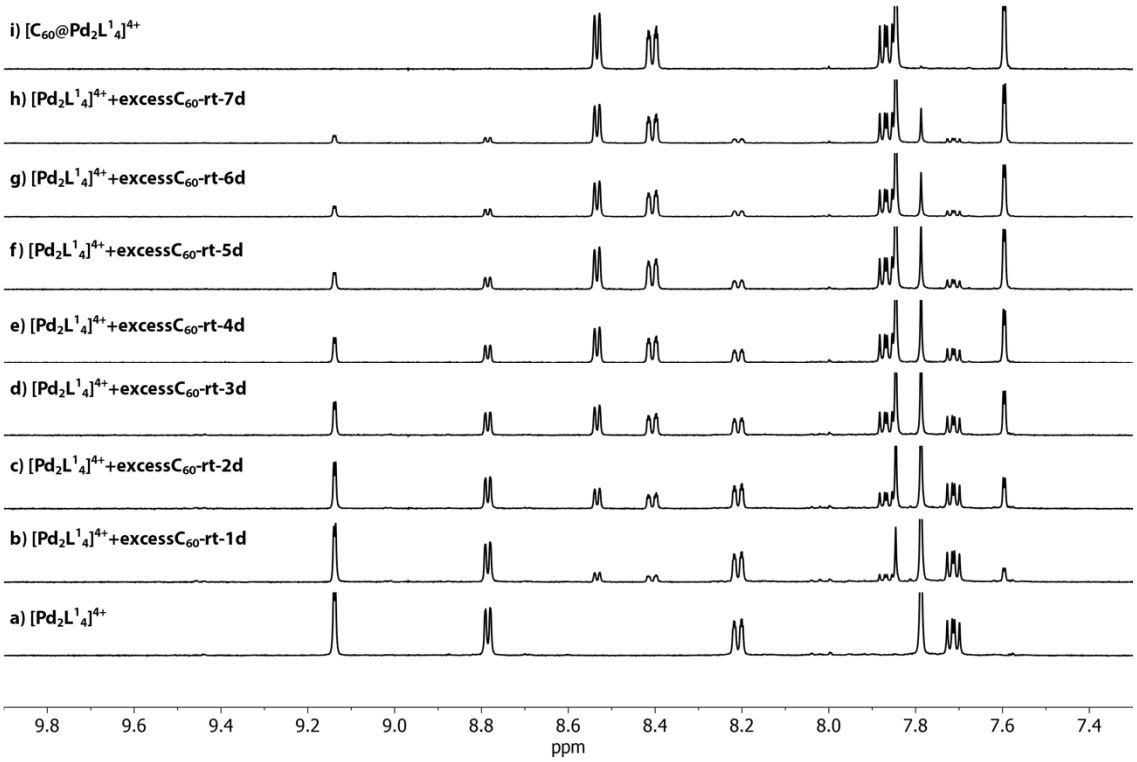

Figure 3.83 ^1H NMR spectra (500 MHz, 298 K, CD_3CN) following the encapsulation of C_{60} in $[Pd_2\mathbf{L^1}_4]^{4+}$ at room temperature.

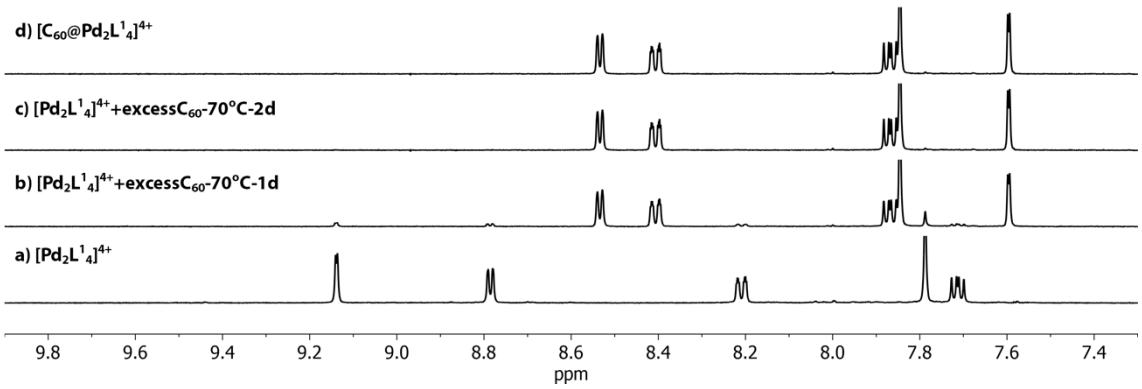

Figure 3.84 ^1H NMR spectra (500 MHz, 298 K, CD_3CN) following the encapsulation of C_{60} in $[Pd_2\mathbf{L^1}_4]^{4+}$ at 70 ^oC, indicating a faster process compared with the encapsulation performed at room temperature.

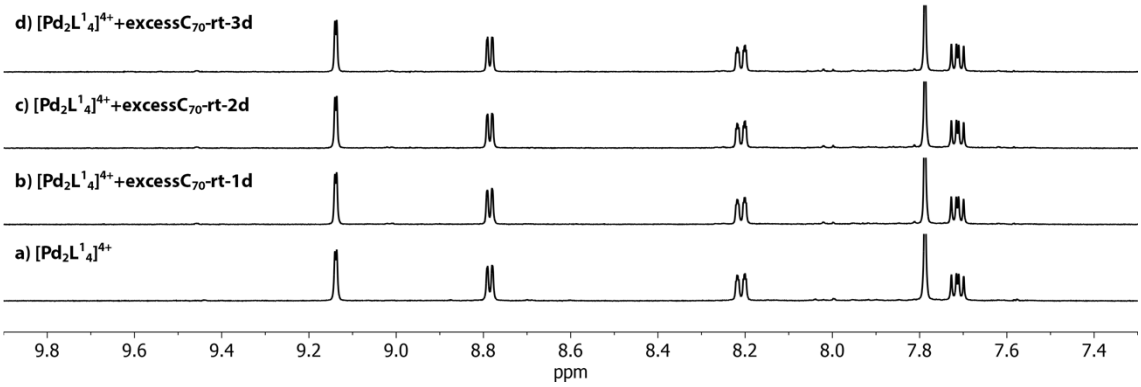

Figure 3.85 ^{1}H NMR spectra (500 MHz, 298 K, CD_3CN) monitoring the test of binding C_{70} in $[Pd_2\mathbf{L^1}_4]^{4+}$ at room temperature, indicating that C_{70} cannot be encapsulated in $[Pd_2\mathbf{L^1}_4]^{4+}$ at room temperature.

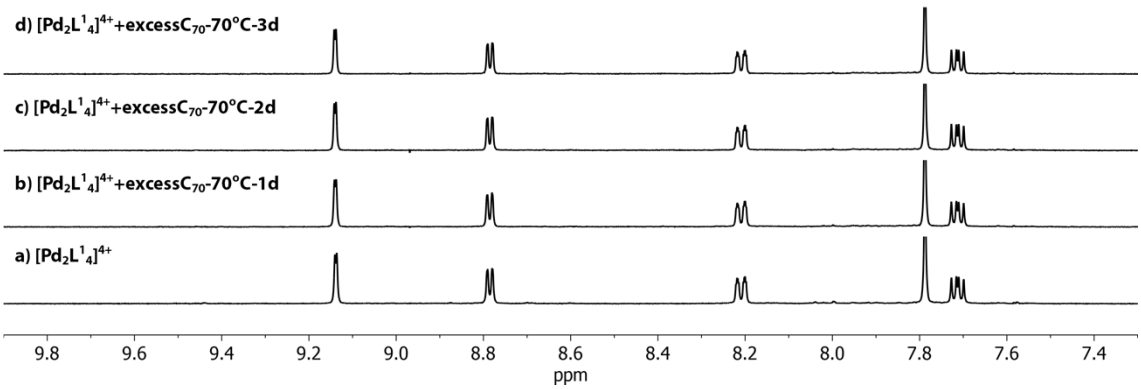

Figure 3.86 ^{1}H NMR spectra (500 MHz, 298 K, CD_3CN) monitoring the test of binding C_{70} in $[Pd_2\mathbf{L^1}_4]^{4+}$ at 70 °C, indicating that C_{70} cannot be encapsulated in $[Pd_2\mathbf{L^1}_4]^{4+}$.

3.8.4.2 Fullerene binding experiment with bowl $[Pd_2\mathbf{L^2}_3(MeCN)_2]^{4+}$

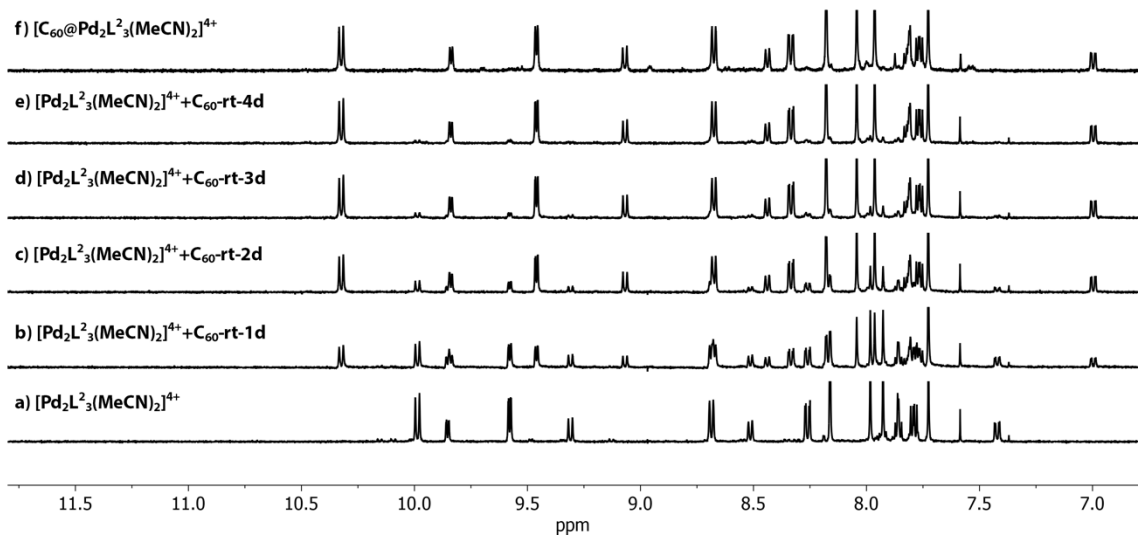

Figure 3.87 ^{1}H NMR spectra (500 MHz, 298 K, CD_3CN) following the encapsulation of C_{60} in $[Pd_2\mathbf{L^2}_3(MeCN)_2]^{4+}$ at room temperature.

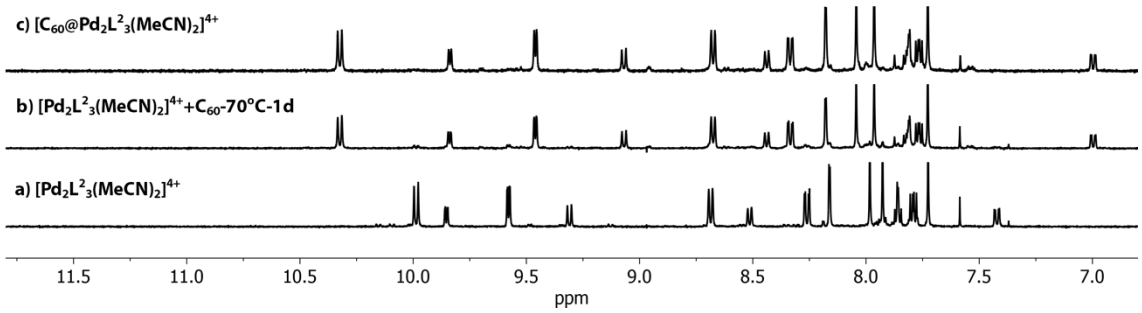

Figure 3.88 ^{1}H NMR spectra (500 MHz, 298 K, CD_3CN) following the encapsulation of C_{60} in $[Pd_2\mathbf{L^2}_3(MeCN)_2]^{4+}$ at 70 °C, indicating a faster process compared with the encapsulation performed at room temperature.

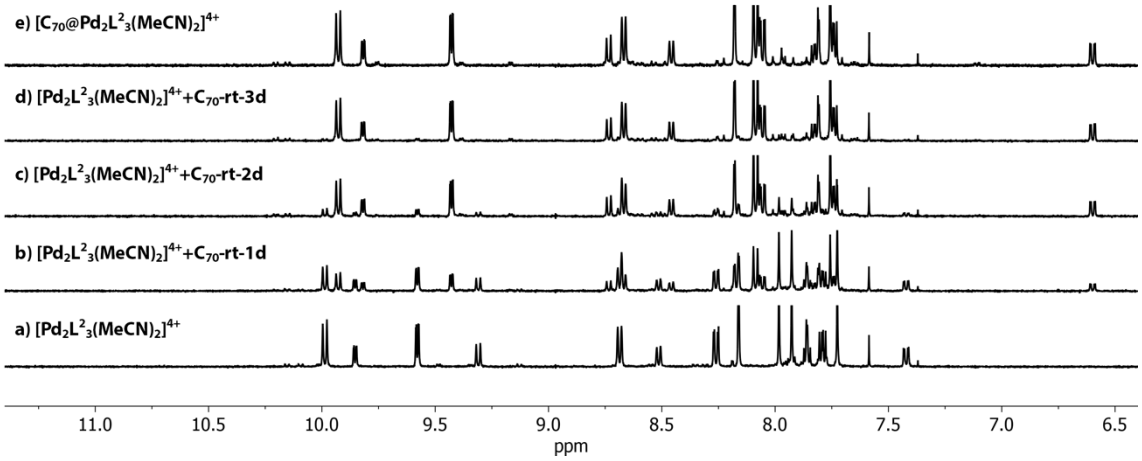

Figure 3.89 ^{1}H NMR spectra (500 MHz, 298 K, CD_3CN) following the encapsulation of C_{70} in $[Pd_2\mathbf{L^2}_3(MeCN)_2]^{4+}$ at room temperature.

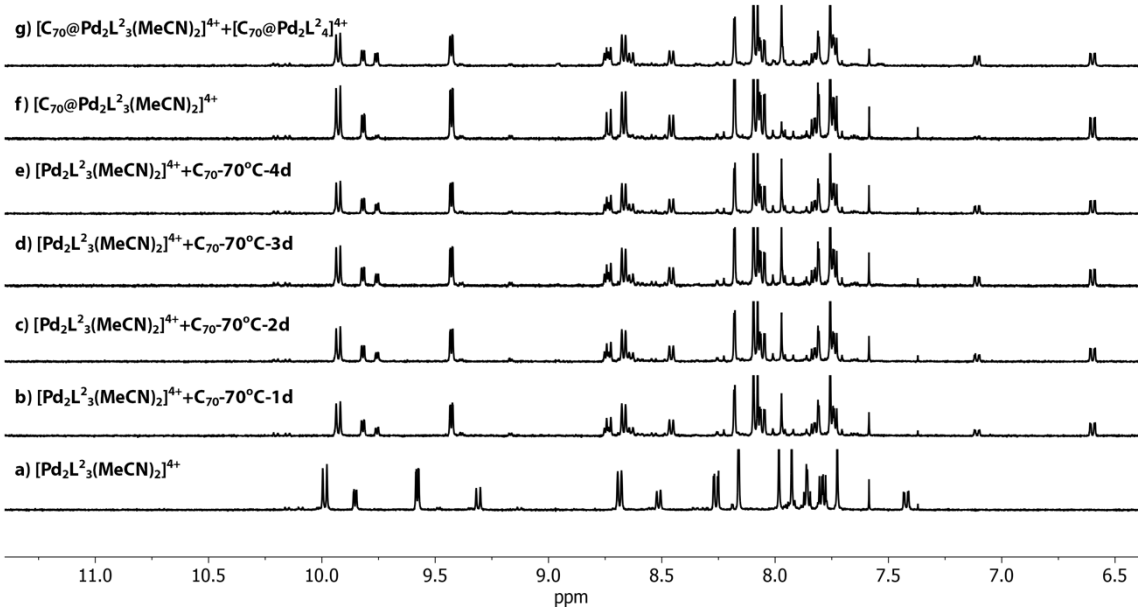

Figure 3.90 ^{1}H NMR spectra (500 MHz, 298 K, CD_3CN) following the reaction between C_{70} and $[Pd_2\mathbf{L^2}_3(MeCN)_2]^{4+}$ at 70 °C, indicating the formation of the mixture of $[C_{70}@Pd_2\mathbf{L^2}_3(MeCN)_2]^{4+}$ and $[C_{70}@Pd_2\mathbf{L^2}_4]^{4+}$.

3.8.4.3 Fullerene binding experiment with bowl $[Pd_2L^2{}_3Cl_2]^{2+}$

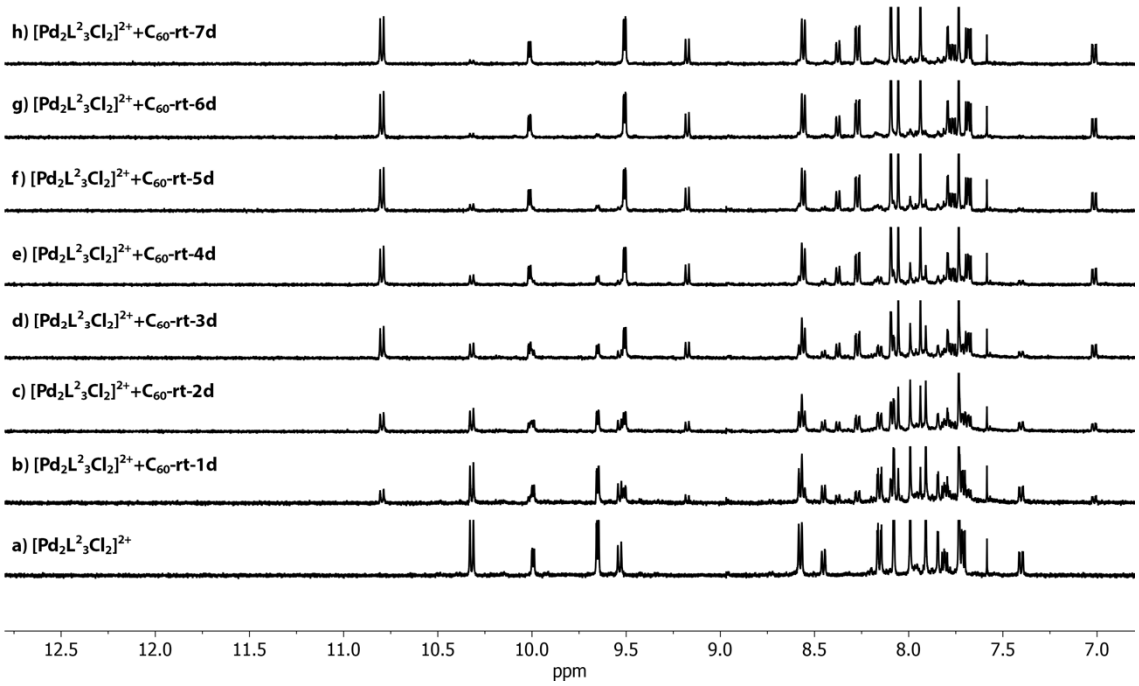

Figure 3.91 ^{1}H NMR spectra (500 MHz, 298 K, CD_3CN) following the encapsulation of C_{60} in $[Pd_2\mathbf{L^2}_3Cl_2]^{2+}$ at room temperature.

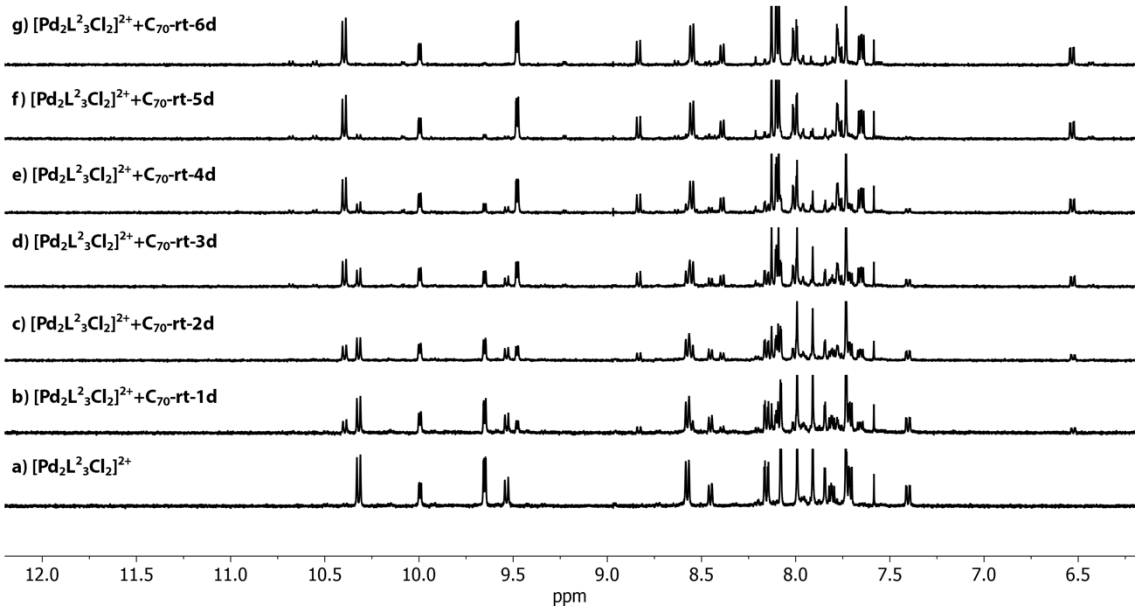

Figure 3.92 ^{1}H NMR spectra (500 MHz, 298 K, CD_3CN) following the encapsulation of C_{70} in $[Pd_2\mathbf{L^2}_3Cl_2]^{2+}$ at room temperature.

3.8.4.4 Fullerene binding experiment with cage $[Pd_2L^3_4]^{4+}$

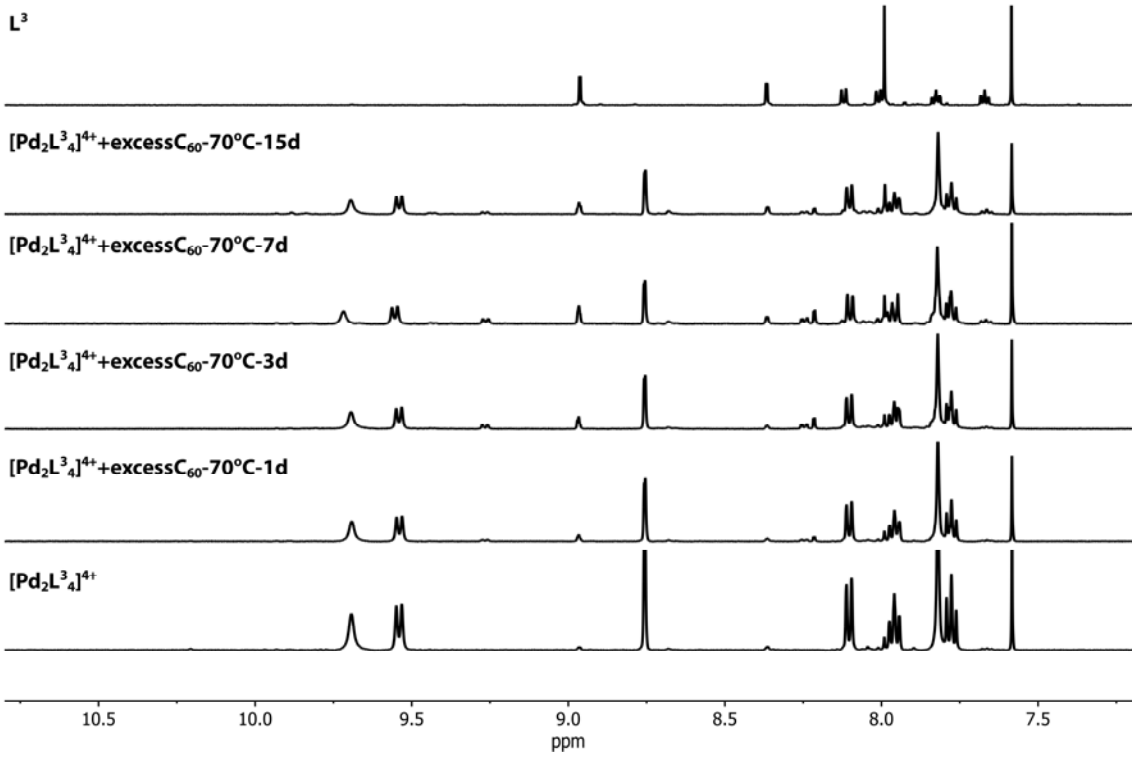

Figure 3.93 ^{1}H NMR spectra (500 MHz, 298 K, CD_3CN) monitoring the test of binding C_{60} in $[Pd_2\mathbf{L^3}_4]^{4+}$ at 70 °C, indicating that C_{60} cannot be encapsulated in $[Pd_2\mathbf{L^3}_4]^{4+}$ and partial decomposition of $[Pd_2\mathbf{L^3}_4]^{4+}$.

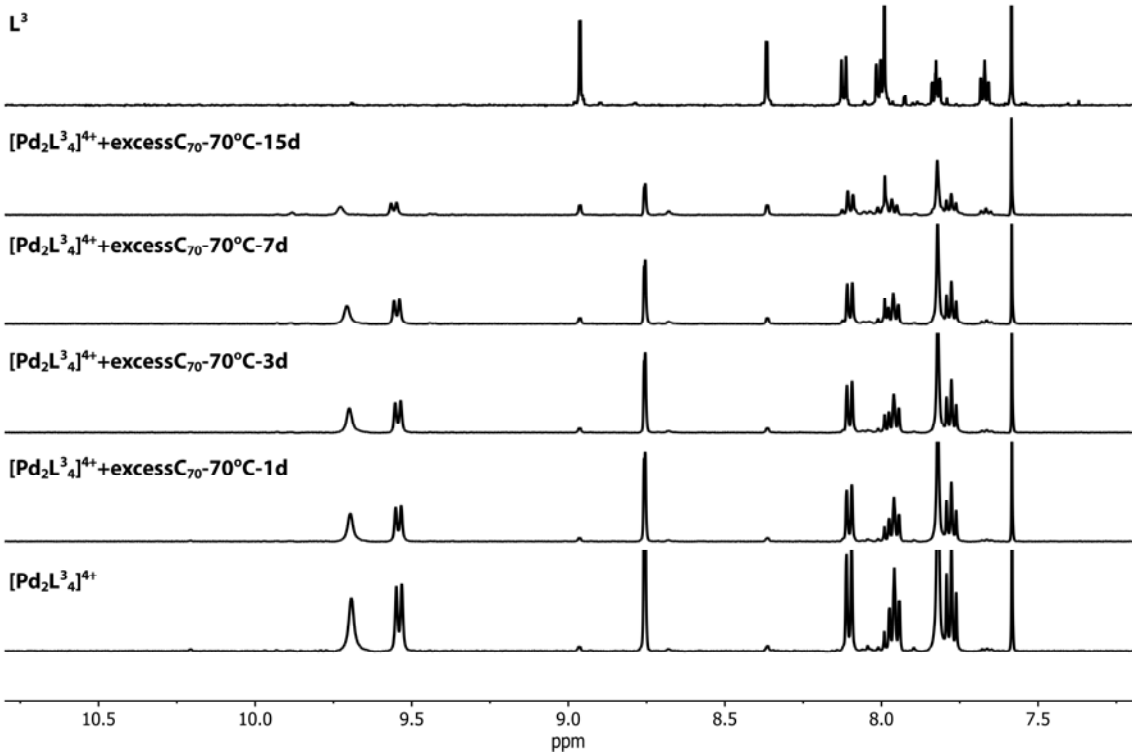

Figure 3.94 ^{1}H NMR spectra (500 MHz, 298 K, CD_3CN) monitoring the test of binding C_{70} in $[Pd_2\mathbf{L^3}_4]^{4+}$ at 70 °C, indicating that C_{70} cannot be encapsulated in $[Pd_2\mathbf{L^3}_4]^{4+}$ and partial decomposition of $[Pd_2\mathbf{L^3}_4]^{4+}$.

3.8.4.5 Fullerene binding experiment with ring $[Pd_2L^4_2(MeCN)_4]^{4+}$

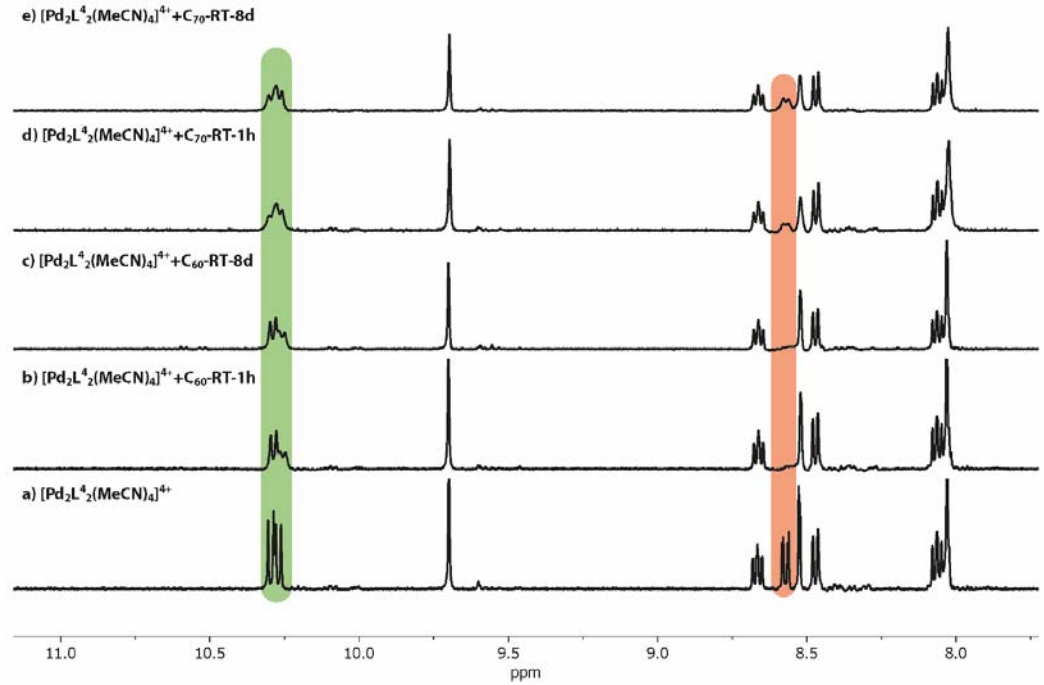

Figure 3.95 ^{1}H NMR spectra (500 MHz, 298 K, CD_3CN) monitoring the test of binding C_{60}/C_{70} in $[Pd_2\mathbf{L^4}_2(MeCN)_4]^{4+}$ at room temperature for 1 h or 8 d, indicating fast exchange between ring and C_{60}/C_{70}. The acridine protons (H_c, H_d) of ring $[Pd_2\mathbf{L^4}_2(MeCN)_4]^{4+}$ and proton H_b are highlighted in green and red, respectively.

3.8.5 UV-Vis spectra

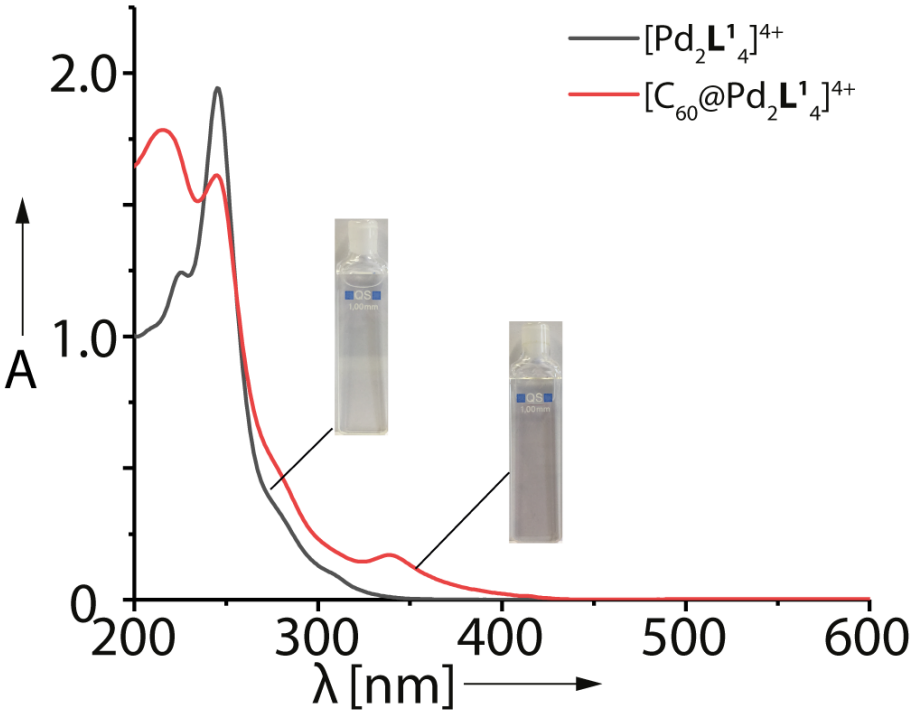

Figure 3.96 UV-Vis spectra (0.064 mM, CH_3CN, 298 K) and photographs of $[Pd_2\mathbf{L^1}_4]^{4+}$ and $[C_{60}@Pd_2\mathbf{L^1}_4]^{4+}$.

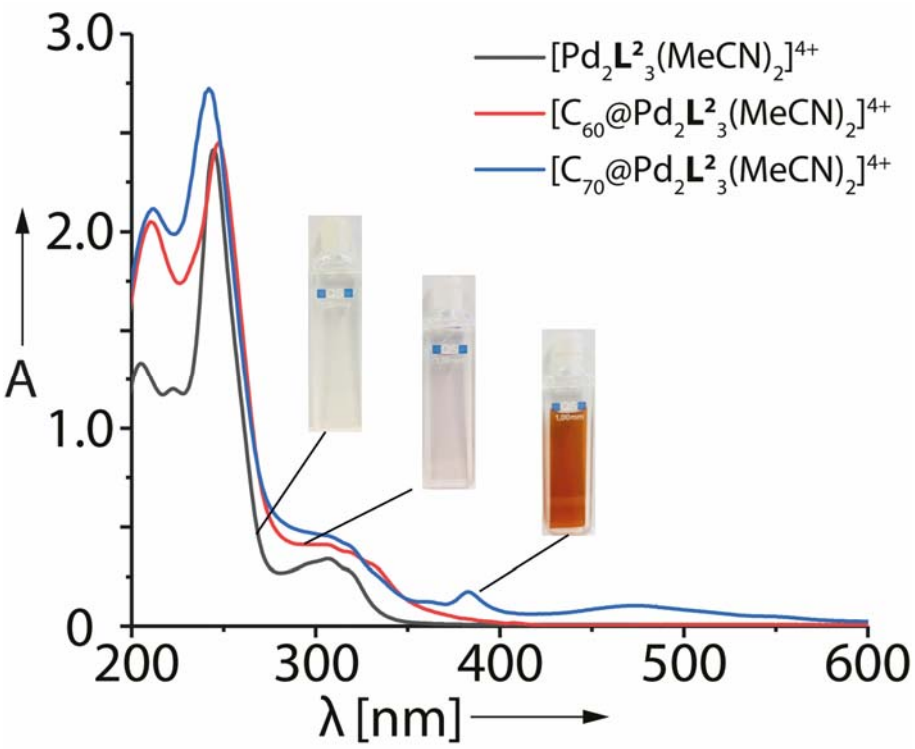

Figure 3.97 UV-Vis spectra (0.064 mM, CH_3CN, 298 K) and photographs of $[Pd_2\mathbf{L^2}_3(MeCN)_2]^{4+}$, $[C_{60}@Pd_2\mathbf{L^2}_3(MeCN)_2]^{4+}$ and $[C_{70}@Pd_2\mathbf{L^2}_3(MeCN)_2]^{4+}$.

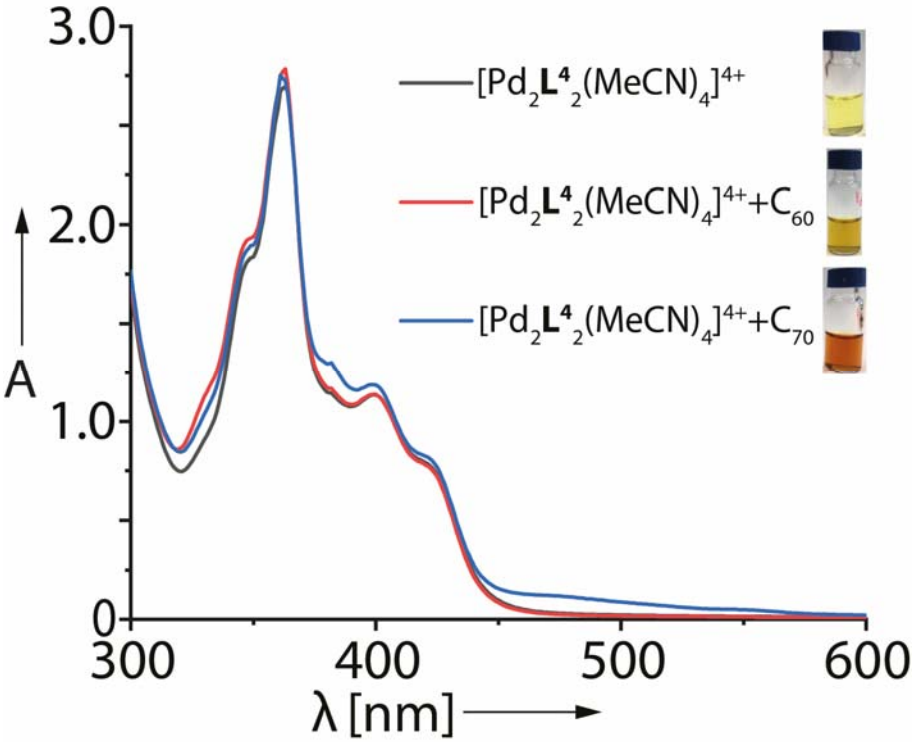

Figure 3.98 UV-Vis spectra (0.64 mM, CH_3CN, 298 K) and photographs of $[Pd_2\mathbf{L^4}_2(MeCN)_4]^{4+}$ with/without fullerenes.

3.8.6 X-Ray data

Table 3.2 Crystallographic data of $[Pd_2\mathbf{L^1}_4](BF_4)_4$, $[C_{60}@Pd_2\mathbf{L^1}_4](BF_4)_4$ and $\mathbf{L^2}$.

Compound	$\mathbf{[Pd_2L^1_4](BF_4)_4}$	$\mathbf{[C_{60}@Pd_2L^1_4](BF_4)_4}$	$\mathbf{L^2}$
CCDC number	1850358	1850359	1850360
Identification code	bc7a_sq	bc16a_sq	bc12d
Empirical formula	$C_{128}H_{88}N_{16}O_{16}Pd_2B_4F_{16}$	$C_{188}H_{88}N_{16}O_{16}Pd_2B_2F_8$	$C_{40}H_{26}N_4O_4$
Formula weight	2666.18	3213.16	626.65
Temperature (K)	80(2)	80(2)	100(2)
Crystal system	Triclinic	Triclinic	Monoclinic
Space group	P-1	P-1	$P2_1$
a (Å)	15.689(3)	29.482(6)	7.3461(2)
b (Å)	17.074(3)	30.095(6)	8.2067(3)
c (Å)	17.522(4)	33.669(7)	23.9093(8)
α (º)	112.90(3)	97.35(3)	90
β (º)	113.54(3)	93.16(3)	93.499(2)
γ (º)	90.59(3)	112.74(3)	90
Volume ($Å^3$)	3886.8(18)	27145(11)	1438.74(8)
Z	1	6	2
Density (calc.) (g/cm^3)	1.139	1.179	1.447
Absorption coefficient (mm^{-1})	0.279	0.246	0.767
F(000)	1352	9780	652
Crystal size (mm^3)	0.200 x 0.020 x 0.020	0.300 x 0.050 x 0.020	0.200 x 0.100 x 0.020
θ range for data collection (º)	1.280 to 26.202	0.595 to 21.512	3.704 to 80.342
Reflections collected	53426	226990	24133
Observed reflections [R(int)]	15802 [0.0413]	64579 [0.0527]	6093 [0.0470]
Goodness-of-fit on F^2	1.049	1.165	1.053
R_1 [$I>2\sigma(I)$]	0.0801	0.0887	0.0290
wR_2 (all data)	0.2626	0.3067	0.0717
Largest diff. peak and hole ($e.Å^{-3}$)	1.537 and -1.238	0.942 and -0.819	0.172 and -0.148
Data / restraints / parameters	15802 / 2120 / 824	64579 / 423903 / 7958	6093 / 1 / 435

Table 3.3 Crystallographic data of $[Pd_2\mathbf{L^2}_4](BF_4)_4$, $[C_{60}@Pd_2\mathbf{L^2}_3(MeCN)_2](BF_4)_4$ and $[C_{70}@Pd_2\mathbf{L^2}_4](BF_4)_2$.

Compound	$\mathbf{[Pd_2L^2_4](BF_4)_4}$	$\mathbf{[C_{60}@Pd_2L^2_3(MeCN)_2](BF_4)_4 \cdot 4MeCN}$	$\mathbf{[C_{70}@Pd_2L^2_4](BF_4)_4}$
CCDC number	1850361	1850362	---
Identification code	bc11c_sq	bc-bg8c_sq	bc19d_sav_sq
Empirical formula	$C_{160}H_{104}N_{16}O_{16}Pd_2B_4F_{16}$	$C_{192}H_{96}N_{18}O_{12}Pd_2B_4F_{16}$	$C_{246}H_{136}N_{16}O_{24}Pd_2B_4F_{16}$
Formula weight	3066.63	3406.90	4259.74
Temperature (K)	80(2)	100(2)	80(2)
Crystal system	Monoclinic	Triclinic	Monoclinic
Space group	$P2_1/n$	P-1	$P2_1/n$
a (Å)	16.884(3)	18.9931(18)	16.617(3)
b (Å)	19.386(4)	20.6975(19)	19.654(4)
c (Å)	32.974(7)	24.287(2)	31.710(6)
α (º)	90	69.678(6)	90
β (º)	103.27(3)	72.978(6)	101.53(3)
γ (º)	90	69.473(6)	90
Volume ($Å^3$)	10505(4)	8224.2(14)	10147(4)
Z	2	2	2
Density (calc.) (g/cm^3)	0.970	1.376	1.394
Absorption coefficient (mm^{-1})	0.213	2.496	0.244
F(000)	3120	3452	4344
Crystal size (mm^3)	0.220 x 0.100 x 0.005	0.300 x 0.200 x 0.100	0.100 x 0.040 x 0.020
θ range for data collection (º)	1.189 to 22.790	1.978 to 41.209	1.188 to 22.490
Reflections collected	102108	56017	98808
Observed reflections [R(int)]	15328 [0.0590]	10167 [0.1148]	14491 [0.0377]
Goodness-of-fit on F^2	1.074	1.063	1.638
R_1 [$I>2\sigma(I)$]	0.0791	0.0994	0.1174
wR_2 (all data)	0.2696	0.2675	0.3936
Largest diff. peak and hole ($e.Å^{-3}$)	1.300 and -0.710	1.282 and -0.934	0.920 and -0.788
Data / restraints / parameters	15328 / 2208 / 964	10167 / 52795 / 2738	14491 / 10841 / 1752

Table 3.4 Crystallographic data of $[Pd_2\mathbf{L^3}_4](BF_4)_4$ and $[Pd_2\mathbf{L^4}_2Cl_4]$.

Compound	$\mathbf{[Pd_2L^3_4](BF_4)_4}$	$\mathbf{[Pd_2L^2_2Cl_4]}$
CCDC number	---	---
Identification code	bc4a_sq	bc23a_sq
Empirical formula	$C_{168}H_{116}N_{20}O_{16}Pd_2B_3F_{12}$	$C_{96}H_{60}N_8O_8Pd_2Cl_4$
Formula weight	3144.03	1808.12
Temperature (K)	80(2)	80(2)
Crystal system	Tetragonal	triclinic
Space group	P4/ncc	P-1
a (Å)	18.445(3)	12.008(2)
b (Å)	18.445(3)	22.155(4)
c (Å)	51.044(10)	24.669(5)
α (º)	90	64.69(3)
β (º)	90	84.73(3)
γ (º)	90	78.34(3)
Volume ($Å^3$)	17366(6)	5810(2)
Z	4	2
Density (calc.) (g/cm^3)	1.203	1.033
Absorption coefficient (mm^{-1})	0.258	0.406
F(000)	6428	1832
Crystal size (mm^3)	0.100 x 0.080 x 0.040	0.080x 0.040 x 0.020
θ range for data collection (º)	0.773 to 20.563	0.885 to 15.359
Reflections collected	113076	18212
Observed reflections [R(int)]	4820 [0.1434]	5322 [0.1197]
Goodness-of-fit on F^2	1.052	1.632
R_1 [I>2σ(I)]	0.1306	0.1607
wR_2 (all data)	0.3537	0.4359
Largest diff. peak and hole ($e.Å^{-3}$)	1.382 and -1.000	1.617 and -0.576
Data / restraints / parameters	4820 / 1398 / 601	5322 / 2719 / 1067

3.8.6.1 Crystal structure of $[Pd_2\mathbf{L^1}_4](BF_4)_4$

Colorless needle crystals of $[Pd_2\mathbf{L^1}_4](BF_4)_4$ were grown over a period of 2 months by slow vapor diffusion of THF into a 0.64 mM CD_3CN solution of $[C_{60}@Pd_2\mathbf{L^1}_4](BF_4)_4$. A single crystal of $[Pd_2\mathbf{L^1}_4](BF_4)_4$ in mother liquor was pipetted onto a glass slide containing NVH oil. To avoid collapse of the crystal lattice, the crystal was quickly mounted onto a 0.3 mm nylon loop and immediately flash cooled in liquid nitrogen. Crystals were stored at cryogenic temperature in dry shippers, in which they were safely transported to macromolecular beamline P11 at Petra III[120], DESY, Germany.

A wavelength of λ = 0.6888 Å was chosen using a liquid N_2 cooled double crystal monochromator. Single crystal X-ray diffraction data was collected at 80(2) K on a single axis goniometer, equipped with an Oxford Cryostream 800 a Pilatus

6M. 1800 diffraction images were collected in a 360° ϕ sweep at a detector distance of 156 mm, 30% filter transmission, 0.2° step width and 0.2 seconds exposure time per image.

Stereochemical restraints for the EAP ligands (**L**[1]) were generated by the GRADE program using the GRADE Web Server (http://grade.globalphasing.org) and applied in the refinement.

Table 3.5 Definition of residues involved in $[Pd_2\mathbf{L}^1_4](BF_4)_4$.

Fragment	Residue class	Occurrence	Residue numbers
Ligand **L**[1]	EAP	2	2,3
BF_4^-	BF4	2	10,11

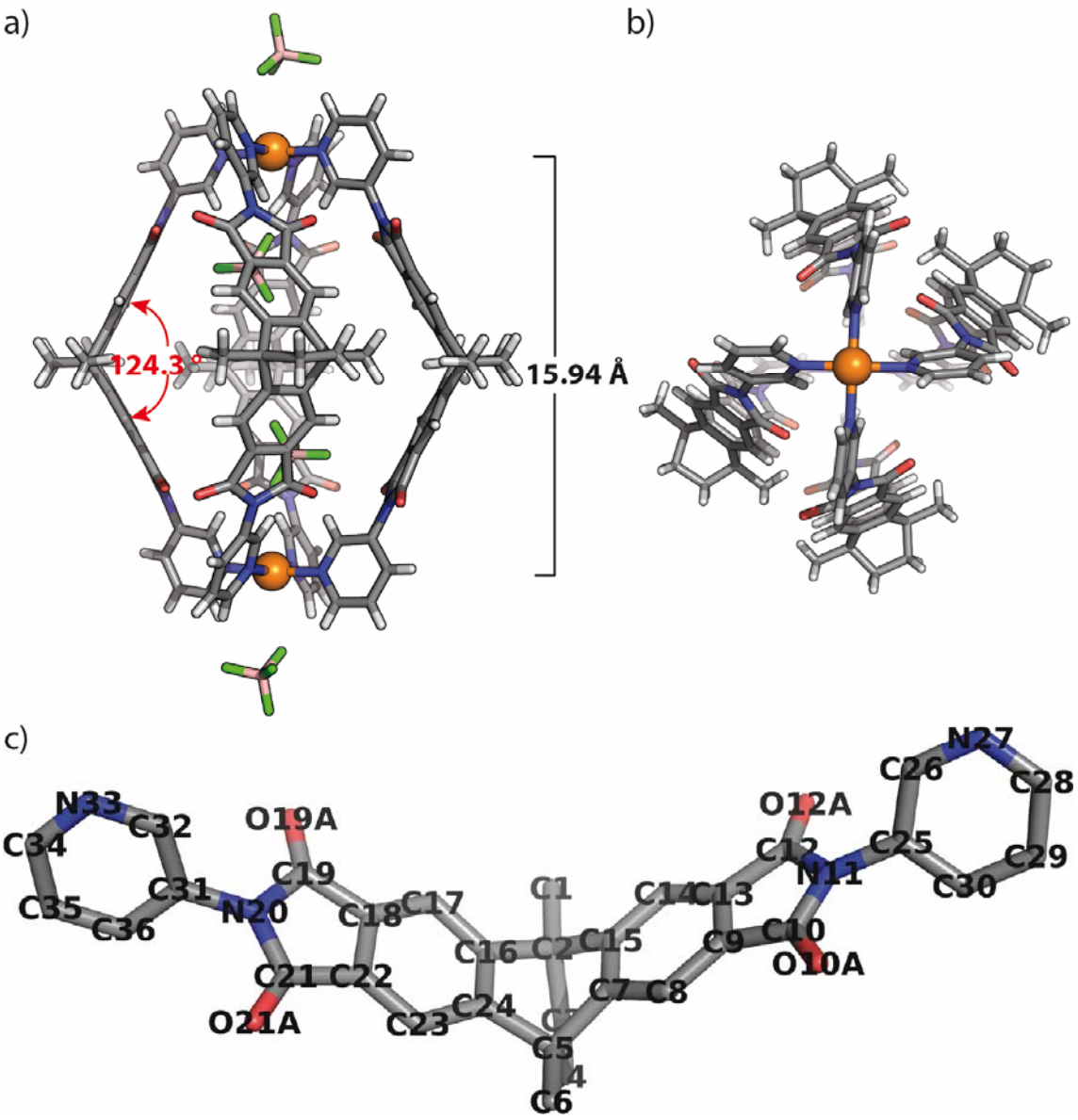

Figure 3.99 X-ray structure of $[Pd_2\mathbf{L}^1_4](BF_4)_4$: (a) The structure showing the occupation of the cavity by two BF_4^- counterions; (b) top view of the structure; (c) atomic naming scheme of ligand **L**[1] (residue class EAP). The same atom labels are used in all other **L**[1] containing structures. Color scheme: H, light grey; B, pink; C, dark grey; N, blue; O, red; F, green; Pd, orange.

Table 3.6 Structural details involved in $[Pd_2\mathbf{L^1}_4](BF_4)_4$.

Residues No.	Dihedral angle (°) between the backbone's benzene planes C16_C17_C18_C22_C23_C24 and C7_C8_C9_C13_C14_C15	Esd	Dihedral angle (°) between planes N27_Pd1_Pd2 and N33_Pd1_Pd2	Esd
2	56.060	0.158	0.715	0.162
3	55.333	0.234	1.264	0.201
Average	55.7		1.0	

3.8.6.2 Crystal structure of $[C_{60}@Pd_2\mathbf{L^1}_4](BF_4)_4$

Red plate crystals of $[C_{60}@Pd_2\mathbf{L^1}_4](BF_4)_4$ were obtained by slow vapor diffusion of isopropyl ether into a 0.64 mM CD_3CN solution of $[C_{60}@Pd_2\mathbf{L^1}_4](BF_4)_4$. A single crystal in mother liquor was pipetted onto a glass slide containing NVH oil. To avoid collapse of the crystal lattice, the crystal was quickly mounted onto a 0.2 mm nylon loop and immediately flash cooled in liquid nitrogen. Crystals were stored at cryogenic temperature in dry shippers, in which they were safely transported to macromolecular beamline P11 at Petra III[120], DESY, Germany.

A wavelength of λ = 0.6888 Å was chosen using a liquid N_2 cooled double crystal monochromator. Single crystal X-ray diffraction data was collected at 80(2) K on a single axis goniometer, equipped with an Oxford Cryostream 800 a Pilatus 6M. 1800 diffraction images were collected in a 360° ϕ sweep at a detector distance of 155 mm, 100% filter transmission, 0.2° step width and 0.1 seconds exposure time per image.

The unit cell contained three crystallographically independent cages. Stereochemical restraints for the EAP ligands ($\mathbf{L^1}$) were generated by the GRADE program using the GRADE Web Server (http://grade.globalphasing.org) and applied in the refinement. Disorder of all three C_{60} guests was modelled with two discrete positions each using the DSR program GUI and its SADI restraints for 1,2-distances and 1,3-distances for C_{60}.[122, 143]

Table 3.7 Definition of residues involved in $[C_{60}@Pd_2\mathbf{L^1}_4](BF_4)_4$.

Fragment	Residue class	Occurrence	Residue numbers
Pd^{2+}	PD	3	60,61,62
Ligand $\mathbf{L^1}$	EAP	12	1,2,3,4,5,6,7,8,9,10,11,12
C_{60}	C60	6	13,14,15,16,17,18 (Three C_{60} with disorder)
BF_4^-	BF4	7	21,22,23,24,25,26,27(One BF_4^- with disorder)

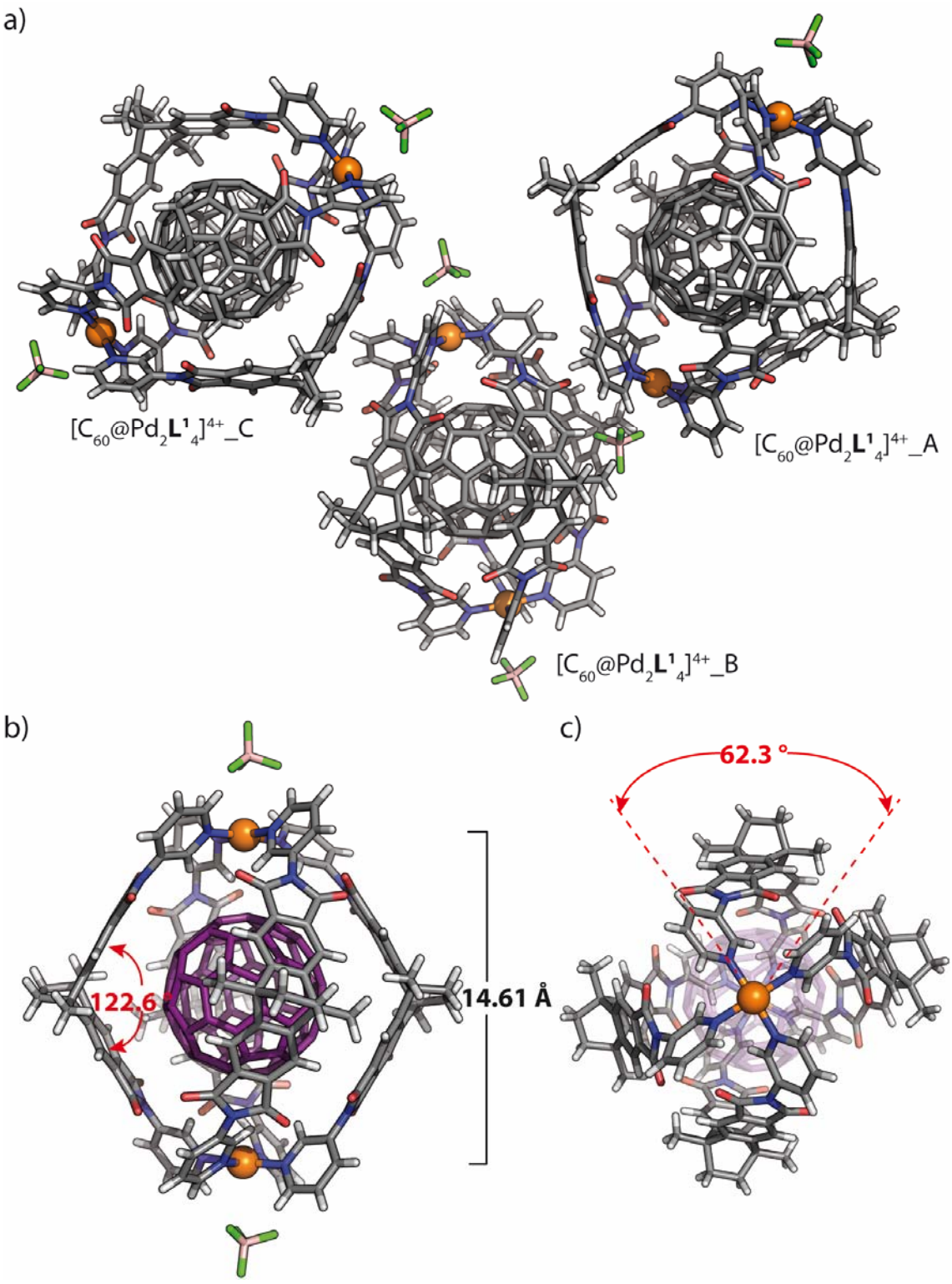

Figure 3.100 X-ray structure of $[C_{60}@Pd_2\mathbf{L^1}_4](BF_4)_4$: (a) The asymmetric unit of three crystallographically independent cages; (b) the structure of $[C_{60}@Pd_2\mathbf{L^1}_4]^{4+}$_C with the Pd–Pd distance of 14.61 Å; (c) top view of the structure of $[C_{60}@Pd_2\mathbf{L^1}_4]^{4+}$_C depicting a dihedral angle of 62.3° in between two pyridine arms of the same ligand. Color scheme: H, light grey; B, pink; C, dark grey; N, blue; O, red; F, green; Pd, orange. Minor disordered position of C_{60} guests was omitted for clarity.

Table 3.8 Structural details involved in $[C_{60}@Pd_2\mathbf{L^1}_4](BF_4)_4$.

Residues No.	Dihedral angle (°) between the backbone's benzene planes C16_C17_C18_C22_C23_C24 and C7_C8_C9_C13_C14_C15	Esd (°)	Dihedral angle (°) between planes N27_Pd1_Pd2 and N33_Pd1_Pd2	Esd (°)
1	58.798	0.174	61.443	0.244
2	56.727	0.252	61.550	0.219
3	56.932	0.219	62.943	0.24
4	56.962	0.250	63.640	0.241
Average	57.4		62.4	
5	60.993	0.239	63.990	0.254
6	59.238	0.228	64.740	0.268
7	58.638	0.292	64.570	0.244
8	57.046	0.203	61.829	0.261
Average	59.0		63.8	
9	58.207	0.282	62.001	0.133
10	59.225	0.343	62.604	0.167
11	55.518	0.273	61.422	0.139
12	56.530	0.264	63.021	0.132
Average	57.4		62.3	

Analysis of the host–guest interaction: At first, the main position of all disordered C_{60} guest (Part 1) was used to create a PDB file for further analysis in the Olex2 program.[126] The 'CENT' and 'MPLN' commands were used to create the centroid of C_{60} and the mean planes of interest situated on the ligands and fullerene surfaces. The corresponding distances in between centroids of the ligands benzene rings, hydrogen atoms, C_{60} centroids and centroids of C_{60} rings were analyzed by using the 'Distances and angles' function.

Table 3.9 Distances associated with the host–guest interaction in $[C_{60}@Pd_2\mathbf{L^1}_4](BF_4)_4$.

Residues No.	Planes	Centroid of plane to centroid of C_{60} (Å)	Centroid of plane to the five or six membered ring centroid of C_{60} (Å)	Hydrogen atoms	Hydrogen atoms to centroid of C_{60} (Å)	Shortest distance to the rings of C_{60} (Å)
1	C7_C8_C9_C13_C14_C15	6.75	3.60	H26	6.07	2.85
1	C16_C17_C18_C22_C23_C24	6.74	3.67	H32	5.96	2.76
2	C7_C8_C9_C13_C14_C15	6.71	3.88	H26	6.22	3.29
2	C16_C17_C18_C22_C23_C24	6.67	3.64	H32	6.06	2.80
3	C7_C8_C9_C13_C14_C15	6.72	3.61	H26	6.25	3.11
3	C16_C17_C18_C22_C23_C24	6.65	3.63	H32	6.04	2.86
4	C7_C8_C9_C13_C14_C15	6.69	3.75	H26	6.14	2.88
4	C16_C17_C18_C22_C23_C24	6.80	3.62	H32	6.18	3.15
5	C7_C8_C9_C13_C14_C15	6.77	3.78	H26	6.03	3.06
5	C16_C17_C18_C22_C23_C24	6.71	3.77	H32	6.01	2.81
6	C7_C8_C9_C13_C14_C15	6.72	3.79	H26	6.04	2.81
6	C16_C17_C18_C22_C23_C24	6.74	3.68	H32	6.20	3.16
7	C7_C8_C9_C13_C14_C15	6.78	3.59	H26	6.26	3.08
7	C16_C17_C18_C22_C23_C24	6.73	3.85	H32	6.13	3.23
8	C7_C8_C9_C13_C14_C15	6.73	3.78	H26	6.12	3.24
8	C16_C17_C18_C22_C23_C24	6.75	3.74	H32	6.01	2.78
9	C7_C8_C9_C13_C14_C15	6.72	3.81	H26	6.13	3.17
9	C16_C17_C18_C22_C23_C24	6.72	3.83	H32	6.10	2.91
10	C7_C8_C9_C13_C14_C15	6.72	3.84	H26	6.05	3.18
10	C16_C17_C18_C22_C23_C24	6.78	3.62	H32	6.12	2.97
11	C7_C8_C9_C13_C14_C15	6.69	3.56	H26	6.10	2.99
11	C16_C17_C18_C22_C23_C24	6.66	3.77	H32	6.12	3.24
12	C7_C8_C9_C13_C14_C15	6.65	3.69	H26	6.17	2.99
12	C16_C17_C18_C22_C23_C24	6.69	3.72	H32	6.20	3.20
Average		6.72	3.72		6.11	3.02

3.8.6.3 Crystal structure of $\mathbf{L^2}$

Colorless block crystals of $\mathbf{L^2}$ were obtained by slow evaporation of a 0.67 mM $CHCl_3$/MeCN (v/v: 1/2) solution of $\mathbf{L^2}$. A single crystal in mother liquor was mounted onto a 0.2 mm nylon loop using NVH oil. Single crystal X-ray diffraction data was collected on a Bruker D8 venture equipped with an Incoatec microfocus source (Iμs 2.0) using Cukα radiation

on a four axis κ-goniometer, equipped with an Oxford Cryostream 800 and a Photon 100 detector. The chiral space group $P2_1$ originated from chiral packing of the achiral EAQ ligand (**L²**).

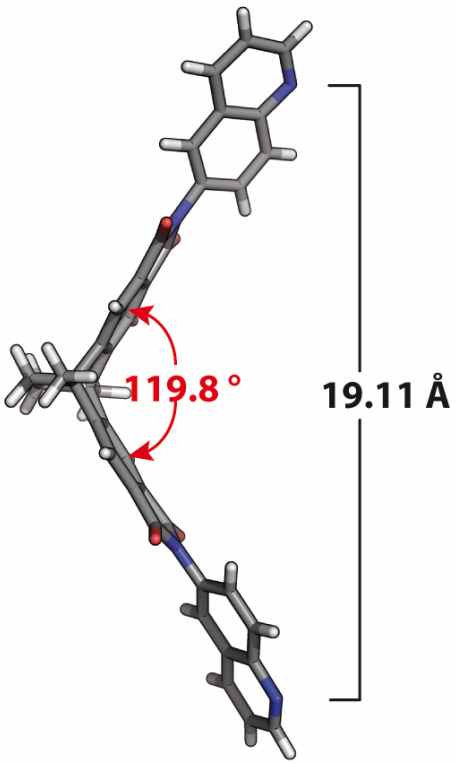

Figure 3.101 X-ray structure of **L²** with the N–N distance of 19.11 Å. Color scheme: H, light grey; C, dark grey; N, blue; O, red.

Table 3.10 Structural details involved in **L²**.

Residues No.	Dihedral angle (°) between the backbone's benzene planes C16_C17_C18_C22_C23_C24 and C7_C8_C9_C13_C14_C15	Esd (°)
-	60.2	0.1

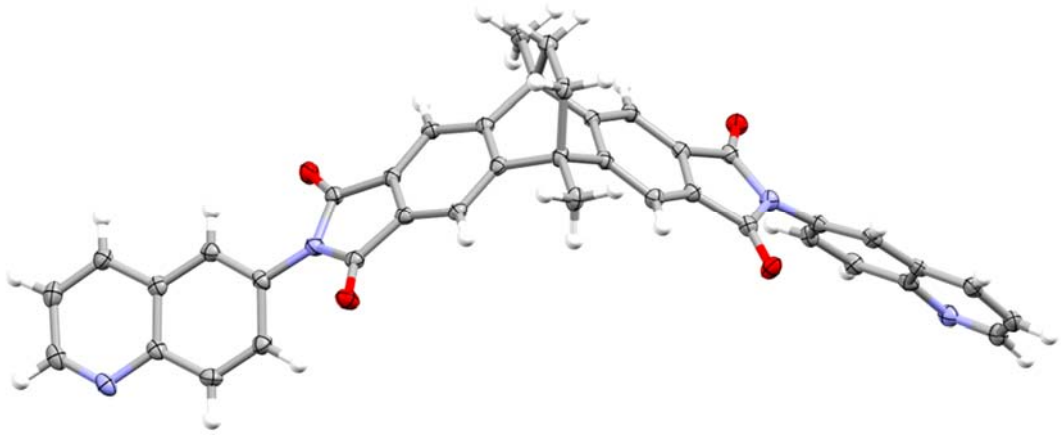

Figure 3.102 The asymmetric unit of the X-ray structure of **L²**, with all non-hydrogen atoms shown as ellipsoids at the 50% probability level. Color scheme: H, white; C, dark grey; N, pale blue; O, red.

3.8.6.4 Crystal structure of $[Pd_2L^2_4](BF_4)_4$

Colorless plate crystals of $[Pd_2\mathbf{L^2}_4](BF_4)_4$ were obtained by slow vapor diffusion of isopropyl ether into a 0.64 mM CD_3CN solution of $[Pd_2\mathbf{L^2}_3(MeCN)_2](BF_4)_4$. A single crystal in mother liquor was pipetted onto a glass slide containing NVH oil. To avoid collapse of the crystal lattice, the crystal was quickly mounted onto a 0.2 mm nylon loop and immediately flash cooled in liquid nitrogen. Crystals were stored at cryogenic temperature in dry shippers, in which they were safely transported to macromolecular beamline P11 at Petra III[120], DESY, Germany.

A wavelength of λ = 0.6888 Å was chosen using a liquid N_2 cooled double crystal monochromator. Single crystal X-ray diffraction data was collected at 80(2) K on a single axis goniometer, equipped with an Oxford Cryostream 800 a Pilatus 6M. 1800 diffraction images were collected in a 360° ϕ sweep at a detector distance of 200 mm, 100% filter transmission, 0.2° step width and 0.2 second exposure time per image.

Stereochemical restraints for the EAQ ligands (**L²**) were generated by the GRADE program using the GRADE Web Server (http://grade.globalphasing.org) and applied in the refinement.

Table 3.11 Definition of residues involved in this structure.

Fragment	Residue class	Occurrence	Residue numbers
Ligand **L²**	EAQ	2	2,3
BF_4^-	BF4	2	4,5

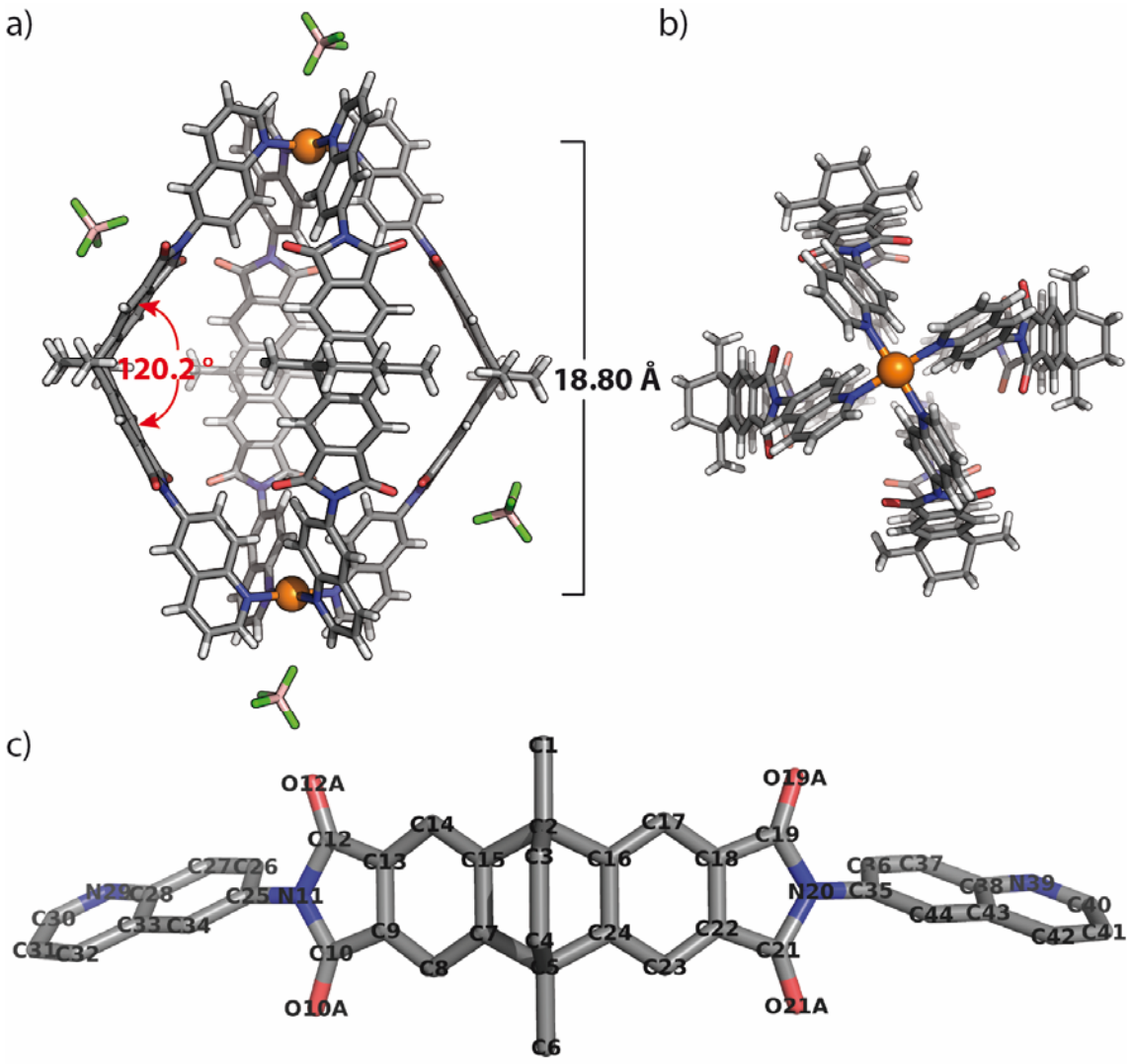

Figure 3.103 X-ray structure of $[Pd_2\mathbf{L^2}_4](BF_4)_4$: (a) The structure showing the Pd–Pd distance of 18.80 Å; (b) top view of the structure; (c) Atomic naming scheme of ligand $\mathbf{L^2}$ (residue class EAQ). The same atom labels are used in all other $\mathbf{L^2}$ containing structures. Color scheme: H, light grey; B, pink; C, dark grey; N, blue; O, red; F, green; Pd, orange.

Table 3.12 Structural details involved in $[Pd_2\mathbf{L^2}_4](BF_4)_4$.

Residues No.	Dihedral angle (°) between the backbone's benzene planes C16_C17_C18_C22_C23_C24 and C7_C8_C9_C13_C14_C15	Esd (°)	Dihedral angle (°) between planes N29_Pd1_Pd2 and N39_Pd1_Pd2	Esd (°)
2	59.298	0.229	1.711	0.255
3	60.300	0.157	0.757	0.181
Average	59.8		1.2	

3.8.6.5 Crystal structure of $[C_{60}@Pd_2L^2_3(MeCN)_2](BF_4)_4$

Pale red block crystals of $[C_{60}@Pd_2\mathbf{L^2}_3(MeCN)_2](BF_4)_4$ were obtained by slow vapor diffusion of isopropyl ether into a 0.64 mM CD_3CN solution of $[C_{60}@Pd_2\mathbf{L^2}_3(MeCN)_2](BF_4)_4$. A single crystal in mother liquor was pipetted onto a glass slide containing NVH oil. To avoid collapse of the crystal lattice, the crystal was quickly mounted onto a 0.2 mm nylon loop and immediately flash cooled in liquid nitrogen. Single crystal X-ray diffraction data was collected on a Bruker D8 venture equipped with an Incoatec microfocus source (Iμs 2.0) using Cukα radiation on a four axis κ-goniometer, equipped with an Oxford Cryostream 800 and a Photon 100 detector.

Stereochemical restraints for the EAQ ligands (**L²**) were generated by the GRADE program using the GRADE Web Server (http://grade.globalphasing.org) and applied in the refinement.

Table 3.13 Definition of residues involved in $[C_{60}@Pd_2\mathbf{L^2}_3(MeCN)_2](BF_4)_4$.

Fragment	Residue class	Occurrence	Residue numbers
Pd^{2+}		1	1
Ligand **L²**	EAQ	3	2,3,4
C_{60}	C60	2	5,6 (One C_{60} with disorder)
BF_4^-	BF4	4	7,8,9,10
MeCN	ACN	6	11,12,13,14,15,16

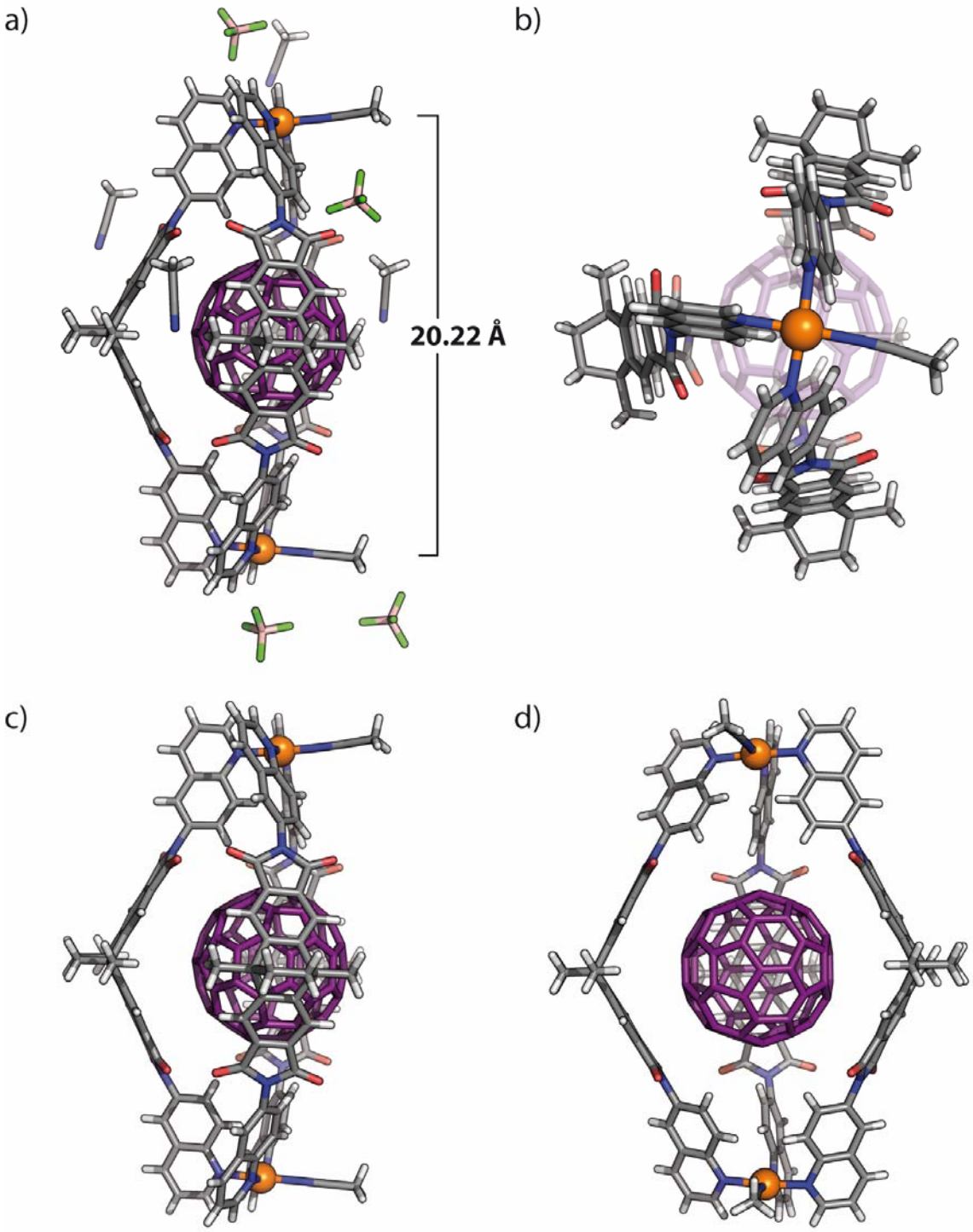

Figure 3.104 X-ray structure of $[C_{60}@Pd_2\mathbf{L^2}_3(MeCN)_2](BF_4)_4$: (a) The asymmetric unit showing the entrapped C_{60} by bowl geometry and the peripheral BF_4^- counterions and acetonitrile; (b) top view of the structure of $[C_{60}@Pd_2\mathbf{L^2}_3(MeCN)_2](BF_4)_4$; (c) and (d) two equatorial views of the structure of $[C_{60}@Pd_2\mathbf{L^2}_3(MeCN)_2](BF_4)_4$. Color scheme: H, light grey; B, pink; C, dark grey; N, blue; O, red; F, green; Pd, orange.

Table 3.14 Structural details involved in $[C_{60}@Pd_2\mathbf{L^2}_3(MeCN)_2](BF_4)_4$.

Residues No.	Dihedral angle (°) between the backbone's benzene planes C16_C17_C18_C22_C23_C24 and C7_C8_C9_C13_C14_C15	Esd (°)	Dihedral angle (°) between planes N29_Pd1_Pd2 and N39_Pd1_Pd2	Esd (°)
2	56.011	0.395	1.098	0.345
3	55.070	0.537	0.165	0.166
4	57.249	0.410	0.446	0.403
Average	56.1		0.6	

Analysis of the host–guest interaction: At first, the main position of all disordered C_{60} guest (Part 1) was used to create a PDB file for further analysis in the Olex2 program.[126] The 'CENT' and 'MPLN' commands were used to create the centroid of C_{60} and the mean planes of interest situated on the ligands and fullerene surfaces. The corresponding distances in between centroids of the ligands benzene rings, hydrogen atoms, C_{60} centroids and centroids of C_{60} rings were analyzed by using the 'Distances and angles' function.

Table 3.15 Distances associated with the host–guest interaction in $[C_{60}@Pd_2\mathbf{L^2}_3(MeCN)_2](BF_4)_4$.

Residues No.	Planes	Centroid of plane to centroid of C_{60} (Å)	Centroid of plane to the five or six membered ring centroid of C_{60} (Å)	Hydrogen atoms	Hydrogen atoms to centroid of C_{60} (Å)	Shortest distance to the rings of C_{60} (Å)
2	C7_C8_C9_C13_C14_C15	6.76	3.88	H26	6.49	3.53
2	C16_C17_C18_C22_C23_C24	6.81	3.93	H36	6.43	3.43
3	C7_C8_C9_C13_C14_C15	6.82	3.76	H26	6.16	3.00
3	C16_C17_C18_C22_C23_C24	6.80	3.74	H36	6.12	2.92
4	C7_C8_C9_C13_C14_C15	6.84	3.77	H26	6.71	3.50
4	C16_C17_C18_C22_C23_C24	6.71	3.67	H36	6.42	3.21
Average		6.79	3.79		6.39	3.27

3.8.6.6 Crystal structure of $[C_{70}@Pd_2L^2_4](BF_4)_4$

Red plate crystals of $[C_{70}@Pd_2\mathbf{L^2}_4](BF_4)_4$ were obtained by slow vapor diffusion of ethyl acetate into a 0.64 mM CD_3CN solution of $[C_{70}@Pd_2\mathbf{L^2}_3(MeCN)_2](BF_4)_4$. A single crystal in mother liquor was pipetted onto a glass slide containing NVH oil. To avoid collapse of the crystal lattice, the crystal was quickly mounted onto a 0.1 mm nylon loop and immediately flash cooled in liquid nitrogen. Crystals were stored at cryogenic temperature in dry shippers, in which they were safely transported to macromolecular beamline P11 at Petra III[120], DESY, Germany.

A wavelength of λ = 0.6888 Å was chosen using a liquid N_2 cooled double crystal monochromator. Single crystal X-ray diffraction data was collected at 80(2) K on a single axis goniometer, equipped with an Oxford Cryostream 800 a Pilatus

6M. 1800 diffraction images were collected in a 360° ϕ sweep at a detector distance of 156 mm, 30% filter transmission, 0.2° step width and 0.2 seconds exposure time per image.

C_2 symmetry center located at the center of the complex. Stereochemical restraints for the EAQ ligands (**L²**) and ethyl acetate (OAC) were generated by the GRADE program using the GRADE Web Server (http://grade.globalphasing.org) and applied in the refinement. Disorder of C_{70} guest was modelled with two discrete positions each using the DSR program GUI and its SADI restraints for 1,2-distances, 1,3-distances and planar groups for C_{70}.[122, 143]

Table 3.16 Definition of residues involved in $[C_{70}@Pd_2\mathbf{L}^2_4](BF_4)_4$.

Fragment	Residue class	Occurrence	Residue numbers
Pd^{2+}		1	1
Ligand **L²**	EAQ	2	2,3
C_{70}	C70	1	4 (One C_{70} with 50% occupation)
BF_4^-	BF4	2	5,6(disorder)
Ethyl acetate	OAC	2	8,9

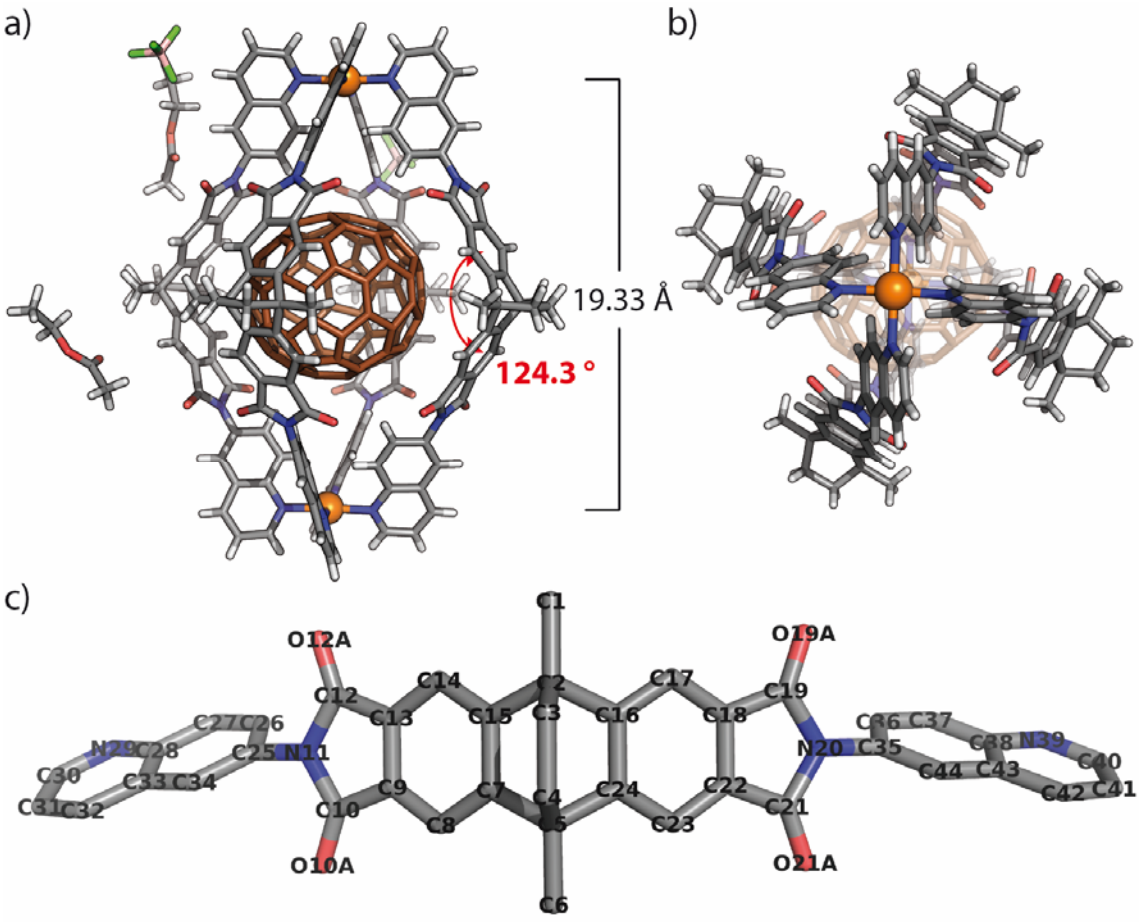

Figure 3.105 X-ray structure of $[C_{70}@Pd_2\mathbf{L}^2_4](BF_4)_4$: (a) Full structure showing the Pd–Pd distance of 19.33 Å; (b) top view; (c) atom naming scheme of ligand **L²** (residue class EAQ). The same atom labels are used in all other **L²** containing structures. Color scheme: H, light grey; B, pink; C, dark grey; N, blue; O, red; F, green; Pd, orange; C_{70}: brown.

Table 3.17 Structural details involved in $[C_{70}@Pd_2\mathbf{L^2}_4](BF_4)_4$.

Residues No.	Dihedral angle (°) between the backbone's benzene planes C16_C17_C18_C22_C23_C24 and C7_C8_C9_C13_C14_C15	Esd (°)	Dihedral angle (°) between planes N29_Pd1_Pd2 and N39_Pd1_Pd2	Esd (°)
2	55.185	0.230	0.685	0.275
3	56.143	0.321	2.065	0.358
Average	55.7		1.4	

3.8.6.7 Crystal structure of $[Pd_2\mathbf{L^3}_4](BF_4)_4$

Colorless plate crystals of $[Pd_2\mathbf{L^3}_4](BF_4)_4$ were obtained by slow vapor diffusion of methyl tert-butyl ether into a 0.64 mM CD_3CN solution of $[Pd_2\mathbf{L^3}_4](BF_4)_4$. A single crystal in mother liquor was pipetted onto a glass slide containing NVH oil. To avoid collapse of the crystal lattice, the crystal was quickly mounted onto a 0.1 mm nylon loop and immediately flash cooled in liquid nitrogen. Crystals were stored at cryogenic temperature in dry shippers, in which they were safely transported to macromolecular beamline P11 at Petra III[120], DESY, Germany.

A wavelength of λ = 0.6888 Å was chosen using a liquid N_2 cooled double crystal monochromator. Single crystal X-ray diffraction data was collected at 80(2) K on a single axis goniometer, equipped with an Oxford Cryostream 800 a Pilatus 6M. 1800 diffraction images were collected in a 360° ϕ sweep at a detector distance of 156 mm, 30% filter transmission, 0.2° step width and 0.2 seconds exposure time per image.

The occupancies of two Pd atoms and three BF_4 moieties were refined with 0.25 in the refinement owing to C_4 symmetry plane oriented along Pd–Pd axis. Stereochemical restraints for the ETQ ligands ($\mathbf{L^3}$) were generated by the GRADE program using the GRADE Web Server (http://grade.globalphasing.org) and applied in the refinement.

Table 3.18 Definition of residues involved in $[Pd_2\mathbf{L^3}_4](BF_4)_4$.

Fragment	Residue class	Occurrence	Residue numbers
Pd^{2+}	PD	1	1 (25 % occupation)
Ligand $\mathbf{L^3}$	ETQ	1	2 (25 % occupation)
BF_4^-	BF4	3	3, 4, 5 (25 % occupation)
Acetonitrile	ACN	1	6

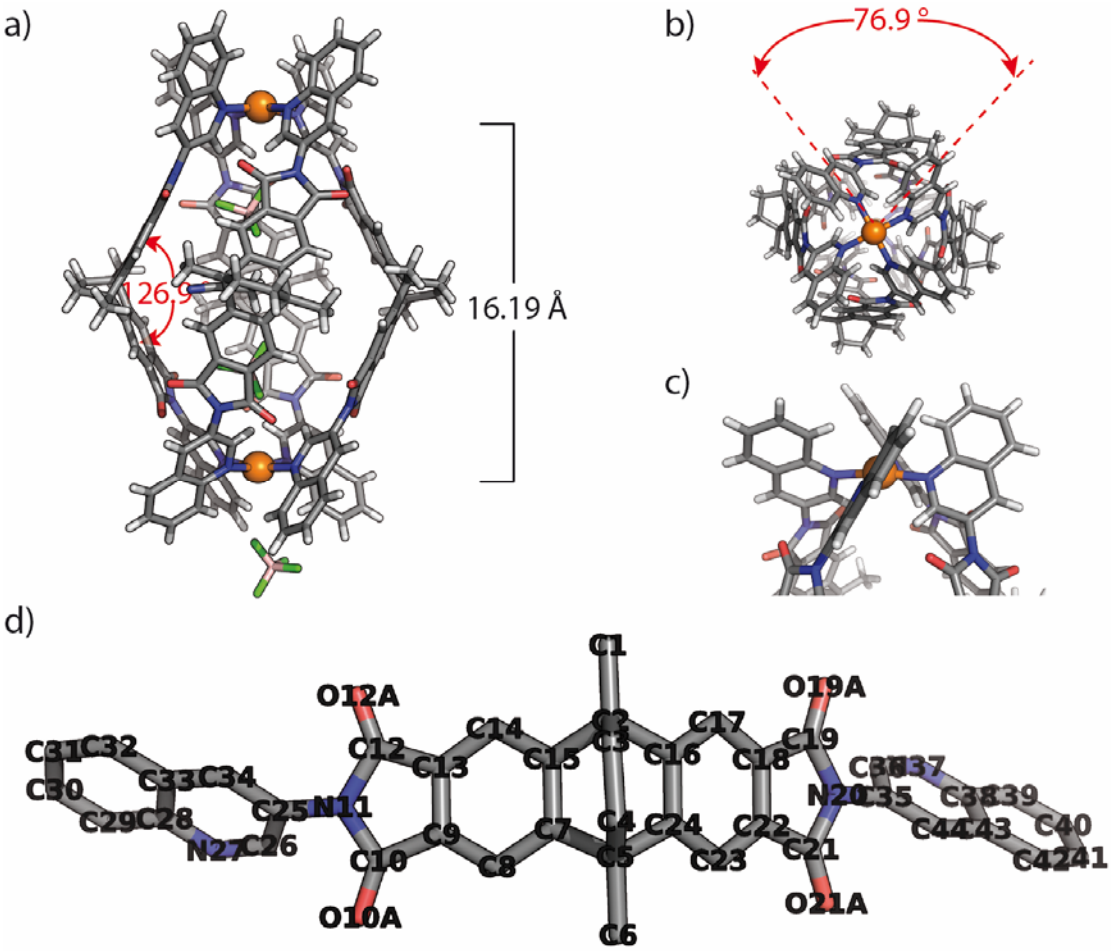

Figure 3.106 X-ray structure of $[Pd_2\mathbf{L^3}_4](BF_4)_4$: (a) Full structure showing the Pd–Pd distance of 16.19 Å; (b) top view depicting a dihedral angle of 76.9° in between two pyridine arms of the same ligand; (c) coordination center showing a highly twisted geometry due to steric hindrance from hydrogen atoms of quinoline moieties; (d) atom naming scheme of ligand $\mathbf{L^3}$ (residue class ETQ). Color scheme: H, light grey; B, pink; C, dark grey; N, blue; O, red; F, green; Pd, orange.

Table 3.19 Structural details involved in $[Pd_2\mathbf{L^3}_4](BF_4)_4$.

Residues No.	Dihedral angle (°) between the backbone's benzene planes C16_C17_C18_C22_C23_C24 and C7_C8_C9_C13_C14_C15	Esd (°)	Dihedral angle (°) between planes N27_Pd1_Pd2 and N37_Pd1_Pd2	Esd (°)
2	53.130	0.432	76.929	0.322

3.8.6.8 Crystal structure of $[Pd_2\mathbf{L^4}_2Cl_4]$

Yellow plate crystals of $[Pd_2\mathbf{L^4}_2Cl_4]$ were obtained by slow vapor diffusion of benzene into a 0.64 mM CD_3CN solution (100 µL) of $[Pd_2\mathbf{L^4}_2(MeCN)_4](BF_4)_4$ in the presence of 5 eq. of tetrabutylammonium periodate ($TBAIO_4$). A single crystal in mother liquor was pipetted onto a glass slide containing NVH oil. To avoid collapse of the crystal lattice, the crystal was quickly mounted onto a 0.1 mm nylon loop and immediately flash cooled in liquid nitrogen. Crystals were stored at cryogenic temperature in dry shippers, in which they were safely transported to macromolecular beamline P11 at Petra III[120], DESY, Germany.

A wavelength of λ = 0.6888 Å was chosen using a liquid N_2 cooled double crystal monochromator. Single crystal X-ray diffraction data was collected at 80(2) K on a single axis goniometer, equipped with an Oxford Cryostream 800 a Pilatus 6M. 1800 diffraction images were collected in a 360° ϕ sweep at a detector distance of 156 mm, 30% filter transmission, 0.2° step width and 0.2 seconds exposure time per image.

The chloride atoms were assigned crystallographically by the electron density and the average bond distances (Pd–Cl: 2.33 Å), although chloride anion does not contain in the crystallization conditions. The chloride ions, presumably, came from a contamination in $TBAIO_4$ or a decomposed product of $CHCl_3$ which was used in purification step for the ligand **L^4**. Stereochemical restraints for the EAA ligands (**L^4**) were generated by the GRADE program using the GRADE Web Server (http://grade.globalphasing.org) and applied in the refinement

Table 3.20 Definition of residues involved in [Pd_2**L^4**$_2Cl_4$].

Fragment	Residue class	Occurrence	Residue numbers
Pd^{2+}	PD	1	1
Ligand **L^4**	EAA	2	2, 3
Cl^-		1	4

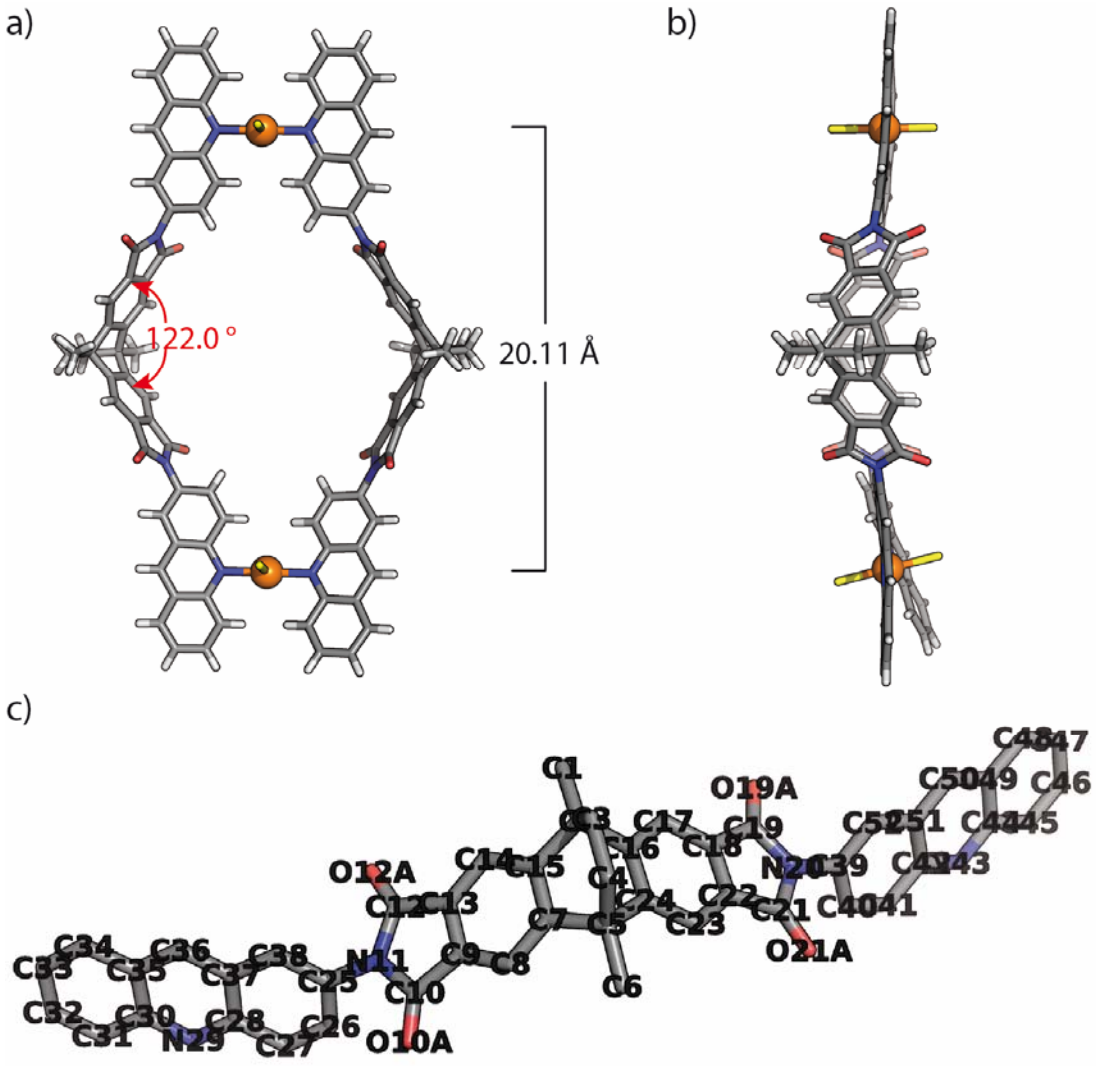

Figure 3.107 X-ray structure of $[Pd_2\mathbf{L}^4{}_2Cl_4]$: (a) Full structure showing the Pd–Pd distance of 20.11 Å; (b) equatorial view; (c) atom naming scheme of ligand $\mathbf{L}^4$ (residue class EAA). Color scheme: H, light grey; C, dark grey; N, blue; O, red; Cl, yellow; Pd, orange.

Table 3.21 Structural details involved in $[Pd_2\mathbf{L}^4{}_2Cl_4]$.

Residues No.	Dihedral angle (°) between the backbone's benzene planes C16_C17_C18_C22_C23_C24 and C7_C8_C9_C13_C14_C15	Esd (°)	Dihedral angle (°) between planes N29_Pd1_Pd2 and N43_Pd1_Pd2	Esd (°)
2	57.732	0.933	3.850	0.337
3	58.288	0.805	4.279	0.346
Average	58.0		4.1	

3.8.6.9 Calculation of the cavity volumes

Crystallographically determined structures of $[Pd_2\mathbf{L}^1{}_4]^{4+}$, $[Pd_2\mathbf{L}^2{}_4]^{4+}$, $[C_{70}@Pd_2\mathbf{L}^2{}_4]^{4+}$and $[Pd_2\mathbf{L}^3{}_4]^{4+}$ were symmetry expanded and encapsulated guest as well as BF_4^- counter ions were removed from the cavity. Resulting inner cavities were calculated with VOIDOO[127] using a primary grid and plot grid spacing of 0.1 Å and 10 cycles of volume refinement

with the size probe radius of 3.2 Å, the minimum radius such that it would not exit the cavity of the structures. Molecular visualization was done using PyMol.[128]

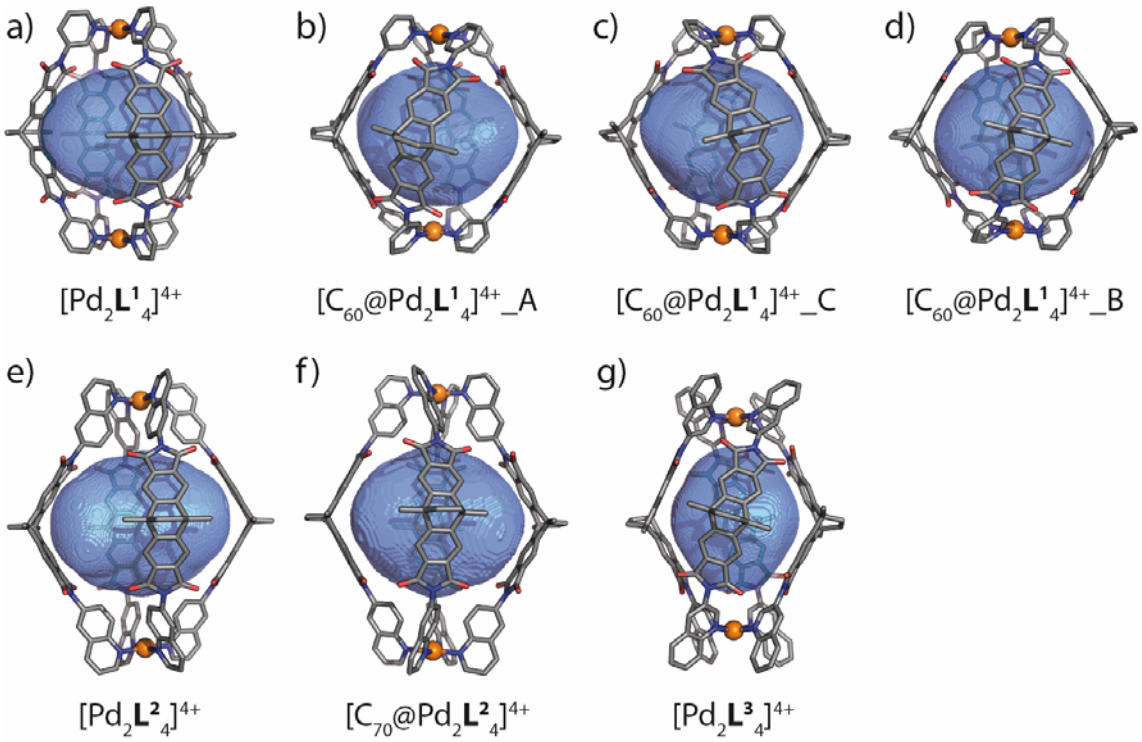

Figure 3.108 The VOIDOO-calculated void space as shown (blue mesh) within the corresponding crystal structures for (a) cage $[Pd_2\mathbf{L^1}_4]^{4+}$ (572 Å^3); (b) cage $[C_{60}@Pd_2\mathbf{L^1}_4]^{4+}$_A (792 Å^3); (c) cage $[C_{60}@Pd_2\mathbf{L^1}_4]^{4+}$_C (780 Å^3); (d) cage $[C_{60}@Pd_2\mathbf{L^1}_4]^{4+}$_B (769 Å^3); (e) cage $[Pd_2\mathbf{L^2}_4]^{4+}$ (1099 Å^3); (f) cage $[C_{70}@Pd_2\mathbf{L^2}_4]^{4+}$ (995 Å^3) and (g) cage $[Pd_2\mathbf{L^3}_4]^{4+}$ (518 Å^3). Color scheme: C, dark grey; N, blue; O, red; Pd, orange.

3.8.6.10 Comparison of photos of $[Pd_2L^1_4](BF_4)_4$ and $[C_{60}@Pd_2L^1_4](BF_4)_4$ crystals

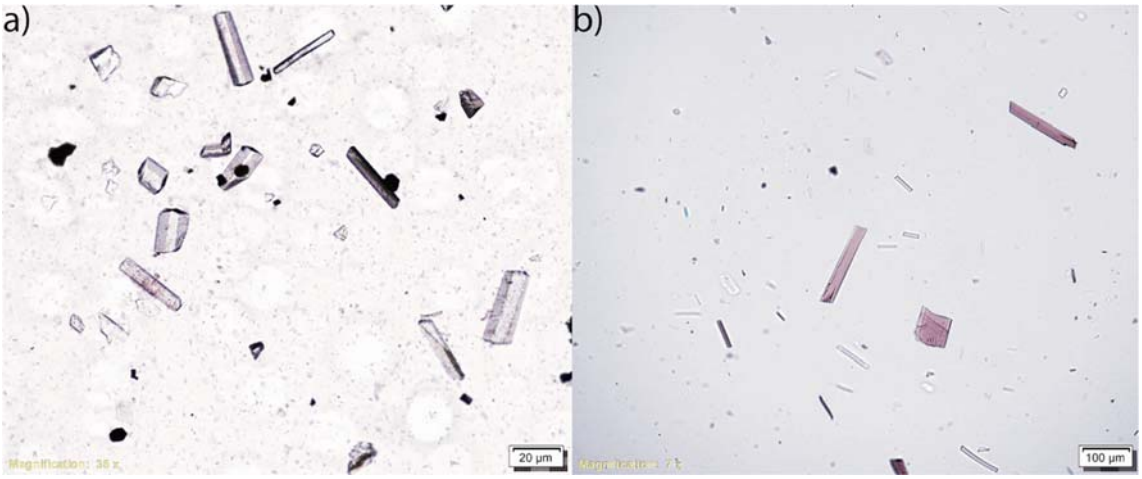

Figure 3.109 Comparison of crystals of $[Pd_2\mathbf{L^1}_4](BF_4)_4$ and $[C_{60}@Pd_2\mathbf{L^1}_4](BF_4)_4$: (a) Colourless block crystals of $[Pd_2\mathbf{L^1}_4](BF_4)_4$ (Magnification: 35X); (b) red thin plate crystals of $[C_{60}@Pd_2\mathbf{L^1}_4](BF_4)_4$ (Magnification: 7X).

3.8.7 Computational studies

All models shown below were constructed using Wavefunction SPARTAN '14[129] and first optimized on semiempiric PM6 level of theory without constraints. The resulting structures were then further refined by DFT structure optimization (B3LYP/C, H, N, O = 6-31g(d)/Pd LANL2DZ) using GAUSSIAN 09.[130]

3.8.7.1 Design of a suitable backbone for the coordination cage as fullerene receptor

Distances within the individually optimized fragments shown in Figure 3.110 c) and d) refer to the same carbon atom position in the final cage-based receptor and the center of C_{60} and the Pd position, respectively, thus indicating that coordinative tethering of four backbones, equipped with *meta*-pyridyl donors, to square-planar Pd(II) should create a C_4-symmetric hollow structure perfectly dimensioned to encapsulate one Buckminster fullerene.

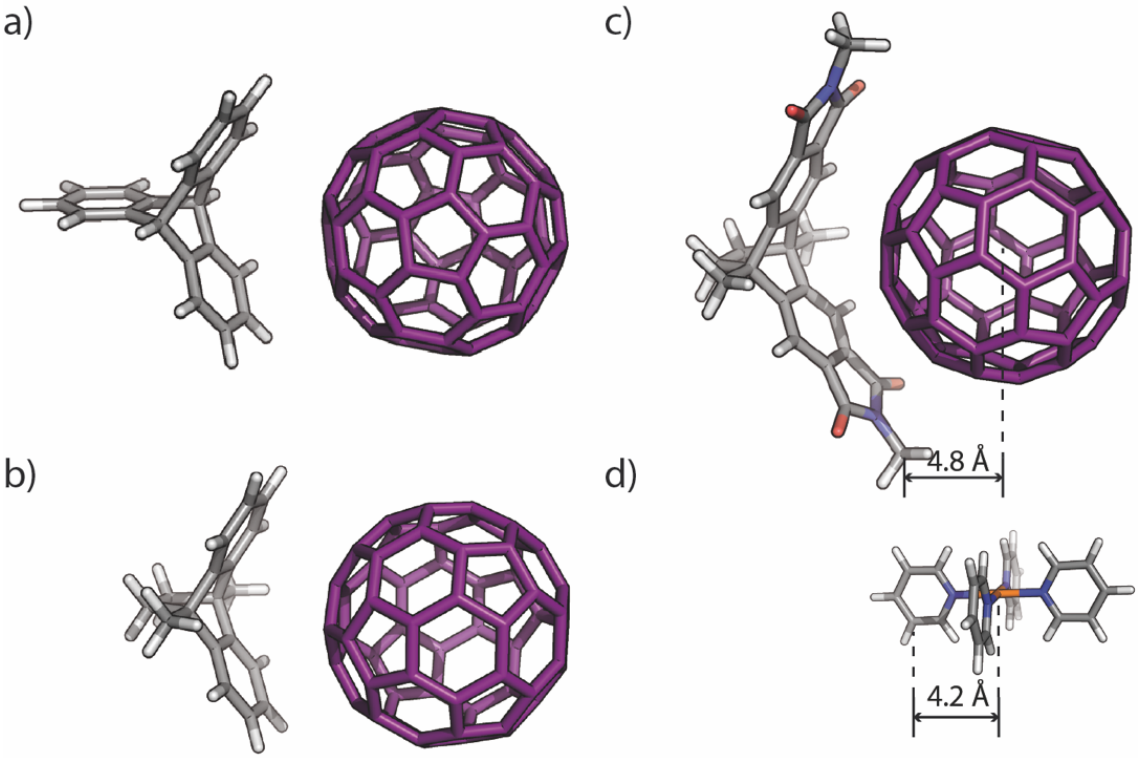

Figure 3.110 DFT optimized structures supporting the host design process.

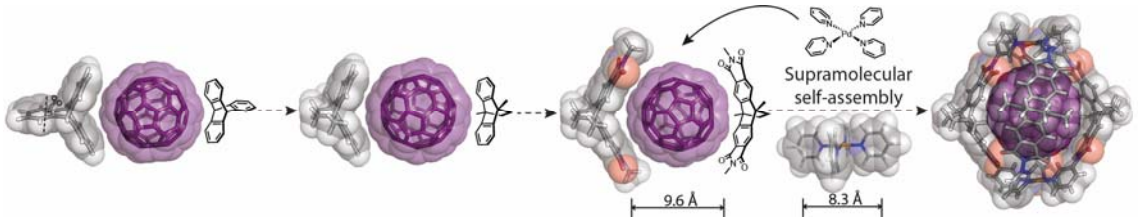

Figure 3.111 Design of a self-assembled, minimal-size metallo-supramolecular fullerene receptor.

3.8.7.2 DFT calculation of the energy change during the conversion from $[Pd_2L^2_3(MeCN)_2]^{4+}$ to $[Pd_2L^2_4]^{4+}$

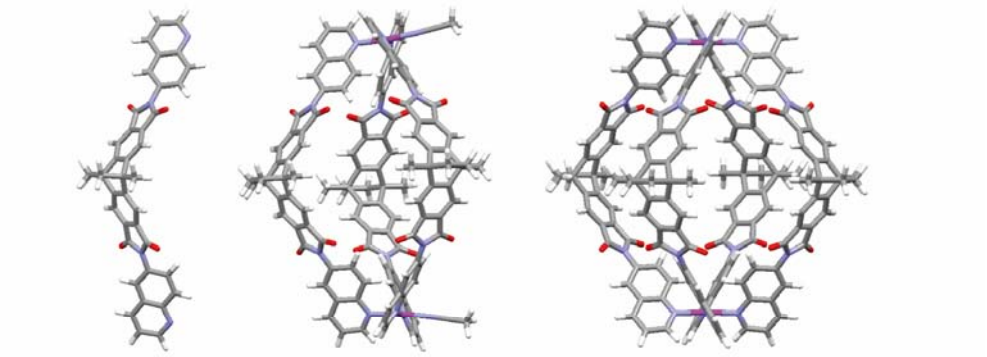

$L^2 + [Pd_2L^2_3(MeCN)_2]^{4+} \rightleftharpoons [Pd_2L^2_4]^{4+} + 2MeCN$

E_{RB3LYP}: -2059.93040025 Ha -6697.78549048 Ha -8492.20342453 Ha -265.50985584 Ha

$\Sigma_{reactants}$: -22993383.07111160 KJ/mol $E_{products}$: -22993376.21760090 KJ/mol

$$E_{products} - \Sigma_{reactants} = 6.9 \text{ KJ/mol}$$

Figure 3.112 Scheme showing the optimized DFT structures of L^2, $[Pd_2L^2_3(MeCN)_2]^{4+}$ and $[Pd_2L^2_4]^{4+}$. Calculated energies obtained from the geometry optimized structures are given below. The computed energy difference for the formation of $[Pd_2L^2_4]^{4+}$ from L^2 and $[Pd_2L^2_3(MeCN)_2]^{4+}$ is positive and supports the experimental finding.

3.8.7.3 DFT calculation of the energy change during the conversion from $[Pd_2L^3_3(MeCN)_2]^{4+}$ to $[Pd_2L^3_4]^{4+}$

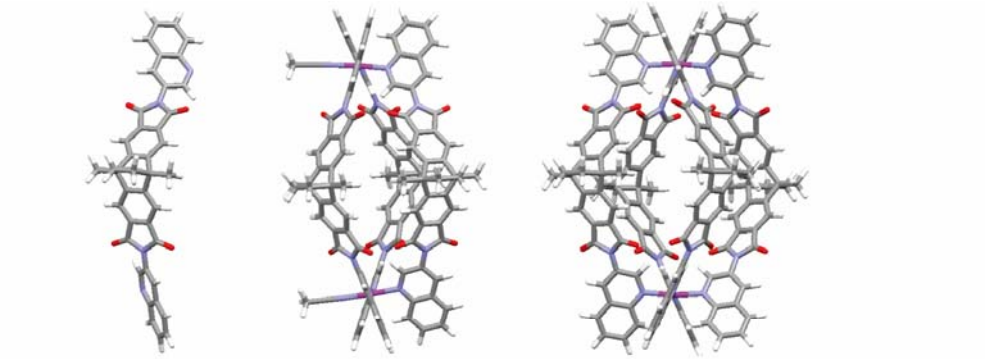

$L^3 + [Pd_2L^3_3(MeCN)_2]^{4+} \rightleftharpoons [Pd_2L^3_4]^{4+} + 2MeCN$

E_{RB3LYP}: -2059.92916787 Ha -6697.79522177 Ha -8492.22184496 Ha -265.50985584 Ha

$\Sigma_{reactants}$: -22993405.38499980 KJ/mol $E_{products}$: -22993424.58043990 KJ/mol

$$E_{products} - \Sigma_{reactants} = -19.2 \text{ KJ/mol}$$

Figure 3.113 Scheme showing the optimized DFT structures of L^3, $[Pd_2L^3_3(MeCN)_2]^{4+}$ and $[Pd_2L^3_4]^{4+}$. Calculated energies obtained from the geometry optimized structures are given below. The energy difference for the formation of $[Pd_2L^3_4]^{4+}$ from L^3 and $[Pd_2L^3_3(MeCN)_2]^{4+}$ is negative and supports the experimental finding.

3.8.7.4 Comparison of the DFT minimized energies of *cis*-$[Pd_2L^4{}_2(MeCN)_4]^{4+}$ and *trans*-$[Pd_2L^4{}_2(MeCN)_4]^{4+}$

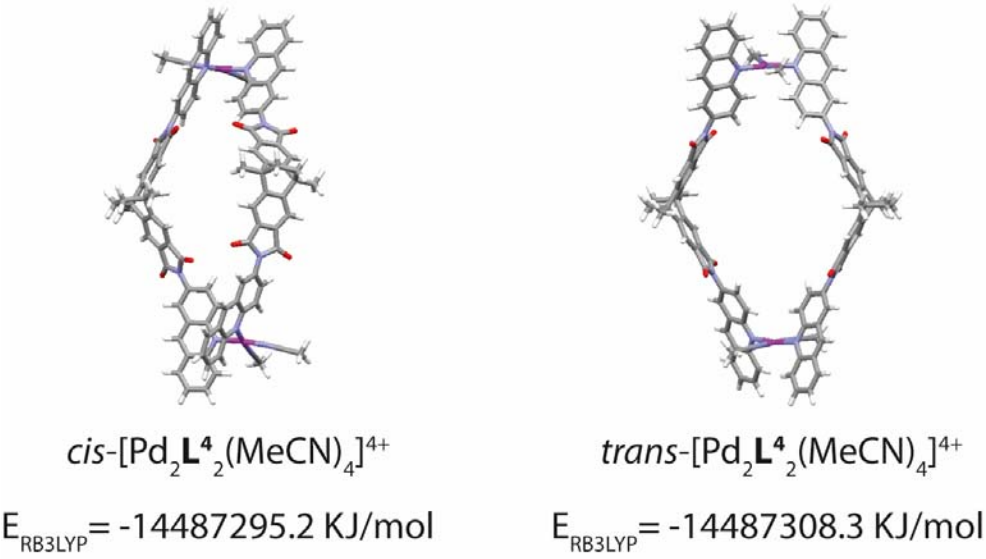

Figure 3.114 DFT energy minimized structures of tentative *cis*-$[Pd_2\mathbf{L^4}_2(MeCN)_4]^{4+}$ and observed *trans*-$[Pd_2\mathbf{L^4}_2(MeCN)_4]^{4+}$. According to the computed energies, *trans*-$[Pd_2\mathbf{L^4}_2(MeCN)_4]^{4+}$ is 13.1 kJ/mol lower in energy.

4 Applications in fullerene chemistry

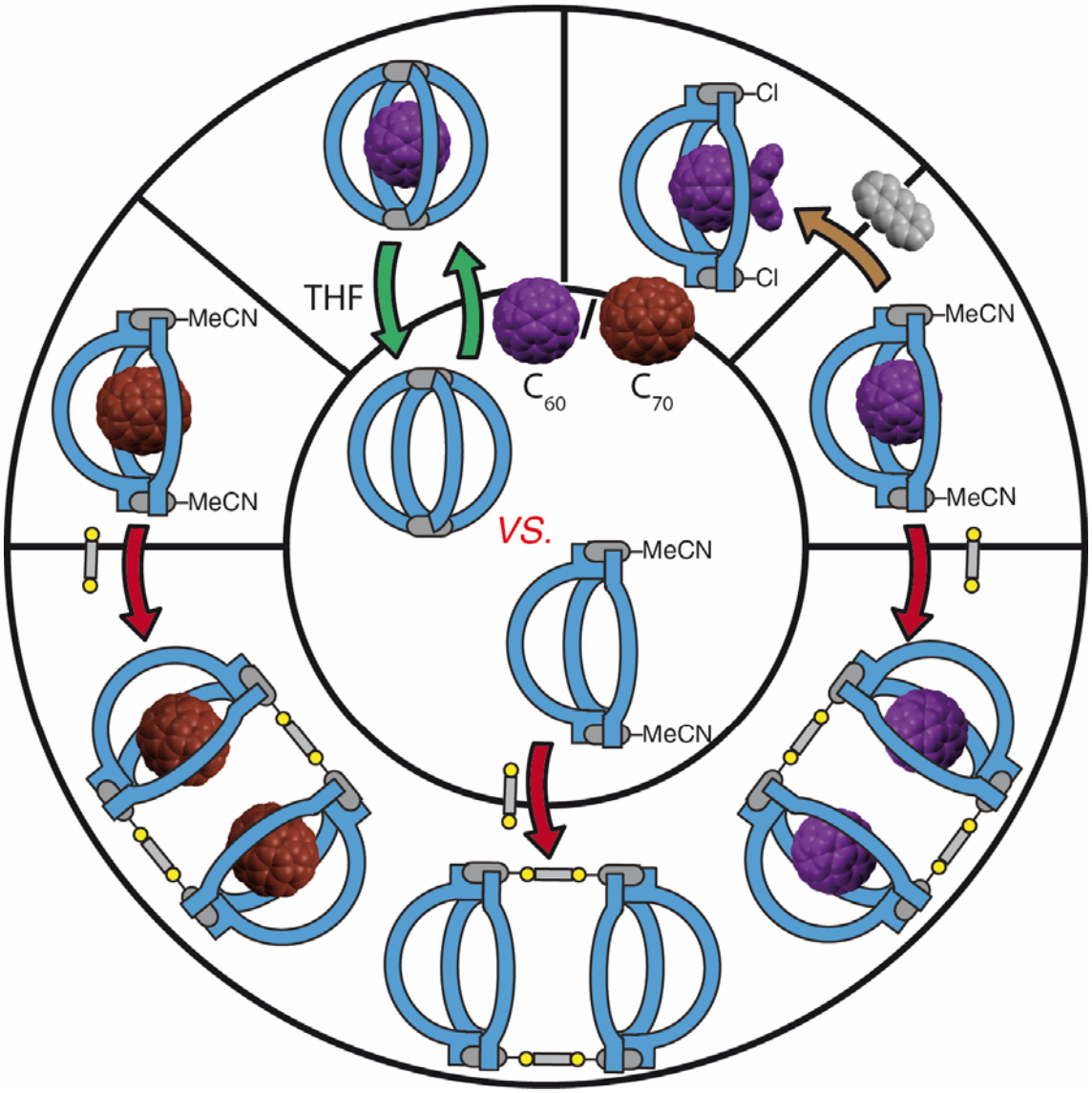

4.1 Introduction

The methodology of solution-phase fullerene handling has raised considerable attention in the last decade, especially for chemical derivatization, surface deposition as well as device fabrication, but is still limited by the scarcity of appropriate solvents owing to the extended π-conjugated structures of fullerenes and their derivatives. Therefore, expanding the fullerene solubility in other solvents, thus substituting for the generally used aromatic and halogenated solvents, can to a certain degree facilitate the further processing of fullerenes with more choices of solvents.

In addition, the tedious purification of fullerenes leads to the high price of pure fullerene compounds in commercial market, which certainly hampers their wide-ranging applications. In recent years, supramolecular chemists have devoted to constructing diverse fullerene receptors, aiming at realizing the fullerene purification at a relatively low cost or in a more environment-friendly way.[144] For this purpose, the prerequisite for promising candidates is that they should be able to exclusively bind one particular fullerene compound from the mixture, as presented in the proven systems for effective separation of C_{60},[59, 61, 77] C_{70}[28-30, 68, 78, 145-149] and other fullerene compounds.[73-74] On the other hand, the controllable release of the entrapped fullerene compounds from the host cavity is also required for the sake of collecting the isolated fullerene compounds and reusing the host for multiple turns. Undoubtedly, build-up of one cyclic purification system satisfying these two requirements is still a challenging project and has been rarely reported.[59]

Inspired by the known functionalities of fullerene derivatives in materials science, chemists turned out attention to achieve efficient protocols for the chemical manipulation of fullerenes. The spherical shape of fullerenes covered with reactive double bonds, determines the poor regioselectivity of chemical reactions on fullerenes, for instance, Diels-Alder reaction. The bowl-shaped structure presented herein can act as a protecting group, thus allowing for the exclusive formation of mono-adduct between C_{60} and anthracene.

Furthermore, one tetrahedral supramolecular cage was published recently with the abilities to bind up to four C_{60} molecules inside the cavity,[65] motivating us to explore fullerene binders able to entrap more than one fullerenes. By means of the strategy of hierarchical assembly, the heteroleptic pill-shaped geometry is constructed and can accommodate two fullerene molecules within the inner cavity concurrently.

4.2 Expanding fullerene solubility

In order to investigate the solubility and stability of cage $[Pd_2\mathbf{L^1}_4](BF_4)_4$ and its C_{60}-containing cage $[C_{60}@Pd_2\mathbf{L^1}_4](BF_4)_4$ in a wider range of organic solvents, the initial acetonitrile solution of cage species was added to NMR tubes, and acetonitrile was evaporated in vacuum, followed by adding different deuterated solvents. Comparison of cage species with ligand in different solvents, allowed us to gain in-depth insight on the possibly suitable solvent systems, thus expanding the scope of solvents for fullerenes.

Given the experimental conclusion deduced from the NMR spectra, nine different solvents can be divided into the following different kinds: (a) in nitromethane (Figure 4.4) and acetone (Figure 4.5), the host as well as host-guest compounds are soluble and stable; (b) the host complex is stable in DMF (Figure 4.6) and DMSO (Figure 4.7), whilst the host-guest complex undergoes partial conversion to the host complex within one day; (c) surprisingly, dichloromethane can induce the transformation from C_{60}-occupied cage to guest-free $[Pd_2\mathbf{L^1}_4](BF_4)_4$ cage after standing one day (Figure 4.8); (d) decomposition of host molecules occurs in chloroform to give unknown species (Figure 4.9), whereas the ligand itself is even labile in methanol, thus undermining the host and host-guest complexes (Figure 4.10); (e) all the cage compounds have extremely poor solubilities in tetrahydrofuran (Figure 4.11) and benzene (Figure 4.12). In conclusion, other solvents, such as acetone, nitromethane and DMF, can be used to dissolve fullerene-containing host-guest complexes.

4.3 Recycling fullerene separation

As a surprising result, crystals of the cage $[Pd_2\mathbf{L^1}_4](BF_4)_4$ were obtained by diffusing THF into a MeCN solution of $[C_{60}@Pd_2\mathbf{L^1}_4](BF_4)_4$. This was inferred to a situation in which the guest escape from the host cavity was presumably triggered by solvent effects. The corresponding test experiments in solution were performed by means of NMR spectroscopy to judge whether the guest liberation happened or not under different ratios of THF and MeCN. Accordingly, to the blue-violet MeCN solution of $[C_{60}@Pd_2\mathbf{L^1}_4]^{4+}$, increasing amounts of d_8-THF were added to prepare a series of mixed solution in the particular CD_3CN/d_8-THF ratios (from 1:1 to 1:5) with the same concentration of cage species (Table 4.1). ^{1}H NMR monitoring showed that the gradually reduced intensity of proton signals for $[C_{60}@Pd_2\mathbf{L^1}_4]^{4+}$ was accompanied by the increasing intensity of proton signals for $[Pd_2\mathbf{L^1}_4]^{4+}$ (Figure 4.15). Also, different amounts of black precipitate were clearly observed in the bottom of these NMR tubes after standing overnight (Figure 4.16). Solids were collected via centrifugation, washed with pure MeCN and dried in vacuum. The ^{13}C NMR spectrum of the isolated solid showed one single peak of C_{60} at 142.8 ppm in deuterated *o*-dichlorobenzene, showcasing the high purity of separated fullerene compounds compared to raw fullerene soot (Figure 4.1c).

Considering that the cage $[Pd_2\mathbf{L^1}_4]^{4+}$ was able to selectively bind C_{60} from the commercially available fullerene soot (Figure 4.13) and the guest could be liberated via the change of the solvent system, this system was recognized to provide a practical solution for the fullerene purification. Indeed, the cyclic purification experiment based on this system was carried out at a milligram scale, as confirmed by ^{1}H NMR spectra of these states in the following procedures (Figure 4.1a and b). Firstly, the pristine cage $[Pd_2\mathbf{L^1}_4]^{4+}$ solution encapsulated C_{60} from the fullerene soot under heating, giving rise to a blue-violent solution of $[C_{60}@Pd_2\mathbf{L^1}_4]^{4+}$ after the filtration of leftover fullerene compounds. Secondly, a five-fold amount of d_8-THF was added to this CD_3CN solution, giving a nearly colorless solution with the black solid in the bottom after precipitating overnight. Thirdly, a CD_3CN solution of the recycled host from the supernatant was obtained via evaporation of the initial mixed solvents and the subsequent addition of CD_3CN. Finally, the recycled $[Pd_2\mathbf{L^1}_4]^{4+}$ was confirmed to possess the ability to selectively bind C_{60} in the second cycle.

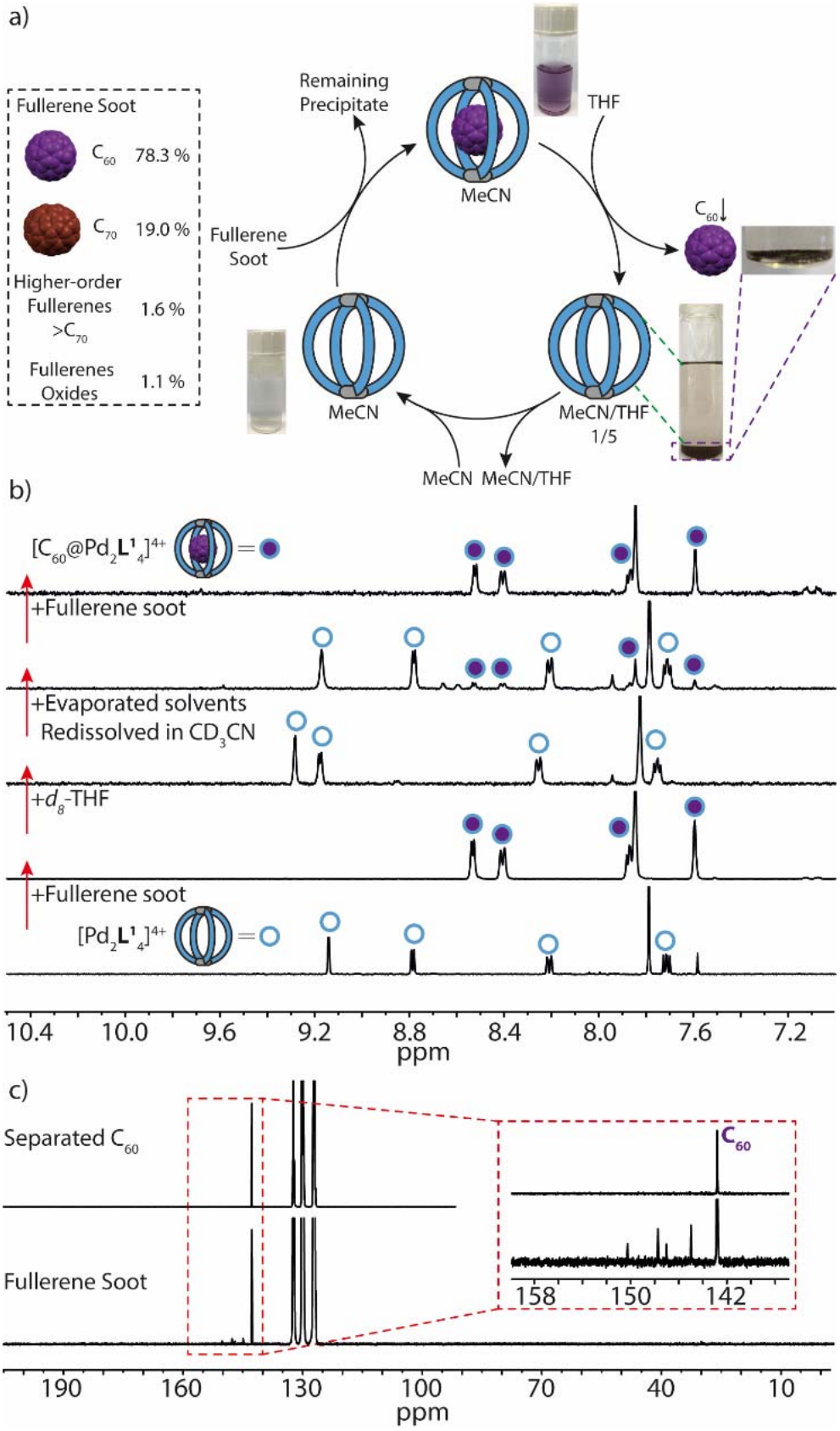

Figure 4.1 Fullerene purification using a recyclable $[Pd_2\mathbf{L^1}_4]^{4+}$ system: (a) Schematic overview; (b) ^{1}H NMR spectra (500 MHz, 298 K) of five different states during the separation process. From bottom to top: initial CD_3CN solution of $[Pd_2\mathbf{L^1}_4]^{4+}$, $[C_{60}@Pd_2\mathbf{L^1}_4]^{4+}$ after encapsulation of C_{60} from soot, CD_3CN:d_8-THF (v/v = 1:5) solution of $[Pd_2\mathbf{L^1}_4]^{4+}$ after precipitation of C_{60}, recycled $[Pd_2\mathbf{L^1}_4]^{4+}$ in CD_3CN, $[C_{60}@Pd_2\mathbf{L^1}_4]^{4+}$ obtained in second purification round; (c) ^{13}C NMR spectra (151 MHz, 298 K, d_4-o-dichlorobenzene) of the separated C_{60} and original fullerene soot.

4.4 Mono-functionalization of fullerene

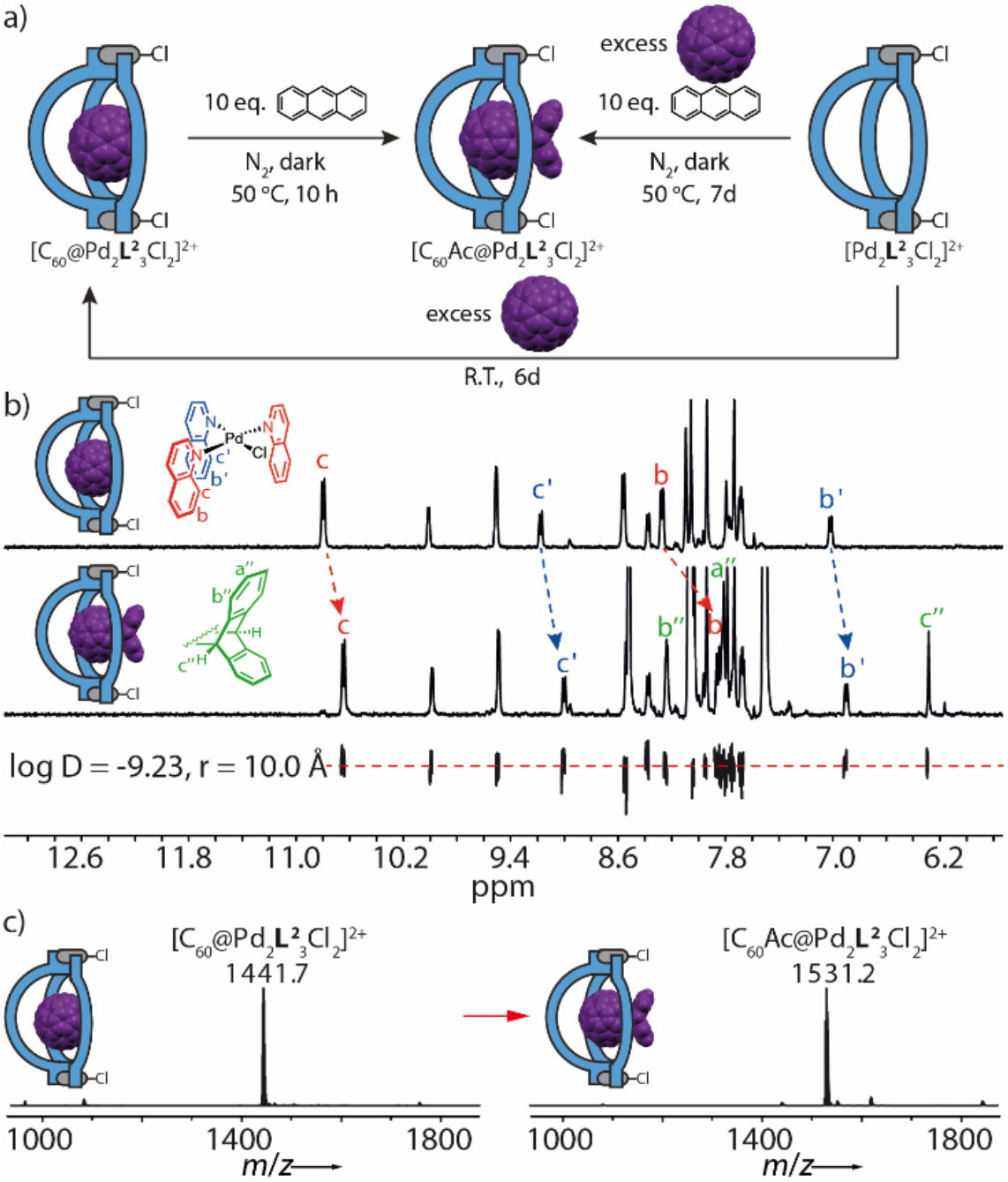

Figure 4.2 Bowl-protected Diels-Alder reaction between encapsulated C_{60} and anthracene: (a) Stepwise or one-pot access to the encapsulated mono-adduct; (b) comparison of ^{1}H NMR spectra (298 K, CD_3CN) of $[C_{60}@Pd_2\mathbf{L^2}_3Cl_2]^{2+}$ (0.56 mM) and $[C_{60}Ac@Pd_2\mathbf{L^2}_3Cl_2]^{2+}$ (0.36 mM), DOSY trace showing all aromatic signals of $[C_{60}Ac@Pd_2\mathbf{L^2}_3Cl_2]^{2+}$ having the same diffusion coefficient; (c) ESI high resolution mass spectra of $[C_{60}@Pd_2\mathbf{L^2}_3Cl_2]^{2+}$ and $[C_{60}Ac@Pd_2\mathbf{L^2}_3Cl_2]^{2+}$.

Inspired by the crystal structure of bowl $[C_{60}@Pd_2\mathbf{L^2}_3(MeCN)_2](BF_4)_4$ showing that approximately 75% of the C_{60} surface was wrapped by the exterior bowl-shaped structure, we hypothesized that the selectivity of Diels-Alder reaction between the encapsulated C_{60} and anthracene could be modulated via this protection mechanism. For this kind of

reaction, solvents with a good solubility towards C_{60}, such as benzene and carbon disulfide, were normally required to be used, ending with mixed products of mono-, di- or even tri-adducts, which were difficult to be separated.[150-151] Recently, the same reaction has been performed within a cubic cavity formed by porphyrin panels, exclusively yielding the bis-adduct.[70, 152] Herein, the bowl $[C_{60}@Pd_2\mathbf{L^2}_3Cl_2]^{2+}$ featuring chloride instead of acetonitrile ligands was selected to react with anthracene on account of the more facile reaction monitoring through mass spectrometry. Eventually, the reaction of an acetonitrile solution of $[C_{60}@Pd_2\mathbf{L^2}_3Cl_2]^{2+}$ (0.56 mM, 1 eq.) with 10 eq. of anthracene was carried out at 50 ^oC for ca. 12 h in the dark under N_2 atmosphere to exclusively form the mono-adduct-occupied bowl $[C_{60}Ac@Pd_2\mathbf{L^2}_3Cl_2]^{2+}$ (Figure 4.26) (equilibrium constant K_{323} = 2210 M^{-1}, Table 4.2).

The formation of mono-adduct within the bowl geometry was unambiguously confirmed by NMR spectroscopy, mass spectrometry as well as single crystal X-ray structural analysis. ^1H NMR spectra suggested signals of proton H_b, $H_{b'}$, H_c, $H_{c'}$ close to the inner cavity underwent slightly up-field shifts. And all the proton signals of the bowl and fullerene mono-adduct shew the same diffusion coefficient in the DOSY spectrum, thus determining the hydrodynamic radius of $[C_{60}Ac@Pd_2\mathbf{L^2}_3Cl_2]^{2+}$ (ca. 10.0 Å) (Figure 4.2b). More convincingly, the ESI mass spectrum revealed the isotopic pattern of a single peak at m/z=1531.2 was in agreement with the formula of the anticipated $[C_{60}Ac@Pd_2\mathbf{L^2}_3Cl_2]^{2+}$ ion (Figure 4.2c and Figure 4.21). Furthermore, single crystals of $[C_{60}Ac@Pd_2\mathbf{L^2}_3Cl_2](BF_4)_2$ were obtained from the fast vapor diffusion of THF into a CD_3CN solution of this cage species, hence giving the first crystallographically observed structure of C_{60}-anthracene mono-adduct, which is usually sensitive to light and oxygen in solution. As clearly observed in the crystal structure, the steric effect hampers the reaction of the entrapped mono-adduct with extra anthracene molecules (Figure 4.30). In contrast to other aforementioned crystal structures of host-guest complexes with disordered C_{60} inside, the encapsulated $C_{60}Ac$ here shows only one co-conformer, but it is rather tilted to one side of the bowl geometry, which is presumably stabilized by the relatively short CH–O contact (2.2 Å) between one of the guest's bridgehead proton and a ligand oxygen. Considering no signal splitting of guest protons in solution, the mono-adduct guest is recognized to rotate freely within the bowl structure in a dynamic manner, like a ball-and-socket joint.

4.5 Dimerization of bowls

The crystal structures of bowl $[C_{60}@Pd_2\mathbf{L^2}_3(MeCN)_2]^{4+}$ and $[C_{60}Ac@Pd_2\mathbf{L^2}_3Cl_2]^{2+}$ suggested that this type of bowl assemblies carrying acetonitrile ligands in Pd^{II}-mediated coordination centers, could be decorated with stronger electron-donating ligands, such as chloride anions. Considering this, the question arose whether a bridging ligand with sterically low-demand and relatively strong electron donating abilities can join two bowls together to form a pill-shaped geometry. Indeed, this assumption was verified by the successful dimerization of two bowls with two terephthalate bridges (Figure 4.3a), similar to the proven strategy of hierarchical assembly involving nitrogen donor and carboxylate ligands.[153-154] Dimerization of monomeric bowls was clearly demonstrated by NMR and MS analyses, forming the guest-free dimer as well as C_{60}- and C_{70}-occupied dimers.

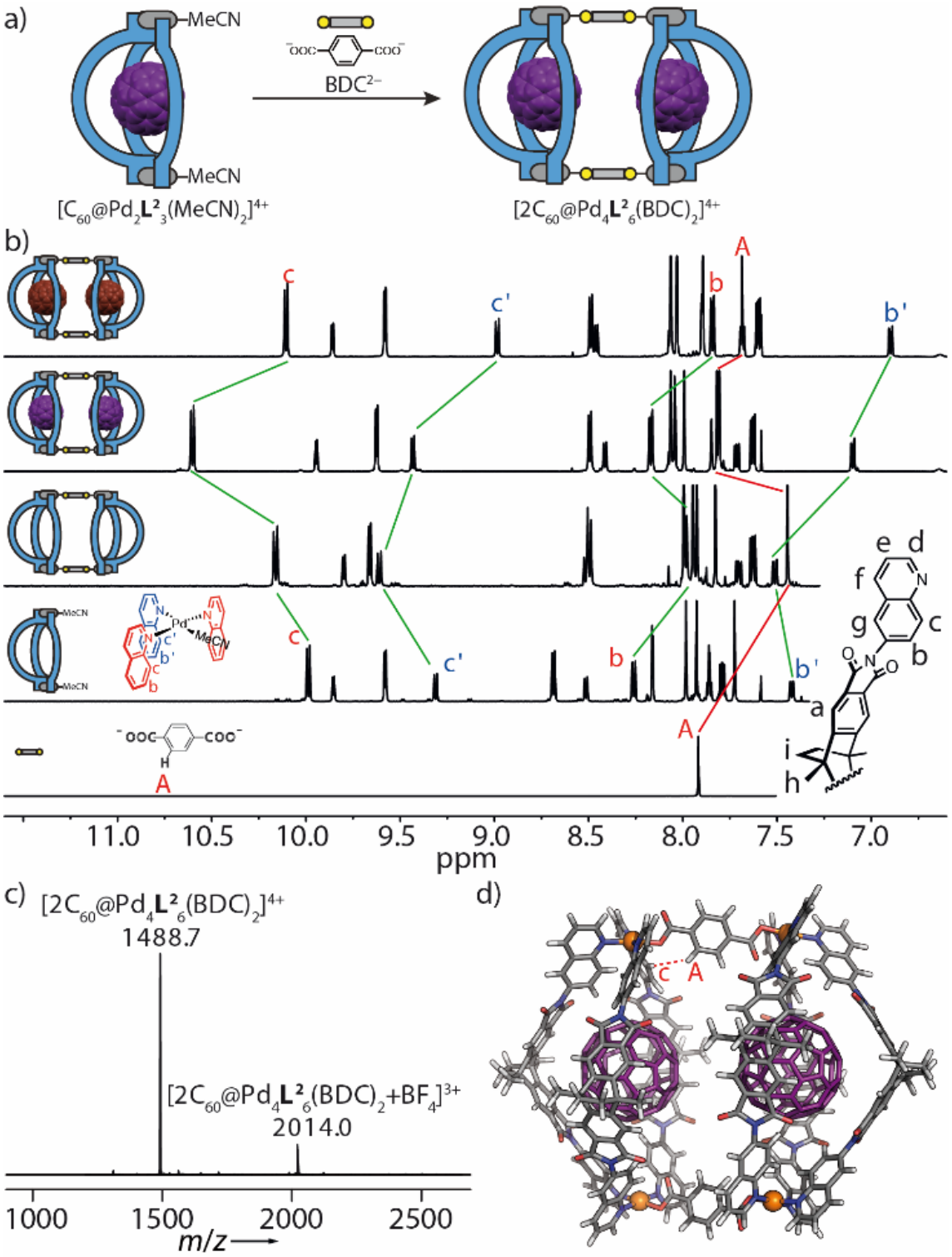

Figure 4.3 Hierarchical assembly and characterization of dimers. (a) Bowl $[C_{60}@Pd_2\mathbf{L^2}_3(MeCN)_2]^{4+}$ reacts with terephthalate (BDC^{2-}) to form dimer $[2C_{60}@Pd_4\mathbf{L^2}_6(BDC)_2]^{4+}$. (b) ^1H NMR spectra (298 K, CD_3CN) of BDC^{2-} (15 mM), $[Pd_2\mathbf{L^2}_3(MeCN)_2]^{4+}$ (0.64 mM), $[Pd_4\mathbf{L^2}_6(BDC)_2]^{4+}$ (0.31 mM), $[2C_{60}@Pd_4\mathbf{L^2}_6(BDC)_2]^{4+}$ (0.31 mM) and $[2C_{70}@Pd_4\mathbf{L^2}_6(BDC)_2]^{4+}$ (0.31 mM) (from bottom to top). Red and blue marked proton signals are assigned to edge and central ligands in the bowl geometries, respectively. (c) High-resolution ESI mass spectrum of $[2C_{60}@Pd_4\mathbf{L^2}_6(BDC)_2]^{4+}$. (d) PM6-optimized structure of $[2C_{60}@Pd_4\mathbf{L^2}_6(BDC)_2]^{4+}$.

^{1}H NMR spectra of dimers showed two sets of proton signals with 2:1 integral ratio for the quinoline moieties, analogous to the monomeric bowl, and a single signal for the terephthalate bridges' protons, indicative of the high symmetry of dimers (Figure 4.3b). Upon binding of fullerenes, chemical shift changes of particular protons (H_b, H_c, $H_{b'}$ and $H_{c'}$) for dimers were similar to the corresponding changes for monomers (compare Figure 4.3b and Figure 3.3b). Moreover, taking the $(C_{60})_2$-containing dimer $[2C_{60}@Pd_4\mathbf{L^2}_6(BDC)_2]^{4+}$ as an example, one cross peak in NOESY spectrum revealed an interligand contact between protons H_c of quinolines and protons H_A of terephthalate bridges, consistent with the relatively short distance between these atoms, measured from the PM6-optimized structure (Figure 4.3d and Figure 4.38). Furthermore, the size expansion from the monomeric bowl $[C_{60}@Pd_2\mathbf{L^2}_3(MeCN)_2]^{4+}$ to the capsule-like dimer $[2C_{60}@Pd_4\mathbf{L^2}_6(BDC)_2]^{4+}$ was confirmed by DOSY spectra (Figure 3.38 and Figure 4.40), corresponding to the diffusion coefficient of 5.20×10^{-10} m^2s^{-1} and 4.08×10^{-10} m^2s^{-1}, respectively. As observed in the ESI mass spectrum, two pronounced peaks at m/z = 1488.7 and 2014.0 were in full agreement with the simulated isotopic patterns of the expected dimer with the formula: $[2C_{60}@Pd_4\mathbf{L^2}_6(BDC)_2+nBF_4]^{(4-n)+}$ (n = 0, 1) (Figure 4.41). Formation of the hollow dimer and C_{70}-trapped dimer was also ascertained by the same analytic techniques (NMR spectroscopy and mass spectrometry), indicating that the fullerene encapsulation was orthogonal to the dimerization process.

4.6 Conclusion

Herein, we discussed multiple applications of the self-assembled cage/bowl system obtained from the previous chapter, concerning the fullerene purification, derivatization as well as advanced trapping in terms of solvent choice and capacity. Firstly, the supramolecular cage $[Pd_2\mathbf{L^1}_4](BF_4)_4$ allows for the transfer of fullerenes into other solvents besides acetonitrile, such as nitromethane, acetone and DMF. Secondly, a cyclic purification system of C_{60} was set up and the guest liberation could be induced by solvent effect. Thirdly, mono-adduct Diels-Alder reaction between the encapsulated C_{60} and anthracene was realized via the protection by exterior bowl-shaped geometry. Lastly, the supramolecular bowl $[Pd_2\mathbf{L^2}_3(MeCN)_2]^{4+}$ can be readily bridged by terephthalate to form dimers that can host two fullerenes within its cavity, which deserves further development to yield more sophisticated structures with higher capacities.

4.7 Experimental section

4.7.1 Solvent effect for $[Pd_2\mathbf{L^1}_4]^{4+}$ and $[C_{60}@Pd_2\mathbf{L^1}_4]^{4+}$

In order to investigate solubility and stability of $[Pd_2\mathbf{L^1}_4]^{4+}$ and $[C_{60}@Pd_2\mathbf{L^1}_4]^{4+}$ in a wider range of organic solvents, the CD_3CN solution of cage compounds $[Pd_2\mathbf{L^1}_4]^{4+}$ and $[C_{60}@Pd_2\mathbf{L^1}_4]^{4+}$ (0.64 mM, 300 µL) was evaporated, followed by adding different deuterated solvents (600 µL). NMR spectra were recorded after 1 h and 24 h.

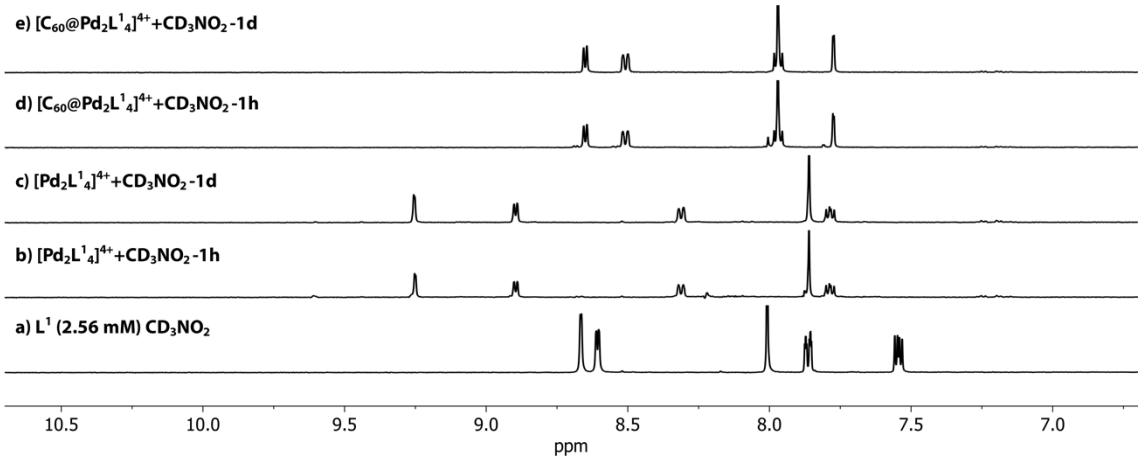

Figure 4.4 ^{1}H NMR spectra (500 MHz, 298 K, CD_3NO_2) of **L^1**, re-dissolved $[Pd_2\mathbf{L^1}_4]^{4+}$ and re-dissolved $[C_{60}@Pd_2\mathbf{L^1}_4]^{4+}$ in CD_3NO_2 for 1 h or 1 d at room temperature, indicating good solubility and stability of $[Pd_2\mathbf{L^1}_4]^{4+}$ and $[C_{60}@Pd_2\mathbf{L^1}_4]^{4+}$ in CD_3NO_2.

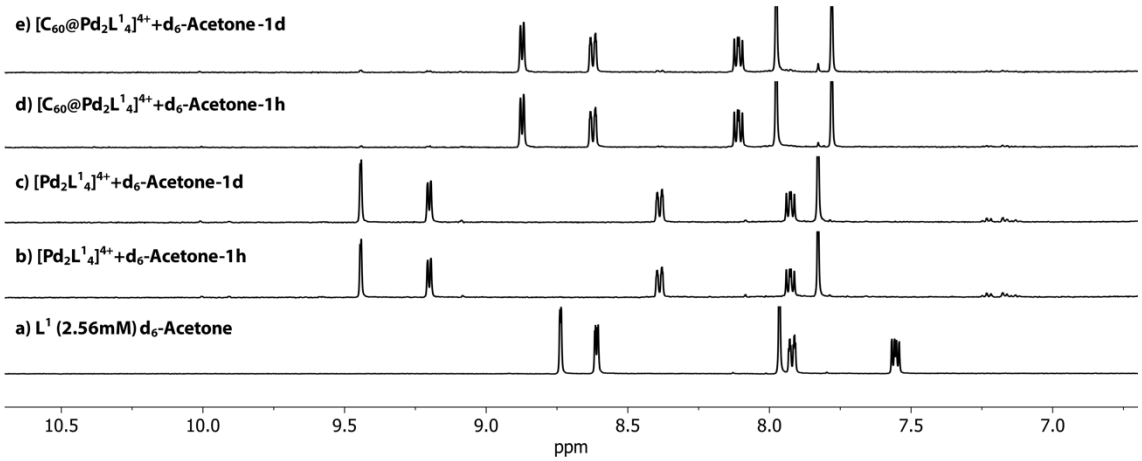

Figure 4.5 ^{1}H NMR spectra (500 MHz, 298 K, d_6-Acetone) of **L^1**, re-dissolved $[Pd_2\mathbf{L^1}_4]^{4+}$ and re-dissolved $[C_{60}@Pd_2\mathbf{L^1}_4]^{4+}$ in d_6-Acetone for 1 h or 1 d at room temperature, indicating good solubility and stability of $[Pd_2\mathbf{L^1}_4]^{4+}$ and $[C_{60}@Pd_2\mathbf{L^1}_4]^{4+}$ in d_6-Acetone.

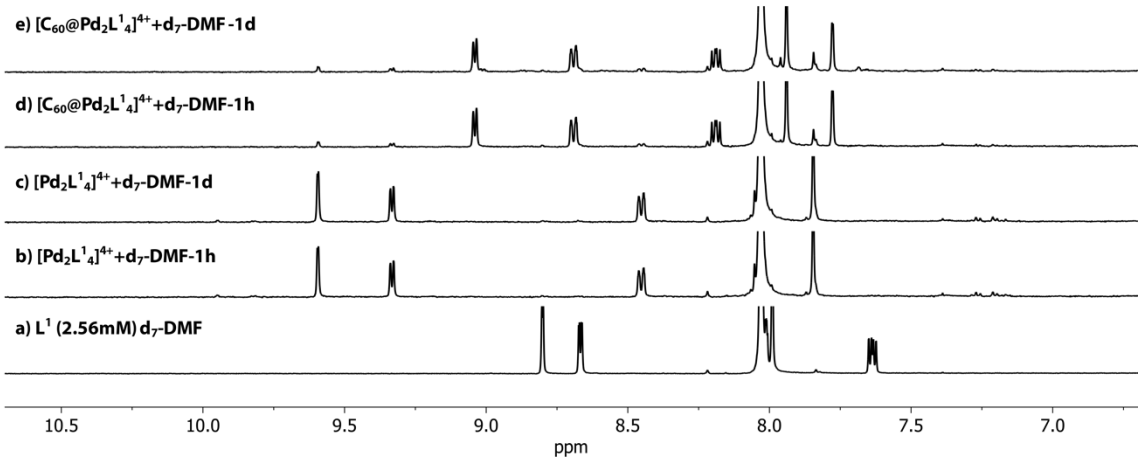

Figure 4.6 ^{1}H NMR spectra (500 MHz, 298 K, d_7-DMF) of **L^1**, re-dissolved $[Pd_2\mathbf{L^1}_4]^{4+}$ and re-dissolved $[C_{60}@Pd_2\mathbf{L^1}_4]^{4+}$ in d_7-DMF for 1 h or 1 d at room temperature, indicating good solubility and stability of $[Pd_2\mathbf{L^1}_4]^{4+}$ and $[C_{60}@Pd_2\mathbf{L^1}_4]^{4+}$ in d_7-DMF.

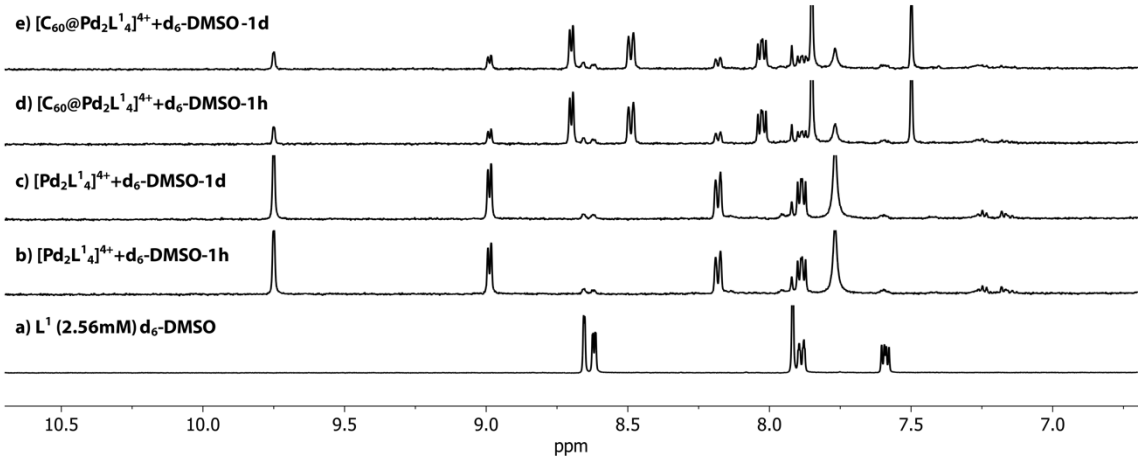

Figure 4.7 ^{1}H NMR spectra (500 MHz, 298 K, d_6-DMSO) of $\mathbf{L^1}$, re-dissolved $[Pd_2\mathbf{L^1}_4]^{4+}$ and re-dissolved $[C_{60}@Pd_2\mathbf{L^1}_4]^{4+}$ in d_6-DMSO for 1 h or 1 d at room temperature, indicating good solubility and stability of $[Pd_2\mathbf{L^1}_4]^{4+}$ but partial conversion of $[C_{60}@Pd_2\mathbf{L^1}_4]^{4+}$ into $[Pd_2\mathbf{L^1}_4]^{4+}$ in d_6-DMSO.

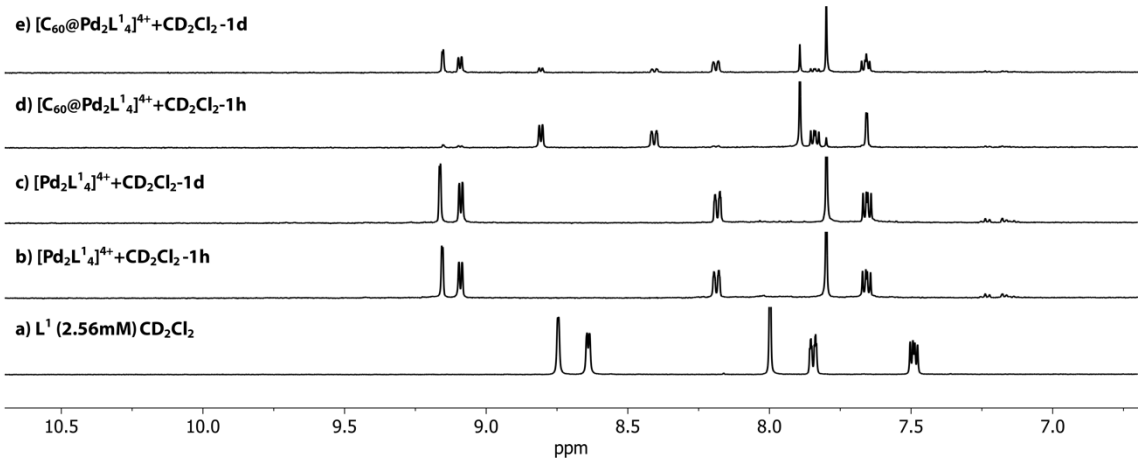

Figure 4.8 ^{1}H NMR spectra (500 MHz, 298 K, CD_2Cl_2) of $\mathbf{L^1}$, re-dissolved $[Pd_2\mathbf{L^1}_4]^{4+}$ and re-dissolved $[C_{60}@Pd_2\mathbf{L^1}_4]^{4+}$ in CD_2Cl_2 for 1 h or 1 d at room temperature, indicating good solubility and stability of $[Pd_2\mathbf{L^1}_4]^{4+}$ in CD_2Cl_2, but conversion of $[C_{60}@Pd_2\mathbf{L^1}_4]^{4+}$ into $[Pd_2\mathbf{L^1}_4]^{4+}$ under ejection of C_{60} in CD_2Cl_2.

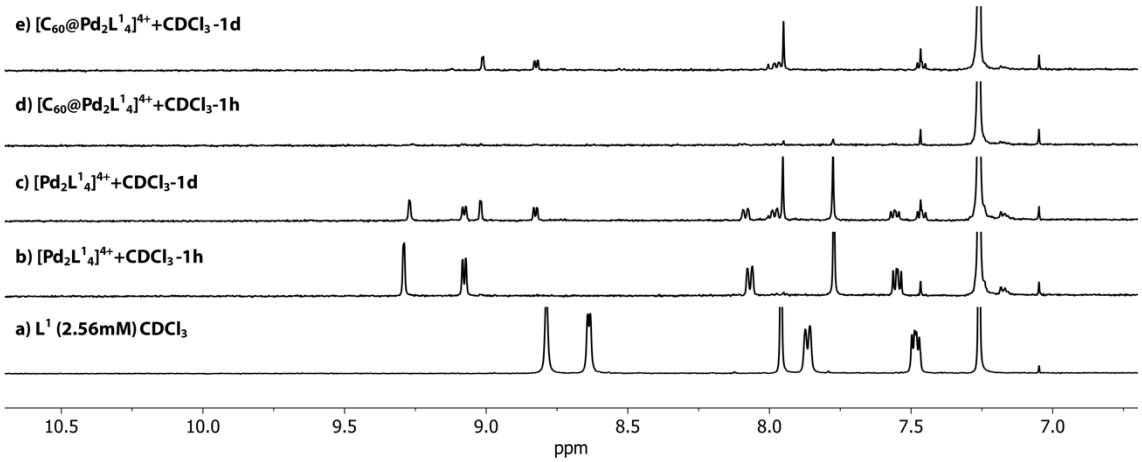

Figure 4.9 ^{1}H NMR spectra (500 MHz, 298 K, $CDCl_3$) of $\mathbf{L^1}$, re-dissolved $[Pd_2\mathbf{L^1}_4]^{4+}$ and re-dissolved $[C_{60}@Pd_2\mathbf{L^1}_4]^{4+}$ in $CDCl_3$ for 1 h or 1 d at room temperature, indicating decomposition of $[Pd_2\mathbf{L^1}_4]^{4+}$ and $[C_{60}@Pd_2\mathbf{L^1}_4]^{4+}$ in $CDCl_3$.

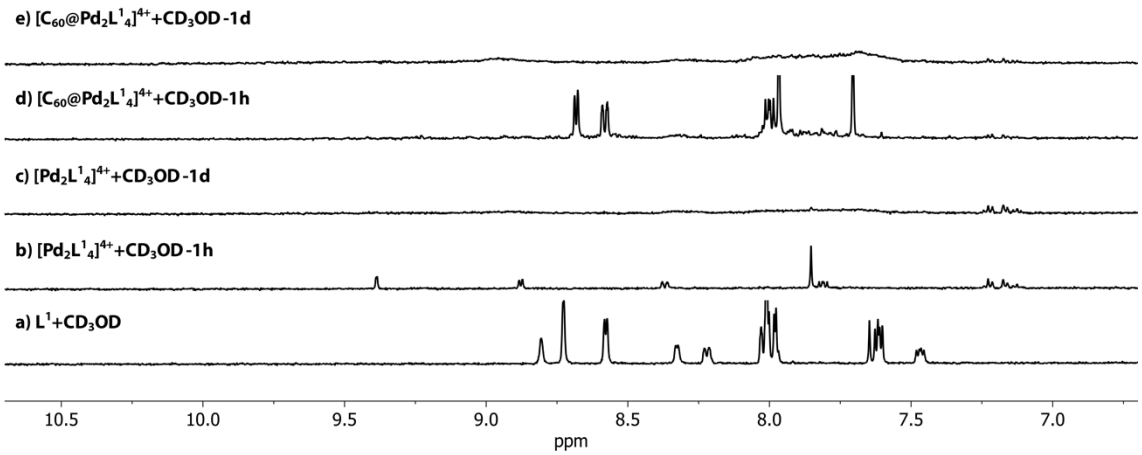

Figure 4.10 ^{1}H NMR spectra (500 MHz, 298 K, CD_3OD) of $\mathbf{L^1}$, re-dissolved $[Pd_2\mathbf{L^1}_4]^{4+}$ and re-dissolved $[C_{60}@Pd_2\mathbf{L^1}_4]^{4+}$ in CD_3OD for 1 h or 1 d at room temperature, indicating decomposition and limited solubility of $\mathbf{L^1}$, $[Pd_2\mathbf{L^1}_4]^{4+}$ and $[C_{60}@Pd_2\mathbf{L^1}_4]^{4+}$ in CD_3OD.

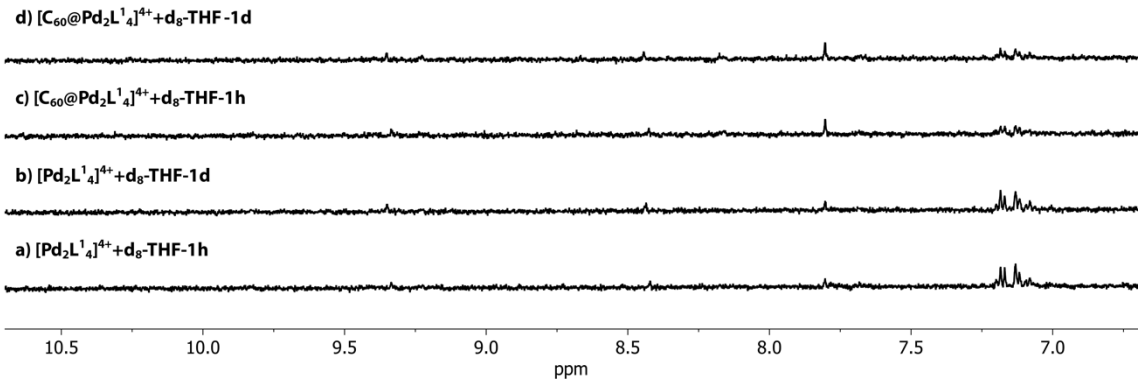

Figure 4.11 ^{1}H NMR spectra (500 MHz, 298 K, d_8-THF) of re-dissolved $[Pd_2\mathbf{L^1}_4]^{4+}$ and re-dissolved $[C_{60}@Pd_2\mathbf{L^1}_4]^{4+}$ in d_8-THF for 1 h or 1 d at room temperature, indicating insolubility of $[Pd_2\mathbf{L^1}_4]^{4+}$ and $[C_{60}@Pd_2\mathbf{L^1}_4]^{4+}$ in d_8-THF.

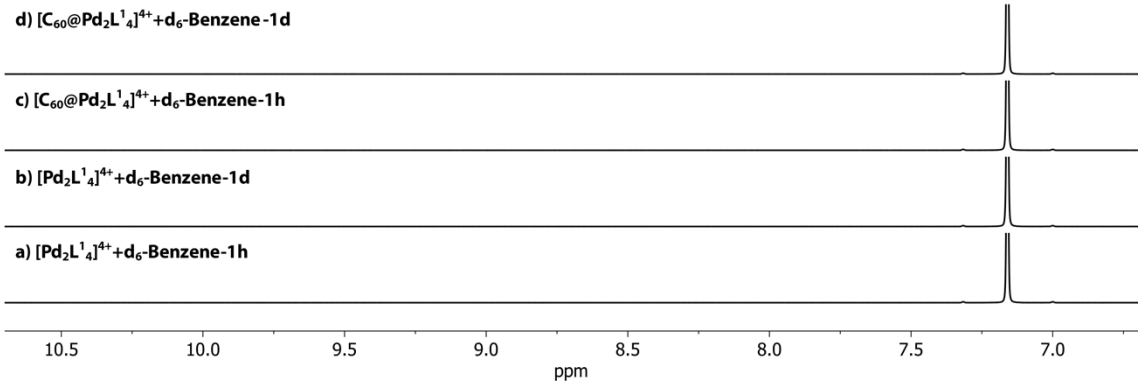

Figure 4.12 ^{1}H NMR spectra (500 MHz, 298 K, d_6-Benzene) of re-dissolved $[Pd_2\mathbf{L^1}_4]^{4+}$ and re-dissolved $[C_{60}@Pd_2\mathbf{L^1}_4]^{4+}$ in d_6-Benzene for 1 h or 1 d at room temperature, indicating insolubility of $[Pd_2\mathbf{L^1}_4]^{4+}$ and $[C_{60}@Pd_2\mathbf{L^1}_4]^{4+}$ in d_6-Benzene.

4.7.2 Fullerene purification by using $[Pd_2\mathbf{L^1}_4]^{4+}$

4.7.2.1 Test of fullerene binding from the mixture

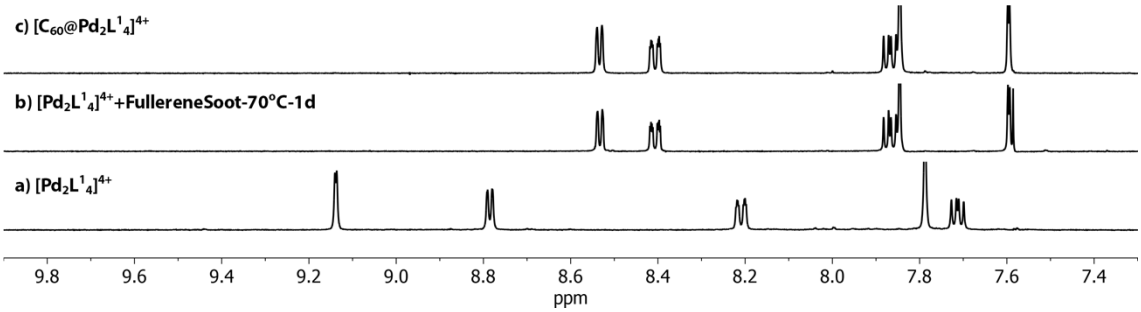

Figure 4.13 ^{1}H NMR spectra (500 MHz, 298 K, CD_3CN) monitoring the test of binding fullerene from the mixture within $[Pd_2\mathbf{L^1}_4]^{4+}$ at 70 °C, indicating $[Pd_2\mathbf{L^1}_4]^{4+}$ is capable of selectively binding C_{60} from the fullerene soot.

4.7.2.2 Addition of THF solution into CD_3CN solution of $[Pd_2\mathbf{L^1}_4]^{4+}$

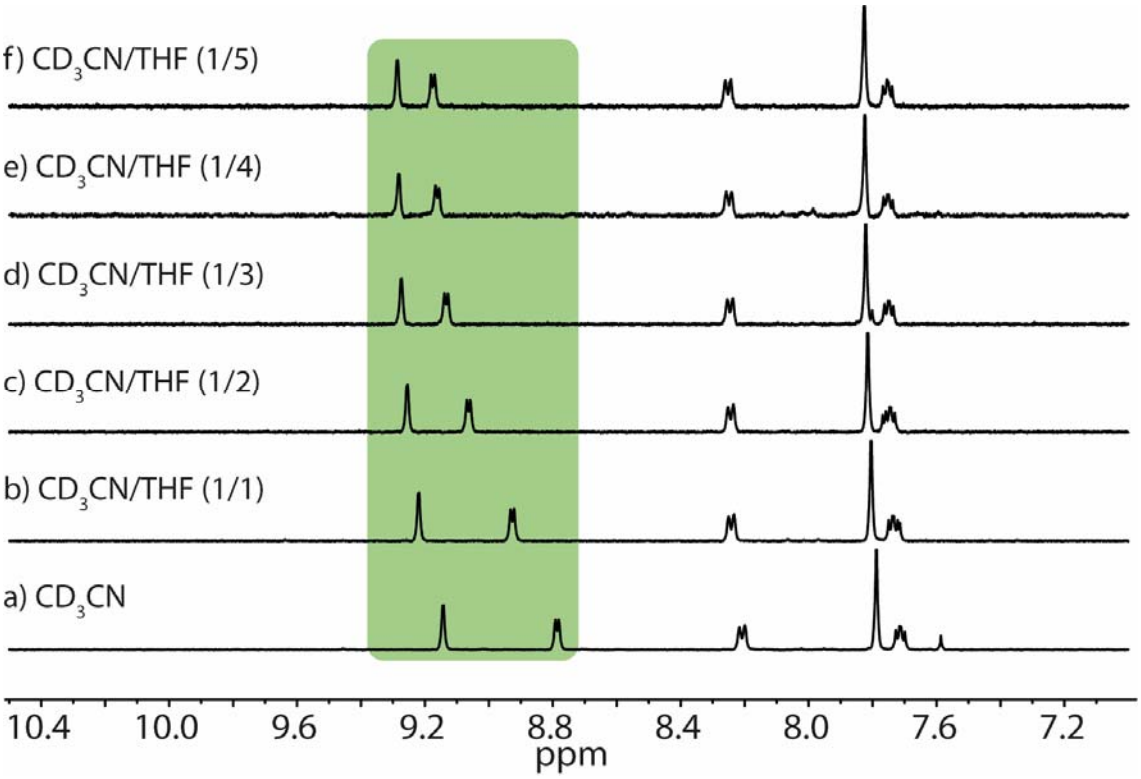

Figure 4.14 Addition of d_8-THF into the standard CD_3CN solution of $[Pd_2\mathbf{L^1}_4]^{4+}$. The pyridine protons b and c of $[Pd_2\mathbf{L^1}_4]^{4+}$ are highlighted in green, indicating the chemical shifts of these two protons due to the solvent effect.

4.7.2.3 Addition of THF solution into CD_3CN solution of $[C_{60}@Pd_2\mathbf{L^1}_4]^{4+}$

To the standard CD_3CN solution of $[C_{60}@Pd_2\mathbf{L^1}_4]^{4+}$ (100 μL, 0.64 mM) in every NMR tube, different amounts of CD_3CN and d_8-THF were added according to the table below, giving a solution with the same concentration of 0.11 mM cage to avoid the effect of concentration on host-guest interaction. ^{1}H NMR spectra were recorded immediately for each sample after adding solvents. After the NMR measurement, the samples were left overnight at room temperature and precipitate arose in the bottom of some NMR tubes.

Table 4.1 Details about the preparation of mixed solvent system.

$[C_{60}@Pd_2\mathbf{L^1}_4]$	100 µL, 0.64 mM,CD_3CN					
CD_3CN	500 µL	200 µL	100 µL	50 µL	20 µL	0 µL
d_8-THF	0 µL	300 µL	400 µL	450 µL	480 µL	500 µL
Ratios of solvents	CD_3CN	CD_3CN/THF 1/1	CD_3CN/THF 1/2	CD_3CN/THF 1/3	CD_3CN/THF 1/4	CD_3CN/THF 1/5
Concentration	0.11 mM					

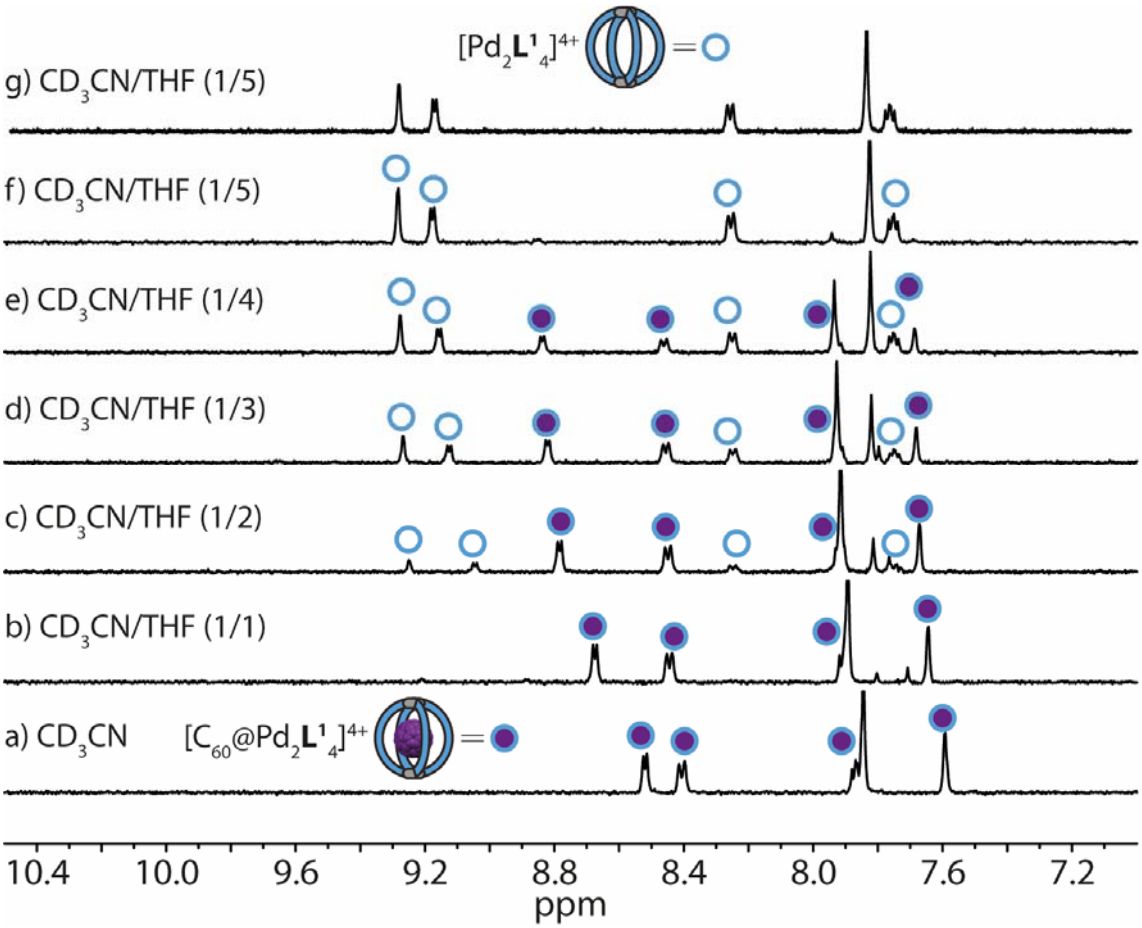

Figure 4.15 Addition of d_8-THF into the standard CD_3CN solution of $[C_{60}@Pd_2\mathbf{L^1}_4]^{4+}$. After formation of solvent mixtures with different ratios (from 1/1 to 1/5), the fullerene-occupied cage $[C_{60}@Pd_2\mathbf{L^1}_4]^{4+}$ converted to free cage $[Pd_2\mathbf{L^1}_4]^{4+}$, gradually.

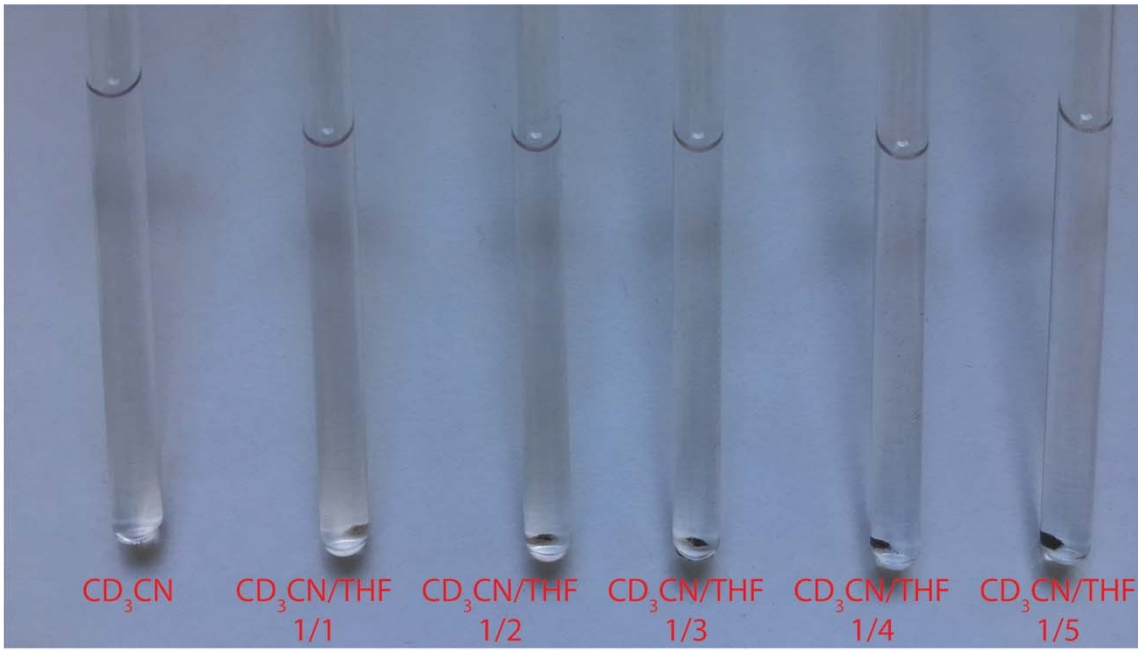

Figure 4.16 Photos of NMR tubes that were left overnight at room temperature. Increasing amounts of precipitate visible in the bottom of the NMR tubes from left to right.

4.7.2.4 Recycling purification of C_{60} from fullerene soot

The separation process is divided into five states as follows: (a) $[Pd_2\mathbf{L^1}_4]^{4+}$ solution (0.64 mM, CD_3CN); (b) $[C_{60}@Pd_2\mathbf{L^1}_4]^{4+}$ solution (0.64 mM, CD_3CN) prepared by liquid-solid extraction of excess fullerene soot (7 mg) with the $[Pd_2\mathbf{L^1}_4]^{4+}$ solution (0.64 mM, CD_3CN, 300 µL) under vigorous stirring at 70 °C for 1 d, followed by filtration; (c) addition of 5-fold excess of d_8-THF (1500 µL) leading to precipitation of pure C_{60} and a 0.11 mM, CD_3CN/d_8-THF(v/v: 1/5) solution of $[Pd_2\mathbf{L^1}_4]^{4+}$ after standing overnight; (d) separation by filtration, followed by evaporation of all solvents under reduced pressure, drying in vacuum and re-solubilization of recycled $[Pd_2\mathbf{L^1}_4]^{4+}$ in CD_3CN (< 0.32 mM, 600 µL); (e) utilization of recycled host in the next cycle.

4.7.3 Diels-Alder reaction with bowl-protected C_{60}

4.7.3.1 Formation and characterization of $[C_{60}Ac@Pd_2\mathbf{L^2}_3Cl_2]^{2+}$

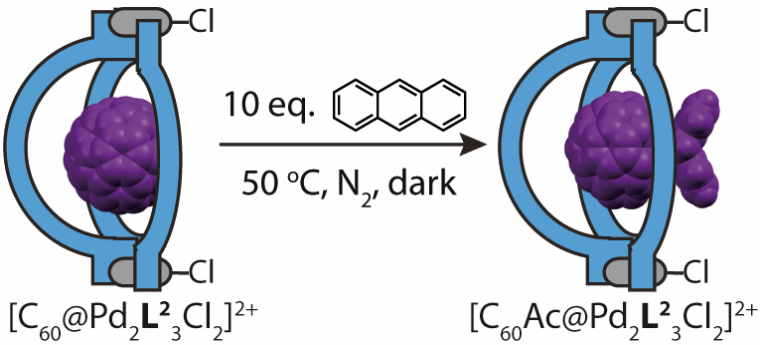

To the CD_3CN solution of $[C_{60}@Pd_2\mathbf{L^2}_3Cl_2]^{2+}$ (500 µL, 0.56 mM, 0.28 µmol, 1 eq.) was added a concentrated CD_3CN solution of anthracene (Ac) (280 µL, 10 mM, 2.80 µmol, 10 eq.) inside an NMR tube under nitrogen protection. The

NMR tube was wrapped with aluminium foil to avoid light irradiation and then heated at 50 °C in the dark overnight (*ca.* 14 h) to give a yellow solution.

^{1}H NMR (500 MHz, 298 K, CD_3CN): δ (ppm) = 10.65 (d, J = 9.2 Hz, 4H), 9.99 (d, J = 5.3 Hz, 2H), 9.49 (d, J = 5.3 Hz, 4H), 9.00 (d, J = 9.2 Hz, 2H), 8.52 (mixed with peaks of unreacted anthracene), 8.37 (d, J = 8.3 Hz, 2H), 8.24 (dd, J = 5.4, 3.3 Hz, 4H), 8.07 (mixed with peaks of unreacted anthracene), 7.95 (s, 4H), 7.89 – 7.77 (m, 14H), 7.73 (m, 6H), 7.67 (dd, J = 8.4, 5.3 Hz, 4H), 7.51 (peaks of unreacted anthracene), 6.95 – 6.83 (m, 2H), 6.28 (s, 2H). Peaks in the aliphatic region overlap with peaks of tetrabutylammonium cation and solvents.

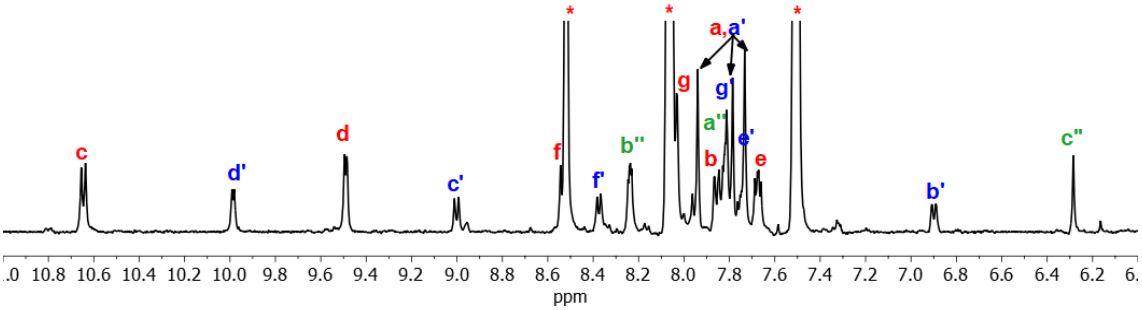

Figure 4.17 ^{1}H NMR spectrum (500 MHz, 298 K, CD_3CN) of $[C_{60}Ac@Pd_2\mathbf{L^2}_3Cl_2]^{2+}$. Relative positons of protons correspond to the case of $[C_{60}@Pd_2\mathbf{L^2}_3(MeCN)_2]^{4+}$. Red asterisks stand for the proton signals of unreacted anthracene.

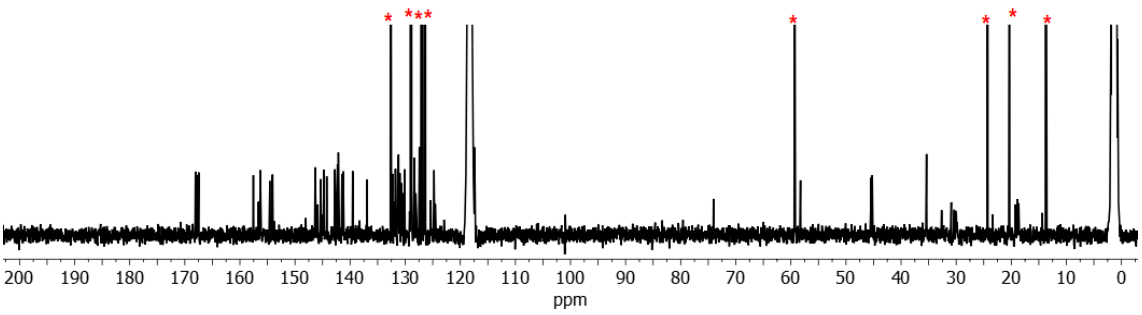

Figure 4.18 ^{13}C NMR spectrum (151 MHz, 298 K, CD_3CN) of $[C_{60}Ac@Pd_2\mathbf{L^2}_3Cl_2]^{2+}$. Red asterisks stand for the carbon signals of unreacted anthracene and tetrabutylammonium ions.

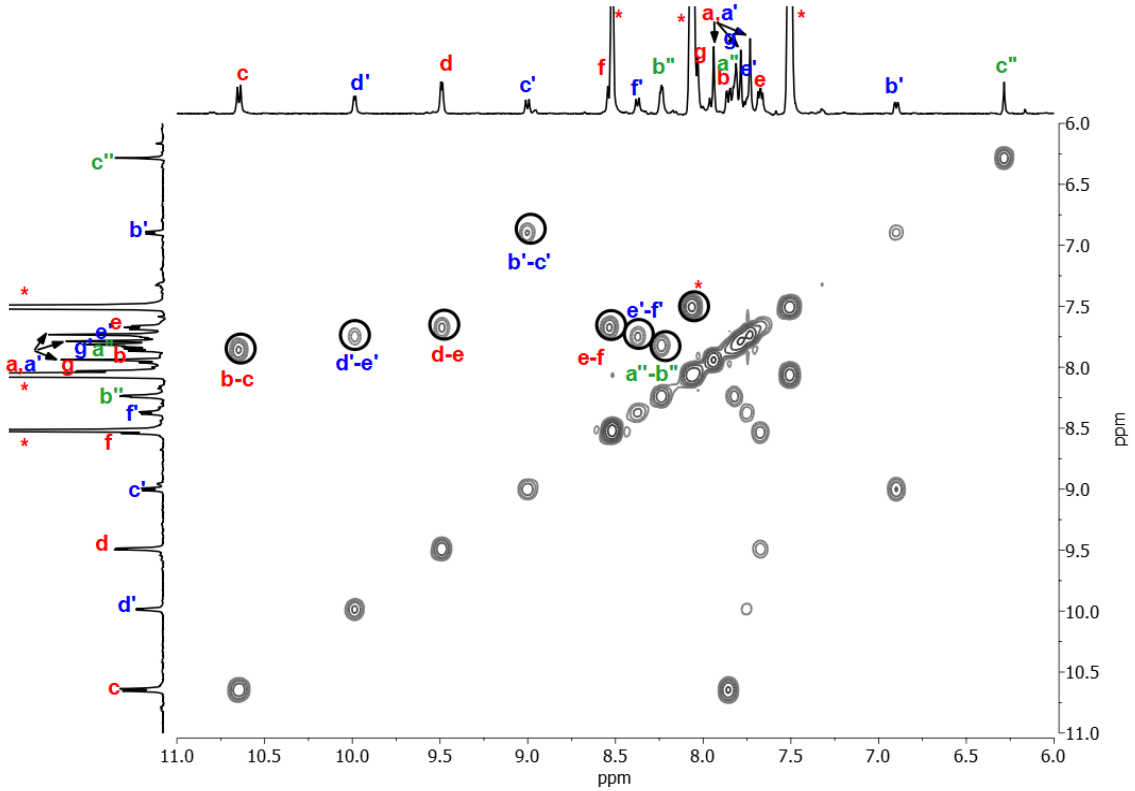

Figure 4.19 Partial $^{1}H - {}^{1}H$ COSY spectrum (500 MHz, 298 K, CD_3CN) of $[C_{60}Ac@Pd_2\mathbf{L^2}_3Cl_2]^{2+}$. Red asterisks stand for the proton signals of unreacted anthracene.

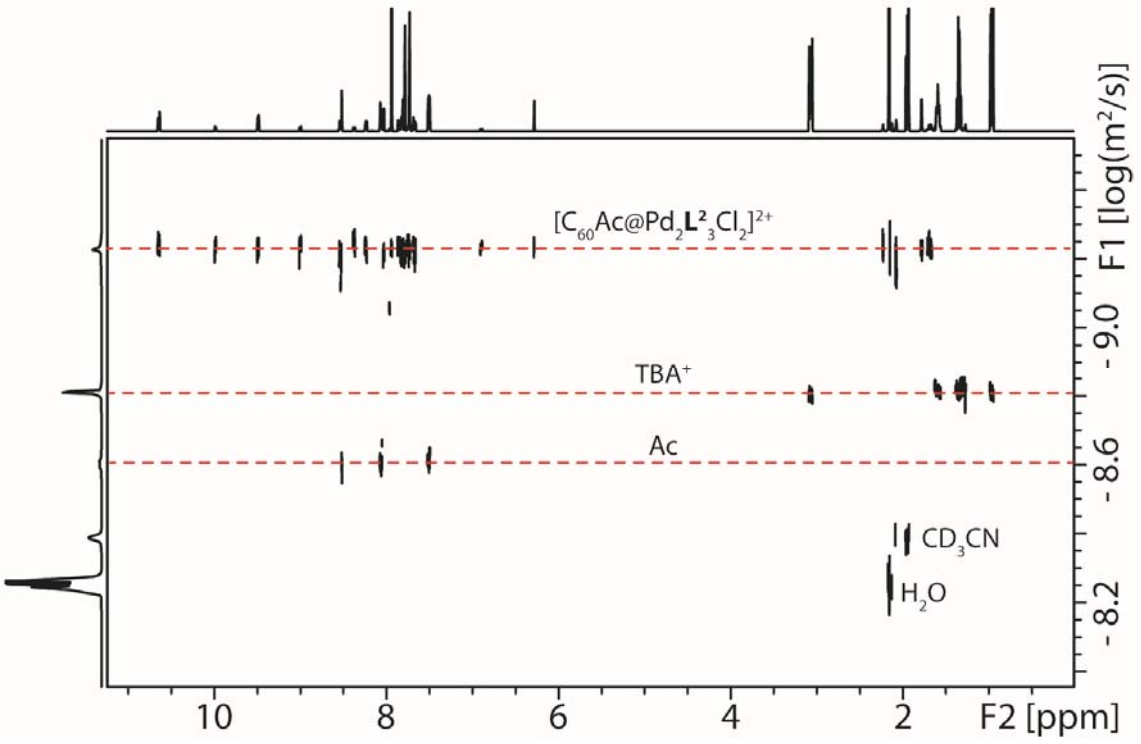

Figure 4.20 DOSY spectrum (500 MHz, 298 K, CD_3CN) of $[C_{60}Ac@Pd_2\mathbf{L^2}_3Cl_2]^{2+}$ with the coexisting tetrabutylammonium ions (TBA^+) and unreacted anthracene. $[C_{60}Ac@Pd_2\mathbf{L^2}_3Cl_2]^{2+}$: diffusion coefficient = 5.9 x 10^{-10} m^2s^{-1}, log D = −9.23, r = 10.7 Å; TBA^+ cation: diffusion coefficient = 1.5 x 10^{-9} m^2s^{-1}, log D = −8.81, r = 4.1 Å; anthracene(Ac): diffusion coefficient = 2.5 x 10^{-9} m^2s^{-1}, log D = −8.60, r = 2.5 Å.

ESI HRMS ($C_{194}H_{88}Cl_2N_{12}O_{12}Pd_2B_2F_8$): $[C_{60}Ac@Pd_2\mathbf{L^2}_3Cl_2]^{2+}$ calcd. for $C_{194}H_{88}Cl_2N_{12}O_{12}Pd_2$ 1531.2074; found 1531.2082.

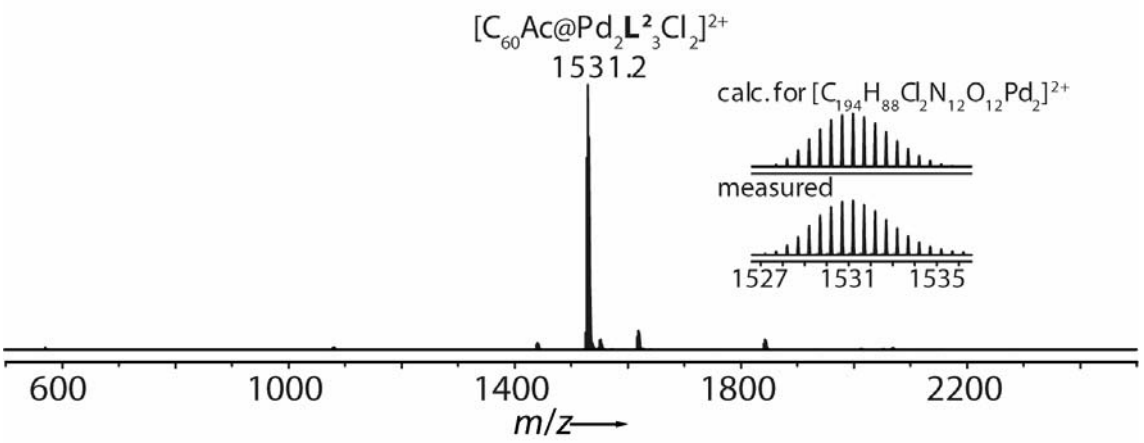

Figure 4.21 ESI mass spectrum of $[C_{60}Ac@Pd_2\mathbf{L^2}_3Cl_2]^{2+}$.

4.7.3.2 Reaction between $[C_{60}@Pd_2L^2_3Cl_2]^{2+}$ and anthracene in different ratios

General procedure: To the standard CD_3CN solution of $[C_{60}@Pd_2\mathbf{L^2}_3Cl_2]^{2+}$ (500 µL, 0.56 mM, 0.28 µmol, 1 eq.) in the bottom of NMR tubes, different equivalents (1, 2, 5, 10 eq.) of the concentrated CD_3CN solution of anthracene (10 mM) were added under nitrogen protection. All NMR tubes were wrapped with aluminium foil to avoid light irradiation and then heated at 50 °C in the dark. After a period of time, a ^1H NMR spectrum was recorded to monitor the partial conversion of $[C_{60}@Pd_2\mathbf{L^2}_3Cl_2]^{2+}$ and anthracene to $[C_{60}Ac@Pd_2\mathbf{L^2}_3Cl_2]^{2+}$.

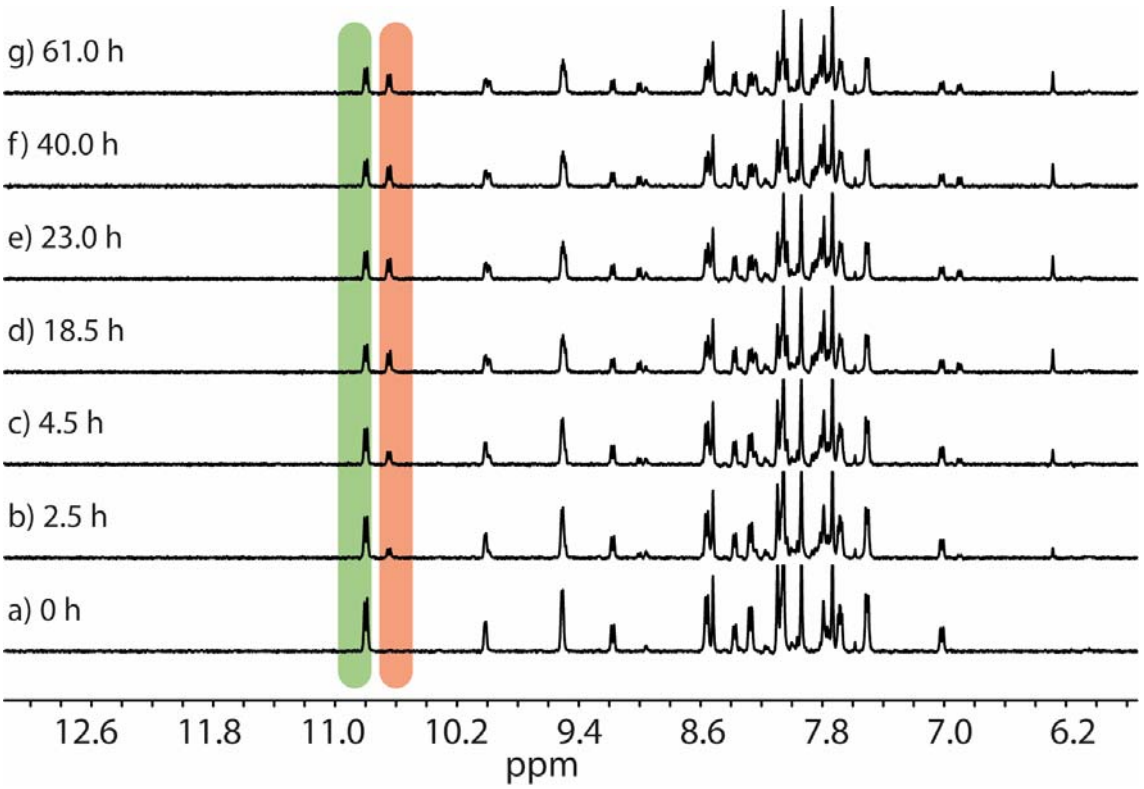

Figure 4.22 ^1H NMR spectra (500 MHz, 298 K, CD_3CN) following the partial conversion of $[C_{60}@Pd_2\mathbf{L^2}_3Cl_2]^{2+}$ and 1 equivalent of Ac to $[C_{60}Ac@Pd_2\mathbf{L^2}_3Cl_2]^{2+}$ after heating at 50 °C. The quinoline proton c of $[C_{60}@Pd_2\mathbf{L^2}_3Cl_2]^{2+}$ and quinoline proton c of $[C_{60}Ac@Pd_2\mathbf{L^2}_3Cl_2]^{2+}$ are highlighted in green and red respectively.

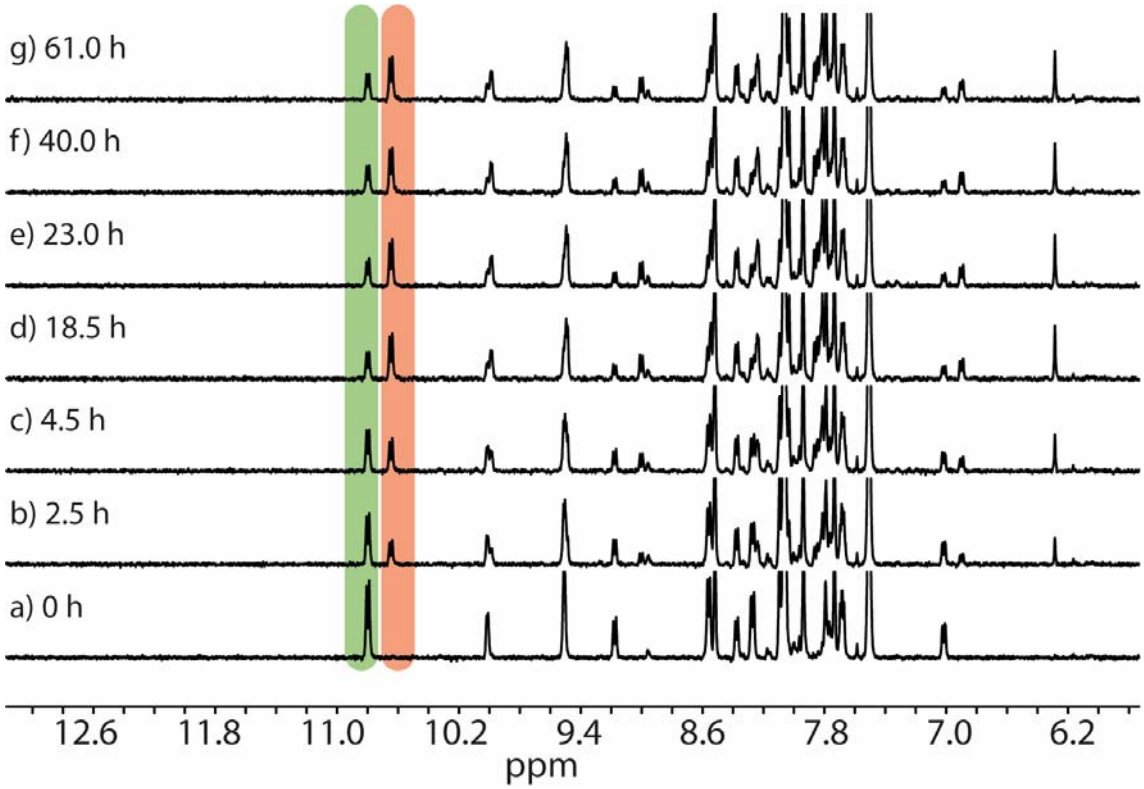

Figure 4.23 ^{1}H NMR spectra (500 MHz, 298 K, CD_3CN) following the partial conversion of $[C_{60}@Pd_2\mathbf{L^2}_3Cl_2]^{2+}$ and 2 equivalent of Ac to $[C_{60}Ac@Pd_2\mathbf{L^2}_3Cl_2]^{2+}$ after heating at 50 °C. The quinoline proton c of $[C_{60}@Pd_2\mathbf{L^2}_3Cl_2]^{2+}$ and quinoline proton c of $[C_{60}Ac@Pd_2\mathbf{L^2}_3Cl_2]^{2+}$ are highlighted in green and red respectively.

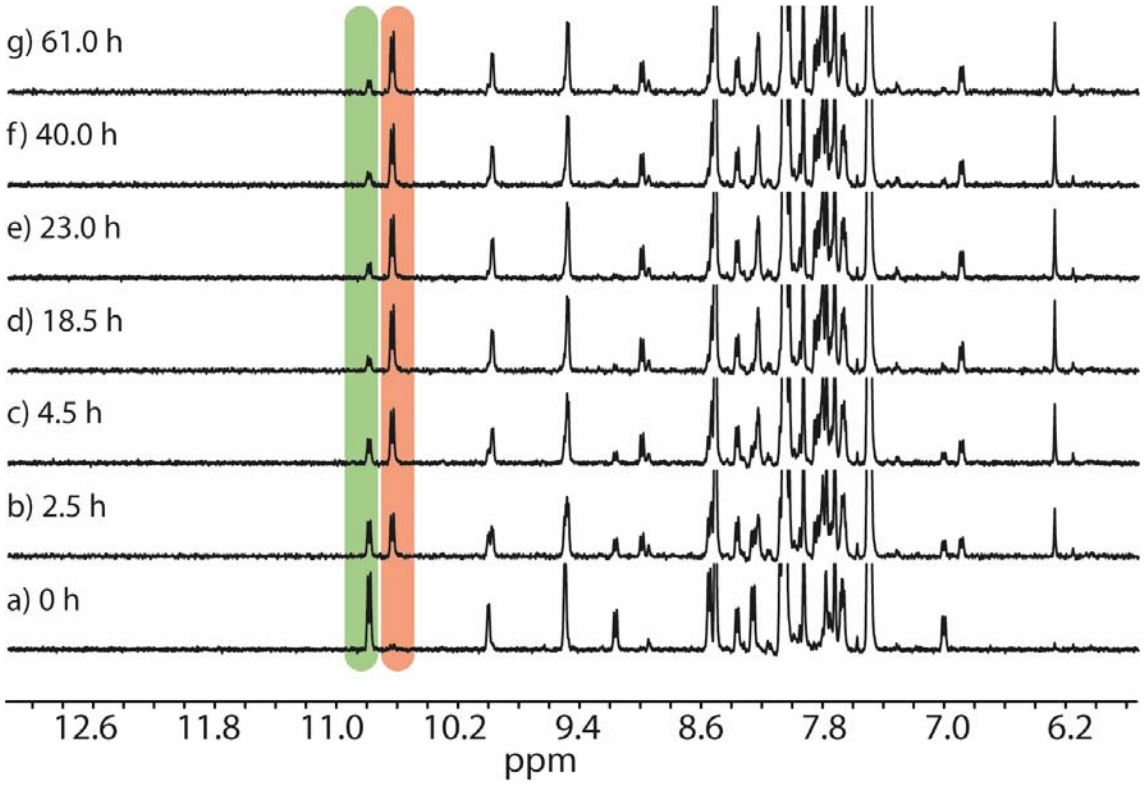

Figure 4.24 ^{1}H NMR spectra (500 MHz, 298 K, CD_3CN) following the partial conversion of $[C_{60}@Pd_2\mathbf{L^2}_3Cl_2]^{2+}$ and 5 equivalent of Ac to $[C_{60}Ac@Pd_2\mathbf{L^2}_3Cl_2]^{2+}$ after heating at 50 °C. The quinoline proton c of $[C_{60}@Pd_2\mathbf{L^2}_3Cl_2]^{2+}$ and quinoline proton c of $[C_{60}Ac@Pd_2\mathbf{L^2}_3Cl_2]^{2+}$ are highlighted in green and red respectively.

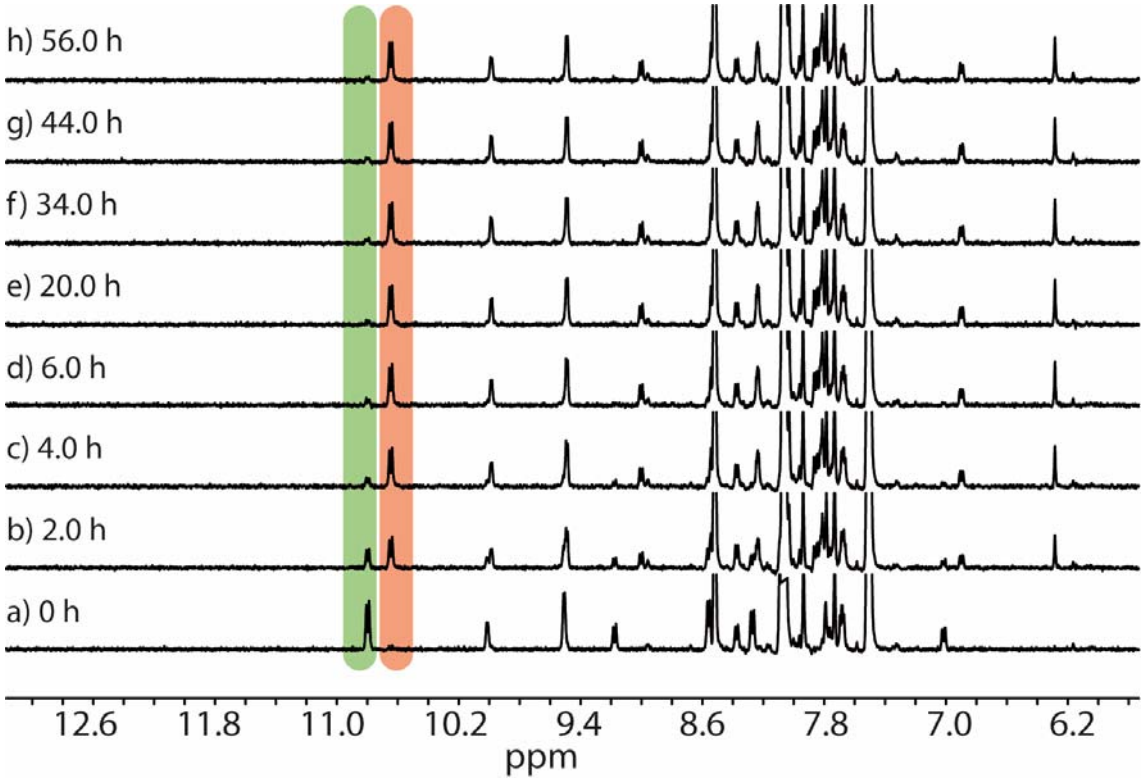

Figure 4.25 ^{1}H NMR spectra (500 MHz, 298 K, CD_3CN) following the partial conversion of $[C_{60}@Pd_2\mathbf{L^2}_3Cl_2]^{2+}$ and 10 equivalent of Ac to $[C_{60}Ac@Pd_2\mathbf{L^2}_3Cl_2]^{2+}$ after heating at 50 ^{o}C. The quinoline proton c of $[C_{60}@Pd_2\mathbf{L^2}_3Cl_2]^{2+}$ and quinoline proton c of $[C_{60}Ac@Pd_2\mathbf{L^2}_3Cl_2]^{2+}$ are highlighted in green and red respectively.

4.7.3.3 Conversion of $[C_{60}@Pd_2L^2{}_3Cl_2]^{2+}$ to $[C_{60}Ac@Pd_2L^2{}_3Cl_2]^{2+}$

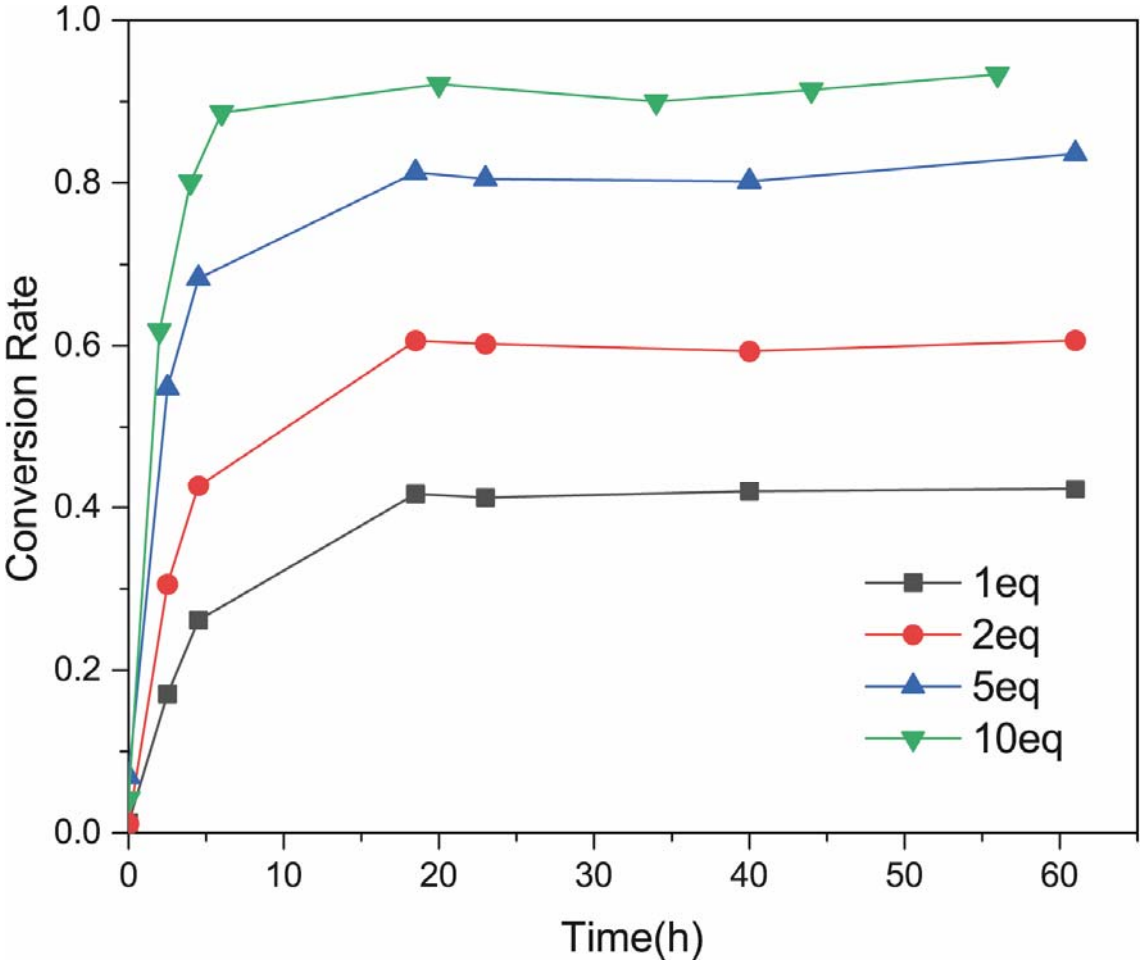

Figure 4.26 Conversion of $[C_{60}@Pd_2\mathbf{L^2}_3Cl_2]^{2+}$ with different equivalents of anthracene to $[C_{60}Ac@Pd_2\mathbf{L^2}_3Cl_2]^{2+}$ after heating at 50 °C for a period of time, concluded from the calculation of integrals of protons in ^{1}H NMR.

4.7.3.4 Determination of equilibrium constant K_c for reaction between $[C_{60}@Pd_2L^2{}_3Cl_2]^{2+}$ and anthracene

$$[C_{60}@Pd_2\mathbf{L^2}_3Cl_2]^{2+} + Ac \rightleftharpoons [C_{60}Ac@Pd_2\mathbf{L^2}_3Cl_2]^{2+}$$

$$K_c = \frac{[C_{60}Ac@Bowl]}{[C_{60}@Bowl][Ac]}$$

where $[C_{60}Ac@Bowl]$, $[C_{60}@Bowl]$ and [Ac] stand for the equilibrium concentrations of $[C_{60}Ac@Pd_2\mathbf{L^2}_3Cl_2]^{2+}$, $[C_{60}@Pd_2\mathbf{L^2}_3Cl_2]^{2+}$ and anthracene at 323 K, respectively. These values are determined by the integration of the H_c signals of $[C_{60}Ac@Pd_2\mathbf{L^2}_3Cl_2]^{2+}$ and $[C_{60}@Pd_2\mathbf{L^2}_3Cl_2]^{2+}$ in ^{1}H NMR spectra. We assumed no change of the equilibrium position during the time required for recording the NMR spectra at 298 K (few minutes).

Table 4.2 Calculation of the equilibrium constant K_c with different amounts of added anthracene. Average value: 2210 L/mol.

Amount of anthracene added	Percent of species in equilibrium		Equilibrium constant K_c (323 K) L/mol
	$[C_{60}@Pd_2\mathbf{L^2}_3Cl_2]^{2+}$	$[C_{60}Ac@Pd_2\mathbf{L^2}_3Cl_2]^{2+}$	
1 eq.	0.580	0.420	2360
2 eq.	0.407	0.593	2061
5 eq.	0.198	0.802	2210

4.7.3.5 One-pot formation of $C_{60}Ac$ inside $[Pd_2L^2{}_3Cl_2]^{2+}$

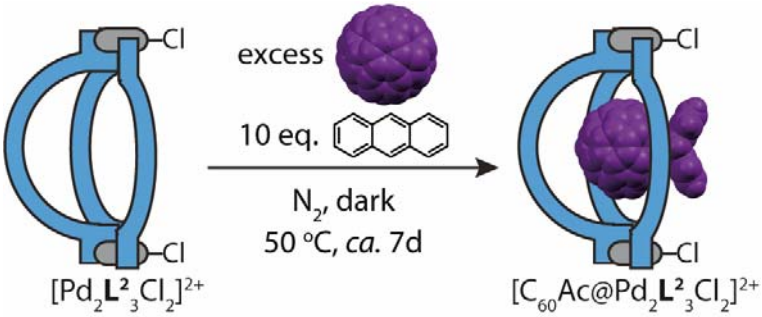

To an excess of C_{60} solid (2.4 mg, 3.36 µmol), the standard CD_3CN solution of $[Pd_2\mathbf{L^2}_3Cl_2]^{2+}$ (500 µL, 0.56 mM, 0.28 µmol, 1 eq.) and a concentrated CD_3CN solution of anthracene (280 µL, 10 mM, 2.80 µmol, 10 eq.) were added under nitrogen protection. NMR tubes were wrapped with aluminium foil to avoid light irradiation and then heated at 50 °C in the dark. After a period of time, ^1H NMR spectra were recorded to monitor the partial conversion of C_{60} to $C_{60}Ac$ inside the bowl $[Pd_2\mathbf{L^2}_3Cl_2]^{2+}$.

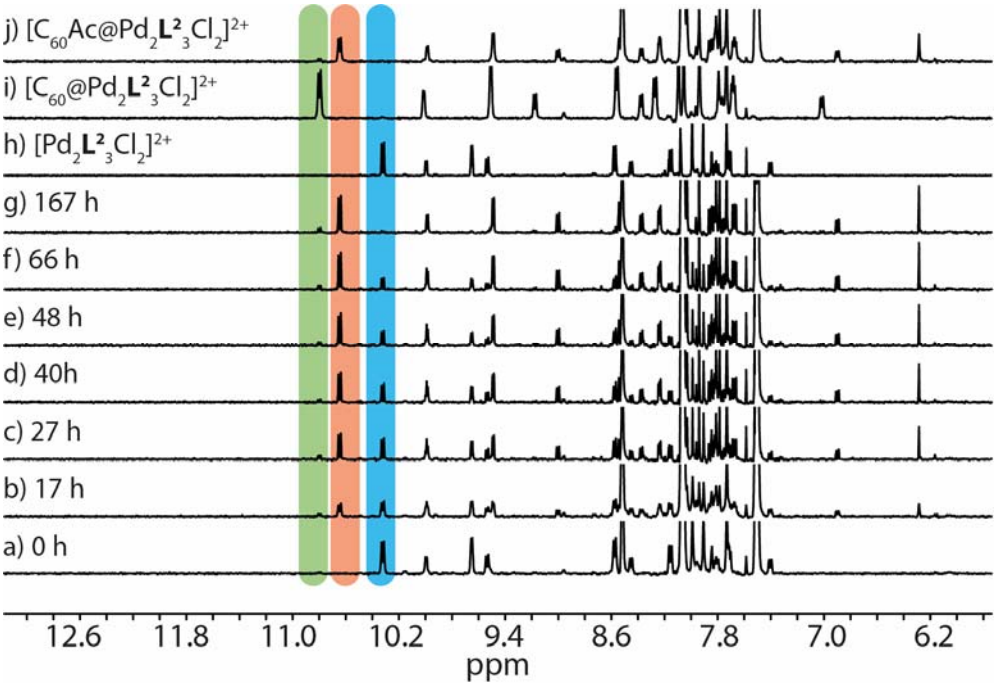

Figure 4.27 ^1H NMR spectra (500 MHz, 298 K, CD_3CN) following the one-pot formation of $[C_{60}Ac@Pd_2\mathbf{L^2}_3Cl_2]^{2+}$ in the presence of 10 equivalents of anthracene and excess C_{60} solid with $[C_{60}Ac@Pd_2\mathbf{L^2}_3Cl_2]^{2+}$ after heating at 50 °C. The quinoline proton c of $[C_{60}@Pd_2\mathbf{L^2}_3Cl_2]^{2+}$, proton c of $[C_{60}Ac@Pd_2\mathbf{L^2}_3Cl_2]^{2+}$ and proton c of $[Pd_2\mathbf{L^2}_3Cl_2]^{2+}$ are highlighted in green, red and blue respectively.

4.7.3.6 Control experiment

To excess C_{60} solid (1.7 mg, 2.36 µmol), CD_3CN (500 µL) and a concentrated CD_3CN solution of anthracene (280 µL, 10 mM, 2.80 µmol) were added under nitrogen protection. NMR tubes were wrapped with aluminium foil to avoid light irradiation and then heated at 50 °C in the dark. After a period of time, ^{1}H NMR spectra were recorded.

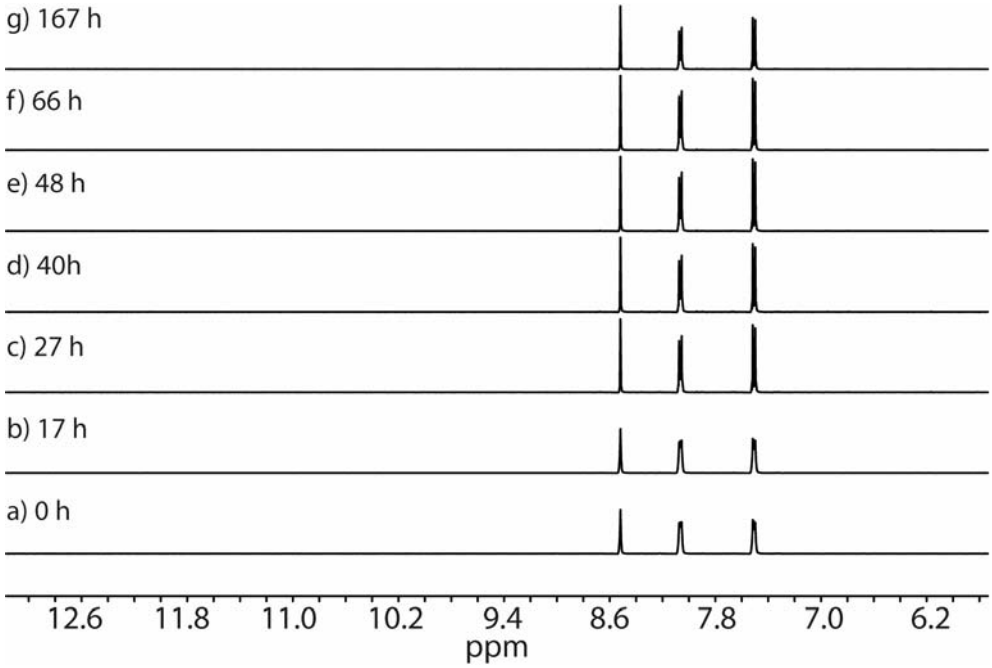

Figure 4.28 ^{1}H NMR spectra (500 MHz, 298 K, CD_3CN) following the control experiment in the presence of 3.59 mM anthracene in CD_3CN with C_{60} solid after heating at 50 °C.

To the CD_3CN solution of $[C_{60}@Pd_2\mathbf{L^1}_4]^{4+}$ (500 µL, 0.64 mM, 0.32 µmol), a concentrated CD_3CN solution of anthracene (320 µL, 10 mM, 3.20 µmol) was added under nitrogen protection. The NMR tube was wrapped with aluminium foil to avoid light irradiation and then heated at 50 °C in the dark. After a period of time, ^{1}H NMR spectra were recorded.

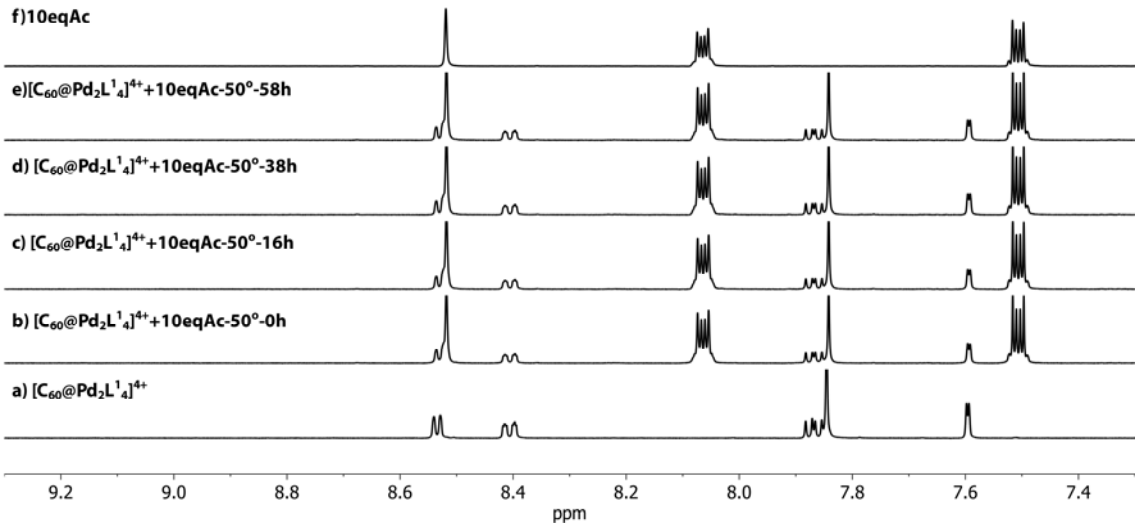

Figure 4.29 ^{1}H NMR spectra (500 MHz, 298 K, CD_3CN) following the control experiment in the presence of $[C_{60}@Pd_2\mathbf{L^1}_4]^{4+}$ and 10 eq. amount of anthracene in CD_3CN after heating at 50 °C, suggesting that the entrapped C_{60} in the cage $[C_{60}@Pd_2\mathbf{L^1}_4]^{4+}$ cannot react with excess anthracene.

4.7.3.7 Crystal structure of $[C_{60}Ac@Pd_2L^2{}_3Cl_2](BF_4)_2$

Table 4.3 Crystallographic data of $[C_{60}Ac@Pd_2\mathbf{L^2}_3Cl_2](BF_4)_2$.

Compound	**$[C_{60}Ac@Pd_2L^2{}_3Cl_2](BF_4)_2\cdot2MeCN\cdot4THF$**
CCDC number	1858158
Identification code	bc20a_plate_sq
Empirical formula	$C_{214}H_{126}N_{14}O_{16}Pd_2B_2F_8Cl_2$
Formula weight	3606.60
Temperature (K)	80(2)
Crystal system	Monoclinic
Space group	$P2_1/n$
a (Å)	18.628(4)
b (Å)	37.428(8)
c (Å)	25.814(5)
α (º)	90
β (º)	92.11(3)
γ (º)	90
Volume ($Å^3$)	17986(6)
Z	4
Density (calc.) (g/cm^3)	1.332
Absorption coefficient (mm^{-1})	0.283
F(000)	7376
Crystal size (mm^3)	0.080 x 0.080 x 0.020
θ range for data collection (º)	0.929 to 23.606
Reflections collected	187883
Observed reflections [R(int)]	29314 [0.0589]
Goodness-of-fit on F^2	1.474
R_1 [I>2σ(I)]	0.1230
wR_2 (all data)	0.3816
Largest diff. peak and hole ($e.Å^{-3}$)	3.312 and -0.683
Data / restraints / parameters	29314 / 5529 / 2461

Red thin plate crystals of $[C_{60}Ac@Pd_2\mathbf{L^2}_3Cl_2](BF_4)_2$ were obtained by fast vapor diffusion of THF into a 0.44 mM CD_3CN solution of $[C_{60}Ac@Pd_2\mathbf{L^2}_3Cl_2](BF_4)_2$ with excess anthracene. A single crystal in mother liquor was pipetted onto a glass slide containing NVH oil. To avoid collapse of the crystal lattice, the crystal was quickly mounted onto a 0.1 mm nylon loop and immediately flash cooled in liquid nitrogen. Crystals were stored at cryogenic temperature in dry shippers, in which they were safely transported to macromolecular beamline P11 at Petra III, DESY, Germany.[120]

A wavelength of λ = 0.6888 Å was chosen using a liquid N_2 cooled double crystal monochromator. Single crystal X-ray diffraction data was collected at 80(2) K on a single axis goniometer, equipped with an Oxford Cryostream 800 a Pilatus

6M. 3600 diffraction images were collected in a 360° ϕ sweep at a detector distance of 155 mm, 100% filter transmission, 0.1° step width and 0.06 seconds exposure time per image.

Stereochemical restraints for the EAQ ligands (**L²**) were generated by the GRADE program using the GRADE Web Server (http://grade.globalphasing.org) and applied in the refinement. The C_{60}Ac Diels-Alder adduct was not disordered and all atomic positions of non-hydrogen atoms were freely refined without the help of any geometrical restraints.

Table 4.4 Definition of residues involved in $[C_{60}Ac@Pd_2\mathbf{L^2}_3Cl_2](BF_4)_2$.

Fragment	Residue class	Occurrence	Residue numbers
Pd^{2+}	PD	1	1
Ligand **L²**	EAQ	3	2,3,4
Cl^-	CL	1	5
$C_{60}Ac$	FAC	1	6
BF_4^-	BF4	2	7,8,9,10 (Two BF_4^- with disorder)
MeCN	ACN	2	11,12
THF	THF	4	13,14,15,16

Table 4.5 Structural details involved in $[C_{60}Ac@Pd_2\mathbf{L^2}_3Cl_2](BF_4)_2$.

Residues No.	Dihedral angle (°) between the backbone's benzene planes C16_C17_C18_C22_C23_C24 and C7_C8_C9_C13_C14_C15	Esd (°)	Dihedral angle (°) between planes N29_Pd1_Pd2 and N39_Pd1_Pd2	Esd (°)
2	56.205	0.179	2.165	0.259
3	55.250	0.206	1.577	0.221
4	49.120	0.284	0.911	0.251
Average	53.5		1.6	

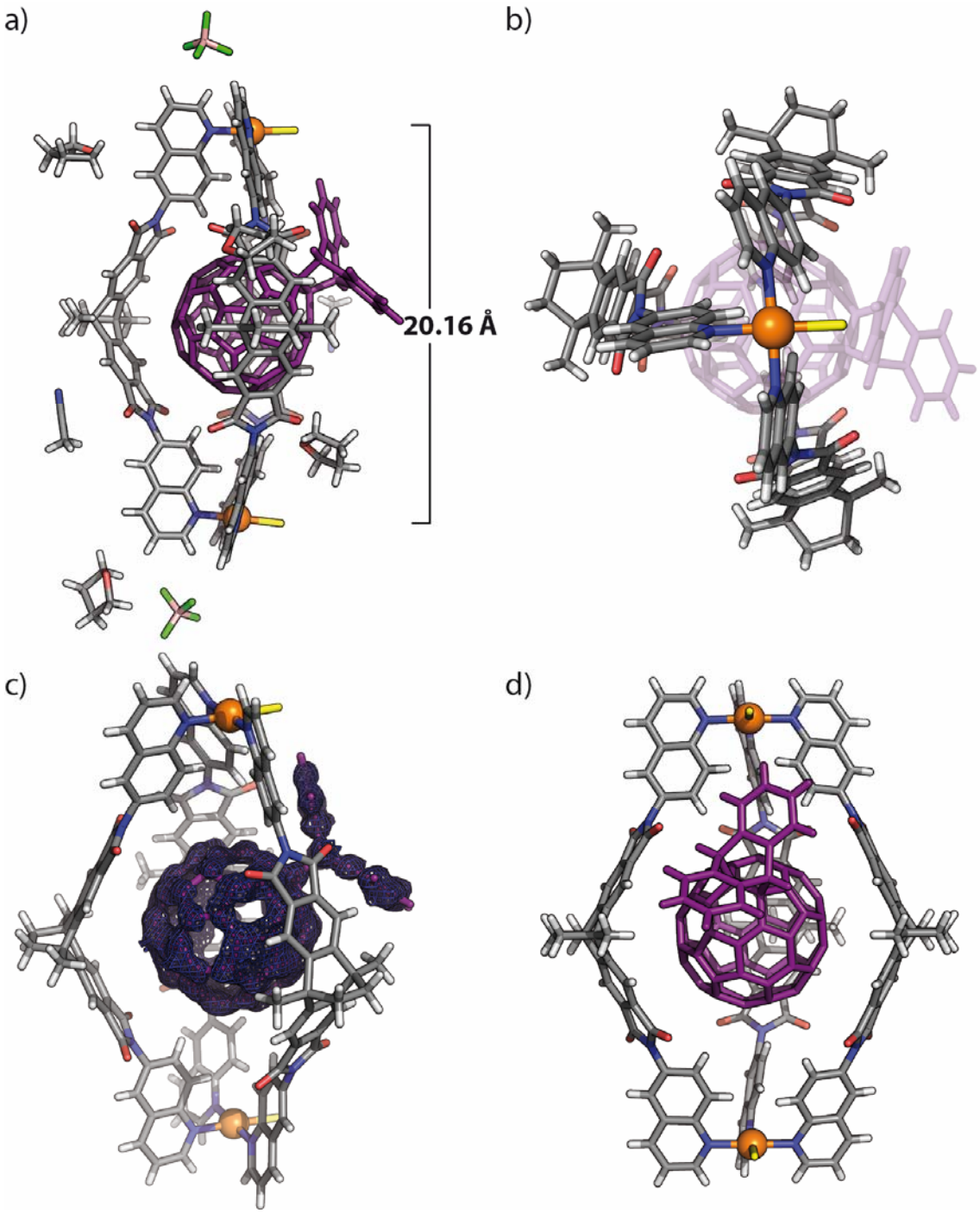

Figure 4.30 X-ray structure of $[C_{60}Ac@Pd_2\mathbf{L^2}_3Cl_2](BF_4)_2$: (a) The asymmetric unit showing the entrapped $C_{60}Ac$ by bowl geometry and the peripheral BF_4^- counterions, acetonitrile and tetrahydrofuran; (b) top view of the structure of $[C_{60}Ac@Pd_2\mathbf{L^2}_3Cl_2](BF_4)_2$; (c) and (d) two orientation views of the structure of $[C_{60}Ac@Pd_2\mathbf{L^2}_3Cl_2](BF_4)_2$, wherein electron density map of $C_{60}Ac$ is represented in blue mesh in (c). Color scheme: H, light grey; B, pink; C, dark grey; N, blue; O, red; F, green; Pd, orange; Cl, yellow; $C_{60}Ac$, purple.

4.7.4 Dimerization of bowls

4.7.4.1 Formation and characterization of dimer $[Pd_4L^2_6(BDC)_2]^{4+}$

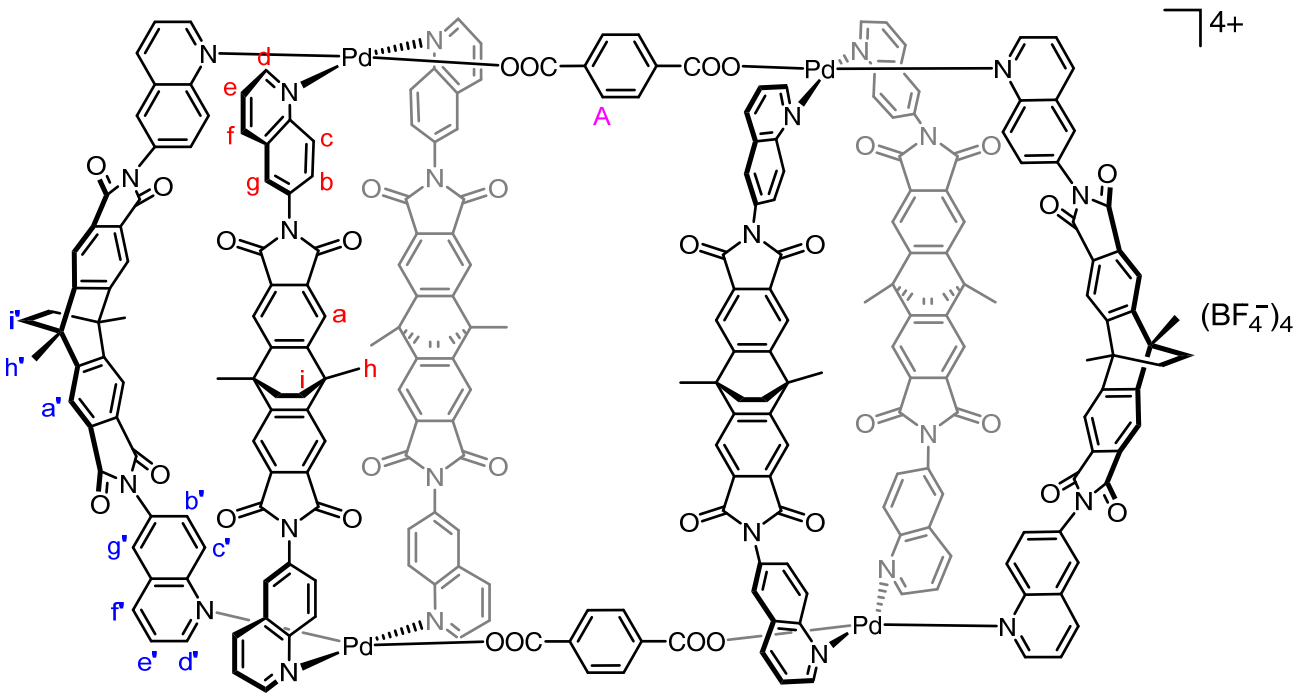

$[Pd_4\mathbf{L^2}_6(BDC)_2]^{4+}$

The CD_3CN solution of $(Et_3NH)_2BDC$ (15 mM) was prepared by mixing 1,4-benzenedioic acid (BDC) and 2 eq. trimethylamine in CD_3CN at room temperature. The CD_3CN solution $[Pd_4\mathbf{L^2}_6(BDC)_2]^{4+}$ (0.31 mM) was formed by stirring a mixture of the CD_3CN solution of $[Pd_2\mathbf{L^2}_3(MeCN)_2]^{4+}$ (500 µL, 0.64 mM, 0.32 µmol, 1 eq.) and CD_3CN solution of $(Et_3NH)_2BDC$ (21.3 µL, 15 mM, 0.32 µmol, 1 eq.) at room temperature for 2 min. NMR spectra was recorded after preparing fresh sample because of its instability.

^{1}H NMR (500 MHz, 298 K, CD_3CN): δ (ppm) = 10.16 (d, J = 9.8 Hz, 8H), 9.80 (dd, J = 5.5, 1.4 Hz, 4H), 9.66 (dd, J = 5.5, 1.4 Hz, 8H), 9.61 (d, J = 9.1 Hz, 4H), 8.53 – 8.47 (m, 12H), 8.00 – 7.96 (m, 16H), 7.96 – 7.93 (m, 12H), 7.92 (s, 8H), 7.83 (s, 8H), 7.70 (dd, J = 8.3, 5.6 Hz, 4H), 7.63 (dd, J = 8.3, 5.4 Hz, 8H), 7.51 (dd, J = 9.1, 2.3 Hz, 4H), 7.44 (s, 8H), 2.26 – 2.19 (m, 24H), 2.16 (s, mixed with water peak in CD_3CN), 1.94 (mixed with solvent residual peak), 1.82 (s, 8H).

Overlapping signals in the aliphatic region could be assigned via 2D NMR spectroscopy.

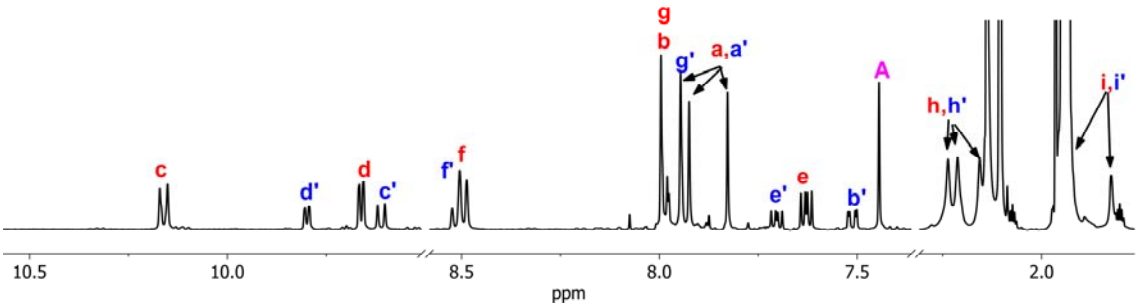

Figure 4.31 ^{1}H NMR spectrum (500 MHz, 298 K, CD_3CN) of $[Pd_4\mathbf{L^2}_6(BDC)_2]^{4+}$.

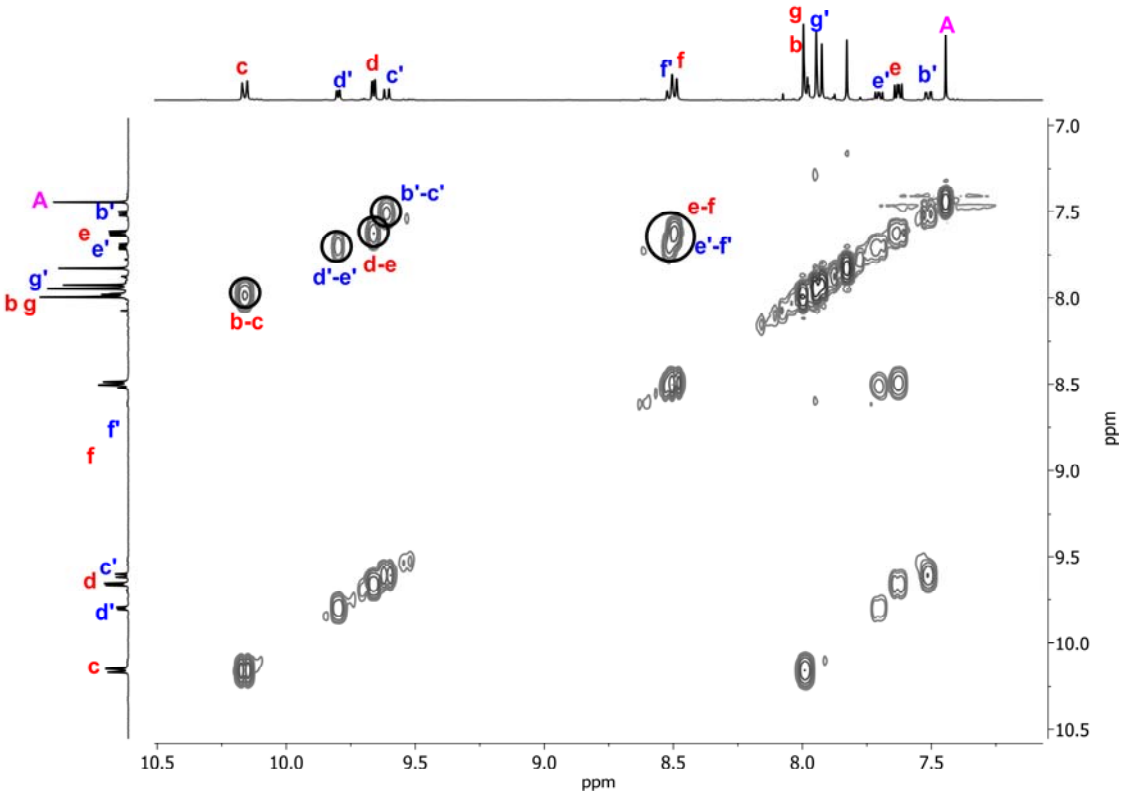

Figure 4.32 Partial ^{1}H – ^{1}H COSY spectrum (500 MHz, 298 K, CD_3CN) of $[Pd_4\mathbf{L^2}_6(BDC)_2]^{4+}$.

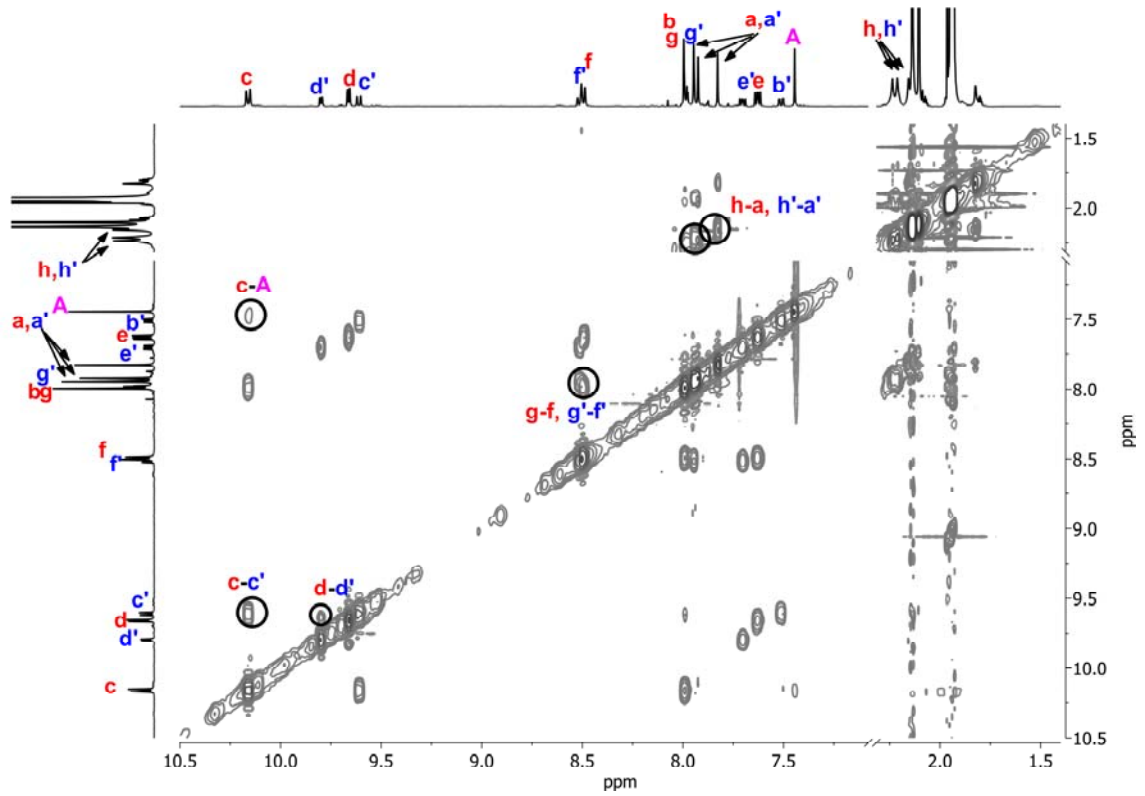

Figure 4.33 Partial $^{1}H - {}^{1}H$ NOESY spectrum (500 MHz, 298 K, CD_3CN) of $[Pd_4\mathbf{L^2}_6(BDC)_2]^{4+}$.

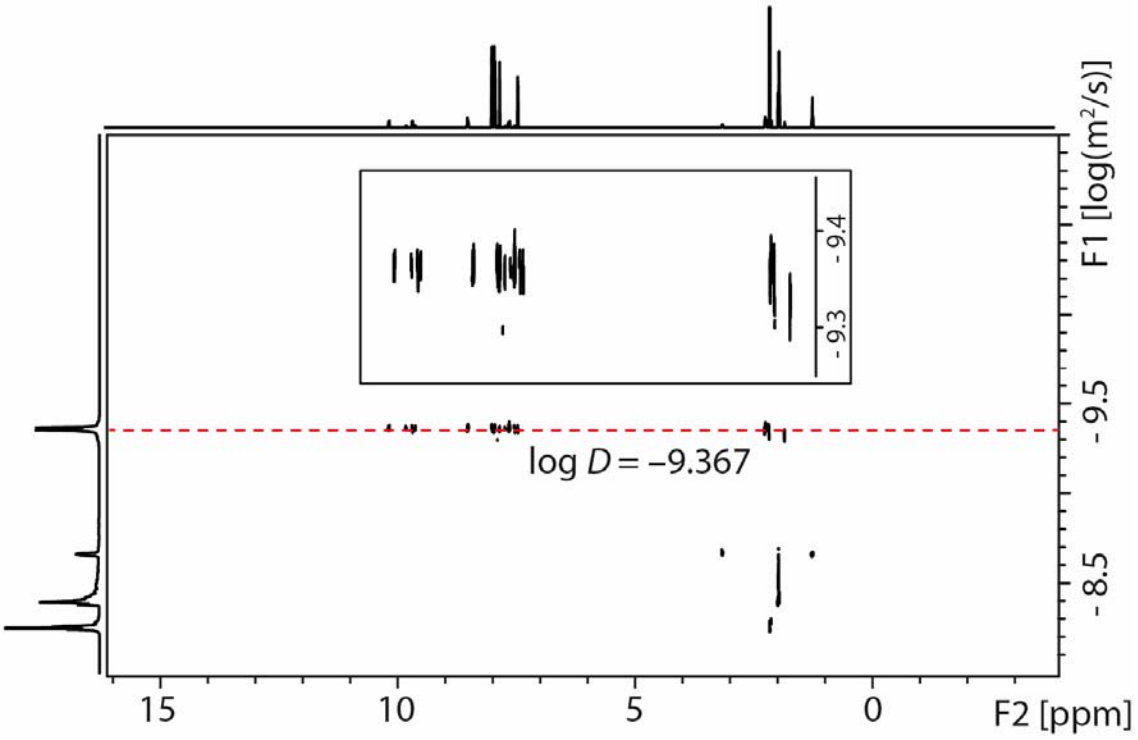

Figure 4.34 DOSY spectrum (500 MHz, 298 K, CD_3CN) of $[Pd_4\mathbf{L^2}_6(BDC)_2]^{4+}$: diffusion coefficient = 4.3 x 10^{-10} m^2s^{-1}, log *D* = −9.37, r = 14.8 Å.

ESI HRMS ($C_{256}H_{164}N_{24}O_{32}Pd_4B_4F_{16}$): $[Pd_4\mathbf{L^2}_6(BDC)_2]^{4+}$ calcd. for $C_{256}H_{164}N_{24}O_{32}Pd_4$ 1128.2015; found 1128.2084; $[Pd_4\mathbf{L^2}_6(BDC)_2{+}BF_4]^{3+}$ calcd. for $C_{256}H_{164}N_{24}O_{32}Pd_4BF_4$ 1533.2740; found 1533.2740.

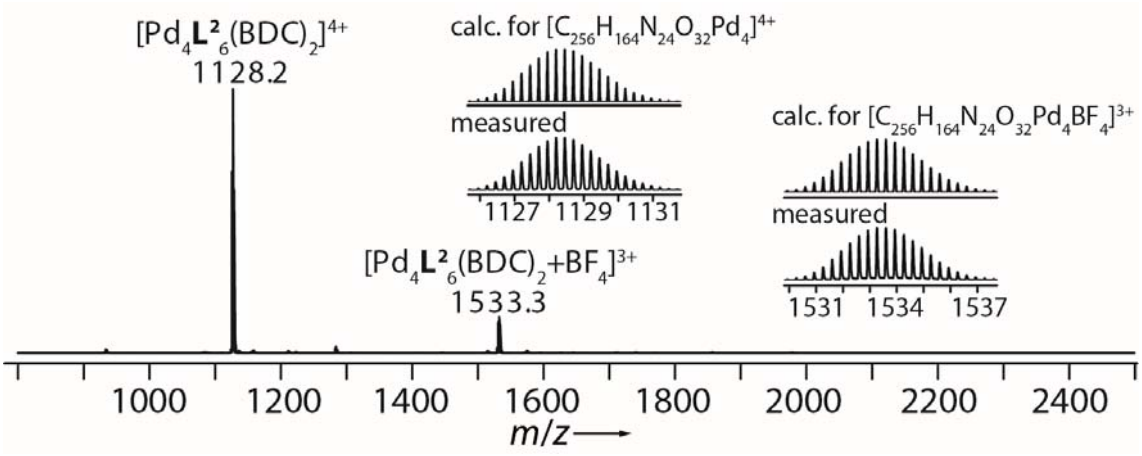

Figure 4.35 ESI mass spectrum of $[Pd_4\mathbf{L^2}_6(BDC)_2]^{4+}$.

4.7.4.2 Formation and characterization of dimer $[2C_{60}@Pd_4\mathbf{L^2}_6(BDC)_2]^{4+}$

The CD_3CN solution $[2C_{60}@Pd_4\mathbf{L^2}_6(BDC)_2]^{4+}$ (0.31 mM) was formed by stirring a mixture of the CD_3CN solution of $[C_{60}@Pd_2\mathbf{L^2}_3(MeCN)_2]^{4+}$ (500 µL, 0.64 mM, 0.32 µmol, 1 eq.) and CD_3CN solution of $(Et_3NH)_2BDC$ (21.3 µL, 15 mM, 0.32 µmol, 1 eq.) at room temperature for 2 min.

^{1}H NMR (600 MHz, 298 K, CD_3CN): δ (ppm) = 10.60 (d, J = 9.0 Hz, 8H), 9.95 (dd, J = 5.5, 1.4 Hz, 4H), 9.62 (dd, J = 5.5, 1.4 Hz, 8H), 9.43 (d, J = 8.9 Hz, 4H), 8.49 (d, J = 8.1 Hz, 8H), 8.41 (d, J = 8.5 Hz, 4H), 8.17 (dd, J = 8.9, 2.3 Hz, 8H), 8.06 (s, 8H), 8.04 (d, J = 2.3 Hz, 8H), 7.99 (s, 8H), 7.85 (d, J = 2.2 Hz, 4H), 7.82 (s, 8H), 7.81 (s, 8H), 7.71 (dd, J = 8.1, 5.6 Hz, 4H), 7.63 (dd, J = 8.1, 5.5 Hz, 8H), 7.10 (dd, J = 8.9, 2.3 Hz, 4H), 2.34 (s, 12H), 2.28 (s, 12H), 2.17 (s, mixed with water peak in CD_3CN), 1.72 (s, 8H).

Overlapping signals in the aliphatic region could be assigned via 2D NMR spectroscopy.

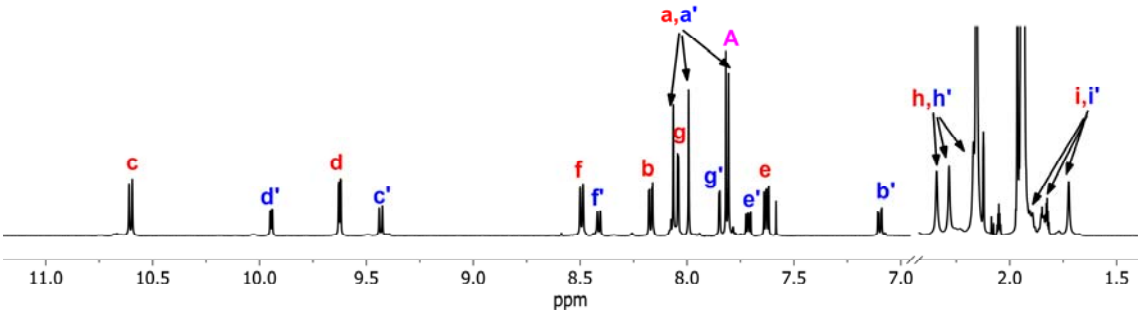

Figure 4.36 ^{1}H NMR spectrum (600 MHz, 298 K, CD_3CN) of $[2C_{60}@Pd_4\mathbf{L^2}_6(BDC)_2]^{4+}$.

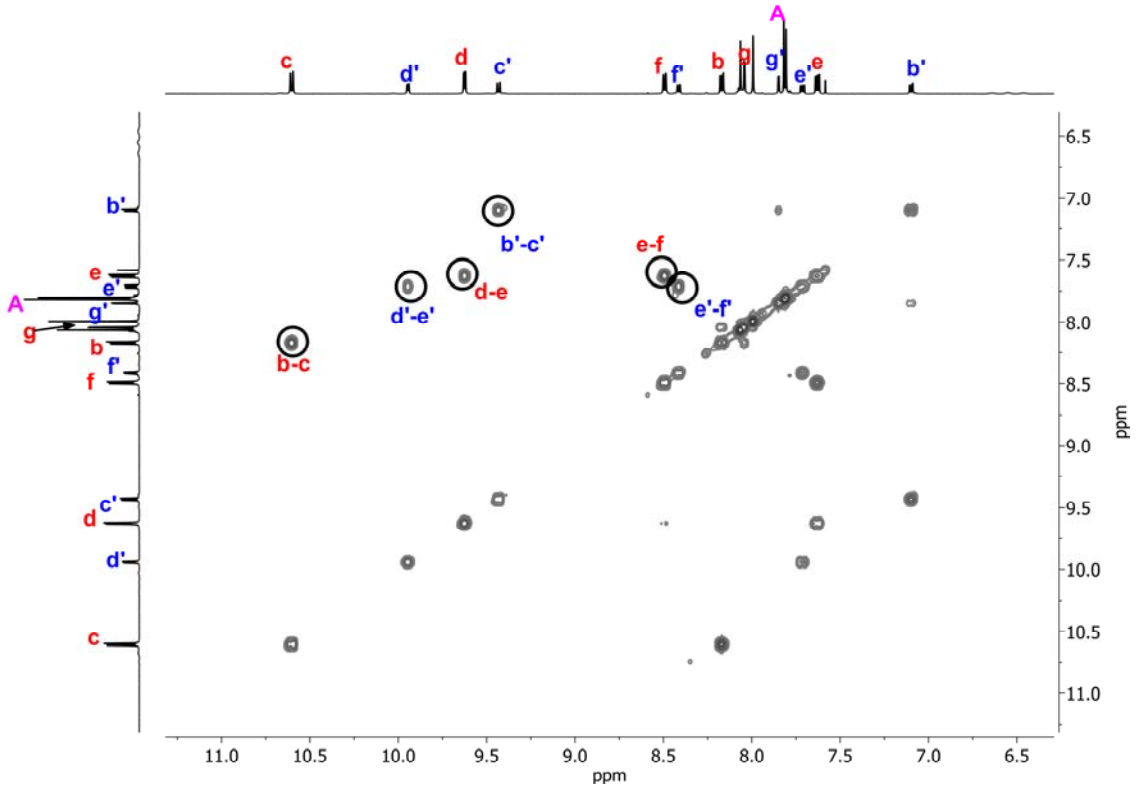

Figure 4.37 Partial $^{1}H - ^{1}H$ COSY spectrum (600 MHz, 298 K, CD_3CN) of $[2C_{60}@Pd_4\mathbf{L^2}_6(BDC)_2]^{4+}$.

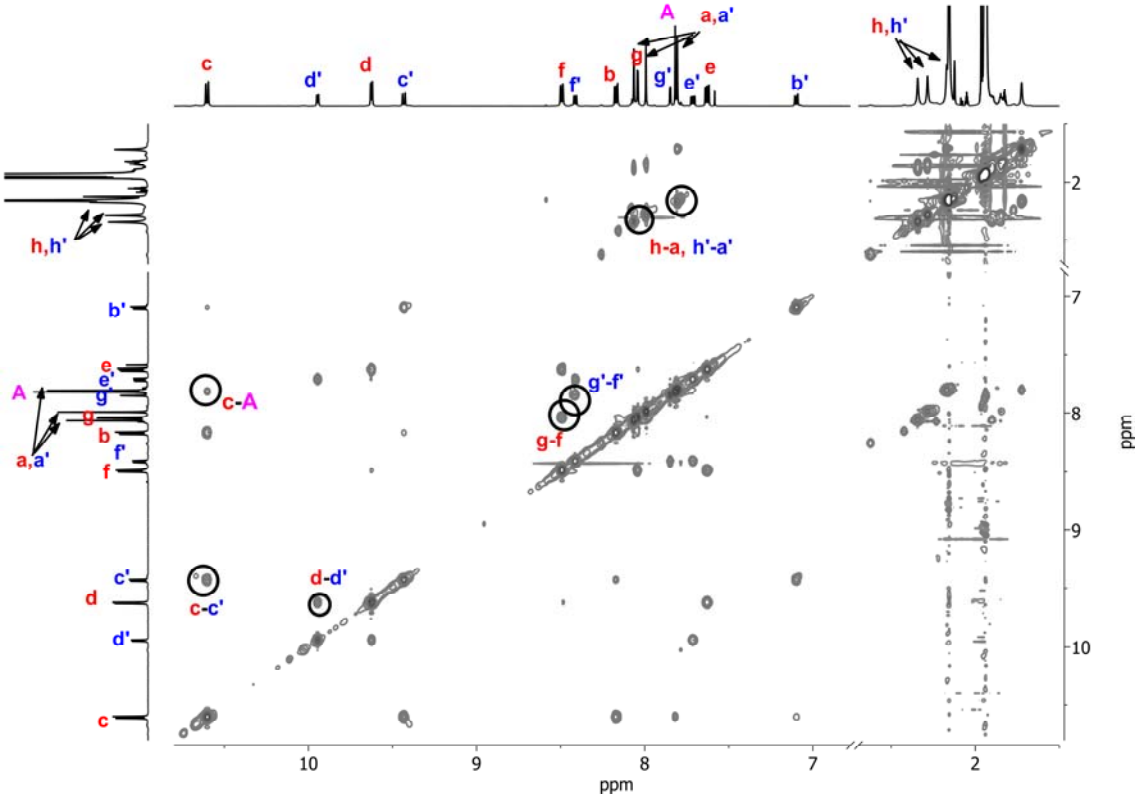

Figure 4.38 Partial $^{1}H - ^{1}H$ NOESY spectrum (600 MHz, 298 K, CD_3CN) of $[2C_{60}@Pd_4\mathbf{L^2}_6(BDC)_2]^{4+}$.

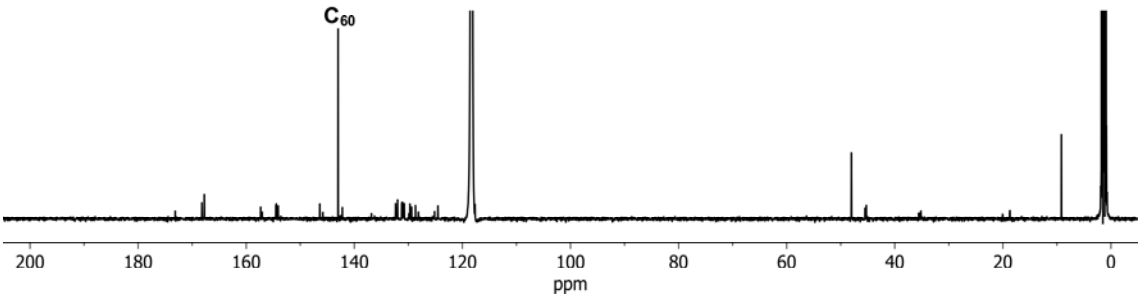

Figure 4.39 ^{13}C NMR spectrum (151 MHz, 298 K, CD_3CN) of $[2C_{60}@Pd_4\mathbf{L^2}_6(BDC)_2]^{4+}$. A single signal at 143.00 ppm corresponds to the encapsulated C_{60}.

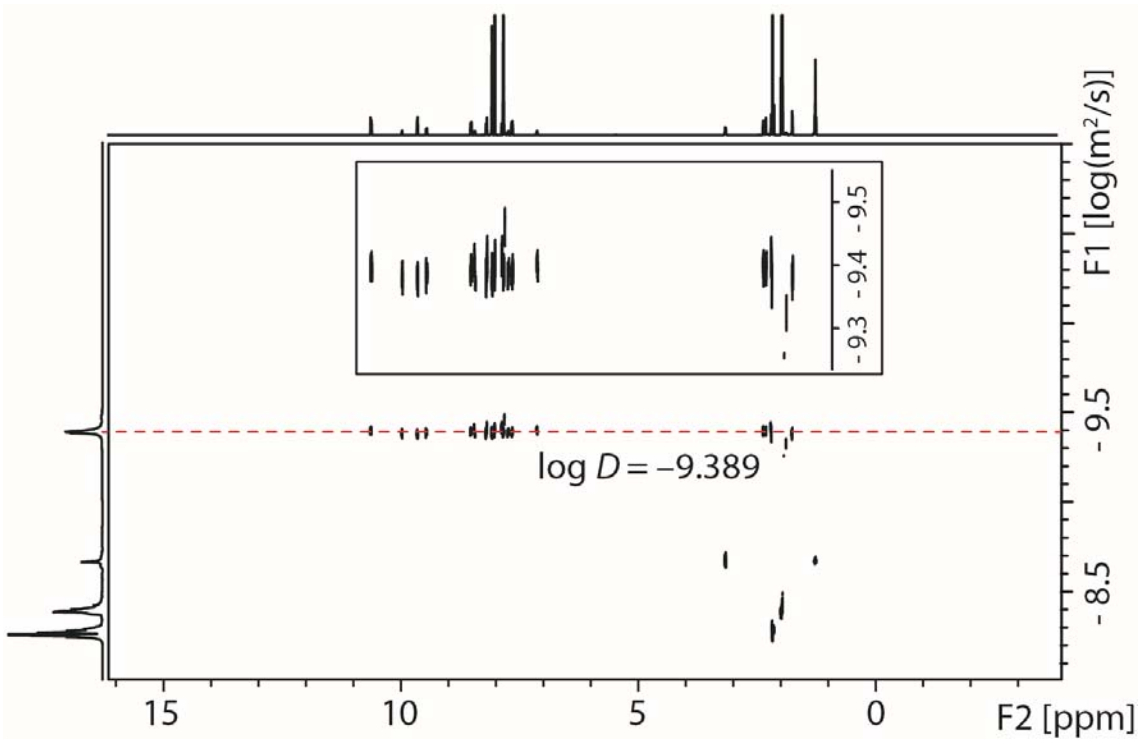

Figure 4.40 DOSY spectrum (500 MHz, 298 K, CD_3CN) of $[2C_{60}@Pd_4\mathbf{L^2}_6(BDC)_2]^{4+}$: diffusion coefficient = 4.1 x 10^{-10} m^2s^{-1}, log *D* = −9.39, r = 15.5 Å.

ESI HRMS ($C_{376}H_{164}N_{24}O_{32}Pd_4B_4F_{16}$): $[2C_{60}@Pd_4\mathbf{L^2}_6(BDC)_2]^{4+}$ calcd. for $C_{376}H_{164}N_{24}O_{32}Pd_4$ 1488.7056; found 1488.7194; $[2C_{60}@Pd_4\mathbf{L^2}_6(BDC)_2{+}BF_4]^{3+}$ calcd. for $C_{376}H_{164}N_{24}O_{32}Pd_4BF_4$ 2013.9422; found 2013.9602.

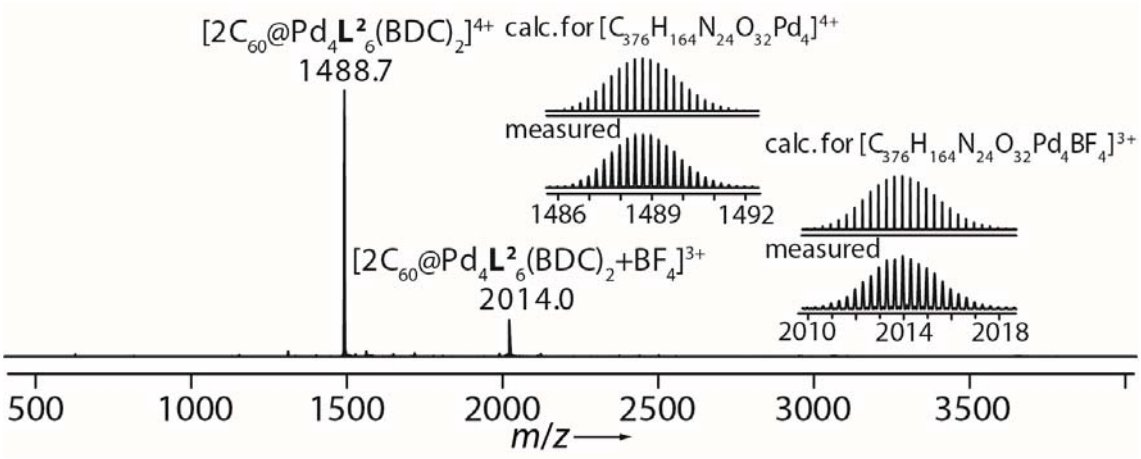

Figure 4.41 ESI mass spectrum of $[2C_{60}@Pd_4\mathbf{L^2}_6(BDC)_2]^{4+}$.

4.7.4.3 Formation and characterization of dimer $[2C_{70}@Pd_4L^2_6(BDC)_2]^{4+}$

The CD_3CN solution $[2C_{70}@Pd_4\mathbf{L^2}_6(BDC)_2]^{4+}$ (0.31 mM) was formed by stirring a mixture of the CD_3CN solution of $[C_{70}@Pd_2\mathbf{L^2}_3(MeCN)_2]^{4+}$ (500 µL, 0.64 mM, 0.32 µmol, 1 eq.) and CD_3CN solution of $(Et_3NH)_2BDC$ (21.3 µL, 15 mM, 0.32 µmol, 1 eq.) at room temperature for 2 min.

^{1}H NMR (600 MHz, 298 K, CD_3CN): δ (ppm) = 10.11 (d, *J* = 9.1 Hz, 8H), 9.86 (dd, *J* = 5.5, 1.4 Hz, 4H), 9.58 (dd, *J* = 5.4, 1.4 Hz, 8H), 8.98 (d, *J* = 9.1 Hz, 4H), 8.49 (dd, *J* = 8.1, 1.2 Hz, 8H), 8.46 (d, *J* = 8.3 Hz, 4H), 8.06 (s, 16H), 8.03 (d, *J* = 2.3 Hz, 8H), 7.91 – 7.89 (m, 12H), 7.84 (dd, *J* = 9.1, 2.3 Hz, 8H), 7.70 – 7.67 (m, 12H), 7.60 (dd, *J* = 8.3, 5.5 Hz, 8H), 6.90 (dd, *J* = 9.1, 2.3 Hz, 4H), 2.40 (s, 12H), 2.34 (s, 12H), 2.22 (s, 12H), 1.75 (s, 8H).

Overlapping signals in the aliphatic region could be assigned via 2D NMR spectroscopy.

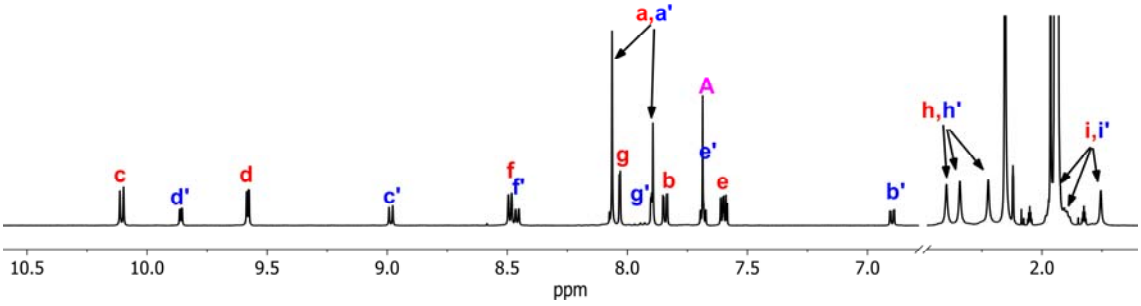

Figure 4.42 ^{1}H NMR spectrum (600 MHz, 298 K, CD_3CN) of $[2C_{70}@Pd_4\mathbf{L^2}_6(BDC)_2]^{4+}$.

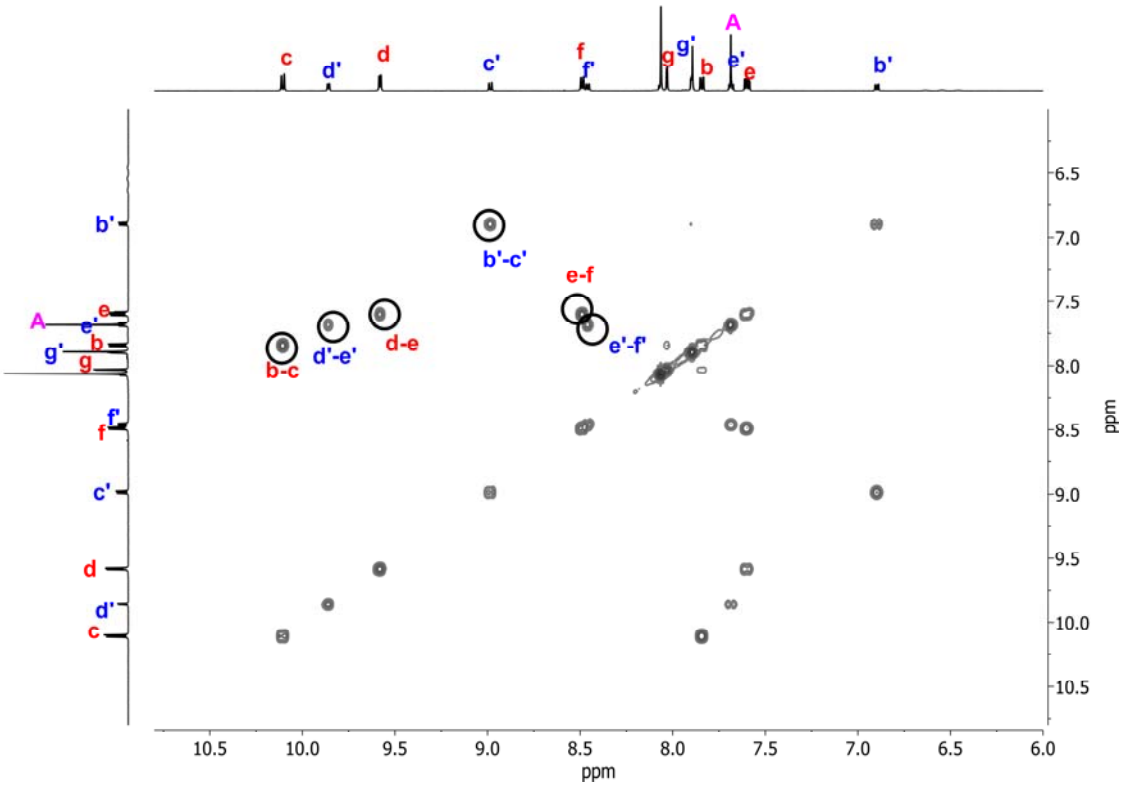

Figure 4.43 Partial $^{1}H - ^{1}H$ COSY spectrum (600 MHz, 298 K, CD_3CN) of $[2C_{70}@Pd_4\mathbf{L^2}_6(BDC)_2]^{4+}$.

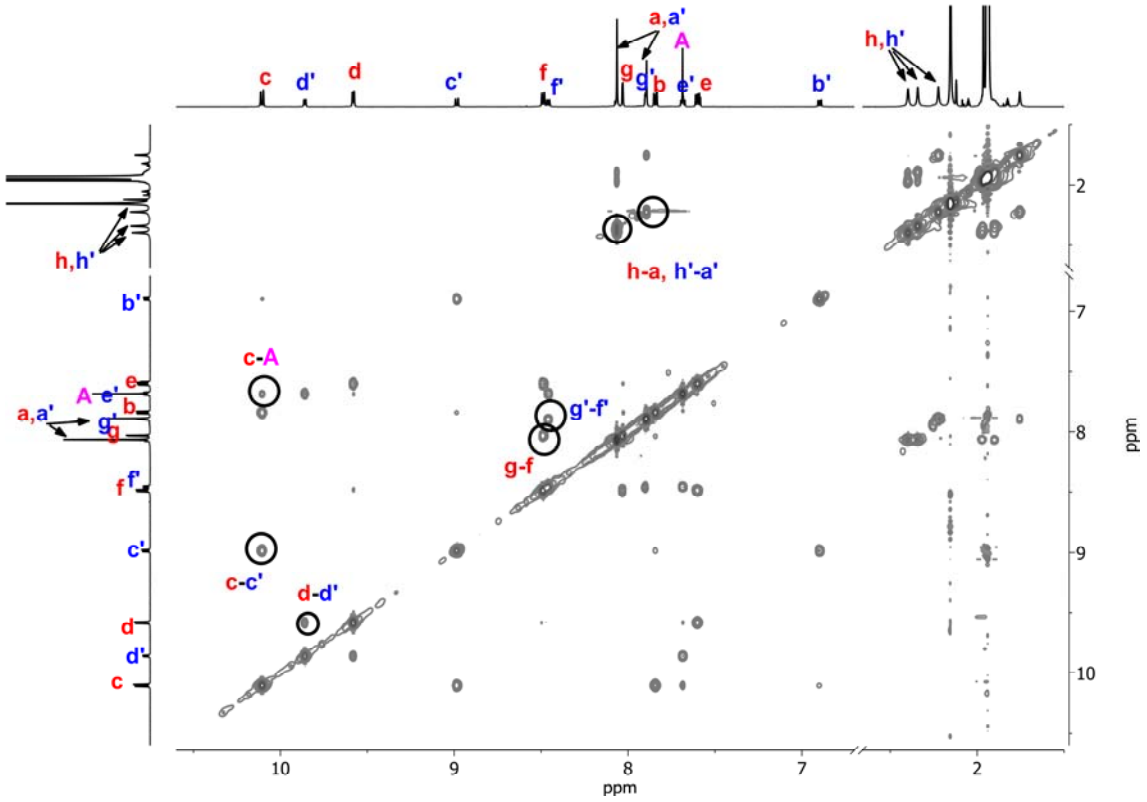

Figure 4.44 Partial $^{1}H - ^{1}H$ NOESY spectrum (600 MHz, 298 K, CD_3CN) of $[2C_{70}@Pd_4\mathbf{L^2}_6(BDC)_2]^{4+}$.

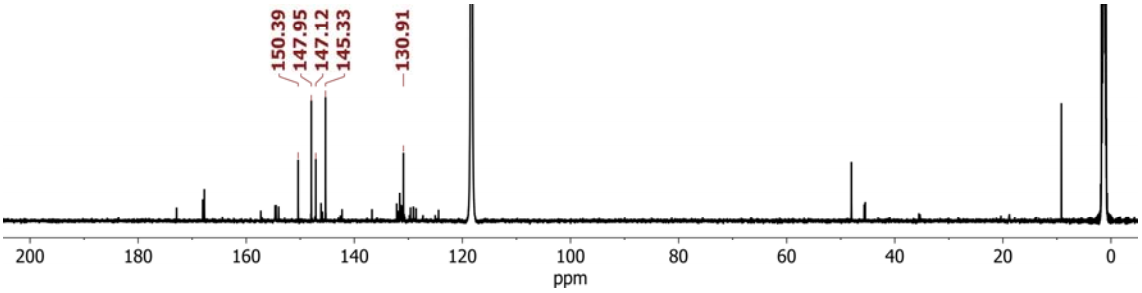

Figure 4.45 ^{13}C NMR spectrum (151 MHz, 298 K, CD_3CN) of $[2C_{70}@Pd_4\mathbf{L^2}_6(BDC)_2]^{4+}$. Five single signals at 150.39, 147.95, 147.12, 145.33, 130.91 ppm correspond to the encapsulated C_{70}.

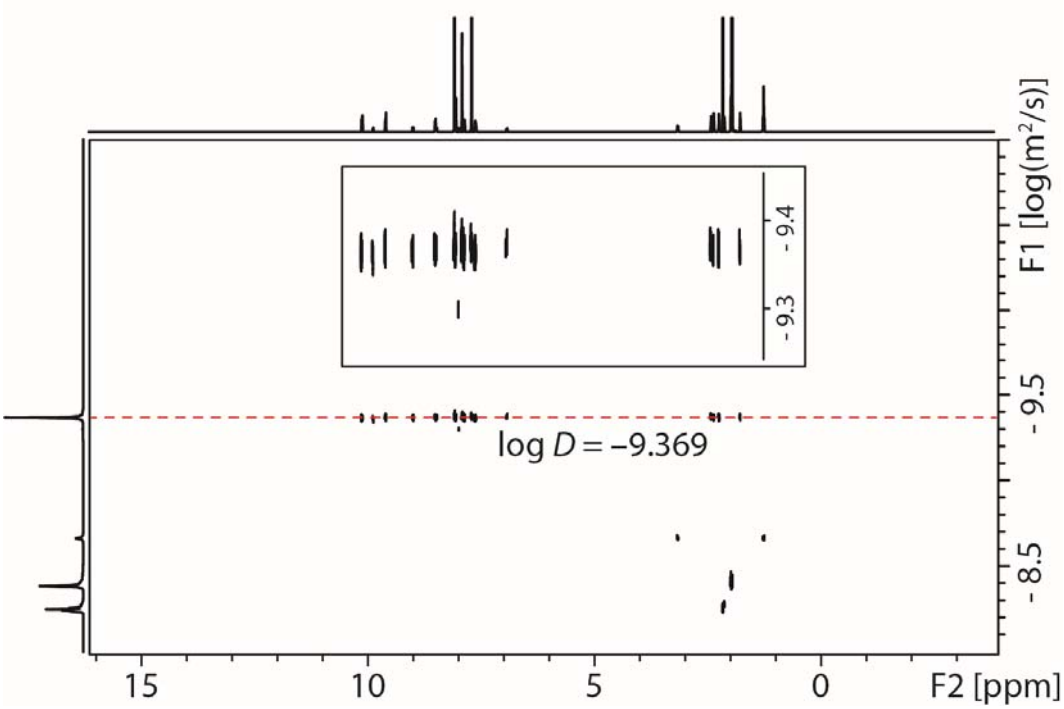

Figure 4.46 DOSY spectrum (500 MHz, 298 K, CD_3CN) of $[2C_{70}@Pd_4\mathbf{L^2}_6(BDC)_2]^{4+}$: diffusion coefficient = 4.3 x 10^{-10} m^2s^{-1}, log D = −9.37, r = 14.8 Å.

ESI HRMS ($C_{396}H_{164}N_{24}O_{32}Pd_4B_4F_{16}$): $[2C_{70}@Pd_4\mathbf{L^2}_6(BDC)_2]^{4+}$ calcd. for $C_{396}H_{164}N_{24}O_{32}Pd_4$ 1548.4563; found 1548.4679; $[2C_{70}@Pd_4\mathbf{L^2}_6(BDC)_2{+}BF_4]^{3+}$ calcd. for $C_{396}H_{164}N_{24}O_{32}Pd_4BF_4$ 2093.9424; found 2093.9582.

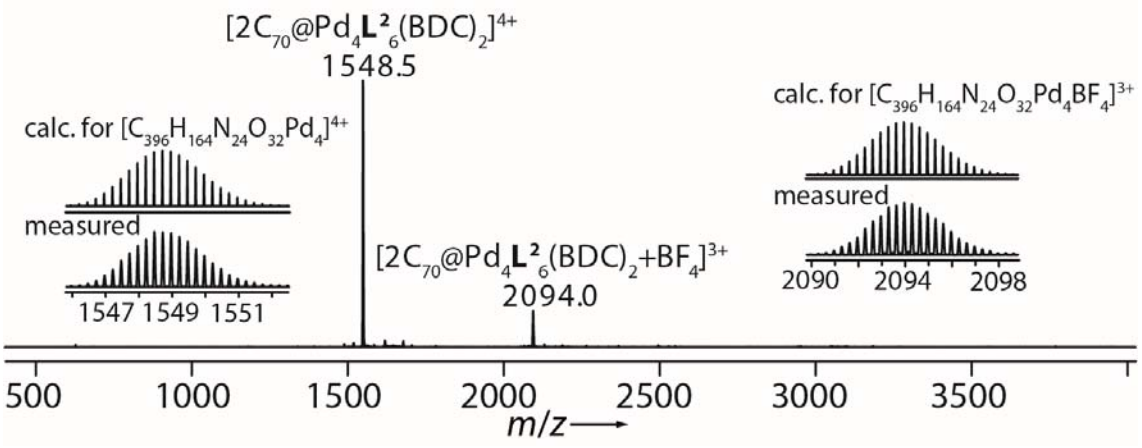

Figure 4.47 ESI mass spectrum of $[2C_{70}@Pd_4\mathbf{L^2}_6(BDC)_2]^{4+}$.

5 Heteroleptic cages based on naphthyridine donor ligand

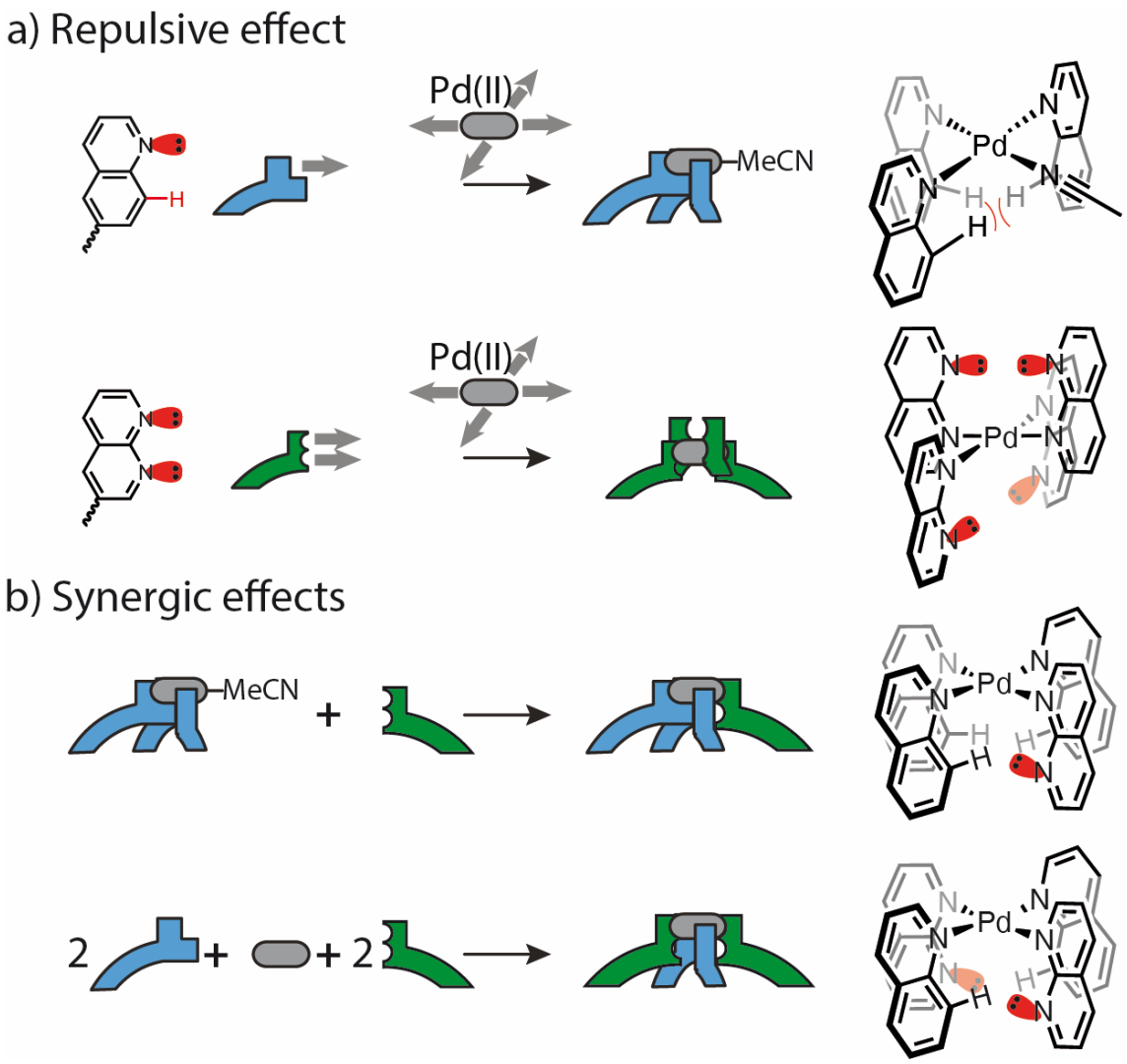

5.1 Introduction

The third chapter described a systemic study of Pd^{II}-mediated coordination self-assemblies of cage-, bowl- and ring-shaped metallosupramolecules, controlled by the steric effect originating from mutually repulsive hydrogen atoms of coordination groups. Inspired by these distinctly terminal-induced geometries in the process of self-assembly, another non-traditional nitrogen donor, namely 1,8-naphthyridine, was utilized as a novel donor group in this chapter. Of great interest are versatile coordination modes that can be possibly produced by this donor, including monodentate,[155-156] bidentate chelating[157-159] and bidentate bridging,[160-164] due to two syn-arranged nitrogen atoms with a short distance of ca. 2.2 Å. When multiple 1,8-naphthyridine donors coordinate to one metal ion in a monodentate fashion, it is

speculated that the electrostatic repulsion between electron-pairs in sp^2 orbitals of non-coordinating nitrogen atoms readily occur around the confined coordination center. In theory, this repulsion between directional electron-pairs surrounding an atom can alter the molecule's geometry to a certain extent, for instance in the H_2O molecule, wherein the H–O–H bond angle is squeezed to 104.5°, deviated away from the bond angle of 109.5° in the methane molecule. Experimentally, this repulsive effect between electron-pairs of adjacent terminals confined in the Pd^{II}-mediated coordination environment leads to dislocated arrangements of ligands in a coordination cage (Figure 5.1a).

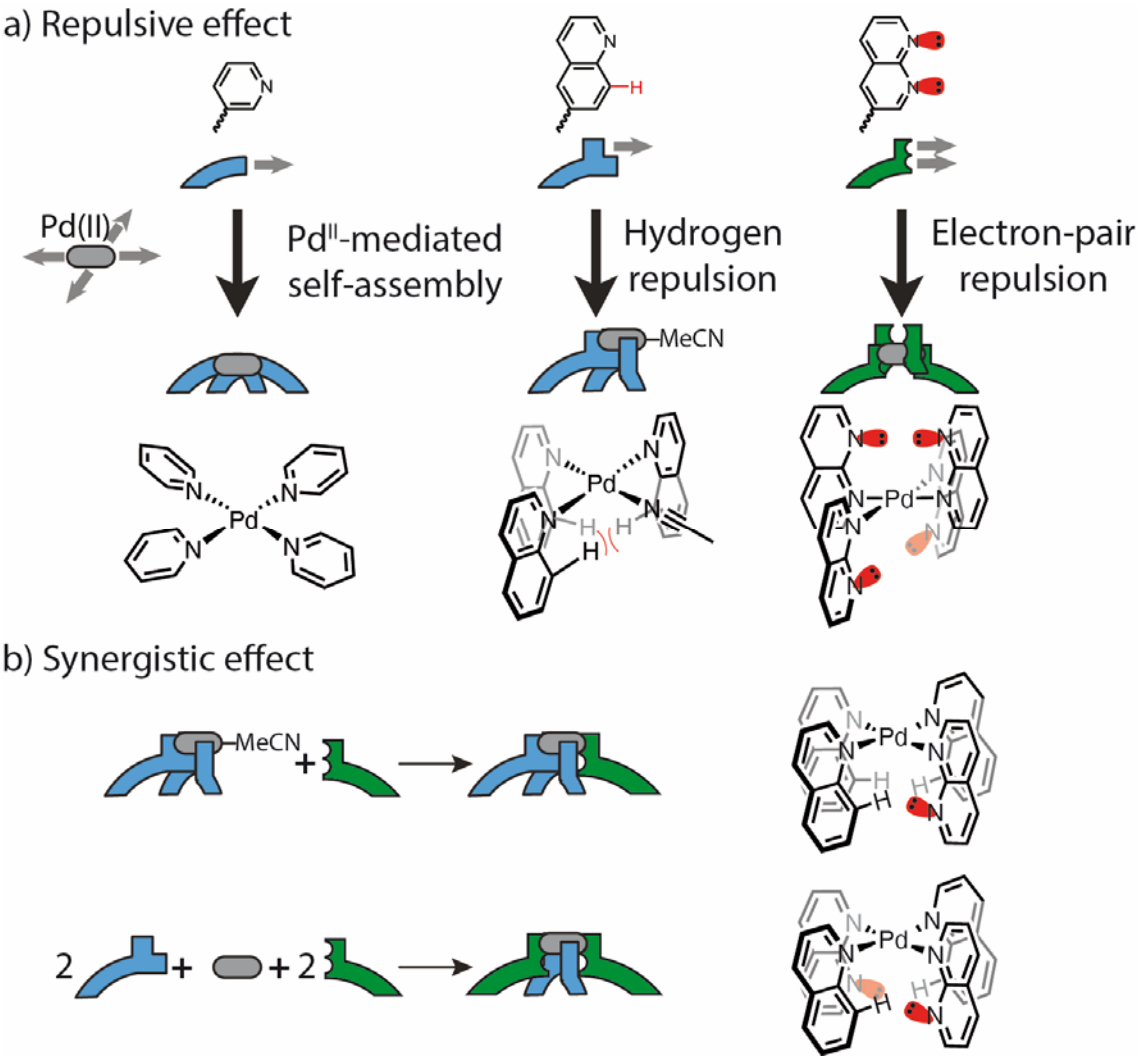

Figure 5.1 Terminal-induced self-assembly: (a) Repulsive effects influenced by directional hydrogen atoms or electron pairs in the congested Pd^{II}-mediated coordination center; (b) synergistic effects between protruding hydrogen atoms and electron-pairs of terminals.

From the perspective of structural diversity, these seemingly unfavorable repulsive effects stemming from adjacent hydrogen atoms or non-bonding electron-pairs in a congested coordination center, however, can induce the formation of diverse metallosupramolecular assemblies. More importantly, these two repulsive effects can be exploited to generate a synergistic effect via the electrostatic attraction between respective hydrogen atoms and lone-pair electrons. Indeed, the combination of quinoline donor ligand (**L^2**) and naphthyridine donor ligand (**L^5**) provides a novel route to access a heteroleptic cage system (Figure 5.1b). Moreover, compared with coordination interaction in the

supramolecular self-assembly, this kind of synergistic effect is still relatively weak and insufficient to result in the exclusive formation of one specific heteroleptic cage due to unfavorable entropic effects. For the purpose of further consolidating the synergy of multiple terminals, a template effect of fullerenes was also introduced to construct two heteroleptic cages effectively.[98]

In this chapter, I present an effective protocol to achieve heteroleptic cages, involving multiple effects: repulsive effect and synergistic effect of terminals as well as template effect of guest molecules, verified by NMR spectroscopy, mass spectrometry as well as X-ray crystallography.

5.2 Homoleptic cage assembly

Ligand **L^5** was prepared according to the proven procedure for other ligands (**L^1**–**L^4**): the dianhydride backbone reacted with excess 3-amino-1,8-naphthyridine at high temperature to afford the desired ligand **L^5** in the yield of 38 % after purification. This 1,8-naphthyridine donor potentially coordinates to metal ions in diverse fashions, rendering the bis-bidentate ligand **L^5** to show different behaviors in Pd^{II}-mediated supramolecular self-assembly, compared with normal banana-shaped ligands. To verify this hypothesis, titration of this ligand with a concentrated solution of $[Pd(MeCN)_4](BF_4)_2$ was performed in CD_3CN, suggesting that the sparingly soluble ligand **L^5** reacted with 0.5 eq. amount of Pd^{II} cations to give a clear solution and the produced species could exist even in the presence of excess Pd^{II} cations (Figure 5.7). ESI mass spectrum provided more convincible evidences, showing a series of peaks belonging to the cage with the formula of $[Pd_2\mathbf{L^5}_4+nBF_4]^{(4-n)+}$ (n = 0, 1, 2) (Figure 5.2b). In general, ^{1}H NMR spectra of normally encountered $[Pd_2L_4]^{4+}$ cages have only one set of ligand proton signals due to the D_{4h}-sysmmetry. However, analyses of 1D and 2D NMR spectra of cage $[Pd_2\mathbf{L^5}_4]^{4+}$ suggested two sets of splitting proton signals for naphthyridine moieties (H_b-H_f) as well as two single peaks of the methyl and methylene proton signals of the backbones (H_g, H_h) (Figure 5.2c). Besides, all these proton signals showed the same diffusion coefficient of 5.3 x 10^{-10} m^2s^{-1} in DOSY spectrum (Figure 5.11). These solution state studies encouraged us to confirm that 1,8-naphthyridine moieties coordinated to Pd^{II} cations in two different monodentate fashions, indicating that the relatively short distance (about 2.2 Å) between these two nitrogen atoms of the identical terminal did not allow them to coordinate to two large-sized Pd^{II} atoms concurrently.

For further verification of the coordination fashion, multiple attempts of crystallization had been done to achieve suitable crystals for X-ray structural analysis. Eventually, long needle crystals were obtained from the diffusion of isopropyl ether into an acetonitrile solution of $[Pd_2\mathbf{L^5}_4]^{4+}$ containing 10 eq. amount of SbF_6^- as counterions. The crystal structure of cage shows two crystallographically independent cages with slightly different Pd–Pd distances in the asymmetrical unit (Figure 5.31), and the cage geometry with a specially dislocated arrangement of ligands fully matches the NMR and MS results. Moreover, this coordination fashion of naphthyridine at both ends of the cage is fully consistent with a recently published crystal structure of $[Pt(Nap)_4](OTf)_2$.[165]

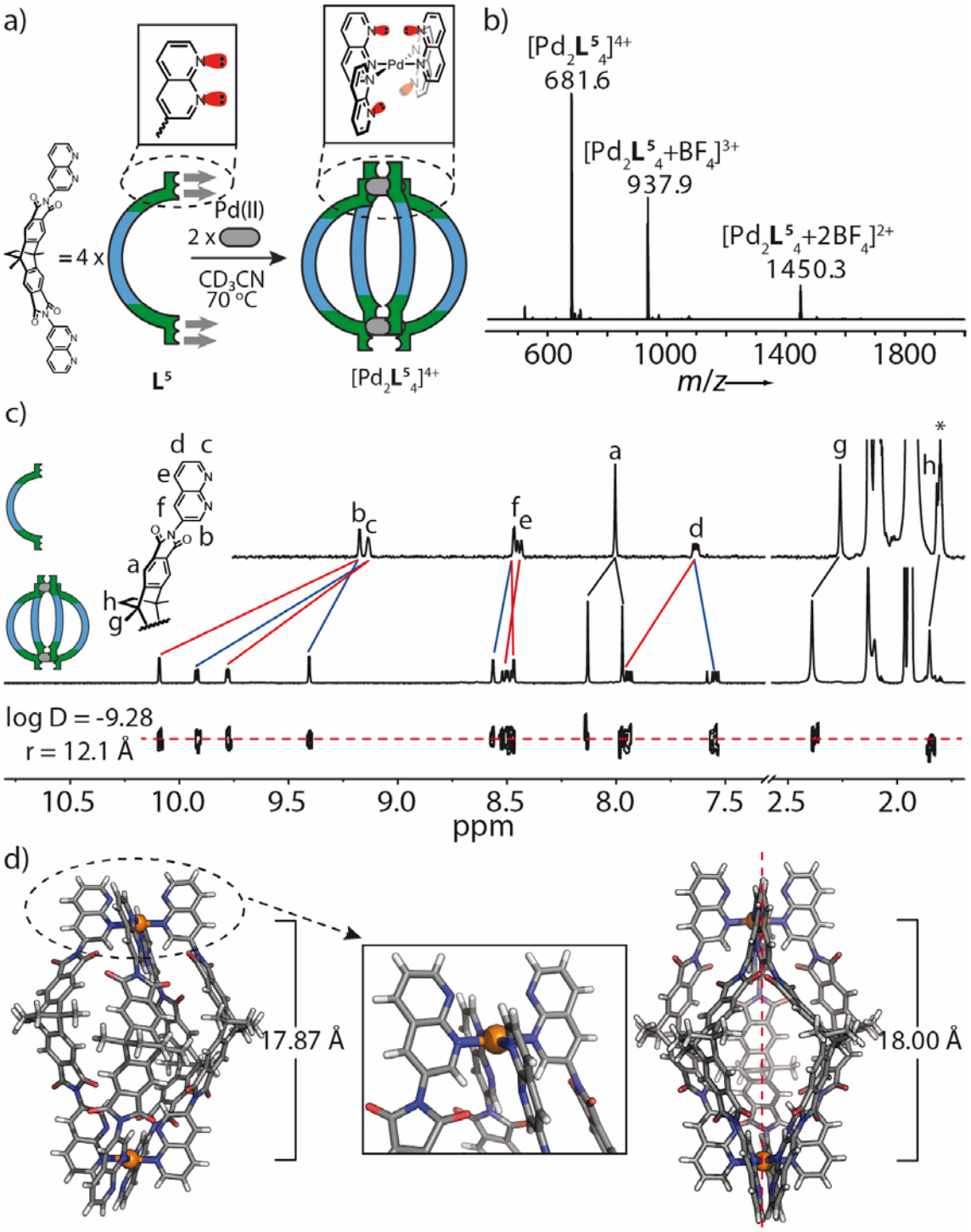

Figure 5.2 Self-assembly and characterization of homoleptic cage $[Pd_2\mathbf{L^5}_4]^{4+}$: (a) Self-assembly of cage $[Pd_2\mathbf{L^5}_4]^{4+}$ based on ligand $\mathbf{L^5}$ and Pd^{II} cations; (b) ESI high resolution mass spectrum of $[Pd_2\mathbf{L^5}_4]^{4+}$; (c) ^{1}H NMR spectra (600 MHz, 298 K, CD_3CN) of ligand $\mathbf{L^5}$ (saturated), cage $[Pd_2\mathbf{L^5}_4]^{4+}$ (0.64 mM); (d) X-ray structure of $[Pd_2\mathbf{L^5}_4]^{4+}$ showing two crystallographically independent cages as well as the dislocated coordination mode.

Another energetically unfavorable, but reasonable isomer of $[Pd_2\mathbf{L^5}_4]^{4+}$, i.e. with the Pd^{II} atoms coordinating to same positioned nitrogen atoms of all four ligands (Figure 5.32), was undetected. It was likely attributed to the remaining four non-coordinating nitrogen atoms located in the congested coordination center, thus generating a strong repulsion between their respective electron-pairs. For the sake of minimizing this kind of repulsive effect, the coordination

fashion with the dislocated arrangement is more energetically stable, as confirmed by DFT calculation: the cage geometry with the dislocated arrangement is 96.4 kJ/mol lower in energy than the congested coordination arrangement (Figure 5.32).

Meanwhile, the dislocated arrangement of ligands resulted in a cage $[Pd_2\mathbf{L^5}_4]^{4+}$ with a smaller cavity relative to the archetypical cage $[Pd_2\mathbf{L^1}_4]^{4+}$, as seen by the shorter vertical distance between inward-pointing hydrogen atoms (H_b). Consequently, it hampers the effective inclusion of C_{60} or C_{70}, as ascertained by fullerene binding tests of the cage $[Pd_2\mathbf{L^5}_4]^{4+}$ (Figure 5.25).

5.3 Heteroleptic cage assembly

Compared with the controlled self-assembly caused by the steric hindrance between adjacent hydrogen atoms as mentioned in the third chapter, the coordination-driven self-assembly of $[Pd_2\mathbf{L^5}_4]^{4+}$ exhibits an analogous repulsive effect, which is induced by electrostatic repulsion between electron-pairs. Additionally, these two repulsive effects, herein could be exploited to produce a synergistic effect between them conversely, inspired by a hydrogen bonding interaction between the electron-pair and the hydrogen atom.

An acetonitrile solution of bowl-shaped structure $[C_{70}@Pd_2\mathbf{L^2}_3(MeCN)_2]^{4+}$ was treated with one equivalent of $\mathbf{L^2}$ under prolonged heating to give a mixture of bowl $[C_{70}@Pd_2\mathbf{L^2}_3(MeCN)_2]^{4+}$ and cage $[C_{70}@Pd_2\mathbf{L^2}_4]^{4+}$ in about 4:1 ratio (Figure 3.48). In contrast, heating a 1:1 mixture of bowl $[C_{70}@Pd_2\mathbf{L^2}_3(MeCN)_2]^{4+}$ and $\mathbf{L^5}$ under the same condition led to the quantitative formation of heteroleptic cage $[C_{70}@Pd_2\mathbf{L^2}_3\mathbf{L^5}]^{4+}$ as a clear brown solution (Figure 5.3). The proton signals of $\mathbf{L^5}$ underwent obvious shifts, particularly for hydrogen atoms around the coordination center, upon the cage formation by capping the bowl structure. By means of 2D NMR spectra, all the proton signals in ^{1}H NMR spectrum were assigned. Further DOSY spectrum also confirmed the presence of cage $[C_{70}@Pd_2\mathbf{L^2}_3\mathbf{L^5}]^{4+}$ with the hydrodynamic radius of 12.5 Å (Figure 5.17). More convincingly, isotopic patterns of a series of signals with a consecutive addition of BF_4^- anions were fully consistent with the simulated ones in the ESI mass spectrum of cage $[C_{70}@Pd_2\mathbf{L^2}_3\mathbf{L^5}]^{4+}$.

In light of the remarkable performance of electronically complementary ligands $\mathbf{L^2}$ and $\mathbf{L^5}$ in the self-assembly of heteroleptic cage $[C_{70}@Pd_2\mathbf{L^2}_3\mathbf{L^5}]^{4+}$, we envisaged to employ this strategy to construct more heteroleptic cages via a simple stoichiometry controlled manner. Screening different ratios of Pd^{II} cations, ligand $\mathbf{L^2}$ and $\mathbf{L^5}$ in acetonitrile was performed and monitored by ^{1}H NMR spectra (Figure 5.26 and Table 5.2), suggesting that this kind of electronic interactions between terminals was not strong enough as expected to induce the exclusive formation of particular heteroleptic cages under the stoichiometric control.

Motivated by the proven template effect of fullerenes in the self-assembly of supramolecular architectures,[98, 166-167] fullerenes (C_{60} and C_{70}) were respectively added to the mixture of $Pd^{II}/\mathbf{L^2}/\mathbf{L^5}$ in different ratios (Figure 5.27 and Figure 5.28). Eventually, two heteroleptic cages could be obtained with high yields on the basis of NMR results: one was the A_3B-type cage, i.e. $[C_{70}@Pd_2\mathbf{L^2}_3\mathbf{L^5}]^{4+}$; another was the A_2B_2-type cage, i.e. $[C_{60}@Pd_2\mathbf{L^2}_2\mathbf{L^5}_2]^{4+}$.

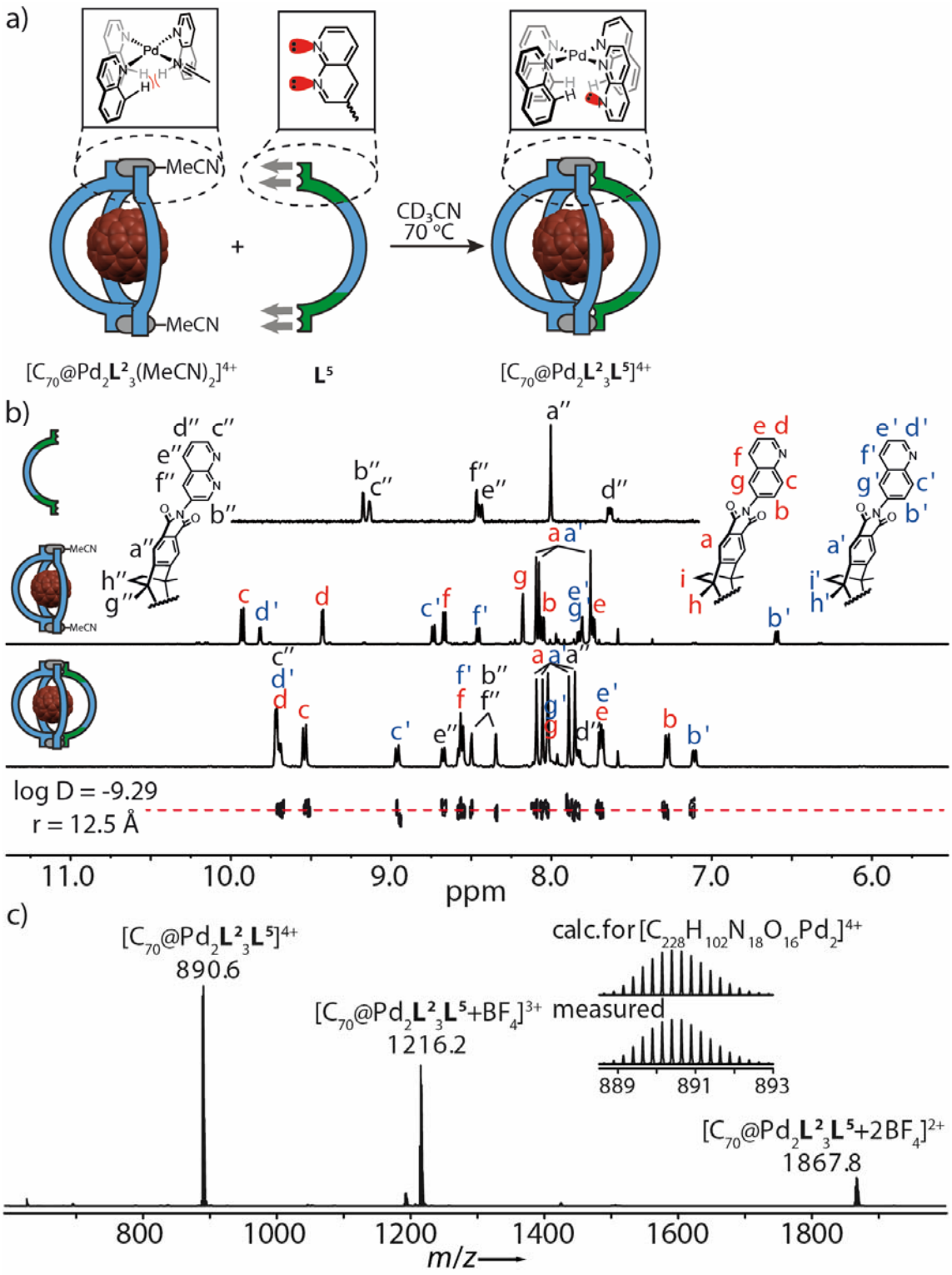

Figure 5.3 Self-assembly and characterization of heteroleptic cage $[C_{70}@Pd_2\mathbf{L^2}_3\mathbf{L^5}]^{4+}$: (a) Bowl $[C_{70}@Pd_2\mathbf{L^2}_3(MeCN)_2]^{4+}$ reacts with ligand $\mathbf{L^5}$ in a 1:1 ratio at 70°C to give cage $[C_{70}@Pd_2\mathbf{L^2}_3\mathbf{L^5}]^{4+}$; (b) ^{1}H NMR spectra (600 MHz, 298 K, CD_3CN) of ligand $\mathbf{L^5}$ (saturated), bowl $[C_{70}@Pd_2\mathbf{L^2}_3(MeCN)_2]^{4+}$ (0.64 mM) and cage $[C_{70}@Pd_2\mathbf{L^2}_3\mathbf{L^5}]^{4+}$ (0.64 mM); (c) ESI high resolution mass spectrum of $[C_{70}@Pd_2\mathbf{L^2}_3\mathbf{L^5}]^{4+}$.

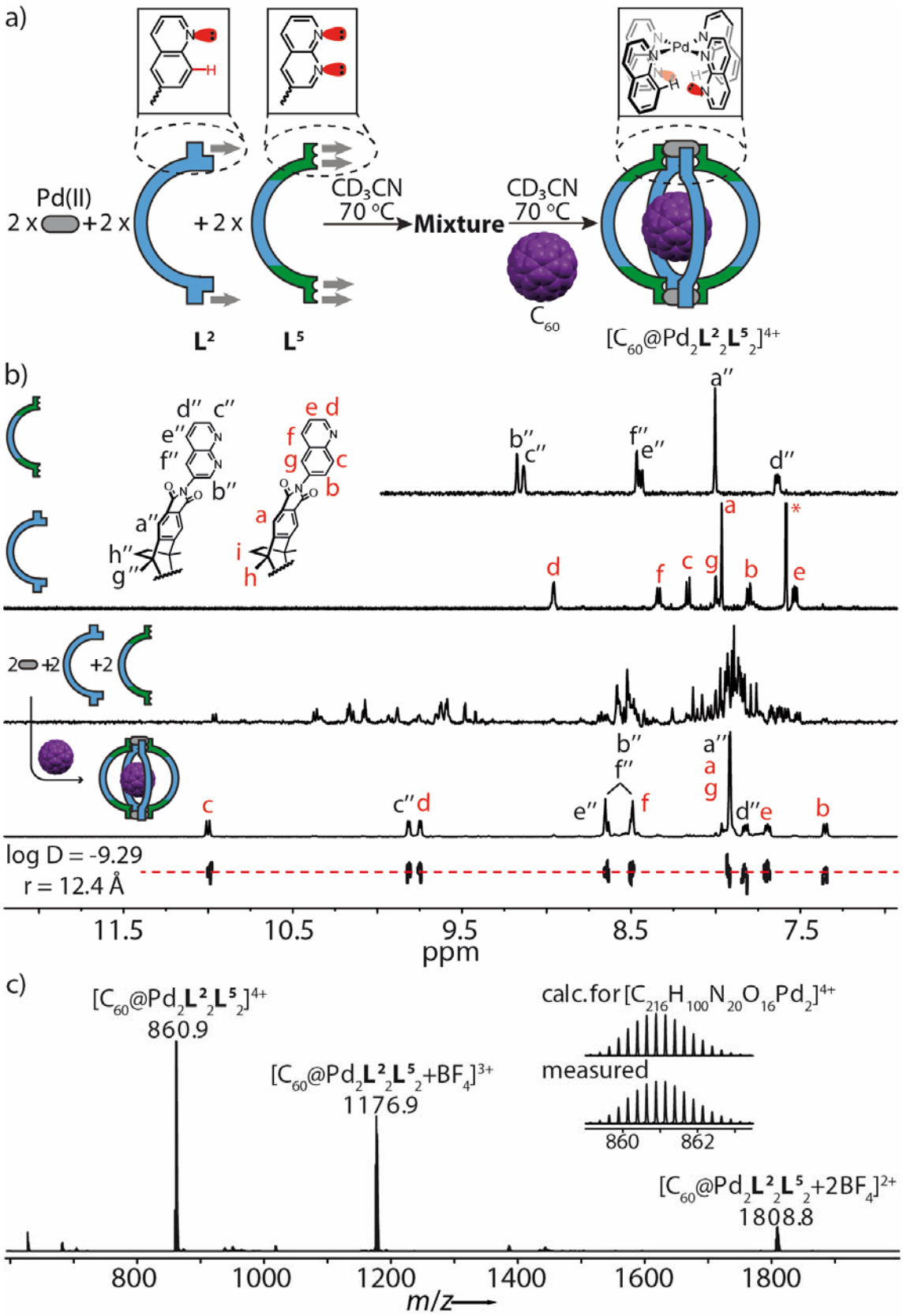

Figure 5.4 Self-assembly and characterization of heteroleptic cage $[C_{60}@Pd_2\mathbf{L^2}_2\mathbf{L^5}_2]^{4+}$: (a) Ligands $\mathbf{L^2}$ and $\mathbf{L^5}$ react with Pd^{II} cations in a 1:1:1 ratio at 70 °C to give a messy mixture, followed by the addition of C_{60}, leading to a social self-sorting of cage $[C_{60}@Pd_2\mathbf{L^2}_2\mathbf{L^5}_2]^{4+}$; (b) ^{1}H NMR spectra (600 MHz, 298 K, CD_3CN) of ligand $\mathbf{L^5}$ (saturated), ligand $\mathbf{L^2}$ (saturated), the reaction mixture based on $Pd^{II}/\mathbf{L^2}/\mathbf{L^5}$ in a 1:1:1 ratio , and cage $[C_{60}@Pd_2\mathbf{L^2}_2\mathbf{L^5}_2]^{4+}$ (0.64 mM); (c) ESI high resolution mass spectrum of $[C_{60}@Pd_2\mathbf{L^2}_2\mathbf{L^5}_2]^{4+}$.

As clearly shown in NMR spectra (Figure 5.29), heating a mixture of Pd^{II}/**L²**/**L⁵** in a 2:3:1 ratio for several days merely gave a messy result. Subsequent addition of C_{70} induced the mixture to transform into the cage $[C_{70}@Pd_2\mathbf{L^2}_3\mathbf{L^5}]^{4+}$ as a major species. However, impurities were more abundant than that achieved through a direct reaction of bowl $[C_{70}@Pd_2\mathbf{L^2}_3(MeCN)_2]^{4+}$ with **L⁵**, likely due to the preorganization of bowl geometry facilitating the structural conversion into cage $[C_{70}@Pd_2\mathbf{L^2}_3\mathbf{L^5}]^{4+}$.

Analogously, a 1:1:1 mixture of Pd^{II}/**L²**/**L⁵** reacted in acetonitrile at 70 °C also gave a messy ^{1}H NMR spectrum, followed by adding excess C_{60} powder to afford a concise spectrum (Figure 5.4b). Considering the resulting blue-violet solution as well as the stoichiometry of the added Pd^{II} cations and ligands, we hypothesized this new species with the formula of A_2B_2-type cage, $[C_{60}@Pd_2\mathbf{L^2}_2\mathbf{L^5}_2]^{4+}$. In addition, reasonable DOSY spectrum and ESI mass spectrum both favored the formation of this host-guest complex $[C_{60}@Pd_2\mathbf{L^2}_2\mathbf{L^5}_2]^{4+}$ (Figure 5.4c).

The analysis of 2D NMR spectra allowed for the assignment of all the proton signals (Figure 5.19), wherein the less and overlapped backbone proton signals (H_a, H_h, H_i for **L²**; $H_{a''}$, $H_{g''}$, $H_{h''}$ for **L⁵**) suggested the cage $[C_{60}@Pd_2\mathbf{L^2}_2\mathbf{L^5}_2]^{4+}$ featuring the high symmetry. Thus, the ligands' arrangement in A_2B_2-type cage could be in *trans*-configuration instead of *cis*-configuration. Moreover, DFT calculation also revealed *trans*-geometry was 13.6 kJ/mol lower in energy than *cis*-geometry (Figure 5.33). Noteworthy is that the chemical shift of quinoline proton H_c in cage $[C_{60}@Pd_2\mathbf{L^2}_2\mathbf{L^5}_2]^{4+}$ is up to 11.0 ppm, a pronounced downfield shift compared with that in other species (Table 5.1). This usual chemical shift of the proton H_c clearly indicates the deshielding effect of adjacent electron-pairs, a direct evidence of electrostatic attraction between quinoline and naphthyridine donors.

It is interesting to notice homoleptic cages based on ligand **L²** or **L⁵**, namely $[C_{60}@Pd_2\mathbf{L^2}_4]^{4+}$ and $[C_{60}@Pd_2\mathbf{L^5}_4]^{4+}$, cannot exist with C_{60} as the guest molecule, however, the heteroleptic cage $[C_{60}@Pd_2\mathbf{L^2}_2\mathbf{L^5}_2]^{4+}$ allows to stably bind C_{60} within the cavity. This highlights the importance of the synergistic effect between electronic complementary terminals (quinoline and naphthyridine) along with the guest to accomplish heteroleptic cage $[C_{60}@Pd_2\mathbf{L^2}_2\mathbf{L^5}_2]^{4+}$.

5.4 Conclusion

Based on the strategy of controlled self-assembly by steric effects as mentioned in the third chapter, the 1,8-naphthyridine was introduced herein as a novel coordination group with the repulsive effect between electron-pairs of non-coordinating nitrogen atoms around the Pd^{II}-coordination center, hence resulting in the formation of uniquely dislocated arrangements of ligands. Moreover, the synergistic effect between quinoline and naphthyridine donors allowed for the readily transformation of bowl geometry into cage geometry, an efficient protocol to achieve the relatively closed systems as well as their internal cavity. Further investigation revealed that this synergistic effect could not determine the exclusive formation of particular heteroleptic cages under stoichiometry control, which additionally entailed the contribution from the template effect of guest molecules. In summary, three different effects—repulsive effect and synergistic effect of terminals as well as template effect of guests, were employed in the self-assemblies of one homoleptic cage and two heteroleptic cages in a comprehensive manner. These strategies will certainly pave the

way for the construction of more heteroleptic supramolecules in the near future, advancing their complexity and functionality.

5.5 Experimental section

5.5.1 Synthesis and characterization

5.5.1.1 Ligand L[5]

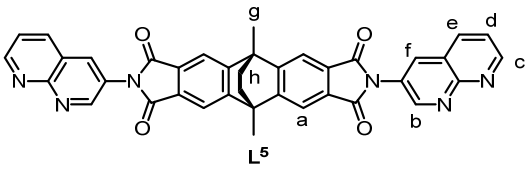

Under a nitrogen atmosphere, ligand **L[5]** was prepared from reported bis-anhydride **S1** (74.8 mg, 0.20 mmol, 1 eq.) and powdered 3-amino-1,8-naphthyridine (145.2 mg, 1.00 mmol, 5 eq.) by heating the mixture of solids without solvent in a preheated oil bath to 170 °C for 10 min. After the black melt cooled to room temperature, it was taken up into 10 mL chloroform, sonificated and the suspension was immediately subjected to flash column chromatography on silica gel ($CHCl_3$: MeOH = 50 : 1) to give the crude product. This was further purified via recycling gel permeation chromatography and the solvent was removed under reduced pressure to yield the desired product as a white powder (48.3 mg, 38 %).

^{1}H NMR (600 MHz, 298 K, $CDCl_3$): δ (ppm) = 9.31 (d, J = 2.7 Hz, 2H), 9.20 (dd, J = 4.3, 1.9 Hz, 2H), 8.39 (d, J = 2.7 Hz, 2H), 8.32 (dd, J = 8.2, 2.0 Hz, 2H), 8.01 (s, 4H), 7.60 (dd, J = 8.2, 4.2 Hz, 2H), 2.25 (s, 6H), 1.83 (s, 4H).

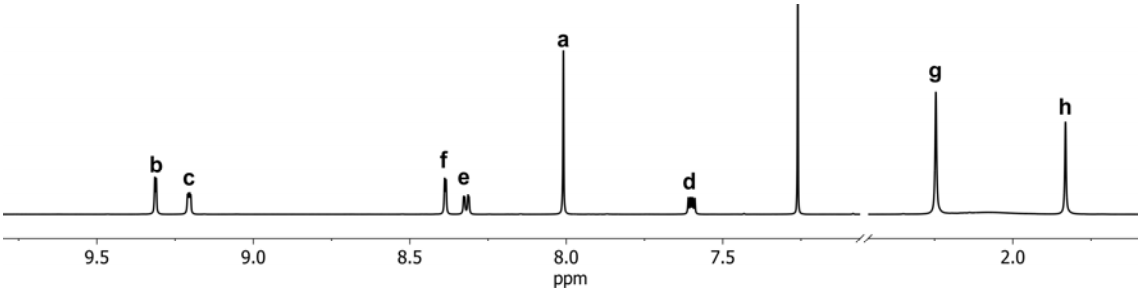

Figure 5.5 ^{1}H NMR spectrum (600 MHz, 298 K, $CDCl_3$) of **L[5]**.

^{13}C NMR (151 MHz, 298 K, $CDCl_3$): δ (ppm) = 166.96, 154.22, 153.95, 153.03, 151.24, 137.91, 132.97, 130.06, 126.95, 122.95, 122.51, 117.12, 44.46, 34.97, 18.86.

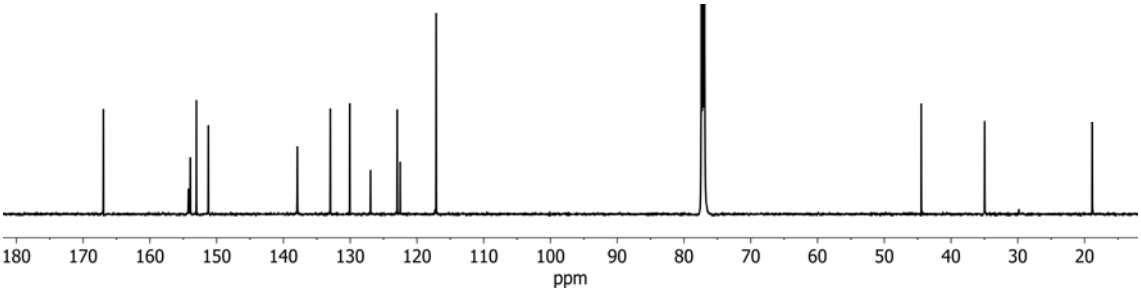

Figure 5.6 ^{13}C NMR spectrum (151 MHz, 298 K, $CDCl_3$) of **L^5**.

ESI HRMS ($C_{38}H_{24}N_6O_4$): $[M + H]^+$ calcd. for $C_{38}H_{25}N_6O_4$ 629.1932; found 629.1910; $[M + 2H]^{2+}$ calcd. for $C_{38}H_{26}N_6O_4$ 315.1002; found 315.0995.

5.5.1.2 Titration of ligand L^5 with $[Pd(MeCN)_4](BF_4)_2$

The sparingly soluble ligand **L^5** (1.1 mg, 1.80 µmol, 1 eq.) in CD_3CN solution (642 µL) was titrated with a concentrated CD_3CN solution of $[Pd(MeCN)_4](BF_4)_2$ (15 mM). Upon each addition of 0.25 eq. $[Pd(MeCN)_4](BF_4)_2$ (15 mM, 30.0 µL, 0.45 µmol), the solution was shaken and heated at 70 °C for 1 d before acquiring the spectrum, which allowed equilibrium to be reached.

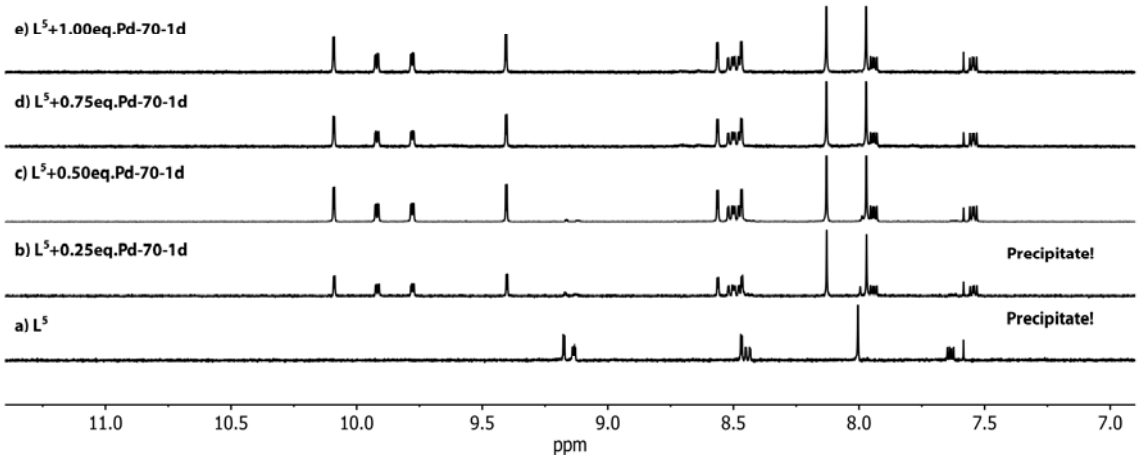

Figure 5.7 ^1H NMR titration (500 MHz, 298 K, CD_3CN) of **L^5** with $[Pd(MeCN)_4](BF_4)_2$. Upon addition of 0.5 eq. $[Pd(MeCN)_4](BF_4)_2$, the solution became clear without precipitate remaining in the bottom. No chemical shifts of proton signals were observed in spectra after continuous addition of Pd^{II} cations.

5.5.1.3 Homoleptic cage $[Pd_2L^5_4]^{4+}$

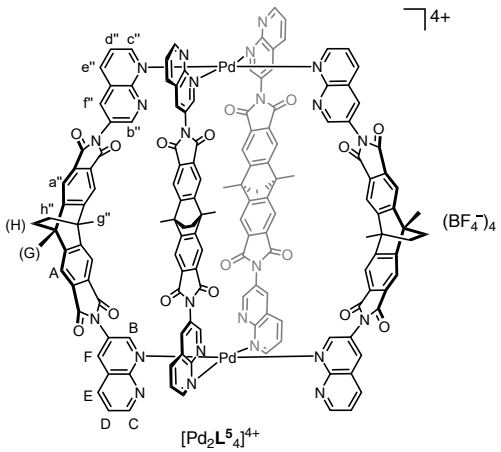

A solution of $[Pd(MeCN)_4](BF_4)_2$ (166.0 µL, 15 mM/CD_3CN, 2.49 µmol, 1 eq.) was combined with ligand **L⁵** (3.1 mg, 4.98 µmol, 2 eq.) in CD_3CN (1778 µL) and heated at 70 °C for 1 d to give a 0.64 mM solution of cage $[Pd_2L^5_4]^{4+}$.

^{1}H NMR (600 MHz, 298 K, CD_3CN): δ (ppm) = 10.09 (d, *J* = 2.4 Hz, 4H), 9.92 (dd, *J* = 5.4, 1.7 Hz, 4H), 9.78 (dd, *J* = 4.5, 1.8 Hz, 4H), 9.40 (d, *J* = 2.5 Hz, 4H), 8.56 (d, *J* = 2.5 Hz, 4H), 8.51 (dd, *J* = 8.3, 1.7 Hz, 4H), 8.49 (dd, *J* = 8.3, 1.8 Hz, 4H), 8.47 (d, *J* = 2.4 Hz, 4H), 8.13 (s, 8H), 7.97 (s, 8H), 7.94 (dd, *J* = 8.1, 4.5 Hz, 4H), 7.55 (dd, *J* = 8.1, 5.4 Hz, 4H), 2.39 (s, 24H), 1.85 (s, 16H).

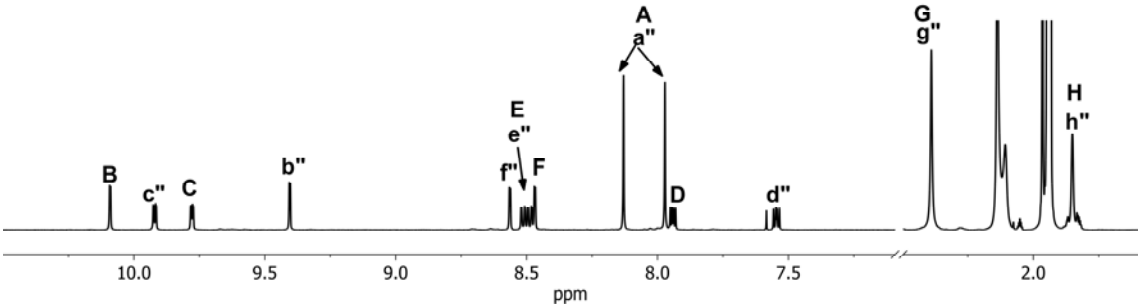

Figure 5.8 ^{1}H NMR spectrum (600 MHz, 298 K, CD_3CN) of $[Pd_2L^5_4]^{4+}$.

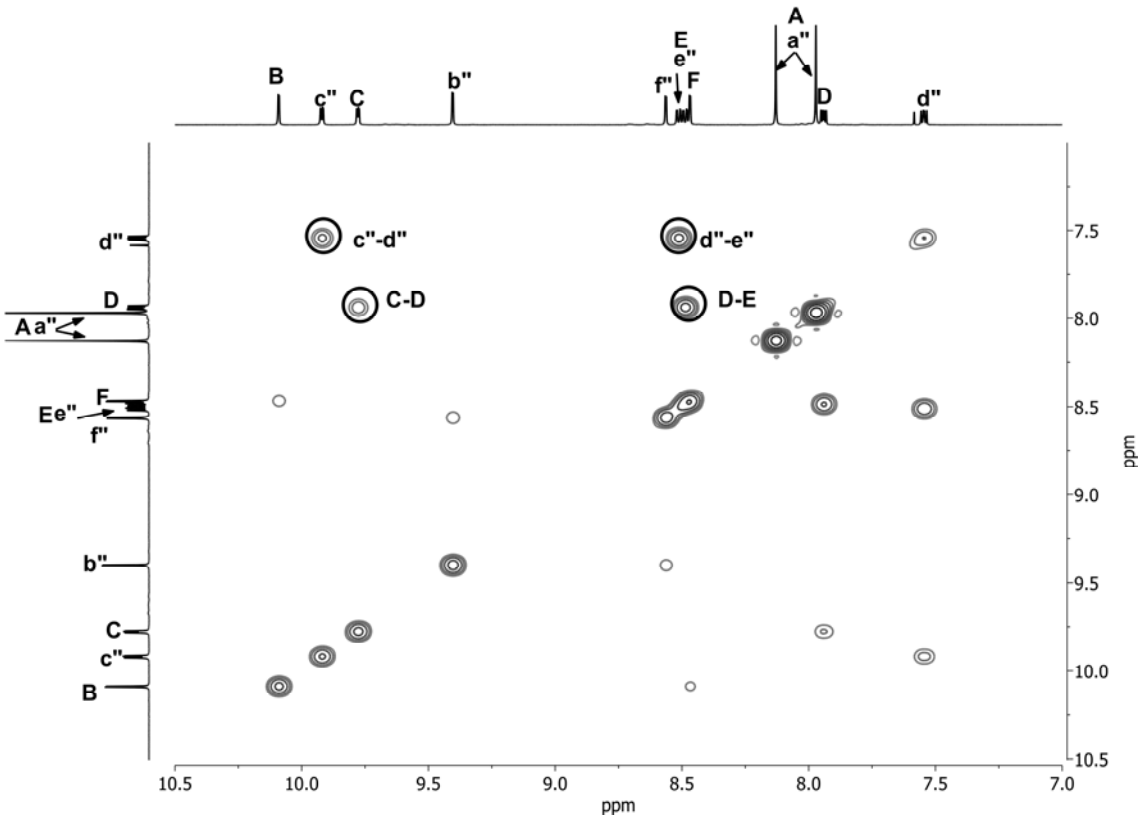

Figure 5.9 Partial $^{1}H - {}^{1}H$ COSY spectrum (600 MHz, 298 K, CD_3CN) of $[Pd_2\mathbf{L^5}_4]^{4+}$.

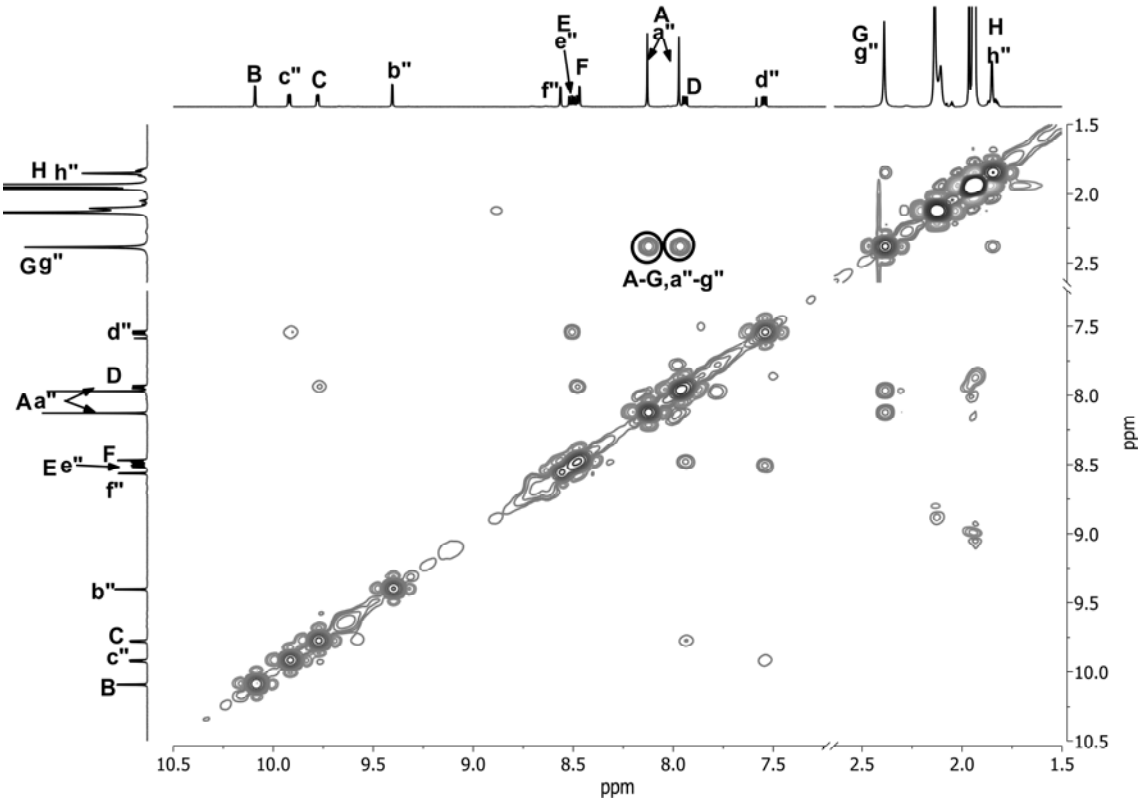

Figure 5.10 Partial $^{1}H - {}^{1}H$ NOESY spectrum (600 MHz, 298 K, CD_3CN) of $[Pd_2\mathbf{L^5}_4]^{4+}$.

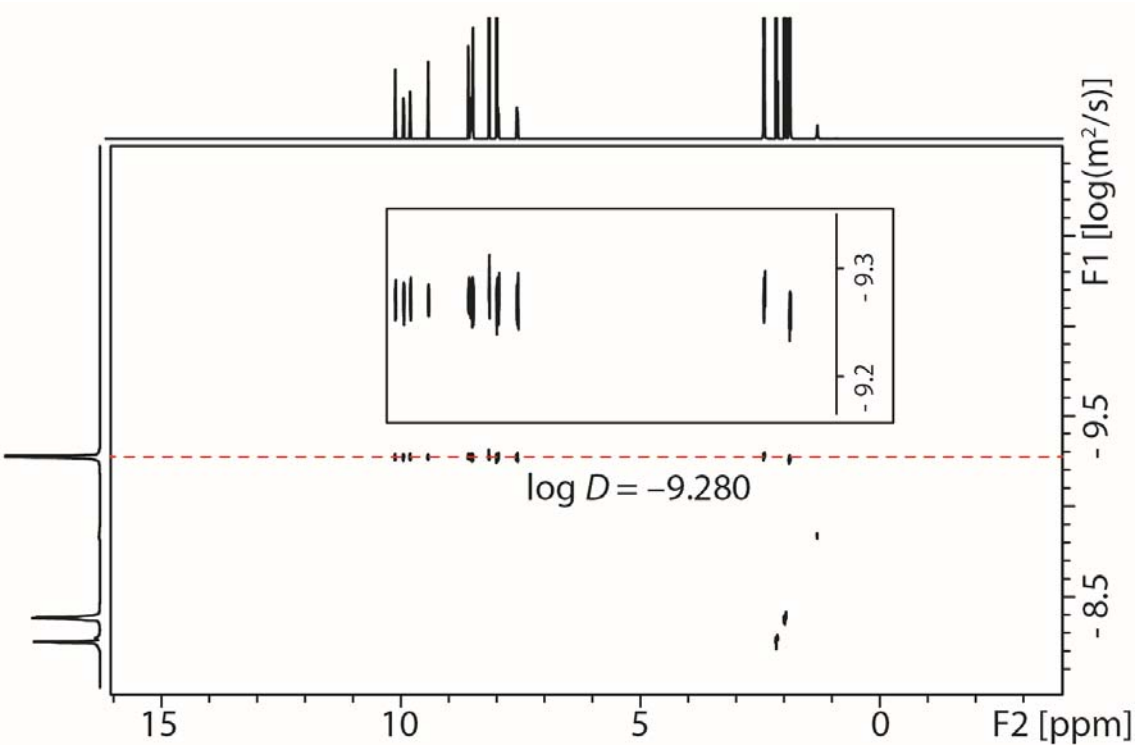

Figure 5.11 DOSY spectrum (500 MHz, 298 K, CD_3CN) of $[Pd_2\mathbf{L^5}_4]^{4+}$: diffusion coefficient = 5.3 x 10^{-10} m^2s^{-1}, log *D* = –9.28, r = 12.1 Å.

ESI HRMS ($C_{152}H_{96}N_{24}O_{16}Pd_2B_4F_{16}$): $[Pd_2\mathbf{L^5}_4]^{4+}$ calcd. for $C_{152}H_{96}N_{24}O_{16}Pd_2$ 681.6386; found 681.6375; $[Pd_2\mathbf{L^5}_4+BF_4]^{3+}$ calcd. for $C_{152}H_{96}N_{24}O_{16}Pd_2BF_4$ 937.8529; found 937.8503; $[Pd_2\mathbf{L^5}_4+2BF_4]^{2+}$ calcd. for $C_{152}H_{96}N_{24}O_{16}Pd_2B_2F_8$ 1450.2815; found 1450.2760.

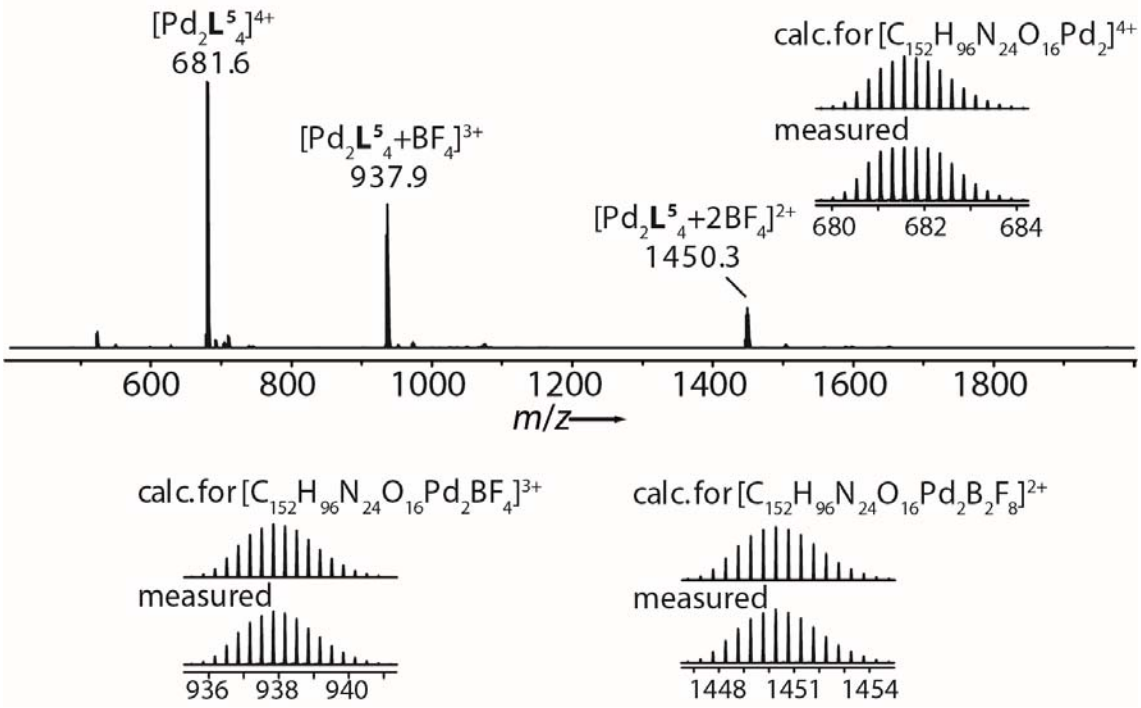

Figure 5.12 ESI mass spectrum of $[Pd_2\mathbf{L^5}_4]^{4+}$.

5.5.1.4 Heteroleptic cage $[C_{70}@Pd_2L^2{}_3L^5]^{4+}$

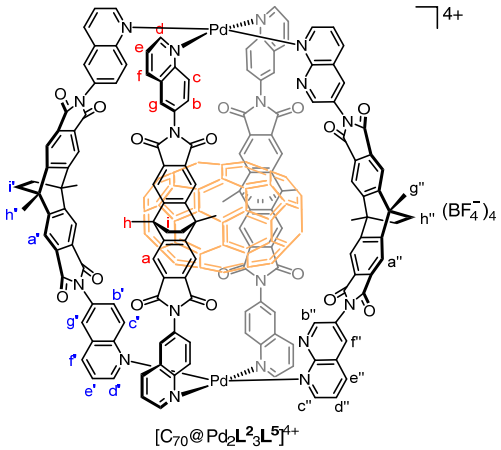

A CD_3CN solution of bowl $[C_{70}@Pd_2L^2{}_3(MeCN)_2](BF_4)_4$ (1000 µL, 0.64 mM, 0.64 µmol, 1 eq.) was combined with ligand L^5 (0.4 mg, 0.64 µmol, 1 eq.) and heated at 70 °C for 1 d to give a 0.64 mM solution of heteroleptic cage $[C_{70}@Pd_2L^2{}_3L^5]^{4+}$.

^{1}H NMR (500 MHz, 298 K, CD_3CN): δ (ppm) = 9.74 – 9.67 (m, 8H), 9.54 (d, *J* = 9.3 Hz, 4H), 8.96 (d, *J* = 9.3 Hz, 2H), 8.71 – 8.64 (m, 2H), 8.59 – 8.54 (m, 6H), 8.50 (d, *J* = 2.5 Hz, 2H), 8.35 (d, *J* = 2.5 Hz, 2H), 8.09 (s, 4H), 8.06 (s, 4H), 8.04 – 8.01 (m, 6H), 7.89 (s, 4H), 7.87 – 7.81 (m, 6H), 7.69 (dd, *J* = 8.3, 5.4 Hz, 6H), 7.28 (dd, *J* = 9.3, 2.3 Hz, 4H), 7.11 (dd, *J* = 9.3, 2.3 Hz, 2H), 2.39 (s, 6H), 2.35 (s, 6H), 2.26 (s, 12H), 1.87 (s, 8H), 1.80 (m, 8H).

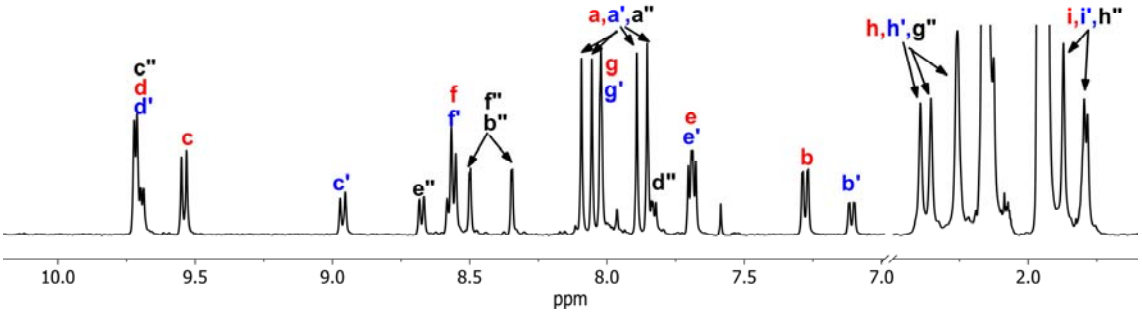

Figure 5.13 ^{1}H NMR spectrum (500 MHz, 298 K, CD_3CN) of $[C_{70}@Pd_2L^2{}_3L^5]^{4+}$.

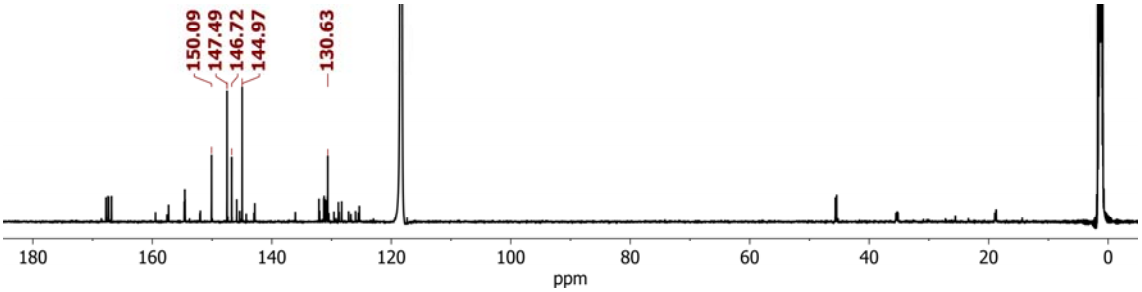

Figure 5.14 ^{13}C NMR spectrum (151 MHz, 298 K, CD_3CN) of $[C_{70}@Pd_2L^2{}_3L^5]^{4+}$. Five single signals at 150.09, 147.49, 146.72, 144.97, 130.63 ppm correspond to the encapsulated C_{70}.

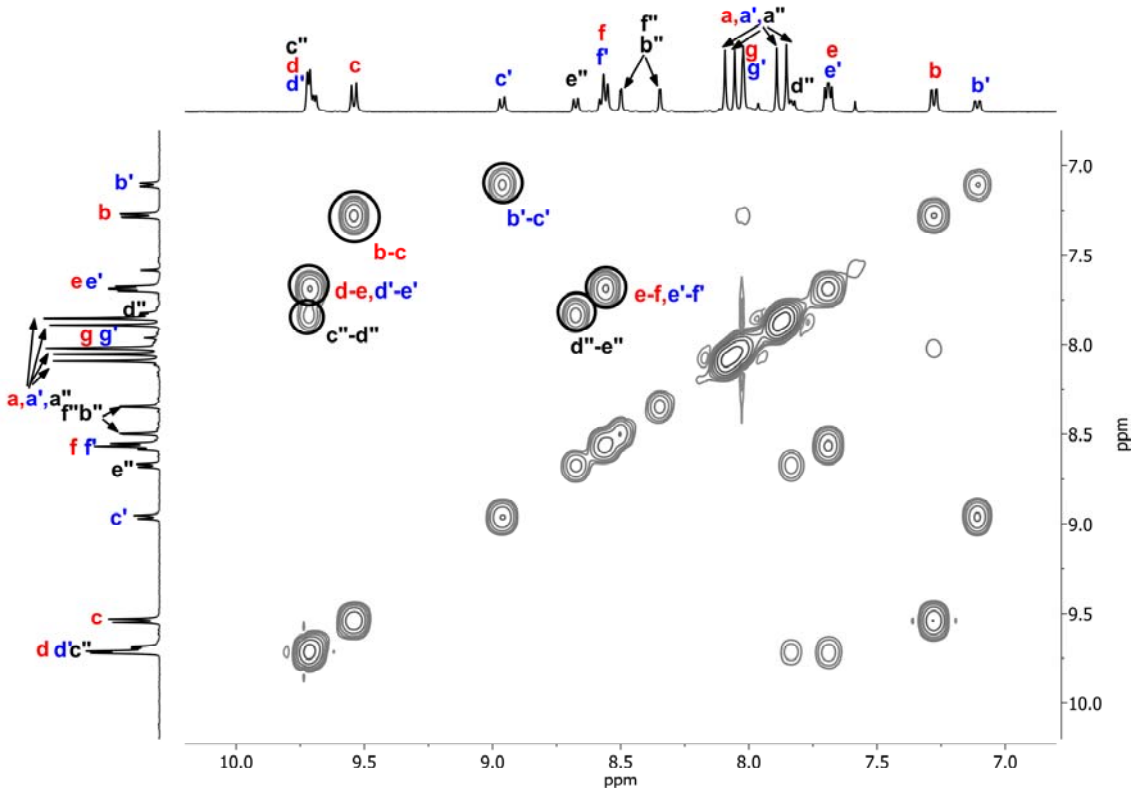

Figure 5.15 Partial $^{1}H - {}^{1}H$ COSY spectrum (500 MHz, 298 K, CD_3CN) of $[C_{70}@Pd_2\mathbf{L^2}_3\mathbf{L^5}]^{4+}$.

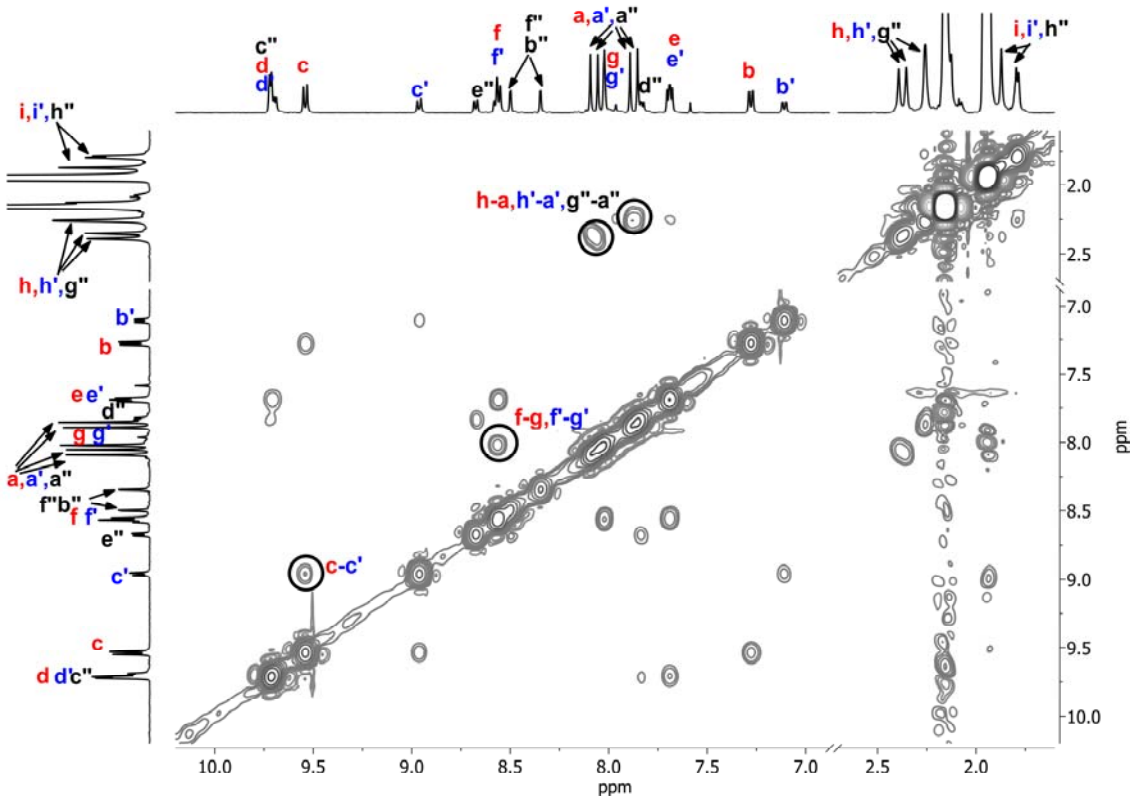

Figure 5.16 Partial $^{1}H - {}^{1}H$ NOESY spectrum (500 MHz, 298 K, CD_3CN) of $[C_{70}@Pd_2\mathbf{L^2}_3\mathbf{L^5}]^{4+}$.

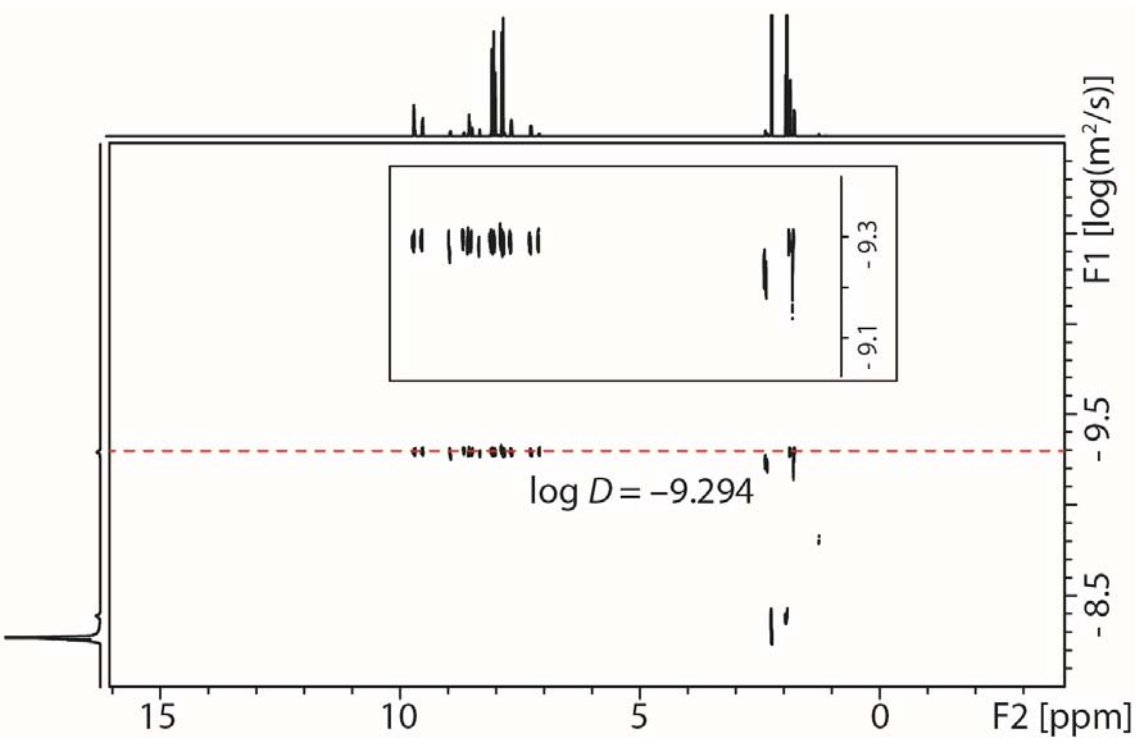

Figure 5.17 DOSY spectrum (500 MHz, 298 K, CD_3CN) of $[C_{70}@Pd_2\mathbf{L^2}_3\mathbf{L^5}]^{4+}$: diffusion coefficient = 5.1 x 10^{-10} m^2s^{-1}, log *D* = −9.29, r = 12.5 Å.

ESI HRMS ($C_{228}H_{102}N_{18}O_{16}Pd_2B_4F_{16}$): $[C_{70}@Pd_2\mathbf{L^2}_3\mathbf{L^5}]^{4+}$ calcd. for $C_{228}H_{102}N_{18}O_{16}Pd_2$ 890.6467; found 890.6458; $[C_{70}@Pd_2\mathbf{L^2}_3\mathbf{L^5}+BF_4]^{3+}$ calcd. for $C_{228}H_{102}N_{18}O_{16}Pd_2BF_4$ 1216.1967; found 1216.1948; $[C_{70}@Pd_2\mathbf{L^2}_3\mathbf{L^5}+2BF_4]^{2+}$ calcd. for $C_{228}H_{102}N_{18}O_{16}Pd_2B_2F_8$ 1867.7973; found 1867.7915.

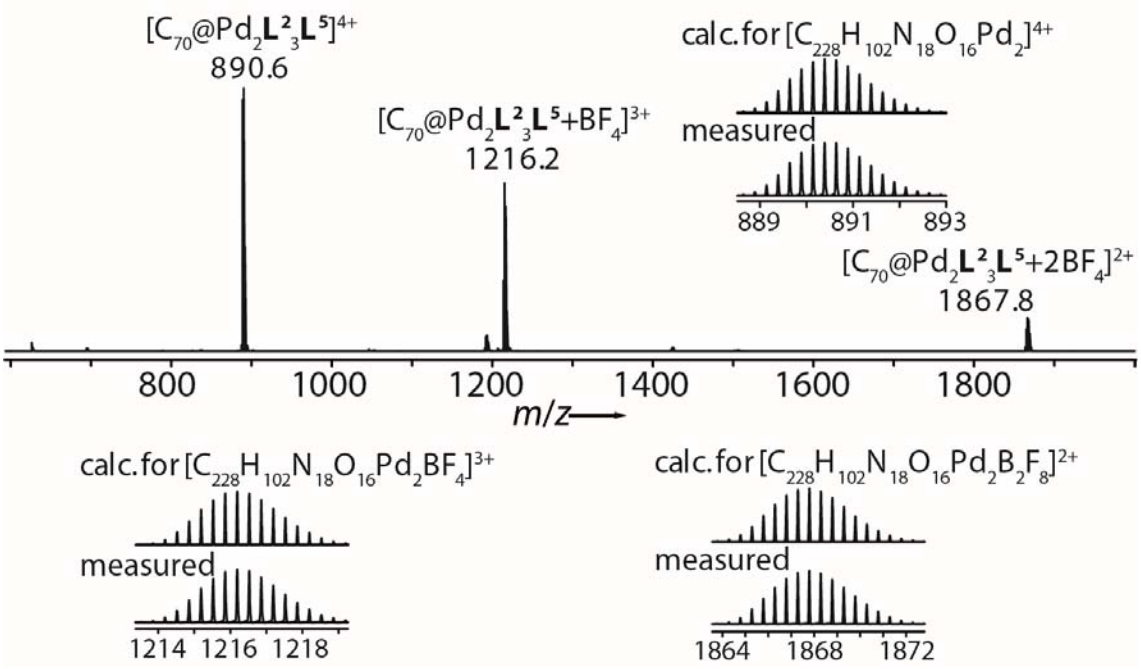

Figure 5.18 ESI mass spectrum of $[C_{70}@Pd_2\mathbf{L^2}_3\mathbf{L^5}]^{4+}$.

5.5.1.5 Heteroleptic cage $[C_{60}@Pd_2L^2_2L^5_2]^{4+}$

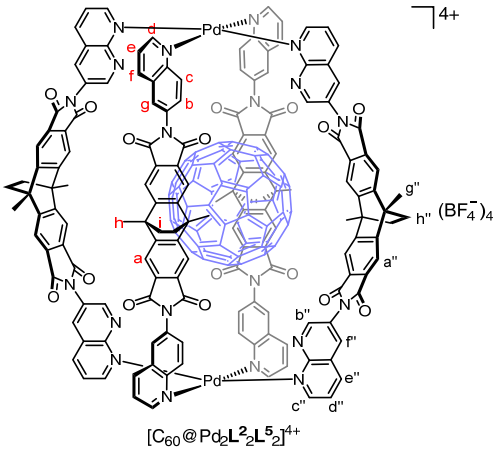

A solution of ligand **L²** (1823 µL, 5 mM/CH_2Cl_2, 9.11 µmol, 1 eq.) was combined with another solution of ligand **L⁵** (1823 µL, 5 mM/CH_2Cl_2, 9.11 µmol, 1 eq.), followed by removing CH_2Cl_2 from the vessel in vacuum. And then a solution of $[Pd(MeCN)_4](BF_4)_2$ (607.6 µL, 15 mM/CD_3CN, 9.11 µmol, 1 eq.), excess C_{60} (6.6 mg, 9.2 µmol, 1.0 eq.) and CD_3CN (6510 µL) were added into the vessel and stirred at 70 °C for 2 d. Excess C_{60} solid was removed by filtration to give a 0.64 mM pale purple solution of heteroleptic cage $[C_{60}@Pd_2\mathbf{L^2}_2\mathbf{L^5}_2]^{4+}$.

^{1}H NMR (500 MHz, 298 K, CD_3CN): δ (ppm) = 11.00 (d, J = 9.3 Hz, 4H), 9.82 (dd, J = 5.3, 1.7 Hz, 4H), 9.75 (d, J = 5.4 Hz, 4H), 8.68 – 8.62 (m, 8H), 8.52 – 8.47 (m, 8H), 7.92 (m, 20H), 7.83 (dd, J = 8.2, 5.4 Hz, 4H), 7.69 (dd, J = 8.3, 5.4 Hz, 4H), 7.35 (dd, J = 9.3, 2.2 Hz, 4H), 2.26 (m, 24H), 1.79 (m, 16H).

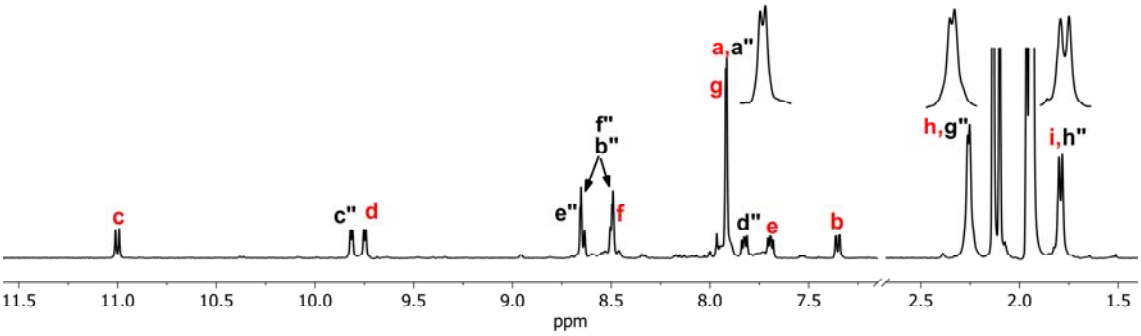

Figure 5.19 ^{1}H NMR spectrum (500 MHz, 298 K, CD_3CN) of $[C_{60}@Pd_2\mathbf{L^2}_2\mathbf{L^5}_2]^{4+}$.

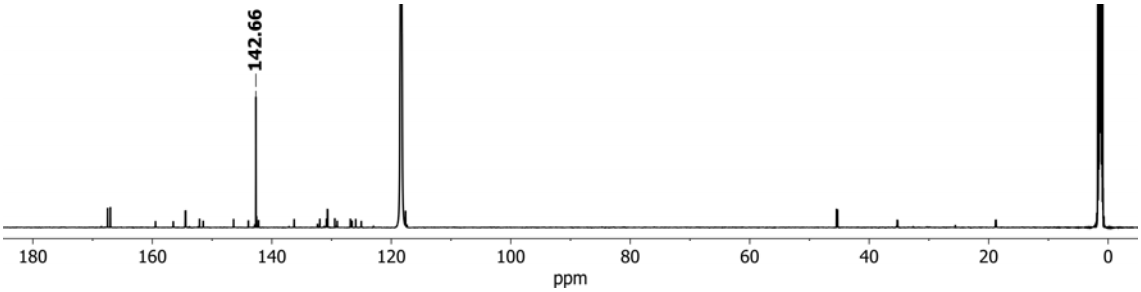

Figure 5.20 ^{13}C NMR spectrum (151 MHz, 298 K, CD_3CN) of $[C_{60}@Pd_2\mathbf{L^2}_2\mathbf{L^5}_2]^{4+}$. A single signal at 142.66 ppm corresponds to the encapsulated C_{60}.

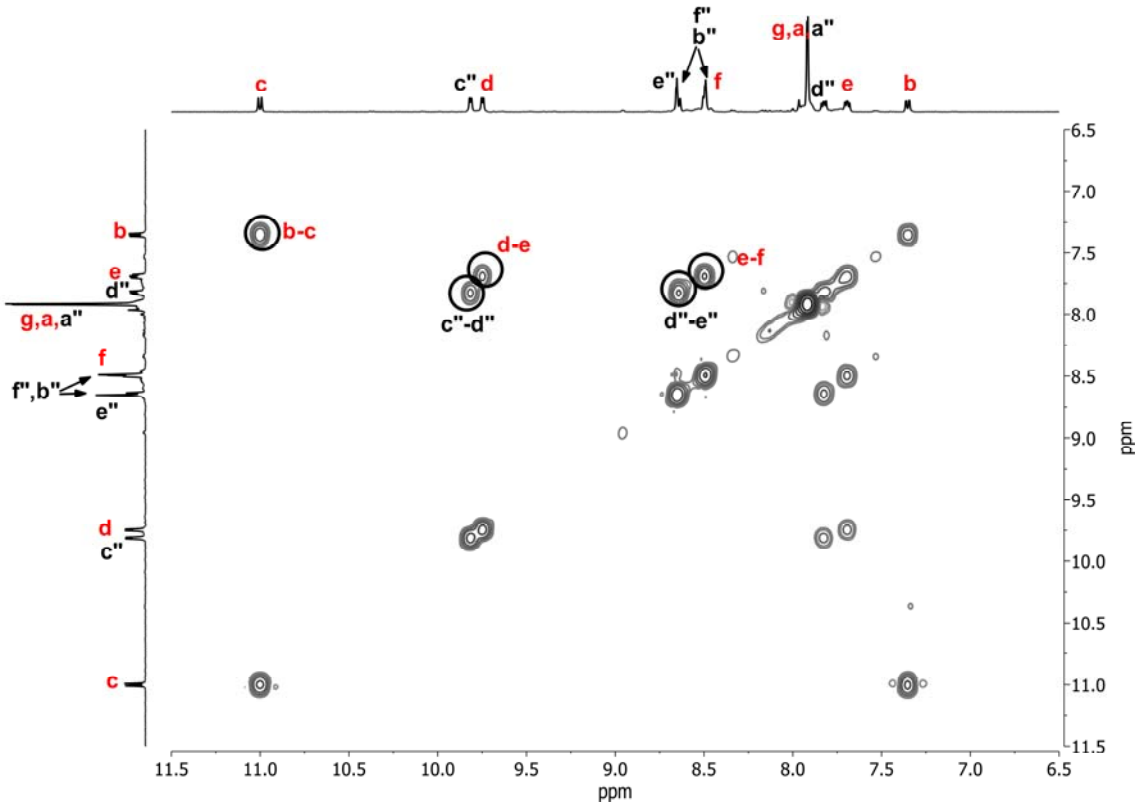

Figure 5.21 Partial $^{1}H - {}^{1}H$ COSY spectrum (500 MHz, 298 K, CD_3CN) of $[C_{60}@Pd_2\mathbf{L^2}_2\mathbf{L^5}_2]^{4+}$.

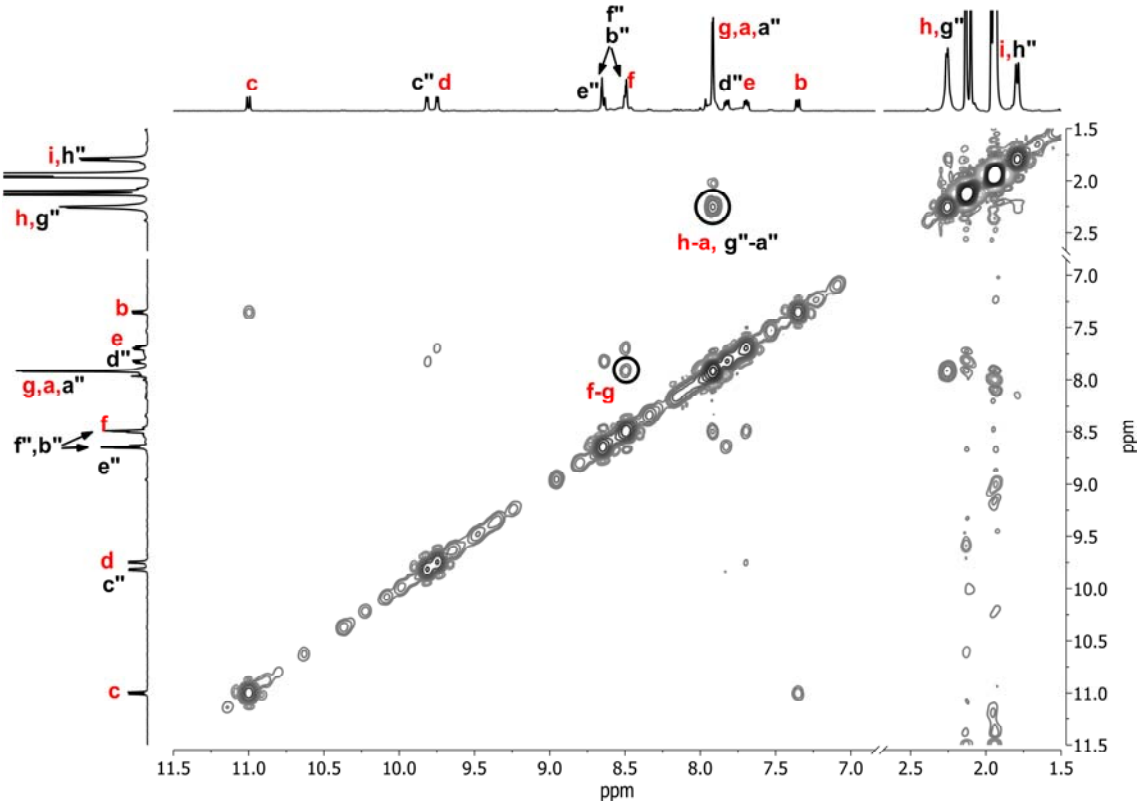

Figure 5.22 Partial $^{1}H - {}^{1}H$ NOESY spectrum (500 MHz, 298 K, CD_3CN) of $[C_{60}@Pd_2\mathbf{L^2}_2\mathbf{L^5}_2]^{4+}$.

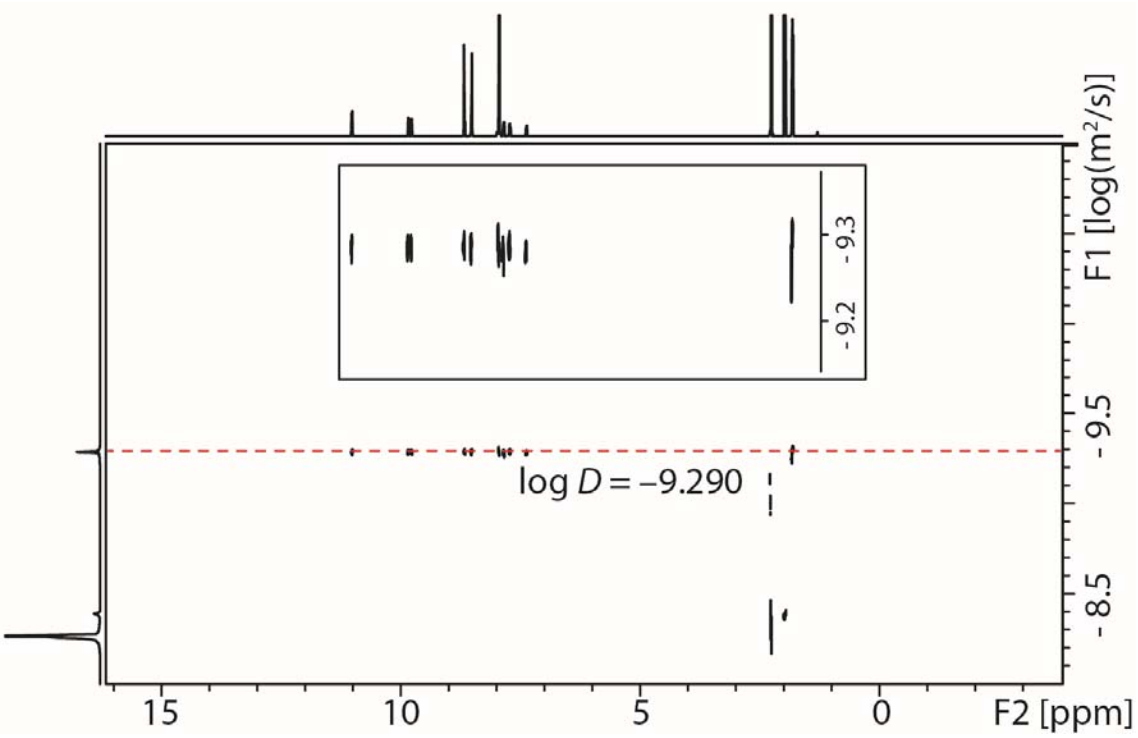

Figure 5.23 DOSY spectrum (500 MHz, 298 K, CD_3CN) of $[C_{60}@Pd_2\mathbf{L^2}_2\mathbf{L^5}_2]^{4+}$: diffusion coefficient = 5.1 x 10^{-10} m^2s^{-1}, log *D* = –9.29, r = 12.4 Å.

ESI HRMS ($C_{216}H_{100}N_{20}O_{16}Pd_2B_4F_{16}$): $[C_{60}@Pd_2\mathbf{L^2}_2\mathbf{L^5}_2]^{4+}$ calcd. for $C_{216}H_{100}N_{20}O_{16}Pd_2$ 860.8940; found 860.8911; $[C_{60}@Pd_2\mathbf{L^2}_2\mathbf{L^5}_2+BF_4]^{3+}$ calcd. for $C_{216}H_{100}N_{20}O_{16}Pd_2BF_4$ 1176.8601; found 1176.8556; $[C_{60}@Pd_2\mathbf{L^2}_2\mathbf{L^5}_2+2BF_4]^{2+}$ calcd. for $C_{216}H_{100}N_{20}O_{16}Pd_2B_2F_8$ 1808.7923; found 1808.7824.

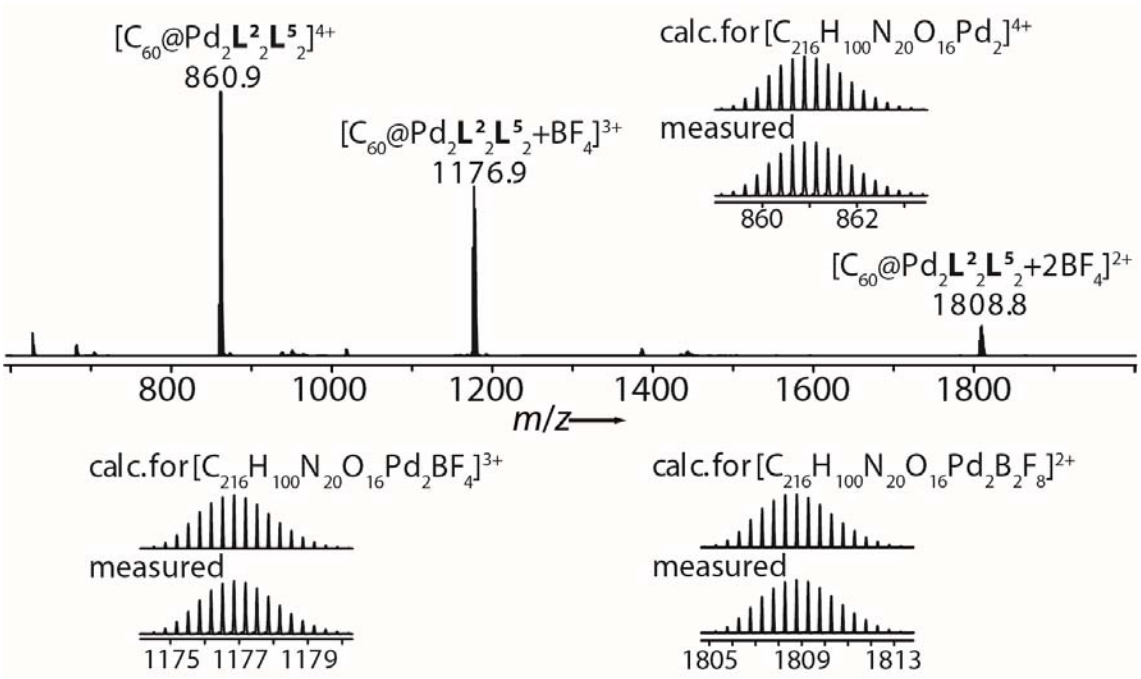

Figure 5.24 ESI mass spectrum of $[C_{60}@Pd_2\mathbf{L^2}_2\mathbf{L^5}_2]^{4+}$.

Table 5.1 Comparison of the chemical shift of quinoline proton (H_c) in different species (CD_3CN, 298K).

Species	Chemical shift (ppm)
$\mathbf{L^2}$	8.16
$[Pd_2\mathbf{L^2}_3(MeCN)_2]^{4+}$	9.99, 9.31
$[Pd_2\mathbf{L^2}_4]^{4+}$	9.54
$[C_{60}@Pd_2\mathbf{L^2}_3(MeCN)_2]^{4+}$	10.32, 9.07
$[C_{70}@Pd_2\mathbf{L^2}_3(MeCN)_2]^{4+}$	9.93, 8.74
$[C_{70}@Pd_2\mathbf{L^2}_4]^{4+}$	8.74
$[C_{70}@Pd_2\mathbf{L^2}_3\mathbf{L^5}]^{4+}$	9.54, 8.96
$[C_{60}@Pd_2\mathbf{L^2}_2\mathbf{L^5}_2]^{4+}$	11.00

5.5.2 Fullerene binding investigation of cage $[Pd_2\mathbf{L^5}_4]^{4+}$

To a CD_3CN solution of $[Pd(MeCN)_4](BF_4)_2$ (1.28 mM, 1 eq.) in the combination of corresponding amount of ligand $\mathbf{L^5}$ (2 eq.) in a sealed vessel, excess fullerene (C_{60} or C_{70}) was added as finely grounded powders, respectively. The mixtures were sonicated for 3 minutes, then stirred at room temperature or left standing at 70 °C for few days. Upon cooling, the supernatant was collected and transferred to NMR tubes.

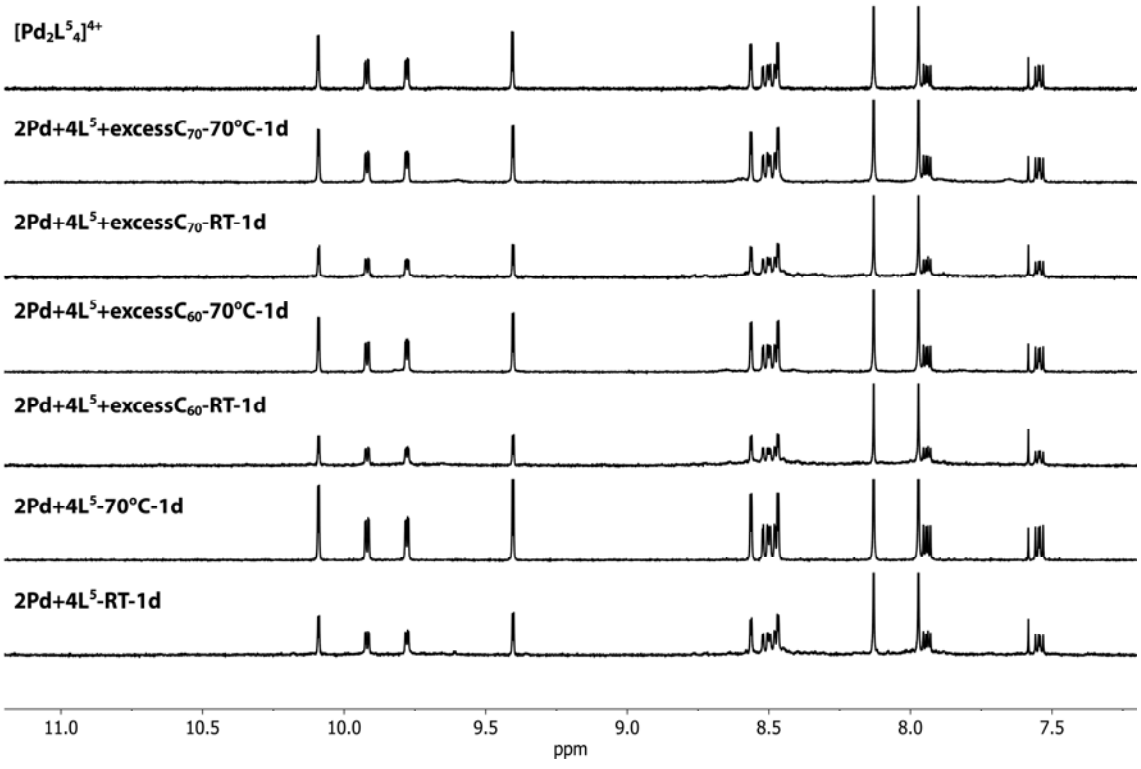

Figure 5.25 ^1H NMR spectra (500 MHz, 298 K, CD_3CN) monitoring the test of binding C_{60} and C_{70} within $[Pd_2\mathbf{L^5}_4]^{4+}$ at room temperature or 70 °C, indicating both of C_{60} and C_{70} cannot be encapsulated in $[Pd_2\mathbf{L^5}_4]^{4+}$. Besides, no further change in NMR spectra was observed after prolonged heating.

5.5.3 Reactions of mixed ligand systems

The CH_2Cl_2 solution of **L²** (5 mM) and the CH_2Cl_2 solution of **L⁵** (5 mM) were respectively added to NMR tubes according to the amounts as shown in the table below, followed by slowly evaporating CH_2Cl_2 from NMR tubes under heating. After sequentially adding the corresponding amounts of CD_3CN and a concentrated solution of $[Pd(MeCN)_4](BF_4)_2$ (CD_3CN, 15 mM) as well as excess fullerene powder, the mixtures were sonicated for 3 minutes and then left standing at 70 °C for several days. Upon cooling, ^1H NMR spectra were recorded immediately for each sample.

Table 5.2 Details about reactions of mixed ligand systems.

Entries	Different amounts of reactants					
	Ratios of Pd^{II}/**L²**/**L⁵**	Pd^{II} (15 mM)	**L²** (5 mM)	**L⁵** (5 mM)	CD_3CN	Excess Fullerenes
1	2:3:1	42.7 μL	192.1 μL	64.0 μL	457.3 μL	-
2	2:2:2	42.7 μL	128.0 μL	128.0 μL	457.3 μL	-
3	2:1:3	42.7 μL	64.0 μL	192.1 μL	457.3 μL	-
4	2:3:1	42.7 μL	192.1 μL	64.0 μL	457.3 μL	C_{60}: 1.5 mg
5	2:2:2	42.7 μL	128.0 μL	128.0 μL	457.3 μL	C_{60}: 1.2 mg
6	2:1:3	42.7 μL	64.0 μL	192.1 μL	457.3 μL	C_{60}: 1.4 mg
7	2:3:1	42.7 μL	192.1 μL	64.0 μL	457.3 μL	C_{70}: 1.1 mg
8	2:2:2	42.7 μL	128.0 μL	128.0 μL	457.3 μL	C_{70}: 2.3 mg
9	2:1:3	42.7 μL	64.0 μL	192.1 μL	457.3 μL	C_{70}: 1.4 mg

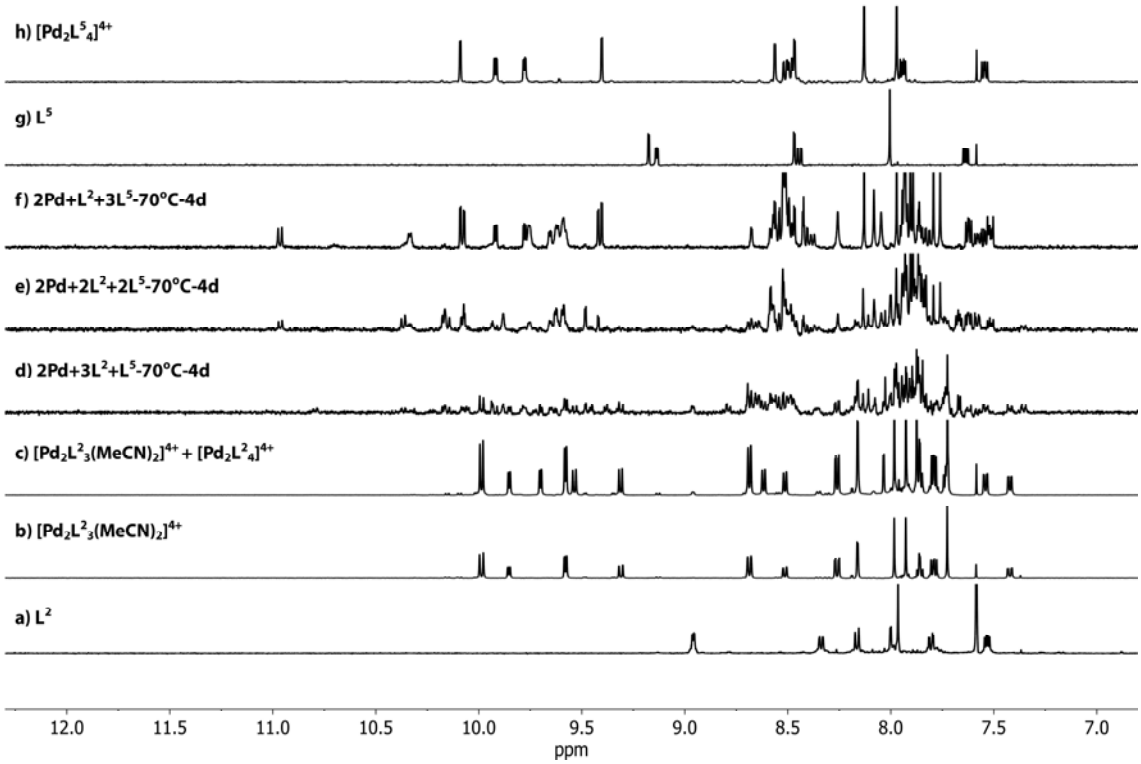

Figure 5.26 ^1H NMR spectra (500 MHz, 298 K, CD_3CN): (a) Ligand **L²**; (b) bowl $[Pd_2\mathbf{L^2}_3(MeCN)_2]^{4+}$; (c) the mixture of bowl $[Pd_2\mathbf{L^2}_3(MeCN)_2]^{4+}$ and cage $[Pd_2\mathbf{L^2}_4]^{4+}$; (d) reaction of Pd^{II}/**L²**/**L⁵** in a 2:3:1 ratio gave an unknown mixture (Entry 1); (e) reaction of Pd^{II}/**L²**/**L⁵** in a 2:2:2 ratio gave an unknown mixture (Entry 2); (f) reaction of Pd^{II}/**L²**/**L⁵** in a 2:1:3 ratio gave an unknown mixture, including cage $[Pd_2\mathbf{L^5}_4]^{4+}$ (Entry 3); (g) ligand **L⁵**; (h) cage $[Pd_2\mathbf{L^5}_4]^{4+}$.

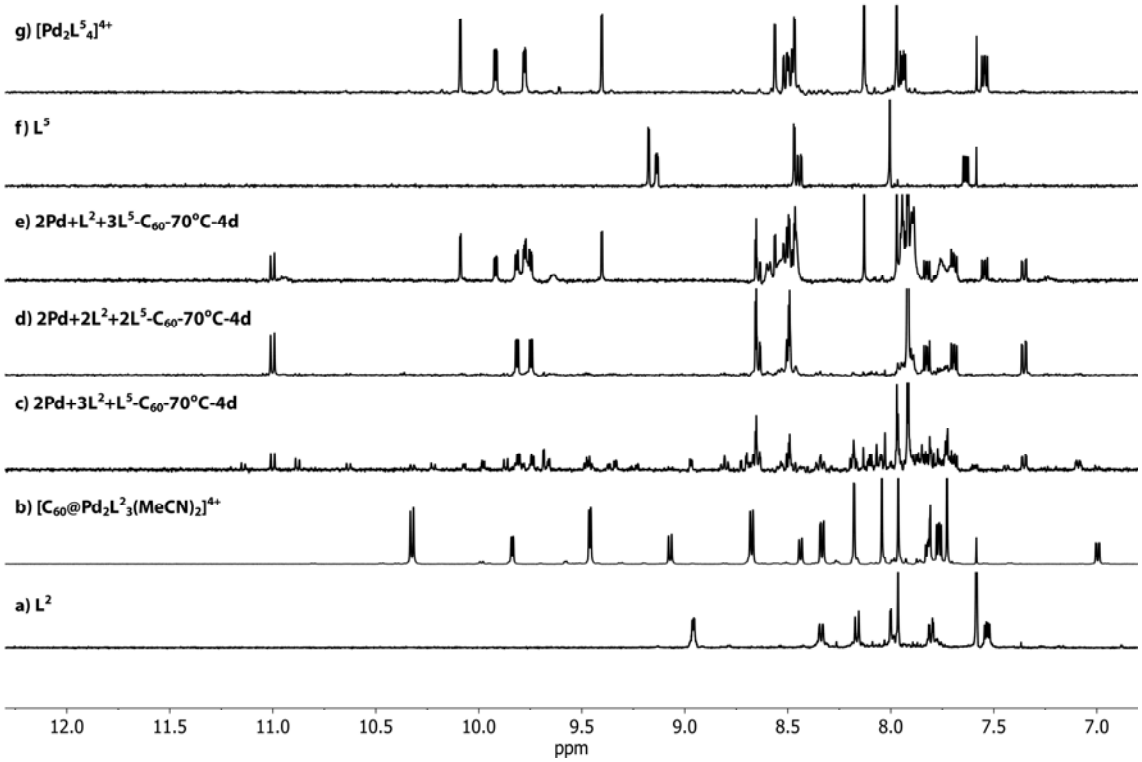

Figure 5.27 ^{1}H NMR spectra (500 MHz, 298 K, CD_3CN): (a) Ligand **L²**; (b) bowl $[C_{60}@Pd_2\mathbf{L^2}_3(MeCN)_2]^{4+}$; (c) reaction of Pd^{II}/**L²**/**L⁵** in a 2:3:1 ratio with excess C_{60} gave an unknown mixture (Entry 4); (d) reaction of Pd^{II}/**L²**/**L⁵** in a 2:2:2 ratio with excess C_{60} gave a concise spectrum, identified as cage $[C_{60}@Pd_2\mathbf{L^2}_2\mathbf{L^5}_2]^{4+}$ (Entry 5); (e) reaction of Pd^{II}/**L²**/**L⁵** in a 2:1:3 ratio with excess C_{60} gave the mixture of cage $[C_{60}@Pd_2\mathbf{L^2}_2\mathbf{L^5}_2]^{4+}$ and cage $[Pd_2\mathbf{L^5}_4]^{4+}$ (Entry 6); (f) ligand **L⁵**; (g) cage $[Pd_2\mathbf{L^5}_4]^{4+}$.

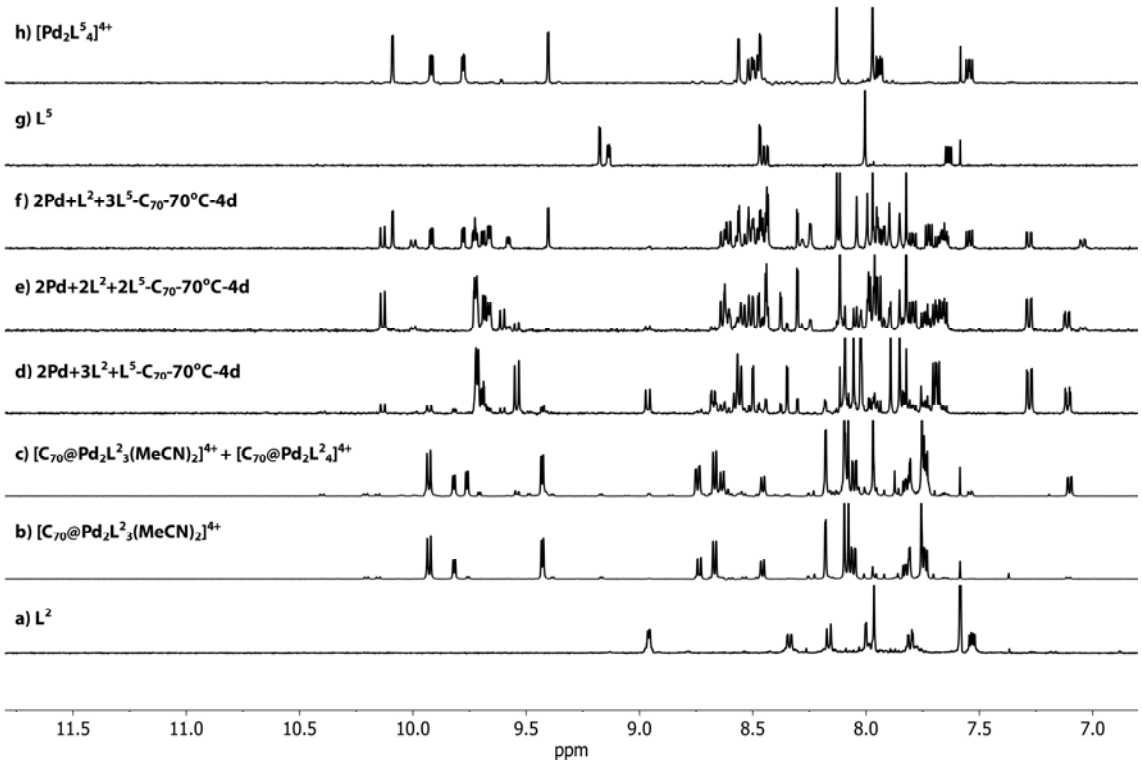

Figure 5.28 ^{1}H NMR spectra (500 MHz, 298 K, CD_3CN): (a) Ligand **L²**; (b) bowl $[C_{70}@Pd_2\mathbf{L^2}_3(MeCN)_2]^{4+}$; (c) the mixture of bowl $[C_{70}@Pd_2\mathbf{L^2}_3(MeCN)_2]^{4+}$ and cage $[C_{70}@Pd_2\mathbf{L^2}_4]^{4+}$; (d) reaction of Pd^{II}/**L²**/**L⁵** in a 2:3:1 ratio with excess C_{70} gave a concise spectrum, identified as cage $[C_{70}@Pd_2\mathbf{L^2}_3\mathbf{L^5}]^{4+}$ (major species) (Entry 7); (e) reaction of Pd^{II}/**L²**/**L⁵** in a 2:2:2 ratio with excess C_{70} gave the cage

$[C_{70}@Pd_2\mathbf{L^2}_2\mathbf{L^5}_2]^{4+}$ as the major product (Entry 8); (f) reaction of Pd^{II}/$\mathbf{L^2}$/$\mathbf{L^5}$ in a 2:1:3 ratio with excess C_{70} gave an unknown mixture, including cage $[Pd_2\mathbf{L^5}_4]^{4+}$ and cage $[C_{70}@Pd_2\mathbf{L^2}_2\mathbf{L^5}_2]^{4+}$ (Entry 9); (g) ligand $\mathbf{L^5}$; (h) cage $[Pd_2\mathbf{L^5}_4]^{4+}$.

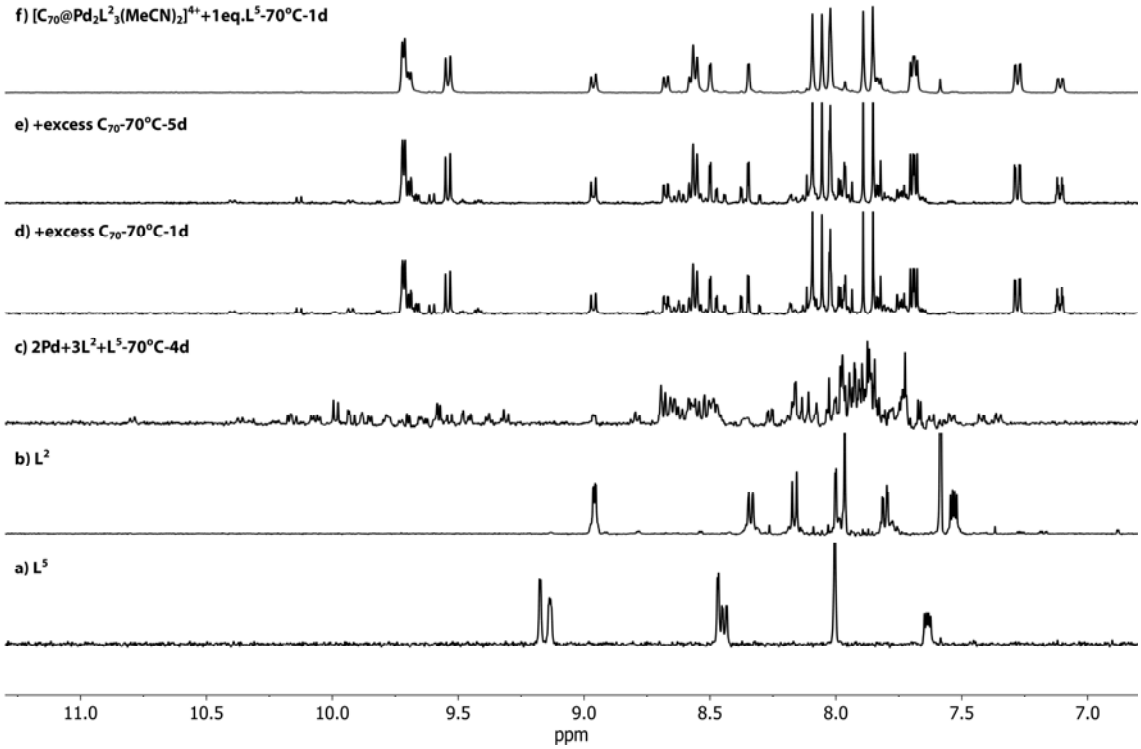

Figure 5.29 ^{1}H NMR spectra (500 MHz, 298 K, CD_3CN): (a) Ligand $\mathbf{L^5}$; (b) ligand $\mathbf{L^2}$; (b) bowl $[C_{70}@Pd_2\mathbf{L^2}_3(MeCN)_2]^{4+}$; (c) reaction of Pd^{II}/$\mathbf{L^2}$/$\mathbf{L^5}$ in a 2:3:1 ratio gave an unknown mixture (Entry 1); (d) and (e) subsequent addition of excess C_{70} powder into the solution (c) gave the concise spectra after one or five days, respectively; (f) cage $[C_{70}@Pd_2\mathbf{L^2}_3\mathbf{L^5}]^{4+}$ achieved through the reaction of bowl $[C_{70}@Pd_2\mathbf{L^2}_3(MeCN)_2]^{4+}$ with 1 equivalent amount of $\mathbf{L^5}$.

5.5.4 X-Ray data

Table 5.3 Crystallographic data of $\mathbf{L^5}$, $[Pd_2\mathbf{L^5}_4](SbF_6)_4$.

Compound	$\mathbf{L^5}$	$\mathbf{[Pd_2L^5_4](SbF_6)_4}$
CCDC number	---	---
Identification code	bc18a	bc24b2_sq
Empirical formula	$C_{38}H_{24}N_6O_4$	$C_{608}H_{384}N_{96}O_{64}Pd_8Sb_{10}F_{60}$
Formula weight	628.63	13266.79
Temperature (K)	100(2)	80(2)
Crystal system	Monoclinic	Orthorhombic
Space group	$P2_1/c$	Pccn
a (Å)	14.0425(5)	41.972(8)
b (Å)	11.2236(4)	70.711(14)
c (Å)	19.5237(7)	27.616(6)
α (º)	90	90
β (º)	103.069(2)	90
γ (º)	90	90
Volume (Å^3)	2997.38(19)	81961(28)
Z	4	4
Density (calc.) (g/cm^3)	1.393	1.075
Absorption coefficient (mm^{-1})	0.093	0.511
F(000)	1304	26536
Crystal size (mm^3)	0.500 x 0.020 x 0.020	0.570 x 0.003 x 0.003
θ range for data collection (º)	2.107 to 36.380	0.547 to 15.734
Reflections collected	90407	97809
Observed reflections [R(int)]	14541 [0.0672]	20884 [0.0936]
Goodness-of-fit on F^2	1.017	1.649
R_1 [$I>2\sigma(I)$]	0.0493	0.1294
wR_2 (all data)	0.1387	0.4033
Largest diff. peak and hole (e.Å^{-3})	0.532 and -0.293	2.053 and -1.725
Data / restraints / parameters	14541 / 0 / 435	20884 / 9789 / 4304

5.5.4.1 Crystal structure of ligand $\mathbf{L^5}$

Colorless needle crystals of $\mathbf{L^5}$ were obtained by slow evaporation of a 1 mM CH_3CN/CH_2Cl_2 (v/v: 1:1) solution of $\mathbf{L^5}$. A single crystal in mother liquor was pipetted onto a glass slide containing NVH oil. Single crystal X-ray diffraction data

was collected on a Bruker D8 venture equipped with an Incoatec microfocus source (Iμs 2.0) using Mokα radiation. All displacements for non-hydrogen atoms were refined anisotropically.

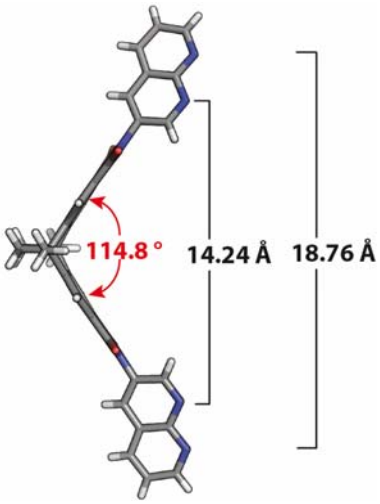

Figure 5.30 X-ray structure of **L⁵** with the longest and shortest N–N distance of 18.76 and 14.24 Å, respectively. Color scheme: H, light grey; C, dark grey; N, blue; O, red.

Table 5.4 Structural details involved in **L⁵**.

Residues No.	Dihedral angle (°) between the backbone's benzene planes C16_C17_C18_C22_C23_C24 and C7_C8_C9_C13_C14_C15	Esd (°)
-	65.222	0.024

5.5.4.2 Crystal structure of cage $[Pd_2L^5_4](SbF_6)_4$

Colorless needle crystals of $[Pd_2L^5_4](SbF_6)_4$ were obtained by slow vapor diffusion of isopropyl ether into a 0.64 mM CD_3CN solution of $[Pd_2L^5_4](BF_4)_4$ containing 10 eq. of $KSbF_6$. A single crystal in mother liquor was pipetted onto a glass slide containing NVH oil. To avoid collapse of the crystal lattice, the crystal was quickly mounted onto a 0.5 mm nylon loop and immediately flash cooled in liquid nitrogen. Single crystal X-ray diffraction data was collected at 80(2) K on a single axis goniometer, equipped with an Oxford Cryostream 800 a Pilatus 6M. 1900 diffraction images were collected in a 360° ϕ sweep at a detector distance of 200 mm, 100% filter transmission, 0.2° step width and 0.06 seconds exposure time per image. And 1650 diffraction images were used for data integration. Stereochemical restraints for the EAN ligands (**L⁵**) were generated by the GRADE program using the GRADE Web Server (http://grade.globalphasing.org) and applied in the refinement.

Table 5.5 Definition of residues involved in $[Pd_2L^5_4](SbF_6)_4$.

Fragment	Residue class	Occurrence	Residue numbers
Pd^{2+}	PD	1	1
Ligand **L⁵**	EAN	9	2-8, 16 (Two EAN with 50% occupation)
SbF_6^-	SBF	6	10-15 (Two SBF with 50% occupation)

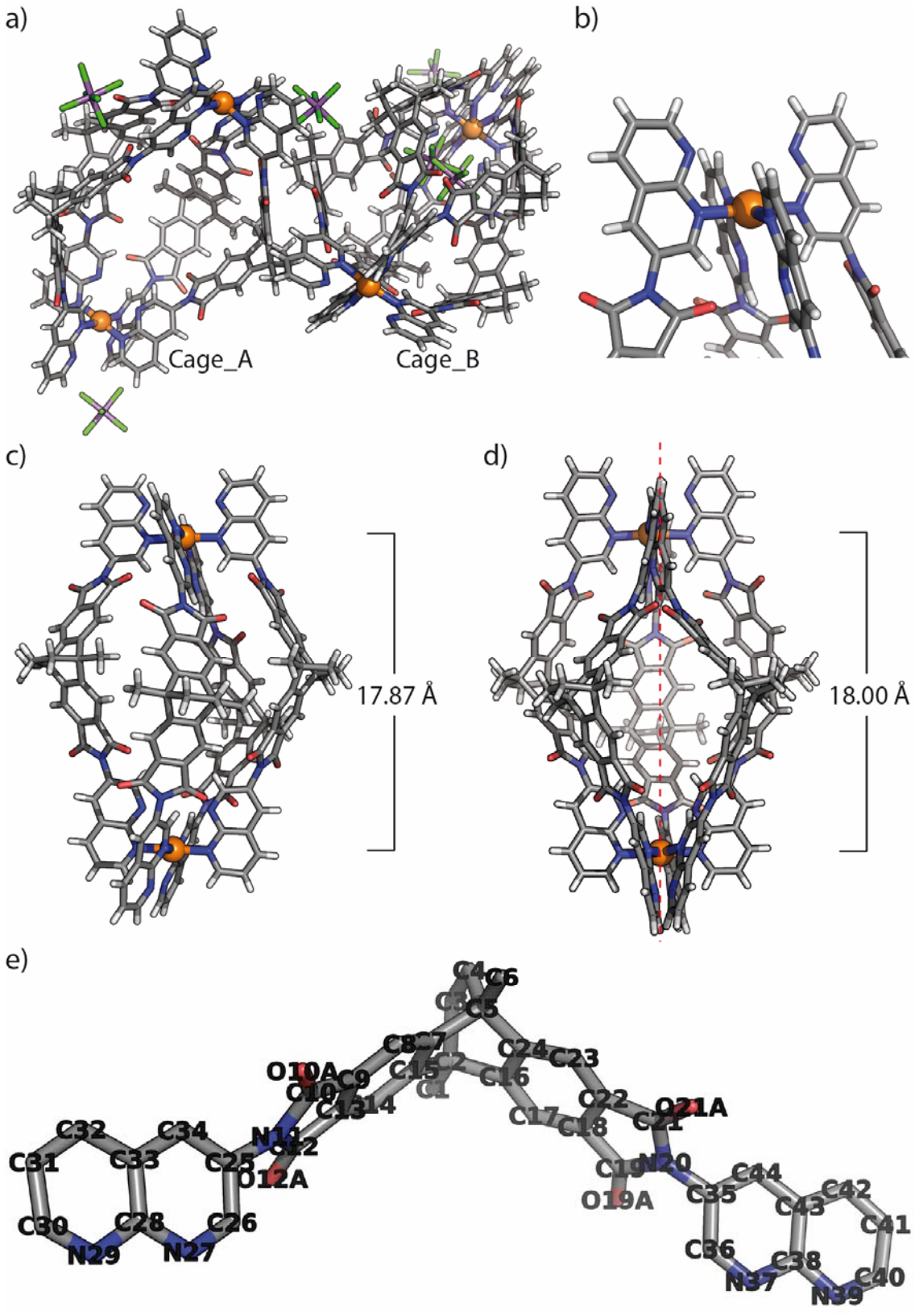

Figure 5.31 X-ray structure of $[Pd_2\mathbf{L}^5{}_4](SbF_6)_4$: (a) The asymmetric unit of two crystallographically independent cages; (b) coordination center showing the dislocation of coordinated terminals; (c) cage_A showing the Pd–Pd distance of 17.87 Å; (d) cage_B showing the Pd–Pd distance of 18.00 Å and one of ligands in two positions with 50% occupation; (e) atomic naming scheme of ligand $\mathbf{L}^5$ (residue class EAN). Color scheme: H, light grey; C, dark grey; N, blue; O, red; F, green; Pd, orange; Sb, violetpurple.

Table 5.6 Structural details involved in $[Pd_2\mathbf{L^5}_4](SbF_6)_4$.

Residues No.	Dihedral angle (°) between the backbone's benzene planes C16_C17_C18_C22_C23_C24 and C7_C8_C9_C13_C14_C15	Esd	Dihedral angle (°) between planes N29_Pd2_Pd1 and N37_Pd1_Pd2, N27_Pd2_Pd1 and N39_Pd1_Pd2	Esd
2	60.182	0.690	3.529	0.412
3	59.264	0.697	0.630	0.267
4	52.863	0.547	0.179	0.388
5	62.371	0.739	3.209	0.390
6	57.592	0.916	0.264	0.153
7	52.732	0.665	1.023	0.324
8	58.882	0.818	2.315	0.145
Average	57.7		1.6	

5.5.5 Computational studies

All models shown below were constructed using Wavefunction SPARTAN '14[129] and first optimized on semiempiric PM6 level of theory without constraints. The resulting structures were then further refined by DFT structure optimization (B3LYP/LANL2DZ) using GAUSSIAN 09.[130]

5.5.5.1 Comparison of the DFT minimized energies of A-type $[Pd_2\mathbf{L^5}_4]^{4+}$ and B-type $[Pd_2\mathbf{L^5}_4]^{4+}$

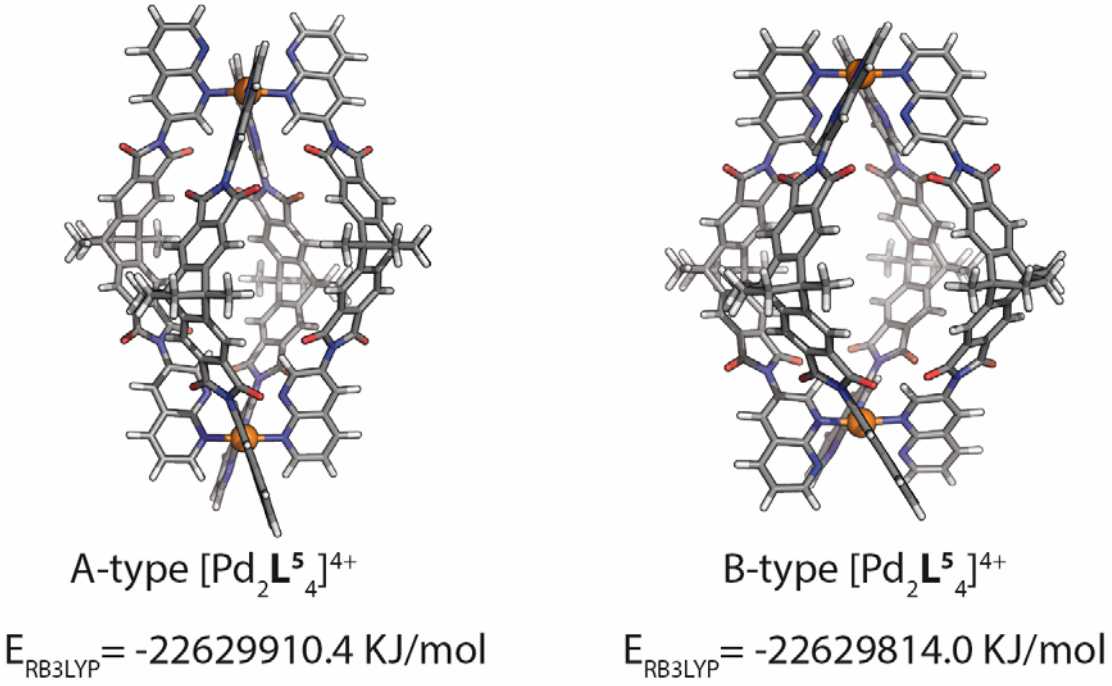

Figure 5.32 DFT energy minimized structures of observed A-type $[Pd_2\mathbf{L^5}_4]^{4+}$ and tentative B-type $[Pd_2\mathbf{L^5}_4]^{4+}$. According to the computed energies, A-type (dislocated) $[Pd_2\mathbf{L^5}_4]^{4+}$ is 96.4 kJ/mol lower in energy.

5.5.5.2 Comparison of the DFT minimized energies of *cis*-$[C_{60}@Pd_2L^2{}_2L^5{}_2]^{4+}$ and *trans*-$[C_{60}@Pd_2L^2{}_2L^5{}_2]^{4+}$

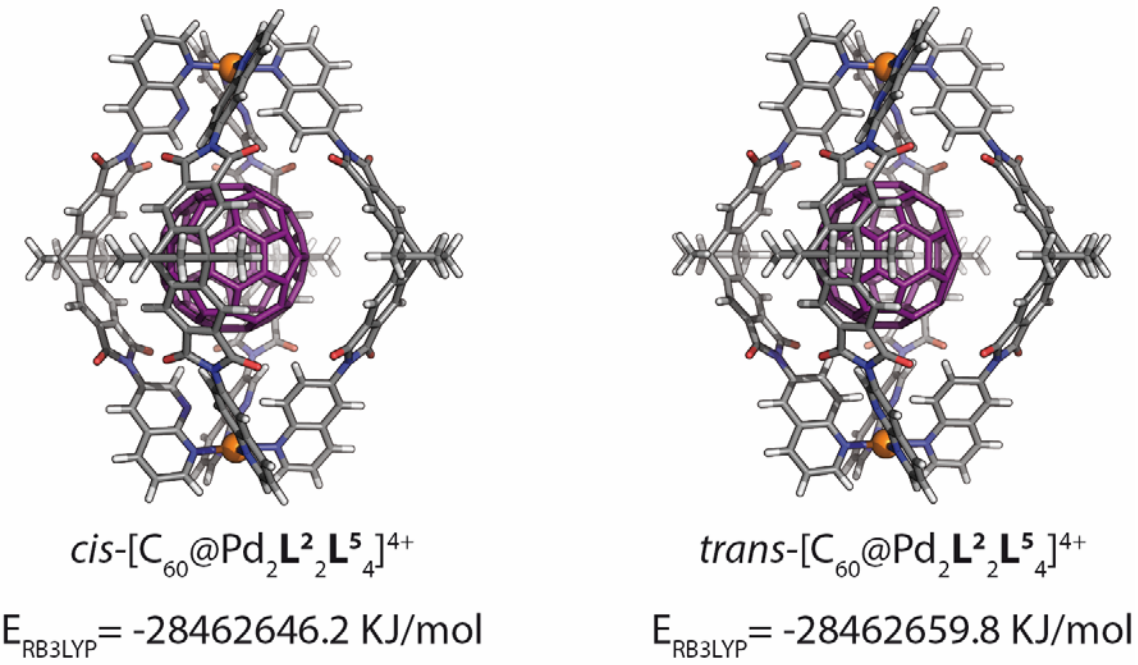

Figure 5.33 DFT energy minimized structures of tentative *cis*-$[C_{60}@Pd_2\mathbf{L^2}_2\mathbf{L^5}_2]^{4+}$ and observed *trans*-$[C_{60}@Pd_2\mathbf{L^2}_2\mathbf{L^5}_2]^{4+}$. According to the computed energies, *trans*-$[C_{60}@Pd_2\mathbf{L^2}_2\mathbf{L^5}_2]^{4+}$ is 13.6 kJ/mol lower in energy.

6 A fullerene-functionalized coordination cage

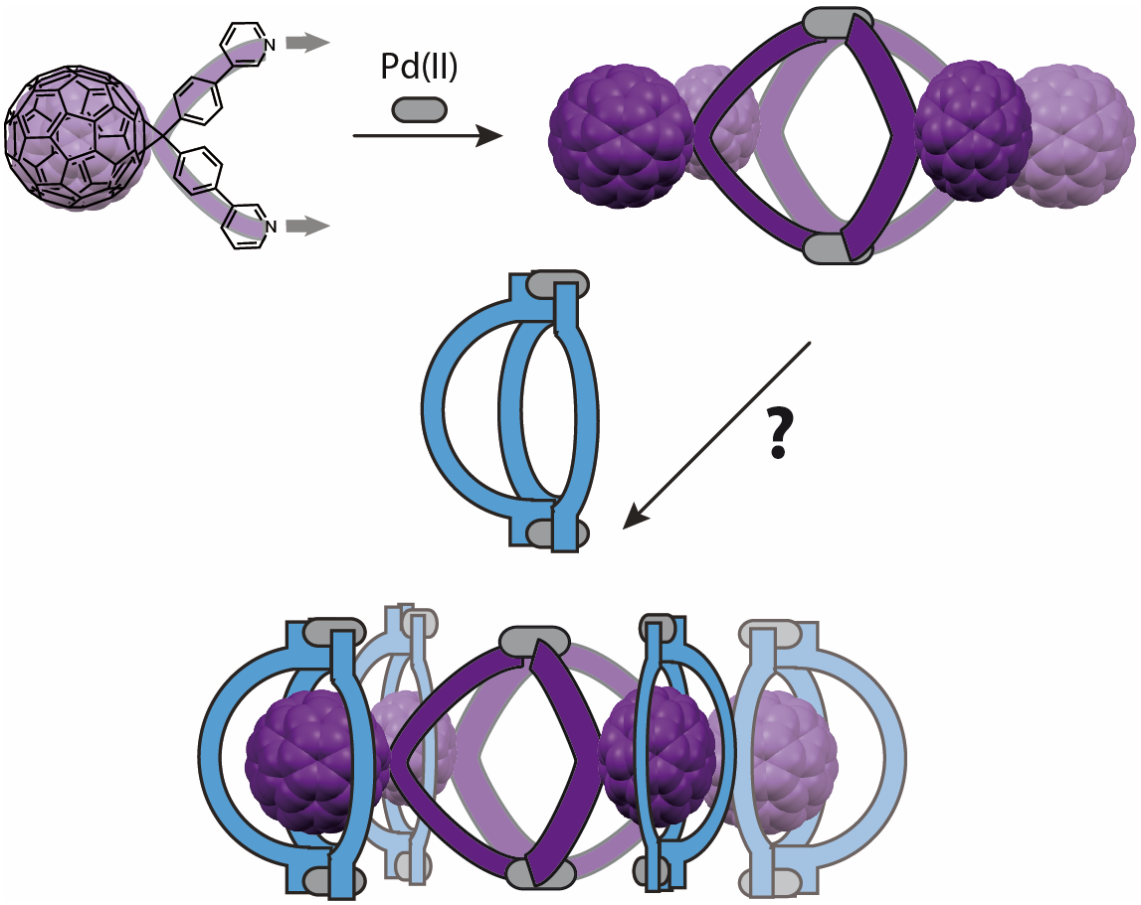

6.1 Introduction

Over the last two decades, the design and synthesis of metal-organic hybrid architectures comprising fullerene derivatives has become a burgeoning area of chemistry research as the combination of unique fullerene-based cage-like structures with functional metal ions, which has been proven to harness the synergistic and complementary properties of both.[168-169] For the purpose of obtaining the fullerene-containing metal complexes with adjustable properties, covalent attachment of the predesigned metal-coordinating moieties to the surface of fullerenes is the most straightforward approach, benefiting from the development of fullerene-based organic chemistry. The implementation of geometrically well-defined metal centers and distinct coordination groups, such as carboxylate,[170-171] pyridine,[172-173] terpyridine[174-175] and other nitrogen donors,[176] allows to gain precise control over the overall geometries of the resulting fullerene-linked metal complexes, which is driven by the intensively studied coordination chemistry. The combination of the electroactive property of fullerene derivatives with inherent properties of metal complexes makes fullerene-metal hybrids attractive candidates for functional molecular materials with widespread applications.[177]

Noteworthy is that covalent modification of pristine C_{60} with metal-binding sites is a synthetically costly process, generally accompanied by the arduous purification of a single fullerene derivative from the reaction mixture, including other adducts or isomers, due to the spherical C_{60} with π-conjugated surface. In this sense, the forward-looking study of fullerene-linked coordination complexes was limited by the laborious purification and relatively low yields of available fullerene-based organic ligands. In order to address this problem, Kräutler and co-workers introduced the method called orthogonal transposition: firstly the C_{60} sphere was symmetrically functionalized with four diethyl malonate groups on the equatorial positions and then the trans-1 positions can be retained for further modification with coordination groups, concurrently enhancing the solubility of this kind of fullerene compounds in organic solvents to a certain extent.[178] By means of this strategy, ligands based on *trans*-1 hexakis-fullerene adducts were obtained and proven to be able to react with transition metals to yield coordination polymers.[173, 176, 179] Similarly, Fujita's group reported a coordination-driven self-assembly of Pd^{II} cations and bis-pyridyl ligands, functionalized on hexakis-fullerene adducts at the sacrifice of the smooth outer surface of fullerenes.[180]

For the sake of maximally retaining fullerene's spherical shape, in other words, to retain the ability to exhibit shape complementary towards particular hosts via its partial convex surface, the modified Bingel reaction is a reliable route to achieve mono-functionalized methanofullerene adduct, thus introducing coordination groups and altering its solubility and electrochemical behavior in the meantime.[181] Few flexible dipyridyl-functionalized methanofullerene ligands have been utilized to construct transition metal complexes.[182-184] In 2015, Stang and co-workers reported a more rigid fullerene-based ligand with the 120° directing dipyridyl donors accessed through Prato reaction, and this ligand could self-assembly with Pt^{II} acceptors into metallocycles, wherein a triplet-state absorption-emission conversion was observed.[185-186]

Herein, the synthesis and characterization of a new bis-monodentate pyridyl ligand bearing a giant C_{60} outside (**L⁶**) as well as its coordination-driven supramolecular assembly with square-planar Pd^{II} cations will also be presented (Figure 6.1).

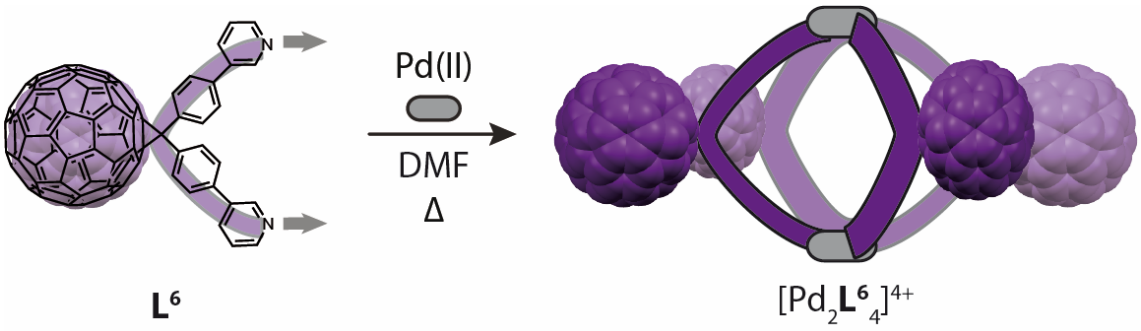

Figure 6.1 A designed fullerene-based ligand with dipyridyl arms (**L⁶**) and its cage formation.

6.2 Ligand synthesis

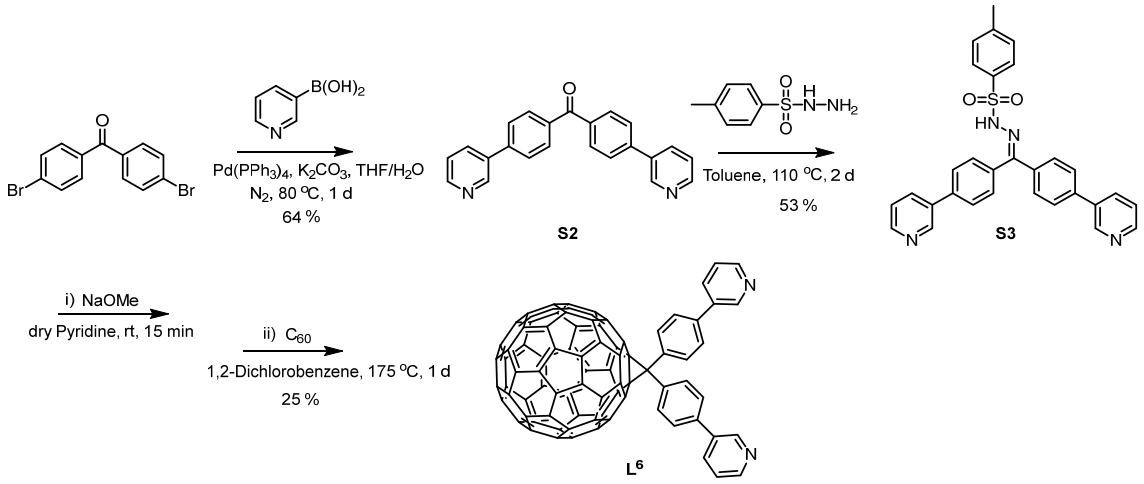

Figure 6.2 Synthesis route of ligand **L^6**.

The synthetic route is depicted in the above figure. Starting from the para-substituted dibromobenzophenone, the coordination groups (3-pyridyl groups) were grafted on benzophenone by a typical Suzuki cross-coupling reaction to give the dipyridyl backbone (**S2**) in 64 % yield. Then the chemical manipulation of this backbone to the surface of C_{60} was realized in a three-step reaction by using a similar synthetic procedure of a known fullerene mono-adduct.[174] First, the dipyridyl benzophenone was reacted with tosylhydrazide to achieve the desired tosyl hydrazone derivative (**S3**) in the yield of 53 %. Then sodium methoxide was added to remove the tosyl group and produce in situ the 1,3-dipolar diazo compound, which was able to react with C_{60} to form a pyrazolinofullerene derivate as an intermediate. Upon heating at high temperature to eliminate molecular nitrogen, the crude product was further purified by column chromatography and GPC to give the pure dipyridyl-functionalized methanofullerene compound in the moderate yield for modified fullerenes (25 %). All these organic compounds were confirmed by NMR spectroscopy and ESI mass spectrometry. Moreover, yellow block crystals of **L^6** were obtained from slow evaporation of its chloroform solution, which unambiguously demonstrated the structure of methanofullerene linked with two phenyl-bridged pyridine arms (Figure 6.3). The asymmetric unit shows two crystallographically unique ligands, featuring slightly different N–N distances (12.94 and 11.44 Å, respectively), due to the quaternary carbons' flexibility.

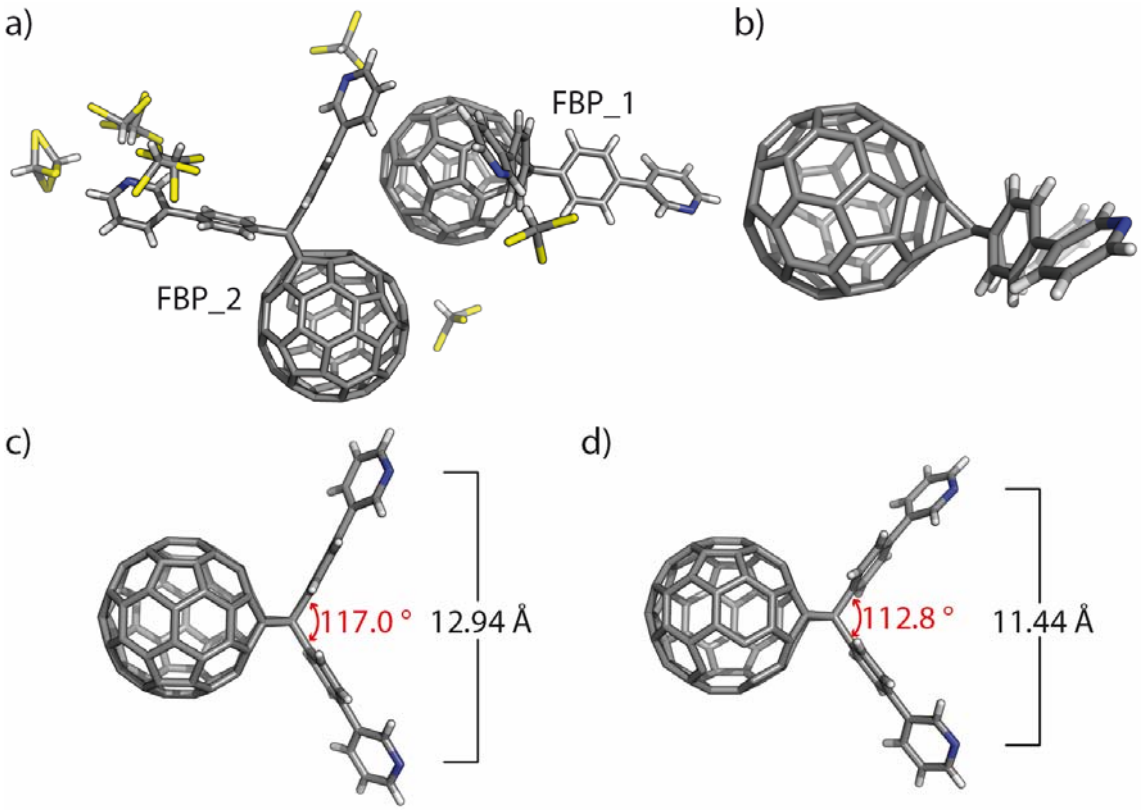

Figure 6.3 X-ray structure of ligand $\mathbf{L^6}$: (a) The asymmetric unit showing two crystallographically independent ligands (FBP_1 and FBP_2) and partially disordered chloroform molecules; (b) top view of the structure of ligand FBP_1; (c) the structure of ligand FBP_1 showing the N–N distance of 12.94 Å and the angle of 117.0° between two arms; (d) the structure of ligand FBP_2 showing the N–N distance of 11.44 Å and the angle of 112.8° between two arms. Color scheme: H, light grey; C, dark grey; N, blue; Cl, yellow.

6.3 Cage assembly

Owing to the low solubility of $\mathbf{L^6}$ in most organic solvents employed for cage formation, such as CH_3CN and DMSO, the cage assembly was found to proceed smoothly only in DMF. Heating a 2:1 mixture of $\mathbf{L^6}$ and $[Pd(MeCN)_4](BF_4)_2$ in DMF-d_7 at 70 °C for 1 d resulted in the quantitative formation of cage $[Pd_2\mathbf{L^6}_4]^{4+}$, undoubtedly characterized by NMR spectroscopy and mass spectrometry. Upon coordination of $\mathbf{L^6}$ to Pd^{II} cations, the downfield shift of proton signals of pyridine moieties was clearly observed in ^1H NMR spectra (Figure 6.4a), which is fully consistent with a reported cage with a similar backbone.[187] The expanded cage structure incorporating four giant fullerenes in the exterior space exhibited larger hydrodynamic radius than that for the ligand itself in DMF solution, as the diffusion coefficient was observed to decrease from 3.7 x 10^{-10} m^2s^{-1} for $\mathbf{L^6}$ to 1.8 x 10^{-10} m^2s^{-1} for $[Pd_2\mathbf{L^6}_4]^{4+}$ in DOSY spectra (Figure 6.4b). It is worth noting that the diameter of the longest axis measured from a C_4-symmetric PM6-optimized model of cage $[Pd_2\mathbf{L^6}_4]^{4+}$ is 30.9 Å, quite close to the double hydrodynamic radius (up to 30.0 Å) determined by DOSY spectrum (Figure 6.19). And the opposing Pd–Pd distance of 12.35 Å in the cage model is also in the range of N–N distances (12.94 and 11.44 Å) measured from crystal structure of $\mathbf{L^6}$. More evidently, the high-resolution ESI mass spectrum of cage $[Pd_2\mathbf{L^6}_4]^{4+}$ revealed prominent signals at m/z = 1094.1 and 1487.8, in line with simulated isotopic patterns of the formula $[Pd_2\mathbf{L^6}_4+nBF_4]^{(4-n)+}$ (n=0, 1) (Figure 6.20).

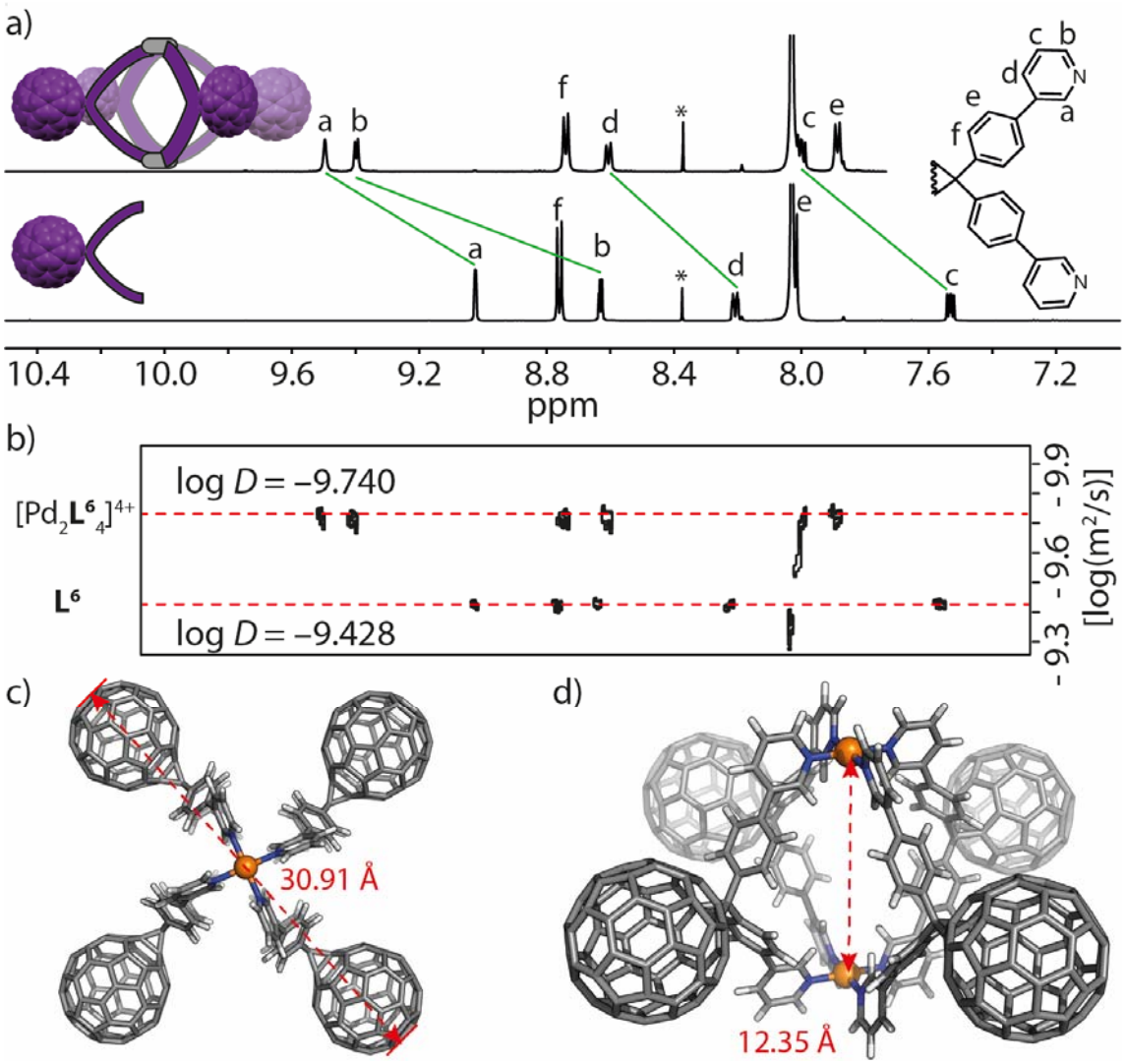

Figure 6.4 Characterization of ligand $\mathbf{L^6}$ and cage $[Pd_2\mathbf{L^6}_4]^{4+}$: (a) Comparison of ^{1}H NMR spectra (600 MHz, 298 K, DMF-d_7) of cage $[Pd_2\mathbf{L^6}_4]^{4+}$ (0.64 mM) and ligand $\mathbf{L^6}$ (2.56 mM); (b) DOSY spectra showing that the diffusion coefficients of $[Pd_2\mathbf{L^6}_4]^{4+}$ and $\mathbf{L^6}$ are 1.8 and 3.7 x 10^{-10} m^2s^{-1}, respectively; (c) and (d) PM6-optimized model of cage $[Pd_2\mathbf{L^6}_4]^{4+}$.

6.4 Conclusion and prospects

This chapter showed the synthesis of a novel fullerene-based ligand $\mathbf{L^6}$ bearing dipyridyl arms, which successfully assembled with the square-planar Pd^{II} acceptors to form a cage structure, characterized by NMR spectroscopy and ESI mass spectrometry.

As mentioned in the introduction of this chapter, we aimed at achieving the organo-fullerene ligand based on the structure of fullerene mono-adduct instead of hexakis-adduct for the purpose of retaining its partially spherical shape, thus allowing for exterior fullerene moieties that can be further wrapped by some bowl-shaped hosts, for example, cyclodextrin or the aforementioned metallosupramolecular bowl $[Pd_2\mathbf{L^2}_3X_2]$ (X= CH_3CN or Cl^-) (Section 3.3), a sophisticated hierarchical assembly driven by coordination bonding and host-guest interaction sequentially. Further

related experiments are still underway and we are looking forward to obtaining the precisely designed supramolecular structures with more complexity based on this strategy.

6.5 Experimental section

6.5.1 Synthesis and characterization

6.5.1.1 Compound S2

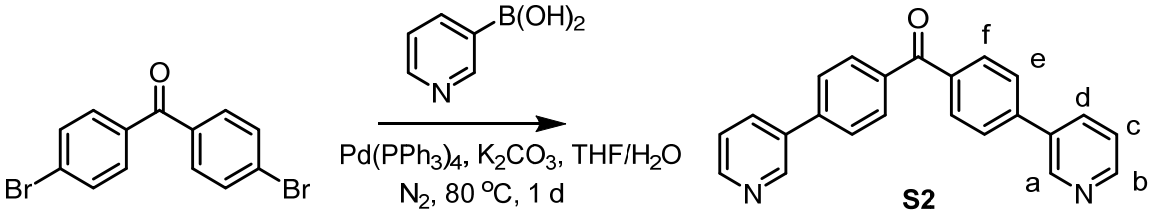

4,4'-Dibromobenzophenone (571.2 mg, 1.68 mmol, 1 eq.), 3-pyridinylboronic acid (826.0 mg, 6.72 mmol, 4 eq.), K_2CO_3 (1857.6 mg, 13.44 mmol, 8 eq.), and $Pd(PPh_3)_4$ (577.8 mg, 0.50 mmol, 0.3 eq.) were placed in a flask and dissolved with THF (100 mL) and water (20 mL). The reaction mixture was stirred at 80 °C for 1 d under nitrogen atmosphere. The reaction was quenched by addition of water and then THF was evaporated by using rotary evaporator. The aqueous layer was extracted with EtOAc, and the organic layer was washed with brine and dried over Na_2SO_4. After removal of the solvent under reduced pressure, the residue was purified by column chromatography on Isolera™ flash purification system to give the crude product (TLC analysis: R_f=0.25 in CH_2Cl_2/CH_3OH=20:1). This was further purified via recycling GPC and the solvent was removed under reduced pressure to yield the desired product (363.0 mg, 64 %).

^{1}H NMR (600 MHz, 298 K, $CDCl_3$): δ (ppm) = 8.93 (d, J = 2.4 Hz, 2H), 8.67 (dd, J = 4.8, 1.6 Hz, 2H), 7.99 – 7.94 (m, 6H), 7.74 (d, J = 8.3 Hz, 4H), 7.44 (dd, J = 7.9, 4.8 Hz, 2H).

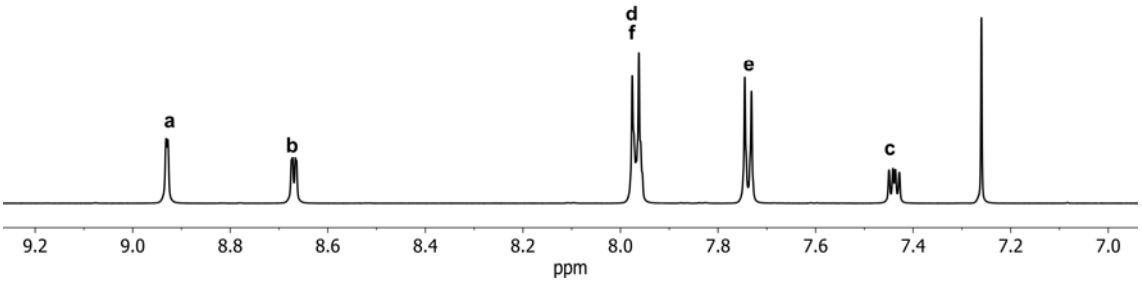

Figure 6.5 ^{1}H NMR spectrum (600 MHz, 298 K, $CDCl_3$) of compound **S2**.

^{13}C NMR (151 MHz, 298 K, $CDCl_3$): δ (ppm) = 195.65, 149.39, 148.44, 142.04, 137.12, 135.71, 134.79, 131.02, 127.28, 123.92.

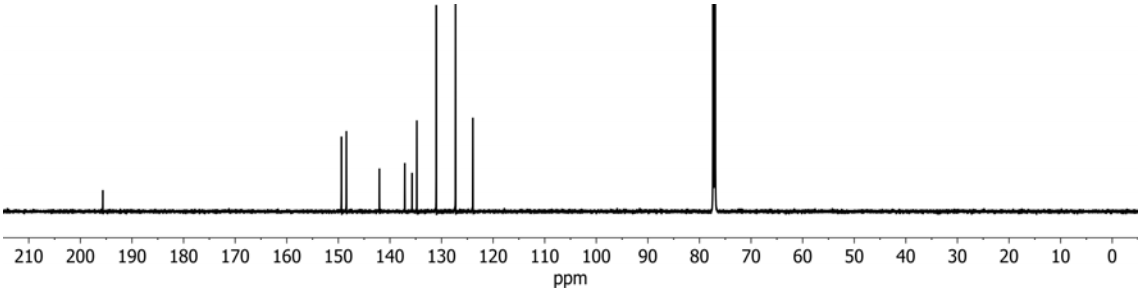

Figure 6.6 ^{13}C NMR spectrum (151 MHz, 298 K, $CDCl_3$) of compound **S2**.

ESI HRMS ($C_{23}H_{16}N_2O$): $[M + H]^+$ calcd. for $C_{23}H_{17}N_2O$ 337.1335; found 337.1285.

6.5.1.2 Compound S3

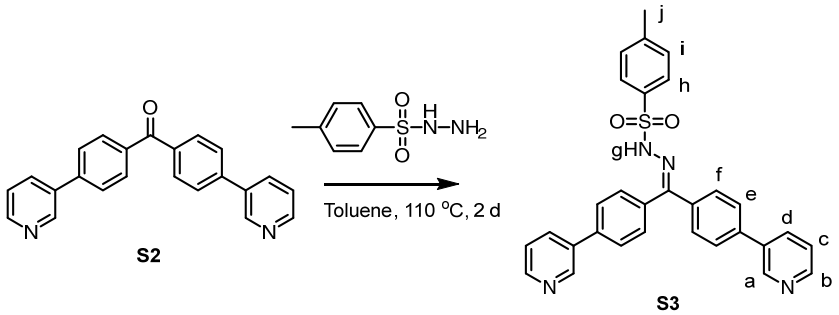

A solution of compound **S2** (336.0 mg, 1.0 mmol, 1 eq.) and p-tosylhydrazide (372.5 mg, 2.0 mmol, 2 eq.) in toluene (50 mL) was heated at 110 °C for 2 d under nitrogen atmosphere. After removal of the solvent under reduced pressure, the crude product was isolated by column chromatography on Isolera™ flash purification system and further purified via recycling GPC to yield the desired product (266.0 mg, 53 %).

The modified tosyl hydrazone unit results in the unsymmetrical chemical shifts of the protons on two 4-(pyridin-3-yl)phenyl groups and all the proton signals are assigned via 2D NMR spectroscopy.

^{1}H NMR (600 MHz, 298 K, $CDCl_3$): δ (ppm) = 8.90 (s, 1H), 8.83 (s, 1H), 8.68 (d, *J* = 4.8 Hz, 1H), 8.64 – 8.57 (m, 1H), 7.94 (dt, *J* = 7.9, 2.0 Hz, 1H), 7.90 (d, *J* = 8.2 Hz, 2H), 7.86 (dt, *J* = 7.9, 2.0 Hz, 1H), 7.77 – 7.74 (m, 2H), 7.60 (d, *J* = 8.4 Hz, 2H), 7.54 (d, *J* = 8.4 Hz, 2H), 7.47 – 7.43 (m, 1H), 7.39 – 7.35 (m, 3H), 7.32 – 7.29 (m, 2H), 2.45 (s, 3H).

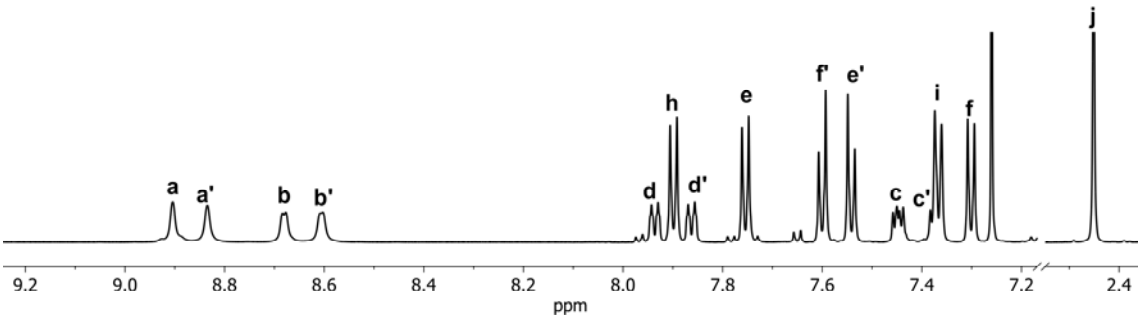

Figure 6.7 ^{1}H NMR spectrum (600 MHz, 298 K, $CDCl_3$) of compound **S3**.

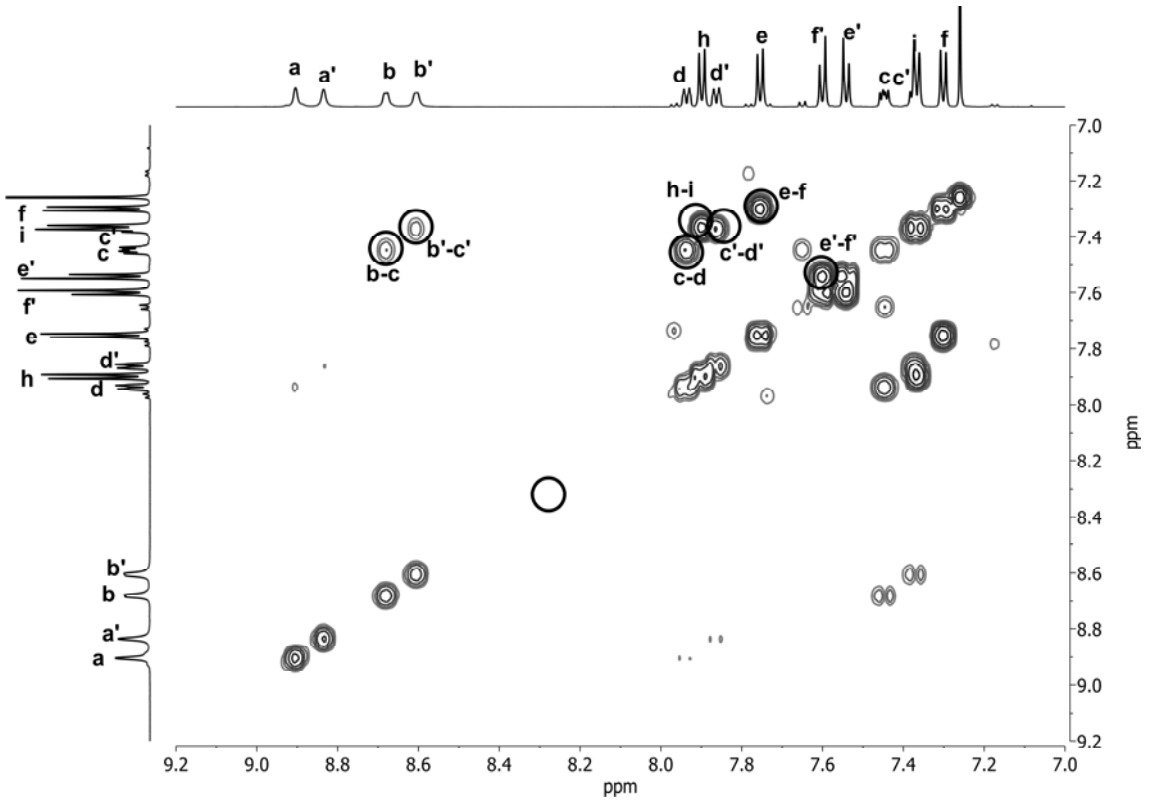

Figure 6.8 Partial $^{1}H - {}^{1}H$ COSY spectrum (600 MHz, 298 K, $CDCl_3$) of compound **S3**.

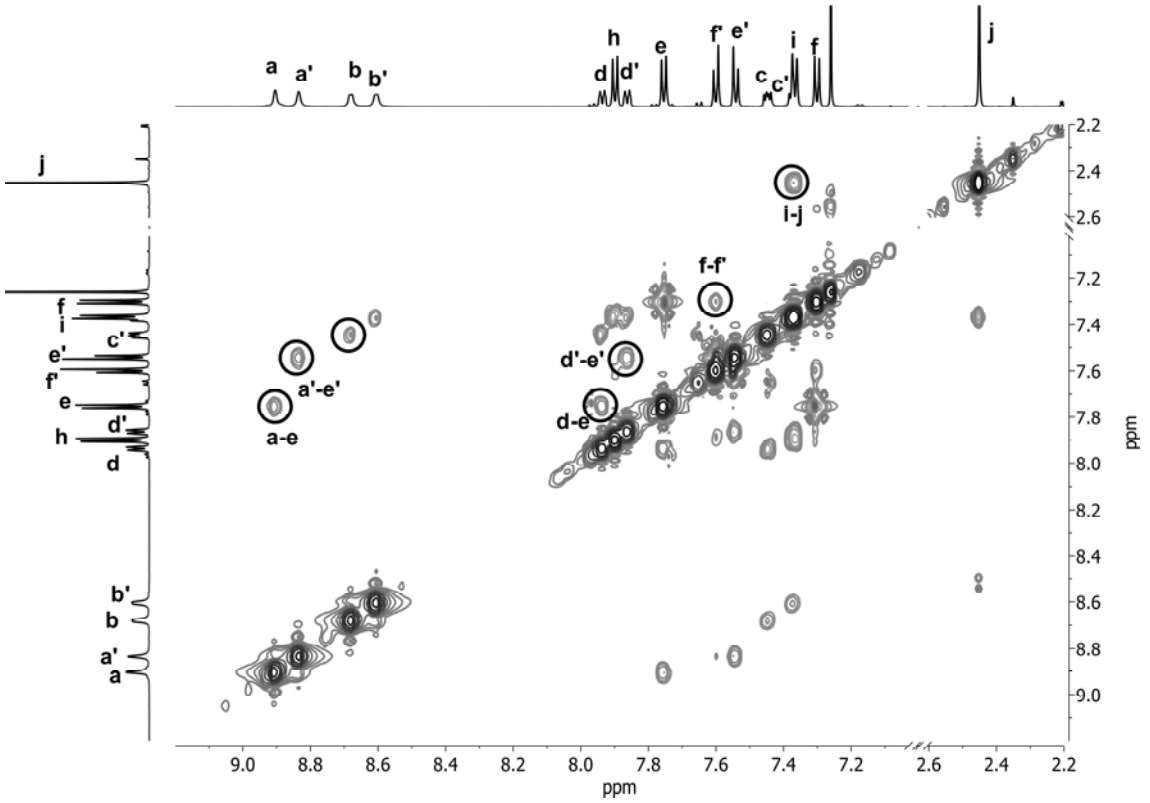

Figure 6.9 Partial $^{1}H - {}^{1}H$ NOESY spectrum (600 MHz, 298 K, $CDCl_3$) of compound **S3**.

ESI HRMS ($C_{30}H_{24}N_4O_2S$): $[M + H]^+$ calcd. for $C_{30}H_{25}N_4O_2S$ 505.1693; found 505.1680.

6.5.1.3 Ligand L[6]

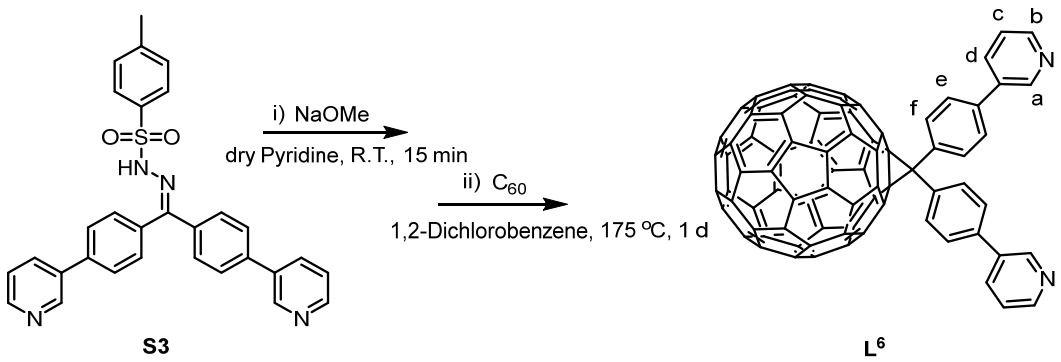

To a suspension of compound **S3** (249.2 mg, 0.49 mmol, 1 eq.) in anhydrous pyridine (10 mL) was added NaOMe (29.2 mg, 0.54 mmol, 1.1 eq). The mixture was stirred for 15 min at ambient temperature with the color change of the solution from yellow to light orange. A solution of C_{60} (1058.4 mg, 1.47 mmol, 2.7 eq.) in dry 1,2-dichlorobenzene (50 mL), prepared by mixing the solvent with C_{60} and being stirred for 1 h, was then added. The mixture was stirred and heated at 180 °C for 18 h. Removal of the solvent by distillation under reduced pressure, gave a dark solid. The unreacted C_{60} was first removed by column chromatography on silica-gel, using toluene as the eluent. Then a black solution was obtained by using CH_2Cl_2/CH_3OH as the eluent and further purified via recycling GPC to yield the desired product (130.0 mg, 25 %).

^{1}H NMR (600 MHz, 298 K, DMF-d_7): δ (ppm) = 9.02 (dd, J = 2.5, 0.9 Hz, 2H), 8.79 – 8.74 (m, 4H), 8.63 (dd, J = 4.8, 1.6 Hz, 2H), 8.21 (ddd, J = 8.0, 2.5, 1.6 Hz, 2H), 8.02 – 8.01 (m, mixed with residual solvent peak), 7.53 (ddd, J = 8.0, 4.7, 0.9 Hz, 2H).

A signal at 8.02 ppm overlapping with the residual solvent peak could be assigned via 2D NMR spectroscopy.

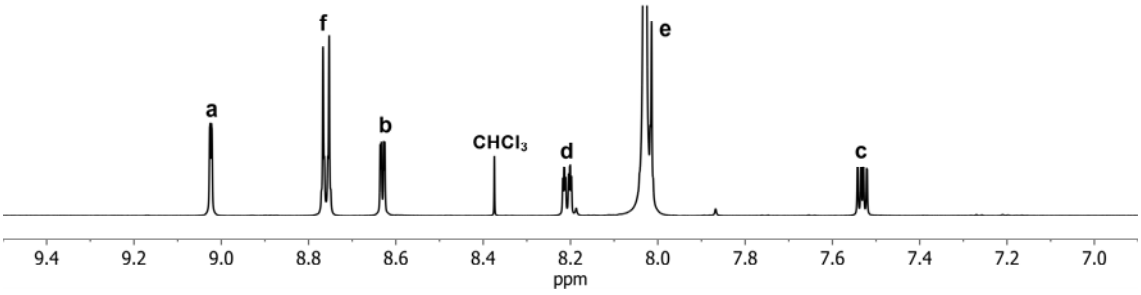

Figure 6.10 ^{1}H NMR spectrum (600 MHz, 298 K, DMF-d_7) of ligand **L[6]** (2.56 mM).

^{13}C NMR (151 MHz, 298 K, DMF-d_7): δ (ppm) = 150.17, 150.01, 149.11, 147.21, 146.04, 145.98, 145.61, 145.54, 145.43, 145.11, 144.73, 143.85, 143.80, 143.76, 143.08, 143.02, 141.49, 140.29, 138.73, 138.57, 136.39, 135.33, 133.32, 128.52, 124.98, 80.65, 59.03.

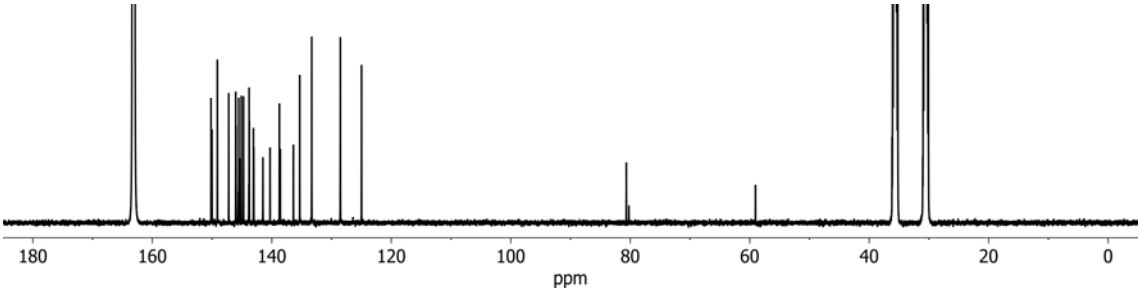

Figure 6.11 ^{13}C NMR spectrum (151 MHz, 298 K, DMF-d_7) of ligand **L^6** (2.56 mM).

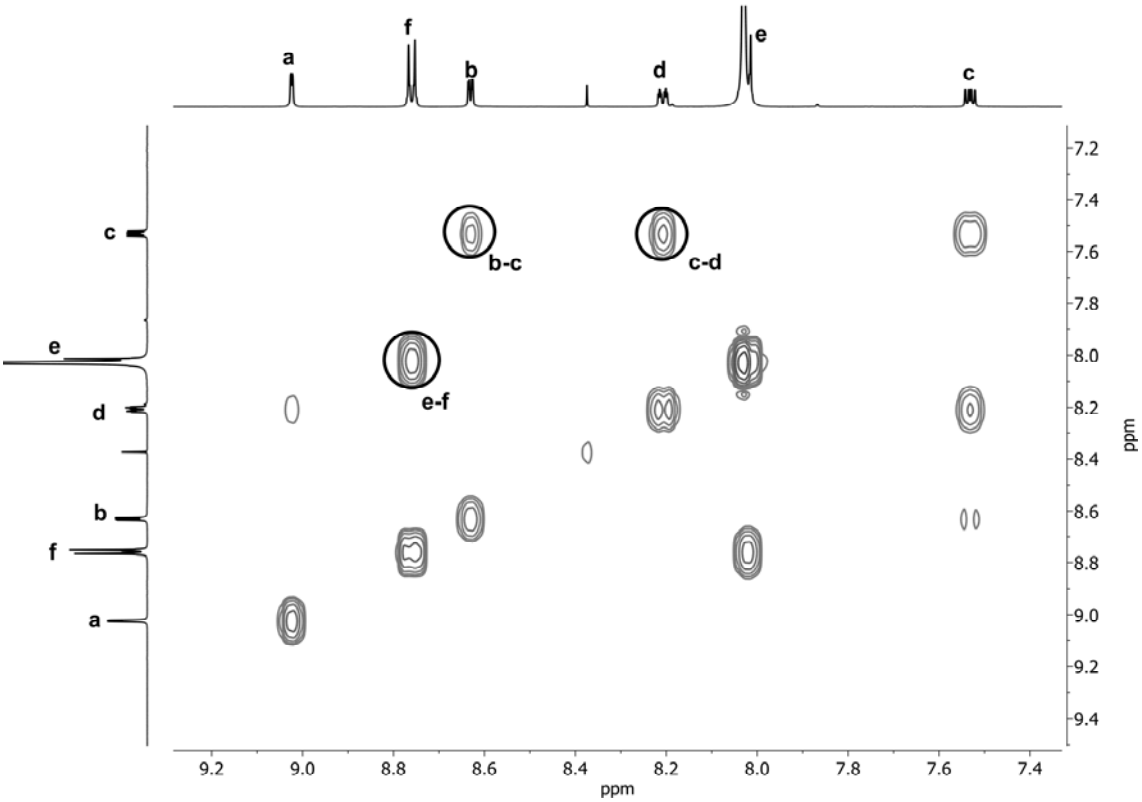

Figure 6.12 Partial $^1H - ^1H$ COSY spectrum (600 MHz, 298 K, DMF-d_7) of ligand **L^6** (2.56 mM).

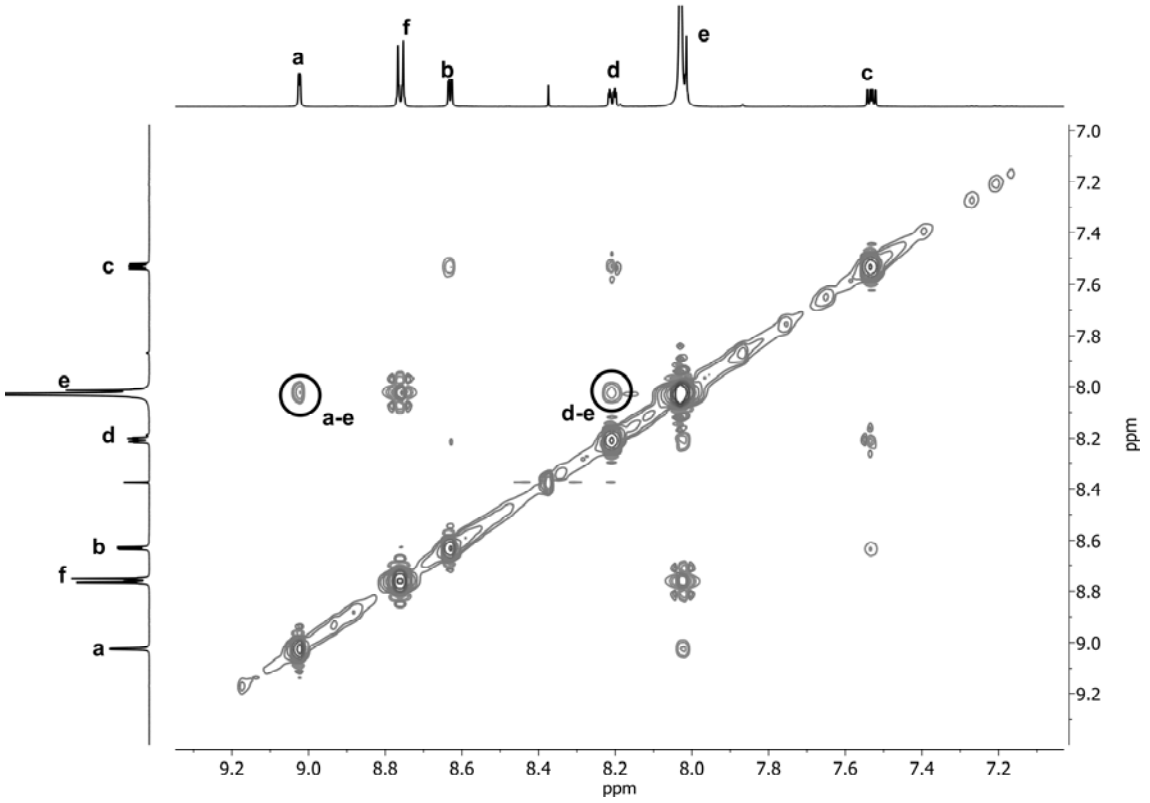

Figure 6.13 Partial ^{1}H – ^{1}H NOESY spectrum (600 MHz, 298 K, DMF-d_7) of ligand **L^{6}** (2.56 mM).

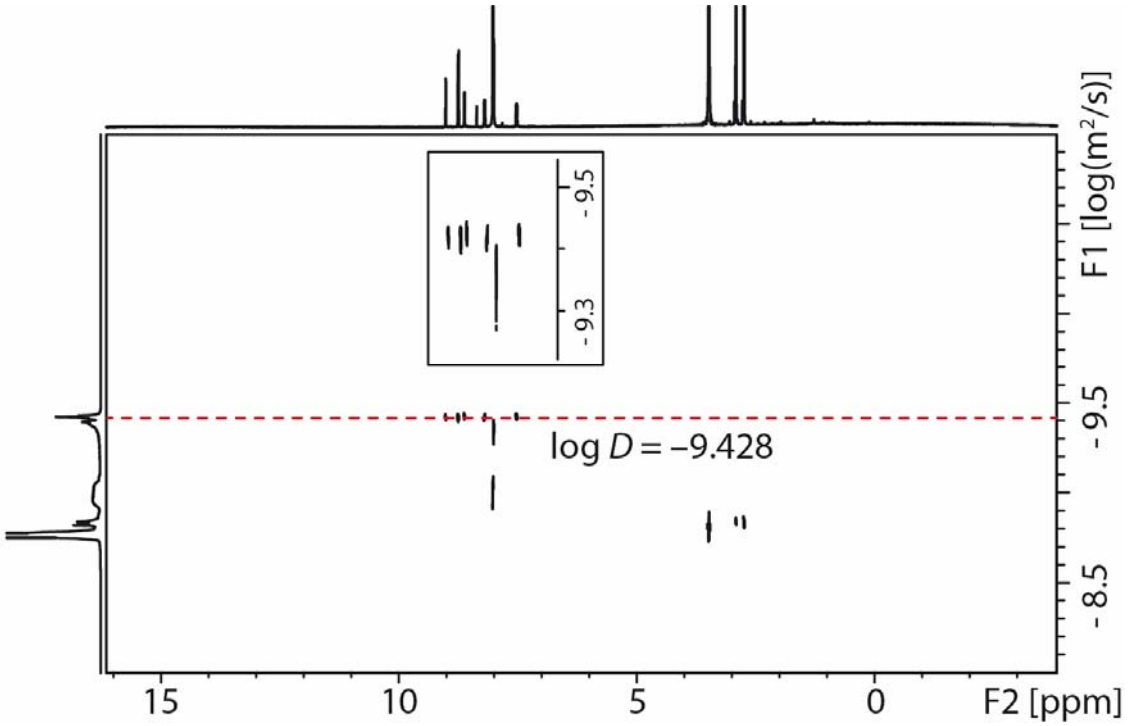

Figure 6.14 DOSY spectrum (500 MHz, 298 K, DMF-d_7) of ligand **L^{6}** (2.56 mM): diffusion coefficient = 3.7 x 10^{-10} m^2s^{-1}, log *D* = −9.43, r = 7.3 Å.

6.5.1.4 Cage $[Pd_2L^6_4]^{4+}$

A solution of $[Pd(MeCN)_4](BF_4)_2$ (129.7 µL, 15 mM/ DMF-d_7, 1.95 µmol, 1 eq.) was combined with ligand **L^{6}** (4.1 mg, 3.90 µmol, 2 eq.) in DMF-d_7 (1389 µL) and heated at 70 °C for 1 d to give a 0.64 mM solution of cage $[Pd_2L^6_4]^{4+}$.

^{1}H NMR (600 MHz, 298 K, DMF-d_7): δ (ppm) = 9.50 (s, 2H), 9.41 – 9.38 (m, 2H), 8.74 (d, J = 7.9 Hz, 4H), 8.61 (dt, J = 8.1, 1.6 Hz, 2H), 8.00 (dd, J = 8.1, 5.6 Hz, mixed with residual solvent peak), 7.89 (d, J = 8.0 Hz, 4H).

A signal at 8.00 ppm overlapping with the residual solvent peak in the aromatic region could be assigned via 2D NMR spectroscopy.

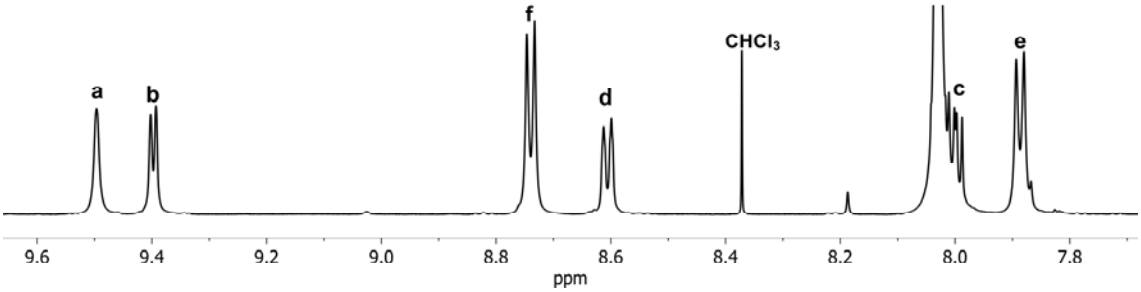

Figure 6.15 ^{1}H NMR spectrum (600 MHz, 298 K, DMF-d_7) of cage $[Pd_2\mathbf{L^6}_4]^{4+}$ (0.64 mM).

^{13}C NMR (151 MHz, 298 K, DMF-d_7): δ (ppm) = 151.53, 149.99, 148.71, 146.09, 145.64, 145.56, 145.12, 145.06, 144.86, 144.69, 144.18, 143.50, 143.43, 143.31, 142.47, 142.42, 141.27, 140.79, 140.05, 138.32, 136.43, 132.88, 129.20, 128.31, 79.48, 57.74.

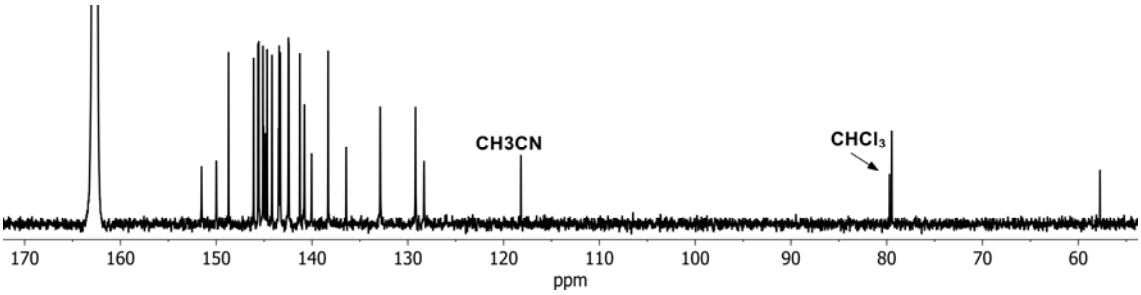

Figure 6.16 ^{13}C NMR spectrum (151 MHz, 298 K, DMF-d_7) of cage $[Pd_2\mathbf{L^6}_4]^{4+}$.

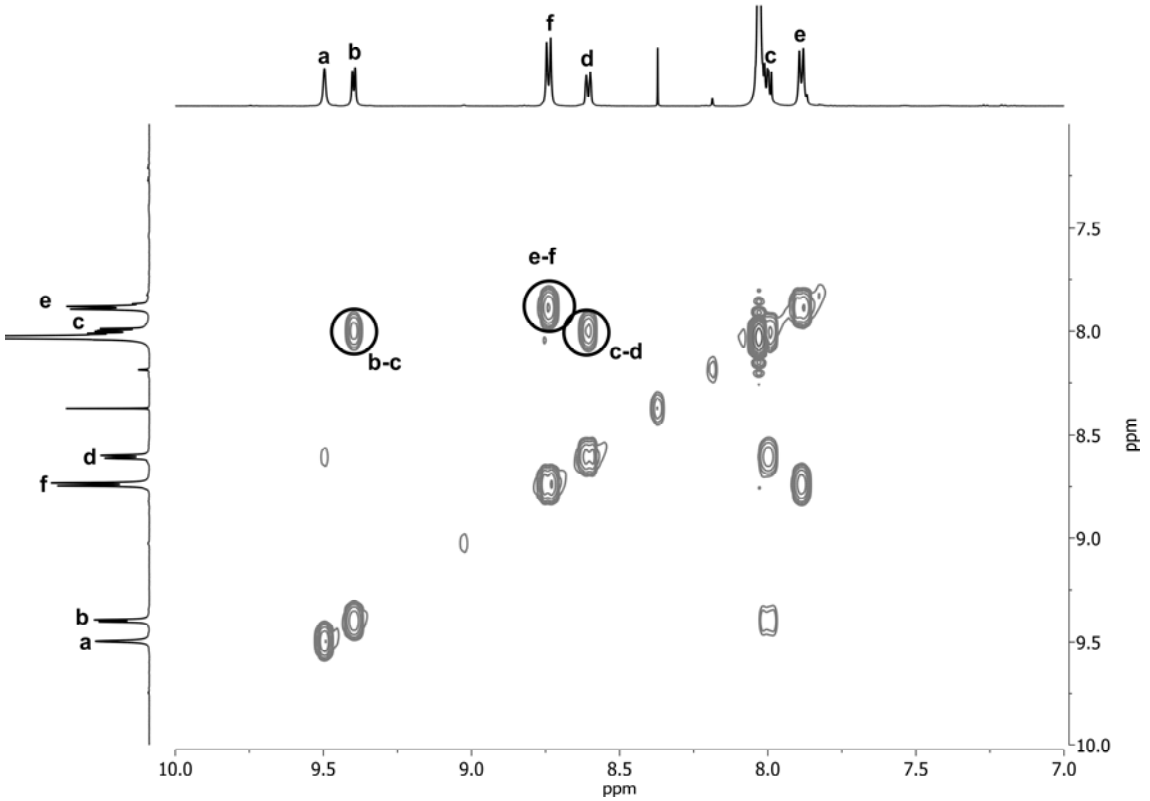

Figure 6.17 Partial $^{1}H - {}^{1}H$ COSY spectrum (600 MHz, 298 K, DMF-d_7) of cage $[Pd_2\mathbf{L^6}_4]^{4+}$.

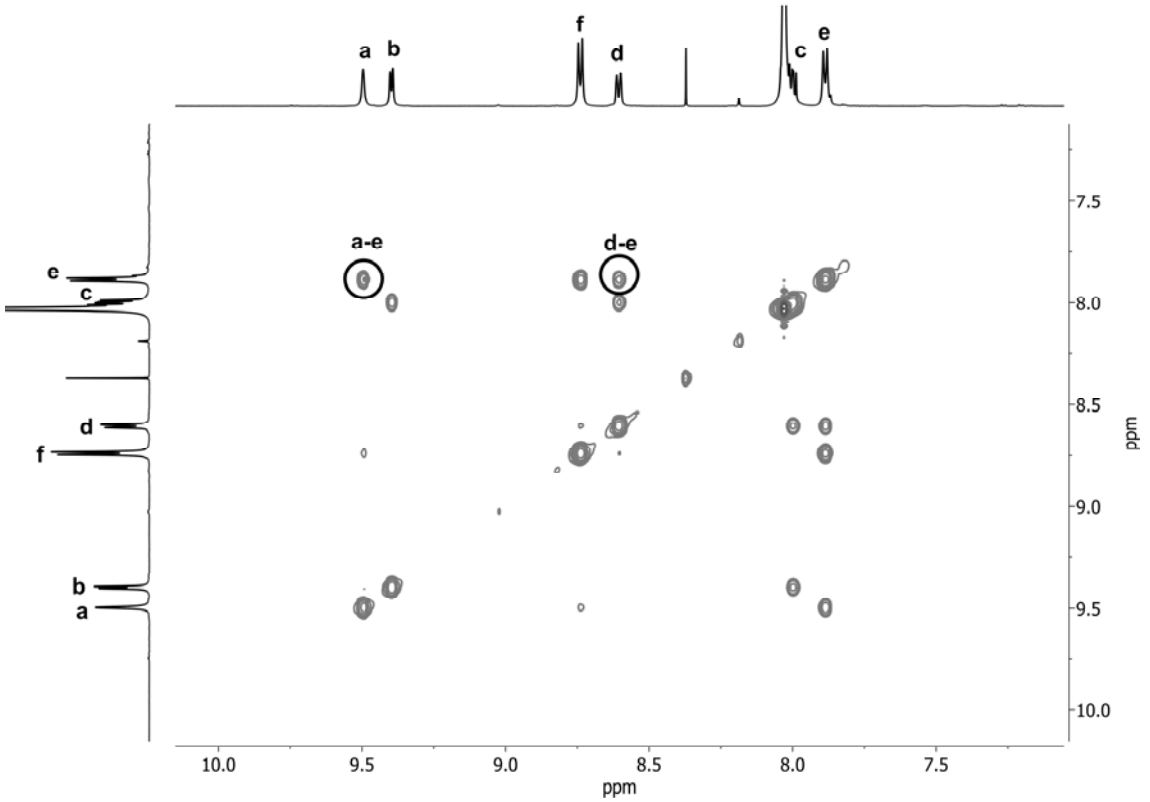

Figure 6.18 Partial $^{1}H - {}^{1}H$ NOESY spectrum (600 MHz, 298 K, DMF-d_7) of cage $[Pd_2\mathbf{L^6}_4]^{4+}$.

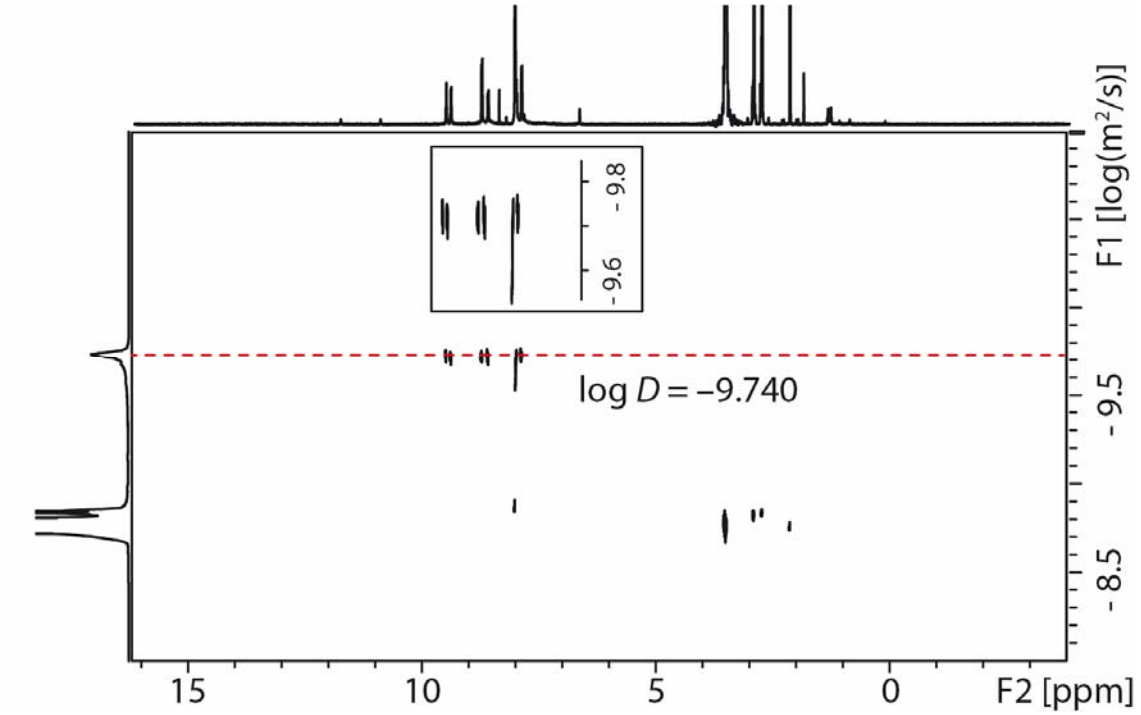

Figure 6.19 DOSY spectrum (500 MHz, 298 K, DMF-d_7) of cage $[Pd_2\mathbf{L^6}_4]^{4+}$: diffusion coefficient = 1.8 x 10^{-10} m^2s^{-1}, log D = –9.74, r = 15.0 Å.

ESI HRMS ($C_{332}H_{64}N_8Pd_2B_4F_{16}$): $[Pd_2\mathbf{L^6}_4]^{4+}$ calcd. for $C_{332}H_{64}N_8Pd_2$ 1094.0857; found 1094.0869; $[Pd_2\mathbf{L^6}_4+BF_4]^{3+}$ calcd. for $C_{332}H_{64}N_8Pd_2BF_4$ 1487.7824; found 1487.7828.

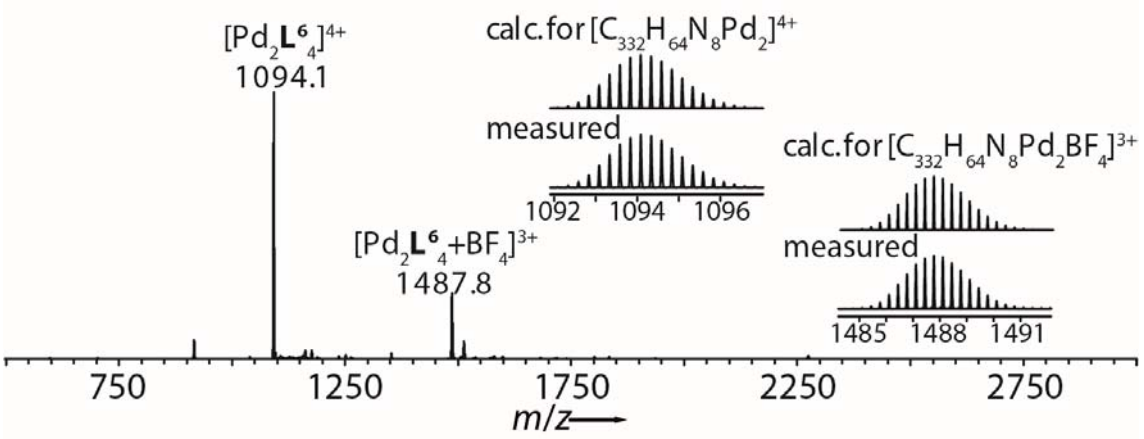

Figure 6.20 ESI mass spectrum of $[Pd_2\mathbf{L^6}_4]^{4+}$.

6.5.2 X-Ray data

Table 6.1 Crystallographic data of **L^6**.

Compound	**L^6·3CHCl$_3$**
CCDC number	---
Identification code	bc29a
Empirical formula	$C_{86}H_{19}Cl_9N_2$
Formula weight	1399.08
Temperature (K)	100(2)
Crystal system	Monoclinic
Space group	$P2_1/c$
a (Å)	30.0739(12)
b (Å)	10.5011(4)
c (Å)	35.2211(13)
α (º)	90
β (º)	92.069(2)
γ (º)	90
Volume (Å^3)	11115.9(7)
Z	8
Density (calc.) (g/cm^3)	1.672
Absorption coefficient (mm^{-1})	4.624
F(000)	5616
Crystal size (mm^3)	0.500 x 0.300 x 0.100
θ range for data collection (º)	2.511 to 70.099
Reflections collected	181579
Observed reflections [R(int)]	21065 [0.1083]
Goodness-of-fit on F^2	1.019
R_1 [I>2σ(I)]	0.0763
wR_2 (all data)	0.2066
Largest diff. peak and hole (e.Å^{-3})	0.950 and -0.845
Data / restraints / parameters	21065 / 4068 / 1858

Yellow block crystals of **L^6** were obtained by slow evaporation of a $CHCl_3$ solution of **L^6**. Stereochemical restraints for the chloroform (residue class CL3) were generated by the GRADE program using the GRADE Web Server and applied in the refinement.

Table 6.2 Definition of residues involved in **L^6**.

Fragment	**Residue class**	**Occurrence**	**Residue numbers**
Ligand **L^6**	FBP	2	1,2
$CHCl_3$	CL3	9	3-11 (three $CHCl_3$ with disorder)

7 Abbreviations

Ac	Anthracene
$BArF^-$	Tetrakis(3,5-bis(trifluoromethyl)phenyl)borate
BDC^{2-}	Terephthalate anion
BF_4^-	Tetrafluoroborate anion
BODIPY	Boron-dipyrromethene
C_{60}PCBM	[6,6]-phenyl-C_{61}-butyric acid methyl ester
CD_3CN	Deuterated acetonitrile
$CHCl_3$	Chloroform
CH_3CN	Acetonitrile
COSY	Correlated spectroscopy
CSI	Cold-spray ionization
CS_2	Carbon disulfide
d	Day(s)
DABCO	1,4-Diazabicyclo[2.2.2]octane
DFT	Density functional theory
DMSO	Dimethyl sulfoxide
DMF	Dimethylformamide
DOSY	Diffusion-ordered spectroscopy
en	Ethylenediamine
eq.	Equivalent
ESI	Electrospray ionization
EtOAc	Ethyl acetate
GPC	Gel permeation chromatography
h	Hour
HR-MS	High resolution mass spectrometry
Hz	Hertz
Ind	Indene
J	Coupling constant
K	Kelvin
L	Ligand
LDI-TOF	laser desorption/ionization–time of flight
m/z	Mass-to-charge ratio
$MeNO_2$	Nitromethane

MeOH	Methanol
MHz	Megahertz
mM	mmol L^{-1}
Nap	1,8-Naphthyridine
NEt_3	Triethylamine
nm	Nanometer
NMR	Nuclear magnetic resonance
NOESY	Nuclear overhauser effect spectroscopy
OAc^-	acetate anion
$OPPh_3$	Triphenylphosphine oxide
OTf^-	Trifluoromethanesulfonate anion
PBI	Perylene bisimide
Pd	Palladium
PEt_3	Triethylphosphine
$PhNO_2$	Nitrobenzene
PPh_3	Triphenylphosphine
ppm	Parts per million
r.t.	Room temperature
Rh	Rhodium
SbF_6^-	Hexafluoroantimonate anion
sol	solvent
THF	Tetrahydrofuran
TLC	Thin layer chromatography
TOF	Time-of-flight
TPT	2,4,6-Tri(4-pyridyl)-1,3,5-triazine
2D	Two dimensional
3D	Three dimensional
δ	Chemical shift
Å	Ångström
°C	Celcius

8 List of figures

9 List of tables

10References

(1) H. W. Kroto, J. R. Heath, S. C. O'Brien, R. F. Curl, R. E. Smalley, *Nature* **1985,** *318,* 162.
(2) F. Langa, J.-F. Nierengarten. *Fullerenes: Principles and Applications*, Edition 2; RSC: Cambridge, 2011; pp 191.
(3) H. Kroto, *Angew. Chem. Int. Ed.* **1997,** *36,* 1578.
(4) R. E. Smalley, *Angew. Chem. Int. Ed.* **1997,** *36,* 1594.
(5) R. F. Curl, *Angew. Chem. Int. Ed.* **1997,** *36,* 1566.
(6) W. Krätschmer, L. D. Lamb, K. Fostiropoulos, D. R. Huffman, *Nature* **1990,** *347,* 354.
(7) J. B. Howard, J. T. McKinnon, Y. Makarovsky, A. L. Lafleur, M. E. Johnson, *Nature* **1991,** *352,* 139.
(8) R. Taylor, G. J. Langley, H. W. Kroto, D. R. M. Walton, *Nature* **1993,** *366,* 728.
(9) L. T. Scott, *Angew. Chem. Int. Ed.* **2004,** *43,* 4994.
(10) A. D. Darwish, H. W. Kroto, R. Taylor, D. R. M. Walton, *Fullerene Sci. Technol.* **2006,** *1,* 571.
(11) R. Taylor, J. P. Hare, A. a. K. Abdul-Sada, H. W. Kroto, *J. Chem. Soc., Chem. Commun.* **1990,** 1423.
(12) A. D. Darwish, H. W. Kroto, R. Taylor, D. R. M. Walton, *J. Chem. Soc., Chem. Commun.* **1994,** 15.
(13) C. A. Martin, D. Ding, J. K. Sorensen, T. Bjornholm, J. M. van Ruitenbeek, H. S. van der Zant, *J. Am. Chem. Soc.* **2008,** *130,* 13198.
(14) T. Chuard, R. Deschenaux, *J. Mater. Chem.* **2002,** *12,* 1944.
(15) A. D. Mendaza, A. Melianas, S. Rossbauer, O. Backe, L. Nordstierna, P. Erhart, E. Olsson, T. D. Anthopoulos, O. Inganas, C. Muller, *Adv. Mater.* **2015,** *27,* 7325.
(16) G. Dennler, M. C. Scharber, C. J. Brabec, *Adv. Mater.* **2009,** *21,* 1323.
(17) C. H. Hsieh, Y. J. Cheng, P. J. Li, C. H. Chen, M. Dubosc, R. M. Liang, C. S. Hsu, *J. Am. Chem. Soc.* **2010,** *132,* 4887.
(18) C.-Z. Li, H.-L. Yip, A. K. Y. Jen, *J. Mater. Chem.* **2012,** *22,* 4161.
(19) H. Tanaka, Y. Abe, Y. Matsuo, J. Kawai, I. Soga, Y. Sato, E. Nakamura, *Adv. Mater.* **2012,** *24,* 3521.
(20) Z. Chen, L. Ma, Y. Liu, C. Chen, *Theranostics* **2012,** *2,* 238.
(21) A. Montellano, T. Da Ros, A. Bianco, M. Prato, *Nanoscale* **2011,** *3,* 4035.
(22) P. Mroz, G. P. Tegos, H. Gali, T. Wharton, T. Sarna, M. R. Hamblin, *Photochem. Photobiol. Sci.* **2007,** *6,* 1139.
(23) J. J. Ryan, H. R. Bateman, A. Stover, G. Gomez, S. K. Norton, W. Zhao, L. B. Schwartz, R. Lenk, C. L. Kepley, *J. Immunol.* **2007,** *179,* 665.
(24) G. B. Adams, M. O'Keeffe, R. S. Ruoff, *J. Phys. Chem.* **1994,** *98,* 9465.
(25) T. Kawase, H. Kurata, *Chem. Rev.* **2006,** *106,* 5250.
(26) P. D. Boyd, C. A. Reed, *Acc. Chem. Res.* **2005,** *38,* 235.
(27) K. Tashiro, T. Aida, *Chem. Soc. Rev.* **2007,** *36,* 189.
(28) M. J. Li, C. H. Huang, C. C. Lai, S. H. Chiu, *Org. Lett.* **2012,** *14,* 6146.
(29) E. Huerta, G. A. Metselaar, A. Fragoso, E. Santos, C. Bo, J. de Mendoza, *Angew. Chem. Int. Ed.* **2007,** *46,* 202.
(30) D. C. Yang, M. Li, C. F. Chen, *Chem. Commun.* **2017,** *53,* 9336.
(31) C. M. Alvarez, G. Aullon, H. Barbero, L. A. Garcia-Escudero, C. Martinez-Perez, J. M. Martin-Alvarez, D. Miguel, *Org. Lett.* **2015,** *17,* 2578.
(32) C. Mejuto, L. Escobar, G. Guisado-Barrios, P. Ballester, D. Gusev, E. Peris, *Chem. Eur. J.* **2017,** *23,* 10644.
(33) A. Sygula, *Synlett* **2016,** *27,* 2070.
(34) H. Isla, M. Gallego, E. M. Perez, R. Viruela, E. Orti, N. Martin, *J. Am. Chem. Soc.* **2010,** *132,* 1772.
(35) B. Grimm, J. Santos, B. M. Illescas, A. Munoz, D. M. Guldi, N. Martin, *J. Am. Chem. Soc.* **2010,** *132,* 17387.
(36) K. Tashiro, T. Aida, J.-Y. Zheng, K. Kinbara, K. Saigo, S. Sakamoto, K. Yamaguchi, *J. Am. Chem. Soc.* **1999,** *121,* 9477.
(37) J. L. Atwood, G. A. Koutsantonis, C. L. Raston, *Nature* **1994,** *368,* 229.
(38) D. Canevet, E. M. Pérez, N. Martín, *Angew. Chem. Int. Ed.* **2011,** *50,* 9248.
(39) E. Huerta, E. Cequier, J. de Mendoza, *Chem. Commun.* **2007,** 5016.
(40) G. Markiewicz, A. Jenczak, M. Kolodziejski, J. J. Holstein, J. K. M. Sanders, A. R. Stefankiewicz, *Nat. Commun.* **2017,** *8,* 15109.
(41) C. García-Simón, M. Costas, X. Ribas, *Chem. Soc. Rev.* **2016,** *45,* 40.
(42) Y. Inokuma, T. Arai, M. Fujita, *Nat. Chem.* **2010,** *2,* 780.
(43) S. Goswami, D. Ray, K. I. Otake, C. W. Kung, S. J. Garibay, T. Islamoglu, A. Atilgan, Y. Cui, C. J. Cramer, O. K. Farha, J. T. Hupp, *Chem. Sci.* **2018,** *9,* 4477.
(44) H. Meng, C. Zhao, Y. Li, M. Nie, C. Wang, T. Wang, *Nanoscale* **2018,** *10,* 3291.
(45) T. E. Shubina, D. I. Sharapa, C. Schubert, D. Zahn, M. Halik, P. A. Keller, S. G. Pyne, S. Jennepalli, D. M. Guldi, T. Clark, *J. Am. Chem. Soc.* **2014,** *136,* 10890.

(46) A. L. Montero-Alejo, E. Menéndez-Proupin, M. E. Fuentes, A. Delgado, F. P. Montforts, L. A. Montero-Cabrera, J. M. García de la Vegab, *Phys. Chem. Chem. Phys.* **2012,** *14,* 13058.
(47) K. Suzuki, K. Takao, S. Sato, M. Fujita, *J. Am. Chem. Soc.* **2010,** *132,* 2544.
(48) M. Tominaga, K. Suzuki, T. Murase, M. Fujita, *J. Am. Chem. Soc.* **2005,** *127,* 11950.
(49) N. Kishi, Z. Li, K. Yoza, M. Akita, M. Yoshizawa, *J. Am. Chem. Soc.* **2011,** *133,* 11438.
(50) D. Zhang, T. K. Ronson, J. R. Nitschke, *Acc. Chem. Res.* **2018,** *51,* 2423.
(51) A. M. Castilla, W. J. Ramsay, J. R. Nitschke, *Acc. Chem. Res.* **2014,** *47,* 2063.
(52) T. K. Ronson, S. Zarra, S. P. Black, J. R. Nitschke, *Chem. Commun.* **2013,** *49,* 2476.
(53) W. Meng, B. Breiner, K. Rissanen, J. D. Thoburn, J. K. Clegg, J. R. Nitschke, *Angew. Chem. Int. Ed.* **2011,** *50,* 3479.
(54) N. Struch, C. Bannwarth, T. K. Ronson, Y. Lorenz, B. Mienert, N. Wagner, M. Engeser, E. Bill, R. Puttreddy, K. Rissanen, J. Beck, S. Grimme, J. R. Nitschke, A. Lutzen, *Angew. Chem. Int. Ed.* **2017,** *56,* 4930.
(55) T. K. Ronson, A. B. League, L. Gagliardi, C. J. Cramer, J. R. Nitschke, *J. Am. Chem. Soc.* **2014,** *136,* 15615.
(56) T. K. Ronson, B. S. Pilgrim, J. R. Nitschke, *J. Am. Chem. Soc.* **2016,** *138,* 10417.
(57) T. K. Ronson, W. Meng, J. R. Nitschke, *J. Am. Chem. Soc.* **2017,** *139,* 9698.
(58) A. J. Musser, P. N. P, J. M. Richter, H. Mori, R. H. Friend, J. R. Nitschke, *J. Am. Chem. Soc.* **2017,** *139,* 12050.
(59) C. García-Simón, M. Garcia-Borràs, L. Gómez, T. Parella, S. Osuna, J. Juanhuix, I. Imaz, D. Maspoch, M. Costas, X. Ribas, *Nat. Commun.* **2014,** *5,* 5557.
(60) C. García-Simón, M. Garcia-Borràs, L. Gómez, I. Garcia-Bosch, S. Osuna, M. Swart, J. M. Luis, C. Rovira, M. Almeida, I. Imaz, D. Maspoch, M. Costas, X. Ribas, *Chem. Eur. J.* **2013,** *19,* 1445.
(61) C. García-Simón, A. Monferrer, M. Garcia-Borràs, I. Imaz, D. Maspoch, M. Costas, X. Ribas, *Chem. Commun.* **2018,** *55,* 798.
(62) K. Mahata, P. D. Frischmann, F. Würthner, *J. Am. Chem. Soc.* **2013,** *135,* 15656.
(63) K. Yazaki, M. Akita, S. Prusty, D. K. Chand, T. Kikuchi, H. Sato, M. Yoshizawa, *Nat. Commun.* **2017,** *8,* 15914.
(64) F. J. Rizzuto, J. R. Nitschke, *Nat. Chem.* **2017,** *9,* 903.
(65) F. J. Rizzuto, D. M. Wood, T. K. Ronson, J. R. Nitschke, *J. Am. Chem. Soc.* **2017,** *139,* 11008.
(66) D. M. Wood, W. Meng, T. K. Ronson, A. R. Stefankiewicz, J. K. Sanders, J. R. Nitschke, *Angew. Chem. Int. Ed.* **2015,** *54,* 3988.
(67) W. K. Han, H. X. Zhang, Y. Wang, W. Liu, X. Yan, T. Li, Z. G. Gu, *Chem. Commun.* **2018,** *54,* 12646.
(68) V. Martínez-Agramunt, D. G. Gusev, E. Peris, *Chem. Eur. J.* **2018,** *24,* 14802.
(69) S. I. Kawano, T. Fukushima, K. Tanaka, *Angew. Chem. Int. Ed.* **2018,** *57,* 14827.
(70) W. Brenner, T. K. Ronson, J. R. Nitschke, *J. Am. Chem. Soc.* **2017,** *139,* 75.
(71) H. Takezawa, T. Murase, G. Resnati, P. Metrangolo, M. Fujita, *J. Am. Chem. Soc.* **2014,** *136,* 1786.
(72) S. Mecozzi, J. J. Rebek, *Chem. Eur. J.* **1998,** *4,* 1016.
(73) C. Fuertes-Espinosa, C. García-Simón, E. Castro, M. Costas, L. Echegoyen, X. Ribas, *Chem. Eur. J.* **2017,** *23,* 3553.
(74) C. Fuertes-Espinosa, A. Gómez-Torres, R. Morales-Martínez, A. Rodríguez-Fortea, C. García-Simón, F. Gandara, I. Imaz, J. Juanhuix, D. Maspoch, J. M. Poblet, L. Echegoyen, X. Ribas, *Angew. Chem. Int. Ed.* **2018,** *57,* 11294.
(75) T. Y. Kim, R. A. S. Vasdev, D. Preston, J. D. Crowley, *Chem. Eur. J.* **2018,** *24,* 14878.
(76) M. J. Li, C. H. Huang, C. C. Lai, S. H. Chiu, *Org. Lett.* **2012,** *14,* 6146.
(77) W. Sun, Y. Wang, L. Ma, L. Zheng, W. Fang, X. Chen, H. Jiang, *J. Org. Chem.* **2018,** 14667.
(78) C. Zhang, Q. Wang, H. Long, W. Zhang, *J. Am. Chem. Soc.* **2011,** *133,* 20995.
(79) A. Ikeda, M. Yoshimura, H. Udzu, C. Fukuhara, S. Shinkai, *J. Am. Chem. Soc.* **1999,** *121,* 4296.
(80) A. Ikeda, H. Udzu, M. Yoshimura, S. Shinkai, *Tetrahedron* **2000,** *56,* 1825.
(81) C. Colomban, G. Szalóki, M. Allain, L. Gómez, S. Goeb, M. Sallé, M. Costas, X. Ribas, *Chem. Eur. J.* **2017,** *23,* 3016.
(82) N. Kishi, M. Akita, M. Kamiya, S. Hayashi, H. F. Hsu, M. Yoshizawa, *J. Am. Chem. Soc.* **2013,** *135,* 12976.
(83) N. Kishi, M. Akita, M. Yoshizawa, *Angew. Chem. Int. Ed.* **2014,** *53,* 3604.
(84) C. S. Wood, C. Browne, D. M. Wood, J. R. Nitschke, *ACS Cent. Sci.* **2015,** *1,* 504.
(85) A. Kaeser, M. Mohankumar, J. Mohanraj, F. Monti, M. Holler, J. J. Cid, O. Moudam, I. Nierengarten, L. Karmazin-Brelot, C. Duhayon, B. Delavaux-Nicot, N. Armaroli, J. F. Nierengarten, *Inorg. Chem.* **2013,** *52,* 12140.
(86) L. D. McPherson, M. Drees, S. I. Khan, T. Strassner, M. M. Abu-Omar, *Inorg. Chem.* **2004,** *43,* 4036.
(87) W. M. Bloch, G. H. Clever, *Chem. Commun.* **2017,** *53,* 8506.
(88) A. Schmidt, A. Casini, F. E. Kühn, *Coord. Chem. Rev.* **2014,** *275,* 19.
(89) M. Han, D. M. Engelhard, G. H. Clever, *Chem. Soc. Rev.* **2014,** *43,* 1848.
(90) S. Saha, I. Regeni, G. H. Clever, *Coord. Chem. Rev.* **2018,** *374,* 1.
(91) S. Pullen, G. H. Clever, *Acc. Chem. Res.* **2018,** *51,* 3052.
(92) Y. Yamauchi, M. Yoshizawa, M. Akita, M. Fujita, *J. Am. Chem. Soc.* **2010,** *132,* 960.
(93) S. Mukherjee, P. S. Mukherjee, *Chem. Commun.* **2014,** *50,* 2239.
(94) Y. R. Zheng, Z. Zhao, M. Wang, K. Ghosh, J. B. Pollock, T. R. Cook, P. J. Stang, *J. Am. Chem. Soc.* **2010,** *132,* 16873.

(95) A. M. Johnson, R. J. Hooley, *Inorg. Chem.* **2011,** *50,* 4671.
(96) P. Liao, B. W. Langloss, A. M. Johnson, E. R. Knudsen, F. S. Tham, R. R. Julian, R. J. Hooley, *Chem. Commun.* **2010,** *46,* 4932.
(97) D. Fujita, K. Suzuki, S. Sato, M. Yagi-Utsumi, Y. Yamaguchi, N. Mizuno, T. Kumasaka, M. Takata, M. Noda, S. Uchiyama, K. Kato, M. Fujita, *Nat. Commun.* **2012,** *3,* 1093.
(98) M. Yamashina, T. Yuki, Y. Sei, M. Akita, M. Yoshizawa, *Chem. Eur. J.* **2015,** *21,* 4200.
(99) M. Schmittel, B. He, P. Mal, *Org. Lett.* **2008,** *10,* 2513.
(100) M. Albrecht, M. Schneider, H. Röttele, *Angew. Chem. Int. Ed.* **1999,** *38,* 557.
(101) W. M. Bloch, J. J. Holstein, W. Hiller, G. H. Clever, *Angew. Chem. Int. Ed.* **2017,** *56,* 8285.
(102) W. M. Bloch, Y. Abe, J. J. Holstein, C. M. Wandtke, B. Dittrich, G. H. Clever, *J. Am. Chem. Soc.* **2016,** *138,* 13750.
(103) R. Zhu, J. Lübben, B. Dittrich, G. H. Clever, *Angew. Chem. Int. Ed.* **2015,** *54,* 2796.
(104) Q. F. Sun, S. Sato, M. Fujita, *Angew. Chem. Int. Ed.* **2014,** *53,* 13510.
(105) Q. F. Sun, T. Murase, S. Sato, M. Fujita, *Angew. Chem. Int. Ed.* **2011,** *50,* 10318.
(106) M. Tominaga, K. Suzuki, M. Kawano, T. Kusukawa, T. Ozeki, S. Sakamoto, K. Yamaguchi, M. Fujita, *Angew. Chem. Int. Ed.* **2004,** *43,* 5621.
(107) R. Zhu, W. M. Bloch, J. J. Holstein, S. Mandal, L. V. Schäfer, G. H. Clever, *Chem. Eur. J.* **2018,** *24,* 12976.
(108) M. L. Saha, S. Neogi, M. Schmittel, *Dalton Trans.* **2014,** *43,* 3815.
(109) M. Yoshizawa, M. Nagao, K. Kumazawa, M. Fujita, *J. Organomet. Chem.* **2005,** *690,* 5383.
(110) D. Preston, J. E. Barnsley, K. C. Gordon, J. D. Crowley, *J. Am. Chem. Soc.* **2016,** *138,* 10578.
(111) A. Company, L. Gómez, J. M. López-Valbuena, R. Mas-Ballesté, J. Benet-Buchholz, A. Llobet, M. Costas, *Inorg. Chem.* **2006,** *45,* 2501.
(112) L. Gómez, A. Company, X. Fontrodona, X. Ribas, M. Costas, *Chem. Commun.* **2007,** 4410.
(113) C. Garcia-Simon, R. Gramage-Doria, S. Raoufmoghaddam, T. Parella, M. Costas, X. Ribas, J. N. Reek, *J. Am. Chem. Soc.* **2015,** *137,* 2680.
(114) S. Bandi, D. K. Chand, *Chem. Eur. J.* **2016,** *22,* 10330.
(115) G. H. Clever, P. Punt, *Acc. Chem. Res.* **2017,** *50,* 2233.
(116) *Bruker-Nonius, APEX, SAINT, SADABS and XPREP*, Bruker AXS Inc.: Madison (USA), 2013.
(117) G. Sheldrick, *Acta Crystallogr. Sect. A* **2015,** *71,* 3.
(118) G. Sheldrick, *Acta Crystallogr. Sect. C* **2015,** *71,* 3.
(119) C. B. Hubschle, G. M. Sheldrick, B. Dittrich, *J. Appl. Crystallogr.* **2011,** *44,* 1281.
(120) A. Burkhardt, T. Pakendorf, B. Reime, J. Meyer, P. Fischer, N. Stube, S. Panneerselvam, O. Lorbeer, K. Stachnik, M. Warmer, P. Rodig, D. Gories, A. Meents, *Eur. Phys. J. Plus* **2016,** *131,* 1.
(121) W. Kabsch, *Acta Crystallogr. Sect. D* **2010,** *66,* 125.
(122) D. Kratzert, J. J. Holstein, I. Krossing, *J. Appl. Crystallogr.* **2015,** *48,* 933.
(123) A. Thorn, B. Dittrich, G. M. Sheldrick, *Acta Crystallogr. Sect. A* **2012,** *68,* 448.
(124) A. Spek, *Acta Crystallogr. Sect. C* **2015,** *71,* 9.
(125) A. Spek, *Acta Crystallogr. Sect. D* **2009,** *65,* 148.
(126) O. V. Dolomanov, L. J. Bourhis, R. J. Gildea, J. A. K. Howard, H. Puschmann, *J. Appl. Crystallogr.* **2009,** *42,* 339.
(127) G. J. Kleywegt, T. A. Jones, *Acta Crystallogr. Sect. D* **1994,** *50,* 178.
(128) W. L. DeLano, The PyMol molecular graphics system. DeLano Scientific LLC: San Carlos (USA).
(129) *Spartan '08 Version 1.2.0*, Wavefunction, Inc.: Irvine (USA), 2009.
(130) M. J. Frisch, et al. *Gaussian09*, Gaussian Inc.: Wallingford (USA), 2009.
(131) A. Hirsch, M. Brettreich. *Fullerenes: Chemistry and Reactions*, VCH: Weinheim, 2005; pp 24.
(132) M. M. Smulders, I. A. Riddell, C. Browne, J. R. Nitschke, *Chem. Soc. Rev.* **2013,** *42,* 1728.
(133) P. L. Abeyratne Kuragama, F. R. Fronczek, A. Sygula, *Org. Lett.* **2015,** *17,* 5292.
(134) Y. Yang, K. Cheng, Y. Lu, D. Ma, D. Shi, Y. Sun, M. Yang, J. Li, J. Wei, *Org. Lett.* **2018,** *20,* 2138.
(135) E. Marc Veen, P. M. Postma, H. T. Jonkman, A. L. Spek, B. L. Feringa, *Chem. Commun.* **1999,** 1709.
(136) T. Murase, K. Otsuka, M. Fujita, *J. Am. Chem. Soc.* **2010,** *132,* 7864.
(137) S. Neogi, Y. Lorenz, M. Engeser, D. Samanta, M. Schmittel, *Inorg. Chem.* **2013,** *52,* 6975.
(138) Y. Rogan, R. Malpass-Evans, M. Carta, M. Lee, J. C. Jansen, P. Bernardo, G. Clarizia, E. Tocci, K. Friess, M. Lanč, N. B. McKeown, *J. Mater. Chem. A* **2014,** *2,* 4874.
(139) Y. M. Liu, D. Xia, B. W. Li, Q. Y. Zhang, T. Sakurai, Y. Z. Tan, S. Seki, S. Y. Xie, L. S. Zheng, *Angew. Chem. Int. Ed.* **2016,** *55,* 13047.
(140) M. Takeda, S. Hiroto, H. Yokoi, S. Lee, D. Kim, H. Shinokubo, *J. Am. Chem. Soc.* **2018,** *140,* 6336.
(141) H. Yokoi, Y. Hiraoka, S. Hiroto, D. Sakamaki, S. Seki, H. Shinokubo, *Nat. Commun.* **2015,** *6,* 8215.
(142) K. Ha, *Acta Crystallogr. Sect. E* **2012,** *68,* m54.
(143) D. Kratzert, I. Krossing, *J. Appl. Crystallogr.* **2018,** *51,* 928.

(144) H. Yi, G. Zeng, C. Lai, D. Huang, L. Tang, J. Gong, M. Chen, P. Xu, H. Wang, M. Cheng, C. Zhang, W. Xiong, *Chem. Eng. J.* **2017,** *330,* 134.
(145) Y. Lu, Z. D. Fu, Q. H. Guo, M. X. Wang, *Org. Lett.* **2017,** *19,* 1590.
(146) G. Gil-Ramírez, S. D. Karlen, A. Shundo, K. Porfyrakis, Y. Ito, G. A. Briggs, J. J. Morton, H. L. Anderson, *Org. Lett.* **2010,** *12,* 3544.
(147) S. Cui, G. Zhuang, D. Lu, Q. Huang, H. Jia, Y. Wang, S. Yang, P. Du, *Angew. Chem. Int. Ed.* **2018,** *57,* 9330.
(148) Q. Wang, C. Zhang, B. C. Noll, H. Long, Y. Jin, W. Zhang, *Angew. Chem. Int. Ed.* **2014,** *53,* 10663.
(149) Y. Shi, K. Cai, H. Xiao, Z. Liu, J. Zhou, D. Shen, Y. Qiu, Q. H. Guo, C. Stern, M. R. Wasielewski, F. Diederich, W. A. Goddard, 3rd, J. F. Stoddart, *J. Am. Chem. Soc.* **2018,** *140,* 13835.
(150) B. Kräutler, T. Müller, A. Duarte-Ruiz, *Chem. Eur. J.* **2001,** *7,* 3223.
(151) Y. Murata, N. Kato, K. Fujiwara, K. Komatsu, *J. Org. Chem.* **1999,** *64,* 3483.
(152) N. Huang, K. Wang, H. Drake, P. Cai, J. Pang, J. Li, S. Che, L. Huang, Q. Wang, H. C. Zhou, *J. Am. Chem. Soc.* **2018,** *140,* 6383.
(153) T. R. Cook, P. J. Stang, *Chem. Rev.* **2015,** *115,* 7001.
(154) Y. Shi, I. Sánchez-Molina, C. Cao, T. R. Cook, P. J. Stang, *PNAS.* **2014,** *111,* 9390.
(155) M. J. Bermejo, J. I. Ruiz, X. Solans, J. Vinaixa, *Inorg. Chem.* **1988,** *27,* 4385.
(156) T. Tanase, H. Ukaji, Y. Yamamoto, *J. Chem. Soc., Dalton Trans.* **1996,** 3059.
(157) H. Nakajima, H. Nagao, K. Tanaka, *J. Chem. Soc., Dalton Trans.* **1996,** 1405.
(158) T.-a. Koizumi, T. Tomon, K. Tanaka, *J. Organomet. Chem.* **2005,** *690,* 4272.
(159) B. G. Harvey, A. M. Arif, R. D. Ernst, *Polyhedron* **2004,** *23,* 2725.
(160) M. Basato, A. Biffis, G. Martinati, C. Tubaro, C. Graiff, A. Tiripicchio, L. A. Aronica, A. M. Caporusso, *J. Organomet. Chem.* **2006,** *691,* 3464.
(161) J. K. Bera, N. Sadhukhan, M. Majumdar, *Eur. J. Inorg. Chem.* **2009,** *2009,* 4023.
(162) D. Gatteschi, C. Mealli, L. Sacconi, *J. Am. Chem. Soc.* **1973,** *95,* 2736.
(163) M. Maekawa, M. Munakata, S. Kitagawa, T. Kuroda-Sowa, Y. Suenaga, M. Yamamoto, *Inorg. Chim. Acta* **1998,** *271,* 129.
(164) A. Bencini, E. Berti, A. Caneschi, D. Gatteschi, E. Giannasi, I. Invernizzi, *Chem. Eur. J.* **2002,** *8,* 3660.
(165) C. Tubaro, G. Greggio, S. Antonello, C. Graiff, A. Biffis, *Inorg. Chim. Acta* **2017,** *466,* 578.
(166) A. R. Mulholland, C. P. Woodward, S. J. Langford, *Chem. Commun.* **2011,** *47,* 1494.
(167) J. L. Wietor, G. D. Pantos, J. K. Sanders, *Angew. Chem. Int. Ed.* **2008,** *47,* 2689.
(168) M. A. Lebedeva, T. W. Chamberlain, A. N. Khlobystov, *Chem. Rev.* **2015,** *115,* 11301.
(169) A. Kraft, F. Beuerle, *Tetrahedron Lett.* **2016,** *57,* 4651.
(170) A. Kraft, C. Roger, D. Schmidt, J. Stangl, K. Muller-Buschbaum, F. Beuerle, *Chem. Eur. J.* **2017,** *23,* 15864.
(171) A. Kraft, P. Roth, D. Schmidt, J. Stangl, K. Muller-Buschbaum, F. Beuerle, *Chem. Eur. J.* **2016,** *22,* 5982.
(172) T. Habicher, J.-F. Nierengarten, V. Gramlich, F. Diederich, *Angew. Chem. Int. Ed.* **1998,** *37,* 1916.
(173) P. Peng, F. F. Li, V. S. Neti, A. J. Metta-Magana, L. Echegoyen, *Angew. Chem. Int. Ed.* **2014,** *53,* 160.
(174) K. Barthelmes, J. Kubel, A. Winter, M. Wachtler, C. Friebe, B. Dietzek, U. S. Schubert, *Inorg. Chem.* **2015,** *54,* 3159.
(175) W. Yan, C. Réthoré, S. Menning, G. Brenner-Weiß, T. Muller, P. Pierrat, S. Bräse, *Chem. Eur. J.* **2016,** *22,* 11522.
(176) P. Peng, F. F. Li, F. L. Bowles, V. S. Neti, A. J. Metta-Magana, M. M. Olmstead, A. L. Balch, L. Echegoyen, *Chem. Commun.* **2013,** *49,* 3209.
(177) A. M. Rice, E. A. Dolgopolova, N. B. Shustova, *Chem. Mater.* **2017,** *29,* 7054.
(178) R. Schwenninger, T. Müller, B. Kräutler, *J. Am. Chem. Soc.* **1997,** *119,* 9317.
(179) C. H. Chen, A. Aghabali, A. J. Metta-Magana, M. M. Olmstead, A. L. Balch, L. Echegoyen, *Dalton Trans.* **2015,** *44,* 18487.
(180) M. Tominaga, K. Suzuki, M. Kawano, T. Kusukawa, T. Ozeki, S. Sakamoto, K. Yamaguchi, M. Fujita, *Angew. Chem. Int. Ed.* **2004,** *43,* 5621.
(181) C. Bingel, *Chem. Ber.* **1993,** *126,* 1957.
(182) P. Pierrat, C. Réthoré, T. Muller, S. Bräse, *Synlett* **2008,** *2008,* 1706.
(183) J. Fan, Y. Wang, A. J. Blake, C. Wilson, E. S. Davies, A. N. Khlobystov, M. Schröder, *Angew. Chem. Int. Ed.* **2007,** *46,* 8013.
(184) D. E. Williams, E. A. Dolgopolova, D. C. Godfrey, E. D. Ermolaeva, P. J. Pellechia, A. B. Greytak, M. D. Smith, S. M. Avdoshenko, A. A. Popov, N. B. Shustova, *Angew. Chem. Int. Ed.* **2016,** *55,* 9070.
(185) V. S. P. K. Neti, M. L. Saha, X. Yan, Z. Zhou, P. J. Stang, *Organometallics* **2015,** *34,* 4813.
(186) R.-L. Zhang, Y. Yang, S.-Q. Yang, V. S. P. K. Neti, H. Sepehrpour, P. J. Stang, K.-L. Han, *J. Phys. Chem. C* **2017,** *121,* 14975.
(187) T. Zhang, G. L. Zhang, Q. Q. Yan, L. P. Zhou, L. X. Cai, X. Q. Guo, Q. F. Sun, *Inorg. Chem.* **2018,** *57,* 3596.